Case studies on fluids and seismicity in submarine environments based on Ocean Bottom Seismometers (OBS) recordings from the Sea of Marmara and application to the Niger Delta

Jean-Baptiste Tary

THÈSE / UNIVERSITÉ DE BRETAGNE OCCIDENTALE

sous le sceau de l'Université européenne de Bretagne

pour obtenir le titre de

DOCTEUR DE L'UNIVERSITÉ DE BRETAGNE OCCIDENTALE

Mention : Géosciences Marines

École Doctorale des Sciences de la Mer

présentée par

Jean-Baptiste Tary

Préparée à l'IFREMER

Département Géosciences Marines

Laboratoire de Géophysique et Géodynamique

Relations entre fluides et sismicité dans le domaine sous-marin à partir de sismographes de fond de mer : étude de cas en Mer de Marmara et Application au Delta du Niger

Thèse soutenue le 15 mars 2011

devant le jury composé de :

Jean-Yves Royer
Professeur, Université Européenne de Bretagne, Plouzané, *Président du jury*

Michel Bouchon
Directeur de Recherche, Université Joseph Fourier, Grenoble, *Rapporteur*

Mustafa Aktar
Professeur, Kandilli Observatory and Earthquake Research Institute, Istanbul, *Rapporteur*

Christophe Delacourt
Professeur, Université Européenne de Bretagne, Plouzané, *Examinateur*

Thomas Bardainne
PhD, Magnitude, Manosque, *Examinateur*

Ramin Nawab
PhD, TOTAL, Pau, *Examinateur*

Louis Géli
Directeur de recherche, IFREMER, *Directeur de thèse*

Pierre Henry
Directeur de Recherche, CEREGE/Collège de France, *Co-directeur de thèse*

Remerciements

Ces remerciements vont tout d'abord à mes directeurs de thèse Louis Géli (Ifremer) et Pierre Henry (CEREGE) qui ont su trouver les clés pour me faire avancer. Grâce à leur enthousiasme et leurs encouragements, de nombreuses difficultés ont ainsi pu être évitées. Je voudrais aussi les remercier de m'avoir mis le pied à l'étrier, spécialement pour m'avoir associé à la campagne Marmesonet en Nov.-Déc. 2009 au large des côtes turques.

La présente thèse ayant un financement triparti, merci à TOTAL et Magnitude pour leur soutien, ainsi que les personnes qui m'ont suivi dans ces deux entreprises, particulièrement Francis Cerda et Ramin Nawab chez TOTAL, et Thomas Bardainne chez Magnitude. En outre, les deux mois que j'ai passé entre Manosque et les locaux de Magnitude ont donné le « La » de mon travail.

Merci aux membres de mon jury, Jean-Yves Royer, Michel Bouchon, Mustafa Aktar, Christophe Delacourt, Ramin Nawab et Thomas Bardainne, d'avoir prêté à mon travail une attention particulière.

Plus proche de la pointe bretonne, mes remerciements vont à toutes les personnes du département Géosciences Marines de l'Ifremer qui ont rendu cet épisode si plaisant, spécialement : Frauke et Stephan pour leurs conseils avisés en programmation et traitement du signal ; Nabil et Sébastien pour l'aide prodiguée en géotechnique ; Pascal, et Yves pour le soin apporté aux appareils et leurs données.

Un grand merci à Jacques Talandier pour ces précieux conseils, à Jean-Luc Got, qui m'a accueilli une semaine dans l'antenne du LGIT à Chambéry pour m'éclairer sur l'épineux problème de la localisation des séismes, ainsi qu'à Mustafa Çomoğlu et ses collègues du KOERI qui m'ont reçu presque un mois dans leurs locaux à Istanbul.

Une chaleureuse accolade à mes colocataires de bureau successifs qui m'ont remonté le moral dans les périodes de troubles : Marie, sans qui Hello Kitty ne serait rien, Jehanne (l'attaque des plantes en pot n'aura pas lieu !), Simon, croulant sous les logs, Vévé, avec son humour à décoller les semelles, sans oublier Bill Baroud.

Je remercie mes acolytes, thésards et ex-thésards : « mon bon » Alexis, DJ Yoann, Thibaud et Sara, pour leur hospitalité et les quelques Tourot bar, Esther, dont les rires tonitruants résonnent encore dans les couloirs, Estelle, dit « la petite », mon colocataire de cabanon Hakan et Céline qui reprend le flambeau.

Enfin, un clin d'œil à ceux qui m'accompagne depuis un long moment : mes parents, sans qui je ne serais pas là aujourd'hui, mes frères et sœurs, mon camarade Loïc, Eloïse la fonceuse, Charles-Henri le dresseur de Mamba vert et Jboul le kitesurfeur des dunes.

Table of contents

Résumé

Le présent travail de thèse aborde la question du couplage entre fluides et déformation en milieu sous-marin, un sujet d'importance dans le domaine des risques, naturels (séismes, glissements de terrain) ou industriels (stabilité des plateformes de forage en mer, par exemple). Trois études de cas sont présentées : les deux premières concernent la Mer de Marmara, en Turquie, une zone fortement exposée au risque sismique, du fait de la proximité de la Faille Nord-Anatolienne ; la troisième concerne une zone pétrolifère offshore, sur la pente continentale du delta profond du Niger.

La **première étude de cas** en Mer de Marmara porte sur l'activité micro-sismique qui caractérise l'escarpement ouest du Bassin de Tekirdag. Notre étude montre que la déformation contribue à maintenir des perméabilités élevées associées au réseau de failles sous l'escarpement, ce qui permet aux fluides de remonter des réservoirs gaziers du Bassin de Thrace jusqu'à la surface.

La **deuxième étude de cas** porte sur des micro-évènements enregistrés par les sismographes de fond de mer, non sismiques, de courtes durées (200 à 600 msec), et caractérisés par des fréquences comprises entre 10 et 30 Hz. Notre étude montre que ces micro-évènements sont liés à des expulsions de gaz. Les OBS fournissent donc des informations inattendues pour l'étude des processus de dégazage naturel en fond de mer.

La **troisième étude de cas,** sur la pente continentale du Nigeria, démontre que la combinaison de piézomètres et d'OBS voisins en fond de mer permet de suivre l'évolution des phases d'accumulation et de vidange de gaz dans les sédiments superficiels. La détection et la surveillance des phénomènes de dégazage naturel en fond de mer est d'une importance qui pourrait s'avérer critique dans les zones d'exploitation pétrolière en domaine offshore.

D'une manière générale, ce travail plaide pour la nécessité : i) de disposer de plusieurs réseaux d'observatoires sous-marins câblés en Mer de Marmara et d'un modèle de vitesse-3D rendant compte du fort gradient de vitesses sismiques dans les couches superficielles (la structure de vitesses du domaine sous-marin étant radicalement différente de celle du domaine émergé, la combinaison des données sismologiques à terre et en mer s'avère très difficile); ii) de développer des approches de surveillance multi-paramètres. Pour chaque paramètre, il est nécessaire de connaître la variabilité naturelle "normale", de manière à détecter les variations anormales. La recherche sur les processus physiques et le développement algorithmique doivent être conduits de front.

Mots clés : sismicité, fluides, risques naturels, sismographes de fond de mer, piézomètre, Mer de Marmara, Delta du Niger, faille.

Abstract

The present work addresses the issue on fluids and deformation coupling in marine environments, a subject of crucial importance for natural (e.g. earthquakes, landslides) and industrial (e. g. stability of drilling platforms) hazards. Three case studies are presented: the first two concern the Sea of Marmara (Turkey), an area highly exposed to earthquake hazards due to its proximity to a seismic gap along the North Anatolian Fault; the third concerns an oilfield area situated on the continental slope offshore Nigeria, in the eastern part of the deep-water Niger Delta.

The **first case study** in the Sea of Marmara concerns the microseismic activity below the western escarpment of the Tekirdag Basin. Our work shows that the tectonic activity in this area contributes to maintain a high permeability in the fault system, enabling fluids, likely related to the oilfields present in the Thrace Basin, to rise up to the seabed.

The **second case study** addresses the question of the origin of non-seismic signals recorded by the OBSs (Ocean Bottom Seismometers). These signals, called micro-events, are characterized by frequency contents between 10 and 30 Hz and short durations (mainly between 200 and 600 msec). Our work shows that these micro-events are related to gas escape on the seafloor. Hence, OBSs provide unexpected information on degassing processes in the upper sediments.

The **third case study**, located on the deep-water Niger Delta, reveals that the combination of closely spaced piezometers and OBSs enables to follow the evolution of gas accumulation and release in superficial sediments, a critical issue for mitigating gas-related geohazards during oil extraction activities offshore.

This work also underlines the necessity to have permanent networks of cabled seafloor observatories in the Sea of Marmara, together with a 3D velocity model taking into account the strong lateral heterogeneities of the velocity structure. The velocity structure of the offshore domain being very different from the onshore domain, the combination of land and marine seismological datasets has proven to be very difficult.

In addition, it is here recommended to develop multi-parameter approaches, including tools and methods for combining all different datasets and detecting anomalous signals that could eventually be identified as indicators that a potentially dangerous situation is developing. To meet such an objective, research on the physical processes must be carried out simultaneously, along with algorithmic developments.

Keywords: seismicity, fluids, natural hazards, ocean bottom seismometers, piezometer, Sea of Marmara, Delta of Niger, fault.

Extended summary (in French)

I. Introduction et objectifs

La sismicité sous-marine diffère de la sismicité terrestre en raison notamment de la vigueur des circulations de fluides dans les failles actives ; son approche diffère également, en raison des difficultés d'observation, à petite comme à grande échelle (tranche d'eau, éloignement ou inadéquation des réseaux terrestres, etc.). Par ailleurs, l'exploration continue des océans au cours des 30 dernières années a permis de révéler la présence systématique de suintements en fond de mer, non seulement au niveau des failles actives, mais aussi au niveau des zones de glissement qui menacent la stabilité des pentes sous-marines.

Le présent travail de thèse aborde la question du couplage entre fluides et déformation en milieu sous-marin, un sujet de recherche de première importance pour un grand nombre d'applications, notamment dans le domaine des risques naturels (séismes, glissements de terrain) et industriels (stabilité des plateformes de forage en mer, par exemple). Le travail étant co-financé par un consortium réunissant des partenaires académiques (Ifremer, CNRS) et industriels (TOTAL, Magnitude), l'étude porte sur deux sites particuliers : la Mer de Marmara et la partie Est du delta profond du Niger, située sur le talus continental au large du Nigeria.

Les objectifs initiaux de la thèse visaient à : i) améliorer la connaissance du bruit de fond et de la micro-sismicité courante dans différents environnements sous-marins destinés à être dotés d'observatoires permanents ; ii) améliorer les méthodes de détection micro-sismique : identifier les points durs, proposer des solutions ; iii) surveiller les variations de pression interstitielle dans le sédiments superficiels et établir des correlations avec la micro-sismicité ; iv) modéliser l'effet des secousses sismiques sur les flux de gaz et de fluides dans les sédiments.

Le dernier point n'a pas pu être abordé comme nous l'aurions souhaité, faute de temps, car l'acquisition, le traitement et l'interprétation des données en mer, à partir d'une approche

multi-paramètres, ont mobilisé toutes nos forces. En revanche, ce travail de thèse apporte des éléments de réponse pour chacun des trois premiers objectifs, que nous avons abordés au travers de 3 études de cas, deux en Mer de Marmara et un dans le delta profond du Niger.

II. La Mer de Marmara (études de cas 1 et 2)

II.1. Cadre général

La Mer de Marmara est située à l'extrémité Ouest de la Faille Nord Anatolienne (FNA), une frontière de plaque majeure longue d'environ 1300 km, séparant la plaque Anatolienne au Sud de la plaque Eurasienne au Nord. La FNA accommode un mouvement relatif d'environ 25 mm/an, par lequel le bloc Anatolie se déplace vers l'ouest et le Sud-ouest. Avant d'entrer en Mer de Marmara, la FNA se sépare en trois branches. Située sur la branche nord, la Mer de Marmara est composée de 3 bassins profonds, le Bassin de Tekirdag, le Bassin Central et le Bassin de Çinarcik, séparés par 2 hauts bathymétriques, les hauts Ouest et Central. Ces bassins, avec des profondeurs d'eau entre 1100 et 1300 m, ont des remplissages sédimentaires Plio-quaternaire épais de 4 à 6 km.

La région d'Istanbul, peuplée de plus de 12 millions d'habitants, est fortement exposée au risque sismique, du fait de la proximité de la FNA en Mer de Marmara. C'est aussi une zone privilégiée pour étudier les relations entre fluides et sismicité en domaine sous-marin. En effet, suite aux séismes de la région d'Izmit en 1999, des émanations de méthane ont été observées le long du segment de faille située dans le Golfe d'Izmit, à l'Est de la Mer de Marmara. Des sorties de fluides et de méthane ont également été documentées le long de la faille lors des campagnes Meteor M44/1 [*Halbach et al.*, 2004] et MarmaraScarps réalisée en 2002 avec le ROV Victor de l'Ifremer [*Armijo et al.*, 2005 ; *Zitter et al.*, 2008]. Les gaz prélevés sur les hauts topographiques (Haut Central et Haut Ouest) au voisinage de la faille ont une origine thermogénique, profonde, qui s'apparente à celle des gaz des réservoirs (en cours d'exploitation) du Bassin de Thrace [*Bourry et al.*, 2009]. Les fluides remontant par la faille à la surface des sédiments proviennent donc de niveaux profonds, proche de la partie supérieure de la zone sismogène. Bien que les relations entre émissions de gaz et activité sismique ne soient pas encore bien comprises, ces résultats sont extrêmement encourageants et posent des questions fondamentales concernant les relations entre la zone sismogène et les

sédiments de surface : quelle est la réponse des fluides interstitiels à la mise en charge de la faille ? Qu'est ce qui fait sortir le gaz et entrer l'eau après un séisme ? Dans quelles conditions et d'après quels processus pourrait-il y avoir des sorties de fluides ou de gaz avant un séisme ? Existe-t-il des signaux précurseurs ***détectables*** au cours de ce cycle ? Et si oui, dans quelles conditions, et suivant quels processus ?

Pour répondre à ces questions, le développement d'un observatoire permanent pour l'acquisition de séries temporelles multi-paramètres est nécessaire. Conduite avec le soutien du réseau d'excellence ESONET (2007-2010), la présente thèse a également pour objectif de contribuer à la conception de cet observatoire.

II.2. Acquisition et traitement des données OBS

Au cours de l'année 2007, 8 OBS courte-période de différents types ont été déployés pour des durées variables (variant, suivant les instruments, entre 10 jours et 3 mois), suivant un réseau triangulaire recouvrant le Bassin de Tekirdag, à l'Ouest de la Mer de Marmara. Au centre du réseau, situé au voisinage d'une sortie active d'eau saumâtre associée à la FNA, cinq instruments (parmi les 8) ont été déployés, dans le but d'effectuer des tests comparatifs des différents OBS, respectivement fournis par l'Ifremer et par CGG-Véritas.

La détection des évènements a été réalisée à l'aide du programme Seiscreen, fourni par la société Magnitude dans le cadre de la convention de thèse. Ce programme Seiscreen prend en compte plusieurs paramètres dont les plus importants sont le calcul du rapport d'une moyenne sur court terme sur une moyenne sur long terme (STA/LTA : Short Term Average/Long Term Average), le nombre de stations, et la décomposition du signal en « chirplets » (sinusoides avec différents contenus fréquentiels et formes d'ondes). Les temps d'arrivées des ondes P et S pour chaque séisme ont ensuite été pointés à la main.

Les sédiments emplissant les bassins de la Mer de Marmara étant caractérisés par des vitesses de propagation sismiques très lentes (comparées à celles du domaine émergé), la question du modèle de vitesses se pose de manière cruciale, notamment lorsqu'il s'agit de combiner les données à terre et en mer. Le seul modèle de vitesse 3D connu pour l'ensemble de la Mer de Marmara est actuellement en cours de construction à partir des travaux de thèse d'Anne Bécel [2006] et de Gaye Bayrakci [2009]. Nous avons donc fabriqué un modèle 1D « composite »

spécifique au Bassin de Tekirdag. Pour les couches supérieures (de profondeur inférieure à 5 km), nous avons utilisé les vitesses déterminées à partir de tirs de sismique réfraction produits par le navire turc Sismik-1, enregistrés avec les OBS et traités dans le cadre de cette thèse. Pour les couches plus profondes (> 5 km), nous avons utilisé un modèle de vitesses 1D, moyen pour toute la Mer de Marmara, établi à partir des résultats de *Bécel* [2006]. Cependant, si ce modèle « composite » 1D rend bien compte de la structure sismique moyenne sous les stations marines, il est inadapté aux stations terrestres. Les tentatives que nous avons faites pour combiner les données à terre se sont toutes avérées infructueuses : le gain obtenu en améliorant la couverture azimutale par l'introduction des stations à terre ne compense pas les erreurs liées aux hétérogénéités de vitesse de propagation. Par conséquent, seuls les microséismes enregistrés par 4 OBSs (aux 3 coins et au centre du réseau) avec 4 temps d'arrivées P et 4 temps d'arrivées S ont été sélectionnés.

Différents programmes de localisation ont été testés pour localiser la micro-sismicité dans et autour du Bassin de Tekirdag, à partir du modèle « composite » 1D et des temps d'arrivées P et S, à savoir : LOC3D, fourni par *Magnitude*, Hyposat et HypoDD.

II.3. Etude de cas 1

La distribution de la microsismicité dans la région du Bassin de Tekirdag montre 2 zones plus actives que les autres pendant la durée de l'enregistrement : le haut Ouest et le Nord-ouest du Bassin de Tekirdag. Les incertitudes associées, en moyenne de 2.7 km horizontalement et de 3.6 km verticalement, reflètent le fait que les évènements soient situés en dehors du réseau.

Les évènements situés au Nord-ouest du Bassin de Tekirdag forment un essaim de 13 microséismes avec des formes d'ondes et des temps d'arrivées P et S très similaires. L'essaim est orienté NW-SE, dans la direction de la contrainte principale maximale. Considérant un plan de faille orienté dans la direction de l'essaim, le mécanisme au foyer calculé pour l'évènement le plus fort de l'essaim (M_w : 2.9, 14/05/2007 20:50) indique une faille normale avec une petite composante décrochante senestre. Un plan de faille Est-Ouest associé avec un régime extensif approximativement Nord-Sud est cohérent avec la présence de fractures orientées N90-N100 sur la pente Ouest du Bassin de Tekirdag.

Un second mécanisme au foyer, calculé pour un évènement situé sous le même escarpement mais à 10 km au Sud de l'essaim, indique une extension SW-NE avec une légère composante décrochante dextre, cohérente avec l'orientation de la contrainte principale minimale et l'observation de fractures ouvertes dans la direction NE-SW observées *in-situ* avec le submersible *Nautile* (site de Boris's bubbler). A terre, des failles normales orientées N270-N330 ont été observées dans la partie Nord-est des montagnes de Ganos.

La cartographie des bulles dans la colonne d'eau par le sondeur multifaisceaux (EM302) du *N/O Le Suroit* [*Géli et al.*, 2010] et les observations visuelles à partir du *Nautile* ont permis de mettre en évidence de nombreuses émissions de gaz au niveau de l'escarpement Ouest du Bassin de Tekirdag. Ces émissions témoignent très probablement du fait que les réservoirs gaziers du Bassin de Thrace « fuient » en Mer de Marmara. Par ailleurs, l'analyse isotopique des gaz prélevés *in situ* indique que l'hélium au niveau du site de Boris's bubbler est d'origine mantellique.

Nous proposons que l'activité tectonique que révèlent les enregistrements OBS contribue à maintenir une forte perméabilité dans le réseau de failles sous l'escarpement Ouest du Bassin de Tekirdag, ce qui permet aux fluides d'origine profonde de remonter en surface.

II.4. Etude de cas 2

Les OBS ont principalement enregistré 2 types de signaux : les séismes et des évènements de courte durée que l'on désignera sous le nom de micro-évènements. Ces signaux sont caractérisés par des durées comprises entre 0.1 et 0.6 s, un contenu fréquentiel compris entre 5 et 30 Hz, et des amplitudes très variables (0.5-50 µm/s). Les micro-évènements sont constitués d'un seul train d'onde et sont enregistrés par l'hydrophone des instruments seulement quand ceux-ci sont proches du fond marin (<0.9 m).

Des micro-évènements ont été enregistrés par tous les types d'OBS posés sur le fond, ce ne sont donc pas des artefacts instrumentaux, ni des bruits résultant de l'activité biologique (poissons, etc). Dans la plupart des cas, les micro-évènements ne sont enregistrés que par un seul OBS à la fois. Seuls les 2 OBS les plus proches (situés à 10 m l'un de l'autre) ont enregistré simultanément certains des micro-évènements. Ceci écarte tous les phénomènes

régionaux (tectonique, courant profond, ondes T, explosions/implosions) comme origines potentielles. Sur la période totale, environ 7300 micro-évènements ont été inventoriés. Les différences dans le nombre de micro-évènements enregistré par les OBS sont très importantes, pouvant aller du simple au triple d'un OBS à l'autre pendant la période d'enregistrement.

Selon leur polarisation dans le repère de l'onde, on peut distinguer deux types de micro-évènements. D'un côté, les micro-évènements avec des durées comprises entre 0.2 et 0.6 s ont une polarisation dans le plan radial-vertical, alors que les micro-évènements très impulsifs appartenant à une crise enregistrée par l'un des OBS (M) sont polarisés selon la composante radiale.

Une attention particulière est donnée aux micro-évènements de cette crise. Pendant la crise, environ 400 micro-évènements ont été enregistrés en 24 heures les 11 et 12 juin 2007. L'analyse en composantes principales de ces micro-évènements a confirmé que, malgré des différences d'amplitude importantes, ces micro-évènements ont les particularités suivantes : (i) ils sont très impulsifs ; (ii) de très courte durée (~0.1 s) ; (iii) très similaires ; (iv) ils présentent des amplitudes sur les composantes horizontales largement supérieures à celles de la composante verticale ; (v) ils sont tous orientés dans le même azimut (à 20° près) par rapport à l'OBS ; (vi) la composante horizontale radiale prédomine largement par rapport à la composante tangentielle.

Parallèlement, les expériences et modélisations de l'échappement de fluides d'une cavité donnent des signaux similaires aux micro-évènements. Le gaz étant très présent dans les sédiments superficiels de la Mer de Marmara, l'expulsion de bulles de gaz semble l'origine la plus probable de ces micro-évènements. L'enregistrement d'une crise de micro-évènements sur un OBS situé à proximité d'une faille et au dessus d'une anomalie acoustique pouvant indiquer la présence de gaz dans les sédiments appuie aussi cette hypothèse.

Finalement, un modèle physique tenant compte des précédents points peut être proposé. En effet, les micro-évènements pourraient être générés par l'expulsion de gaz sur les fonds marins à travers des conduits subverticaux.

III. Partie Est du delta profond du Niger (Afrique de l'Ouest)

III.1. Cadre général

Le Nord-est du Golf de Guinée, et plus particulièrement la zone du delta du fleuve Niger, est une région pétrolifère en cours d'exploitation. Dans le but d'évaluer les risques d'instabilité de la couverture sédimentaire, fortement chargée en gaz, située à l'Est du delta profond du Niger, des mesures complémentaires ont été collectées pendant la campagne ERIG3D conduite en 2008 par l'Ifremer en partenariat avec TOTAL. Notamment, des OBS et des piézomètres ont été déployés, pour contribuer à étudier les risques, qu'ils soient naturels (liés au fluage du pli argileux) ou industriels (liés à l'implantation d'infrastructures lourdes).

Un des objectifs principaux du déploiement d'OBS était d'obtenir un état zéro du bruit de fond et de la micro-sismicité, précédant la phase d'exploitation des réservoirs. Il s'agit là d'un enjeu primordial, permettant de mieux comprendre les phénomènes associés au pompage d'hydrocarbures ou à l'injection de fluides dans la formation. La micro-sismicité induite par injection de fluides dans les réservoirs est en effet un phénomène bien connu : l'augmentation de pression interstitielle entraîne une diminution de la contrainte effective et donc, une diminution de la résistance de la roche au cisaillement.

III.2. Etude de cas 3

Des profils sismiques très haute résolution (système SYSIF), ainsi que des mesures géotechniques (piézo-cônes CPTu) ont permis d'identifier la distribution des couches sableuses, du gaz libre et des gaz hydrates dans les premiers 60 m de sédiments. De plus, 3 piézomètres et 9 OBS ont été déployés autour d'une faille orientée E-W connectée à des réservoirs d'hydrocarbures. L'essentiel du travail d'interprétation a été effectué sous la coordination de Michel Voisset et Nabil Sultan, que nous remercions de nous avoir donné accès aux enregistrements OBS.

Durant les 65 jours de déploiement des OBS aucun séisme n'a été détecté par les OBS. En revanche, environ 11960 micro-évènements ont été inventoriés. L'analyse en composantes principales d'un peu moins de 1000 micro-évènements enregistrés par l'OBS 4 a montré que

ces micro-évènements ont des caractéristiques similaires à ceux de la Mer de Marmara (i. e. des amplitudes variables généralement comprises entre 0.5 et 50 µm/s, des durées comprises entre 0.2 et 0.6 s, un contenu fréquentiel entre 4 et 30 Hz). Certains des micro-évènements sont visibles sur l'hydrophone des OBS, situé à ~0.4 m au dessus du fond marin.

Le 21 Juin 2008, une crise de ~300 évènements a été enregistrée par l'OBS 4 tandis que le cinquième capteur (-11.48 m) du piézomètre PZS12, situé à 400 m de l'OBS au niveau d'une couche sablo-silteuse, enregistrait de son côté des variations significatives de la pression interstitielle. L'OBS 4 et le piézomètre PZS12 ont tous deux enregistré un épisode d'accumulation et de vidange de gaz dans les sédiments superficiels. L'analyse combinée des données permet de proposer un scénario en 4 étapes : (i) remontée de gaz canalisée par un conduit pré-existant (faille) ; (ii) accumulation du gaz et augmentation de la pression interstitielle dans la couche sablo-silteuse ; (iii) surpression et échappement du gaz à travers de multiple conduits ; (iv) diffusion de la pression.

IV. Conclusions

1. Recommandations pour les futurs observatoires pluridisciplinaires permanents en Mer de Marmara:

Les bassins de la Mer de Marmara s'apparentant à des fosses emplies de 4 à 6 km de sédiments Plio-Quaternaires, la structure de vitesses du domaine sous-marin est radicalement différente de celle du domaine émergé. De ce fait, la combinaison des données à terre et en mer s'avère très difficile.

Pour améliorer la caractérisation de la sismicité (précision des localisations, recherche des tremors sismiques [*Bouchon et al.*, 2011], il est nécessaire de disposer de plusieurs réseaux d'observatoires sous-marins câblés. Chacun de ces réseaux doit être cohérent en lui-même, de manière à permettre de caractériser la sismicité avec la meilleure résolution possible.

Un objectif prioritaire est l'obtention d'un modèle de vitesse 3D rendant compte du fort gradient de vitesses sismiques dans les couches superficielles. Ceci devrait être faisable en utilisant les données disponibles de sismique multi-traces en Mer de Marmara.

Il est impératif de développer des approches multi-paramètres. Pour chaque paramètre, il est nécessaire de connaître la variabilité naturelle "normale", de manière à détecter les variations anormales. La recherche sur les processus physiques et le développement algorithmique doivent être conduits de front.

2. Etude de cas 1 :

2.1 Notre étude de la micro-sismicité montre une importante activité tectonique sous l'escarpement Ouest du Bassin de Tekirdag. La déformation engendrée par cette activité tectonique pourrait contribuer à augmenter la perméabilité des zones de failles, permettant à des fluides, provenant vraisemblablement des réservoirs gaziers du Bassin de Thrace, de remonter à la surface.

2.2 Nos résultats pourraient expliquer l'existence des sites d'émissions de gaz découverts au pied de l'escarpement Ouest du Bassin de Tekirdag, qui témoignent du fait que les réservoirs de gaz naturel du Bassin de Thrace "fuient" à l'intérieur de la Mer de Marmara.

3. Etude de cas 2:

3.1 Les nombreux profils sismiques "Chirp" (2 à 4 kHz) disponibles montrent que les sédiments superficiels qui recouvrent la Mer de Marmara contiennent du gaz en de très nombreux endroits.

3.2 Des micro-évènements non-sismiques ont été enregistrés avec différents types d'OBS, en différents sites du Bassin de Tekirdag. Ces évènements de courte durée (généralement inférieure à 0.6 s) sont d'amplitude très variable et caractérisés par des fréquences comprises entre 10 et 30 Hz. De surcroît, les micro-évènements ne sont pas corrélés d'un OBS à l'autre, dès lors que la distance séparant les instruments dépasse quelques dizaines de mètres.

3.3 Notre étude indique que ces micro-évènements pourraint être liés à des expulsions de gaz sur les fonds marins. Les OBS pourraient donc fournir des informations inattendues pour l'étude des processus de dégazage naturel en fond de mer.

4. Etude de cas 3:

4.1 La détection et la surveillance des phénomènes de dégazage naturel en fond de mer est d'une importance capitale dans les zones d'exploitation pétrolière en domaine offshore.

4.2 Notre travail sur le delta profond du Niger démontre les avantages des approches pluridisciplinaires dans l'analyse et la compréhension des phénomènes naturels. La combinaison de piézomètres et d'OBS voisins a permis de détecter et de suivre l'évolution d'un épisode d'accumulation et de vidange de gaz dans les sédiments superficiels.

Chapter 1. Introduction

It has been recognized for some time that the hydrogeologic system is directly coupled to the fault system through the interaction of fluid pressure and stress state, leading the scientific community to hypothesize that at least some faults channel fluids from deep levels within the sediments and, possibly, from the seismogenic zone [e.g. *Moore et al.*, 1990; *Le Pichon et al.*, 1992; *Tryon et al.*, 1999; *Henry et al.*, 2002]. Hence, in actively tectonic environments, coupling between deformation and fluid flow may lead to post-seismic fluid release, precursor events, and/or systematic variations of flow rates, fluid chemistry and pore pressure during inter-seismic phases

Compared to land, submarine environments are more favorable to test this hypothesis, as they are characterized by an infinite supply of water above seafloor and by very high permeabilities at the formation scale revealed by unexpectedly high flow rates (compared to land) of fluids circulating along the fault plane. In addition, observations of fluid seepage in submarine environments are commonly associated not only with active tectonic features, but also with sliding surfaces at steep slopes. Fluid circulation at passive continental margins – a phenomenon ignored until a recent past – can lead to catastrophic geological events, such as gas or mud eruptions or huge landslides. Fluids are now considered to be the governing parameter that control mass wasting in hydrocarbon prone areas that are presently being exploited.

In this specific context, the initial ambition of the present PhD was to develop methods to better understand the relations between micro-seismicity and pore pressure in sub-surface marine sediments. Because the work benefited from the sponsorship of a consortium including academic (Ifremer, CNRS) and industrial partners (Total, Magnitude), it was decided to work in a variety of settings, namely:

- the Sea of Marmara, which has been identified as a prioritary site for the implementation of permanent, multi-parameter seafloor observatories within ESONET

(the European Seafloor Observatory Network). A systematic correlation is documented between active faulting and gas emissions along the submerged section of the North Anatolian Fault in the Sea of Marmara. Hence, a critical issue of direct, societal implication is to determine whether or not gas can generate **detectable** signals related to the stress building process during the seismic cycle. Major questions are: what are the governing parameters that drive the observed gas outflows and water inflows after submarine earthquakes ? What are the processes through which gas could escape prior to large earthquakes ?

- the continental slope of the deep-water Niger Delta, where Ifremer and Total have conducted a joint-research programme, ERIG3D, in 2008. Seafloor sedimentary features such as pockmarks, slides and carbonate build-ups associated with fluid flow and gas hydrates affect the Nigerian continental slope. These observations make the deep-water Niger delta a prime interest target to study the active interplay of fluid flow processes, gas hydrate dynamics and seafloor deformation, a subject of critical importance with respect to industrial geohazards [*e.g. Sultan et al.*, 2011 and references herein].

The initial, specific objectives of the work were: i) to gain knowledge on the background submarine micro-seismicity, in order to identify the recorded signals; ii) to improve the accuracy of the detection techniques; iii) to monitor sediment pore pressure variations and establish correlations with micro-seismicity; iv) to model the influence of earthquake ground shaking on gas and water fluxes through the sediment-water interface.

I have to admit that these initial objectives were too ambitious. The present work provides some new contributions on the first three objectives, but the latter objective (on modelling) turned out to be out of reach. Understanding the behaviour of gassy sediments before, during and after earthquakes is a challenge that requires, besides field measurements, a combination of laboratory work and modelling. But field measurements (data acquisition and interpretation) mobilized all our forces, as we had to spend considerable time in trying to secure the observations and the interpretations through a multi-parameter approach, for **three case studies**: two in the Sea of Marmara and one in the area of the Niger Delta.

In the Sea of Marmara, acoustic surveys carried out in 2007 and 2009 have revealed numerous sites of gas emissions on the slope bordering the Tekirdag Basin to the west, suggesting that gas from the Thrace Basin reservoir is presently leaking into the water column. Therefore, for the **first case study**, focus was given to the relation between the micro-seismicity and other observations we had from the seafloor, most particularly: fluid sampling and analysis (performed by Pete Burnard and Sylvain Bourlange, from CRPG, Nancy, using samples collected in 2007 during the MarNaut cruise) and detailed micro-bathymetry (based on AUV data collected in 2009 during the Marmesonet cruise). After this work, there is now little doubt that *« tectonic strain below the western slope of the Tekirdag Basin contributes to maintain a high permeability in faults zones, and that the fault network provides conduits for deep-seated fluids to rise up to the seafloor [Tary et al., 2011] ».*

During the Marmesonet cruise of R/V Le Suroit (from October 4th to December 14th, 2009), I was in charge of the processing of the high resolution, seismic data collected with the sediment penetrator (3.5 kHz). I then realized that gas occurrence is ubiquitous in the sub-surface sediments covering the Marmara seafloor. Therefore, for the **second case study**, we decided to focus on the detailed analysis of non-seismic micro-events recorded with Ocean Bottom Seismometers and hypothetically attributed to degassing episodes from the upper sediment layers. Our analysis confirms our hypothesis and provides unprecedented insights on how gas is expelled from the uppermost sediment layers: the recorded micro-events seem to be related to natural degassing from the seafloor and to the building and collapsing process of gas chimneys near the subsurface.

Submarine degassing processes may be either natural (continuous exploration efforts and progress in multi-beam sonar techniques in the recent years have shown that natural seafloor degassing is a wide spread phenomenon), either artificial resulting from human activities (e. g. sediment destabilization related to oil exploration, pipe leaking, etc). Whether natural or artificial, degassing processes require a number of generic tools for their detection and monitoring, a subject of critical importance for mitigating gas-related geohazards. However, the pre-requisite -prior to any step forward- is to gain more and more experience on the natural, background degassing activity in a variety of environments.

We thus applied the knowledge gained in the Sea of Marmara to the **third case study**, the continental slope of the eastern part of the deep-water Niger Delta. For this part, I am deeply indebted to Michel Voisset and Nabil Sultan, who drew our attention on the importance of the dataset collected in this area during the ERIG3D cruise in 2008. Our interpretation of the OBS data usefully complements Nabil Sultan's analysis of the piezometric data, which clearly documents an episode of slow upward migration and accumulation of free gaz in the uppermost sediment layers, followed by an episode of gas outbursts.

This manuscript presents the three case studies, each of them being summarized in papers in press, submitted in peer review journals, or in preparation. The two case studies concerning the Sea of Marmara are preceded by two long sections, that we think, are of critical importance to understand the general framework of the present work: one section concerns the geological setting; the other concerns specific methodological aspects for earthquake location in the Sea of Marmara.

Chapter 2. The Sea of Marmara: Case studies (1 & 2)

2.1. Present-day plate motions

The Sea of Marmara is located in NW Turkey, on the North Anatolian Fault (NAF), a right-lateral strike-slip fault separating the Eurasian and the Anatolian Plates [e.g. *Barka,* 1992; *Straub et al.,* 1997; *Okay et al.,* 2000; *İmren et al.,* 2001; *Le Pichon et al.,* 2001, 2003; *Armijo et al.,* 2002; *Şengör et al.,* 2004]. The present-day NAF extends over ~ 1200 km, from the Eurasia-Anatolia-Arabia triple junction near Karliova (~41°E) in eastern Turkey, to the Gulf of Saros in western Turkey.

Based on GPS measurements analysis [e.g. *McClusky et al.,* 2000; *Reilinger et al.,* 2006], the relative plate motion is ~ 24 ± 1 mm/y east of the Sea of Marmara, where the NAF is mainly a single vertical fault that follows the small circle of the rotation of the Anatolian Plate (Fig. 2.1). In contrast, to the west of N31°30'E (~ city of Bolu), the NAF splits into three main branches: the Main Marmara Fault (MMF) and the middle and southern branches (Fig. 2.2). Based on GPS analysis, slip rate estimates on the MMF range between 17 and 27.9 mm/yr *[Meade et al, 2002; Flerit et al, 2003; Reilinger et al, 2006]*. However, using a 3D geomechanical model incorporating the structural complexities of the sea of Marmara, *Hergert and Heidbach* [2010] recently predicted that right-lateral slip rate on the MMF is lower than previously estimated, likely not greater than 18 mm/yr.

2.2. Geological evolution

The present-day NAF more or less follows the late Cretaceaous Intra-Pontide suture zone, which formed after the closure and subduction of the Tethyan Ocean [*Şengör and Yilmaz,* 1981; *Okay et al.,* 1996; *Okay and Tüysüz,* 1999] (Fig. 2.3 and 2.4). The fault thus results from a complex evolutionary history, from the late Cretaceous to present. It is not the scope of

the present study to review all the abundant literature on the subject. Instead, we here provide focus on some specifities of the tectonic heritage and geological background, which, we think, are of direct relevance for our work:

- The relation with the Thrace Basin
- The late Pliocene evolution of the NAF / Basin formation
- Late marine transgression

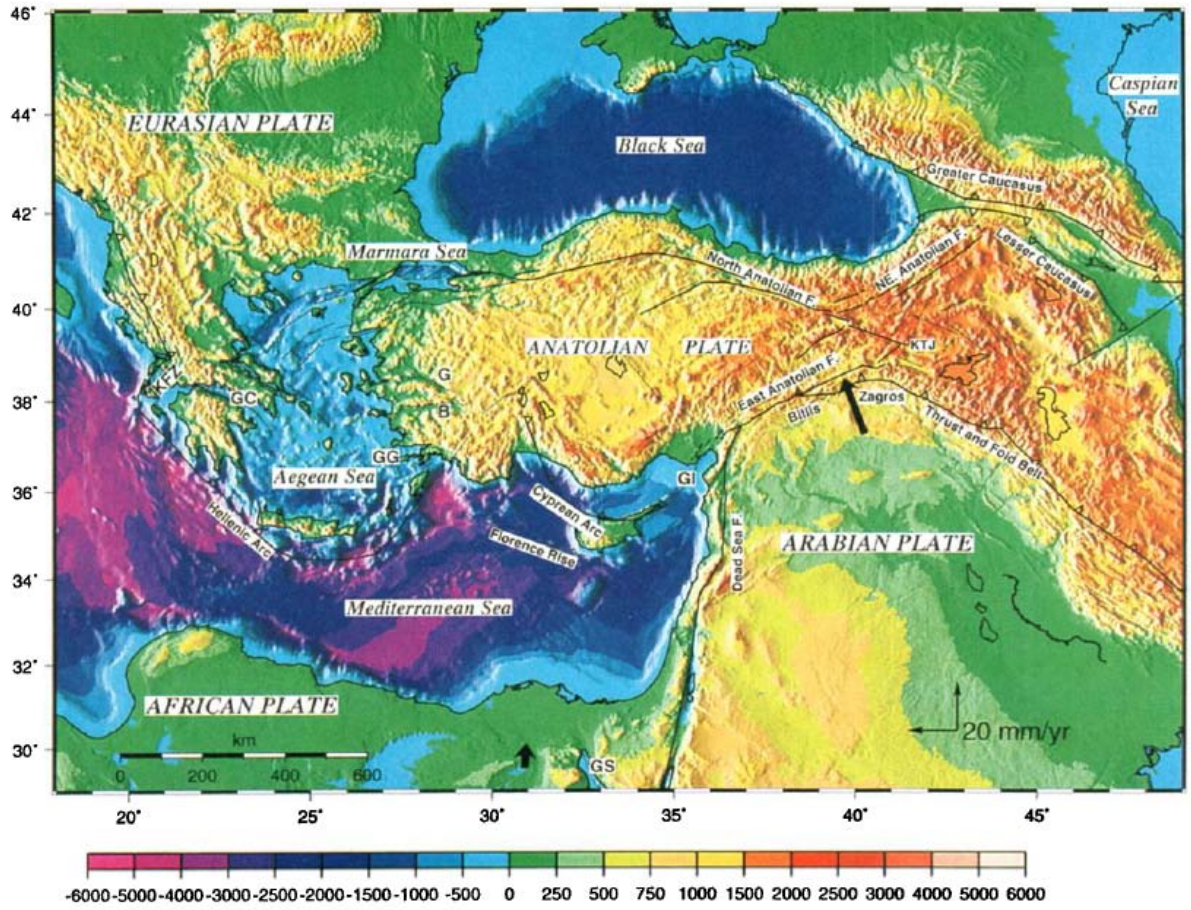

Fig. 2.1. Reproduced from McClusky et al. [2000]. Tectonic map of the eastern Mediterranean region together with the topography and bathymetry. Strike-slip, normal and thrust faults are indicated by black solid lines, black solid lines with ticks, and black solid lines with triangles, respectively. Heavy arrows show NUVEL-1A plate motions relative to Eurasia. Abbreviations: G, Gediz graben; B, Buyuk Menderes graben; KTJ, Karliova triple junction; GG, Gulf of Gokova; KFZ, Kephalonia fault zone; GI, Gulf of Iskenderum; GC, Gulf of Corinth; GS, Golf of Suez.

2.2.1. Relationships with the Thrace Basin

The first focus concerns the relations between the Thrace Basin and the present-day Sea of Marmara. Our work is indeed a part of a larger project, which aims at implementing multi-parameter seafloor observatories in the Sea of Marmara for monitoring interactions between

fluids and seismicity. We will show later that some of these fluids are hydrocarbons that have been proven to be of the same origin as those found in the Thrace Basin.

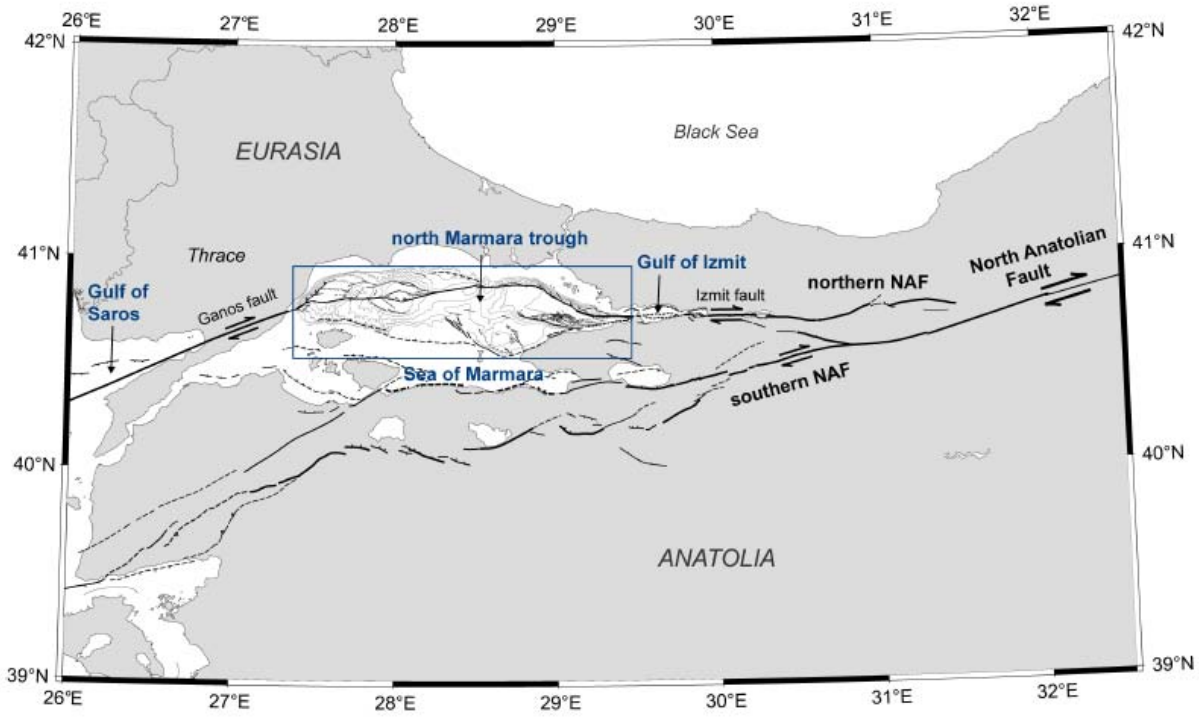

Fig. 2.2. Reproduced from Carton [2005]. North Anatolian Fault zone in the Sea of Marmara region. The North Anatolian Fault splits in two strands before the Izmit Gulf, the northern and southern strands. The southern part splits in two again, as one of its strands delimits the southern margin of the Sea of Marmara, and the other goes to the southwest.

Based on the stratigraphy, structure and the regional geology (Fig. 2.5), it has been proposed that, quoting *Sen and Yıllar* [*2009*], *« the Thrace Basin is a fore-arc basin because of its location between a magmatic arc to the north and a subduction-accretion complex to the south [Görür and Okay, 1996; Elmas, 2003; Zattin et al., 2005]. The development of the Thrace Basin as a fore-arc basin occurred by closure of the Neotethys Ocean (Late Cretaceous - early Eocene), Neotethys Ocean and Istranca massif collision (middle Eocene-lower Miocene), and post-collisional process (middle Miocene-Quaternary).»*

In this context, the North Anatolian fault zone formed during the Middle-Late Miocene as a broad shear zone which, according to [e.g. *Perinçek*, 1991], *«developed with a number of strands splaying westward in a horsetail pattern. Later, the movement became localized along a central strand, and the southerly and northerly splays became inactive. The West Northwest-striking Thrace fault slip system is one of these right-lateral, presently inactive splays. The Thrace fault zone probably connected to the southeast with the presently active North Anatolian Fault in the Marmara Sea.»*

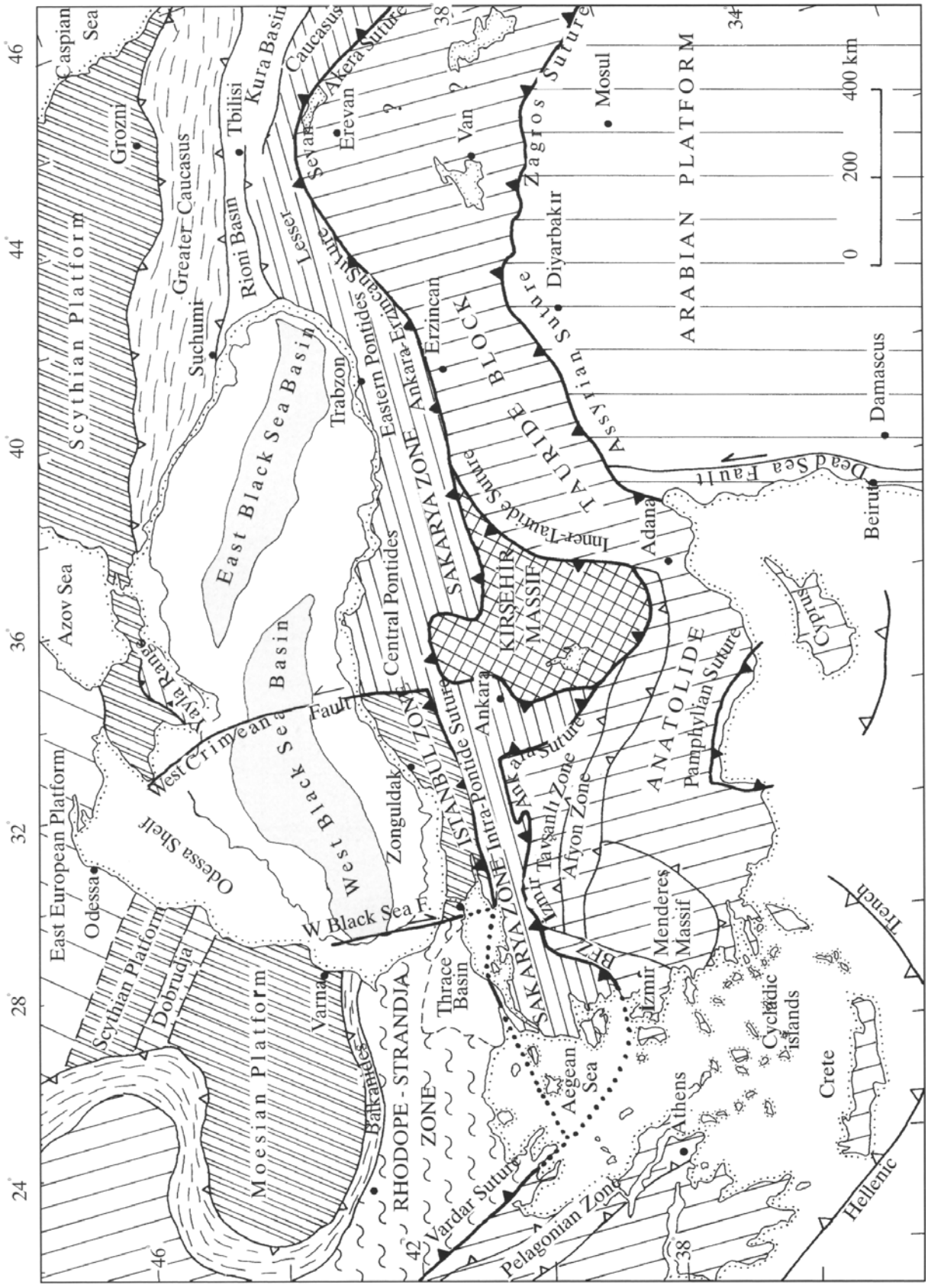

Fig. 2.3. Reproduced from Okay and Tüysüz [1999]. Tectonic map of the eastern Mediterranean area. Active and former subduction zones are indicated by heavy lines with open and filled triangles, respectively. The vergence of major thrust faults and folds are shown by small open triangles.

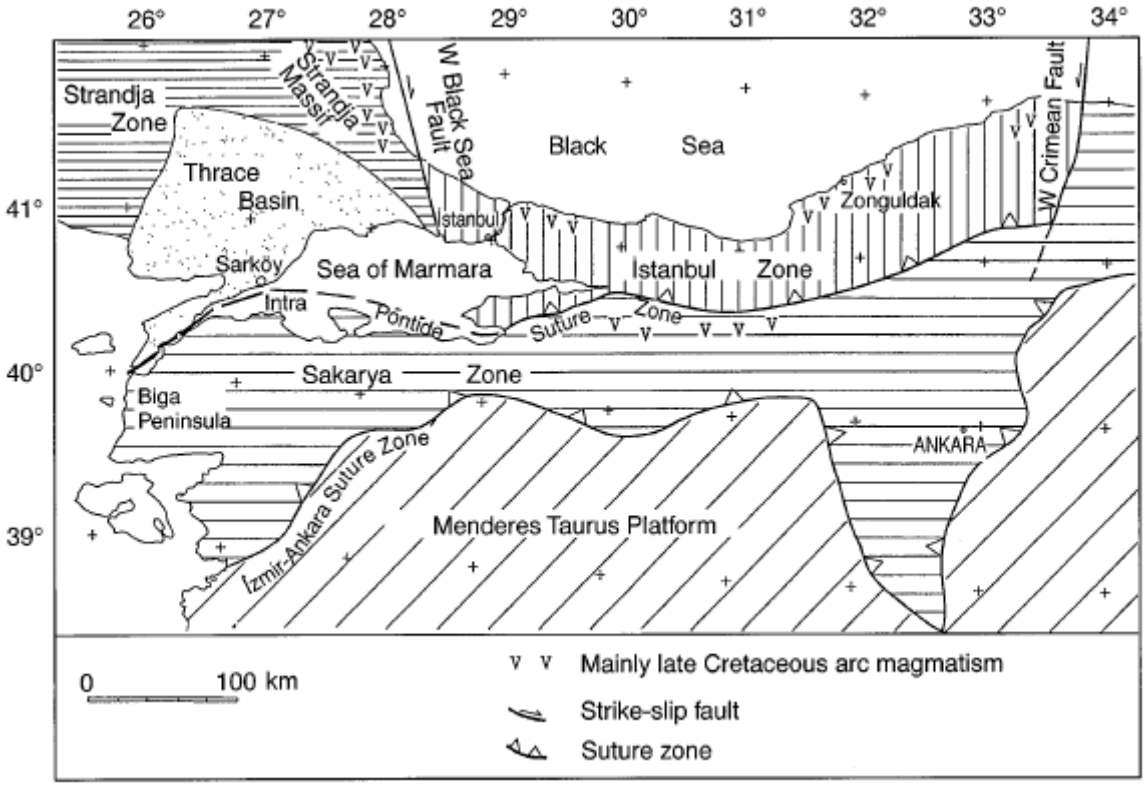

Fig. 2.4. Reproduced from Görür and Okay [1996]. Tectonic map of the Sea of Marmara region.

Also, *Yaltırak* [2002] pointed out that *«the present-day Sea of Marmara results from the superimposed evolutionary history defined by two different- aged fault systems: the early Miocene Early Pliocene Thrace-Eskisehir Fault Zone and its branches, and the late Pliocene Recent North Anatolian Fault and its branches [Fig. 2.6]. […] The branches of the North Anatolian Fault Zone (NAFZ) caused the evolution of a number of basins, which differ in character depending on the trend and past characteristics of the older branches that became connected.»*

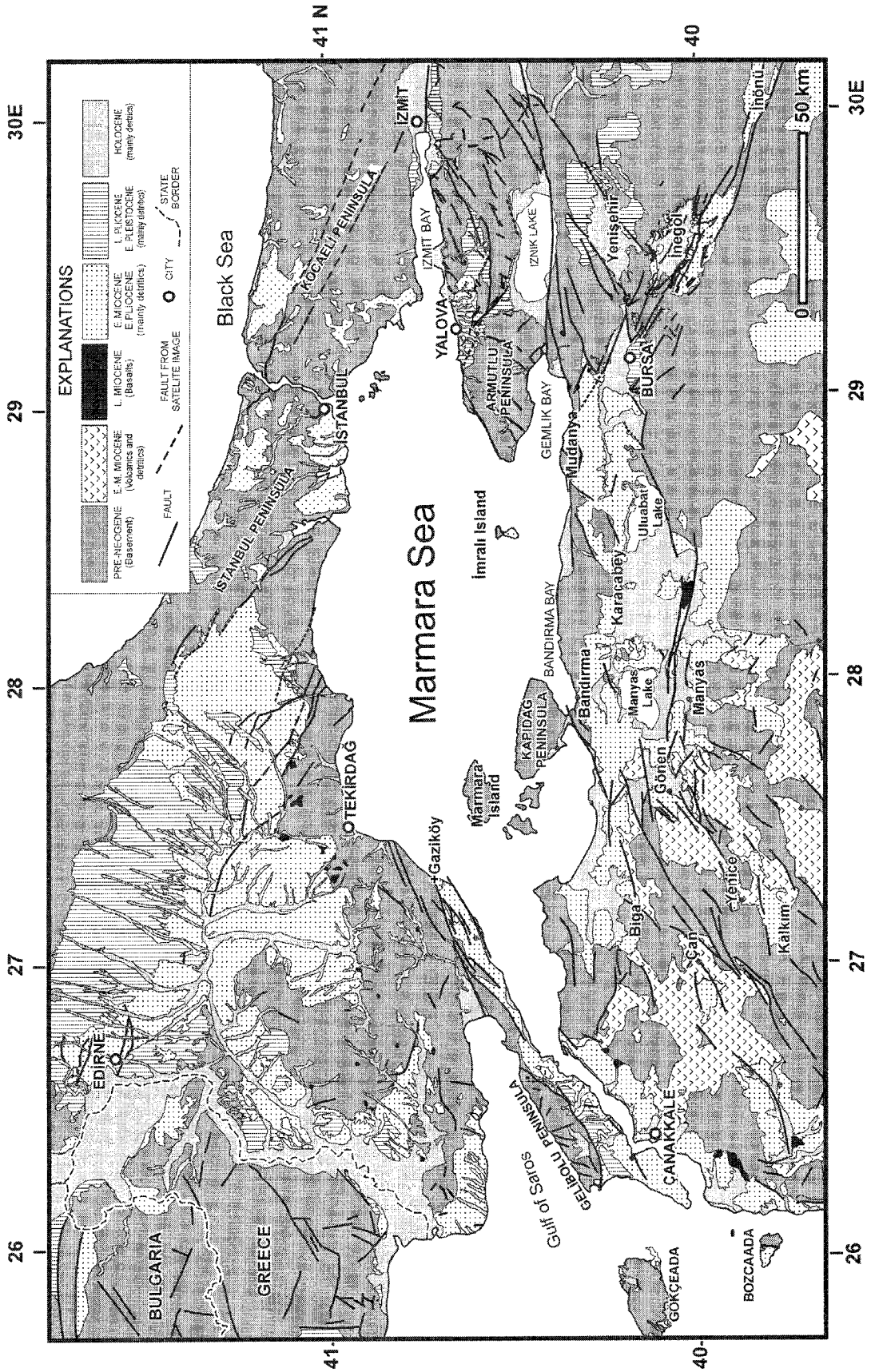

Fig. 2.5. Reproduced from Yaltirak [2002]. Geological map of the surroundings of the Sea of Marmara (after Yaltirak [2002] and references therein).

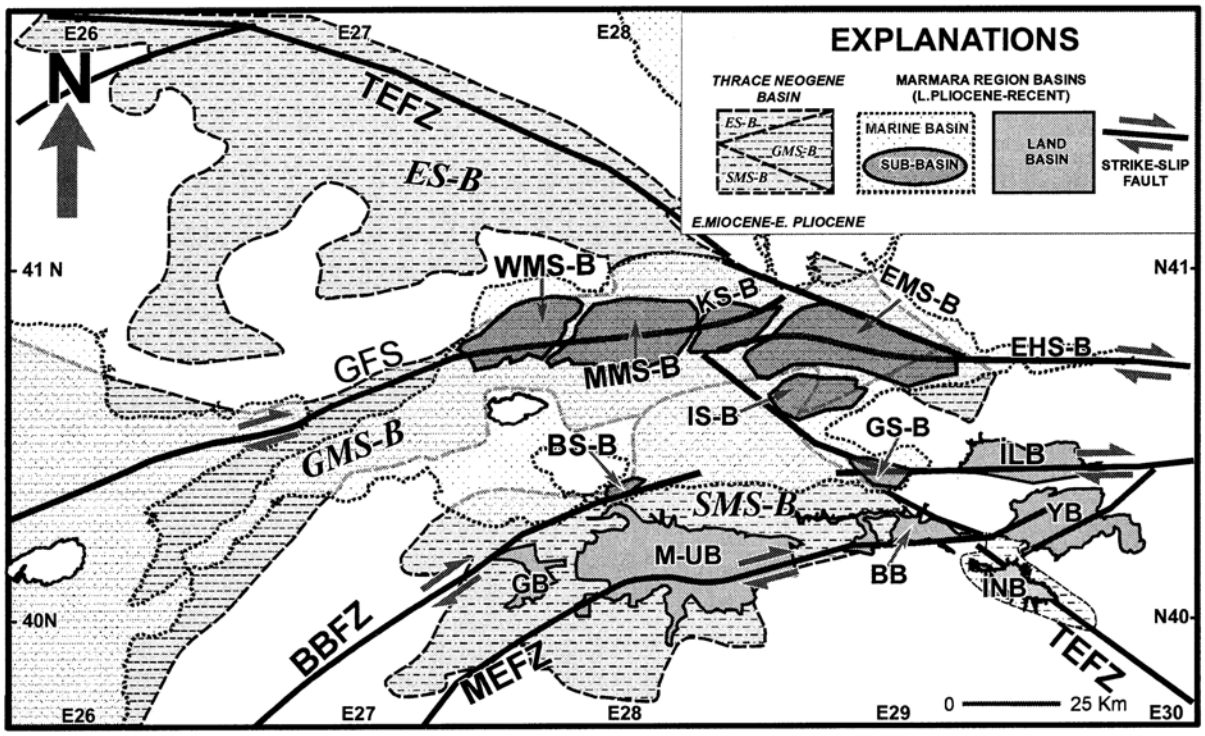

Fig. 2.6. Reproduced from Yaltirak [2002].Geological structures of the Sea of Marmara region showing the interplay between the Thrace-Eskişehir Fault Zone (TEFZ) and the strands of the NAFZ. Abbreviations: GFZ, Ganos Fault Zone; BBFZ, Bandirma-Behramkale Fault Zone; MEFZ, Manyas-Edremit Fault Zone; ES-B, Ergene Sub-Basin; GMS-B, Gelibolu-Marmara Sub-Basin; SMS-B, South Marmara Sub-Basin; WMS-B, West Marmara Sub-Basin; MMS-B, Middle Marmara Sub-Basin; KS-B, Kumburgaz Sub-Basin; EMS-B, East Marmara Sub-Basin; BS-B, Bandirma Sub-Basin; GS-B, Gemlik Sub-Basin; EHS-B, Izmit Sub-Basin; ILB, Iznik Lake Basin; YB, Yenişehir Basin; INB, Inegöl Basin; BB, Bursa Basin; M-UB, Manyas-Uluabat Basin; GB, Gönen Basin.

2.2.2. Late Pliocene evolution / Basin Formation

The second focus concerns the Late Pliocene evolution of the NAF in the Sea of Marmara region. The specific inheritance here above described explains that under the Sea of Marmara, the NAF splits into a complex fault network with numerous fault strands of varying dip and strike, forming, most particularly, three prominent ~1250 m-deep basins, separated by NE-trending transpressional highs (Fig. 2.7). These basins, respectively from east to west, the Çinarcik, Central and Tekirdag basins, are characterized by high sedimentation and deformation rates. The sedimentation rate, averaged over a period going from the marine transgression (~12 kyr BP) to present, is about ~1 mm/yr in basin margins and up to 2.5 mm/yr in the deep basins [*Çagatay et al.*, 2000; *Çagatay et al.*, 2009]. Sedimentation is in competition with basin extension, reaching 6 mm/yr in the Central Basin [*Armijo et al.*, 2005].

Consequently these deep basins are troughs, filled by about 4 km (Tekirdag Basin, Fig. 2.8) or 6 km (Çinarcik and Central basins, Fig. 2.9 and 2.10) of Plio-quaternary sediments [*Bécel,* 2006; *Carton et al.,* 2007; *Bécel et al.,* 2010]. We will see later that this specific situation controls the distribution of seismic velocities below the Sea of Marmara, and ultimately, the accuracy of earthquake locations based on OBSs arrays.

The Late Pliocene tectonic history of the NAF system in the Sea of Marmara that controlled the evolution of these deep basins is a question of critical importance to predict the location and magnitude of the most probable, large earthquake in the Istanbul area. This question has long been the subject of debate. Even though this debate is not critical for the present work, we just recall here that two main families of models have been proposed: the first considers the Sea of Marmara as a large pull-apart-like area [e. g. *Barka and Kadinsky-Kade,* 1988; *Wong et al.,* 1995; *Armijo et al.,* 1999]; the second considers a single and localized, through-going strike-slip fault [e. g. *Aksu et al.,* 2000; *Le Pichon et al.,* 2001, 2003; *Imren et al.,* 2001; *Meade et al.,* 2002].

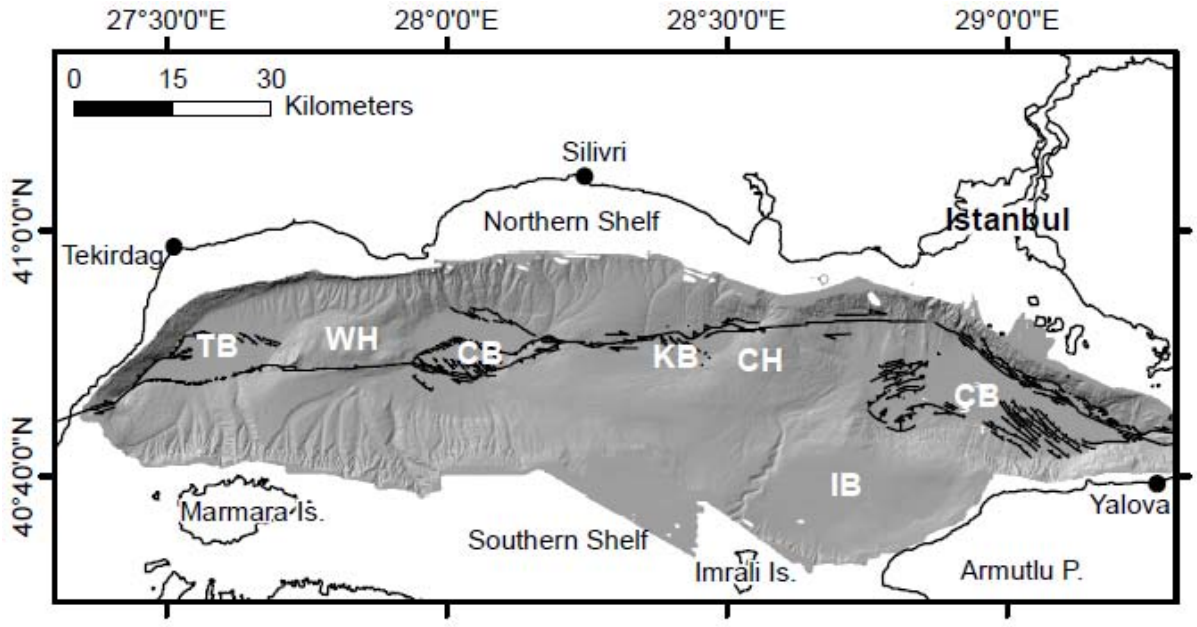

Fig. 2.7. Location of the main geological structures in the Sea of Marmara referred to in the text, with active faults shown by black lines (after Imren et al. [2001] and Rangin et al. [2004]). Abbreviations: TB, Tekirdag Basin; WH, Western High; CB, Central Basin; KB, Kumburgaz Basin; CH, Central High; ÇB, Çinarcik Basin; IB, Imrali Basin; Is.: Island ; P. : Peninsula.

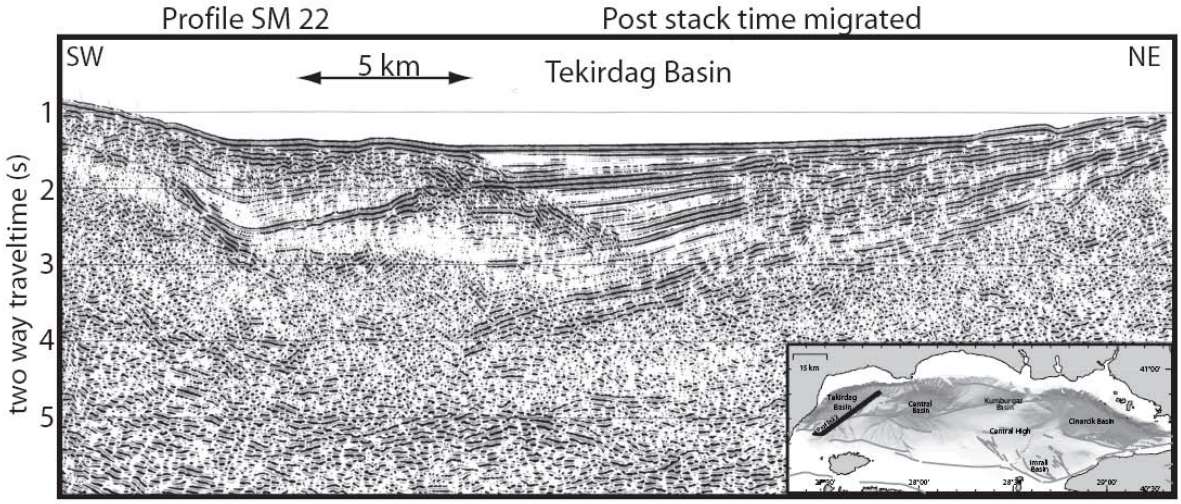

Fig. 2.8. Reproduced from Bécel [2006]. Post stack time migrated section of the Tekirdag Basin: profile SM22. The sedimentary infill reaches at least ~4 km (with a velocity of 2 km/s) in this profile.

Rangin et al. [2004] proposed a model belonging to the second family but slightly different, where an initial extensional stage controlled by the Thrace Basin fault system, evolves first to a pull-apart system, then to a transpressional regime, and finally to the progressive, recent (~ 200 ka) strain localization of the NAF in the Sea of Marmara (Fig. 2.11). This model integrates the Pre-Pliocene tectonic inheritance, by considering that the Sea of Marmara originates from the interplay between a ~N120 E fault zone, likely related to the Thrace Basin, and the East-West NAF [*Okay et al.*, 2000; *Yaltirak,* 2002]. Since the middle-late Miocene, the area that gave birth to the present-day Sea of Marmara, is a broad shear zone, which has been characterized by a succession of episodes of strain localization and of strain partitioning.

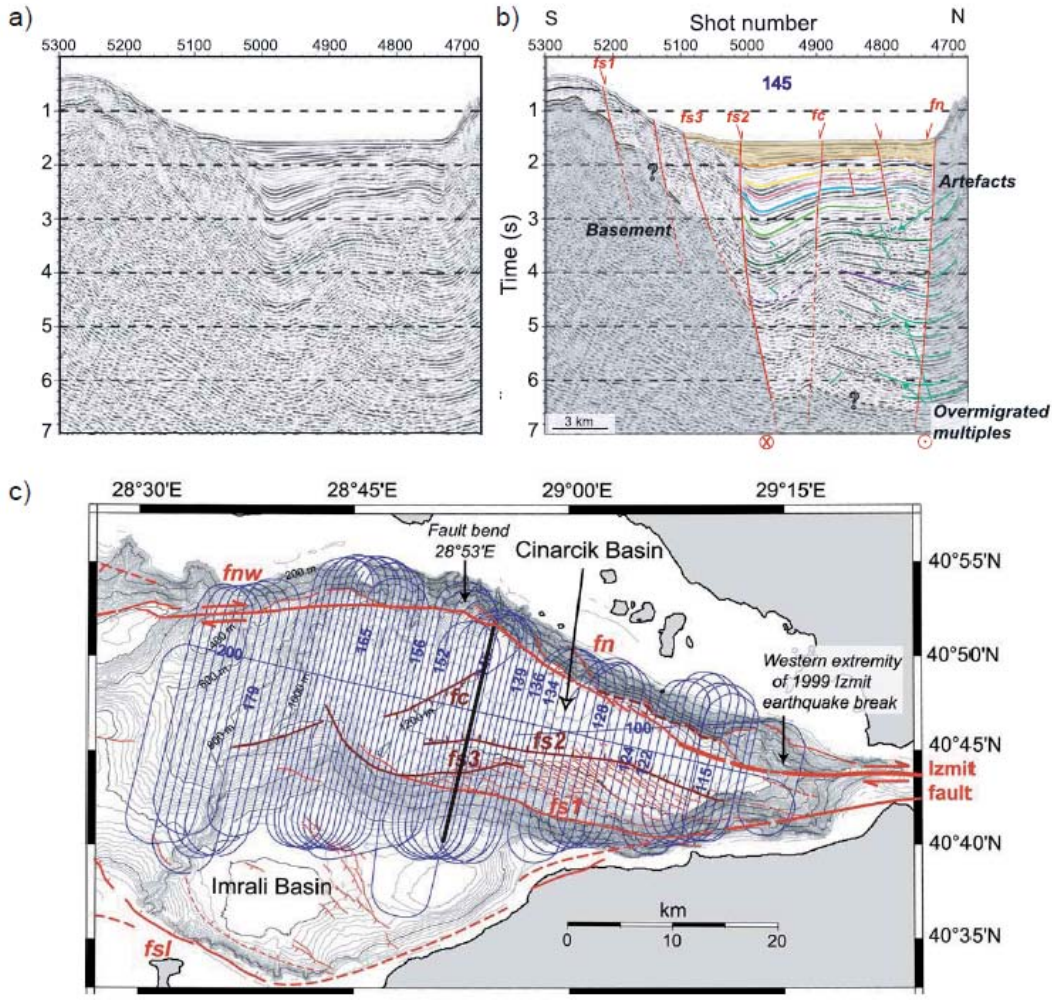

Fig. 2.9. Modified from Carton et al. [2007]. a) Time-migrated section of the Çinarcik Basin: profile 145 (black line in c)). b) Profile 145 structural interpretation. c) Seismic profiles (blue lines) acquired during the SEISMARMARA cruise (2001) in the Çinarcik Basin. Faults are indicated by red [Armijo et al., 2002] and brown [Carton et al., 2007] lines. The sedimentary infill reaches ~6 km (with a velocity of 2 km/s) in this profile.

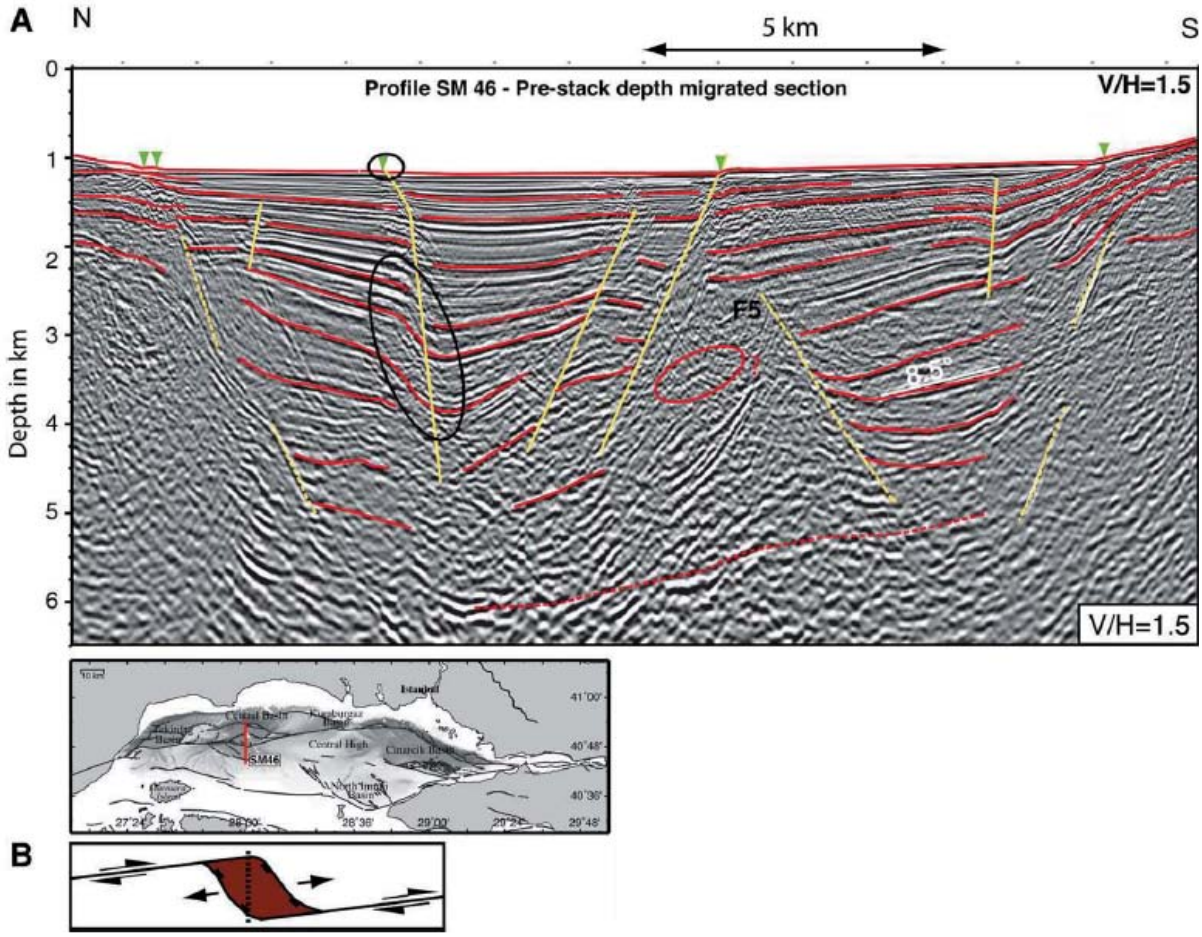

Fig. 2.10. Modified from Bécel et al. [2010]. A) Pre-stack depth-migrated section of the Tekirdag Basin: profile SM 46 (vertical exaggeration: 1.5). Fault scarps reported by Armijo et al. [2002] are indicated by green triangles. B) Map of the Sea of Marmara showing the location profile SM 46 (red line). The profile position is also indicated on the sketch of a pull-apart basin by the black dashed line.

2.2.3. Late marine transgressions

High resolution seismic data (Appendix B) show the ubiquitous presence of a very characteristic, impermeable sediment layer, covering the bottom of the Sea of Marmara. Focus is given here to this layer due to its relevance to the present work. The base of this layer acts as an impervious cap. Gas of deep origin can only escape through unsealed, fault conduits. Where this cap is unfaulted, deeper levels are isolated from the sea surface and thermogenic gases are prevented to escape. Stratigraphic analysis of Late Quaternary sediments indicates that the base of this layer corresponds to the last marine transgression that occurred ca 12,000 yr BP, when the Marmara Lake was inundated by the Mediterranean waters and gradually converted into a marine realm. The sedimentary sequence also recorded

the sea-level variations that occurred during the Upper Pleistocene, as pointed by *Çagatay et al. [2009]* : *"chirp sub-bottom profiling, multibeam bathymetric mapping and a combination of faunal and isotopic analysis of molluscs and foraminifera in sediment cores on the northern shelf of the Sea of Marmara (SoM) provide evidence of sea-level excursions, water exchanges between the adjacent Mediterranean and Black Seas, and oscillating salinity over the last 160 ka bp"*.

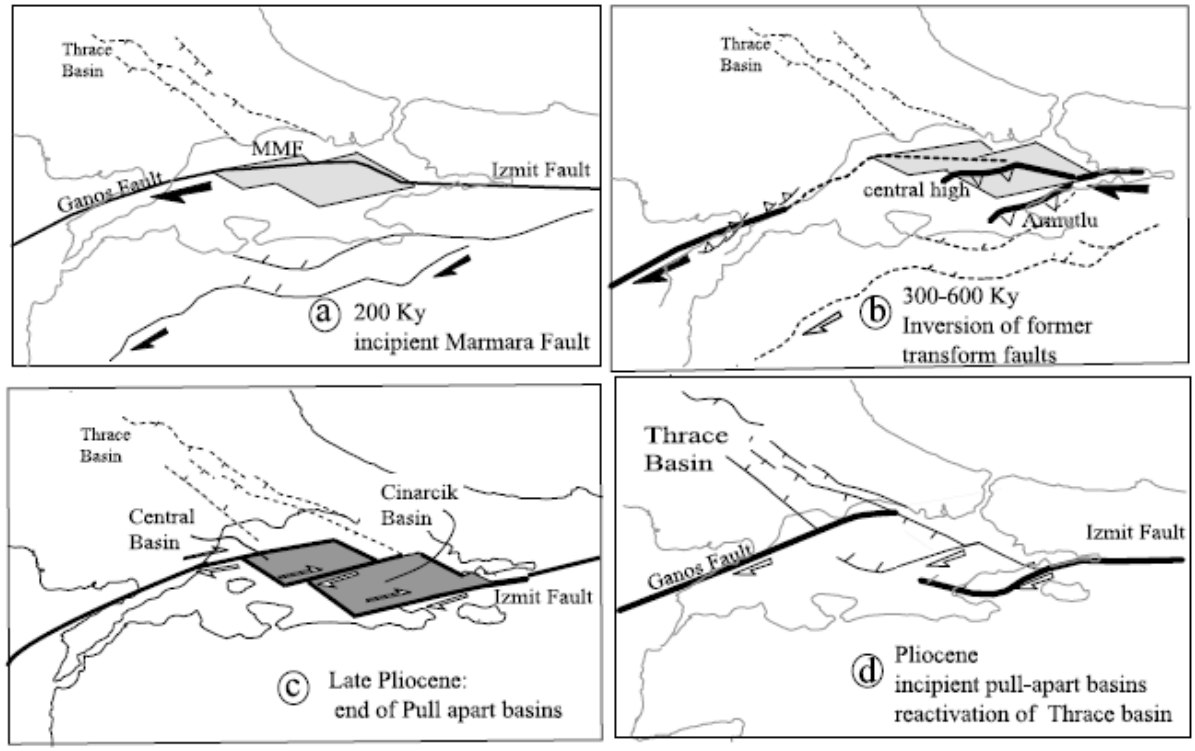

Fig. 2.11. Reproduced from Rangin et al. [2004]. Backward development of the fault system in the Sea of Marmara. (d) Extensional regime controlled by Thrace Basin normal faults during Pliocene. (c) Development of a "Marmara block" composed by pull-apart basins (Miocene-Pliocene). (b) Transition between pull-apart and transpressional regimes (300-600 kyr). (a) Current tectonic regime with a single strike-slip fault (~200 ± 100 kyr - present).

2.3. Earthquake Hazards in the Sea of Marmara

2.3.1. Historical Seismicity

Concerning the pre-instrumental period, important studies were conducted by Professor Nicolas Ambraseys, who spent decades of his life investigating the historical record of the region over the last 20 centuries, based on the *« sustained tradition of historiography of the lower Roman, Byzantine and Ottoman empires »* [*Ambraseys, 2002*]. The reader is thus

invited to refer to the abundant litterature published on the subject by Ambraseys and his group, particularly: on « *the seismicity of Turkey and Adjacent areas, 1500-1800* » [*Ambraseys and Finkel,* 1995]; on *« the seismic activity of the Marmara Sea Region over the last 2000 years »* [*Ambraseys,* 2002]; on the *« Seismicity of the Sea of Marmara Areas since 1500 »* [*Ambraseys and Jackson,* 2000] (Fig. 2.12).

It is interesting to note here that the intensive, marine studies conducted in the Sea of Marmara since the 1999 Izmit (M 7.4) and Düzce (M 7.2) earthquakes, valuably complement the record on the historical seismicity. Quoting [*Görür and Çagatay,* 2010]: *« Large sea-floor rupturing earthquakes seem to have played an important role also in the filling of the deep depressions of the SoM. These basins are filled predominantly with intercalated sequences of turbidite–homogenite units […] directly linked to earthquakes and tsunamis (Beck et al. 2007). Recently, by studying the turbidite–homogenite units in the basins of the SoM, evidence for a number of large historical earthquakes was documented (McHugh et al. 2006; Sarı and Çagatay 2006; Çagatay et al. 2008). According to these studies, large earthquakes occurred in the SoM in 181 AD, 740 AD, 1063 AD, 1343 AD, 1509 AD, 1766 AD, 1894 AD and 1912 AD ».*

The instrumental period (starting from the early XXth century) in Western Turkey is dominated by a 60-year sequence (between 1941 and 1999) of large earthquakes rupturing along the NAF, with a westward propagation towards Istanbul, with one event promoting the next [*Toksöz et al.,* 1979; *Stein et al.,* 1997; *Armijo et al.,* 1999; *Hubert-Ferrari et al.,* 2000; *Parsons et al.,* 2000; *Parsons* 2004; *Meade et al.,* 2002]. Prior to this sequence, which ended with the 1999 earthquakes at the eastern end of the Sea of Marmara, the fault ruptured in 1912 in Ganos, at the western end of the Sea of Marmara, with an estimated moment magnitude of 7.4. Therefore, the northern branch of the NAF in the Sea of Marmara is considered to be a seismic gap threatening the heavily populated Istanbul area.

Using detailed fault mapping based on high resolution bathymetric images and improved historical earthquake catalogs for the [1500-2004] period, [*Parsons,* 2004] estimated that « *the regional time-dependent probability of Magnitude 7 earthquakes in the Sea of Marmara is 44 ± 18%, and incorporation of stress transfer raises it to 53 ± 18%. The 30 year Poisson probability at Istanbul is 21%, and the addition of time dependence and stress transfer raises it to 41 ± 14%. »*

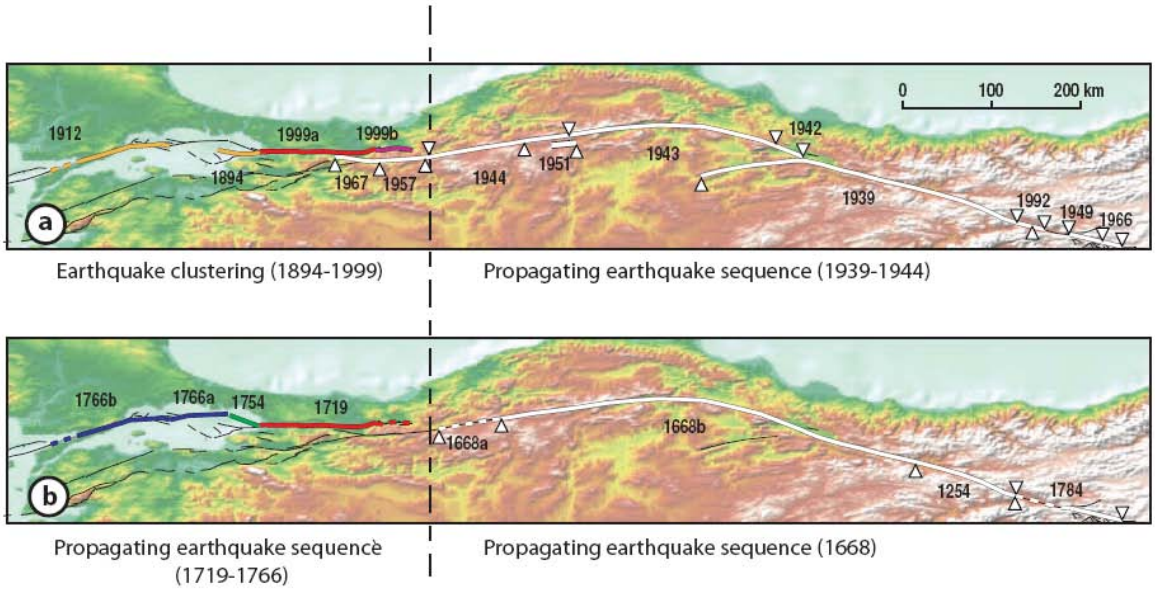

Fig. 2.12. Reproduced from Pondard et al. [2007]. Twentieth and seventeenth-eighteenth centuries earthquakes sequences (M ≥ 7) along the North Anatolian Fault. For each earthquake is shown its rupture length. A compilation of observations [Toksöz et al., 1979; Ikeda et al., 1991; Barka, 1996], historical data [Ambraseys and Finkel, 1995] and Coulomb stress analysis [Pondard et al., 2007]. The vertical dashed line separates two regions with different seismic activities, the linear portion of the North Anatolian Fault and the Sea of Marmara region.

2.3.2. Present day micro-seismic activity in the Sea of Marmara

2.3.2.1. Studies from land stations

A number of studies, dedicated especially to microseismicity location, have already been done in the Sea of Marmara Region. In October – September 1995, 48 land stations were deployed around the Marmara Sea [*Gürbüz et al.*, 2000]. The microseismicity distribution for this period and a 1D velocity model specific to the Sea of Marmara has been simultaneously inverted (VELEST). The events distribution shows an important activity along the main trace of the North Anatolian Fault, and defines two seismic gaps, one located in the Izmit Gulf (where the Izmit earthquake occurred) and one in the Kumburgaz Basin. The micro-seismic activity in the South of the Sea of Marmara is more diffuse.

Following Izmit (M_w = 7.4) and Düzce (M_w = 7.2) earthquakes in 1999, aftershocks distribution and focal mechanisms in the eastern Marmara region were extensively studied [e. g. *Örgülü and Aktar*, 2001; *Ozalaybey et al.*, 2002; *Karabulut et al.*, 2002; *Bohnhoff et al.*, 2006]. Based on the aftershocks distribution, *Ozalaybey et al.* [2002] and *Karabulut et al.*,

[2002] proposed that the rupture of the Izmit earthquake offshore extends farther in the Çinarcik Basin than previously assessed from ground motion inversion and GPS measurements [e. g. *Bouchon et al.*, 2000; *Reilinger et al.*, 2000]. Aftershocks distribution and focal mechanisms also emphasised the complexity of the NAF system as it enters in the Sea of Marmara. West of the Izmit Gulf (and Izmit earthquake mainshock), aftershocks define three main zones: one next to the fault delineating the northern escarpment of the Çinarcik Basin, one in the continuation of the NAF in the Çinarcik Basin, and one in the North of the Armutlu Peninsula ("Yalova cluster"). Focal mechanisms calculated for numerous aftershocks shown mainly strike-slip and normal regimes [*Örgülü and Aktar*, 2001; *Karabulut et al.*, 2002; *Bohnhoff et al.*, 2006].

In order to determine the micro-seismic activity in the Çinarcik Basin, *Bulut et al.* [2009] combined data from sea (OBSs) and land networks (KOERI land stations and PIRES array) for the period November 2005 – December 2007. For the location of micro-earthquakes that were not recorded by the KOERI network, *Bulut et al.* [2009] used specific methods dedicated to arrays of closely spaced stations. The micro-earthquakes distribution shows mainly two NW-SE alignments. These alignments unite at a depth of ~20 km in a single fault.

2.3.2.2. Studies from seabottom networks

From April to July 2000, a network of 10 OBSs was deployed during 70 days for the first time in the Sea of Marmara [*Sato et al.*, 2004] (Fig. 2.13). The microseismicity has been located with HYPOMH algorithm [*Hirata and Matsu'ura*, 1987] and the 1D velocity model of *Gürbüz et al.* [2000]. Station corrections have been used to compensate variations in the sedimentary basins thickness. The 350 earthquakes having the best precision were discussed (Fig. 2.13). A high seismic activity has been found along the northern trace of the North Anatolian Fault in the Sea of Marmara, close to the Gulf of Izmit and the Armutlu peninsula. In the Izmit Gulf and Armutlu peninsula, the seismic activity might be related to stress transfer from the Izmit and Duzce earthquakes in 1999. In addition, focal mechanisms were calculated for micro-earthquakes located in the Western High area and the Çinarcik Basin, showing subvertical strike-slip and extensional mechanisms, respectively.

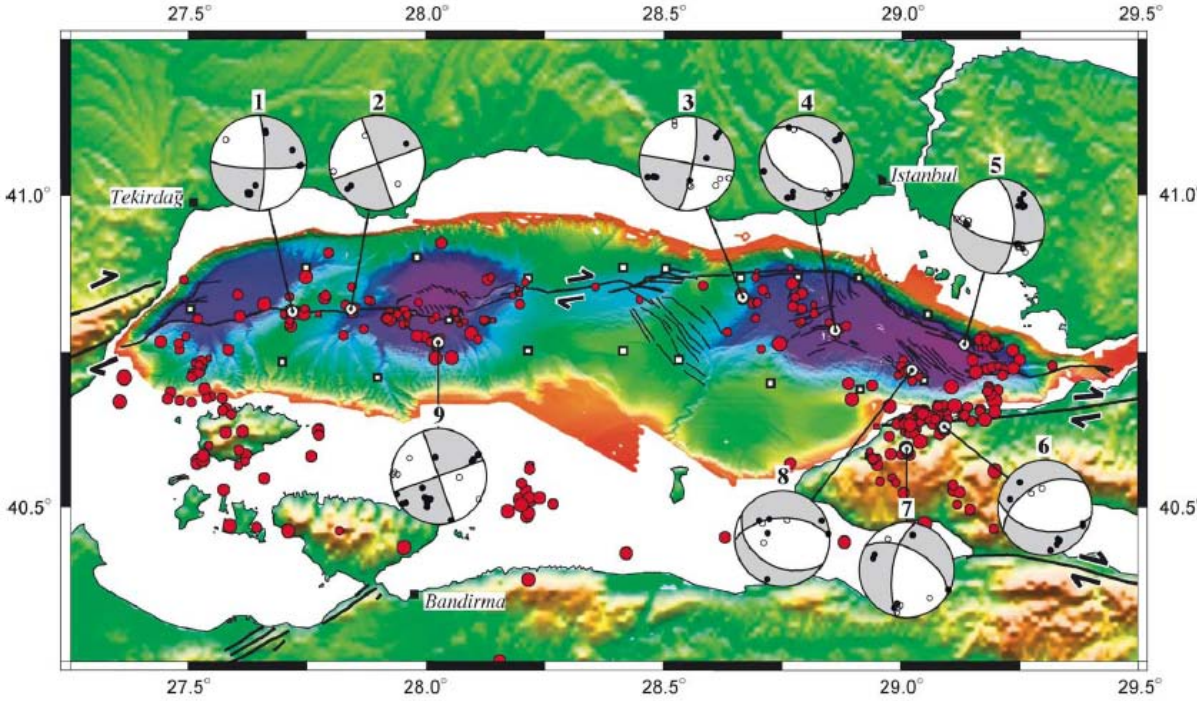

Fig. 2.13. Reproduced from Sato et al. [2004]. Microseismicity distribution (period April-July, 2000) in the Sea of Marmara, and composite focal mechanisms represented as equal-area projections on the lower hemisphere. OBS are shown by the white squares. Gray and white quadrants indicate compression and dilatation, respectively, with solid circles corresponding to wave's first motion in compression, and open circles corresponding to wave's first motion in dilatation.

In 2001, a network of 37 OBS (Seismarmara cruise) and 60 land stations was deployed in and around the Marmara Sea, recording continuously during 6 weeks. A powerful source and a long streamer were also used to image the supracrustal and deep structures [*Bécel,* 2006; *Bécel et al.*, 2009].

The earthquakes locations and deep structure geometry have been inverted simultaneously. The microseismicity is concentrated in a 50 km wide zone including the Central Basin and the Western High (Fig. 2.14). Several clusters are visible in North-South cross-sections of the Central Basin, often located in the continuation at depth of the surface fault traces.

During the Seismarmara cruise, only a few micro-earthquakes were found in the Çinarcik and Tekirdag basins. In the Kumburgaz Basin, no micro-earthquakes of magnitude >0.6 were located, indicating that this segment might be either creeping or blocked.

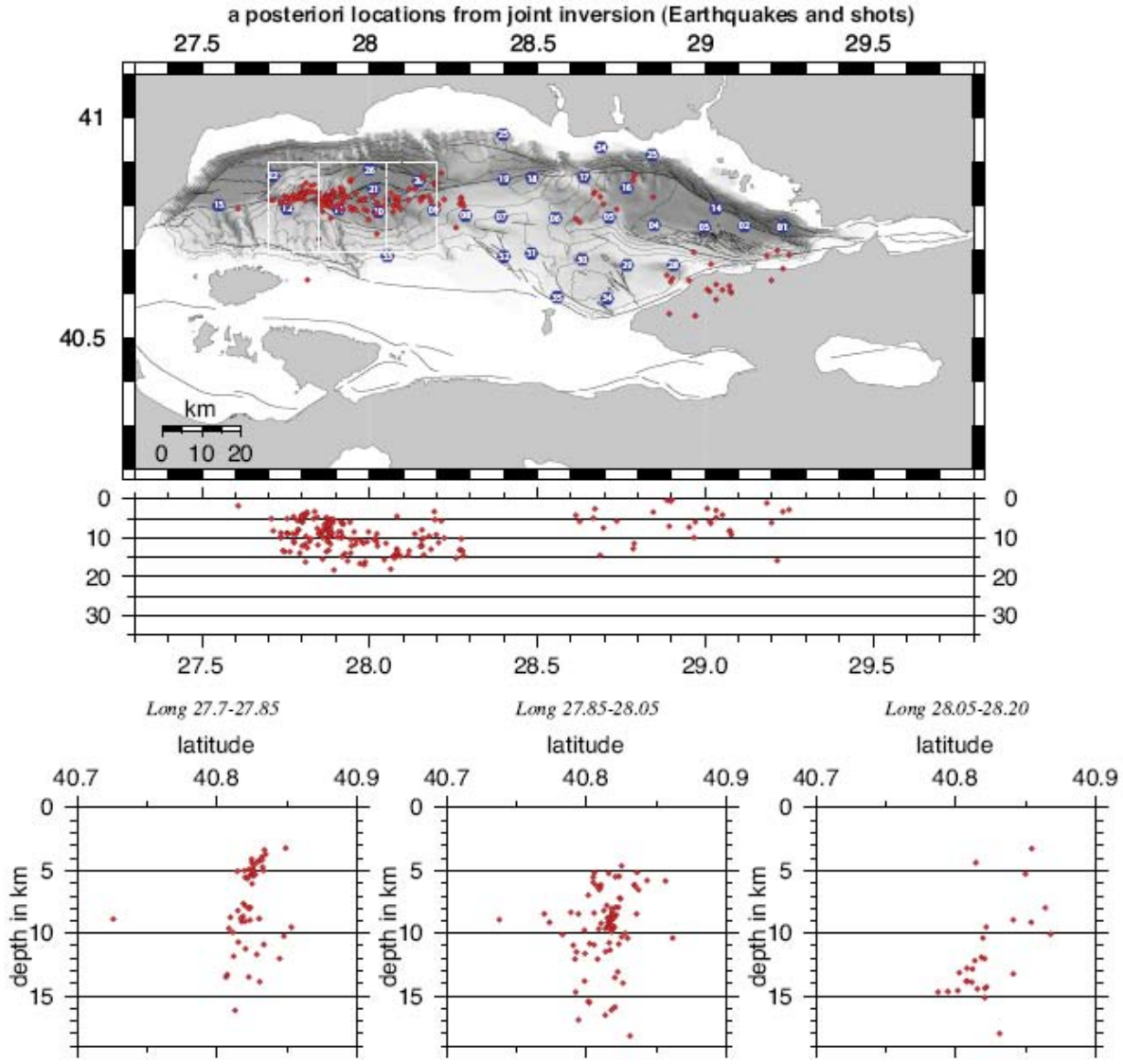

Fig. 2.14. Reproduced from Bécel [2006]. Microseismicity distribution in the Sea of Marmara after the simultaneous inversion of earthquakes and seismic shots arrival times. The white rectangles correspond to the cross-sections shown below the map.

2.4. Fluids manifestations

Fluid expulsion is a common phenomenon in marine sediments. Gas expulsions, often designated as cold seeps, are observed on continental shelves and slopes worldwide. [*Paull et al.*, 1984; *Juniper and Sibuet*, 1987; *Dimitrov and Woodside*, 2003; *Judd and Hovland*, 2007]. Cold seeps are often, but not always, associated to active faults [*Moore et al.*, 1990; *Le Pichon et al.*, 1992; *Henry et al.*, 2002], indicating that faults may channel fluids from depth to the seafloor (Fig. 2.15).

Fluid-earthquakes relationships have been highlighted during the Mw 7.4 1999 Kocaeli earthquake, when gas expulsions were observed in the Gulf of Izmit (eastern end of the Sea of Marmara) after the earthquake [*Alpar,* 1999; *Halbach et al.,* 2004; *Kusçu et al.,* 2005]. Hereafter, we report observations of fluid manifestations from the deep parts of the Sea of Marmara.

2.4.1. Field observations from the deep basins

During Marmarascarps (2002) and MarNaut (2007) cruises, ROV data (microbathymetry, photos and videos), cores, chirp profiles and Nautile dives (Fig. 2.15) were conducted along the active fault traces in the Sea of Marmara. Numerous fluid-related observations were made along the faults traces [*Zitter et al.*, 2008] (Fig. 2.16).

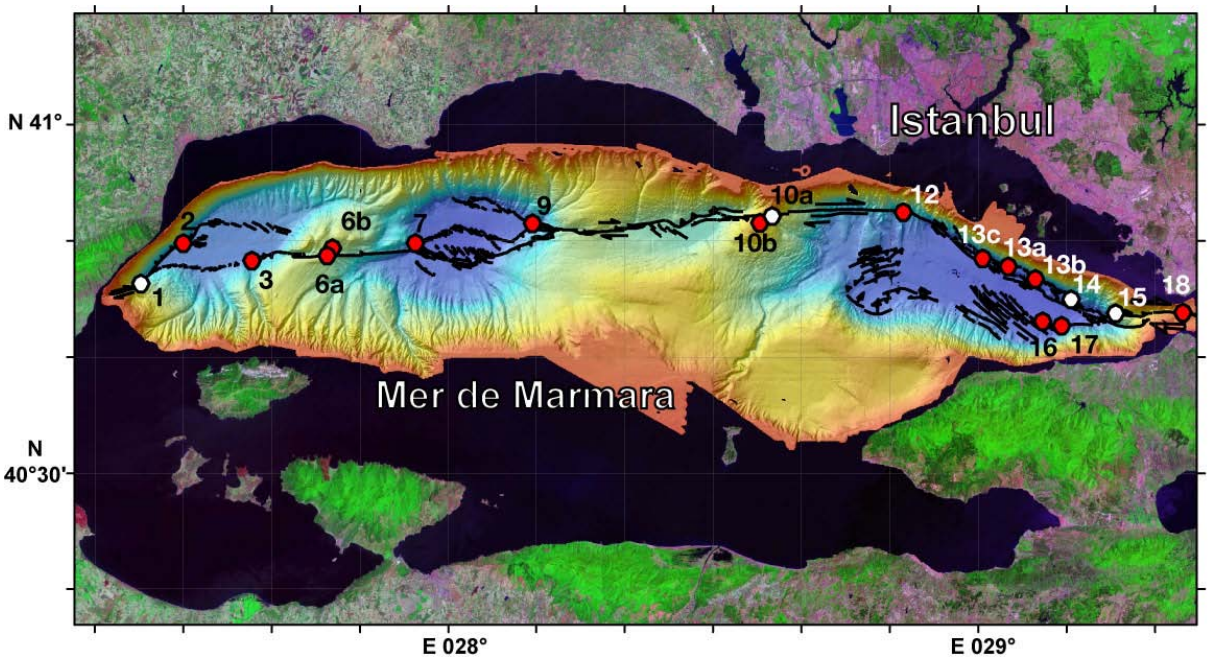

Fig. 2.15. Map of the Sea of Marmara with active fault traces over a Landsat image of the area. The Nautile dive sites explored during Marnaut are shown by red dots where fluid seepage were observed, and by white dots otherwise. Numbers refer to dive sites and follow the definition of dive targets in the cruise plan (http://cdf.u-3mrs.fr/~henry/marmara/marnaut_web/meeting1.html) ©CNRS. Pierre Henry.

Zitter et al. [2008] inventoried two types of fluid migration. The first is the migration of free gas (methane) in sediments inferred from echo sounder acoustic anomalies and bubble emission triggered by coring. At the seafloor, methane emissions are related to the occurrence of black patches of reduced sediments.

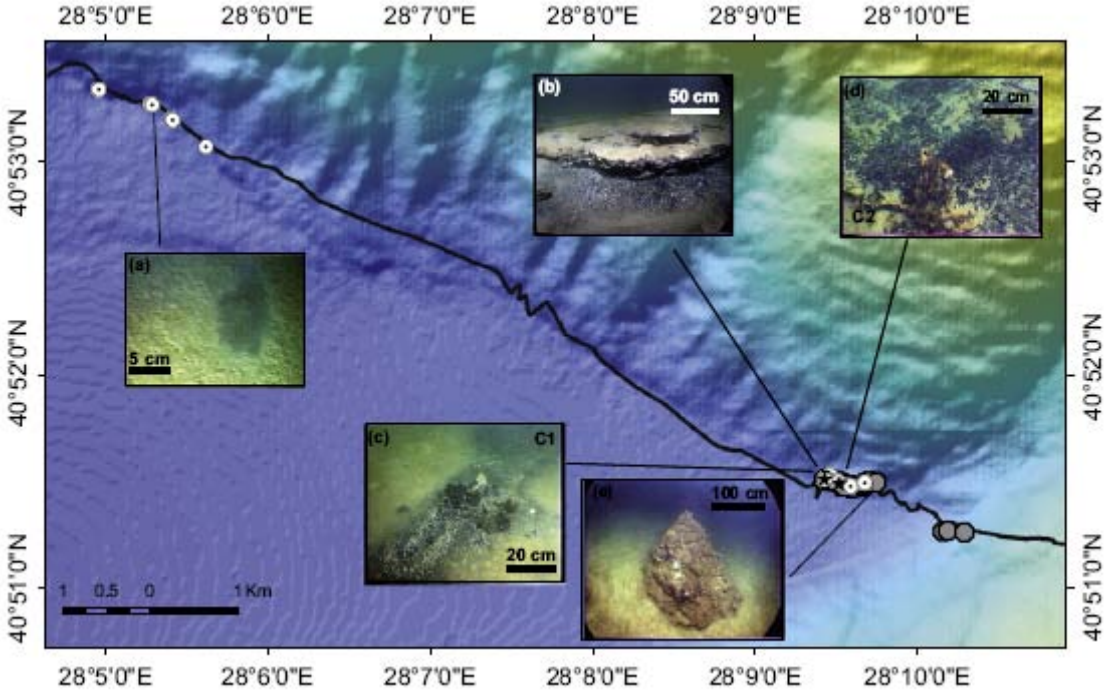

Fig. 2.16. Reproduced from Zitter et al. [2008]. Map of the eastern end of the Central Basin (dive 9 in Fig. 2.15) showing the locations of seafloor observations: black patches (a), carbonate crust (b), carbonate chimneys (c, d) and carbonate edifice (e).

Black patches observed on the seafloor (Fig. 2.17)

These black patches result from the anaerobic oxidation of methane, through which the methane contained in the upper sediments layer is oxidized by sulfates contained in the sea water [*Boetius et al.*, 2000; *Hensen et al.*, 2003].

The second type of fluid migration reported by *Zitter et al.* [2008] is brackish pore water expulsion at the seabed. The fluids are expelled through authigenic carbonate chimneys like in the Tekirdag or Central basins. A possible explanation for these expulsions is that fluids might migrate through high permeability layers, until they are released in areas prone to intense erosion.

Fig. 2.17. Photograph of a black patch taken by Nautile submersible during the MarNaut cruise.

2.4.2. Acoustic anomalies in the water column

During the Marnaut cruise of R/V L'Atalante in May – June 2007, gas plumes have been detected in the water column by echo sounder operating at 38 kHz [*Géli et al.,* 2008] (Fig. 2.18). All sites where acoustic anomalies were detected in a previous cruise in 2000 [*Rangin et al.,* 2001; *Le Pichon et al.,* 2001] were still active in 2007. These gas plumes have been confirmed in situ by dives observation of the Nautile submersible (black patches of reduced sediments).

However, the EK-60 profiles were concentrated only on fault zones. During the Marmesonet cruise in Nov.-Dec. 2009, a Simrad EM302 multibeam echosounder (27-33 kHz) was systematically used to detect gas plumes in the water column over all the northern part of the Sea of Marmara (Fig. 2.19 and 2.20).

Acoustic anomalies have been observed mainly along faults, active or not, on anticlines summit and in basins (Fig. 2.20).

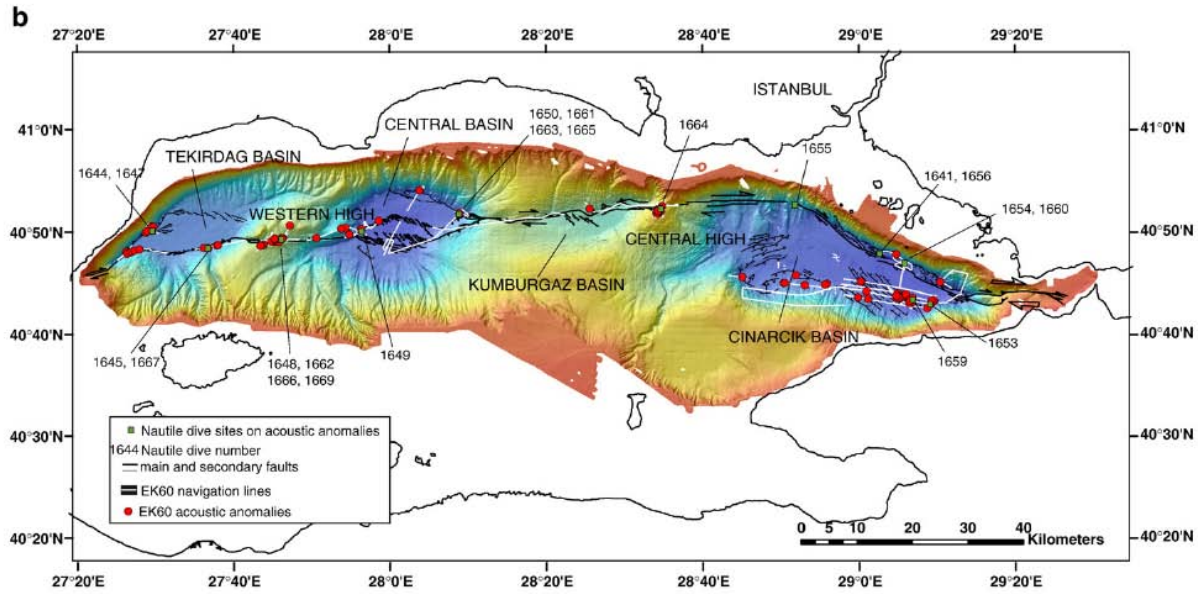

Fig. 2.18. Reproduced from Géli et al. [2008]. Bathymetric map of the Sea of Marmara with the acoustic anomalies (red dots) detected with an EK-60 sonar during the MarNaut cruise (May-June 2007). Black and white lines indicate active faults (after Imren et al., [2001] and Rangin et al., [2004]) and the R/V L'Atalante tracks during the MarNaut cruise.

- Çinarcik Basin

In the Çinarcik Basin, acoustic anomalies were found mainly along the prolongation of the northern strand of the NAF in the Sea of Marmara, i. e. along the northern fault and the highly faulted, southern part of the basin.

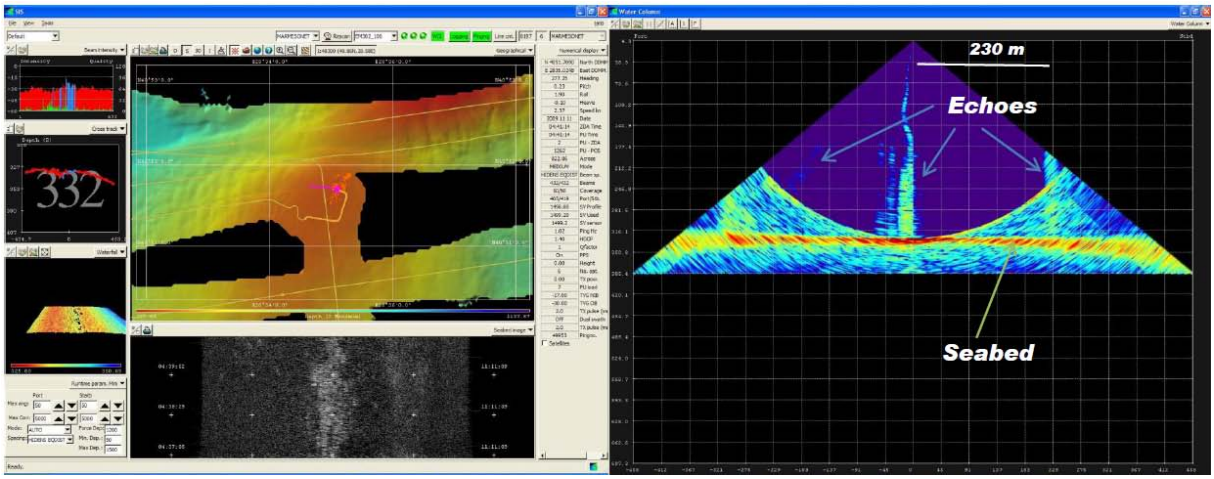

Fig. 2.19. Modified from Dupré et al. [2010]. Example of R/V Le Suroit EM302 onboard screen showing the bathymetry (left) and water column (right) of the Central High area ("Istanbulle area"). The flat high amplitude reflector and the high amplitude echoes in the water column correspond to the seabed and gas plumes, respectively.

-Central and western highs

The structural highs (Western and Central) show numerous sites of gas emissions. The bubbles observed on the anticlines could either result from material squeezing followed by the escape of fluids through extrados fracture, or originate from the main fault and then channeled through high-permeability layers to the anticline. In the Western High area, two pockmarks zones are associated with intense bubbling.

-Central Basin

In the Central Basin, bubble emissions are concentred at the two corners of the basin where it connects to the main strike-slip fault and, to a lesser extent, along the northern escarpment. They are aligned along preferential orientations controlled by fractures. The main inner faults of this basin show less acoustic anomalies related to bubble emissions in the water column.

-Tekirdag Basin

Acoustic anomalies in the Tekirdag Basin follow the basin boundaries, i. e. the southern strike-slip fault trace, and the western and northern escarpments. The WNW-ESE normal faults crossing the northern part of the basin were covered by EM302 profiles, but no acoustic anomalies were found. Acoustic anomalies were found at known sites of gas emissions, Boris's bubbler [*Burnard et al.*, 2011 *in preparation*], and brackish water escape, Jack the smoker [*Armijo et al.*, 2005; *Imren et al.*, 2001; *Géli et al.*, 2008] (Fig. 2.20).

As acoustic anomalies were found mainly on fault traces (Fig. 2.20), the faults networks, experiencing seismically-induced fracturing, may serve as conduits for fluids to rise up to the sea floor. In some places, the fluid outflow might be diverted by low permeability materials (clayey sediments, slump deposits…), like in the southern part of the Tekirdag Basin [*Zitter et al.*, 2008].

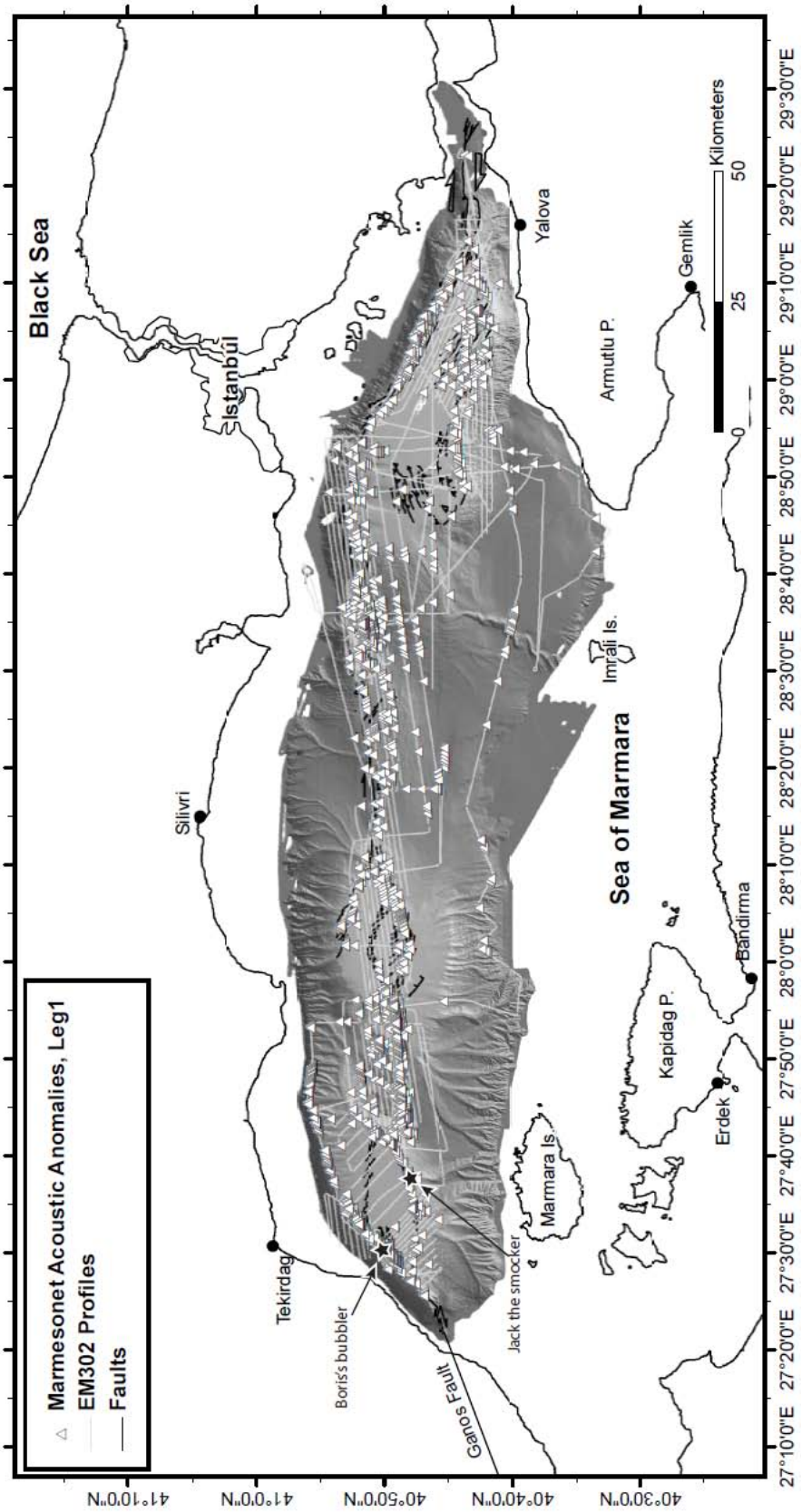

Fig. 2.20. Preliminary acoustic anomalies distribution detected by the Simrad EM302 multibeam system in the water column during Marmesonet cruise, leg 1. The acoustic anomalies have been positioned on the ship's track, even though this position can be shifted by up to about 1 km from the "real" one depending on the water depth (Fig. 2.19). Abbreviations: Is., Island; P., Peninsula.

2.4.3. Gas distribution from Marmesonet chirp profiles

The northern part of the Sea of Marmara was systematically covered by chirp profiles during the Marmesonet cruise in 2009 (see Appendix B). Depending on lithology, chirp profiles image up to the first 100 m of sediments. These profiles were used to document the gas distribution in marine sediments, and the possible connections between gas occurrence and the North Anatolian Fault system.
Gas evidence was found mainly in sedimentary basins, but also on structural highs as shown in Fig. 2.21 and 2.22.

- Next to the western escarpment in the western part of the Tekirdag Basin, where gas bubbles of deep origin were observed escaping from tensile cracks on the seafloor [*Burnard et al.,* 2008].

- On the southern side of the Western High, close to the site of OBS K (MarNaut cruise, 2007, see section 2.6 for location).

- On the top of the Central High and on the southeastern part of the Çinarcik Basin are two particular areas where intense gas emissions were detected in the water column by the EM302 echosounder and numerous gas signatures found on chirp profiles.

- In the Central, Kumburgaz and Imrali basins.

Although, it is known that the North Anatolian Fault is connected to deep reservoirs having the same origin as those of the Thrace Basin [*Bourry et al.,* 2009], gas occurrence in sediments were found only in a few places close to the Main Marmara Fault. Gas occurence is visible on chirp profiles where gasses cause a significantly high impedance contrast with the surrounding sediments. The distribution of acoustic anomalies in the water column shown that the fault zone in the Sea of Marmara is characterized by a high permeability. Hence gas escapes could prevent gas accumulation and thus explain why only few gas evidences were found next to the fault system.

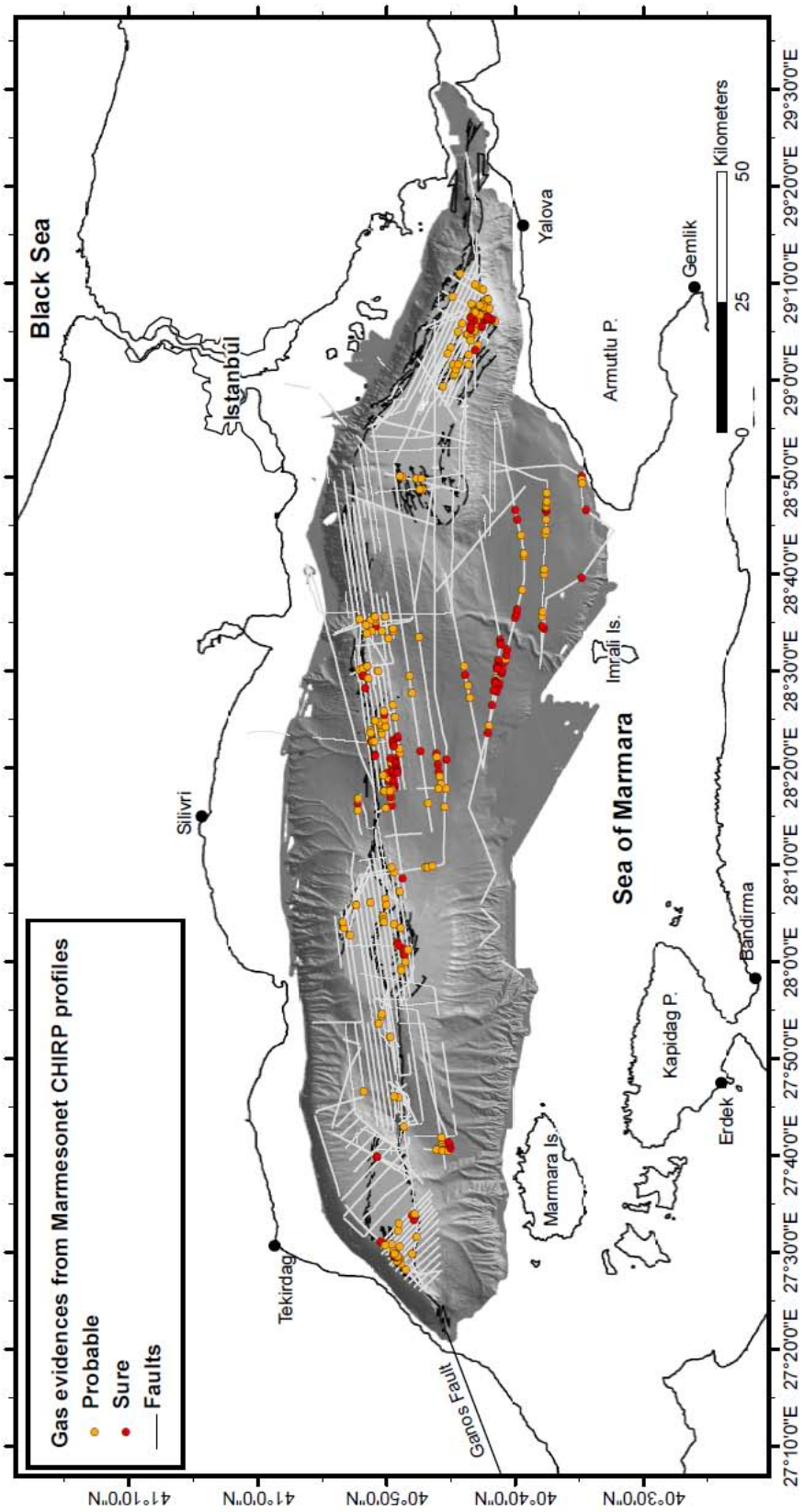

Fig. 2.21. Distribution of gas evidences in sediments from Marmesonet CHIRP profiles. Gas evidences that we considered as "sure" are indicated by red dots while the ones we considered as "probable" are indicated by orange dots. Black and gray lines correspond to active faults traces (after Imren et al. [2001] and Rangin et al. [2004]) and CHIRP profiles acquired during the Marmesonet cruise, respectively. Abbreviations: Is., Island ; P., Peninsula.

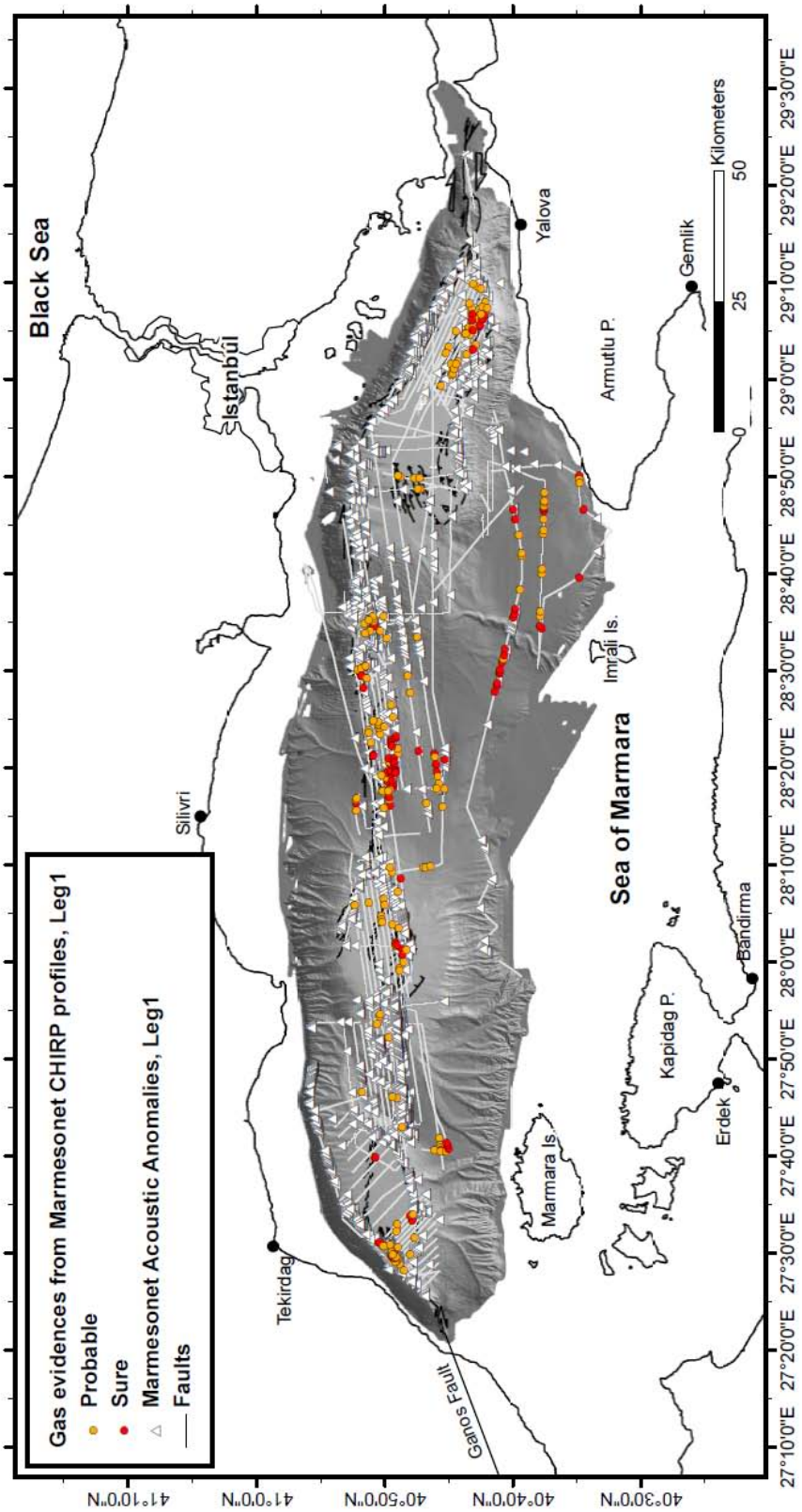

Fig. 2.22. Distribution of gas evidences in sediments from CHIRP profiles and acoustic anomalies in the water column (white triangles) detected by the Simrad EM302 multibeam system during the Marmesonet cruise, leg 1, in the Sea of Marmara. Gas evidences that we considered as "sure" are indicated by red dots while the ones we considered as "probable" are indicated by orange dots. Gray lines corresponds to CHIRP profiles acquired during the Marmesonet cruise. Abbreviations: Is., Island ; P., Peninsula.

Gas occurrence in sediments is generally correlated with gas emissions in the water column but the reverse is not true (Fig. 2.22). Thereby, only a fraction of the fluids is able to reach the seafloor, through fractures, pre-existent or not, in the upper sediments (~0-100 m). It is also important to note that seepage sites reported by *Géli et al.* [2008] were still active in 2009, ~2.5 years after the MarNaut cruise. Therefore, gas emissions seem to be a stable phenomenon at the scale of a few years in the Sea of Marmara.

2.4.4. Origin of fluids

Whether fluids come from shallow or deep sediments give important insight on fluids circulation from the surface to seismogenic depths. The most common gas in sediments is methane. Methane can be produced either in superficial sediments by carbon dioxide reduction or acetate fermentation (biogenic methane), or by thermal degradation of kerogen and oil in deeper sediments (thermogenic methane). The origin of methane can be determined by the analysis of carbon and hydrogen isotopic ratios.

2.4.4.1. Geochemical analyses: hydrocarbons and carbon isotopic ratio

-Structural highs (Western High and Central High)

Clusters of gas plumes have been detected in the Western High fault valley and on top of the Central High, about 1 km southward of the fault (Fig. 2.18 and 2.20). Gas bubbles sampled on Western (PG-1662) and Central (PG-1664) Highs, and gas hydrates sampled on Western High (MNTKS27), show isotopic and molecular composition typical of a thermogenic origin [*Bourry et al.,* 2009] (Fig. 2.23). Consequently, the sources of these gases are petroleum or rocks filled by thermally mature organic matter.

The gas samples coming from the Western High have a composition similar to the *K.Marmara-af* natural gas field [*Gürgey et al.*, 2005; *Bourry et al.*, 2009]. The *K.Marmara-af* is one of the natural gas fields originating from the Thrace Basin. The similarities in gas composition between the Western High samples and the *K.Marmara-af* indicate that the North Anatolian Fault cross-cuts gas reservoirs from the southern continuation of the Thrace Basin gas field, and that gas probably follows the fracture network of the North Anatolian Fault to rise up to the sea floor.

- Çinarcik Basin

In contrast, gas samples taken from the southern part of the Çinarcik Basin (PG-1659, Fig. 2.23) show that the methane and ethane have a biogenic and thermogenic origin, respectively. It seems that biogenic and thermogenic gases are mixed in this area [*Bourry et al.*, 2009].

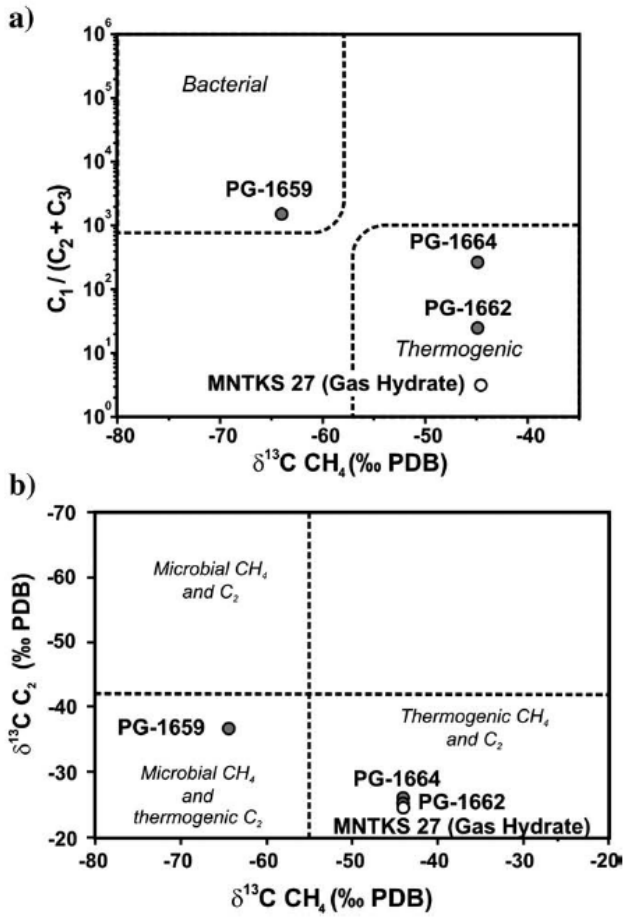

Fig. 2.23. Reproduced from Bourry et al. [2009]. Hydrocarbons and carbon isotopic ratio analysis for gas bubbles and gas hydrates origin determination. a) Stable carbon isotope composition ($\delta^{13}C$) of CH_4 in function of the $C_1/(C_2+C_3)$ ratio. b) Stable carbon isotope composition ($\delta^{13}C$) of CH_4 in function of the table carbon isotope composition ($\delta^{13}C$) of C2. Carbon isotopic ratio ($\delta^{13}C$) is given as parts per thousand (‰) relative to the PeeDee Belemnite standard (PDB).

2.4.4.2. Geochemical analyses: helium isotopes

Fluid samples from the Marnaut cruise have been analyzed for Helium isotopes and for Ne/He ratios. In nature, there are only 2 stable isotopes of helium, ^{3}He and ^{4}He. The only source of ^{3}He in geological fluids is the mantle (i.e. primordial He trapped in the earth during

accretion). The isotope ^{4}He is produced over time by radioactive decay of Uranium and Thorium. The measurements are normalized to the ^{3}He/^{4}He ratio of atmosphere ($(^3He/^4He)_{air}$ = 1.39x10^{-6} = 1 Ra). Atmospheric He escapes to space, so the Ne/He ratio is high for air and seawater, and low for the crust and the mantle. This ratio, combined with the ^{3}He/^{4}He ratio, is a powerful tool for tracing the origin of fluids.

Fluid samples were recovered during the Marnaut cruise in 2007. Eight of the recovered samples have He/Ne ratios similar to the atmosphere, one has a ratio corresponding to pure crust, and the remaining 10 samples have variable amounts of mantle helium (Fig. 2.24). Almost all of these samples have less than 25 % of mantle helium. Only one sample, coming from the northwest corner of the Tekirdag Basin, is composed of 70 % mantle helium. This ratio shows that the fluids of this site have a deep source [*Burnard et al.*, 2008; *Burnard et al.*, 2011 *in preparation*].

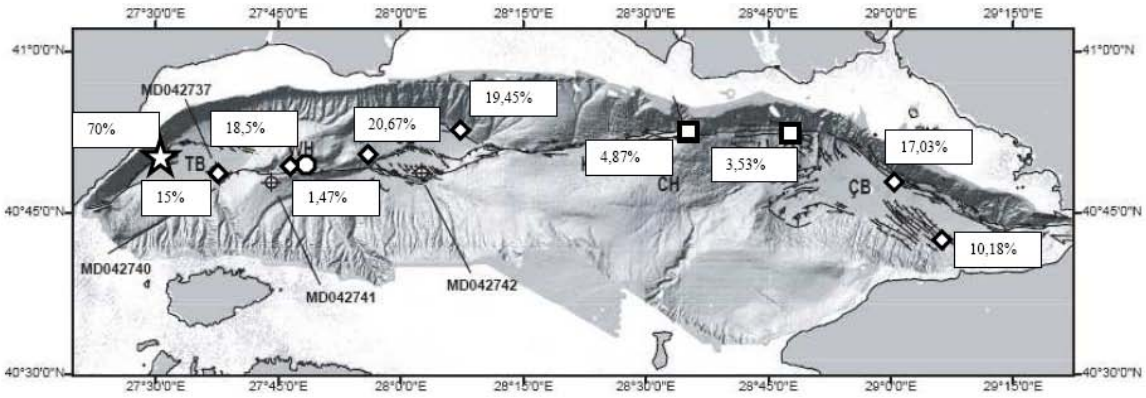

Fig. 2.24. Reproduced from Burnard et al. [2011] in preparation. Helium isotope data analysis for fluids emanating from the North Anatolian Fault and related splays. The percentages correspond to the amount of mantle fluids. TB: Tekirdag Basin. WH: Western High. CH: Central High. ÇB: Çinarcik Basin.

2.4.5. Occurrence of piercement structures

The fact that emissions of thermogenic gases, and, in some places, hydrocarbon seapages have been found on the seafloor in the close vicinity of the main fault, within the fault valley or on top of neighboring anticlines, clearly indicates that there is a direct connection between the sediment surface and the hydrocarbon reservoirs at depth. In addition, high-resolution 3D seismic data reveal a 300 meters wide, chimney-like conduit, rising from below the Western High, up to the site where gas hydrates were sampled at the sea surface. Geochemical analysis

of sediment pore waters suggests that the maximum source temperature inferred for the fluids at this site is 100-150°C (Livio Ruffine, personnal communication, 2010). From Géli (personnal communication) "*Thermal gradients of 50°C/km were measured within the uppermost sediment layers, yielding depths between 6 and 8 km, assuming that the thermal conductivity increases with depth, from 0.8 to 2* $Wm^{-1}K^{-1}$*. Hence, it is likely that fluids from the top of the seismogenic reach (at least locally and episodically) the sediment surface".*

Also from Géli (personnal communication): "*The existence of one chimney at this site, located less than 600 m away from the main fault suggest that shear movement along the fault perturbs the hydrogeological system, likely affecting the precarious equilibrium of over-pressured units, and thereby allowing fluids to be flushed along the fault pathway.*

Piercement structures (such as hydrothermal vent complexes, pockmarks and mud volcanoes) are found in various geological settings but are often associated with faults or other fluid-focussing features. To explain these observations, it has been proposed that the critical fluid pressure required to induce sediment deformation is dramatically reduced when strike-slip faulting is active [Mazzini et al, 2009]. Fluid expulsion then occurs when overpressure at depth is sufficient to fracture the overburden sedimentary units [e.g. Kopf, 2002 and references therein]. When a threshold is reached due to continuous generation of fluids (e.g. water, hydrocarbons, gas) at depth, a system of fractures propagates towards the surface breaching the seal.

Inversely, one can reasonably expect that when the total stress approaches the failure strength immediately prior to an earthquake (reaching 90 to 95 % of the yield stress), the critical overpressure to fracture the overburden layers is approached, causing fluids to escape along the fault. Therefore, in the very specific case of the submerged section of the North Anatolian Fault in the Sea of Marmara, we may have detectable fluid emissions as precursory phenomena prior to earthquakes. This assertion must not be generalized to other geological settings. It may be applied to the Sea of Marmara because of the presence of the main fault hydrocarbon reservoirs, resulting in oil and gas seepages documented on the seafloor".

2.5. Selected sites for multi-parameter seafloor observatories

The Marmara Demonstration Mission (april 2008 to september 2010) was conducted within the EU-funded ESONET programme to characterize the temporal and spatial relations between fluid expulsion, fluid chemistry and seismic activity in the Sea of Marmara and to test the relevance of permanent seafloor observatories for an innovative monitoring of earthquake related hazards, appropriate to the Marmara Sea specific environment.

The following sites were proposed for the implementation of seafloor observatories (Fig. 2.25):

Site 1, entrance of Izmit Gulf. At this site, the principal deformation zone of the North Anatolian Fault is less than some tens of meters wide. In addition, the site is close to the western end of the surface rupture associated with the 1999 Izmit earthquake, where the next earthquake affecting the fault strand towards Istanbul may nucleate.

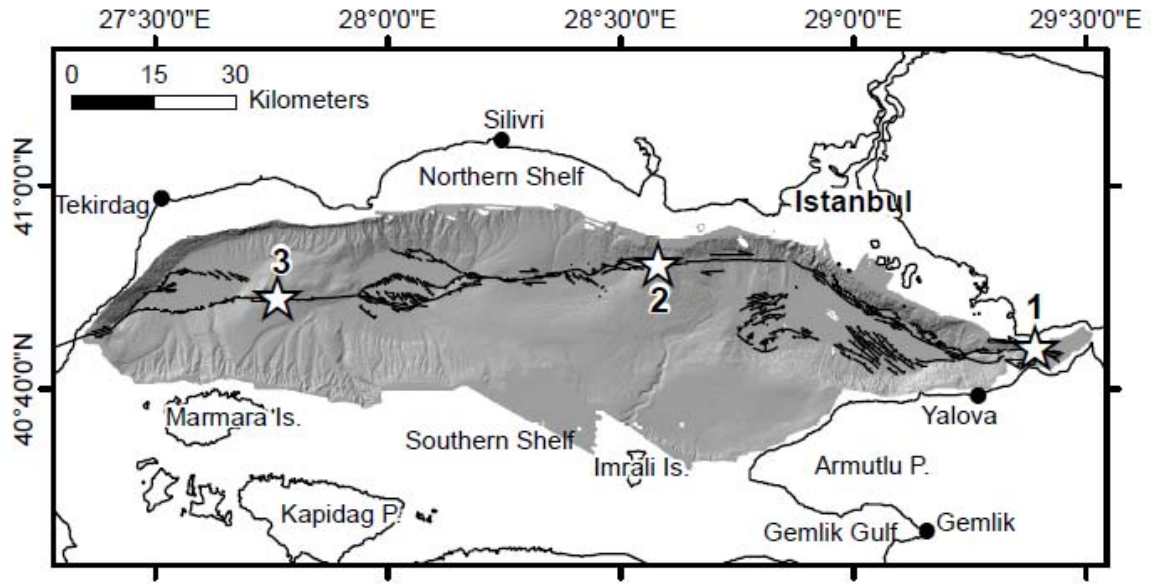

Fig. 2.25. Map of the Sea of Marmara with active faults traces (black lines) after Imren et al. [2001] and Rangin et al. [2004]. The white stars indicate the implementation sites of the future seafloor observatories.

Site 2, on Istanbul-Silivri segment. This site located in the seismic gap immediately south of Istanbul where intense bubbling is observed on a structural High, 1 km south of the main fault trace, while no evidence of fluid expulsion is found on the fault itself. Here, it is of critical importance to monitor micro-seismic activity, with a view to determine if the fault segment is locked or creeping.

Site 3, on the Western High / Gas Hydrates area. This site is located where oil and gas seeps from the Thrace Basin were found and where the connections between the fluid migration conduits and the main fault system were imaged using 3D, High-Resolution seismics.

2.6. MarNaut cruise (May-August, 2007): OBS data analysis

2.6.1. Network configuration and instrument characteristics

During the MarNaut cruise, 8 short-period OBSs were deployed for various periods in the Tekirdag Basin (western part of the Sea of Marmara, Fig. 2.26 and 2.27). Five OBSs, called J, J2, K, L and M, were provided by IFREMER and three by CGG-Veritas, called ARMSS, NEEDLE and SPAN. All OBSs were 3 components velocity sensors with a hydrophone. Except the ARMSS, in which the geophones are in Galperin configuration, all other OBSs have their sensors set orthogonally.

Based on laboratory measurements in similar temperature and pressure conditions, the clock drift was linearly corrected for all instruments. Moreover, as mentioned in *Tary et al.* [2011], *"seismic shots triggered using a GPS-synchronized clock were recorded by the OBSs on May 23 and 24, 2007 providing estimates of the drift of the instruments after 10 days of deployment (between May 14 and May 24). These estimates confirmed that the instruments internal clocks drifted almost linearly during the first 25-days period."*

For the first recording period (14 May – 9 June, 2007), clock drifts were obtained after the instruments recovery. However, OBSs recordings stopped before the second recovery, preventing the measurement of clock drifts for the second period (9 June – 12 September, 2007). Therefore, clock drifts of the second period were corrected by extrapolating clock drifts obtained for the first period. The instruments recording periods are listed in Table 2.1 and their technical characteristics are detailed in Appendix C.

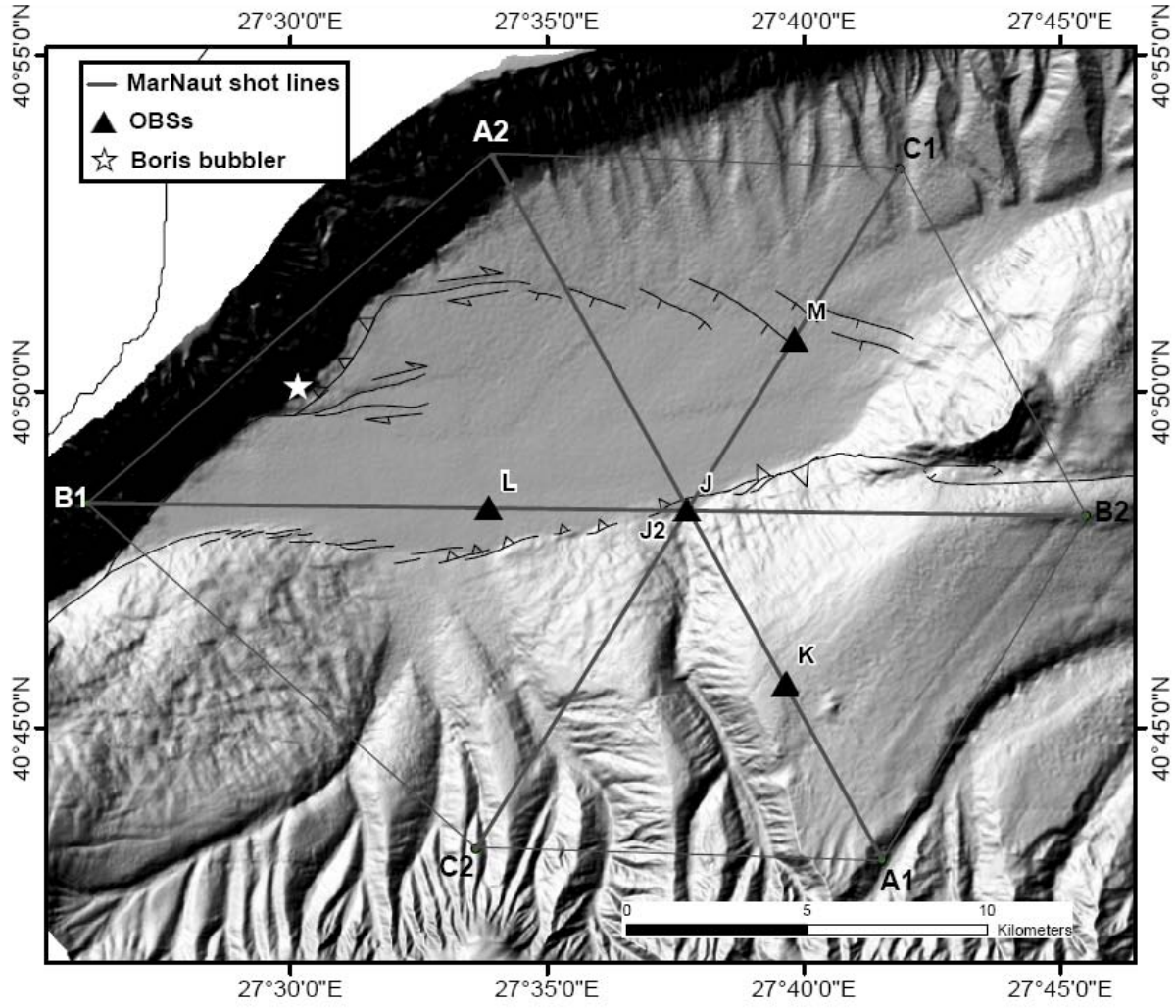

Fig. 2.26. Reproduced from Tary et al. [2011] (presented in section 2.7). Tectonic map of the Tekirdag Basin. The OBSs deployed during the MarNaut cruise are indicated by black triangles. Gray lines show the location of the wide-angle seismic profiles acquired during the MarNaut cruise by the R/V Sismik-1. OBSs J2, ARMSS, NEEDLE and ARMSS are situated close to OBS J (see Fig. 2.27).

During the first period, from May 14 to June 9, 2007, between 4 and 8 OBSs worked simultaneously. However, during the second period, from June 9 to August 28, 2007, only 3 instruments worked. In our configuration, three stations are not enough to locate micro-earthquakes with reasonable uncertainties. Consequently, the recordings of the 2nd period were not used for locating earthquakes.

During the MarNaut cruise, 5 types of OBS have been layed down to the sea floor: OldOBS (J, K, L, and M), MicrOBS (J2), ARMSS, SPAN, and NEEDLE. Each one is equipped with different coupling devices. Thereby, an inter-comparison of OBSs response to known solicitations as well as a noise analysis has been carried out to determine the performance of each instrument (Appendix C).

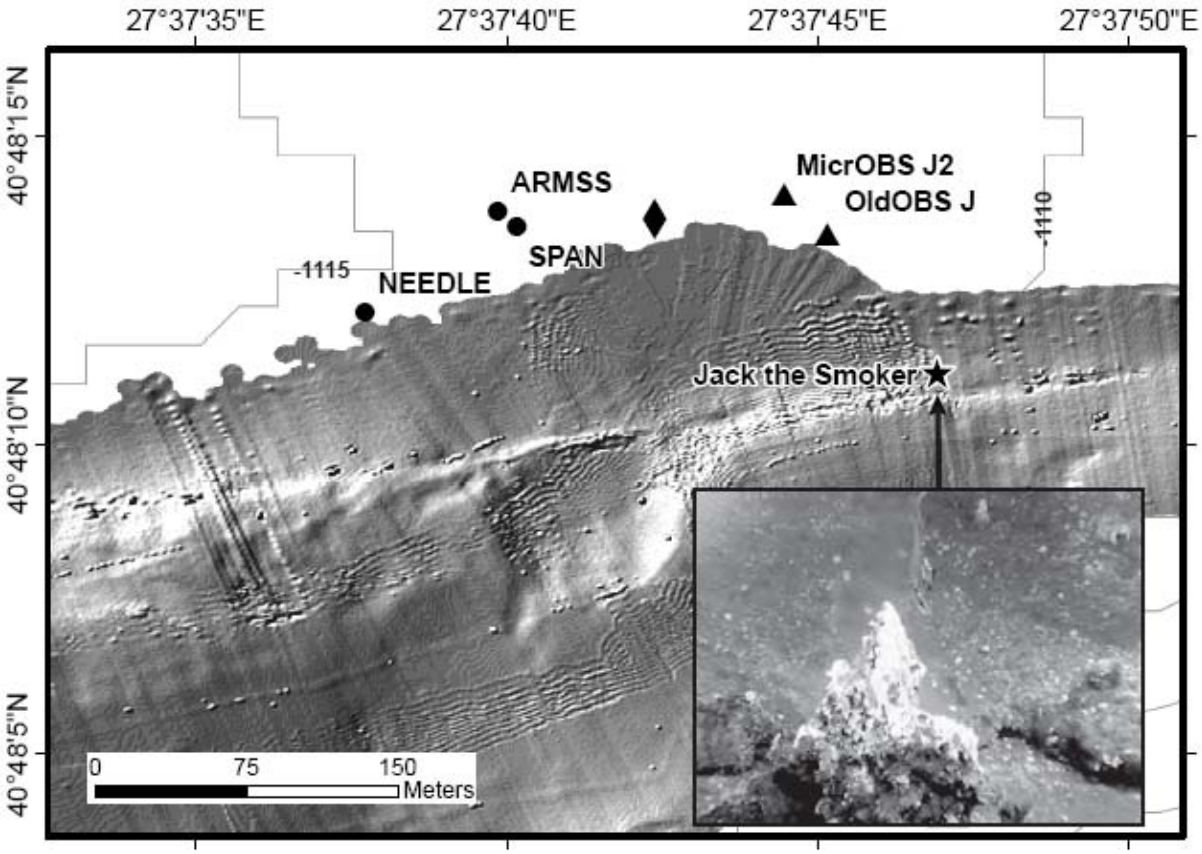

Fig. 2.27. Reproduced from Tary et al. [2011], submitted (presented in section 2.8.2). Zoom in the area close to OBS J. Microbathymetric data were acquired during the MARMARASCARPS cruise in 2002 by the R.O.V. Victor. OBS provided by IFREMER and CGG-Veritas are indicated by black triangles and black dots respectively. The black star shows the location of "Jack the Smoker" site where fresh water escapes from the seafloor through carbonate chimneys. The seismic shot used for OBSs amplitude inter-calibration is indicated by the black diamond (Fig. 2.28).

Stations	Longitude (deg)	Latitude (deg)	Depth (m)	Recording period used	F_0 (Hz)	Fs(Hz)
J	E 27.62921	N 40.80372	1112	14 May - 30 Aug. 2007	4.5	250
J2	E 27.62902	N 40.80390	1112	22 May - 28 May 2007	4.5	250
K	E 27.6608	N 40.7613	546	14 May - 19 Aug. 2007	4.5	250
L	E 27.5645	N 40.8044	1132	14 May - 09 June 2007	4.5	250
M	E 27.6637	N 40.8466	1110	14 May - 26 Aug. 2007	4.5	250
ARMSS	E 27.62774	N 40.80382	1115	14 May - 09 June 2007	14	500
SPAN	E 27.62782	N 40.80376	1117	14 May - 28 May 2007	4.5	500
NEEDLE	E 27.62714	N 40.80337	1115	14 May - 28 May 2007	4.5	500

Table 2.1. OBS position, main technical characteristics and recording period. F_0: geophones natural frequency; Fs: sampling frequency.

2.6.2. Tentative calibration for hydrophones and geophones

Each OBS type has a specific descaling factor to convert digital (counts) into physical (µm/s or Pa) amplitudes, which depends on the ADC coefficient (counts to volts), on the pre-amplifier and amplifier gains, and geophone or hydrophone sensibility. Unfortunately, the descaling factors of the different instruments are not known, except for the hydrophone of the MicrOBS and for the geophones of the OldOBS, which will be used hereafter as references. To compare the amplitudes of the signals recorded by the different instruments, we have used seismic shots fired with a surface vessel above the OBSs (Fig. 2.27). Conversion factors were derived, assuming that the amplitude of the first P-arrival peak in response to one given shot is the same for all different OBSs (Fig. 2.28, Table 2.2)

	Hydrophone	Geophone (Z)
OldOBS (J, K, L, M)	4.822E-06	2.286E-04
MicrOBS (J2)	5.813E-06	2.125E-04
ARMSS	-7.170E-05	1.058E-05
NEEDLE	2.847E-05	1.996E-03
SPAN	No signal	2.870E-04

Table 2.2. Conversion factors for vertical geophones (counts to µm/s) and hydrophones (counts to Pa) of all OBSs.

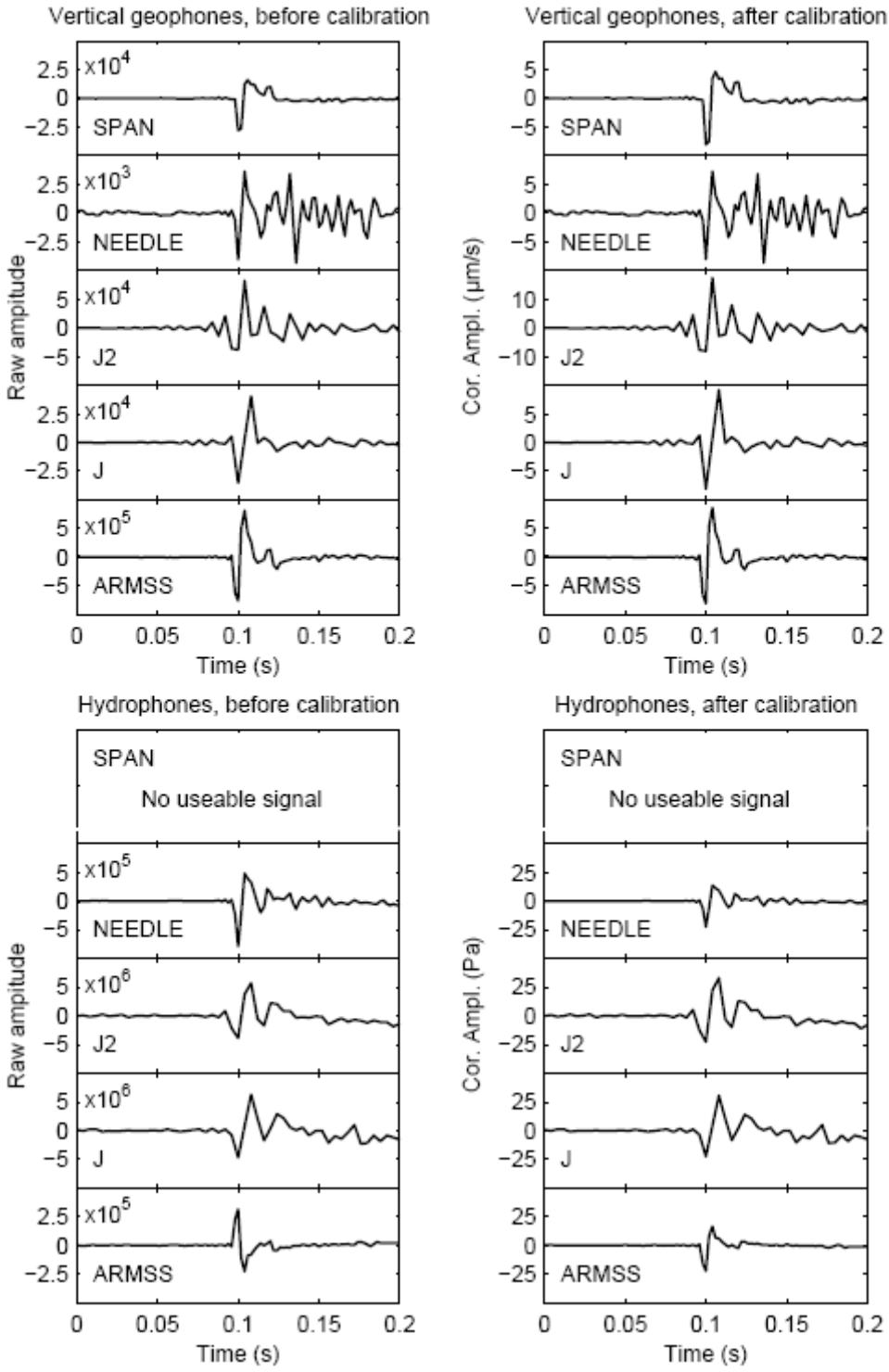

Fig. 2.28. Recordings of a seismic shot (May 24, 2007, 07:04:21.6) by the 5 OBSs before and after inter-calibration (see Fig. 2.27 for locations). Despite the resonance of OBS J2 geophones, the seismic shot amplitudes on OBSs J2 and J are in the same order of magnitude. Cor. Ampl., Corrected amplitudes.

2.6.3. Microseismicity location

2.6.3.1. Detection and location programs

- Micro-earthquakes detection

The dataset was first converted from continuous SAC files to SEG-2 files of 10 minutes including all the OBSs. The events were then detected using dedicated software developed by Magnitude (Sainte Tulle, France), a company specialized in microseismicity monitoring in relation with the petroleum and mining industries (http://www.magnitude-geo.com/).

The event detection procedure follows these steps:

(1) Events detection with seiscreen program (©Magnitude). The detection algorithm is based on the ratio between the short-term and long-term average convolved by chirplets (sinusoids of different waveforms and frequency contents, [*Bardainne*, 2005]), the duration of events, and the number of stations. In our case, a pick is made if the STA/LTA ratio exceeds 20 at a minimum of 3 stations and at least 5 seconds after the previous pick (Fig. 2.29).

The aim of the STA/LTA ratio is to detect sudden changes in the signal amplitude. This technique computes the ratio between the mean for a short window (STA) and the mean for a long window (LTA). A wave is detected when the ratio exceeds a given threshold.
To improve the detection program efficiency, the signal is decomposed in a sum of chirplets before the STA/LTA ratio computation. As most of the earthquakes energy is below 30 Hz (Fig. 2.30), the triggering has been made over the frequency bandwidth 7 – 50 Hz.

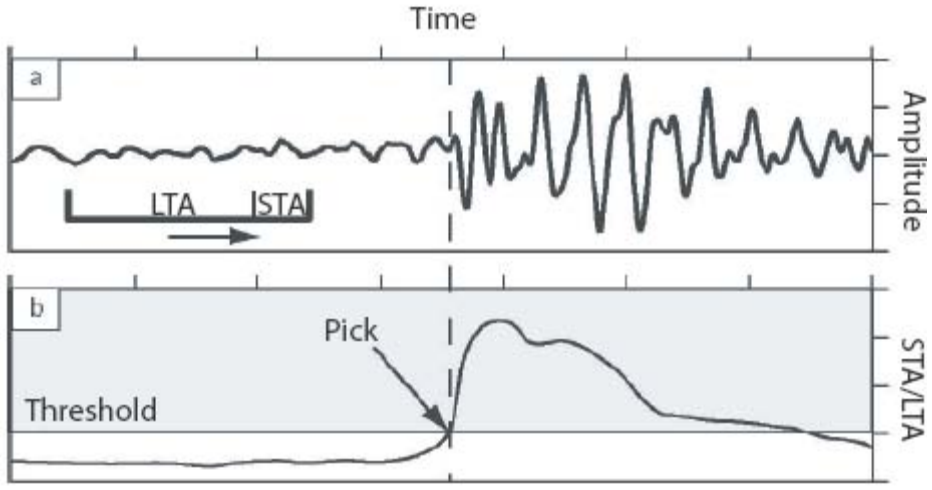

Fig. 2.29. Modified from Bardainne [2005]. STA/LTA ratio computation. (a) Seismograms with the 2 windows STA and LTA. (b) STA/LTA ratio, a picks is made when the ratio exceeds a given threshold.

(2) Manually inspect all detections and picked arrivals, assigning a subjective uncertainty to each pick. P waves picks uncertainties are included between 0.012 and 0.99 with a mean of 0.31, and S waves picks uncertainties are included between 0.03 and 1.56 with a mean of 0.4. Unclear events or events with picks for only one phase type (P or S) have been removed.

For events with a low signal-to-noise ratio, a band pass filter (4 – 25 Hz) was applied. Sometimes the waveforms were too litigious to be picked independently. In some cases, a "master" event with clear picks and very similar waveforms (i.e. with the same source and ray path) was used to remove the ambiguity and pick at the litigious station(s);

Based on the above, 270 events have been picked, among which 110 events for the first period (May 14 to June 9, 2007).

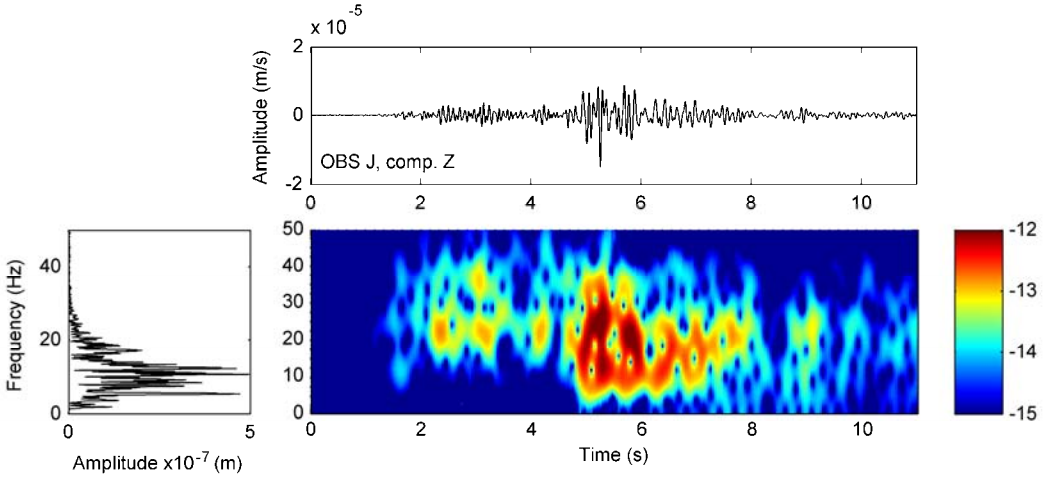

Fig. 2.30. Top: Micro-earthquake recorded by OBS J (Component Z) on 14 May, 2007 at 20:50:35 (M_w 2.9). Bottom left: micro-earthquake frequency content. Bottom right: temporal evolution of the micro-earthquake frequency content.

- Location programs

With P and S waves picks, several programs can be used to solve the earthquake location problem. We have therefore compared different softwares, thanks particularly to Mustafa Çomoğlu, working for the KOERI (Kandilli Observatory and Earthquake Institute). The day-to-day earthquakes location in Turkey is done by the KOERI with the program zSacWin based on HYPO-71 [*Lee and Lahr*, 1972]. This program minimizes iteratively the residues between calculated and observed travel times.

Given an *a priori* hypocenter and a 1D velocity model, the algorithm follows the steepest slope of decreasing residues. This is the linearized least-squares solution to the earthquake location problem. However, the parameters space in the location problem is not linear. Thereby, this method is very sensitive to local minima and is highly dependent on the *a priori* hypocenter. HYPO-71 does not take into account the station elevation. This obviously introduces time shifts in the calculated travel times. *Lienert et al.* [1986] showed that the capability of the location algorithm to locate shallow events is enhanced when stations elevations are included.

To avoid those problems, LOC3D software has been used [*Bardainne and Gaucher*, 2010]. It takes into account the stations elevation and uses a non-linear algorithm. It follows the

probabilistic formulation of inversion presented in *Tarantola and Valette* [1982]. First the program computes the travel times for all x-y-z nodes using a finite-difference code based on the 3D Eikonal equation developed by *Podvin and Lecomte* [1991].

Then LOC3D proceeds to a probability grid search with a 3D or a 1D velocity model, using P and S waves arrival times and/or wave polarisation. The hypocenter is positioned on the local probability maximum. As probability density functions are calculated for all grid points, local minima are avoided. Since probability distributions obtained are rarely Gaussian, they cannot be approximated by an ellipsoid (Fig. 2.31). The uncertainties computed by LOC3D correspond to 68 % of the probability integral.

The wave polarization has not been used for the location owing to the lack of information about the orientation of OBSs horizontal components. Therefore, earthquakes location was performed using only P and S waves picks.

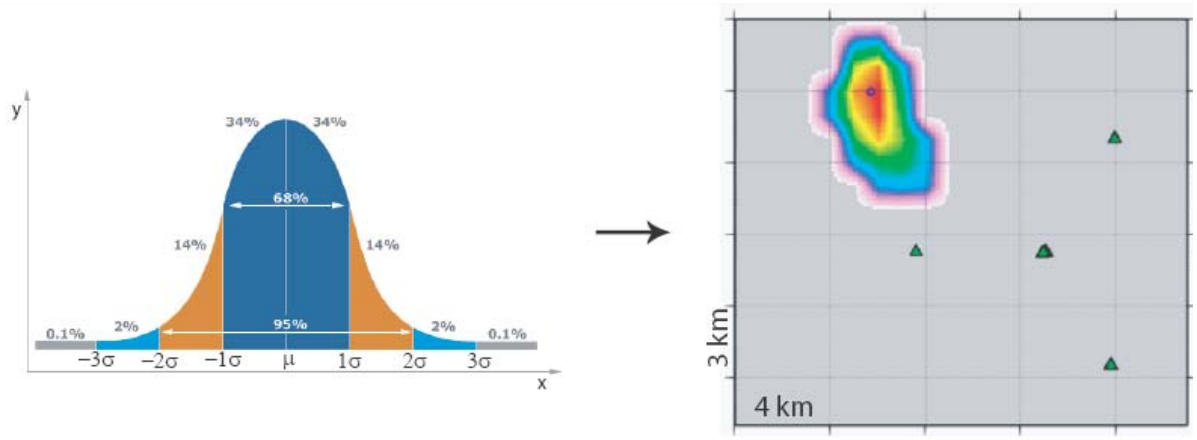

Fig. 2.31. (Left) Normal distribution of a parameter x with the 1, 2 and 3 standard deviations (σ). (Right) A located event with its uncertainty. The red and white-pink colours correspond to the maximum of probability and the 68 % contour of the probability integral, respectively. It can be seen that the shape of the probability distribution is not Gaussian.

- Micro-earthquakes magnitude

As specified by *Lee and Stewart* [1981] for microseismicity, the magnitude of the micro-earthquakes has been determined by the formula,

$$M = \frac{2}{3}\log(M_0) - 10.7 .$$

Following *Brune* [1970], the seismic moment M_0 (N.m) can be estimated from the source and ray path parameters:

$$M_0 = \frac{4\pi\rho\Omega_0 R\beta^3}{0.85}$$

With:

ρ: earth density (2700 kg/m^3),

Ω_0: long period limit of the shear wave displacement spectrum (m.s; Fig. 2.32),

R: distance (m),

β: S-wave velocity (3000 m/s),

0.85 takes into account an average radiation pattern factor.

- Magnitude detection threshold

Out of the 110 micro-earthquakes detected during the first period (14 May - 9 June, 2007), P and S waves were picked at a minimum of 4 stations only for 30 events. Their respective magnitudes range from 1.5 to 2.9. During the same period, the KOERI located 8 earthquakes with magnitudes between 2.1 and 3 in the same area (Fig. 2.33). This highlights the ability of OBSs to lower the magnitude detection threshold in the Sea of Marmara.

In Fig. 2.34 is shown the differences between the locations made by the KOERI using land stations only, and our best locations using seabottom stations only (see section 2.6.3.2: a tailored 1D model was used with LOC3D software). For the three examples shown, the distance between KOERI and our locations ranges from ~5 to ~10 km. This result addresses the difficult question on the accuracy of earthquake location in the Sea of Marmara. Indeed, relatively to land stations, OBSs are generally closer to micro-earthquakes, involving a gain in accuracy. However, seismometers networks onshore oppose their numerous stations providing good azimuth coverage of seismic events to the proximity and the limited size of seabottom networks.

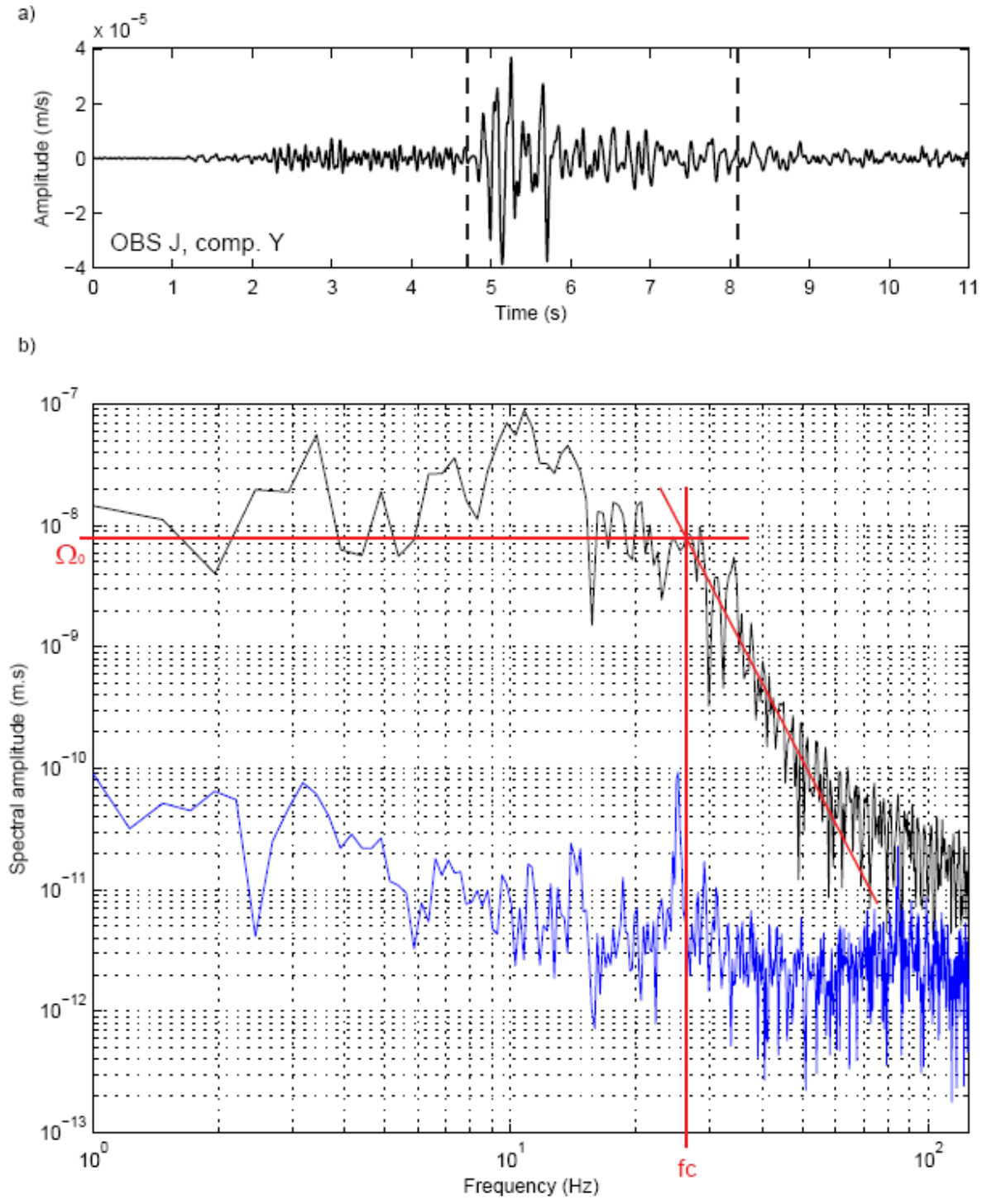

Fig. 2.32. a) Seismogram of a micro-earthquake recorded by OBS J (component Y) on 14 May 2007 (M_w 2.9). The part of the seismogram used to calculate the S-wave displacement spectrum presented in b) is included between the two dashed lines. b) S-wave displacement spectrum of the micro-earthquake shown in a) (black line). The blue line shows the noise displacement spectrum (over 6 s taken before the micro-earthquake). Ω_0: long period limit of the S-wave displacement spectrum; fc: S-wave spectrum corner frequency.

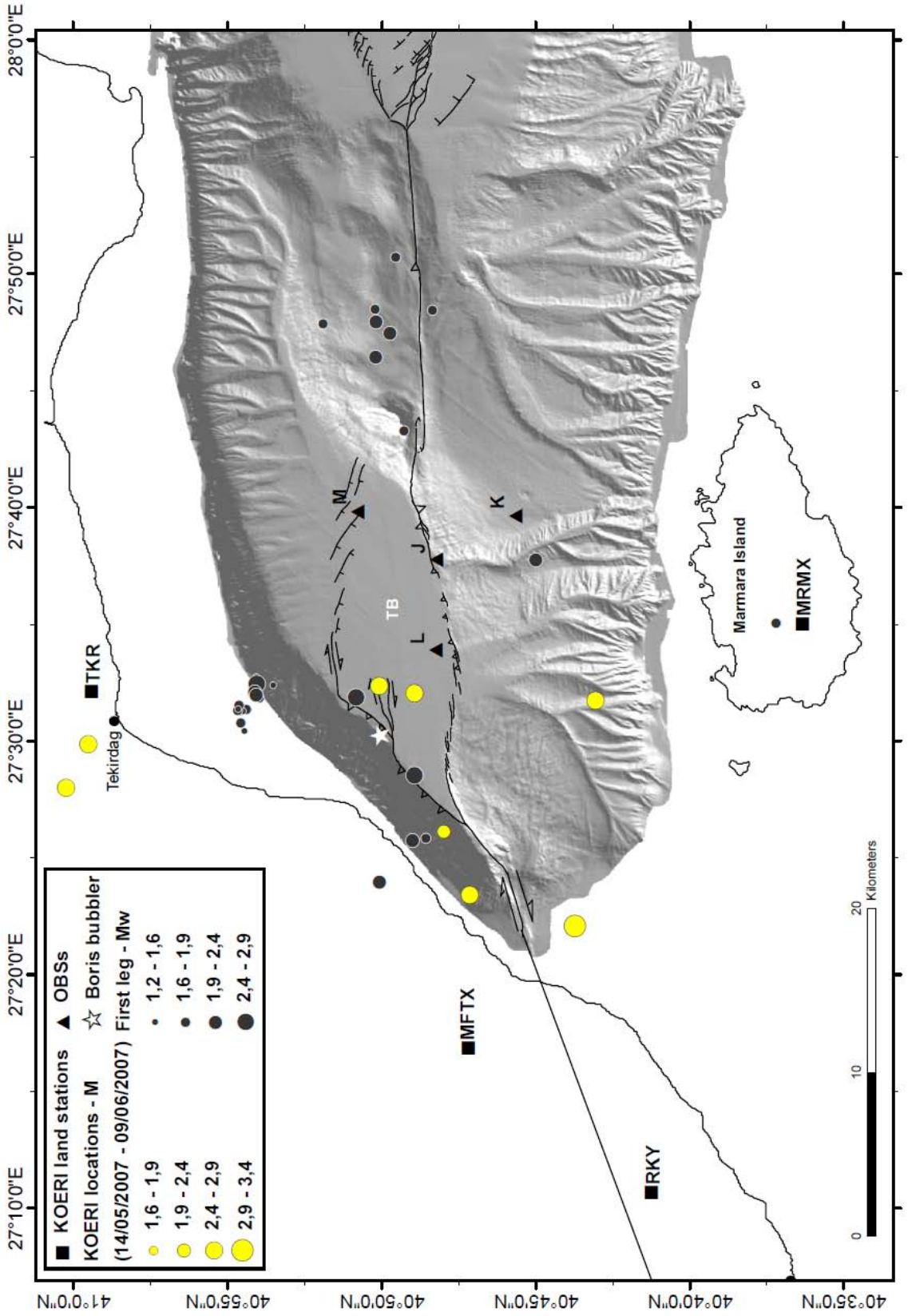

Fig. 2.33. Microseismicity distribution in the Tekirdag Basin (TB) during the period 14 May – 09 June 2007. This figure illustrates the ability of OBSs to lower the detection threshold in the Sea of Marmara. The location of the selected earthquakes using LOC3D and our composite 1D model are indicated by gray dots. Locations from the KOERI catalogue are indicated by yellow dots. The dots size depends on the magnitude. Boris's bubbler site is shown by the white star.

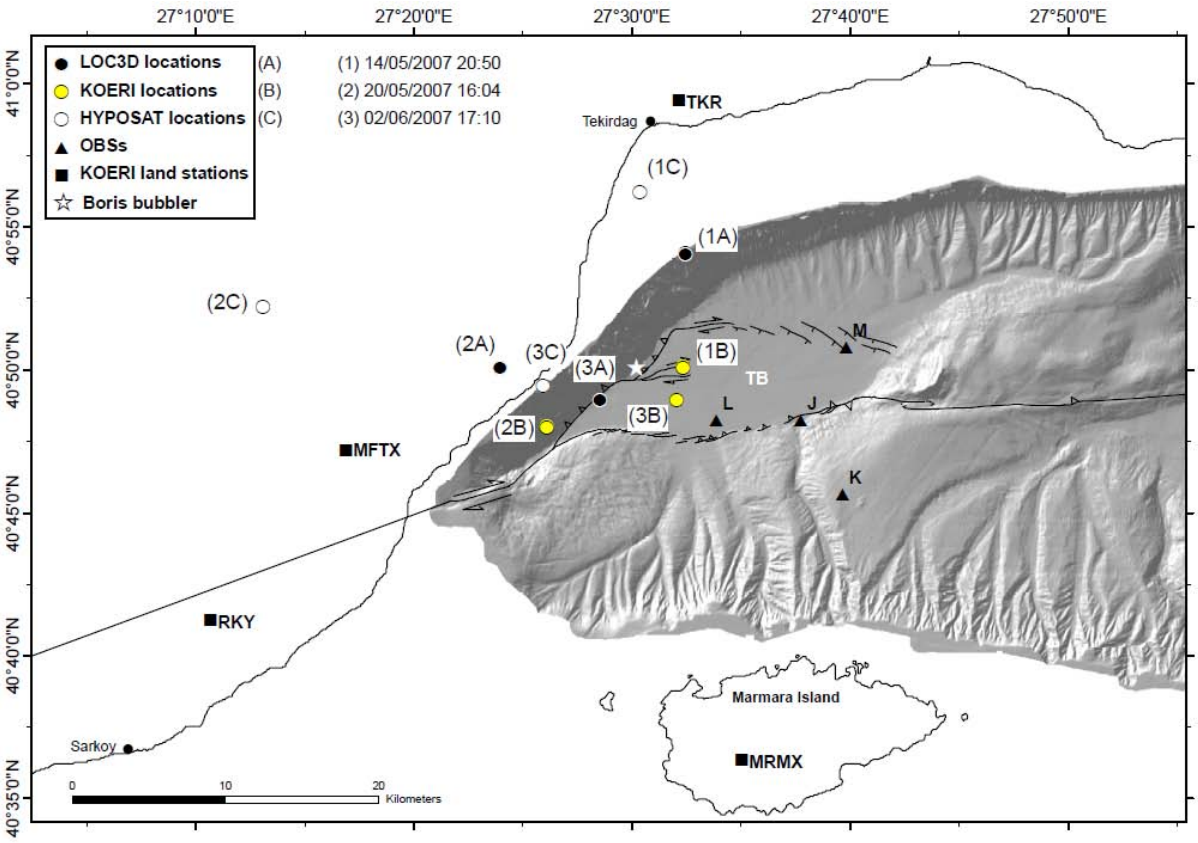

Fig. 2.34. Comparison between locations of 3 micro-earthquakes. Locations from the KOERI catalogue, obtained using land stations data, are indicated by yellow dots and labelled 1B, 2B, 3B. Our locations, obtained using only seabottom stations data, are shown by black dots and labelled 1A, 2A, 3A. HYPOSAT locations (white dots) performed using seabottom and land stations data are also indicated and labelled 1C, 2C, 3C (see section 2.6.3.3).

2.6.3.2. Velocity models

Previous workers used three different 1D velocity models for earthquake location in the Sea of Marmara.

(1) First the NEMC model [*Kalafat et al.,* 1987], used by the KOERI for day-to-day location, is a standard model for the whole Turkey (Fig. 2.35). This very simple model does not consider the specific velocity structure of the Sea of Marmara region due to the presence of deep troughs filled by low-velocity sediments.

(2) The Gürbüz 1D velocity model [*Gürbüz et al.,* 2000; *Sato et al.,* 2004] has been obtained by the simultaneous inversion (VELEST) of hypocenters (between October and

December 1995) and velocity structure. Station corrections were also calculated. The *a priori* velocity model came from an earlier refraction data modelling [*Gürbüz et al.*, 1992]. This model has been performed specifically for the Sea of Marmara region. It is more accurate than the NEMC model and has a lower supracrustal velocity. However, like the NEMC model, this model is adapted to land networks.

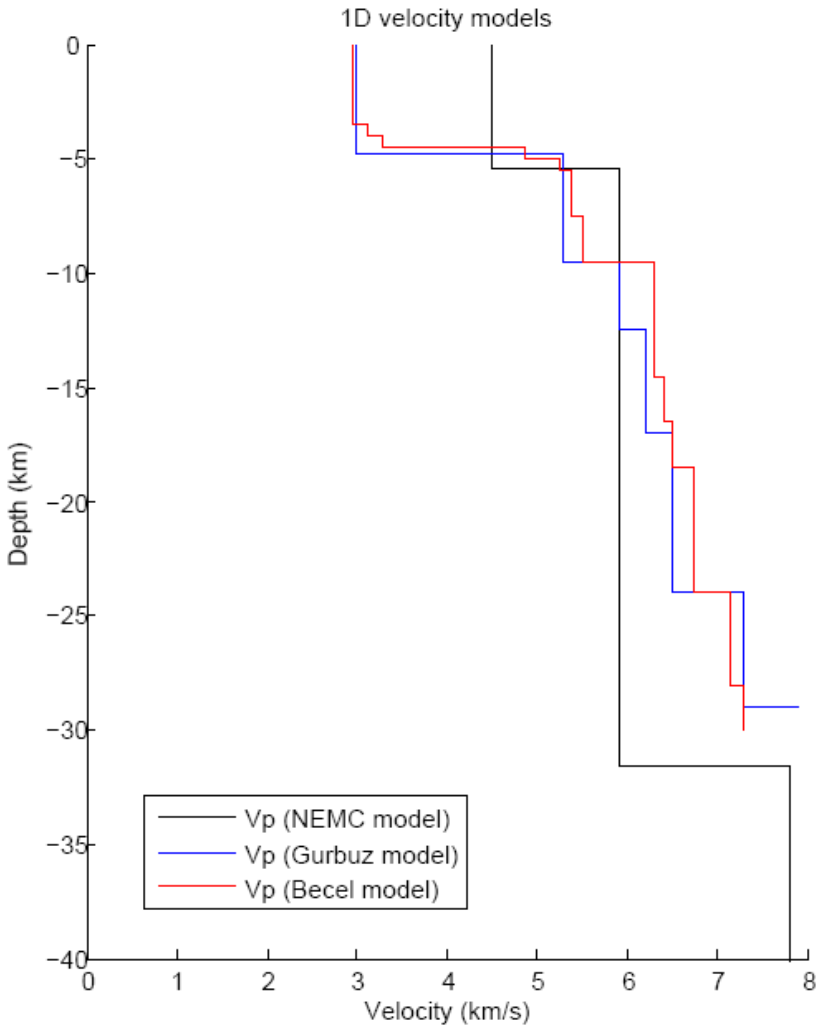

Fig. 2.35. Three 1D velocity models for the region of the Sea of Marmara, in black the NEMC model [Kalafat et al., 1987], in blue the Gürbüz model [Gürbüz et al., 2000], and in red the model of Bécel [2006].

(3) The model of *Bécel* [2006] is based on the simultaneous 1D inversion of hypocenters, seismic shots and velocity structure (Seismarmara cruise in 2001). The *a priori* velocity model is the model of *Gürbüz et al.* [2000]. Both P and S waves velocity structure have been inversed. The Vp/Vs ratio is about 1.79 and almost constant with depth. Therefore, in the present study a constant Vp/Vs ratio of 1.79 is assumed.

While this model has the advantage to take into account the specific structure of the Sea of Marmara, the averaged velocity structure of the upper 5 km does not correspond to the one in sedimentary basins. Therefore, wide-angle profiles acquired during the MarNaut cruise by the R/V Sismik-1 in the Tekirdag Basin were modelled to obtain its velocity structure in the upper 4 km (see Appendix A in *Tary et al.* [2011], presented in section 2.7). Finally, the deep velocity structure of *Bécel* [2006], and our result on the superficial structure were combined to a "composite" 1D model (Fig. 2.36). This "composite" model was used in the present study for locating micro-earthquakes within the Sea of Marmara.

The influence of the velocity model in the micro-seismicity location is shown in Fig. 2.37. Selected earthquakes were located based on OBS data only with the program LOC3D, using two different 1D velocity models: the NEMC velocity model, and our "composite" velocity model. Relatively to the locations using the composite velocity model (gray dots), the locations using the NEMC model (black squares) are pushed away from the OBS network (up to 10-15 km). This arises from the fact that the NEMC model has higher velocities than the composite model in the upper layers. Thus, at the scale of the Tekirdag Basin, major errors can be introduced by the velocity model.

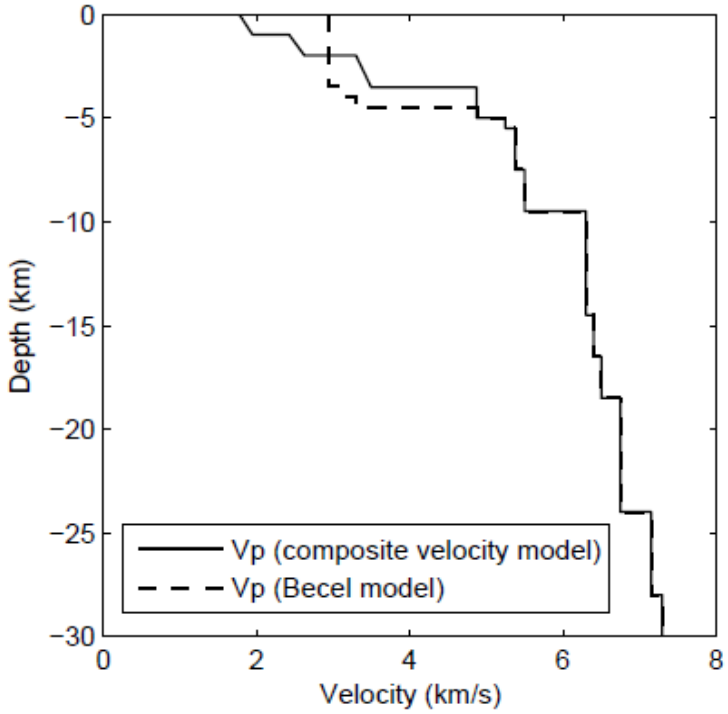

Fig. 2.36. Composite 1D velocity model (solid black line) in the upper 30 km of the Tekirdag Basin. The velocity model of Bécel [2006] is indicated by the dashed black line.

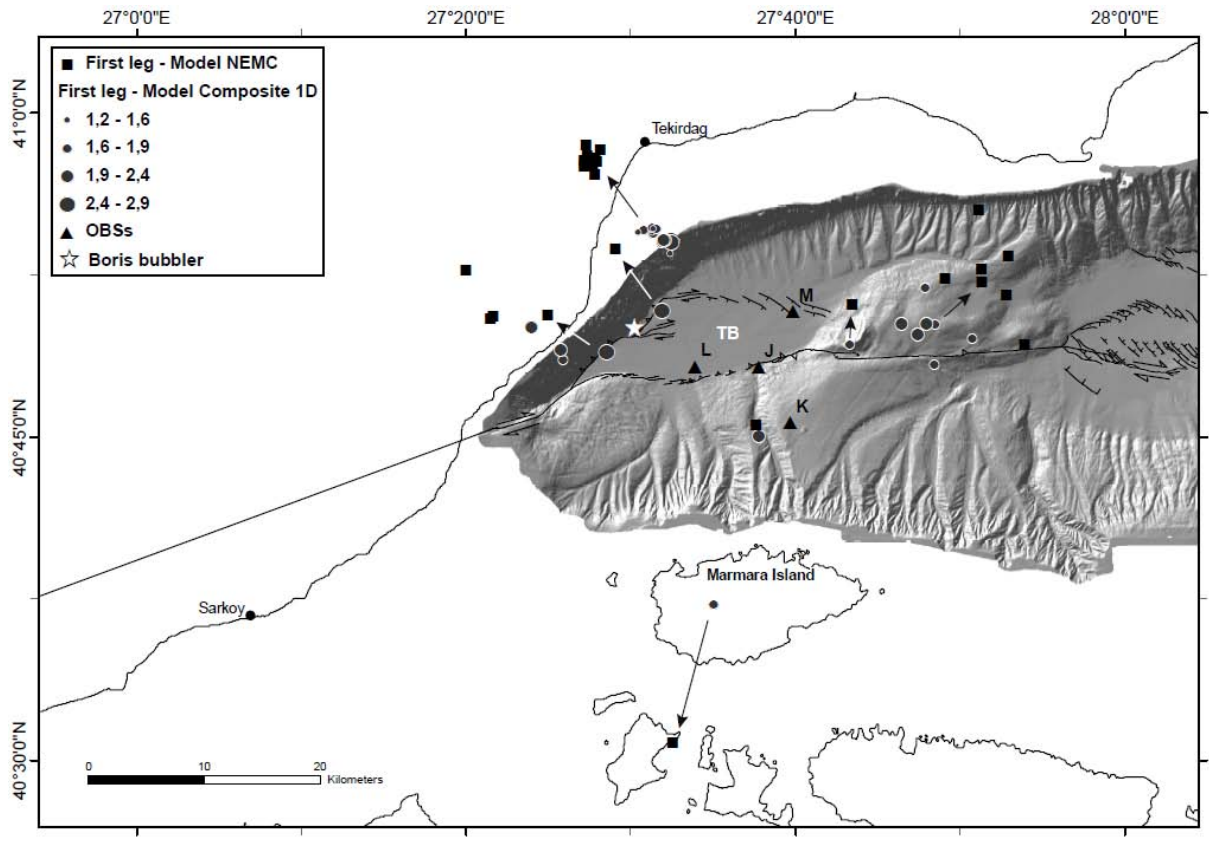

Fig. 2.37. Influence of the velocity model in hypocenter determination. Selected earthquakes have been located based on OBS data, using either the composite 1D model (gray dots), or the NEMC model (black squares). The locations have been performed using the same program, LOC3D, and the same P and S waves picks. Black triangles show the OBSs position. Boris's bubbler site is indicated by the white star. TB: Tekirdag Basin.

2.6.3.3. Constitency problems when merging land and sea networks

- Microseismicity location

To improve the location precision, we tried to combine the datasets coming from land (KOERI) and sea networks (Fig. 2.38). However, velocity structures below land and sea stations are greatly different, and inconsistencies in travel times have frequently been observed. Fig. 2.39 represents a micro-earthquake strong enough to be recorded by the two networks. It can be seen that P waves arrive sooner at sea stations (J, K, L and M) than at land station MRMX. Typically, this indicates that the micro-earthquake is closer to the OBSs than to the land station. On the other hand, the difference between S and P waves arrival times, proportional to the distance source-receiver, is larger for seabottom stations, indicating that

the land station is closer to the micro-earthquake hypocenter. This incompatibility arises due to the wave propagation in low-velocity sediments in the Tekirdag Basin, which involves a time delay at seabottom stations.

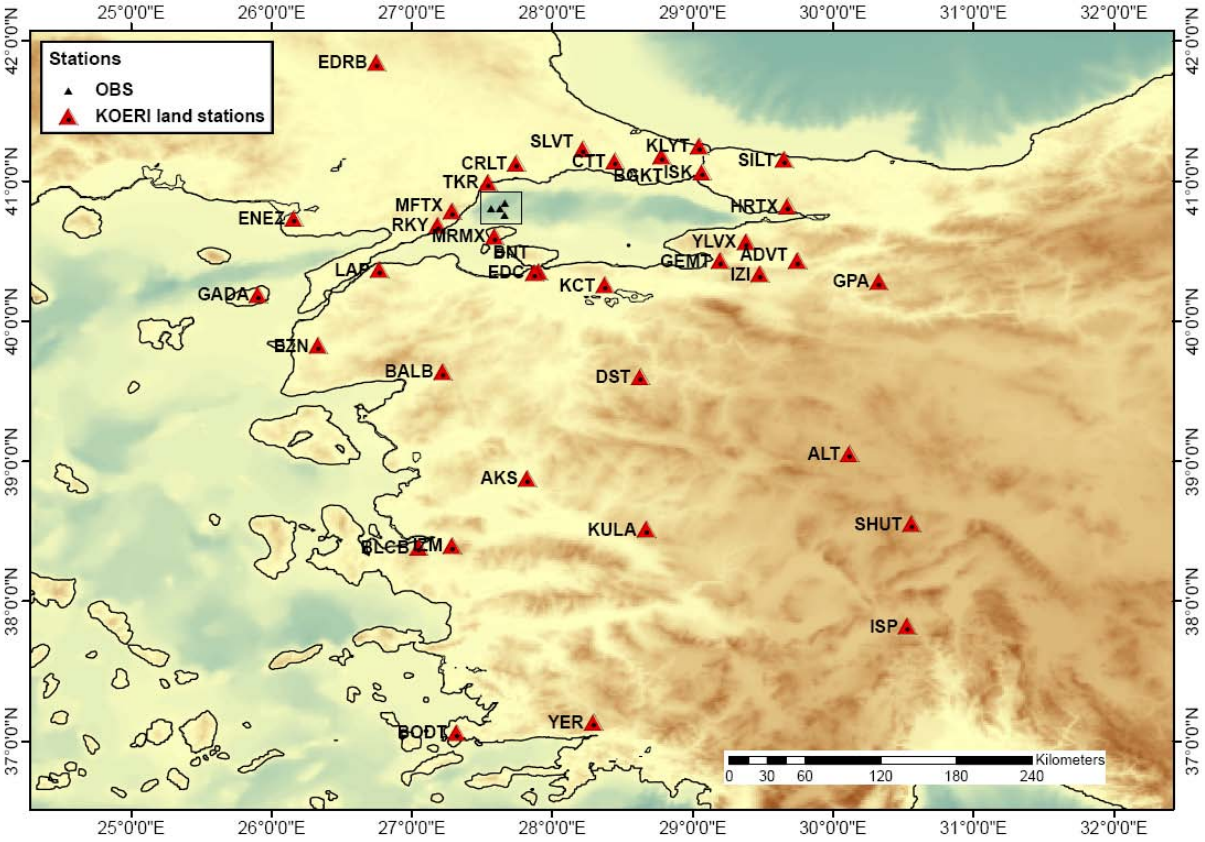

Fig. 2.38. Location of KOERI land stations (red triangles) in western Turkey and MarNaut OBSs (black triangles).

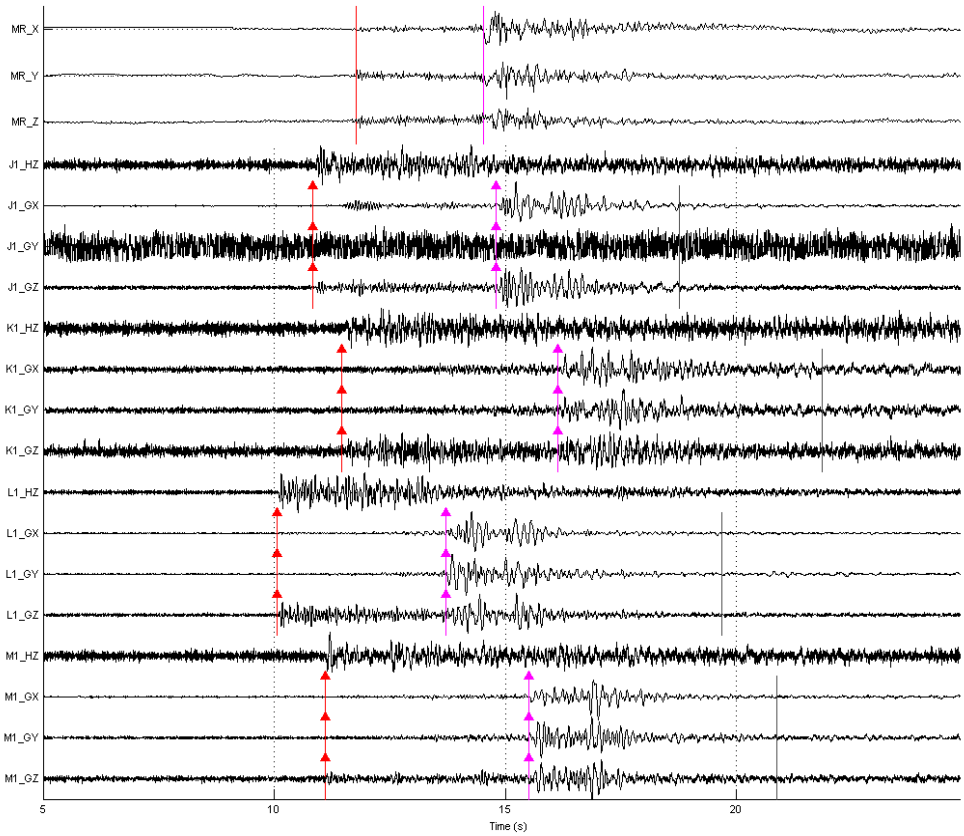

Fig. 2.39. Seismograms of MRMX (MR_) land station, and OBS J, K, L, M for the same event (origin time: 01/06/2007 12:40:32). X and Y are horizontal components, Z is vertical and H is hydrophone. Seismograms are not filtered. P (red lines) and S (purple lines) wave arrivals are indicated. Vertical black lines indicate the end of the time windows used for displacement spectrum and magnitude calculations. Note that the P waves are clearly visible on the hydrophone, which is very helpful for phase picking.

Therefore, with a 1D velocity model and a unique Vp/Vs ratio, we do not recommend a joint location using land and seabottom stations because it introduces important location errors. In large networks, velocity structure heterogeneities can be compensated by the removal of stations with large travel-times residues. When we deal with 3D velocity structure heterogeneities, stations corrections would solve only partly this problem, as they are dependent on the position of the micro-earthquakes.

A 3D velocity model or several 1D velocity models could be used to combine the land and seabottom datasets in a joint location. The 2nd solution was tested, as no 3D velocity model of the Sea of Marmara was available when we performed the micro-earthquakes location. LOC3D does not allow to use different 1D models for land and seabottom stations. Therefore, we instead used HYPOSAT, which assigns a 1D local velocity model below every single

epicenter [*Schweitzer*, 2001]. The local model is assigned to the stations near the epicenter, while a global model is assigned to the stations located away from the epicenter (Fig. 2.40). The size of the area around the epicenter, where the local model is prescribed, is defined by the user. The algorithm used in HYPOSAT is similar to the one used in HYPO-71 (HYPOSAT takes into account the station elevation, while HYPO-71 does not). HYPOSAT solves the non-linear problem of earthquake location with a stepwise linearized least-squares algorithm and needs *a priori* locations. Depending on the locations reliability, either LOC3D or KOERI locations have been used as *a priori* locations. For events that were not located by the KOERI or events located by LOC3D with uncertainties inferior to 10 km, we used LOC3D locations as *a priori* locations. In the other cases, mainly for events situated too far from the OBS network, we used KOERI locations as *a priori* locations.

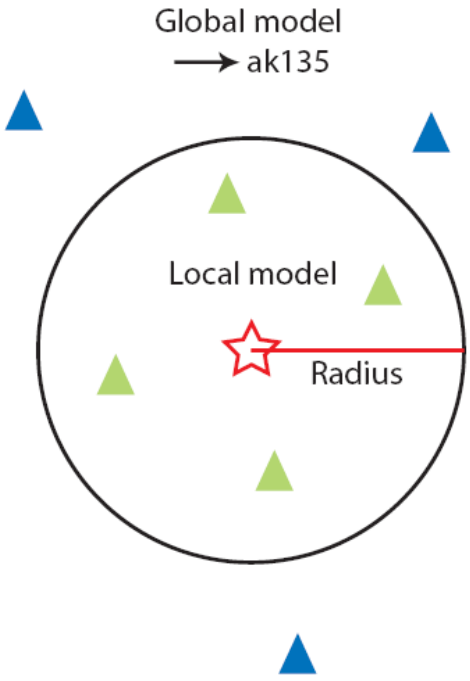

Fig. 2.40. Sketch illustrating how velocity models are prescribed in HYPOSAT. The disk defined by the epicenter (red star) and the radius corresponds to the influence of the local model. The global (ak135, [Kennet et al., 1995]) and local models are assigned to the stations located outside the circle (blue triangles) and inside the circle (green triangles), respectively.

Three different local models have been used. The composite 1D model has been used for the events located in the Tekirdag Basin and its vicinity. Either the NEMC or Gürbüz models have been assigned to epicenters situated close to the land stations. The global model, called ak135 [*Kennet et al.*, 1995] (Table 2.3), corresponds to the velocity structure of an average continental crust. Elevation corrections are applied at each OBS.

Finally, 67 events were located with uncertainties ranging from 0.5 to 8 km horizontally (mean 1.6 km), and from 0.5 and 7 km in depth (mean 2.4 km). The RMS range from 0.03 to 0.65 s, with a mean of 0.2 s (Fig. 2.41). These events were located using 3 or 4 OBSs and between 1 and 37 land stations. Among those 67 events, 25 were recorded only by OBSs, and thus located using only OBSs. In Fig. 2.42 are shown the HYPOSAT locations of these 25 events together with their locations performed by LOC3D. As the 25 events are close enough to the OBS network, locations were all performed using the same velocity model, i. e. the "composite" 1D model. In average, the distance between HYPOSAT and LOC3D locations is about 3.8 km. This shows that the location software has significant influence on the locations.

The other 42 events were located using OBSs and land stations. The resulting locations are generally very different (with an offset ranging from 1 and 47 km) from the *a priori* locations. These results clearly show the influence of, by order of consequence: 1) the velocity structure; 2) merging data from land and seabottom stations; and 3) the location software.

Depth (Km)	P wave velocity (km/s)	S wave velocity (km/s)
0.0	5.800	3.460
20.0	6.500	3.850
35.0	8.040	4.480
77.5	8.045	4.490
120.0	8.050	4.500

Table 2.3. Ak135 model [Kennet et al., 1995] corresponding to HYPOSAT global model.

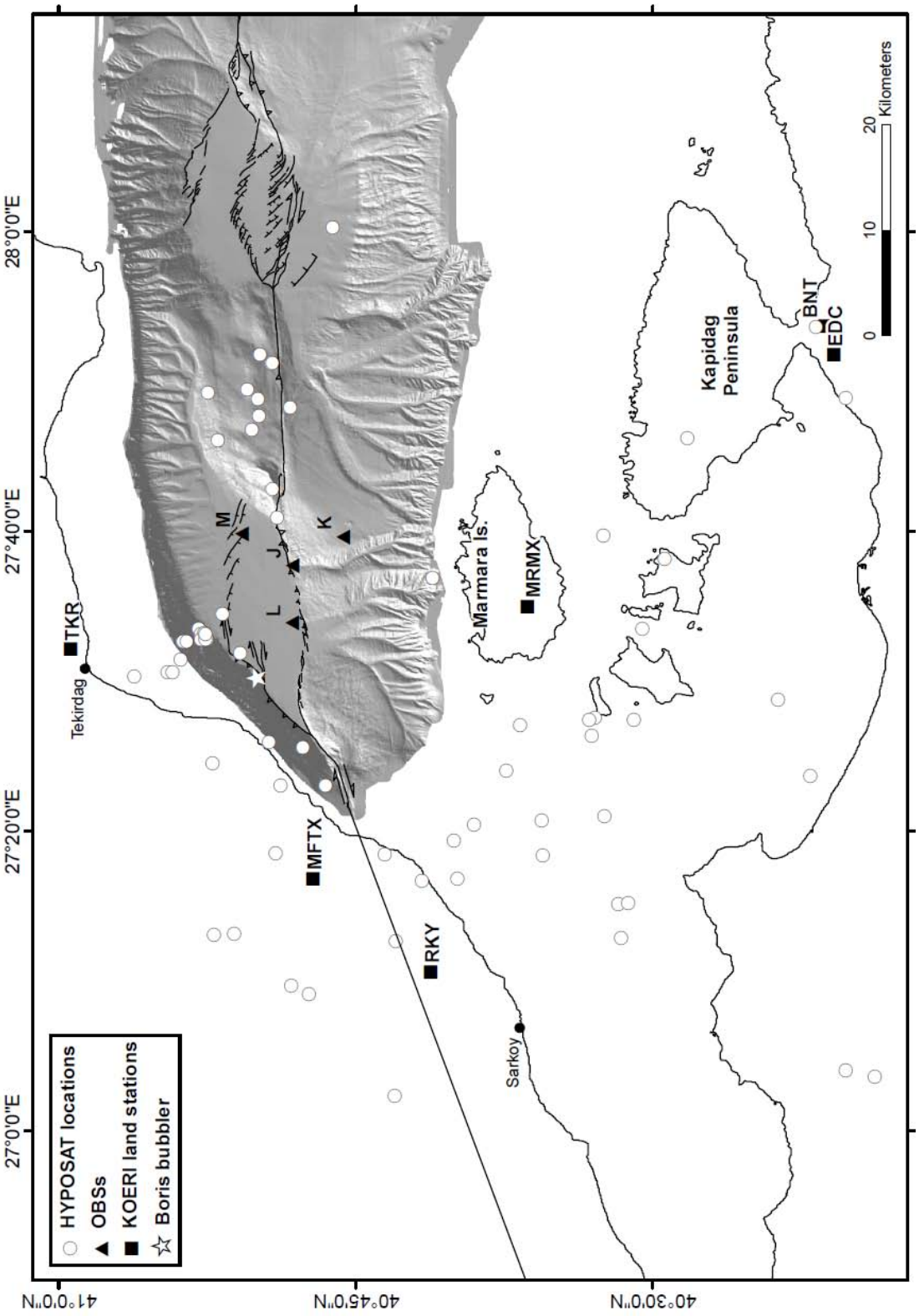

Fig. 2.41. All HYPOSAT locations (white dots) obtained during the complete recording period (14 May – 31 August, 2007) using seabottom and land stations. The black triangles and black squares indicate the OBSs and KOERI land stations, respectively. TB: Tekirdag Basin; Is: Island.

In summary, distances between HYPOSAT locations, computed using only OBSs data and LOC3D locations as *a priori* locations, and LOC3D locations are in the order of magnitude of the locations uncertainties. Adding land stations allows a better azimuth coverage. However, these earthquakes have to be strong enough to be recorded by the two networks.

In addition, the definition of the local velocity model below the epicenters is not convenient in our case. It would have been better to define local models at station locations. Except for large events detected at a lot of stations, the gain in precision obtained by the addition of 1 or 2 land stations is lower than the errors introduced by the combination of 2 very different velocity models. Whether land stations are useful or not depends on the objective. In the present study, we focus on micro-earthquakes within or around the Tekirdag Basin which are generally recorded by less than 2 land stations. Then, from our point of view, it is more rigorous to show locations based on a consistent dataset, along with representative uncertainties, than locations based on land and seabottom stations.

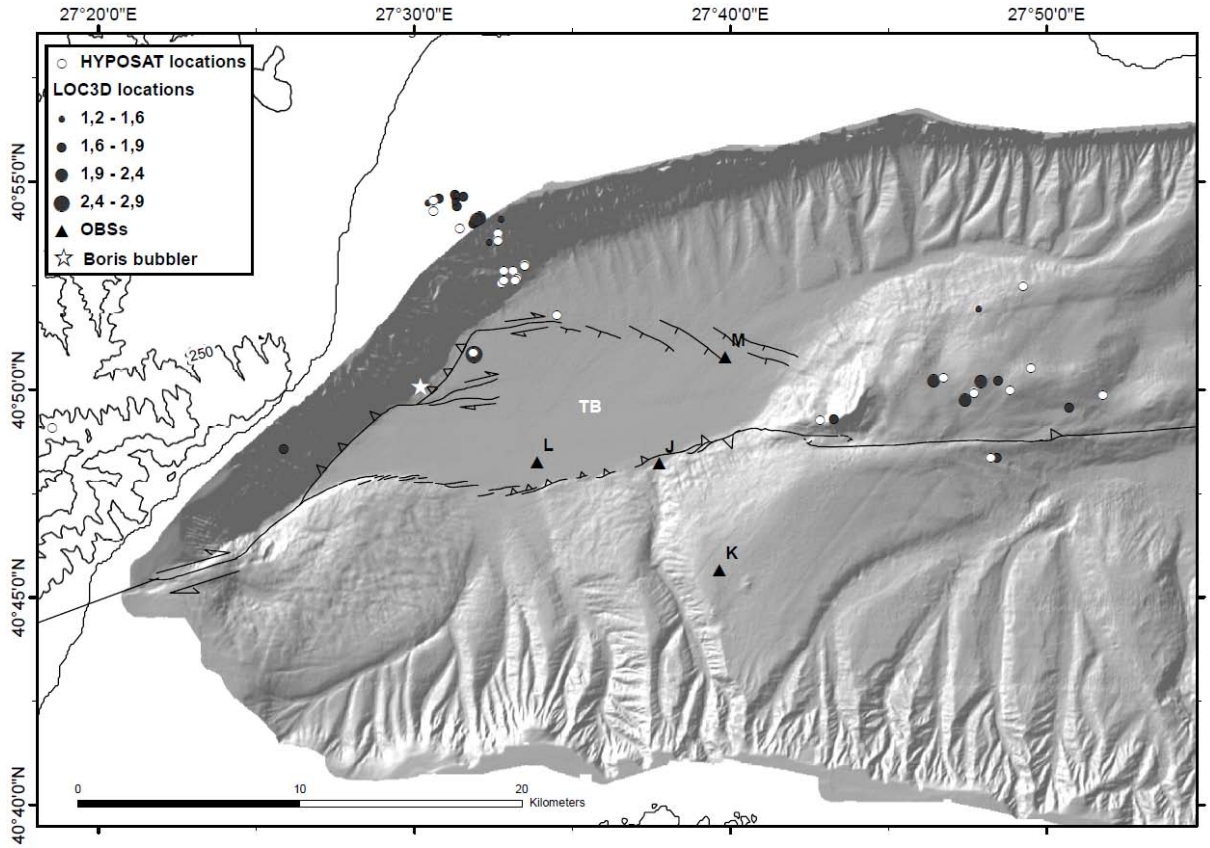

Fig. 2.42. HYPOSAT (white dots) and LOC3D (gray dots) locations using only seabottom stations. The gray dots size depends on the magnitude. The black triangles indicate the OBSs stations.

- Focal mechanisms calculation

The focal mechanisms have been calculated using land and seabottom networks in order to improve the azimuth coverage for each given events. To determine the stability of the focal mechanism calculations regarding the velocity model problem, we have performed two calculations: one with our composite 1D velocity model and one with the NEMC velocity model (Fig. 2.43).

Because focal mechanisms calculations mainly depend on the geographical distribution of stations, the 2 solutions are relatively similar (Fig. 2.43). This conclusion holds even if we use the velocity model of *Gürbüz et al.* [2000], which is known to be more appropriate for the Sea of Marmara region. The velocity model is of critical importance for locating earthquakes, but it has less impact on focal mechanism calculations in our 2 cases (M_w 2.9 May 14, 20:50:35 and M_w 2.6 June 2, 17:10:34).

Hence, we here consider that it is adequate to merge land and sea-bottom stations for deriving focal mechanisms, whereas it is not adequate to do so for locating earthquakes.

A)

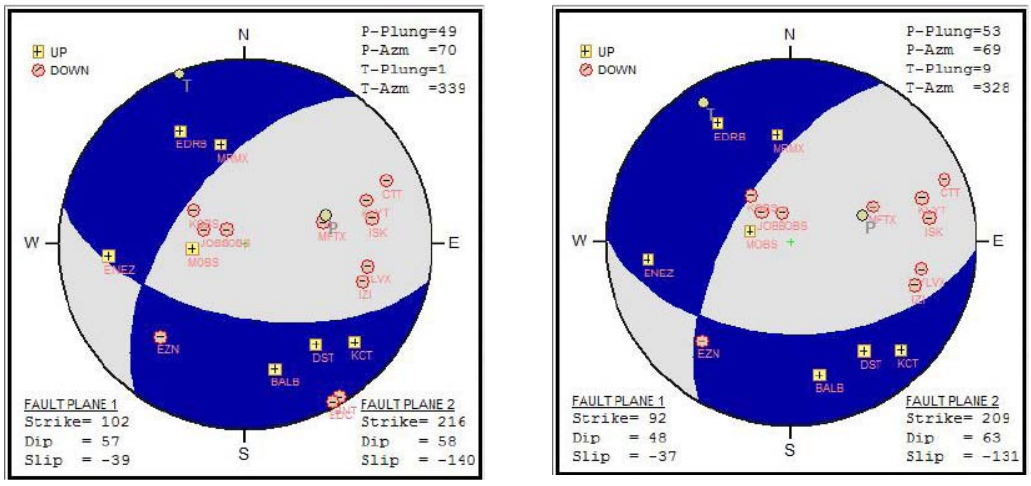

B)

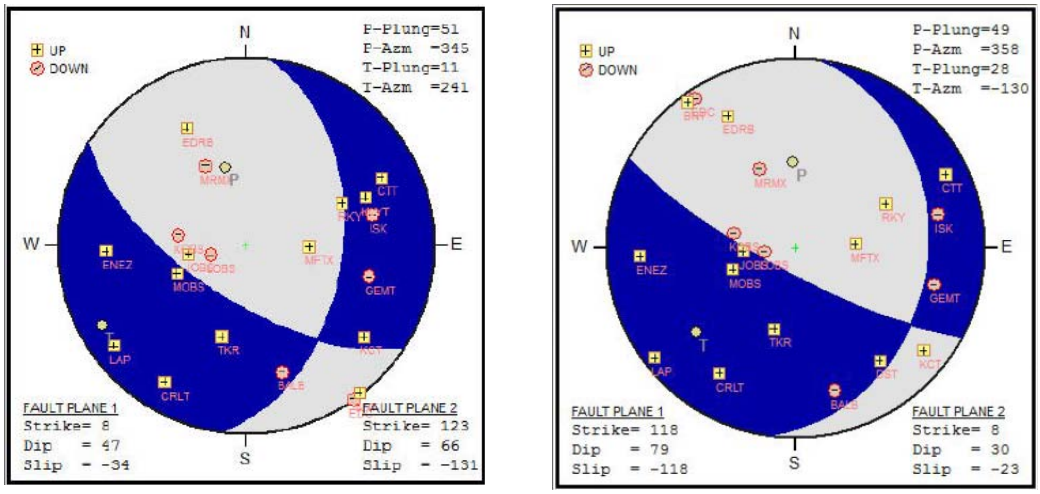

Fig. 2.43. Focal mechanisms of (A) the largest micro-earthquake (northern event in Fig. 2.36, May 14, 2007, 20:50:35) and (B) the micro-earthquake located close to the western escarpment of the Tekirdag Basin, ~10 km south of the one presented in (A) (June 2, 2007, 17:10:34), lower hemisphere projection. On the right are the focal mechanisms calculated with our composite 1D velocity model, and on the left the focal mechanisms calculated with NEMC velocity model. (+) indicates Upward and (-) Downward first motion at a given station.

2.7. Case study 1: Sea Bottom Observations from the Western Escarpment of the Sea of Marmara

Article published in the Bulletin of the Seismological Society of America.

Bulletin of the Seismological Society of America, Vol. 101, No. 2, pp. 775–791, April 2011, doi: 10.1785/0120100014

Sea-Bottom Observations from the Western Escarpment of the Sea of Marmara

by J. B. Tary, L. Géli, P. Henry, B. Natalin, L. Gasperini, M. Çomoğlu, N. Çağatay, and T. Bardainne

Abstract The western escarpment of the Sea of Marmara has recently been recognized as the site of intensive gas emissions escaping from the seafloor. Visual observations with the Nautile submersible indicate that gas escapes from elongated tensile cracks oriented to the northwest in the direction of the maximum principal stress. Here, we report results from a 25-day test in 2007 with four ocean-bottom seismometers (OBSs) showing that this area is also characterized by microseismic activity. A cluster of 13 small-magnitude earthquakes aligned northwest occurred in less than 30 hr at shallow crustal depth below the western slope of the Tekirdag basin. The only two focal mechanisms resolvable using land and sea-bottom data reveal normal faulting with strike-slip components, consistent with the stress field expected in this area. It is suggested that tectonic strain below the western slope of the Tekirdag basin contributes to maintaining a high permeability in fault zones and that the fault network provides conduits for deep-seated fluids to rise up to the seafloor.

Introduction

The Sea of Marmara (Fig. 1) is located on the North Anatolian fault (NAF) zone in northwestern Turkey, a major transform-plate boundary that has produced devastating historical earthquakes along its 1600-km length (see, e.g., Ambraseys & Jackson, 2000). The deeper part of the Sea of Marmara is composed of recent basins with water depths greater than 1000 m (respectively, from east to west, the Çinarcik basin, the Central basin, and the Tekirdag basin), separated by two bathymetric highs oriented northeast–southwest, the central and western highs (Fig. 1). A sequence of eight $M > 7$ earthquakes has ruptured the NAF boundary progressively from east to west over the last century. The most recent and westernmost events in this sequence, the M_w 7.4 Izmit and M_w 7.2 Duzce mainshocks in 1999, were particularly destructive. Together, they ruptured about 160 km of this fault system, including the submarine portion of the fault in the Gulf of Izmit, eastern Marmara Sea (Barka *et al.*, 2002). Relatively little strain, however, is thought to have been released by earthquakes along 150 km of the transform through the Marmara Sea since the mid 1700s. In fact, the previous strongest earthquake to affect the westernmost Marmara region was the 1912 M_w 7.2 Ganos earthquake that ruptured the entire 50-km-long segment across the Gelibolu peninsula plus submarine portions on either side (Aksoy *et al.*, 2009). For this reason, the NAF below the Sea of Marmara is identified as a seismic gap, and the study of the two end members of this gap, in other words, the Izmit Gulf to the east and the Tekirdag basin to the west, is particularly important for seismic risk assessment in this region.

In the deeper parts of the Sea of Marmara, fluid outflow sites manifested by carbonate crusts, black patches, and bacterial mats are commonly observed along or near active faults (e.g., Armijo *et al.*, 2005; Zitter *et al.*, 2008; Géli *et al.*, 2008). Such features are indicators of relatively continuous emission of dissolved methane at the seafloor. The anaerobic oxidation of methane triggers a suite of geochemical reactions that ultimately result in the production of black iron (Fe) and manganese (Mn) sulphide mineral assemblages (e.g., Boetius *et al.*, 2000; Hensen *et al.*, 2003). Methane originates from microbial degradation of organic matter or from deeper thermogenic hydrocarbon generation and passes upwards as a dissolved component in pore fluid advection or as a buoyant gas phase. The sulphate source is the overlying water column, with sulphate diffusing across the sediment-water boundary. The product of the anaerobic oxidation of methane is used by the microbial mats, and the black patches are related to Fe and perhaps Mn minerals precipitating with the sulphide. Black sediment patches are hence indicators of rapid, prolonged, and current methane emissions. The emissions must be rapid enough to keep the bottom boundary layer completely anoxic (Tryon *et al.*, 2002). Free gas emissions are common and appear to be influenced by earthquake occurrence (Alpar, 1999; Alpar *et al.*, 2005). While gas emitted from the Çınarcik basin is predominantly of relatively shallow origin, hydrocarbon gases expelled from faults

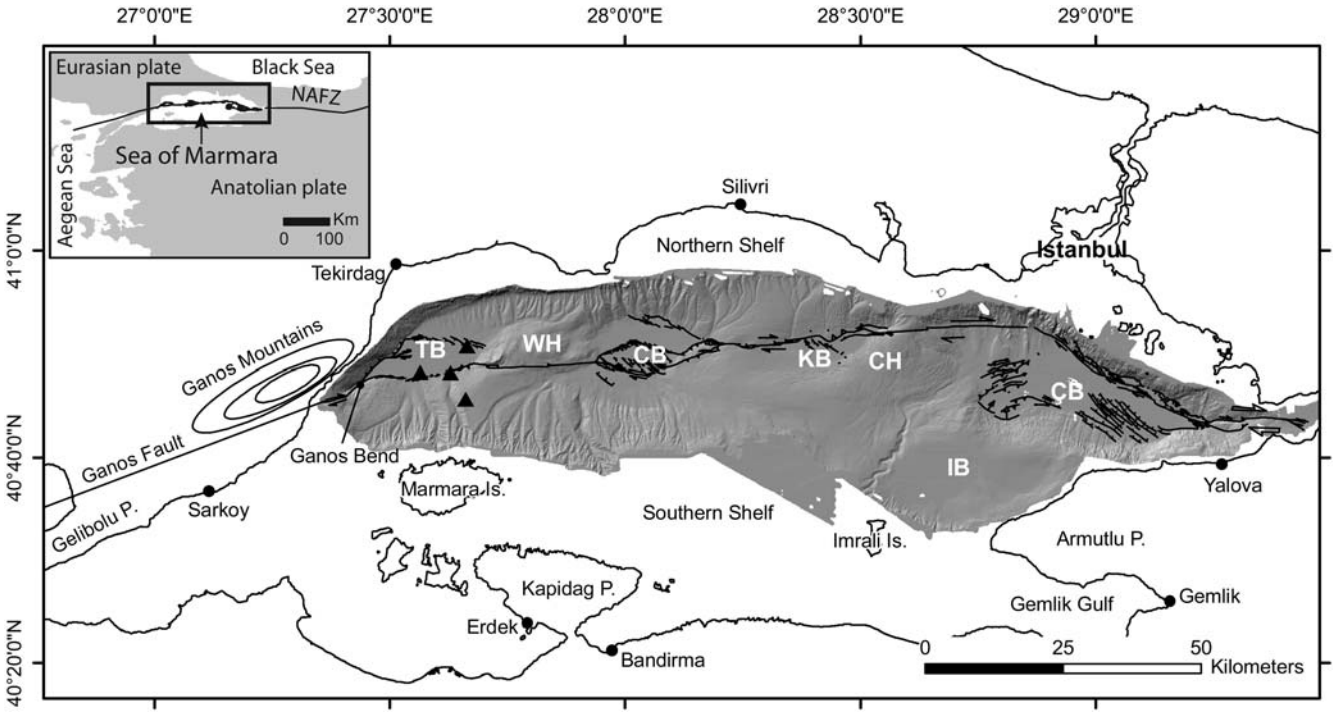

Figure 1. Map of the Sea of Marmara based on bathymetric data collected with R/V Le Suroit in 2000 (Rangin *et al.* 2001) with main active fault traces after Imren *et al.* (2001) and Rangin *et al.* (2004). The black triangles indicate OBSs deployed during the Marnaut cruise in May–August 2007. The exact OBS coordinates are listed in Appendix A. Abbreviations: TB, Tekirdag basin; WH, Western high; CB, Central basin; KB, Kumburgaz basin; CH, Central high; ÇB, Çinarcik basin; IB, Imrali basin; Is.: Island ; NAFZ, North Anatolian Fault Zone. The inset shows the map's location at the boundary between the Anatolian and Eurasian plates.

cutting the topographic highs are of deep thermal origin (Bourry *et al.*, 2009). Near the foot of the western escarpment of the Tekirdag basin, gas bubbles of deep origin (Burnard *et al.*, 2008) have been found escaping from open fractures, elongated in the northwestern direction.

These observations and the high geohazard potential of the area are the reason that the Sea of Marmara has been identified as a unique, natural laboratory for studying the relationships between fluids and seismicity through the European Seas Observatory Network (ESONET) Network of Excellence (NoE) project cofunded by the European Commission. Here, we report results from a preparatory test carried out in 2007 with four ocean-bottom seismometers (OBSs) deployed during the MarNaut Cruise in the western part of the Sea of Marmara. Combined with other submarine observations, the results of this test provide useful information on the tectonic regime characterizing the western slope of the Tekirdag basin. The Tekirdag basin is the westernmost topographic depression of the Marmara Sea and develops at the connection of the North Anatolian fault northern strand and the Ganos fault onshore (Fig. 1). Water depth reaches over 1.1 km in the basin, while thickness of the sediment infill, estimated from analysis of seismic reflection profiles, is over 4 km (Okay *et al.*, 1999). This setting is complicated by the presence of compressive deformation affecting the western edge of the basin, likely caused by the change in orientation of the principal plate boundary along which the southern block moves to the west and to the southwest (Le Pichon *et al.*, 2001; Armijo *et al.*, 2002 ; Okay *et al.*, 2004 ; Seeber *et al.*, 2004). Compressional deformation at or near the Ganos bend probably led to crustal shortening that gave rise to the formation of the Ganos mountains, which bound the Sea of Marmara following the western slope of the Tekirdag basin.

Previous OBS Surveys in the Sea of Marmara

The potential of OBSs to record microseismicity and lower the detection threshold in the Sea of Marmara has been largely proven by previous experiments. In 2000, two successive, one-month-long deployments of 10 OBSs enabled the determination of 350 earthquakes, showing strike-slip activity on subvertical fault planes in the western part of the Sea of Marmara in contrast to extensional focal mechanisms found in the eastern part (Sato *et al.*, 2004; Bulut *et al.*, 2009). In 2001, 60 land stations were installed, and a network of 37 OBSs were deployed with the Research Vessel (R/V) L'Atalante in and around the Sea of Marmara, providing continuous recording over six weeks (Bécel, 2006; Bécel *et al.*, 2009, 2010). Based on these two experiments, no particular microseismic pattern has been reported for the western slope of the Tekirdag basin due to two possible causes: the absence of microseismicity during the recording periods or the fact that the OBS distribution was inadequate to detect low-level microseismicity from this area.

The MarNaut OBS Data

Four short-period (4.5 Hz) OBSs were deployed in the Tekirdag basin (Fig. 1) during the summer of 2007 (see coordinates in Appendix A). From 14 May to 9 June (25 days), the four instruments functioned simultaneously, recording data at a sampling rate of 250 Hz. During the remaining period, from 9 June to 30 August, the data were recorded by three OBSs only. The instruments were equipped with three velocity sensors (one vertical and two nonoriented horizontal components) and one hydrophone. *In situ* photographs taken by the Nautile submersible showed that the sensor capsule was entirely covered by sediments, providing reasonable coupling with the seafloor. Based on laboratory results obtained in comparable pressure and temperature, the drifts of the OBSs' internal clocks were linearly corrected for each instrument. In addition, seismic shots triggered using a Global Positioning System (GPS)-synchronized clock were recorded by the OBSs on 24 May 2007, providing estimates of the drift of the instruments after 10 days of deployment (between 14 May and 24 May). These estimates confirmed that the instruments' internal clocks drifted almost linearly during the first 25-day period.

Seismological Data

A total of 270 events were detected by the OBSs (including 110 in the first 25 days), while only ~50 events were recorded with land stations from the KOERI (Kandilli Observatory and Earthquake Research Institute) network. Expressed in terms of the moment-magnitude scale M by

$$M = \frac{2}{3}\log(M_0) - 10.7, \tag{1}$$

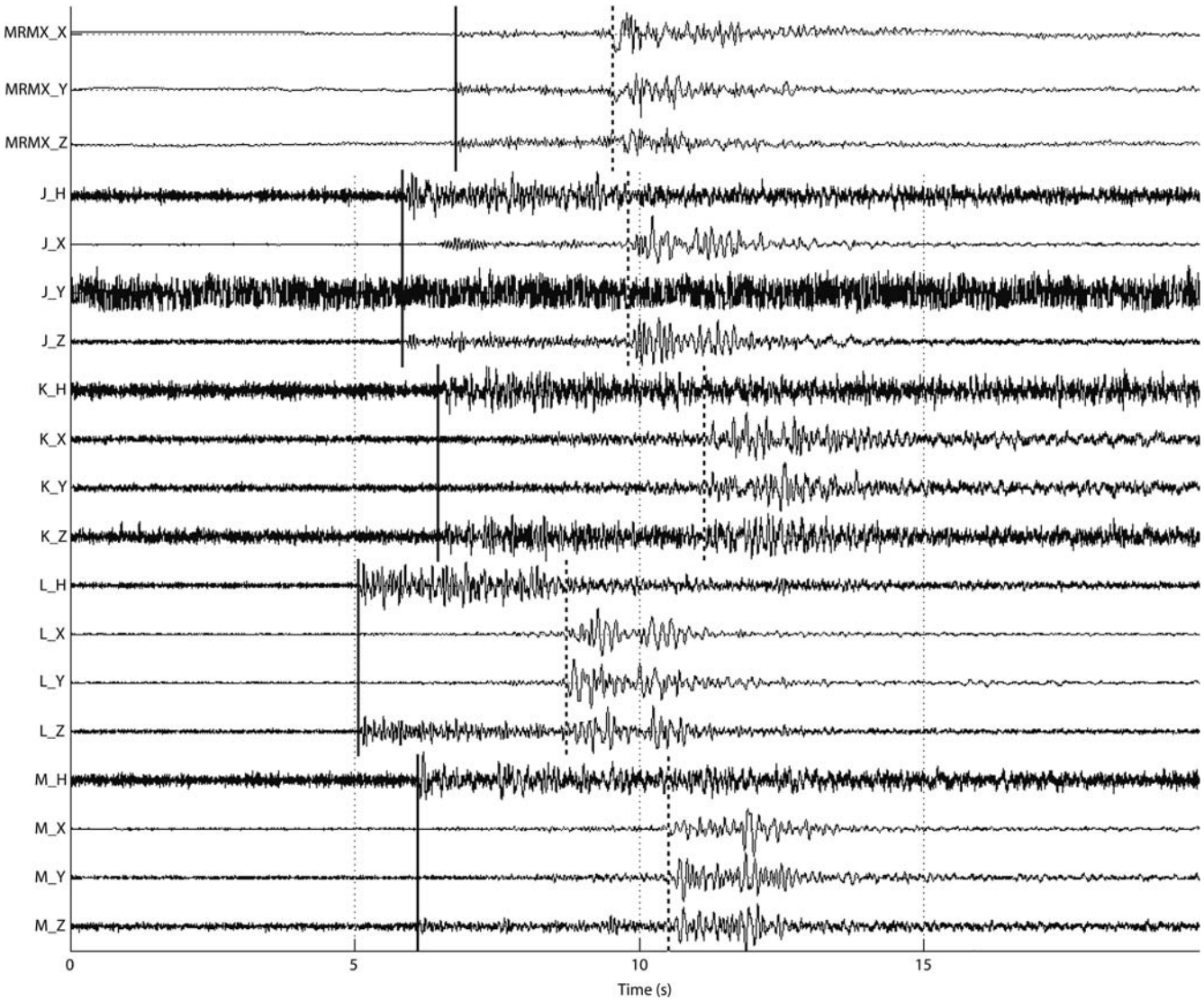

Figure 2. Seismograms of MRMX land station, and OBS J, K, L, M for the same event (origin time: 06/01/2007 12:40:32). *X* and *Y* are horizontal components, *Z* is vertical, and *H* is hydrophone. Seismograms are not filtered. *P* (solid lines) and *S* (dashed lines) wave arrivals are indicated. Note that the *P* wave is clearly visible on the hydrophone, which is very helpful for phase picking.

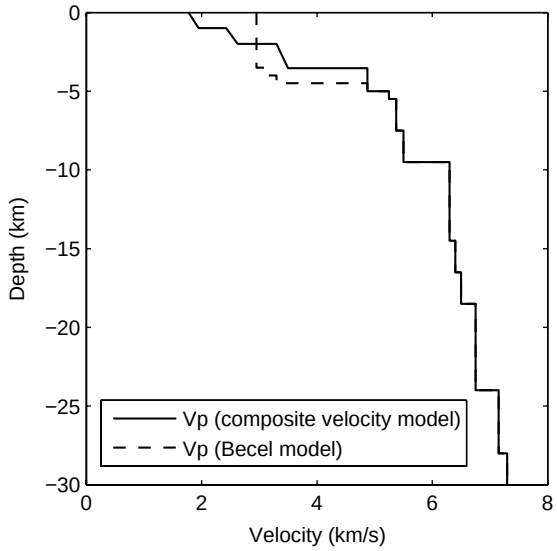

Figure 3. Composite 1D velocity model (solid black line) in the upper 30 km of the Tekirdag basin area, based on the velocity model of Bécel (2006, dashed black line) and our new velocity model (see Appendix A). The composite velocity model was used in this study to initially locate earthquakes.

where M_0 is the seismic moment, as specified by Lee and Stewart (1981) for microseismicity, the detection threshold was lowered from $M = 2.7$ for land stations to $M = 1$ for OBSs.

The main limitation in locating earthquakes is the limited number of OBSs. Hence, we have tried to merge the land and sea-bottom data sets. As the Tekirdag basin is a trough filled with more than 4 km of Plio-Quaternary soft (slow) sediments, the velocity structure in the basin is drastically different from the one below the onshore area that surrounds the Sea of Marmara. This is particularly well illustrated in Figure 2, which clearly shows important discrepancies in $t_S - t_P$ differences for a distant earthquake recorded at one land station and OBSs with comparable source-receiver distances.

For the deep offshore domain, our preferred one-dimensional (1D)-velocity model is a composite (Fig. 3) based on new high-resolution, wide-angle OBS data for the 4-km thick, syn-rift Plio-Quaternary sediment sequence and on the Bécel (2006) model for depths > 4 km below the seafloor (see Appendix A). This composite velocity model is reasonable for the submarine domain, but inappropriate for the onshore domain. A 3D, simultaneous inversion of earthquake locations performed using seismic shots recorded in 2001 and structure velocity is presently being finalized but is not yet available (Anne Bécel, personal comm., 2010). In the absence of a 3D velocity model encompassing the onshore and offshore domains and due to the limited number of OBSs, our attempts to merge the land and sea-bottom data sets have proven unsuccessful. Many attempts have been made using different relocation software that enable the use of different 1D velocity models for the offshore and onshore domains, but all attempts

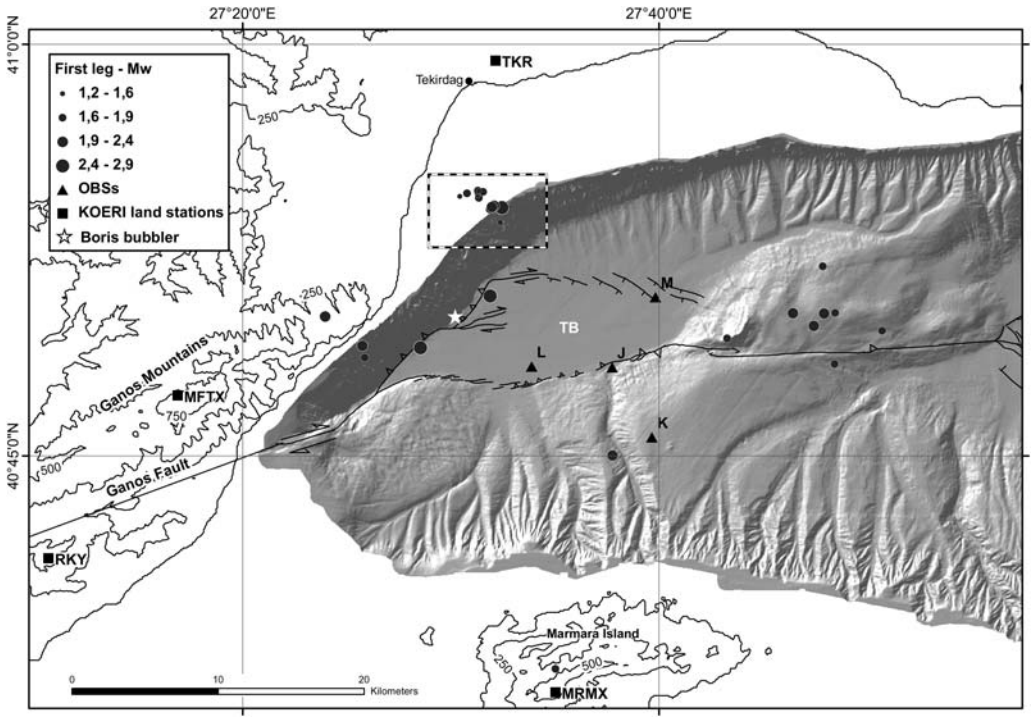

Figure 4. Map of the Tekirdag basin showing location of selected earthquakes (gray circles). The symbol sizes indicate magnitude. The black triangles and black squares are OBS locations (labeled J, K, L, and M) deployed during the Marnaut cruise and KOERI land stations locations, respectively. The rectangle outlines the zone of the earthquake cluster that was recorded on 14–15 May. Boris Bubbler (white star) is a site of intense gas emanations of deep origin escaping from tensile cracks oriented northwest, observed by the Nautile on 16 May 2007. TB: Tekirdag basin.

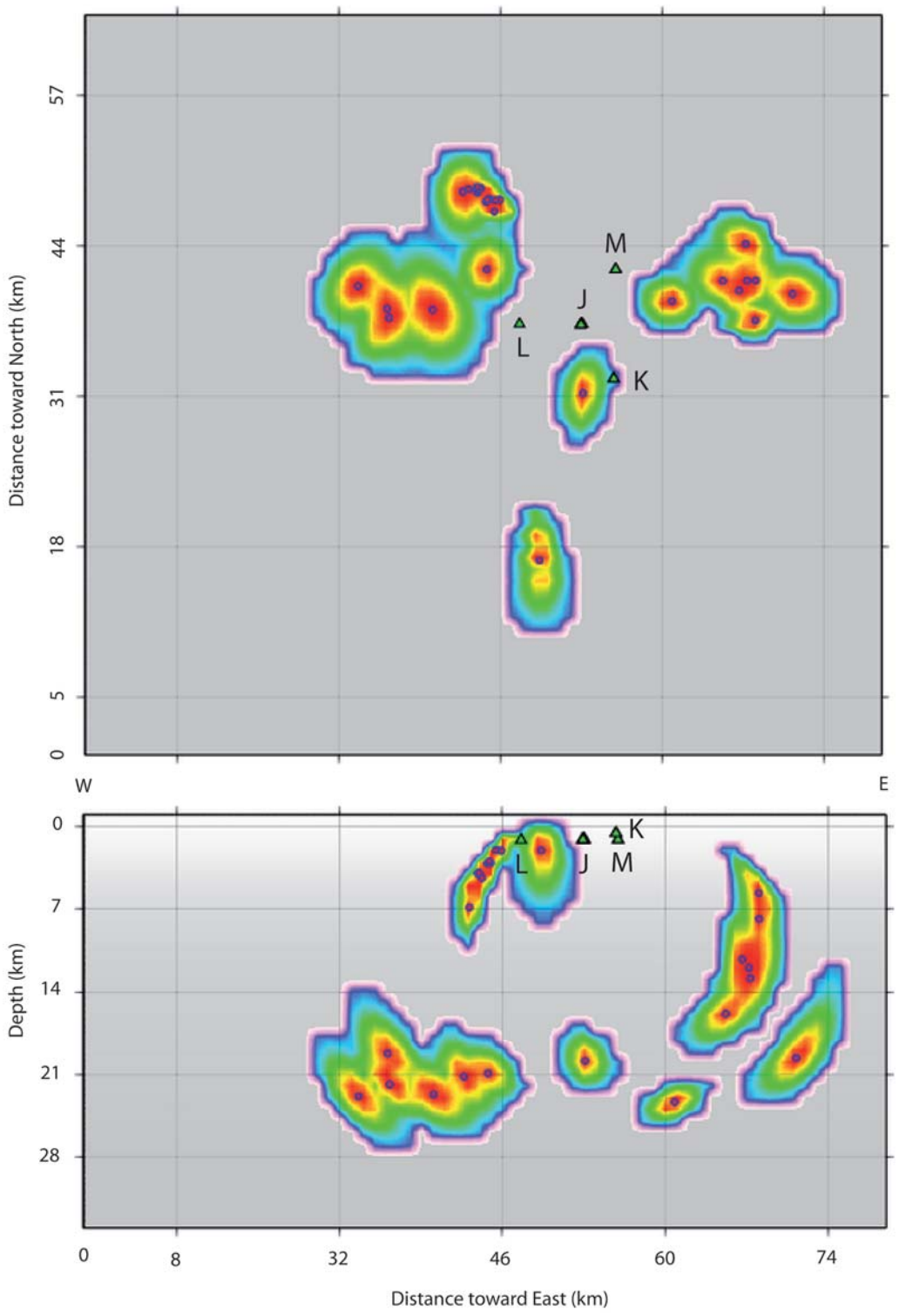

Figure 5. Map view (top) and cross-sectional view (bottom) of horizontal and vertical uncertainties, respectively, for the selected earthquakes (blue circles). The white-pink edges correspond to a 68% probability of earthquake location. The red color corresponds to the maximum probability of the earthquake location.

have failed to provide consistent results. Consequently, to locate earthquakes, we have restricted our study to the events located in the offshore domain and have only used the OBS data set from the first monitoring period, consisting of 25 days of continuous recording with four instruments.

Earthquake locations were first performed using LOC3D software, which performed a grid-search method based on the calculation of a probability density function. The probability density function could be calculated using any velocity model (1D or 3D) from the *P*- and *S*-wave arrival

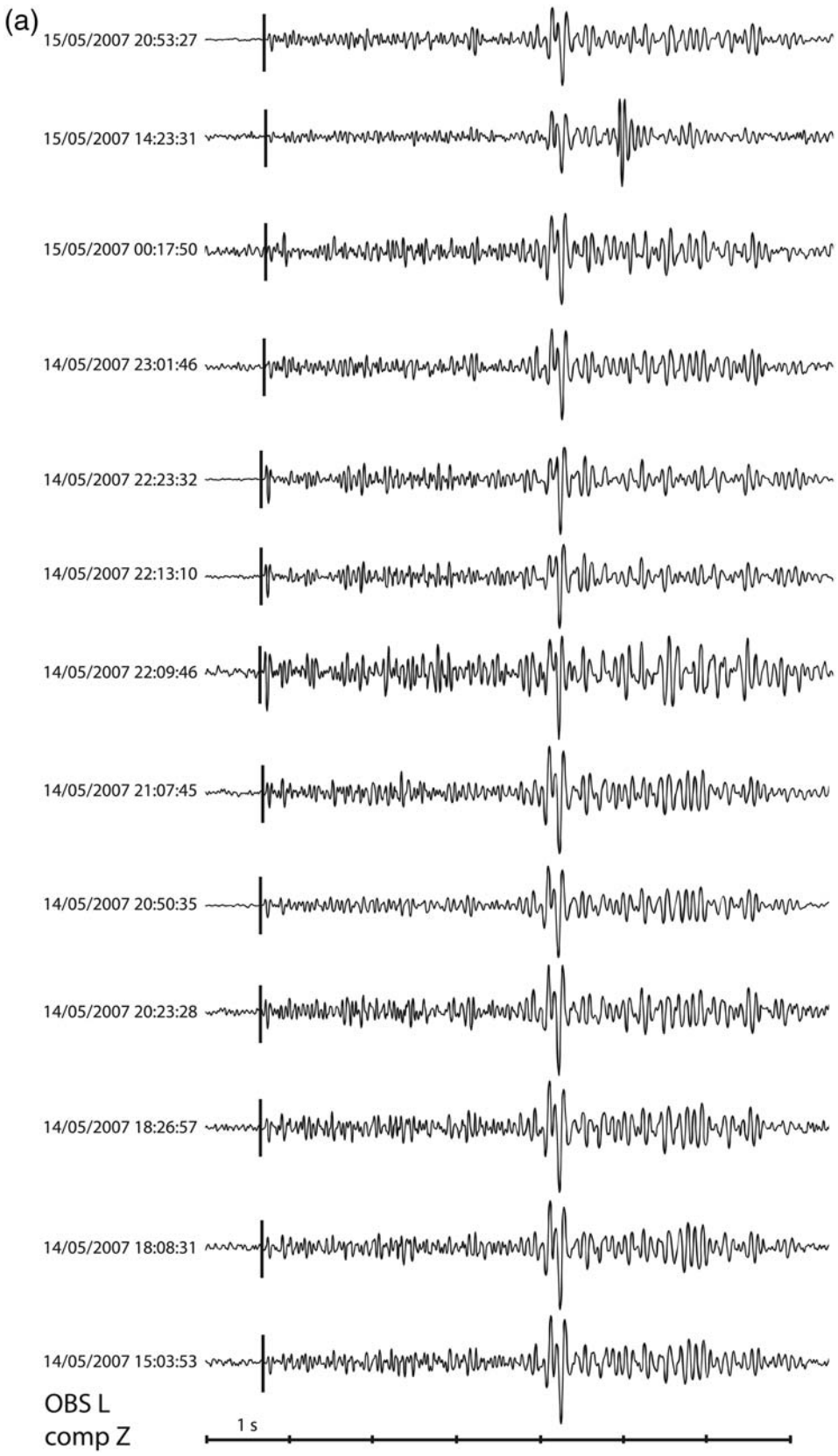

Figure 6. Seismograms recorded at OBS (a) L and (b) M of the 13 events of the Tekirdag basin earthquake cluster recorded between 14 May, 15:03 and 15 May, 20:53 (vertical component, filtered between 0 and 30 Hz). (*Continued*)

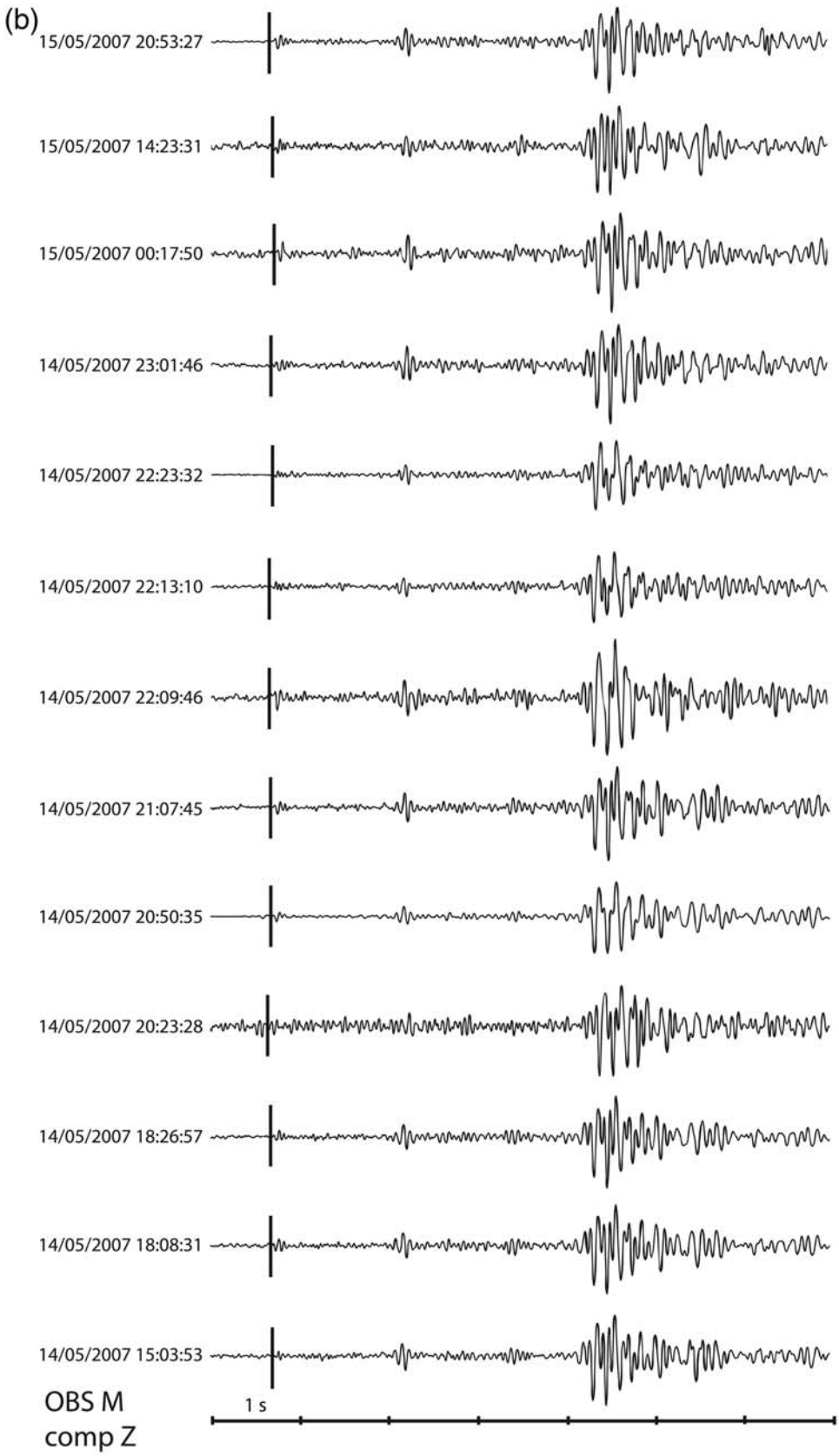

Figure 6. Continued.

times, according to the probabilistic formulation of inversion presented by Tarantola and Valette (1982), and *P*-wave polarization measurements.

Arrival times were first computed using a finite-difference code based on the 3D Eikonal equation developed by Podvin and Lecomte (1991). Then, a probabilistic grid search was performed using $t_S - t_P$ and/or wave polarization to find the local probability maximum with uncertainties corresponding to 68% (one standard deviation) of the probability integral. In the present case, our 1D composite model (Fig. 3) was used with *P*- and *S*-wave picks. Wave polarizations were not used due to the lack of information regarding the orientation of the horizontal sensors.

Out of the 110 events detected during the first 25 days, 81 were located with our location algorithm (LOC3D), but we selected only those 30 events having at least four *P* and four *S* picks. Most events were geographically distributed in two areas, the western slope of the Tekirdag basin and the Western high (Fig. 4). All were located outside the network, and this clearly affected location uncertainties, which increased with distance. Computed uncertainties ranged in average from 1 to 6 km horizontally, with a mean of 2.7 km, and from 1.5 to 7 km in depth, with a mean of 3.6 km (Fig. 5).

Because uncertainties in absolute locations are large, we strictly focused on the events of a cluster that are prone to relative determinations. These events occurred in the upper crust (less than ~5 km) below the western slope of the Tekirdag basin. Relative determinations were not possible for the events that occurred below the Western high, which were not in clusters. The events of the cluster had similar waveforms and similar $t_S - t_P$ differences (Fig. 6 and 7), which indicate that they had similar sources and similar ray paths from source to station. As the distance between two events was small relative to the event-station distance, ray paths were indeed nearly the same. In addition, travel-time differences between two closely spaced events did not depend on the velocity structure along the source-receiver travel path. This observation allowed the use of the double-difference method, which provided very precise hypocenter determinations by minimizing time differences for event pairs (Waldhauser and Ellsworth, 2000), increasing our confidence in the proposed absolute location of the cluster. Double-difference also annihilated the effect of time synchronization error between the different stations. We also used a homemade algorithm that allows the relative determination of hypocenters with respect to a supposedly well-located reference event (Appendix B). The relative locations inferred from this method were consistent with locations based on hypoDD and LOC3D (Appendix B).

The events of the cluster were not unevenly distributed but defined northwest-oriented alignments (Fig. 8a). The main compressive stress in this area that leads to the uplift of the Ganos mountain and the subsidence of the Tekirdag basin was also oriented northwest–southeast (Seeber *et al.*, 2004; Janssen *et al.*, 2009). The largest event of the cluster (14 May 2007, 20:50), an M_w 2.9 magnitude earthquake, was detected by the OBSs and by 15 land stations of the KOERI network. This enabled the determination of a focal mechanism (Fig. 8b), a normal fault with a strike-slip component. Similarities in waveforms suggest that this focal mechanism is likely to be representative of the other events in the cluster. Assuming the cluster reflects slip on a fault, striking approximately parallel to the axis of the cluster, the focal mechanism implies normal faulting with a small sinistral strike-slip component. An east–west oriented fault plane is consistent with bathymetric observations on the slope of fractures oriented N90-100 (Géli *et al.*, 2010). The cluster was situated at the junction between compression to the west and extension to the east (Seeber *et al.*, 2004). A local stress reorientation in this transitional area could explain the roughly north–south extensional stress regime shown by the focal mechanism.

The second focal mechanism, calculated for an event located ~10 km south of the cluster (Fig. 8c) showed a normal fault with a dextral component striking to the northwest. This mechanism is consistent with the local southwest–northeast extension that affects the western slope of the Tekirdag basin as it approaches the Ganos bend. On land, the northeastern part of the Ganos mountain is cut by many normal faults oriented N270 to N330, with a strike-slip component for some of them (Okay *et al.*, 1999).

Field Observations

Detailed multibeam bathymetry data (Le Pichon *et al.*, 2001) showed that the foot of the western slope of the Tekirdag basin comprises a series of *en-échelon* fault segments oriented to the northeast, relayed by short, dextral strike-slip segments oriented approximately east–west (Fig. 8a). The trails of two strike-slip faults extending into

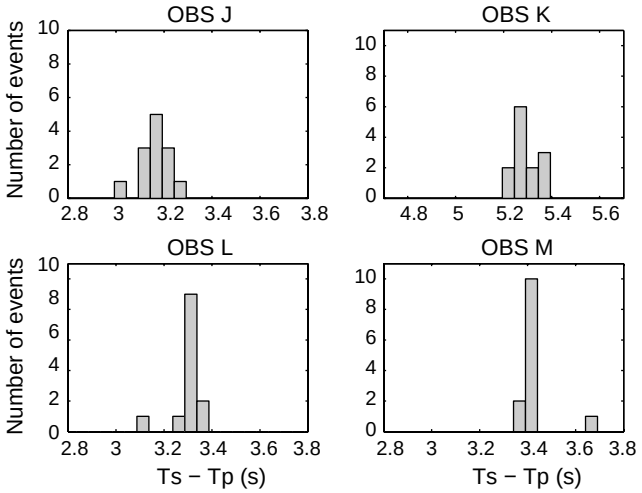

Figure 7. Travel-time difference $t_S - t_P$ histograms at each OBS for the 13 events of the Tekirdag basin cluster that occurred on 14 and 15 May 2007.

the Tekirdag basin were particularly visible in the bathymetry near 40° 49.5' N and near 40° 51.5' N. Between these two strike-slip segments, traces of compressive deformation affecting the uppermost (< 50 m) sedimentary structure are visible in high-resolution seismic reflection profiles (Fig. 9).

Acoustic data collected in 2007 with a 38-kHz sonar (Géli *et al.*, 2008) and in 2009 with a SIMRAD EM302 multibeam system, allowing water column mapping (Fig. 8a), indicate that the western slope of the Tekirdag basin is the site of intensive gas emissions escaping from the seafloor. On 16 May 2007, during the Marnaut cruise, the Nautile submersible explored the western slope of the Tekirdag basin a few kilometers to the southwest of the swarm that occurred on 14 May. It has been established that small northwest-trending canyons (dive 1644, Fig. 8a) are controlled by northwest-striking, closely spaced fractures. Different types of black patches were found on the slope with different shapes and orientations (Fig. 9). Elongated black patches (~300 m long and 30 m wide) were commonly found striking N320–350 together with gas emanations escaping from narrow (7- to 15-cm wide) tensile cracks oriented northwest in the bedrock. In contrast, equidimensional black patches are characteristic of segments located in zones of transpression striking in the northeast direction and coinciding with the Ganos Fault. Isotopic analysis indicates the Helium contained in the gas has a deep-seated origin (Burnard *et al.*, 2008). In the absence of evidence for local magmatic sources, it seems likely that the fault system located below the western slope of the Tekirdag basin allows gas to escape through the crust.

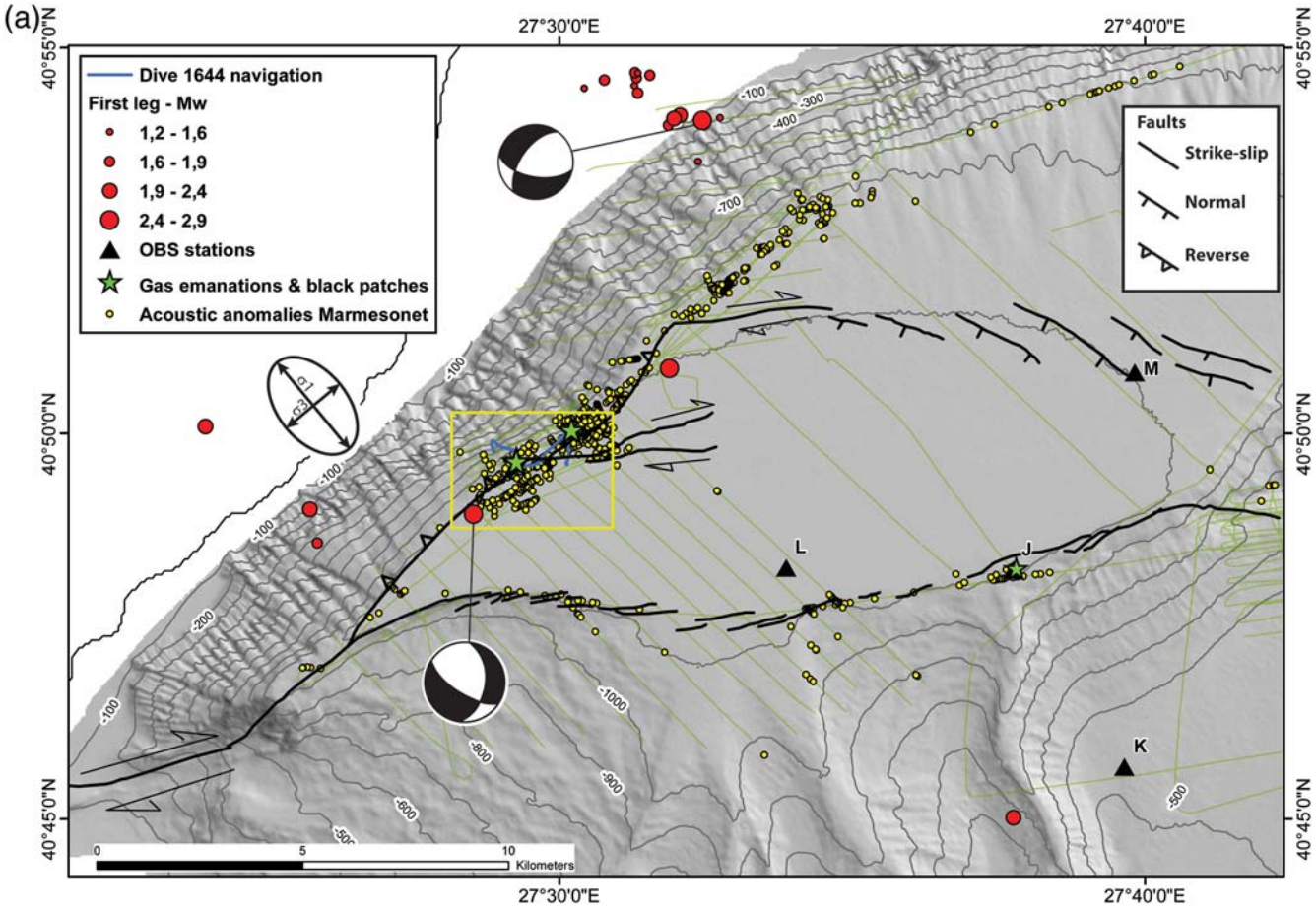

Figure 8. (a) Detailed bathymetric map of the western slope of the Tekirdag basin with active fault traces (after Le Pichon *et al.*, 2001 and Rangin *et al.*, 2004). Sites of gas emanations and black patches (green stars), and epicenters detected with the OBS deployed between 14 May and 8 June 2007 (red dots) are indicated. Green lines and yellow dots indicate, respectively, the routes followed by the R/V Le Suroit in November–December 2009 and the acoustic anomalies detected in the water column using the SIMRAD EM302 multibeam system. The blue line indicates navigation of the Nautile submersible during dive number 1644. Coordinates of the gas sampling site are N40°50.046, E27° 30.206. Yellow rectangle indicates location of Figure 9; Focal mechanisms of (b) the largest microearthquake of the Tekirdag basin cluster (14 May, 20:50:35) and (c) the microearthquake located ~10 km south of the cluster (2 June, 17:10:34), lower-hemisphere projection. Symbol + indicates upward and − downward first motion at a given station. Panels on the right show the KOERI land stations (red triangles) and OBSs (small black triangles) used to calculate each focal mechanism (also shown in (a)). Red dots are the absolute location of the microearthquakes. (*Continued*)

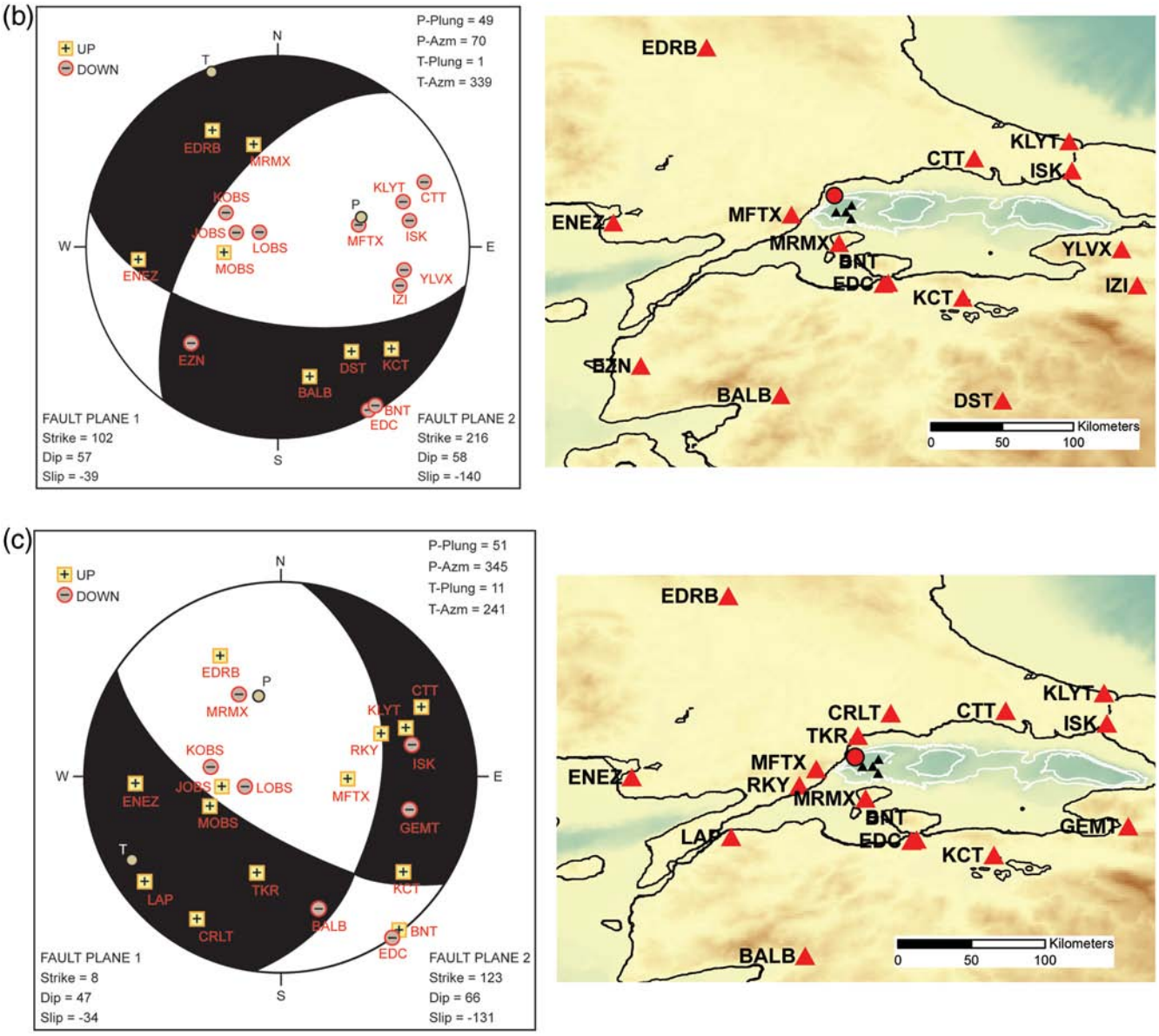

Figure 8. Continued.

Conclusions

Field data (mainly, detailed bathymetry, sounder profiles, and submersible observations) indicate that the western slope of the Tekirdag basin is affected by at least three structural directions: transpressive southeast–northwest with faults along the main scarp, right-lateral east–west faults in the basin, and southeast–northwest normal faults and tension gashes. These directions are consistent with the regional stress field in the Sea of Marmara with a minimal principal stress oriented in the northeast direction and a maximum (compressive) principal stress oriented to the northwest. In this context, gas bubbles with a mantle source component (based on Helium isotopes) have been found escaping from northwestern tensile cracks through the sedimentary rock formations exposed near the base of the main escarpment.

The seismological results presented here are consistent with northeast–southwest to north–south extension in the northeastern prolongation of the Ganos fault. A cluster of 13 small-magnitude earthquakes, occurring over a duration of less than 30 hr, below the western slope of the Tekirdag basin were detected on 14 and 15 May by the OBSs deployed during the MarNaut cruise. These events occurred at shallow crustal depth and were aligned in the northwestern direction. The only focal mechanism for the cluster events that was resolvable using land and sea-bottom data is compatible with a slip on a fault oriented along the trend of the cluster with major normal and minor strike-slip components. The

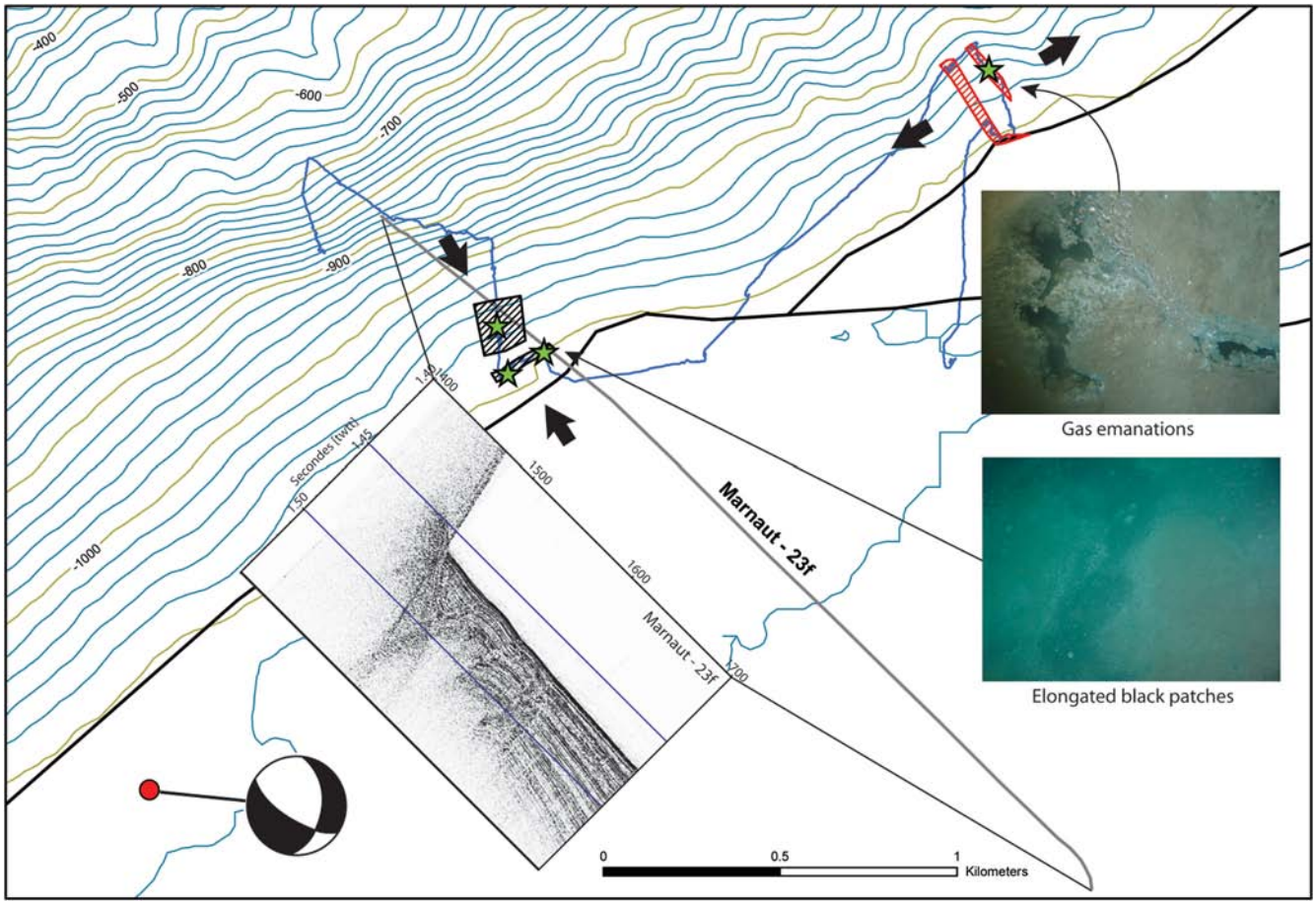

Figure 9. Summary figure to describe dive 1644 to explore the structural geology of the base of the western slope of the Tekirdag basin (yellow rectangle in Fig. 8a). Blue line indicates navigation of the Nautile submersible during dive number 1644. Red and black hatched areas show locations of elongated and equidimensional black patches, respectively. Sites of seafloor gas bubble escape are indicated by green stars. Thick black arrows, depending on their orientations, show extension or compression direction. Chirp profile (high-resolution seismics using a chirp source with frequency ranging between 2 and 4 kHz) indicating compression affecting the sediments in the Tekirdag basin (gray line). Photograph locations are indicated by small black arrows.

other focal mechanism calculated for an event near the western slope of the Tekirdag basin is consistent with observations at the seafloor indicating a southwest-northeast extension. This event could be related to the observation of a series of normal faults striking N270 to N330 along the coast on the Ganos mountain (Okay *et al.*, 1999). We suggest this normal fault system extends northward at least to the area of the microseismicity cluster even though the fault at the base of the northwest Tekirdag cliff has not been considered active this far north (Rangin *et al.*, 2004; Armijo *et al.*, 2005).

Associations between fluid expulsion sites and active fault systems in submarine environments have been recognized for some time (e.g., Moore *et al.*, 1990). Some observations suggest that it is very difficult to pass free gas through sediment but relatively easy to pass it through fractures, which leads to water seeps being found in many places, such as outcrops of sand layers, while gas seeps more often are found associated with fractures (Tryon *et al.*, 2002).

A recent acoustic survey (conducted in November 2009 with the SIMRAD EM302 multibeam echosounder) shows that gas emanations occur continuously all along the base of the northwestern Tekirdag basin slope. It appears likely that tectonic activity along the western slope of the Tekirdag basin contributes to maintaining a high-permeability fault network and enables deep-seated fluids to rise up to the seafloor.

Data and Resources

The mapping of acoustic anomalies detected during the Marmesonet cruise (4 November to 15 December 2009) has not yet been published. The cruise report is available by a request to the authors. All other data used in this paper come from published sources listed in the references.

Acknowledgments

We wish to acknowledge all the actors that initiated the Turkish–French collaboration since 2000. We also warmly acknowledge the Captain and crew of R/V L'Atalante (MarNaut Cruise, 2007) and R/V Le Suroit (Marmesonet cruise, 2009) and the very efficient assistance of the Turkish Navy in the zones of heavy ship traffic. The present work is part of the Ph.D.

Thesis of J. B. Tary, cofunded by TOTAL, Baker Hughes, and IFREMER. Financial support from Agence Nationale de la Recherche (project ANR/ISIS) and ESONET is also acknowledged. We thank M. Yilmazer, F. Klingelhoefer, P. Pelleau, J.-L. Got, P. Burnard, S. Bourlange, and S. Dupré for very helpful discussions and support. Very thorough reviews, particularly from the Associate Editor, greatly helped improve the manuscript.

References

Aksoy, E. M., M. Meghraoui, M. Vallée, and Z. Cakir (2009). Rupture characteristics of the 1912 Mürefte (Ganos) earthquake segment of the North Anatolian fault (Western Turkey), *Eos Trans. AGU* **90,** 52, Fall Meet. Suppl., abstract no. T13C-1884.

Alpar, B. (1999). Underwater signatures of the Kocaeli earthquake of 17 August 1999 in Turkey, *Turk. J. Mar. Sci.* **5,** 111–130.

Alpar, B., S. Burak, and E. Doğan (2005). Environmental and hydrological management of the Golden Horn Estuary, Istanbul, *J. of Coast. Res.* **21,** 4, 646–654.

Ambraseys, N., and J. Jackson (2000). Seismicity of the Sea of Marmara (Turkey) since 1500, *Geophys. J. Int.* **141,** F1–F6.

Armijo, R., B. Meyer, S. Navarro, G. King, and A. Barka (2002). Slip partitioning in the Sea of Marmara pull-apart: A clue to propagation processes of the North Anatolian Fault?, *Terra Nova* **14,** 80–86.

Armijo, R., N. Pondard, B. Meyer, and G. Uçarkus (2005). Submarine fault scarps in the Sea of Marmara pull-apart (North Anatolian Fault): Implications for seismic hazard in Istanbul, G^3, **6,** Q06009.

Barka, A., H. S. Akyüz, E. Altunel, G. Sunal, Z. Çakir, A. Dikbas, B. Yerli, R. Armijo, B. Meyer, J. B. de Chabalier, T. Rockwell, J. R. Dolan, R. Hartleb, T. Dawson, S. Christofferson, A. Tucker, T. Fumal, R. Langridge, H. Stenner, W. Lettis, J. Bachhuber, and W. Page (2002). The surface rupture and slip distribution of the 17 August 1999 Izmit earthquake (*M* 7.4), North Anatolian fault, *Bull. Seismol. Soc. Am.* **92,** 43–60.

Bécel, A. (2006). Structure Sismique de la Faille Nord Anatolienne en Mer de Marmara, *Ph.D. Thesis*, Institut de physique du globe de Paris (IPGP), Paris, France.

Bécel, A., M. Laigle, B. de Voogd, A. Hirn, T. Taymaz, A. Galvé, H. Shimamura, Y. Murai, J. C. Lépine, M. Sapin, and S. Özalaybey (2009). Moho, crustal architecture and deep deformation under the North Marmara Trough, from the SEISMARMARA Leg 1 offshore —onshore reflection—refraction survey, *Tectonophysics* **467,** 1–21.

Bécel, A., M. Laigle, B. de Voogd, A. Hirn, T. Taymaz, S. Yolsal-Cevikbilen, and H. Shimamura (2010). North Marmara Trough architecture of basin infill, basement and faults, from PSDM reflection and OBS refraction seismics, *Tectonophysics* **490,** 1–14.

Boetius, A., K. Ravenschlag, C. J. Schubert, D. Rickert, F. Widdel, A. Giesecke, R. Amann, B. B. Jørgensen, U. Witte, and O. Pfannkuche (2000). A marine microbial consortium apparently mediating anaerobic oxidation of methane, *Nature* **407,** 623–626.

Bourry, C., B. Chazallon, J. L. Charlou, J. P. Donval, L. Ruffine, P. Henry, L. Geli, N. Çagatay, S. İnan, and M. Moreau (2009). Free gas and gas hydrates from the Sea of Marmara, Turkey Chemical and structural characterization, *Chem. Geol.* **264,** 197–206.

Bulut, F., M. Bohnhoff, W. L. Ellsworth, M. Aktar, and G. Dresen (2009). Microseismicity at the North Anatolian fault in the Sea of Marmara offshore Istanbul, NW Turkey, *J. Geophys. Res.* **114,** B09302.

Burnard, P., S. Bourlange, P. Henry, L. Géli, B. Marty, B. Natalin, and C. Sengor (2008). Fluid Sources on the North Anatolian Fault in the Sea of Marmara From He Isotope Measurements, *Eos Trans. AGU* **89,** 53, Fall Meet. Suppl., abstract no. U53A-0069.

Géli, L., P. Henry, T. Zitter, S. Dupré, M. Tryon, N. M. Çagatay, B. Mercier de Lépinay, X. Le Pichon, A. M. C. Şengör, N. Görür, B. Natalin, G. Uçarkuş, S. Özeren, D. Volker, L. Gasperini, S. Bourlange, and The Marnaut Scientific Party (2008). Gas emissions and active tectonics within the submerged section of the North Anatolian Fault zone in the Sea of Marmara, *Earth Planet. Sci. Lett.* **274,** 34–39.

Géli, L., P. Henry, and N. Çagatay (2010). *Marmesonet Leg1 Cruise Report, November 4th—November 25th, 2009*, http://www.esonet.marmara-dm.itu.edu.tr/, December 2010.

Gürbüz, C., M. Aktar, H. Eyidogan, A. Cisternas, H. Haessler, A. Barka, M. Ergin, N. Türkelli, O. Polat, S. B. Üçer, S. Kuleli, S. Baris, B. Kaypak, T. Bekler, E. Zor, F. Bicmen, and A. Yoruk (2000). The seismotectonics of the Marmara Region (Turkey): Results from a micro-seismic experiment, *Tectonophysics* **316,** 1–17.

Hensen, C., M. Zabel, A. Boetius, K. Pfeifer, T. Schwenk, S. Kasten, N. Riedinger, and H. D. Schulz (2003). Control of sulfate pore-water profiles by sedimentary events and the significance of anaerobic oxidation of methane for the burial of sulfur in marine sediments, *Geochem. Cosmochim. Acta* **67,** 14, 2631–2647.

Imren, C., X. Le Pichon, C. Rangin, E. Demirbağ, B. Ecevitoğlu, and N. Görür (2001). The North Anatolian fault within the Sea of Marmara: A new interpretation based on multichannel seismic and multi-beam bathymetry data, *Earth Planet. Sci. Lett.* **186,** 143–158.

Janssen, C., M. Bohnhoff, Y. Vapnik, E. Görgün, F. Bulut, B. Plessen, D. Pohl, M. Aktar, A. I. Okay, and G. Dresen (2009). Tectonic evolution of the Ganos segment of the North Anatolian fault (NW Turkey), *J. Struct. Geol.* **31,** 11–28.

Lee, W. H., and S. W. Stewart (1981). Principles and applications of micro-earthquake network, *Adv. Geophys.*, Supplement 2, Academic Press, New York, 293 pp.

Le Pichon, X., A. M. C. Şengör, E. Demirbağ, R. Rangin, C. Imren, R. Armijo, N. Görür, N. Çağatay, Lepinay B. Mercier de, B. Meyer, R. Saatcilar, and B. Tok (2001). The main Marmara fault, *Earth Planet. Sci. Lett.* **192,** 595–616.

Moore, J. C., D. Orange, and L. D. Kulm (1990). Interrelationship of fluid venting and structural evolution—Alvin observations from the frontal accretionary prism, Oregon, *J. Geophys. Res.* **95,** B6, 8795–8808.

Podvin, P., and I. Lecomte (1991). Finite difference computation of traveltimes in very contrasted velocity model: a massively parallel approach and its associated tools, *Geophys. J. Int.* **105,** 271–284.

Okay, A. I., E. Demirbağ, H. Kurt, N. Okay, and I. Kuşçu (1999). An active, deep marine strike-slip basin along the North Anatolian fault in Turkey, *Tectonics* **18,** 129–147.

Okay, A. I., O. Tüysüz, and Ş. Kaya (2004). From transpression to transtension: Changes in morphology and structure around a bend on the North Anatolian fault in the Marmara region, *Tectonophysics* **391,** 259–282.

Rangin, C., E. Demirbağ, C. Imren, A. Crusson, A. Normand, E. Le Drezen, and A. Le Bot (2001). *Marine Atlas of the Sea of Marmara (Turkey)*, French Research Institute for Exploitation of the Sea (IFREMER), France.

Rangin, C., X. Le Pichon, E. Demirbağ, and C. Imren (2004). Strain localization in the Sea of Marmara: Propagation of the North Anatolian fault in a now inactive pull-apart, *Tectonics* **23,** 2, TC2014, 18 pp.

Sato, T., J. Kasahara, T. Taymaz, M. Ito, A. Kamimura, T. Hayakawa, and O. Tan (2004). A study of microearthquake seismicity and focal mechanisms within the Sea of Marmara (NW Turkey) using ocean bottom seismometers (OBSs), *Tectonophysics* **391,** 303–314.

Seeber, L., O. Emre, M.-H. Cormier, C. C. Sorlien, C. M. G. McHugh, A. Polonia, N. Ozer, and N. Cağatay (2004). Uplift and subsidence from oblique slip: The Ganos—Marmara bend of the North Anatolian transform, Western Turkey, *Tectonophysics* **391,** 239–258.

Tarantola, A., and B. Valette (1982). Inverse problems = quest for information, *J. Geophys. Res.* **50,** 159–170.

Tryon, M. D., K. M. Brown, and M. E. Torres (2002). Fluid and chemical fluxes in and out of sediments hosting hydrate deposits on Hydrate Ridge, OR, II: Hydrological processes, *Earth Planet. Sci. Lett.* **201,** 3–4, 541–557.

Waldhauser, F., and W. L. Ellsworth (2000). A double-difference earthquake location algorithm: Method and application to the Northern Hayward fault, California, *Bull. Seismol. Soc. Am.* **90,** 1353–1368.

Zelt, C. A. (1999). Modelling strategies and model assessment for wide-angle seismic traveltime data, *Geophys. J. Int.* **139,** 183–204.

Zelt, C. A., and R. B. Smith (1992). Seismic traveltime inversion for 2-D crustal velocity structure, *Geophys. J. Int.* **108,** 16–34.

Zitter, T. A. C., P. Henry, G. Aloisi, G. Delaygue, M. N. Çagatay, Lepinay B. Mercier de , M. Al-Samir, F. Fornacciari, M. Tesmer, A. Pekdeger, K. Wallmann, and G. Lericolais (2008). Cold seeps along the main Marmara fault in the Sea of Marmara (Turkey), *Deep Sea Res.* **55,** 552–570.

Appendix A

The northern part of the Marmara Sea is composed of four recent basins, from east to west, the Çinarcik basin, the Kumburgaz basin, the Central basin, and the Tekirdag basin. An average 1D velocity model for these basins was proposed by Bécel (2006). The average velocity structure (constant velocity for the first 3.5 km) is not precise enough to perform microearthquake location in a specific basin. The Tekirdag basin, where the OBSs are located, is filled by 4 km of syn-rift Plio-Quaternary sediments; in contrast, the Central and Çinarcik basins are filled by 5–6 km of sediments, and the Kumburgaz basin is filled by 2–3 km of sediments. Therefore, to perform accurate microearthquake locations, a new velocity model, specific to the Tekirdag basin, is required.

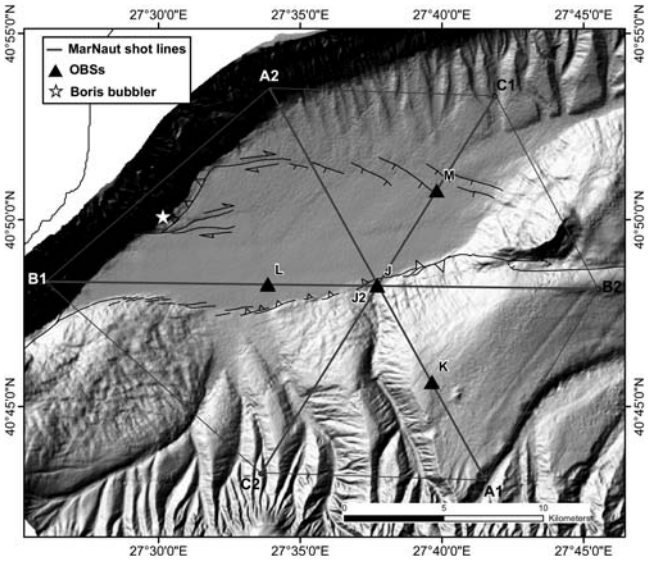

Figure A1. Location of the wide-angle seismic profiles acquired during the MarNaut cruise in the Tekirdag basin (gray lines). Thick lines indicate the profiles used for the velocity inversion. OBSs (black triangles) and Boris Bubbler positions (white star) are indicated. OBS J2, situated near OBS J, was deployed for a short period (22–28 May), centered on the wide-angle profiles acquisition.

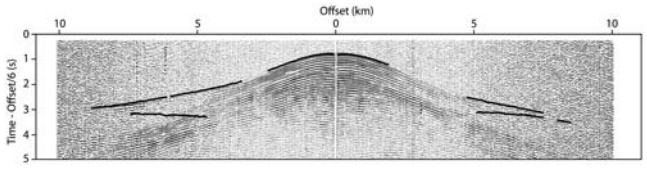

Figure A2. Receiver gather from profile A2–A1 (see location on Fig. A1) recorded on horizontal geophone at OBS J (filtered between 0 and 30 Hz) with the observed travel times superimposed (black lines). The data are displayed with a gain proportional to source-receiver offset and are reduced at a velocity of 6 km/s.

Table A1
OBS Positions and Water Depth

Stations	Longitude (deg)	Latitude (deg)	Water Depth (m)
J	E 27.6290	N 40.8039	1112
J2	E 27.6290	N 40.8038	1112
K	E 27.6608	N 40.7613	546
L	E 27.5645	N 40.8044	1132
M	E 27.6637	N 40.8466	1110

Natural frequency of geophones: 4.5 Hz; sampling frequency: 250 Hz.

During the MarNaut cruise, twelve wide-angle profiles were acquired in the Tekirdag basin by the R/V Sismik-1 (on 23 and 24 May 2007), using five short-period ocean-bottom instruments (Fig. A1). Six profiles were shot across the basin (A1-A2, A2-A1, B1-B2, B2-B1, C1-C2, and C2-C1) and six around the basin (A1-B2, B2-C1, C1-A2, A2-B1, B1-C2, and C2-A1; Fig. A2). All instruments were equipped with three-component velocity sensors (one vertical and two non-oriented, horizontal components) and a hydrophone. Their position and main technical features are summarized in Table A1.

For each profile that crosses the basin (A1-A2, A2-A1, B1-B2, B2-B1, C1-C2 and C2-C1), the reflected and refracted waves were identified. An uncertainty of 0.02 s was assigned to each pick. The velocity model was determined by inversion of the first-arrival travel times using the RAYINVR package (Zelt and Smith, 1992; Zelt, 1999). Each individual profile was considered separately, assuming a 2D isotropic medium. Due to uncertainties in picking, we did not attempt to use secondary arrivals or *S* waves. The initial velocity model consisted of a sequence of five horizontal layers (except for sediment/water interface, which mimics

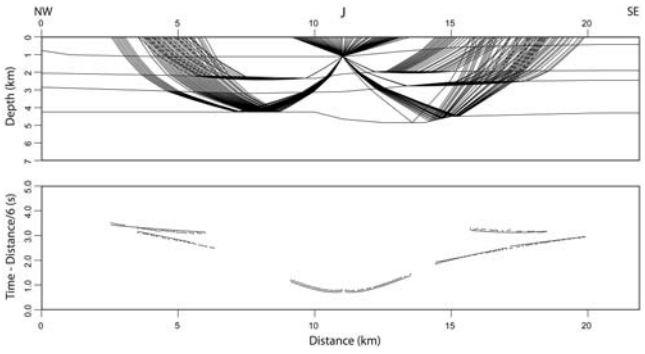

Figure A3. (Top) Ray coverage of OBS J in the profile A2-A1. The black lines indicate the ray paths. (Bottom) Travel-time fit of the associated rays. The dots mark the refracted and reflected wave picks. The black lines correspond to the calculated hodochrones for the rays shown in the top part of the figure. The travel times are reduced at a velocity of 6 km/s.

Table A2
Number of Picks, Number of Blocks, and rms Travel-Time Residual for All Profiles

Profile	No. of Picks	No. of Blocks	rms Travel-Time Residual
A1A2	82	36	0.064
A2A1	312	69	0.086
B1B2	131	51	0.054
B2B1	201	62	0.064
C1C2	322	61	0.068
C2C1	320	66	0.075

The number of blocks in the model depends on the layer geometry, the velocity structure, and the data coverage.

the bathymetry): the water layer (1.52 km/s) and four sedimentary layers (1.8, 2.2, 3.1, and 3.4 km/s). Travel times were calculated by numerical integration along ray paths. The final velocity model was then adjusted iteratively via a trial-and-error, forward-modeling process by adjusting interface geometries and medium velocity. A total of 1368 picks were used to calculate the velocity models along the six 2D profiles, with root mean square (rms) residuals ranging from 0.054 to 0.086 s (Fig. A3). The rms travel-time residual, number of picks, and blocks for all profiles are listed in Table A2. The six velocity profiles were combined to determine the velocity structure beneath OBS J, the OBS network center, for the upper 4-km layer (Fig. A4). The corresponding surficial 1D velocity model underneath OBS J (Fig. A5a) was used to modify Bécel's (2006) velocity model for the upper 4 km of sediments (Fig. A5b) specific to the Tekirdag basin. A constant V_P/V_S ratio equal to 1.79 (Bécel, 2006) was used for microearthquake locations.

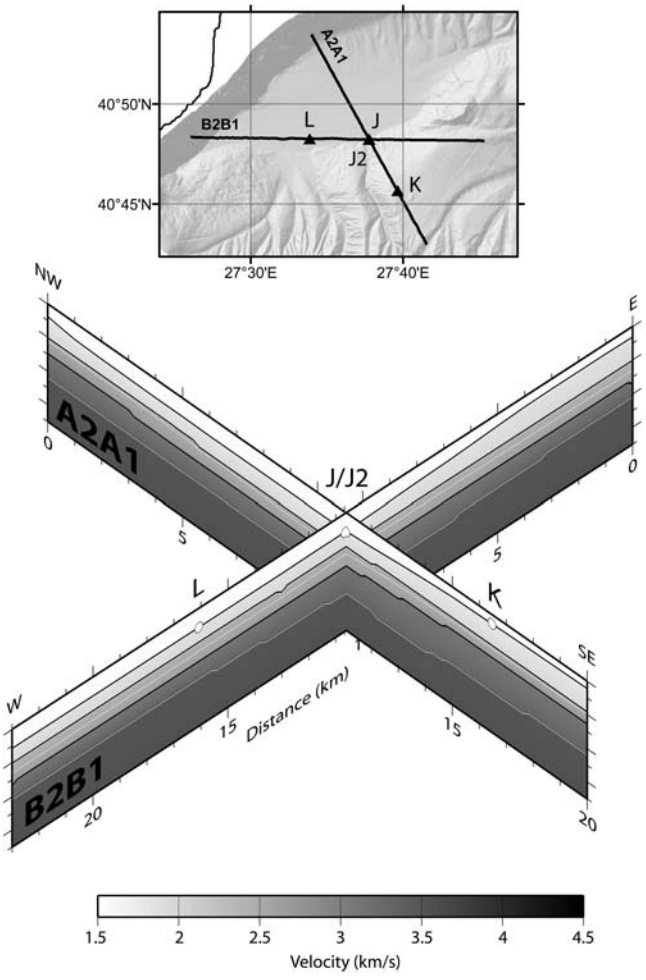

Figure A4. (Top) Location of the wide-angle seismic profiles A2-A1 and B2-B1. (Bottom) Final velocity models for profiles A2-A1 and B2-B1. White dots indicate OBS positions. White lines are the layer boundaries, and black lines the velocity boundaries.

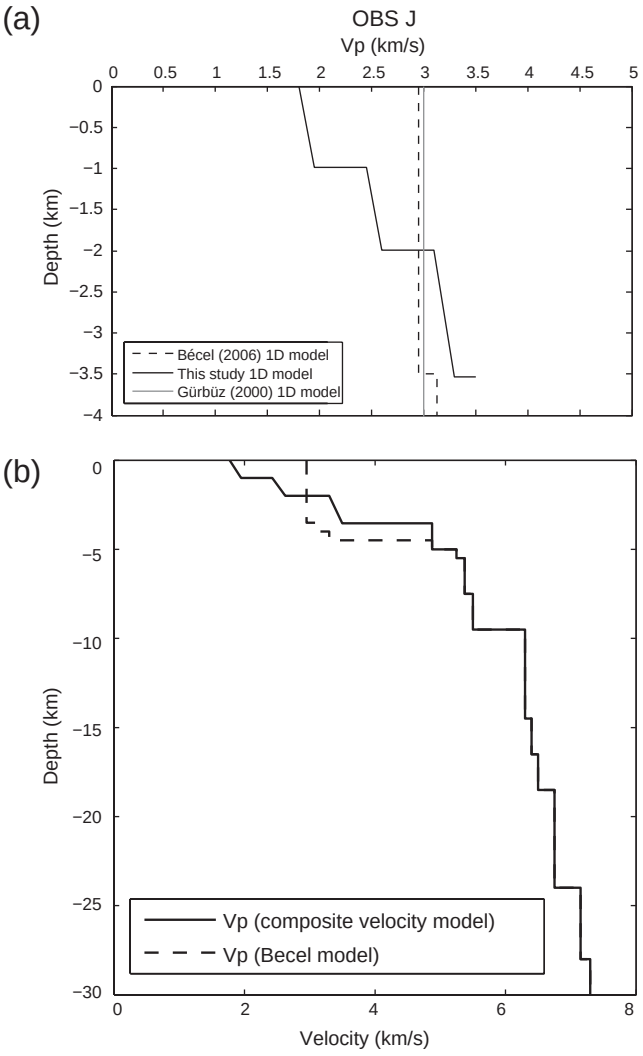

Figure A5. (a) Comparison of 1D velocity models in the upper 4 km beneath OBS J with the velocity model of Gürbüz (2000) shown as the gray line, the velocity model of Bécel (2006) shown as the black dashed line, and our final velocity model shown as the black solid line. (b) Composite 1D velocity model (solid black line) in the upper 30 km of the Tekirdag basin area based on the velocity model of Bécel (2006, dashed black line) and our new velocity model. The composite velocity model was used in this study to initially locate earthquakes.

Appendix B

Here, we present a homemade technique in which $N-1$ events are determined relative to the location of a master event, which is supposed to be perfectly well located (where N is the number of events, equal to 13). Let us assume that the biggest event of the cluster (E_0), is accurately located. The cluster events are then relocated relative to E_0.

For a given earthquake (E_i) station (S) pair, the travel time can be expressed as

$$(t_S - t_P)_{E_iS} = A_{E_iS} E_i S \quad \text{with} \quad A_{E_iS} = \left(\frac{1}{V_P} - \frac{1}{V_S}\right)_{E_iS}, \tag{B1}$$

where t_S and t_P are the P- and S-wave arrival times at station S, and A_{E_iS} is the mean slowness difference along the source-receiver distance (E_iS). In Cartesian coordinates, the source-receiver distance is thus

$$\|E_iS\| = \sqrt{(x_i - x_S)^2 + (y_i - y_S)^2 + (z_i - z_S)^2} = \frac{(t_S - t_P)_{E_iS}}{(\frac{1}{V_P} - \frac{1}{V_S})_{E_iS}}. \tag{B2}$$

For each microearthquake, the distance E_iS can be decomposed into a main part, the reference earthquake (E_0)-station distance (E_0S), and a small part, the reference earthquake-event distance (E_0E_i):

$$\begin{aligned} x_i - x_S &= (x_0 - x_S) + (x_0 - x_i) = (x_0 - x_S)\left(1 + \frac{x_0 - x_i}{x_0 - x_S}\right), \\ y_i - y_S &= (y_0 - y_S) + (y_0 - y_i) = (y_0 - y_S)\left(1 + \frac{y_0 - y_i}{y_0 - y_S}\right), \\ z_i - z_S &= (z_0 - z_S) + (z_0 - z_i) = (z_0 - z_S)\left(1 + \frac{z_0 - z_i}{z_0 - z_S}\right). \end{aligned} \tag{B3}$$

Given that the distance between two events is small relative to the event-station distance, (B3) is linearized as

$$\begin{aligned} (x_i - x_S)^2 &= (x_0 - x_S)^2\left(1 + 2\frac{x_i - x_0}{x_0 - x_S}\right), \\ (y_i - y_S)^2 &= (y_0 - y_S)^2\left(1 + 2\frac{y_i - y_0}{y_0 - y_S}\right), \\ (z_i - z_S)^2 &= (z_0 - z_S)^2\left(1 + 2\frac{z_i - z_0}{z_0 - z_S}\right). \end{aligned} \tag{B4}$$

The source-receiver distance, E_iS, becomes

$$\begin{aligned} \|E_iS\| &= \sqrt{(x_0 - x_S)^2\left(1 + 2\frac{x_i - x_0}{x_0 - x_S}\right) + (y_0 - y_S)^2\left(1 + 2\frac{y_i - y_0}{y_0 - y_S}\right) + (z_0 - z_S)^2\left(1 + 2\frac{z_i - z_0}{z_0 - z_S}\right)} \\ &= \|E_0S\|\sqrt{1 + 2\frac{(x_i - x_0)(x_0 - x_S) + (y_i - y_0)(y_0 - y_S) + (z_i - z_0)(z_0 - z_S)}{\|E_0S\|^2}} \\ &= \|E_0S\|\left(1 + \frac{(x_i - x_0)(x_0 - x_S) + (y_i - y_0)(y_0 - y_S) + (z_i - z_0)(z_0 - z_S)}{\|E_0S\|^2}\right). \end{aligned} \tag{B5}$$

In (B1), we can replace E_iS by its linearized form

$$(t_S - t_P)_{E_iS} = A_{E_iS}\|E_0S\|\left(1 + \frac{LA_1}{\|E_0S\|^2}\right) \quad \text{with} \quad \begin{aligned} LA_1 &= (x_i - x_0)(x_0 - x_S) \\ &+ (y_i - y_0)(y_0 - y_S) \\ &+ (z_i - z_0)(z_0 - z_S). \end{aligned} \tag{B6}$$

The mean slowness difference, A_{E_iS}, can also be decomposed like the source-receiver distance E_iS, and (B6) becomes

$$(t_S - t_P)_{E_iS} = (A_{E_0S} + A_{E_iE_0})\|E_0S\|\left(1 + \frac{LA_1}{\|E_0S\|^2}\right), \tag{B7}$$

where A_{E_0S} is the mean slowness difference along station-reference distance, and $A_{E_iE_0}$ the small difference in slowness from A_{E_0S} along reference-event distance. Equation (B7) can also be linearized, and we obtain

$$\begin{aligned} (t_S - t_P)_{E_iS} &= A_{E_0S}\left(1 + \frac{A_{E_iE_0}}{A_{E_0S}}\right)\|E_0S\|\left(1 + \frac{LA_1}{\|E_0S\|^2}\right), \\ &= A_{E_0S}\|E_0S\|\left(1 + \frac{A_{E_iE_0}}{A_{E_0S}} + \frac{LA_1}{\|E_0S\|^2}\right). \end{aligned} \tag{B8}$$

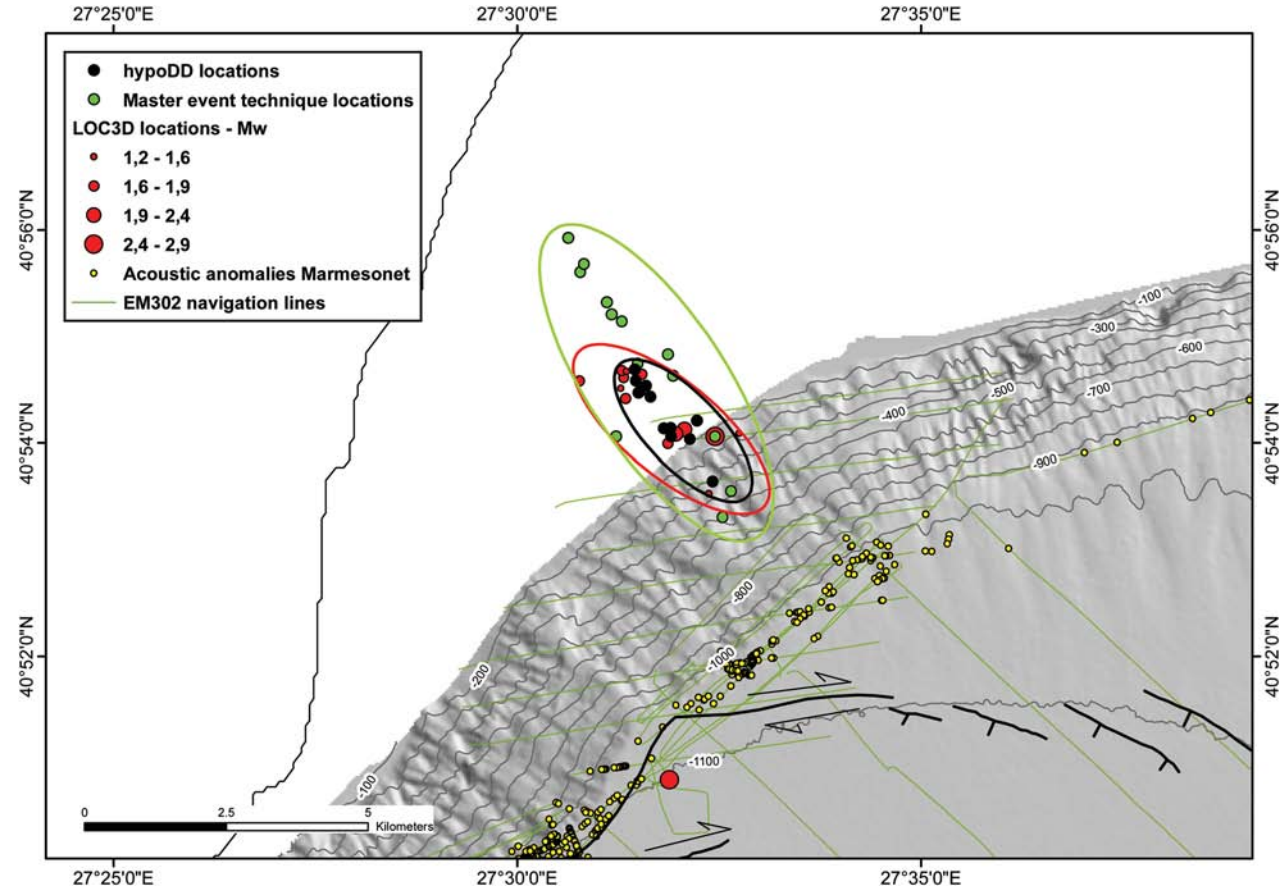

Figure B1. Earthquake locations using LOC3D (red circles), hypoDD (black circles, singular value decomposition solution), and our master event technique (green circles). Green lines indicate the routes followed by the R/V Le Suroit in November–December 2009. Yellow dots show locations of acoustic anomalies detected using the SIMRAD EM302 multibeam system.

With $(t_S - t_P)_{E_0S} = A_{E_0S}\|E_0S\|$ and (B8) appear the double-difference equation

$$(t_S - t_P)_{E_iS} - (t_S - t_P)_{E_0S} = A_{E_iE_0}\|E_0S\| + A_{E_0S}\frac{LA_1}{\|E_0S\|}. \tag{B9}$$

Finally, we normalize (B9) by $(t_S - t_P)_{E_0S}$ and obtain

$$\begin{aligned}\frac{(t_S - t_P)_{E_iS} - (t_S - t_P)_{E_0S}}{(t_S - t_P)_{E_0S}} = &\frac{(x_0 - x_S)(x_i - x_0)}{\|E_0S\|^2} \\ &+ \frac{(y_0 - y_S)(y_i - y_0)}{\|E_0S\|^2} \\ &+ \frac{(z_0 - z_S)(z_i - z_0)}{\|E_0S\|^2} \\ &+ A_{E_iE_0}\frac{\|E_0S\|}{(t_S - t_P)_{E_0S}}.\end{aligned} \tag{B10}$$

In equation (B10), the unknowns are the event positions (x_i, y_i, z_i) and the slowness changes along reference-event distance ($A_{E_iE_0}$). This gives a system of four equations (four stations) for four unknowns to solve:

$$\begin{pmatrix} \frac{(x_0-x_J)}{\|E_0J\|^2} & \frac{(y_0-y_J)}{\|E_0J\|^2} & \frac{(z_0-z_J)}{\|E_0J\|^2} & \frac{\|E_0J\|}{(t_S-t_P)_{E_0J}} \\ \frac{(x_0-x_K)}{\|E_0K\|^2} & \frac{(y_0-y_K)}{\|E_0K\|^2} & \frac{(z_0-z_K)}{\|E_0K\|^2} & \frac{\|E_0K\|}{(t_S-t_P)_{E_0K}} \\ \frac{(x_0-x_L)}{\|E_0L\|^2} & \frac{(y_0-y_L)}{\|E_0L\|^2} & \frac{(z_0-z_L)}{\|E_0L\|^2} & \frac{\|E_0L\|}{(t_S-t_P)_{E_0L}} \\ \frac{(x_0-x_M)}{\|E_0M\|^2} & \frac{(y_0-y_M)}{\|E_0M\|^2} & \frac{(z_0-z_M)}{\|E_0M\|^2} & \frac{\|E_0M\|}{(t_S-t_P)_{E_0M}} \end{pmatrix} \begin{pmatrix} x_i - x_0 \\ y_i - y_0 \\ z_i - z_0 \\ A_{E_iE_0} \end{pmatrix}$$

$$= \begin{pmatrix} \frac{(t_S-t_P)_{E_iJ} - (t_S-t_P)_{E_0J}}{(t_S-t_P)_{E_0J}} \\ \frac{(t_S-t_P)_{E_iK} - (t_S-t_P)_{E_0K}}{(t_S-t_P)_{E_0K}} \\ \frac{(t_S-t_P)_{E_iL} - (t_S-t_P)_{E_0L}}{(t_S-t_P)_{E_0L}} \\ \frac{(t_S-t_P)_{E_iM} - (t_S-t_P)_{E_0M}}{(t_S-t_P)_{E_0M}} \end{pmatrix}. \tag{B11}$$

However, due to the large event-station distance, the depth ($\frac{(z_0-z_S)(z_i-z_0)}{\|E_0S\|^2}$) and slowness ($A_{E_iE_0}\frac{\|E_0S\|}{(t_S-t_P)_{E_0S}}$) terms are small compared to the others. Consequently, their contributions in the solution are small, and only the horizontal terms (x-y) are well constrained.

The results are consistent with locations obtained by hypoDD and absolute locations obtained by LOC3D. However, the dispersion of the epicenters using the master event technique is larger than the one obtained with hypoDD (Fig. B1). The main reason for this is that the four values produced by each inversion are actually not independent but are linked via the slowness term ($A_{E_0E_i}$).

French Research Institute for Exploitation of the Sea (IFREMER)
Marine Geosciences Department
BP 70, 29280
Plouzané, France
(J.B.T., L.G.)

Centre Européen de Recherche et d'Enseignement des Géosciences de l'Environnement (CEREGE)
Chaire de géodynamique du Collège de France
Europôle de l'Arbois, BP80, 13545
Aix-en-Provence Cedex 04, France
(P.H.)

Istanbul Technical University
Faculty of Mines, Geology Department
Maslak, 34469
Istanbul, Turkey
(B.N., N.Ç.)

Istituto di Scienze Marine (ISMAR)
Consiglio Nazionale delle Ricerche (CNR)
101 Via Gobetti, 40129
Bologna, Italy
(L.G.)

Kandilli Observatory and Earthquake Research Institute
34684 Cengelköy
Istanbul, Turkey
(M.Ç.)

Magnitude, Centre Regain
route de Marseille, 04220
Sainte-Tulle, France
(T.B.)

Manuscript received 13 January 2010

2.8. Case study 2: Micro-events observed on OBS recordings

2.8.1. Introduction

Besides micro-earthquakes, the OBSs deployed during the MarNaut cruise recorded numerous non-seismic micro-events. These micro-events are very common on OBS recordings [*Buskirk et al.*, 1981; *Diaz et al.*, 2007], but generally they are not detected by the procedure described earlier for micro-earthquakes, as they are most of the time not recorded by more than one station. Micro-events differ from micro-earthquakes by several aspects (Fig. 2.44 and 2.45).

Micro-events have short durations of less than 0.8 s, a monochromatic frequency content between 5 and 30 Hz, and highly variable amplitudes (0.5-50 µm/s). Even though micro-earthquakes have peak amplitudes in the same range, they have a richest frequency spectrum and longer durations (3 s-few minutes) than micro-events. In addition, earthquakes are composed by different waves (P-wave, S-wave, surface waves…) while micro-events show only one arrival. Finally, while micro-earthquakes are well recorded by the hydrophones, micro-events are visible only on those hydrophones that are close enough to the sediment/water interface (<0.9 m).

Based on OBS recordings in various geologic contexts, *Buskirk et al.* [1981] and *Diaz et al.* [2007] proposed two explanations for the origin of the observed micro-events. Following the observations of micro-events distribution with depth, which could mimics the repartition of biomass in oceans, and observations of eggs of unknown biologic organism fixed on the frame of several instruments, *Buskirk et al.* [1981] proposed that micro-events could be produced by some living organisms “bumping” on the instruments.

On the other hand, following the fluid-filled cracks modeling of *Chouet* [1988, 1996], *Diaz et al.* [2007] suggested that micro-events could be produced by pressure transients involving the resonance of fluid-filled cracks.

In the following section, we propose that gas emissions on the seafloor through fractures, pre-existent or not, are likely the source of the recorded micro-events.

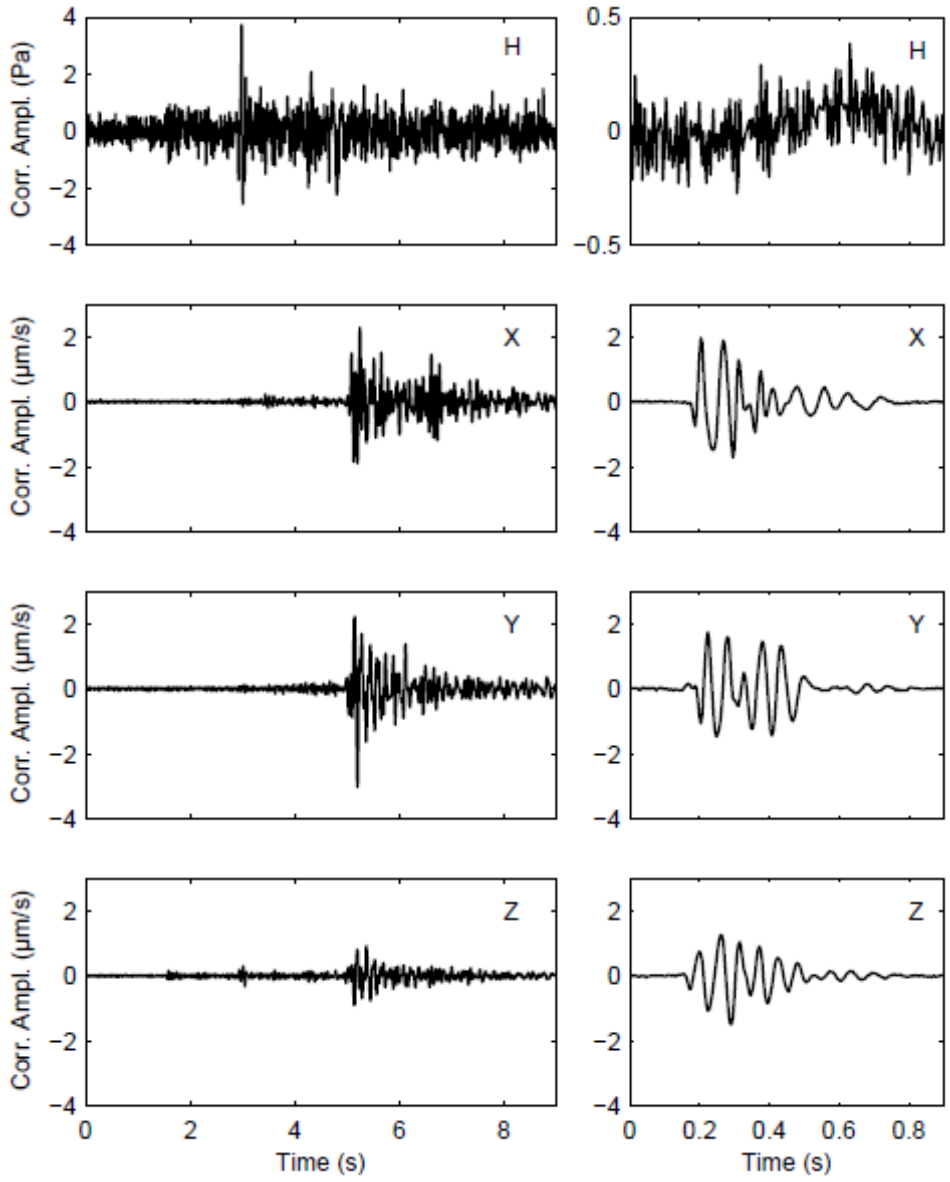

Fig. 2.44. OBS M recordings (H: hydrophone, X and Y: geophone horizontal components, Z: geophone vertical component), showing a micro-earthquake (M_w 1.98, May 14, 2007, 22:23:32) on the left and a micro-event on the right (May 14, 2007, 14:01:57).

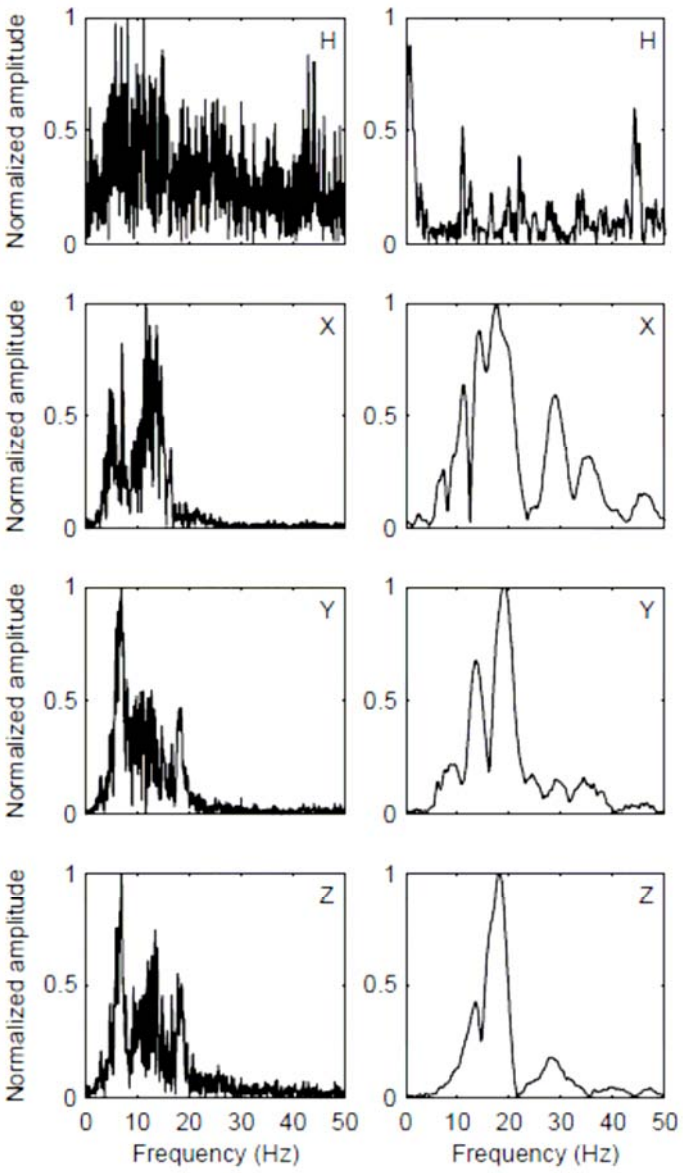

Fig. 2.45. Frequency spectrum of the micro-earthquake (left) and the micro-event (right) shown in Fig. 2.44 (H: hydrophone, X and Y: geophone horizontal components, Z: geophone vertical component).

2.8.2. Micro-events produced by gas migration and expulsion at the seabed: a study based on sea bottom recordings from the Sea of Marmara

In the following is presented the analysis of the micro-events recorded by the OBSs deployed in the Sea of Marmara. This section is presented hereafter as an article that was submitted to the Journal of Geophysical Research – Solid Earth.

Micro-events produced by gas migration and expulsion at the seabed: a study based on sea bottom recordings from the Sea of Marmara

Jean-Baptiste Tary,[1] Louis Géli,[1] Claude Guennou,[2] Pierre Henry,[3] Nabil Sultan,[1] Namik Çağatay,[4] and Valérie Vidal[5]

Abstract

Different types of 4-Components Ocean Bottom Seismometers (OBS) were deployed in 2007, over soft sediments covering the seafloor of the Tekirdag Basin (western part of the Sea of Marmara, Turkey). Non-seismic micro-events were recorded by the geophones, but generally not by the hydrophones, except when the hydrophone is located less than a few tens of cm above the seafloor. The micro-events are characterized by short durations of less than 0.6 seconds, frequencies ranging between 5 and 30 Hz, and highly variable amplitudes. In addition, no correlation between OBSs was observed, except for those OBSs located 10 meters apart. Interestingly, a swarm of ~400 very similar micro-events (based on principal component analysis) was recorded in less than one day by an OBS located in the close vicinity of an active, gas-prone fault cutting through the upper sedimentary layers. The presence of gas in superficial sediments, together with analogies with laboratory experiments, suggest that gas migration followed by the collapse of fluid-filled cavities or conduits could be the source of the observed micro-events. This work shows that OBSs may provide valuable information to improve our understanding of natural degassing processes from the seafloor.

[1] IFREMER, Marine Geosciences Department, 29280 Plouzané, France

[2] UMR 6538, Domaines Océaniques, Institut Universitaire Européen de la Mer, 29280 Plouzané, France

[3] CEREGE, Chaire de géodynamique du Collège de France, Europôle de l'Arbois, 13545 Aix-en-Provence, France

[4] Mining Faculty, Istanbul Technical University (ITU), 34469 Istanbul, Turkey

[5] Laboratoire de Physique, Université de Lyon, Ecole Normale Supérieure, CNRS, 69364 Lyon, France

1. Introduction – general context

The Sea of Marmara is located on the North Anatolian Fault zone in NW Turkey, a major transform-plate boundary that has produced devastating historical earthquakes along its 1600 km length. After the 1999 Izmit and Düzce earthquakes, the next large (Mw > 7) earthquake is expected close to the heavily populated (>15 million inhabitants) Istanbul Area (Fig. 1). Hence, the Sea of Marmara has been extensively surveyed during the last decade.

Several marine expeditions found gas emissions sites and brackish water seeps, along or near the main active faults scarps in the Sea of Marmara [*Alpar*, 1999; *Halbach et al.*, 2004; *Armijo et al.*, 2005; *Zitter et al.*, 2008; *Géli et al.*, 2008]. However, recent sediment sounder (chirp) profiles and multibeam echosounder data acquired during MARMESONET cruise of R/V Le Suroit [*Géli et al.*, 2010], show the widespread presence of gas in the upper sediments and water column [*Dupré et al.*, 2010; *Tary*, 2011]. Geochemical analysis indicates that the gas is mainly methane, and has two different origins: 1) in basins, gas is dominantly of bacterial origin, likely resulting from the decomposition of organic material in the Pleistocene sediments; 2) on the Western High and Central High, gas is dominantly thermogenic, originating from the Eocene-Oligocene Thrace Basin source rocks [*Bourry et al.*, 2009].

These observations and the high geohazard potential of the area are such that the Sea of Marmara has been identified as an unique, natural laboratory to study the relationships between fluids and seismicity through the EC-funded ESONET Network of Excellence (**E**uropean **S**eafloor **O**bservatory **Net**work). In order to prepare the implementation of permanent multidisciplinary seafloor observatories, two preparatory experiments were conducted in 2007 and 2009-2010. Here, we report observations of non-seismic micro-events detected by Ocean Bottom Seismometers (OBS) and show that these events are related to gas emissions from shallow sediment layers (<5 m). These findings provide a better understanding of degassing processes from the seafloor. In the perspective of future pluri-disciplinary seafloor observatories, our results may help establish a method to detect and characterize episodes of gas accumulation and release in shallow sediments.

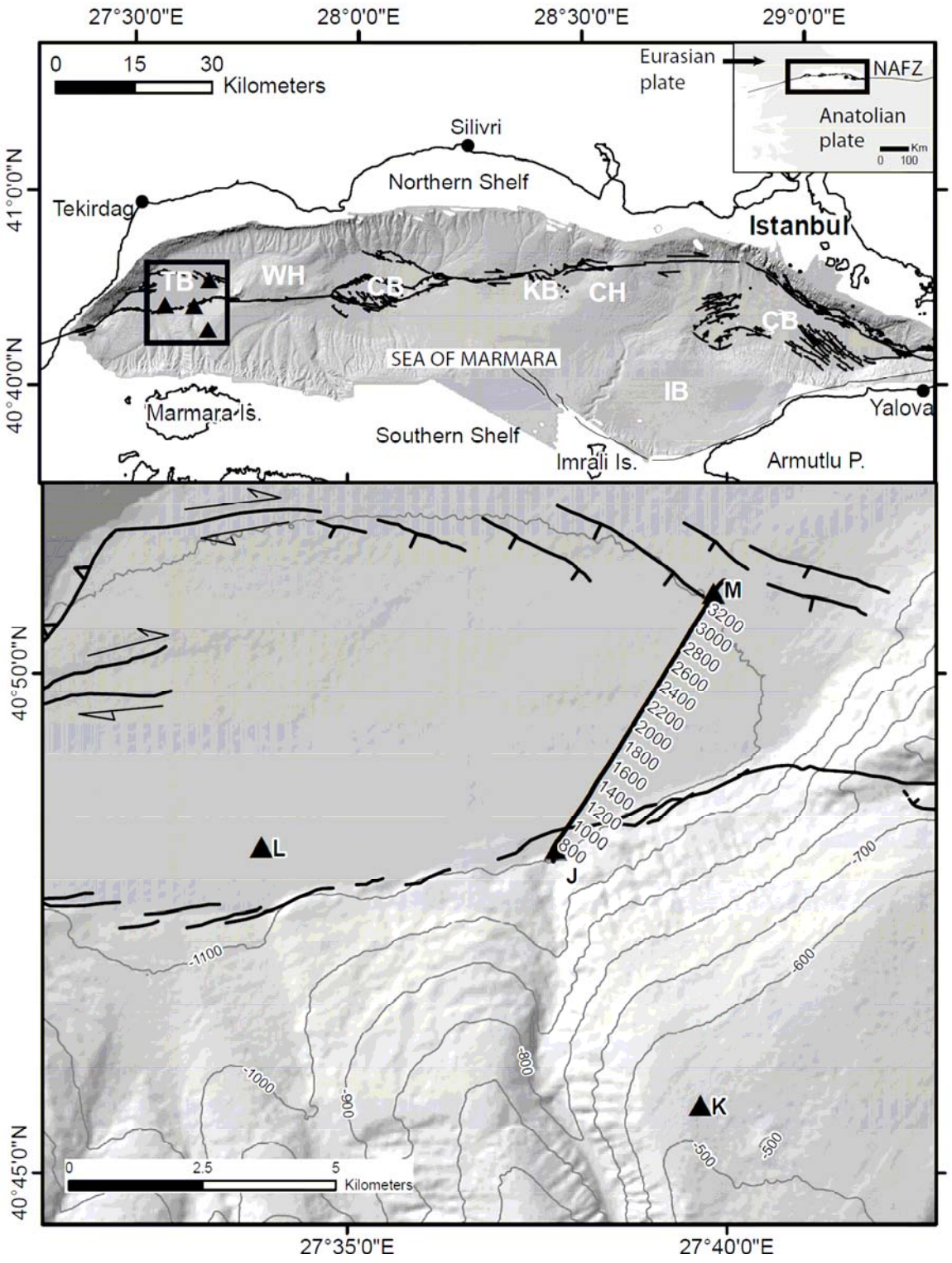

Figure 1. (Top) Map of the Sea of Marmara with active fault traces [Rangin et al., 2001, 2004; Imren et al., 2001; Armijo et al., 2005]. Abbreviations: NAFZ, North Anatolian Fault Zone; TB, Tekirdag Basin; WH, Western High; CB, Central Basin; KB, Kumburgaz Basin; CH, Central High; ÇB, Çinarcik Basin; IB: Imrali Basin; P., Peninsula; Is., Island. (Bottom) Bathymetric map of the Tekirdag Basin. Indicated by black triangles are the OldOBS deployed during MarNaut cruise in 2007. In the same place as J are located J2, ARMSS, NEEDLE and SPAN (see Fig. 2). The black line with numbers corresponds to the ship's track and trace numbers of the chirp profile in Fig. 7. The faults are indicated by the other black lines.

2. Instrument characteristics and environmental settings

2.1. Instrument characteristics

From May 14 to August 30, 2007, a total of eight, autonomous OBSs equipped with three component geophones and one hydrophone were deployed in the western part of the Sea of Marmara: five, provided by Ifremer, were launched off board from the operating vessel, R/V L'Atalante; three, provided by CGG-Veritas were installed on the sea bottom with Nautile, the Ifremer submersible (Fig. 1 and 2). In order to test different coupling devices, 5 types of OBSs with different design (respectively OldOBS, MicrOBS, ARMSS, NEEDLE and SPAN) were deployed during different, not always overlapping periods. The instruments locations, technical characteristics and recording periods are summarized in Table 1. Specific details, useful for the present paper, are given hereafter:

- OldOBS (deployed at sites J, K, L and M) are large instruments (1.5 m in height, weighing 240 kg in air) from Ifremer. The geophones are contained in an outer, pressure-resistant case resting on the seafloor, while the hydrophone is fixed on the instrument's frame, ~0.9 m above the seafloor (Fig. 3).
- MicrOBS (deployed at site J2) is also an Ifremer instrument, weighing less than 20 kg in air, packaged within a 13" glass sphere, which includes the electronics, the batteries and the geophones. The hydrophone is fixed on the instrument's frame, ~0.3 m above the seafloor.
- ARMSS (from CGG-Veritas) consists in a 0.9 m long cylinder lying horizontally on the seafloor, with a head containing both the geophones (arranged in a Galperin configuration) and the hydrophone. A vibrating system mounted around the instrument's head optimizes the coupling with the seafloor.
- SPAN (from CGG-Veritas) is a ~1 m bullet shaped instrument, with geophones integrated in a titanium container three-fourth buried in the soil, or a little more due to the soft character of sediments. The data of this instrument were too noisy to be used for quantitative signals analysis.
- NEEDLE (from CGG-Veritas) consists in a 4.5 m long pipe inserted in the sediments. After penetration, a self corroding system was activated, which divided the pipe into 2 mechanically decoupled sections, the sensors (three geophones and a hydrophone) being at the end of the lower section (~3 m long).

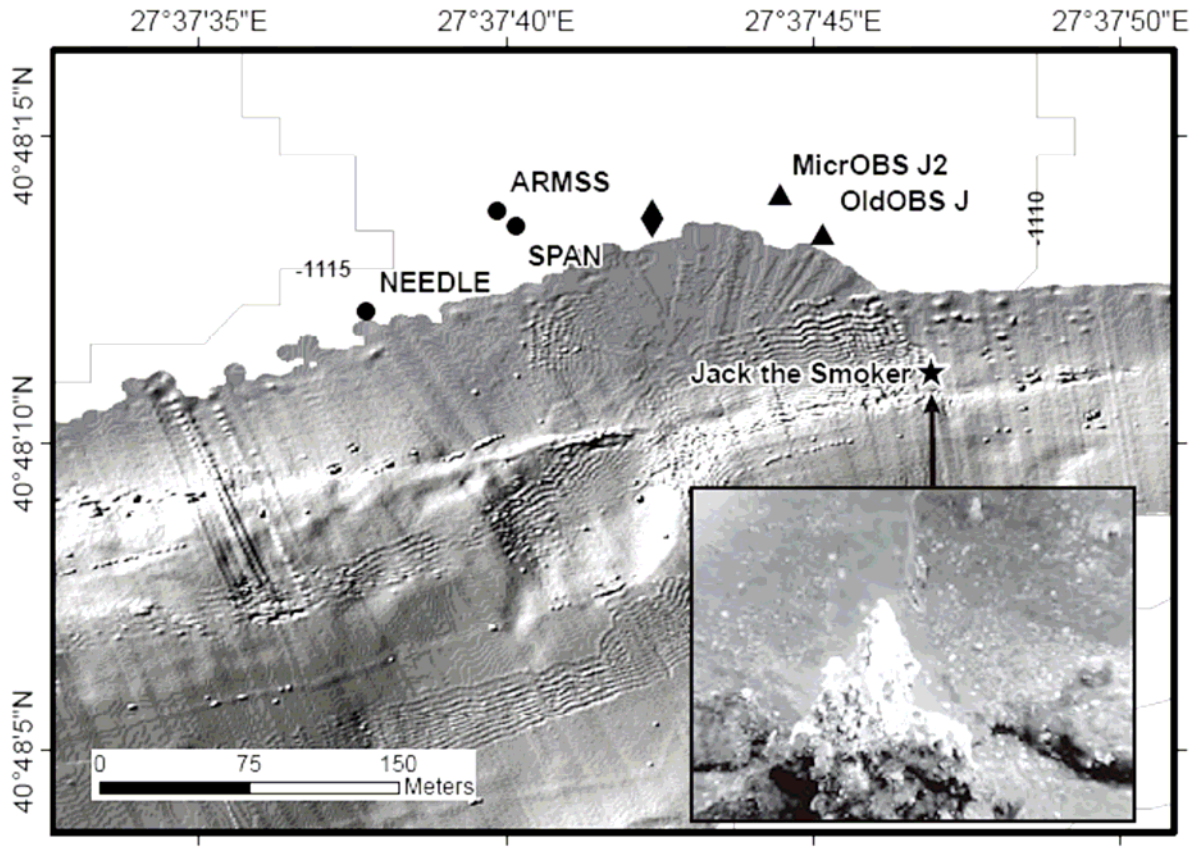

Figure 2. Zoom in the OBS network center. Microbathymetric data were acquired during the MARMARASCARPS cruise in 2002 by the R.O.V. Victor [Armijo et al., 2005]. OBS provided by IFREMER and CGG-Veritas are indicated by black triangles and black dots respectively. The black star shows the location of "Jack the Smoker" site where fresh water escapes from the seafloor through carbonate chimneys. The black diamond shows the location of the seismic shot used for OBSs amplitude inter-calibration (Section 2.6.2).

Stations	Longitude (deg)	Latitude (deg)	Depth (m)	Recorded period used	F_0 (Hz)	Fs (Hz)	Observations
J	E 27.62921	N 40.80372	1112	14 May - 30 Aug. 2007	4.5	250	
J2	E 27.62902	N 40.80390	1112	22 May - 28 May 2007	4.5	250	Y comp. resonance
K	E 27.6608	N 40.7613	546	14 May - 19 Aug. 2007	4.5	250	
L	E 27.5645	N 40.8044	1132	14 May - 09 June 2007	4.5	250	
M	E 27.6637	N 40.8466	1110	14 May - 26 Aug. 2007	4.5	250	
ARMSS	E 27.62774	N 40.80382	1115	14 May - 09 June 2007	14	500	
SPAN	E 27.62782	N 40.80376	1117	14 May - 28 May 2007	4.5	500	Low quality
NEEDLE	E 27.62714	N 40.80337	1115	14 May - 28 May 2007	4.5	500	

Table 1. OBS position, technical characteristics and recording period. F_0: geophones natural frequency; Fs : sampling frequency; comp.: component.

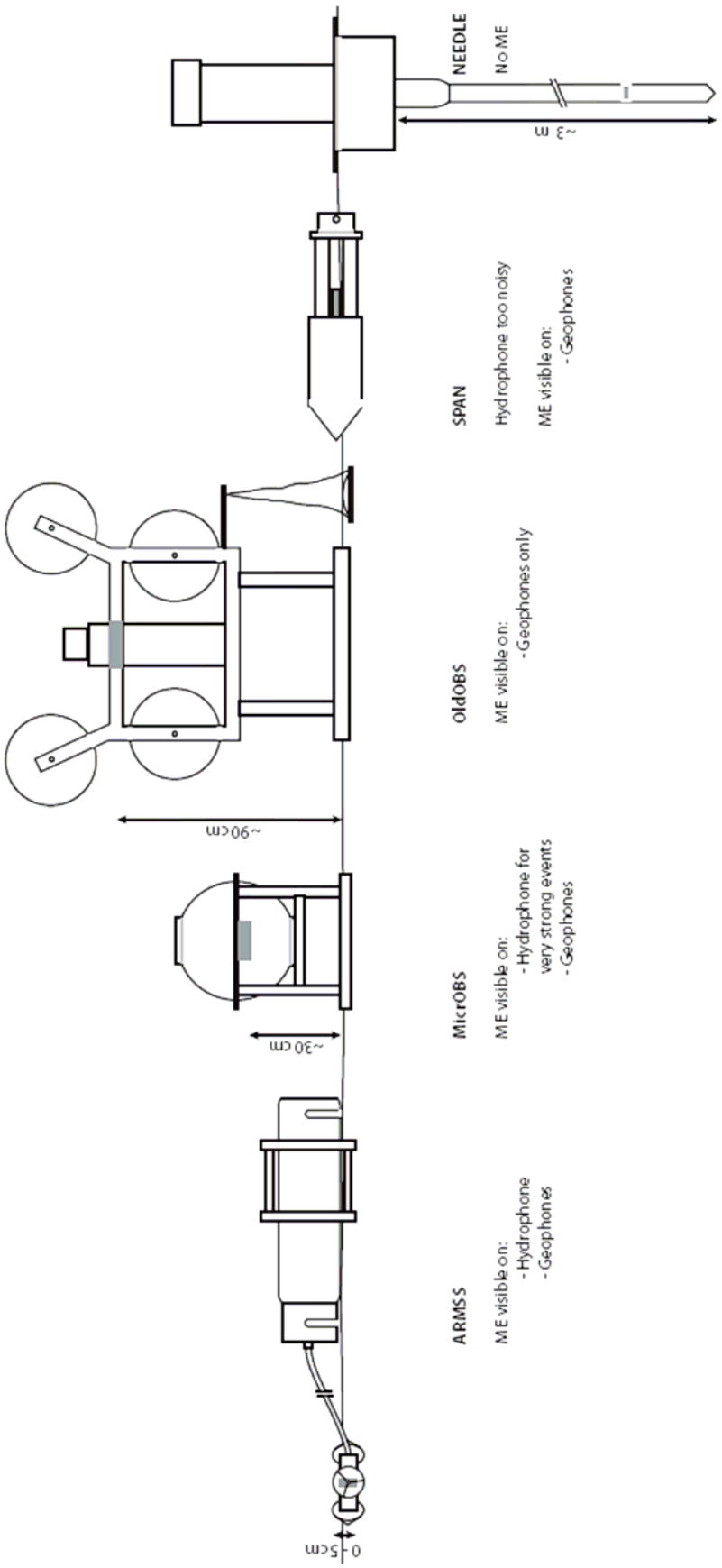

Figure 3. Schematic structure of the OBSs deployed during the MarNaut cruise. For each OBS, the hydrophone location is indicated by the gray rectangle. ME: micro-events.

For each OBS, the drifts of the internal clocks were linearly corrected, based on laboratory results obtained in comparable pressure and temperature. In addition, as reported in *Tary et al.* [2011], *"seismic shots triggered using a GPS-synchronized clock were recorded by the OBSs on May 23 and 24, 2007 providing estimates of the drift of the instruments after 10 days of deployment (between May 14 and May 24). These estimates confirmed that the instruments internal clocks drifted almost linearly during the first 25-days period."*

Descaling factors to convert digital (counts) into physical (µm/s or Pa) units are different for each type of OBSs. Unexpected high amplitudes were obtained for CGG-Veritas sensors and OldOBS hydrophones, raising doubts on their descaling factors. Hence, seismic shots have been used to calibrate the instruments sensors relatively to well-known sensors (MicrOBS hydrophone and OldOBS geophones). This procedure is described in Section 2.6.2. The amplitudes given hereafter correspond to calibrated, relative amplitudes.

2.2. Environmental settings

Three OldOBSs (K, L, M) were deployed so as to define a triangular network having equal sides, 10 km long, covering the North Anatolian Fault (Fig. 1). OBS M was positioned in the northern part of the Tekirdag Basin, near WNW-ESE oriented normal faults [*Le Pichon et al.*, 2001; *Rangin et al.*, 2004], while OBS K was positioned on the southern flank of the fault, by water depth of 546 m. Based on sediment sounder profiles (chirp data), the upper sediment layers near OBSs K and M are filled by gas [*Tary*, 2011].

The 5 remaining OBSs (OldOBS J, MicrOBS J2, ARMSS, NEEDLE and SPAN), were positioned near the center of the triangle, within a distance of ~100 to 400 m from a cold seep called "Jack the Smoker" located on a seafloor rupture of the North Anatolian Fault [*Armijo et al.*, 2005; *Zitter et al.*, 2008]. These OBSs are very close from each other, the closest ones, ARMSS and SPAN, being separated by only 10 m (Fig. 2).

3. Micro-events general characteristics

The dataset was first analyzed to characterize the micro-seismicity in the area. The results were published in [*Tary et al.*, 2011]. An algorithm, based on the ratio Short Term Average/Long Term Average (STA/LTA) and a minimum number of stations, was applied to detect the seismic events. Over the whole period, 270 seismic events recorded at least at 3 stations were identified.

OBSs also recorded a large number of micro-events that were not detected by the above mentioned procedure, as they are generally not recorded by more than one station although their amplitudes are comparable to earthquakes (Fig. 4). These events of short duration are very common on ocean bottom recordings [*Buskirk et al.*, 1981; *Diaz et al.*, 2007].

Except NEEDLE, all OBSs, whatever their structures, have recorded micro-events (NEEDLE only recorded aseismic signals related to its post-penetration stabilization mainly the first two days of the experiment). The general characteristics of the micro-events are:

- Short duration, in average between 0.3 and 0.6 s,
- Frequency spectrum between 5 and 30 Hz,
- Large amplitude range, between 0.5 and 50 µm/s in relative amplitude,
- No clear secondary arrival.

These characteristics may change slightly depending on the instrumental response of each OBS type. The signals recorded by the OldOBS have a higher frequency content (5 – 30 Hz) and are shorter (0.1 – 0.6 s) than the ones of the other instruments (4 – 12 Hz, 0.5 – 0.8 s).
The micro-events are visible on hydrophones only when these are close enough to the sediments surface. The hydrophones of ARMSS and J2, situated at the seafloor and ~30 cm above the seafloor respectively, recorded only micro-events having amplitude on the vertical geophone exceeding ~2-3 µm/s (ARMSS) and ~15 µm/s (J2). Earthquakes and seismic shots with lower amplitudes on the vertical geophone (~1 µm/s) are clearly visible on all hydrophones. The absence or low amplitudes of the signals recorded by hydrophones appear to be specific to micro-events. This could be explained by a propagation mainly along the water/sediment interface, transmitting very little motions to the water column. Hydrophones from other OBSs (OldOBS and NEEDLE) are too far from the water/sediment interface to be able to record any micro-events.
Diaz et al. [2007] reported signals very similar to the micro-events described in this paper (designed by *Diaz et al.* [2007] as short duration events). They are characterized by durations between 0.5 and 1 s, and frequency contents constituted by one or two narrow peaks between 3 and 23 Hz. *Diaz et al.* [2007] also observed no clear secondary arrivals and large differences in the number of micro-events recorded by different OBS. No correlations were found between micro-events recorded by 2 different OBSs (~10 km apart).

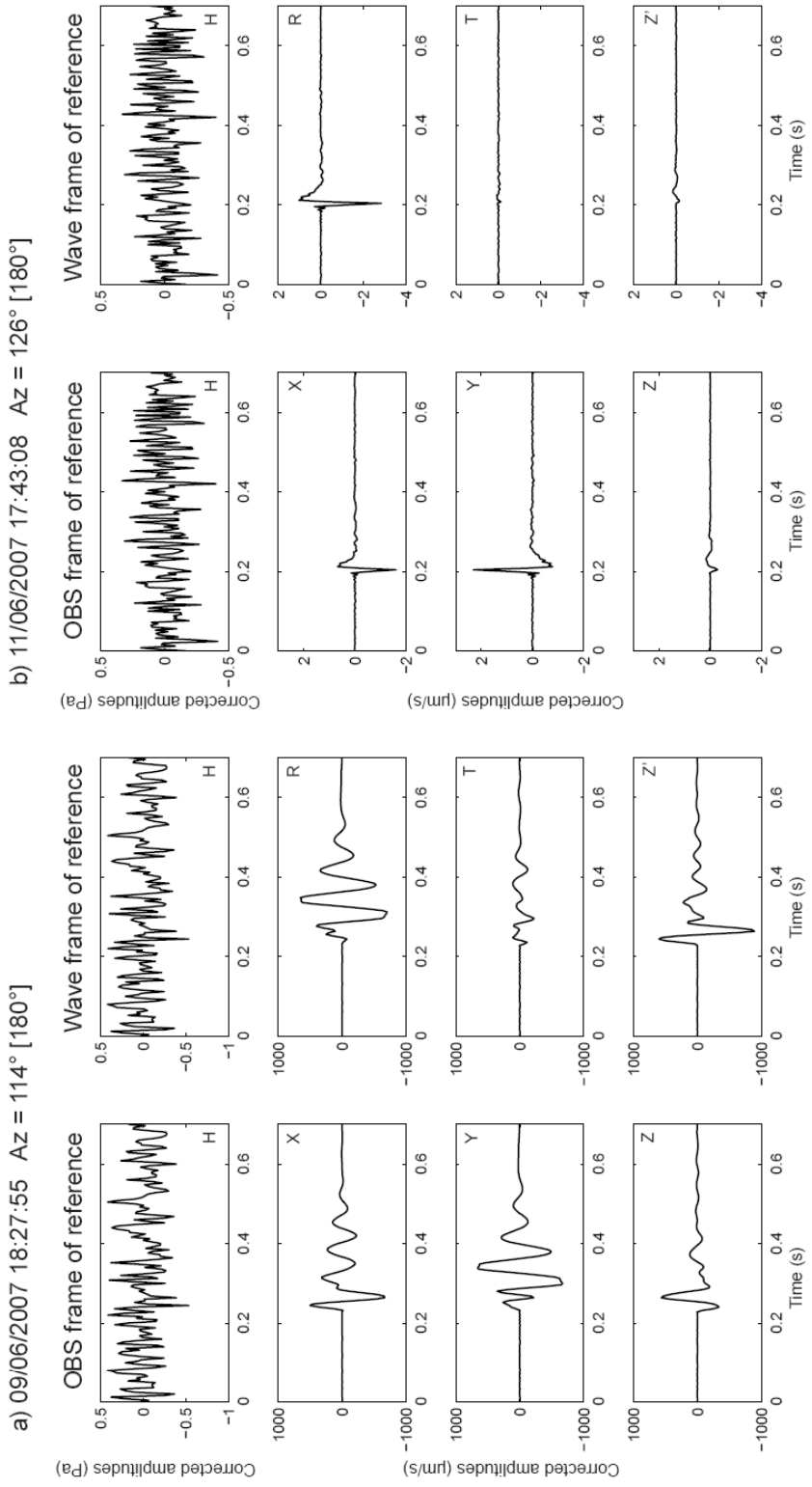

Figure 4. Two examples of micro-events recorded by OBS M. The three-components seismograms are presented before (H: hydrophone, X and Y: horizontal components, Z: vertical component) and after rotation in the wave frame of reference (R: radial component, T: transverse component, Z': vertical component). Azimuths calculation was performed assuming a wave polarization in the vertical plane along the direction of propagation (radial-vertical). a) Very high amplitude micro-event recorded on 09 June 2007 at 18:27:55. b) Micro-event recorded on 11 June 2007 at 17:43:08. This micro-event is typical of the ones constituting the swarm. Note that the two micro-events have similar azimuth. OBS M amplitudes have been corrected according to Section 2.6.2 methodology.

In our case, micro-events are most of the time not correlated from an OBS to another, implying that the source is in the very close vicinity of the OBS. Some strong micro-events are simultaneously recorded only by the closest stations, ARMSS and SPAN which are 10 m apart. On the other hand J2 and J, distant by 25 m, did not record any correlated micro-events. The maximum spacing for OBSs to simultaneously record micro-events ranges between 10 and 25 m. Thus, micro-events seem to be strongly attenuated both horizontally in the sediments and vertically in the water column.

The number of micro-events and the temporal distribution of inventoried micro-events for each instrument are shown in Fig. 5 and 6. About 7310 micro-events were detected. The number of micro-events is variable from one OBS to the other, ranging from 915 recorded by J to 3168 by K (same instrument and recording period). In term of number of micro-events, the most active sites are near ARMSS and K locations (Fig. 5 and 6).

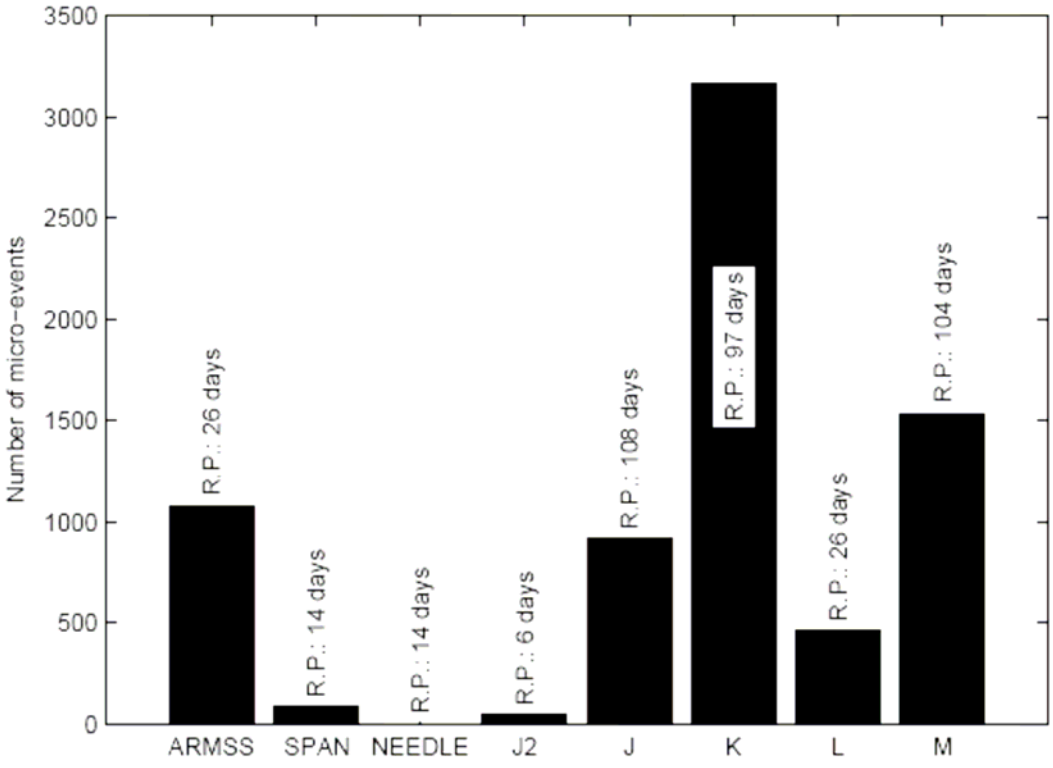

Figure 5. Number of micro-events and recording period (R.P) for all instruments.

No clear cycles, as the tidal cycles (less than 10 cm in the Sea of Marmara [*Alpar and Yüce*, 1997]), are visible on the micro-events temporal distribution (Fig. 6). In addition, no correlation between the number of micro-events and the hour of the day has been found, as it could be expected if these signals resulted from the activity of some living organisms.

4. Interpretation

Except NEEDLE, all instruments have recorded micro-events, discarding the hypothesis of an instrumental noise to explain their origin. These brief and impulsive signals, generally discarded as environmental noise, appear commonly on OBS data [*Buskirk et al.*, 1981; *Diaz et al.*, 2007]. *Buskirk et al.* [1981] and *Diaz et al.* [2007] described very similar signals in varying environmental and geodynamical settings, the Pacific borders and the Galicia passive margin respectively. According to *Buskirk et al.* [1981], the number of micro-events depends on the hour of the day for instruments at depths shallower than 1000 m. In addition, the number of events decreases with the depth of the instrument, suggesting a possible relationship with the vertical distribution of biomass in the ocean. These observations, and the recovery of living organisms (eggs of unknown origin) attached to two OBSs, lead *Buskirk et al.* [1981] to suggest a biological origin of the signals.

The number of micro-events recorded by OldOBS K (depth: 546 m) does not show any dependence on the hour of the day. However, relatively to the other OldOBS at greater immersion depths (J, K and L), the number of micro-events recorded by K is two to three times more important (Fig. 5). Apart from biologic activity, pressure effects on gas bubbles can also explain the decrease in the number of micro-events with depth. Indeed, as pressure decreases, bubbles size and gas exsolution will increase while gas solubility will decrease. Hence, for a same gas source and similar sediments, more bubbles will be created at lower pressure (i. e. at shallower depths). So, a decrease of biological activity is not the only parameter that could explain the decrease of the number of micro-events with depth. Moreover, as already noticed by *Diaz et al.* [2007], the fact that swarms consist in very similar signals during an extended period of time is incompatible with a biological origin.

As mentioned earlier, the origin of micro-events is very close to the instruments. Regional phenomena, such as tectonic, deep currents, resonating clouds of bubbles [*Pontoise and Hello*, 2002] and T-waves [*Talandier and Okal*, 1996], can be discarded in our case. In addition, sources in the water column (deep currents, resonating bubbles, T-waves and explosions/implosions) are very unlikely because micro-events were not recorded by OldOBS hydrophones.

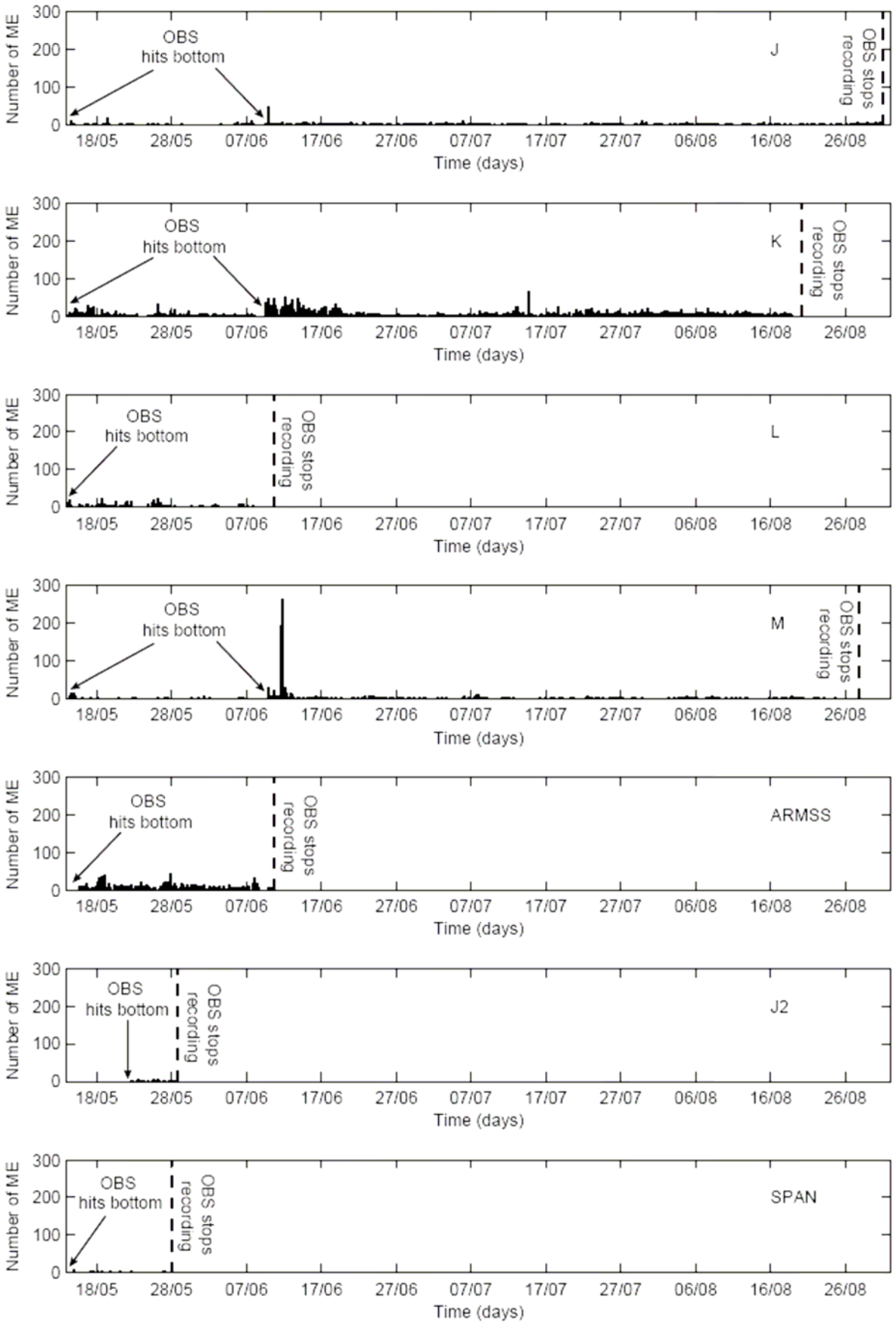

Figure 6. Temporal evolution of the number of micro-events recorded by OBSs J, K, L, M, ARMSS, J2 and SPAN. ME: micro-events.

On the other hand, gas is known to be common in marine sediments, and the Sea of Marmara is not an exception. Active venting sites have been found throughout the Sea of Marmara by geophysical means [*Alpar et al.*, 1999; *Géli et al.*, 2008; *Dupré et al.*, 2010] and visual observations [*Zitter et al.*, 2008]. A chirp profile, crossing the position of OBS J and M, was collected during the Marmesonet cruise in 2009 ([*Géli et al.*, 2010], Fig. 7). On this profile, a high-amplitude reflector followed by a strong attenuation of the seismic waves is clearly visible close to the fault situated below OBS M. These signatures are characteristic of the presence of gas. In addition, experiences and modeling [*Vidal et al.*, 2006; *Varas et al.*, 2009; *Diaz et al.*, 2007; *Chouet* 1988, 1996] of the opening and resonance of a cavity filled by fluids generate signals with waveforms qualitatively consistent with our data.

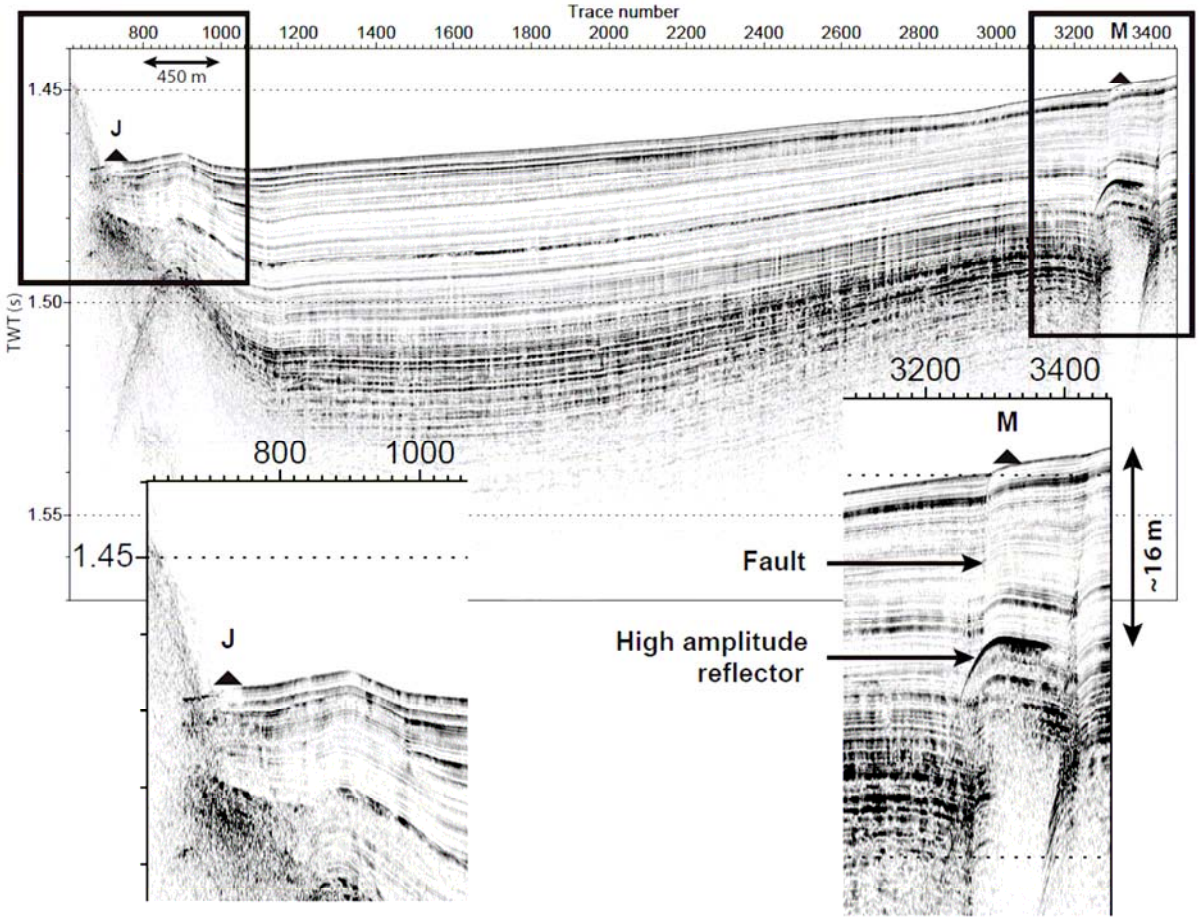

Figure 7. Chirp profile acquired during the MARMESONET cruise in Nov.-Dec. 2009 ([Géli et al., 2010], see location in Fig. 1). OBS J and M are indicated on the profile by black triangles. Below M is visible a high amplitude reflector followed by a strong attenuation of the seismic waves (zoom on the right). No seismic anomaly is visible below J (zoom on the left).

Interestingly, OBS M recorded a swarm of 400 micro-events in 24 hours on June 11 and 12 (Fig. 8). Despite large amplitude differences, the micro-events recorded during this crisis have very similar waveforms (Fig. 4b) and frequency contents (dominant frequency between 10 and 20 Hz). The number of micro-events increases gradually over the crisis, reaching a maximum after 6 hours with 96 micro-events in 2 hours (the background rate was ~ 5 micro-events/hours, Fig. 8). Hence, in the following we suggest that the micro-events could result from gas emission on the seafloor, considering (i) the presence of gas and a fault near OBS M (where the swarm of micro-events was recorded); (ii) Modeling of source and wave propagation. The source of the micro-events is likely quite superficial, as no correlation is observed from one OBS to another, unless they are less than 25 m apart.

5. Specific sequence on OBS M

5.1. Sequence chronology

One day before the swarm of micro-events, a very strong micro-event with a peak-to-peak amplitude >1000 µm/s was recorded by OBS M (Fig. 4a and 9). Despite its very high amplitude, the signal is not visible on the hydrophone.

As it occurred only ~40 minutes after OBS M hits the sea bottom (09/06/2007 17:48:04), it seems likely that the impact of the instrument on the seafloor has indirectly caused this strong signal. Indeed, the impact produced by the OBS deployment could have significantly destabilized the gas-prone sediments close to this OBS, involving a gas break-through in the superficial sediments. Then, after about 40.5 h of relative quiescence, OBS M recorded the swarm. This oscillatory phase constituted by signals of relatively low amplitudes could correspond to the escape of numerous gas bubbles through conduits.

5.2. Principal Component Analysis (PCA)

In order to propose some physical explanations, a PCA was applied to determine the most characteristic micro-events of the swarm. First, the signals were detected with an automatic algorithm based on a STA/LTA threshold and visually controlled. Secondly, for each micro-event, one temporal series of N samples was extracted in order to control the origin time and average.

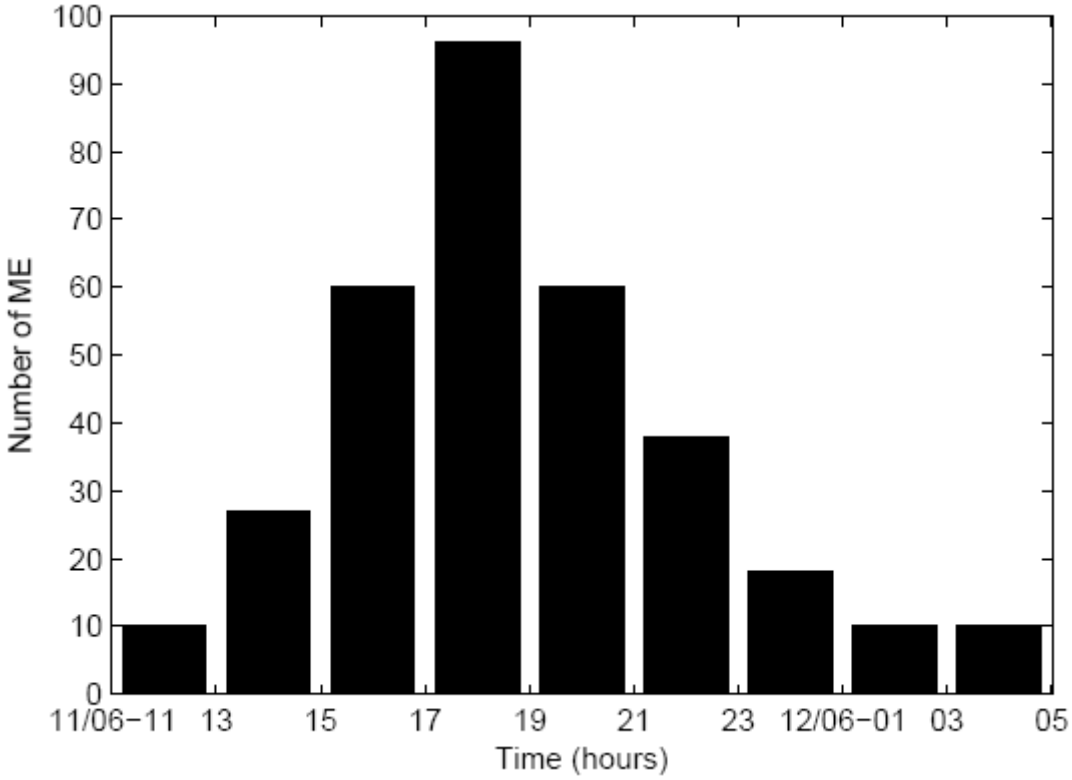

Figure 8. Temporal distribution of the micro-events constituting the swarm recorded by OBS M. The crisis has been divided in 9 two-hour periods, from June 11, 11:00:00, to June 12, 05:00:00.

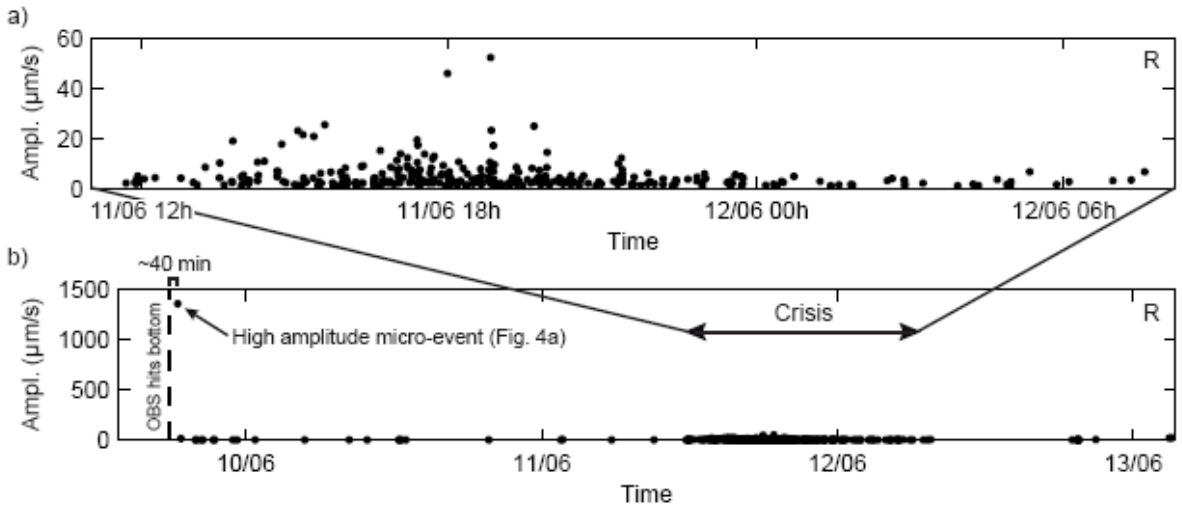

Figure 9. Peak to peak amplitudes of the micro-events inventoried on OBS M between the OBS deployment and the 13 June 2007 at 03:20 (b), and during the crisis (11/06 11:00 – 12/06 08:10) (a). R: radial component.

Using a method based on *Jurkevics* [1988], the three-component temporal series in the OBS frame of reference were rotated in the waves frame of reference. The three components in the wave frame of reference will be referred as the radial, transverse and vertical components

(Fig. 4). Then the covariance matrix between all signals, with a common origin and a zero-average, was calculated following this formula,

$$\left[C_{tp,tq}\right] = \sum_{1 \le i,\, j \le M} f_i(t_p)\, f_j(t_q) \text{ where } t_1 \le t_p, t_q \le t_N, \quad (1)$$

with f_i and f_j the temporal series, M the number of micro-events, and N the number of samples.

Eventually, the characteristic signals (eigenvectors, $\boldsymbol{V_i}$, i = 1, M) and their data representativeness (eigenvalues, λ_i, i = 1, M) are calculated from the covariance matrix. Hereafter, the representativeness of each eigenvector will be given as a percentage of the total energy ($\lambda_i^2/\Sigma\lambda_i^2$).

The micro-events constituting the swarm recorded by OBS M on June 11 and 12 present four particularities: (i) they are very impulsive; (ii) of short duration (mainly around 0.1 s); (iii) very similar; (iv) and present higher amplitudes on the horizontal components than on the vertical one (Fig. 4b). The PCA performed with this dataset indicates that the first eigenvector has a data representativeness of ~83 % on the radial component (Fig. 10). The relatively low data representativeness of the first eigenvectors of the transverse and vertical components, ~35 and 58 % respectively, result likely from the lower amplitude of the recorded signals on these components (Fig. 4b).

This characteristic signal is very impulsive and has a duration around 0.15 s on the radial component. Frequency spectra of the eigenvectors of the three components show one main peak between 13 and 20 Hz. Noticeably, the frequency spectrum of the first eigenvector of the radial component show a higher frequency content than the other components (Fig. 10). The main characteristics of the first eigenvectors are summarized in Table 2.

Eigenvector 1			
Components	%	Freq. (Hz)	Dur. (s)
OBS M swarm (368 ME)			
Radial	83	13 - 20	0.14
Transverse	35	14.2	0.21
Vertical	58	14.5 - 17	0.23

Table 2. First eigenvector characteristics of the PCA performed on the micro-events of the swarm recorded by OBS M. The number of micro-events used in the PCA is also indicated (ME: micro-events). %: data representativeness (energy); Freq.: dominant frequency; Dur.: duration.

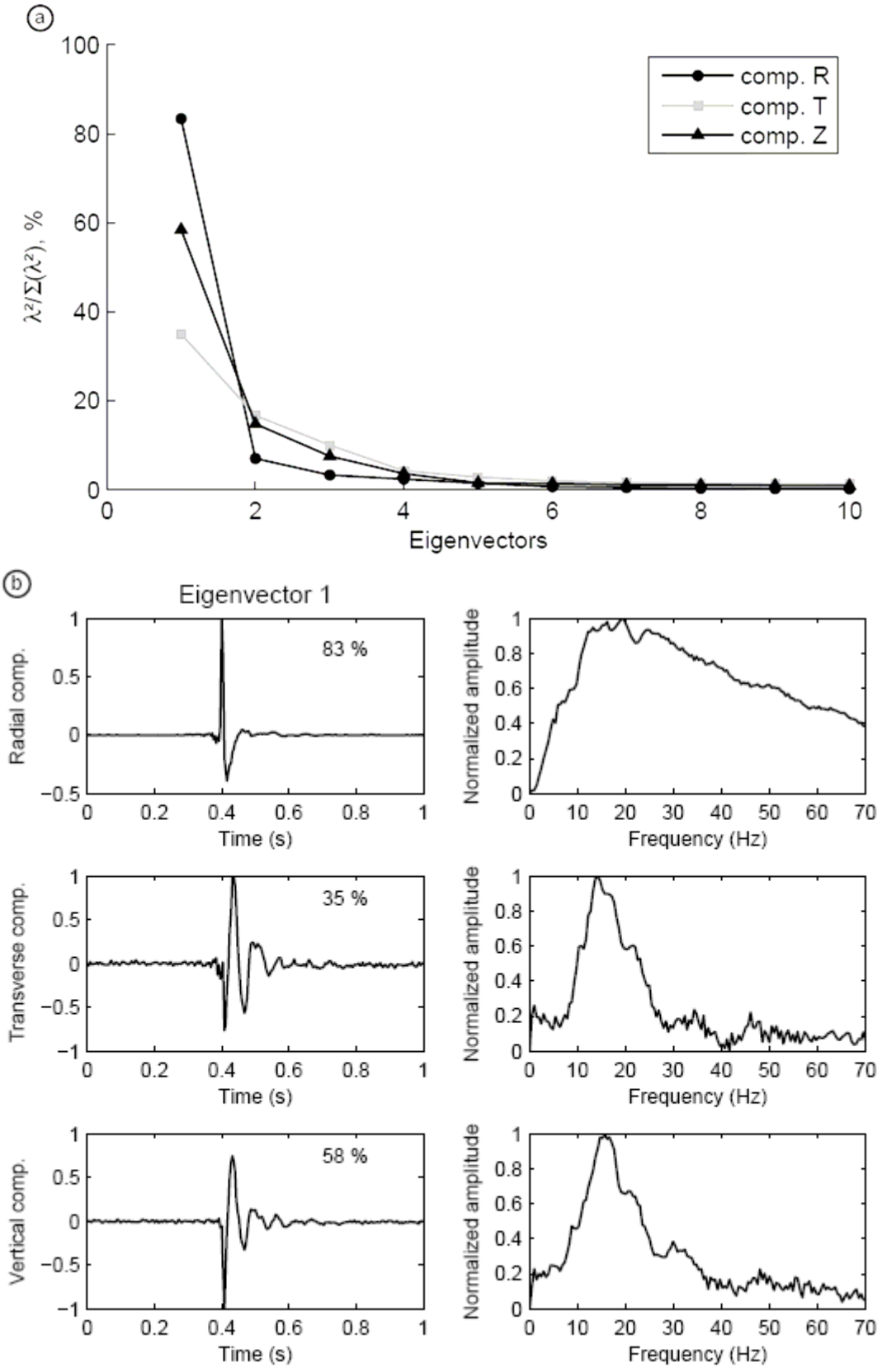

Figure 10. PCA of the micro-events constituting the crisis identified on OBS M. a) Representativeness of the first 10 eigenvectors (R: radial, T: transverse, Z: vertical). b) First eigenvector for the 3 components in the wave frame of reference. The representativeness of each eigenvector is indicated by its eigenvalue given in percentage of the total energy. On the right is given the eigenvector spectrum.

5.3. Wave polarization analysis

In the wave frame of reference, the polarization of the two micro-events presented in Fig. 4 is very different. In one case, the particle motion is mainly in the radial-vertical plane (Fig. 4a), which is consistent with surface waves (Stoneley-Scholte waves, *Zakharia* [2002]). In the other case, the particle motion is in the radial direction (Fig. 4b), which in principle is consistent with P-waves. Then, the wave decomposition on OBS M components of the micro-events constituting the crisis was analyzed in order to obtain the sources azimuth and tilt (Fig. 11 and 12). The source direction in the geographical frame of reference could not be determined due to the lack of information regarding the orientation of the horizontal geophones. As azimuths are computed with a 180° ambiguity, only the direction of propagation in the OBS frame of reference is resolved.

The orientation of the sources is very stable over the crisis, around 105° – 135° [180°] in the OBS frame of reference (Fig. 11), suggesting a localized source. The waves tilt ranges mainly between 0 and 15° (Fig. 12). With a maximum source-receiver distance of about 20 m, this leads to a maximum source depth of ~5.4 m.

Noticeably, the strong micro-event and the micro-events constituting the swarm recorded by OBS M have similar azimuths, 114° [180°] and 105° – 135° [180°], respectively. One possibility is that both could result from fluid migration along the fault visible on the chirp profile located close to OBS M (Fig. 7).

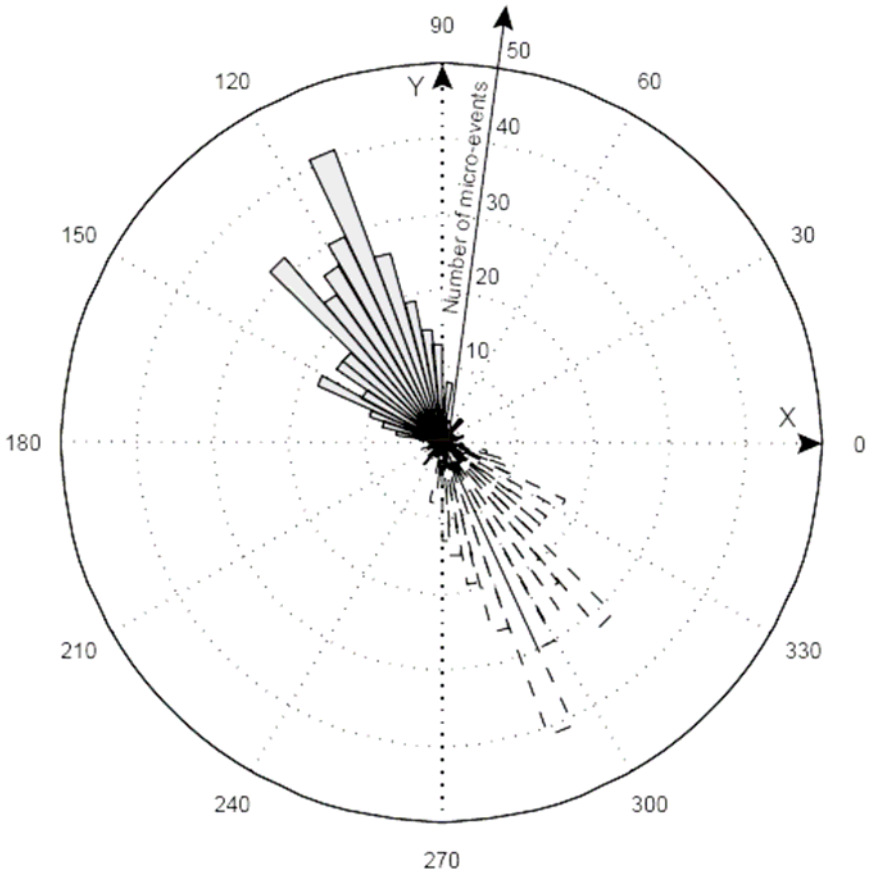

Figure 11. Wave direction of propagation (solid line) in the OBS frame of reference of the micro-events constituting the crisis recorded on OBS M. OBS horizontal components X and Y are directed toward 0 and 90 degrees respectively. The 180°-shifted azimuths (dashed line) account for the 180° ambiguity in azimuths calculation. Numbers near the dotted circles inside the diagram indicate the number of micro-events. Each gray bin represents 5 degrees.

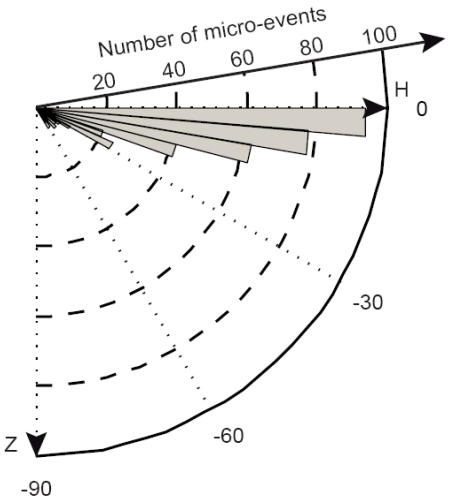

Figure 12. Wave tilt in the OBS frame of reference of the micro-events constituting the crisis recorded on OBS M (H: horizontal, Z: vertical). The line at 0 degree separates the seawater quadrant above from the sediment quadrant below. Numbers near the dotted circles indicate the number of micro-events. Each gray bin represents 5 degrees.

6. Source and wave propagation modeling

The numerical simulations were carried out using the SKB code [*Dietrich*, 1988]. This code computes, as a function of frequency and wave number, the response in terms of stress and displacement of a 3D, horizontally stratified, half-space subjected to a source positioned anywhere in the stratification. Fluid layers, within or bounding the stratification can be taken into account. The attenuation is included by working with complex wave velocities [*Toksöz and Johnston*, 1981]. The computation is based on a recursive algorithm using reflection-transmission coefficients as wave vector propagators [*Kennet and Kerry*, 1979]. The last steps of the computation are to integrate in discrete wave numbers [*Bouchon*, 1981], and make a convolution with a spectrum of a signal source followed by an inverse Fourier transform in time, in order to recover stresses and displacements in space and time.

According to *Biot* [1956], water saturation induces an attenuation that can be accounted for by a complex formulation of waves velocities, as in visco-elastic media (see also *Géli et al.* [1987]). Therefore, our computation method is adapted to the modeling of wave propagation in strongly attenuating, marine sub-surface sediments, [e. g. *Meunier and Guennou*, 1991]. This computation method takes into account the complete wave field (direct, transmitted, reflected waves…), including both far-field and near-field terms [*Dietrich and Bouchon*, 1985]. The representation of the source in terms of forces or moment tensor appears within the SKB code in terms of equivalent stress or displacement discontinuity, allowing the calculation of stress and displacement at the receivers by using reflection-transmission coefficients. The source signal used is the phase null Ricker signal.

The model consists in a 1110 m thick water layer, with typical density of 1000 kg/m^3 and P-wave velocity of 1500 m/s, overlying a homogeneous half-space. Sediment properties measured on cores (MSCL core logging system: P-wave velocity and sediments density) collected near OBS J have been used for the numerical seismograms calculation. The acoustical properties of the homogeneous half-space correspond to those of a soft and very attenuating sediment, i.e. a density of 1500 kg/m^3, P-wave velocity and quality factor of 1550 m/s and 10, S-wave velocity and quality factor of 100 m/s and 10 [*Wang et al.*, 1994; *Sultan et al.*, 2007; *Campbell*, 2009]. Two types of point source were tested: an isotropic explosive source generating P-waves with the same energy in all directions, and an unidirectional horizontal force generating P-waves with the maximum of energy in the horizontal direction. In all simulations, the source signal has a constant frequency content of 15 Hz, consistent with

micro-events frequency content. Numerical seismograms were calculated for 100 horizontally aligned receivers (spaced by 1 m) at four different levels (0.01 m below and 0.1, 0.3, 0.9 m above the water-sediment interface), and two source depths, respectively 2 and 5 m below the water/sediment interface (Fig. 13).

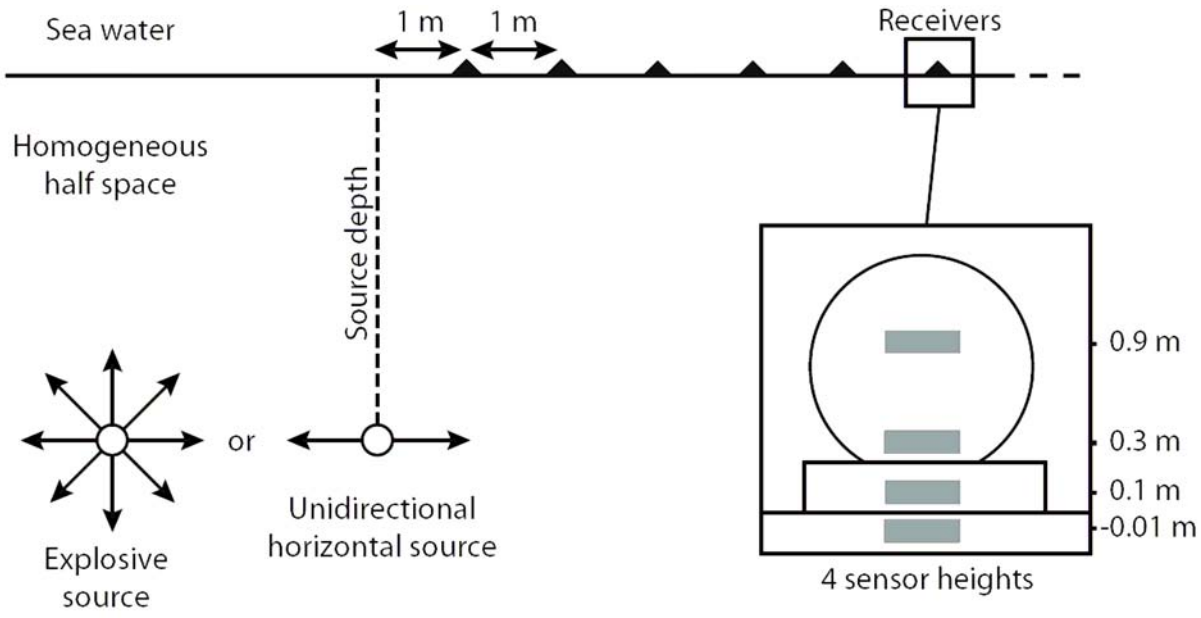

Figure 13. Configuration of the model used for micro-events modeling. A point source (horizontal unidirectional or explosive) located in a homogeneous half space produces either P- or surface waves recorded by a set of equally-spaced receivers on the surface (4 sensor heights: 0.01 below and 0.1, 0.3 and 0.9 above the interface).

Whatever the type and depth of the source, the computed signals are attenuated very quickly in the sediments (Fig. 14). Surface waves (Stoneley-Scholte waves) are produced by both the unidirectional horizontal force and the explosive source in superficial sediments. These waves, propagating at ~77 m/s in our configuration, are attenuated both horizontally in sediments and vertically in the water column (Fig. 14 and 15). However, in the case of an explosive source, P-waves with significant amplitudes are clearly visible on the horizontal component.

The micro-event shown in Fig. 4a has a higher amplitude on the radial component than on the vertical component (while still of the same order of magnitude), which could be compatible with Stoneley-Scholte waves produced by a shallow source. The waveforms of the vertical and radial components appear dissimilar, but it is unlikely that significant energy occurs as P-waves, as this P-wave should have also been recorded by the hydrophone.

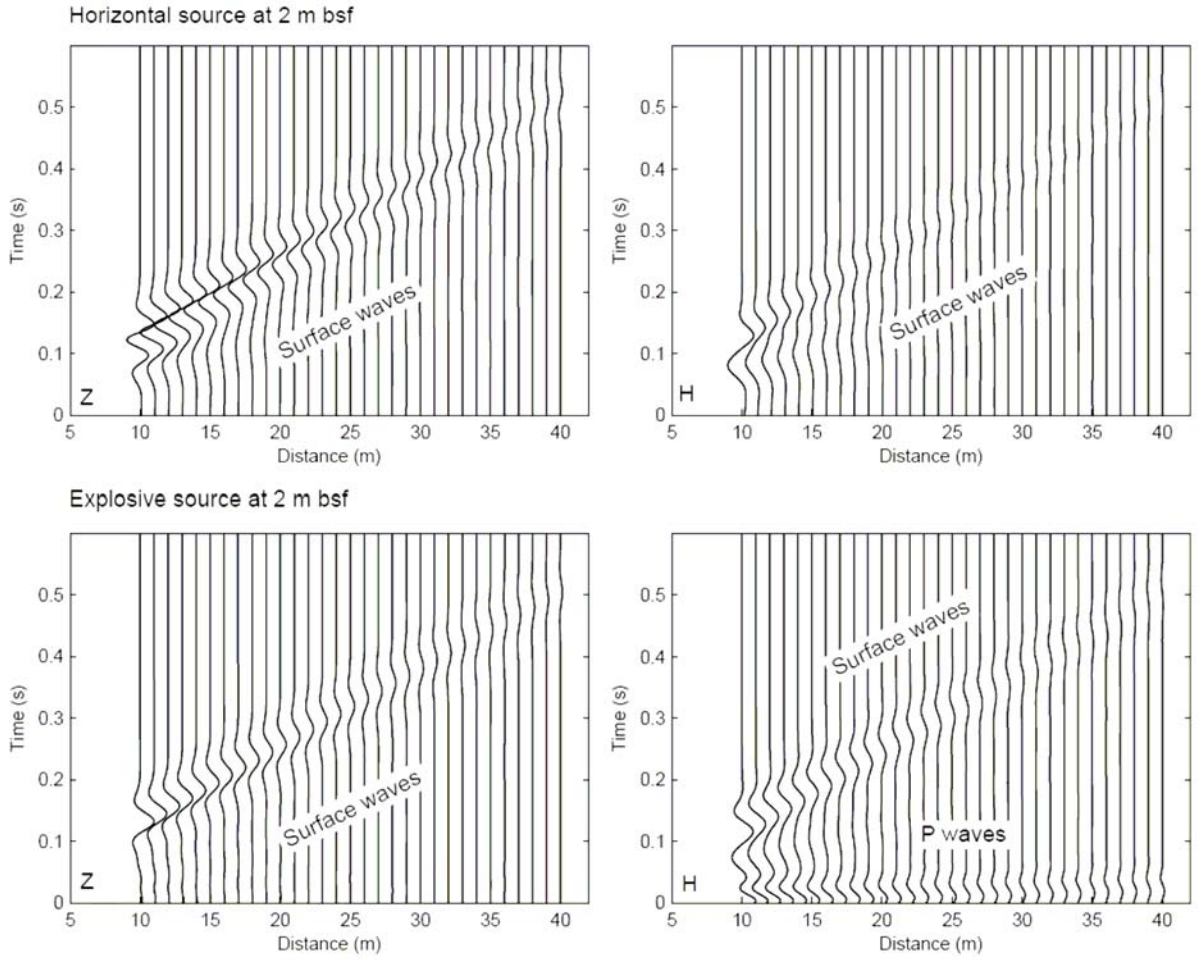

Figure 14. Micro-events numerical simulations using the SKB code [Dietrich, 1988] for a horizontal and an explosive source located at 2 m bsf (below sea floor), and sensors 1 cm within the sediments. H: horizontal motion; Z: vertical motion. Note the strong attenuation of P- and surface waves.

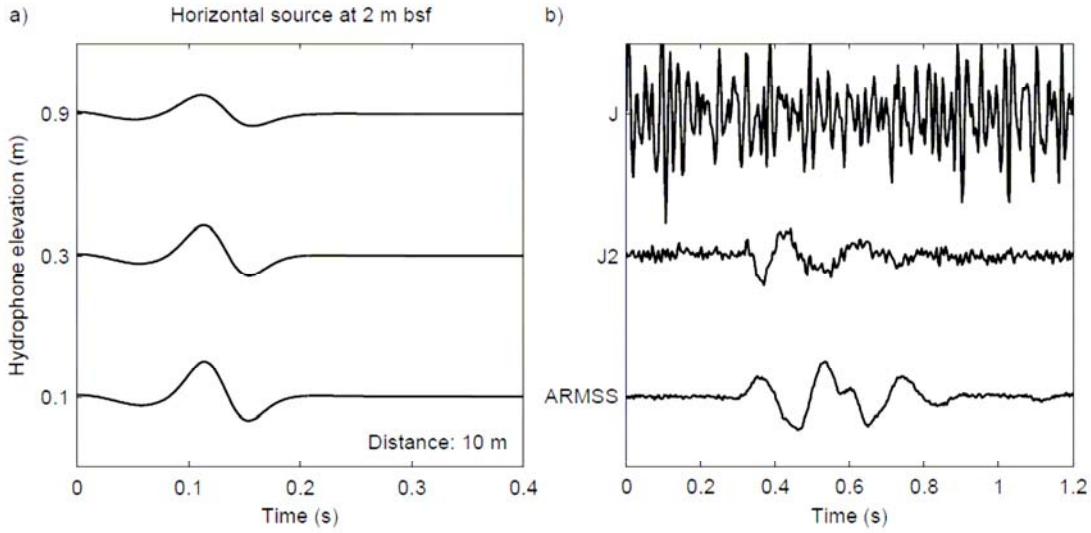

Figure 15. a) Micro-events numerical simulations for a horizontal source at 2 m bsf and sensors at 10, 30 and 90 cm above the interface (distance: 10 m), showing the vertical attenuation of surface waves. b) Hydrophone recordings of OBSs ARMSS (~0.05 m), J2 (~0.3 m) and J (~0.9 m), for three signals of similar calibrated amplitudes (~15 µm/s) recorded by these OBSs. The signals are normalized by those situated close to the seawater/sediments interface (0.1 m – ARMSS).

The impulsive micro-events of the crisis have most of their energy on the radial component and thus cannot be interpreted as Stoneley-Scholte waves (Fig. 4b). They could in principle be better explained by a P-wave hitting the sediments/water interface with a high incidence angle, transmitting little energy to the water column (see Appendix A). However, the corresponding wavelength would be of the order of 100 m, which is probably much more than the distance to the source. Most likely, these impulsive signals are non-propagative and generated by a weak but very close source of deformation causing horizontal displacement, which could be a pulsing conduit.

7. Physical hypotheses and interpretation

7.1. Physical hypotheses

Bubbles in sands are spherical, grow and migrate by displacing grains, whereas bubbles in clay are presumably oblate spheroid, and migrate by fracturing the sediments [*Johnson et al.*, 2002; *Boudreau et al.*, 2005]. Hence, gas migration in fine-grained sediments is expected to depend on fractures propagation, which is function of the mechanical properties of the medium through its Young's modulus E, shear strength, and fracture toughness K_{1c} [*van Kessel and van Kesteren*, 2002; *Algar et al.*, 2009]. However, it is often observed at the seafloor that bubbles escape continuously through tubular conduits, which are sometime recovered as cemented chimneys in the sediments. Such open conduits may be maintained to a few meters depth in the sediment and enable bubble-induced pore water mixing [*Haeckel et al.*, 2007].

Other experiments, where gas (air) is injected in a granular media (sodosilica grains with diameters of 100 and 400 µm), have shown that gas escapes through numerous conduits that look-like tree branches [*Varas et al.*, 2009; *Varas et al.*, 2010]. Gas conduits seem to be intrinsically unstable, because, even without variations of the gas injection rate, conduits are created or closed continuously. The superficial sediments of the Sea of Marmara are mainly clay-rich cohesive sediments with particles smaller than 5 µm. Nevertheless, open conduits in compacting sediments are expected to be mechanically unstable except very close to the seafloor. We suspect that the opening and collapse of conduits or gas filled fractures could explain the characteristics of micro-events (Fig. 4).

Then, our preferred mechanism consists in a subvertical fracture, pre-existent or not, gradually filled by gas within a porous, saturated medium (Fig. 16). The fracture is located close to the sediment/water interface. Gas pressure increase as a crack fills and progressively opens (step 0). When the fracture toughness threshold is reached, the gas will rise up to the sediment/water interface in a moving crack (step 1), where it will escape to the seawater (step 2) without major deformation of the sedimentary matrix [*Johnson et al.*, 2002; *Boudreau et al.*, 2005; *Algar et al.*, 2009]. After the gas release, the confining pressure will close the fracture.

The partitioning of the signal recorded by the OBSs in horizontal and vertical motions will depend on fractures tilt and depth, and on wave propagation processes.

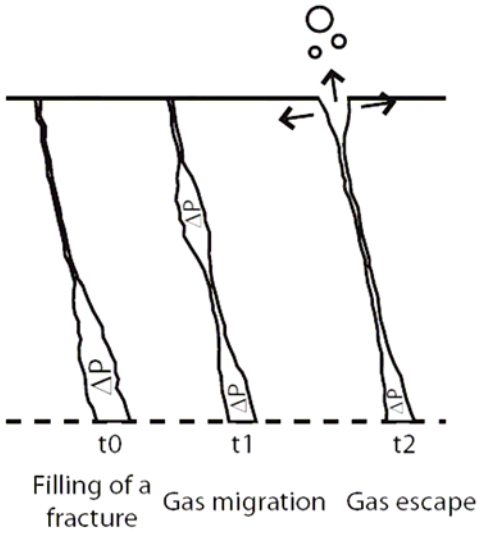

Figure 16. Schematic explanation in 3 steps of the mechanism proposed for the micro-events source: gas migration and escape through a subvertical conduit.

7.2. Interpretation of the micro-events crisis

We identified two types of micro-events: small impulsive repetitive events and larger amplitude oscillatory signals, which appear less frequently and display more variability and could correspond to Stoneley-Scholte waves.

Varas et al. [2009] described two regimes of bubbles emission in granular media depending on the gas injection rate. At low flow rate, large and independent bubbles are formed ("bubbling regime"), whereas at high flow rate, small bubbles supplied by a continuous channel are produced ("open-channel regime"). Except the swarm recorded by OBS M, all

OBSs displayed a low daily rate of micro-events. We propose that the larger micro-events correspond to the collapse of a cavity or fracture that trapped gas at a relatively shallow depth below the sediments. The crisis recorded by OBS M followed such an event and could, hypothetically, result from a nearby continuous flow of bubbles in an open-channel regime which followed the expulsion of the gas from the main cavity.

8. Conclusions

The characteristics of the micro-events recorded by OBS M during the crisis that occurred on June 11-12, 2007 are such that they cannot be explained by instrumental artifacts, nor noise related to biological activity. The presence of gas in the superficial layers and the source modeling we performed strongly suggest that these micro-events are likely related to natural degassing from the seafloor. Hence, the micro-events could possibly be related to the opening and closure of a conduit induced by degassing near the subsurface. The present work shows that OBSs can detect episodes of gas accumulation and release in shallow sediment layers. In combination with piezometers and bubble recorders, OBS could be used in the Sea of Marmara to monitor the evolution of such episodes, hence to better understand the relationships between deformation and non-seismic transients related to degassing from the sub-seafloor layers near the fault zone.

9. Appendix A - Static pressure on the seafloor in response to P-waves

Here we adapt notations and formulations provided by Okal and Talandier (personnal communication, 2011). We consider a P-wave coming from below hitting the sediments/water interface. Then, the resulting waves system at this interface will be:

- The incident P-wave,
- A reflected P-wave in the sediments,
- A reflected S-wave in the sediments,
- A transmitted P-wave in the seawater.

Hereafter, we will note α and β the P- and S-waves velocities in the sediment, α_l the P-waves velocity in the seawater, and ρ_s and ρ_l the sediment and seawater densities. Together with the P-wave incidence angle (i_P), we introduce the S-wave reflection (i_S) and the P-wave transmission angles (i_l) as

$$\frac{\sin i_P}{\alpha} = \frac{\sin i_S}{\beta} = \frac{\sin i_l}{\alpha_l}.$$

To determine the static pressure associated with the transmitted P-wave in the seawater, we will use the transmission coefficient *PL* given by *Ben-Menahem and Singh* [1981, p. 478] in the case of an interface solid-liquid.

$PL = \dfrac{2\cos i_P \cos 2i_S}{D}$, where D is the determinant given by

$$D = \left(\frac{\beta}{\alpha}\right)^2 \sin 2i_P \sin 2i_S \cos i_l + \frac{\rho_l}{\rho_S}\frac{\alpha_l}{\alpha}\cos i_P + \cos^2 2i_S \cos i_l .$$

Then, the static pressure associated with the P-wave transmitted in the seawater can be expressed as

$p_S = \rho_l \alpha_l^2 k \cdot PL$, where k is the wave number ($k = \omega/\alpha_l$).

Considering a P-wave with an amplitude of 1 mm propagating in a very soft sediment (α = 1550 m/s, β = 100 m/s and ρ_s = 1500 kg/m^3), the transmission coefficient *PL* and the static pressure associated with the P-wave transmitted in seawater (α_l = 1500 m/s, ρ_l = 1000 kg/m^3) are shown in Fig. A1.

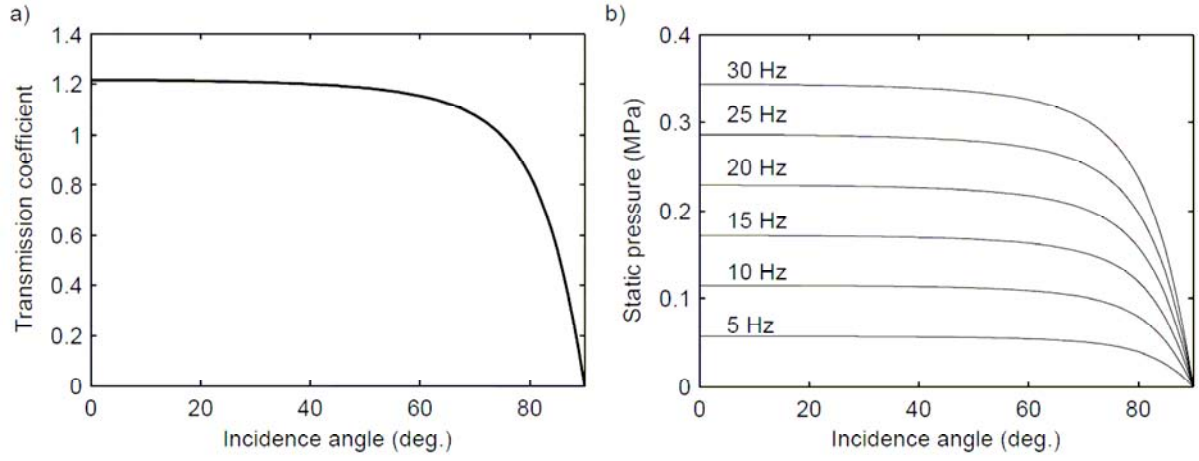

Fig. A1. Transmission coefficient PL (a) and static pressure (b) in function of the P-wave incidence angle. The static pressure (in MPa) is given for different frequencies ranging from 5 to 30 Hz.

10. References

Algar, C. K., and B. P. Boudreau (2009), Transient growth of an isolated bubble in muddy, fine grained sediments, *Geochim. Cosmochim. Acta, 73*, 2581-2591, doi: 10.1016/j.gca.2009.02.008.

Alpar, B. (1999), Underwater signatures of the Kocaeli earthquake of 17 August 1999 in Turkey, *Turkish J. Mar. Sci., 5*, 111-130.

Alpar, B., and H. Yüce (1997), Short and tidal period sea-level variations along the turkish strait system, *Turkish J. Mar. Sci., 3*, 11-22.

Armijo, R., Pondard, N., Meyer, B., Uçarkus, G., Mercier de Lépinay, B., Malavieille, J., Dominguez, S., Gustcher, M.-A., Schmidt, S., Beck, C., Çagatay, N., Çakir, Z., Imren, C., Eris, K., Natalin, B., Özalaybey, S., Tolun, L., Lefèvre, I., Seeber, L., Gasperini, L., Rangin, C., Emre, O., and K. Sarikavak (2005), Submarine fault scarps in the Sea of Marmara pull-apart (North Anatolian Fault): implications for seismic hazard in Istanbul, *Geochem. Geophys. Geosyst., 6*, Q06009, doi: 10.1029/2004GC000896.

Ben-Menahem, A., and S. J. Singh (1981), *Seismic Waves and Sources*, Springer-Verlag, New York.

Biot, M. A. (1956), Theory of the propagation of elastic waves in a fluid saturated porous solid, 1, Low-frequency range, *J. Acoustic Soc. Am., 28*, 168-178.

Bouchon, M. (1981), A simple method to calculate Green's functions for elastic layered media, *Bull. Seism. Soc. Am., 71*, 959-971.

Boudreau, B. P., Algar., C., Johnson, B. D., Croudace, I., Reed, A., Furukawa, Y., Dorgan, K. M., Jumars, P. A., Grader, A. S., and B. S. Gardiner (2005), Bubble growth and rise in soft sediments, *Geology, 33(6)*, 517-520, doi: 10.1130/G21259.1.

Bourry, C., Chazallon, B., Charlou, J. L., Donval, J. P., Ruffine, L., Henry, P., Geli, L., Çagatay, N., İnan, S., and M. Moreau (2009), Free gas and gas hydrates from the Sea of Marmara, Turkey Chemical and structural characterization, *Chemical Geology, 264*, 197-206, doi: 10.1016/j.chemgeo.2009.03.007.

Buskirk, R.E., Frohlich, C., Latham, G. V., Chen, A. T., and J. Lawton (1981), Evidence that biological activity affects ocean bottom seismograph recordings, *Mar. Geophys. Res., 5 (2)*, 189-205.

Campbell, K. W. (2009). Estimates of shear-wave Q and κ0 for unconsolidated and semiconsolidated sediments in Eastern North America, *Bull. Seism. Soc. Am., 99,* 2365-2392, doi: 10.1785/0120080116.

Chouet, B. (1988), Resonance of fluid-driven crack : radiation properties and implications for the source of long-period events and harmonic tremor, *J. Geophys. Res., 93,* 4375-4400.

Chouet, B. (1996), Long-period volcano seismicity : its source and use in eruption forecasting, *Nature, 380,* 309-316, doi: 10.1038/380309a0.

Diaz, J., Gallart, J., and O. Gaspà (2007), Atypical seismic signals at the Galicia Margin, North Atlantic Ocean, related to the resonance of subsurface fluid-filled cracks, *Tectonophysics, 433,* 1-13, doi: 10.1016/j.tecto.2007.01.004.

Dietrich, M. (1988), Modeling of marine seismic profiles in the t-x and tau-p domains, *Geophysics, 53,* 453-465, doi: 10.1190/1.1442477.

Dietrich, M., and M. Bouchon (1985), Synthetic vertical seismic profiles in elastic media, *Geophysics, 50(2),* 224-234.

Dupré, S., Scalabrin, C., Géli, L., Henry, P., Grall, C., Tary, J. B., Çagatay, N., Imren, C., and the MARMESONET Scientific Party (2010), Widespread gas emissions in the Sea of Marmara in relation with the tectonic and sedimentary environments: results from shipborne multibeam echosounder water column imagery (MARMESONET expedition, 2009), EGU General Assembly, Vienna, Abstract EGU2010-9429-2.

Géli, L., Bard, P.-Y., and D. P. Schmitt (1987), Seismic wave propagation in a very permeable water-saturated surface layer, *J. Geophys. Res., 92*, 7931-7944.

Géli, L., Henry, P., Zitter, T., Dupré, S., Tryon, M., Çagatay N. M., Mercier de Lépinay, B., Le Pichon, X., Şengör, A.M.C., Görür, N., Natalin, B., Uçarkuş, G., Özeren, S., Volker, D., Gasperini, L., Bourlange, S., the Marnaut Scientific Party (2008), Gas emissions and active tectonics within the submerged section of the North Anatolian Fault zone in the Sea of Marmara, *Earth Planet. Sci. Lett., 274*, 34-39, doi: 10.1016/j.epsl.2008.06.047.

Géli, L., Henry, P., and N. Çagatay, (2010). Marmesonet Leg1 Cruise Report, November 4th – November 25th, 2009, http://www.esonet.marmara-dm.itu.edu.tr/ (12,2010).

Haeckel, M., Boudreau, B. P., and K. Wallmann (2007), Bubble-induced porewater mixing: A 3-D model for deep porewater irrigation, *Geochim. Cosmochim. Acta, 71,* 5135-5154, doi: 10.1016/j.gca.2007.08.011.

Halbach, P., Holzbecher, E., Reichel, Th., and R. Moche (2004), Migration of the sulphate-methane reaction zone in marine sediments of the Sea of Marmara – can this mechanism be tectonically induced ?, *Chemical Geology, 205*, 73-82, doi: 10.1016/j.chemgeo.2003.12.013.

Imren, C., Le Pichon, X., Rangin, C., Demirbağ, E., Ecevitoğlu, B., and N. Görür (2001), the North Anatolian Fault within the Sea of Marmara: a new interpretation based on multichannel seismic and multi-beam bathymetry data, *Earth Planet. Sci. Lett., 186*,143–158, doi: 10.1016/S0012-821X(01)00241-2

Johnson, B. D., Boudreau, B. P., Gardiner, B. S., and R. Maass (2002), Mechanical response of sediments to bubble growth, *Marine Geology, 187*, 347-363.

Jurkevics, A. (1988), Polarization analysis of three-component array data, *Bull. Seism. Soc. Am., 78*, 1725-1743.

Le Pichon, X., Şengör, A. M. C., Demirbağ, E., Rangin, R., Imren, C., Armijo, R., Görür, N., Çağatay, N., Mercier de Lepinay, B., Meyer, B., Saatcilar, R., and B. Tok (2001), The main Marmara fault, *Earth Planet. Sci. Lett., 192*, 595-616.

Kennet, B. L. N., and N. J. Kerry (1979), Seismic waves in a stratified half-space, *Geophys. J. Roy. Astr. Soc., 57*, 557-583.

Meunier, J., and C. Guennou (1991), Computation of shear waves by integral methods in stratified media, in *Shear waves in Marine Sediments*, edited by J. M. Hovem et al., pp. 495-502, Kluwer Academic Publishers, printed in the Netherlands.

Pontoise, B., and Y. Hello (2002), Monochromatic infra-sound waves recorded offshore Ecuador : possible evidence of methane release, *Terra Nova, 14*, 425-435.

Rangin, C., Demirbağ, E., Imren, C., Crusson, A., Normand, A., Le Drezen, E., and A. Le Bot (2001), Marine Atlas of the Sea of Marmara (Turkey), IFREMER, France.

Rangin, C., Le Pichon, X., Demirbağ, E., and C. Imren (2004), Strain localization in the Sea of Marmara: propagation of the North Anatolian Fault in a now inactive pull-apart, *Tectonics, 23(2)*, TC2014, doi: 10.1029/2002TC001437.

Sultan, N., Voisset, M., Marsset, T., Vernant, A. M., Cauquil, E., Colliat, J. L., and V. Curinier (2007), Detection of free gas and gas hydrate based on 3D seismic data and cone penetration testing: An example from the Nigerian Continental Slope, *Marine Geology, 240*, 235-255, doi:10.1016/j.margeo.2007.02.012.

Talandier, J., and E. A. Okal (1996), T waves from underwater volcanoes in the Pacific Ocean: ringing witnesses to geyser processes ?, *Bull. Seismol. Soc. Am., 86(5)*, 1529-1544.

Tary, J. B. (2011), Relations entre fluides et sismicité dans le domaine sous-marin à partir de sismographes de fond de mer : étude de cas en Mer de Marmara et Application au Delta du Niger, PhD Thesis, IFREMER, Université de Bretagne Occidentale, Brest, France.

Tary, J. B., Géli, L., Henry, H., Natalin, B., Gasperini, B., Çomoglu, M., Çagatay, N., and T. Bardainne (2011), Sea bottom observations from the western escarpment of the Sea of Marmara, *Bull. Seismolog. Soc. Am., 101*, 775-791, doi: 10.1785/0120100014.

Toksöz, M. N., and D. H. Johnson (Eds.) (1981), Seismic wave attenuation, *Geophysics Reprint Series, 2*, Tulsa, OK: Society of Exploration Geophysicists.

van Kessel, T., and W. G. M. van Kesteren (2002), Gas production and transport in artificial sludge depots, *Waste Management, 22*, 19-28.

Varas, G., Vidal, V., and J. C. Géminard (2009), Dynamics of crater formations in immersed granular materials, *Phys. Rev. E., 79*, 021301, doi: 10.1103/PhysRevE.79.021301.

Varas, G., Vidal, V., and J. C. Géminard (2010), Venting dynamics of an immersed granular layer, *Phys. Rev. E.*, (in review).

Vidal, V., Géminard, J.-C., Divoux, T., and F. Melo (2006), Acoustic signal associated with the bursting of a soap film which initially closes an overpressurized cavity, *Eur. Phys. J. B., 54*, 321-329, doi: 10.1140/epjb/e2006-00450-0.

Wang, Z., Street, R., Woolery, E. and J. Harris (1994). *Qs* estimation for unconsolidated sediments using first-arrival *SH* wave critical refractions, *J. Geophys. Res., 99*, 13543-13551.

Zakharia, M. E. (2002), Sub-bottom variability characterization using surface acoustic waves, in *Impact of Littoral Environmental Variability on Acoustic Predictions and Sonar Performance*, edited by N. G. Pace and F. B. Jensen, pp. 131-138.

Zitter, T.A.C., Henry, P., Aloisi, G., Delaygue, G., Çagatay, M.N., Mercier de Lepinay, B., Al-Samir, M., Fornacciari, F., Tesmer, M., Pekdeger, A.,Wallmann, K., and G. Lericolais (2008), Cold seeps along the main Marmara Fault in the Sea of Marmara (Turkey), *Deep-Sea Res., 55*, 552-570, doi:10.1016/j.dsr.2008.01.002.

Chapter 3. Application to the ERIG3D cruise (2008-2009), eastern part of the deep-water Niger Delta: case study 3

3.1. Study area and OBS data analysis

3.1.1. The study area

The study area is located on the continental slope offshore Nigeria, on the eastern part of the deep-water Niger Delta (Fig. 3.1). The Niger Delta is widely known for its numerous oil fields and is heavily exploited. This zone is undergoing gravity driven extensional tectonics [*Damuth,* 1994] due to the weight of important deposits that come mainly from the Niger river. Thereby, gravitational forces cause large sediment masses to slowly propagate seaward involving growth normal faults, extensive diapirism and imbricate compressional thrusts [*Damuth,* 1994 *and references therein*].

The study area, with water depth ranging from 700 to 800 m, presents pressure and temperature conditions, as well as free gas supplies that are suitable for gas hydrates formation. Gas hydrates presence and evolution is considered as an important hazard source for edifices rooted in the seafloor and hence for oil fields exploitation.

In order to determine free gas and gas hydrates distribution and free gas circulation, complementary instruments were deployed during the ERIG3D cruise (from May 2008 to June 2009). High resolution 3D seismic data provided by TOTAL were used to define faults, and associations between gas hydrates and free gas. Very high resolution seismic data acquired with the SYSIF deep towed system [*Ker et al.,* 2008; *Marsset et al.,* 2010], together with CPTu piezocone (PENFELD) measurements (Sultan et al., 2010), were used to identify layers of silty-sandy sediments, free gas and gas hydrates in the first ~60 m of sediments. Key mechanical properties were obtained by geotechnical measurements conducted on sediment

and gas hydrates samples recovered using piston corers (calypso). Four long-term piezometers, deployed near an E-W normal fault, were used to measure the pore pressure in the superficial sediments (up to ~11.5 m) and highlight fluids circulation (Fig. 3.2). Detailed description of these instruments, results and discussion are reported in the Appendix A. Hereafter is described the preliminary analysis of the data of OBSs that were also deployed in this area during the ERIG3D cruise (Fig. 3.2).

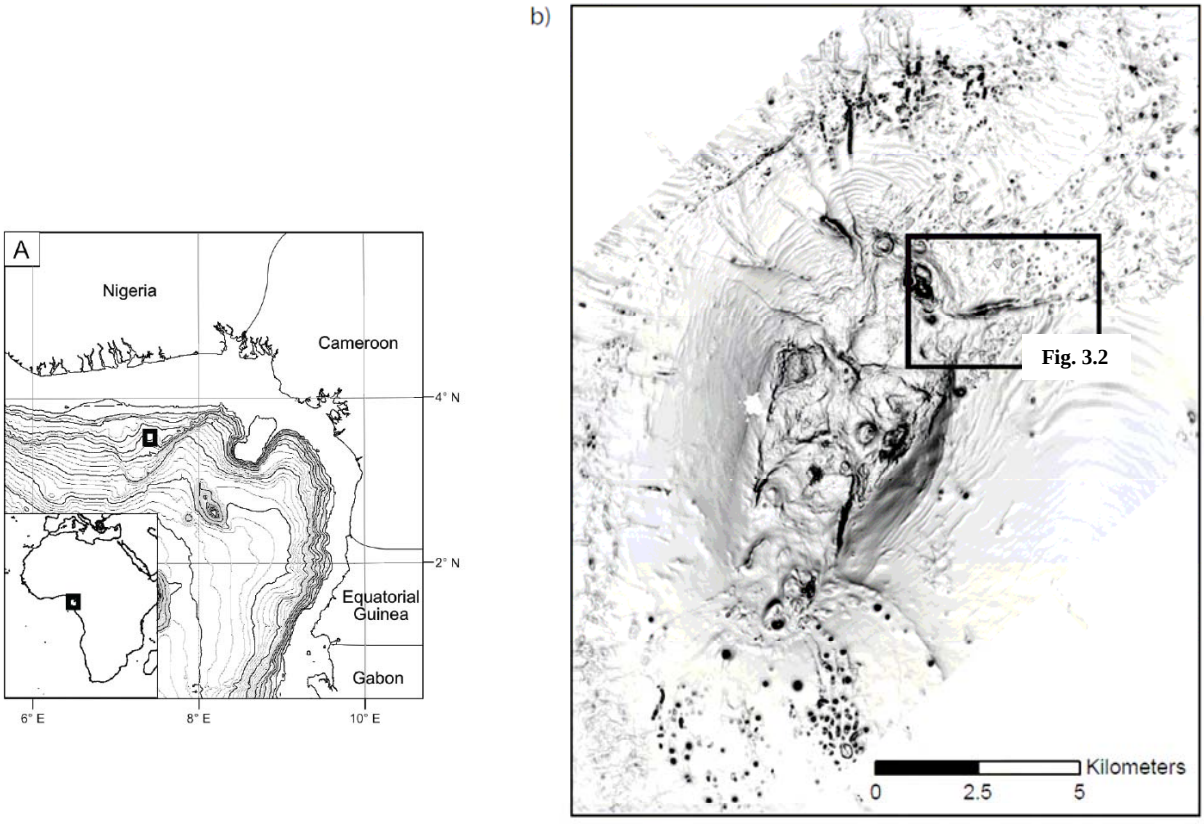

Fig. 3.1. a) Reproduced from Sultan et al. [2011], submitted (presented in Appendix A). Map of Gulf of Guinea showing the location of the study area (black rectangle). b) Dip map of the study area (AUV bathymetry). The position of Fig. 3.2 is indicated by the black rectangle.

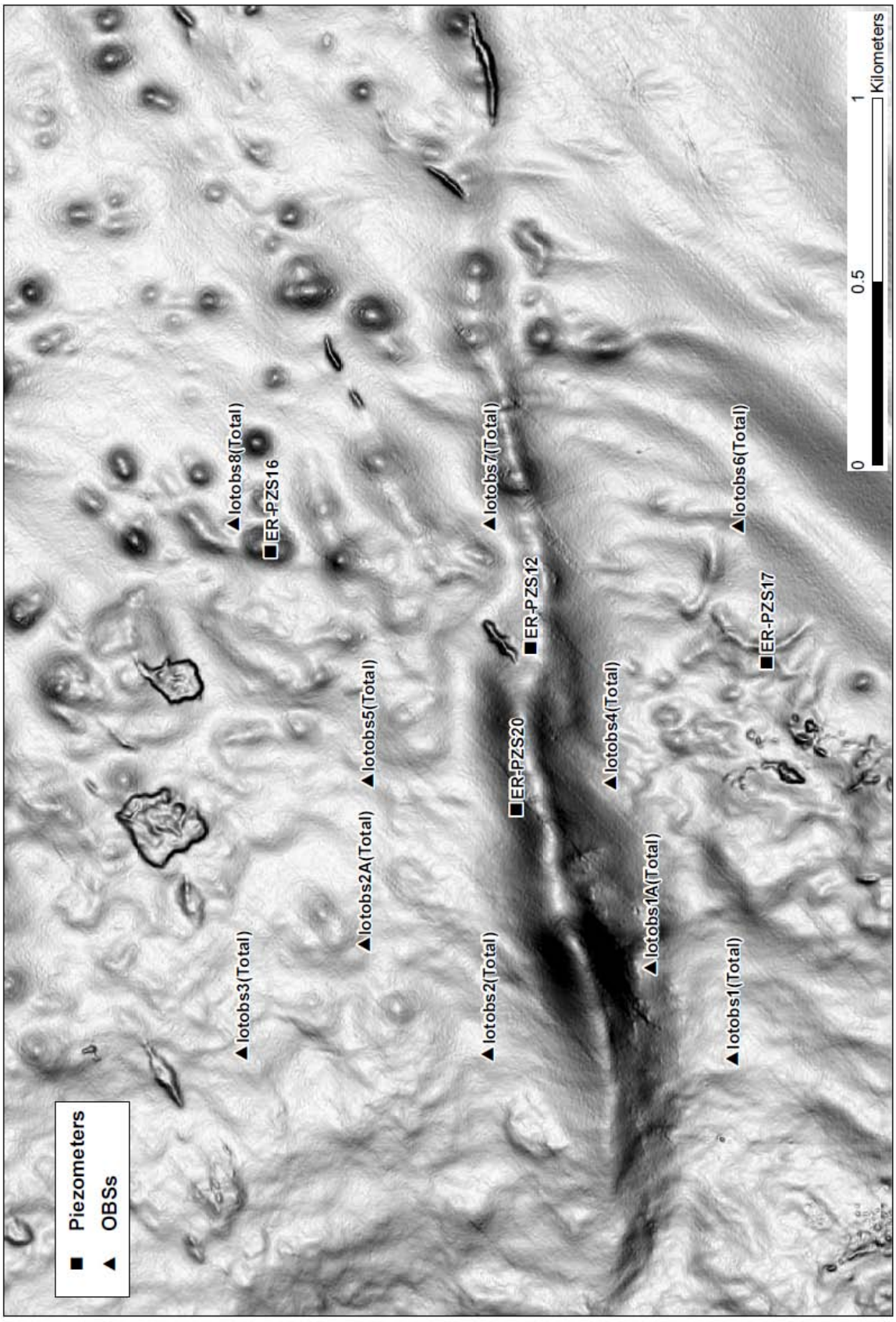

Fig. 3.2. Zoom in the OBS network (black triangles) deployed near an E-W normal fault in the study area. The piezometers deployed during the ERIG3D cruise are also indicated (black squares).

3.1.2. ERIG 3D cruise: OBS data analysis

During the ERIG3D cruise, 9 OBS were deployed close to a major E-W normal fault. This fault is connected at depth with a hydrocarbon reservoir. In the perspective of oil exploitation, the reservoir depletion could induce instabilities on the seafloor (seafloor settling, landslides, earthquakes ground shaking) hazardous for oil structures. Thereby, the purpose of the present study was to characterize the level of the seismic activity of this fault.

The OBS network configuration was set up by TOTAL to ensure precise location of the microseismicity associated to the superficial fault network. The OBSs were provided by IFREMER (LotOBS, see Appendix C for detailed technical description) and laid down to the seafloor using a cable with relative positioning system. The OBSs main technical features and recording period are summarized in Table 3.1.

Stations	Water depth (m)	Recording period
1A	726	10/06/2008 02:00 - 28/06/2008 01:26
2A	735	10/06/2008 02:00 - 08/07/2008 01:43
02	728	10/06/2008 02:00 - 23/06/2008 12:12
03	733	10/06/2008 02:00 - 11/08/2008 04:54
04	734	10/06/2008 02:00 - 22/06/2008 14:22
05	739	10/06/2008 02:00 - 21/06/2008 16:31
06	743	10/06/2008 02:00 - 20/06/2008 18:40
07	748	10/06/2008 02:00 - 15/08/2008 01:58
08	716	10/06/2008 02:00 - 11/06/2008 16:14

Table 3.1. OBSs water depth and recording period. Natural frequency of geophones: 4.5 Hz; Sampling frequency: 250 Hz.

Unfortunately, most of the instruments (except OBS 07) did not record during the whole deployment period, preventing the measurements of the internal clock drifts. Therefore, the OBSs were prepared again in the laboratory. The drift of the clock of each instrument were measured after the same recording period (e. g. 18 days for OBS 1A, 28 days for OBS 2A, 13 days for OBS 02…). A linear clock drift is assumed.

Apart from the shortened recording periods, the instruments worked well and the data quality is good. Some seismic shots have been recorded during the first week of the deployment due to 3D seismic acquisition in the area. High amplitude noise due to the ship traffic have also been recorded several times.

The microseismicity processing was conducted with the SYTMIS software package. This software have been developed by INERIS, which is an institution specialized in the seismic monitoring of abandoned mines. SYTMIS was used to import and convert the data, and for the micro-earthquakes automatic detection. A detection is made when a given amplitude threshold is overcome at a given number of stations.

However, during the ERIG3D cruise, no micro-earthquake was identified. Only micro-events were detected (Fig. 3.3).

- Micro-events analysis

These micro-events have the same characteristics as the ones observed in the Sea of Marmara (section 2.8), that is

- Large amplitudes range, between 0.1 and 50 µm/s,
- Short duration, between 0.2 and 0.6 s,
- Frequency spectrum between 4 and 30 Hz,
- No secondary arrival.

Only limited number of micro-events were recorded by the LotOBS hydrophones (Fig. 3.3), positioned at ~0.5 m above the seafloor (Fig. B6).

No correlated micro-events were observed on two or more OBSs. The minimum distance between OBSs during the ERIG3D cruise is about 440 m. This indicates, as in the case of the Sea of Marmara, that the micro-events origin is close to the instruments.

About 11960 micro-events on the nine OBSs were inventoried by *Maury et al.* [2009] (Fig. 3.4). Micro-events temporal distributions for each OBS are given in Fig. 3.5 and Fig. 3.6.

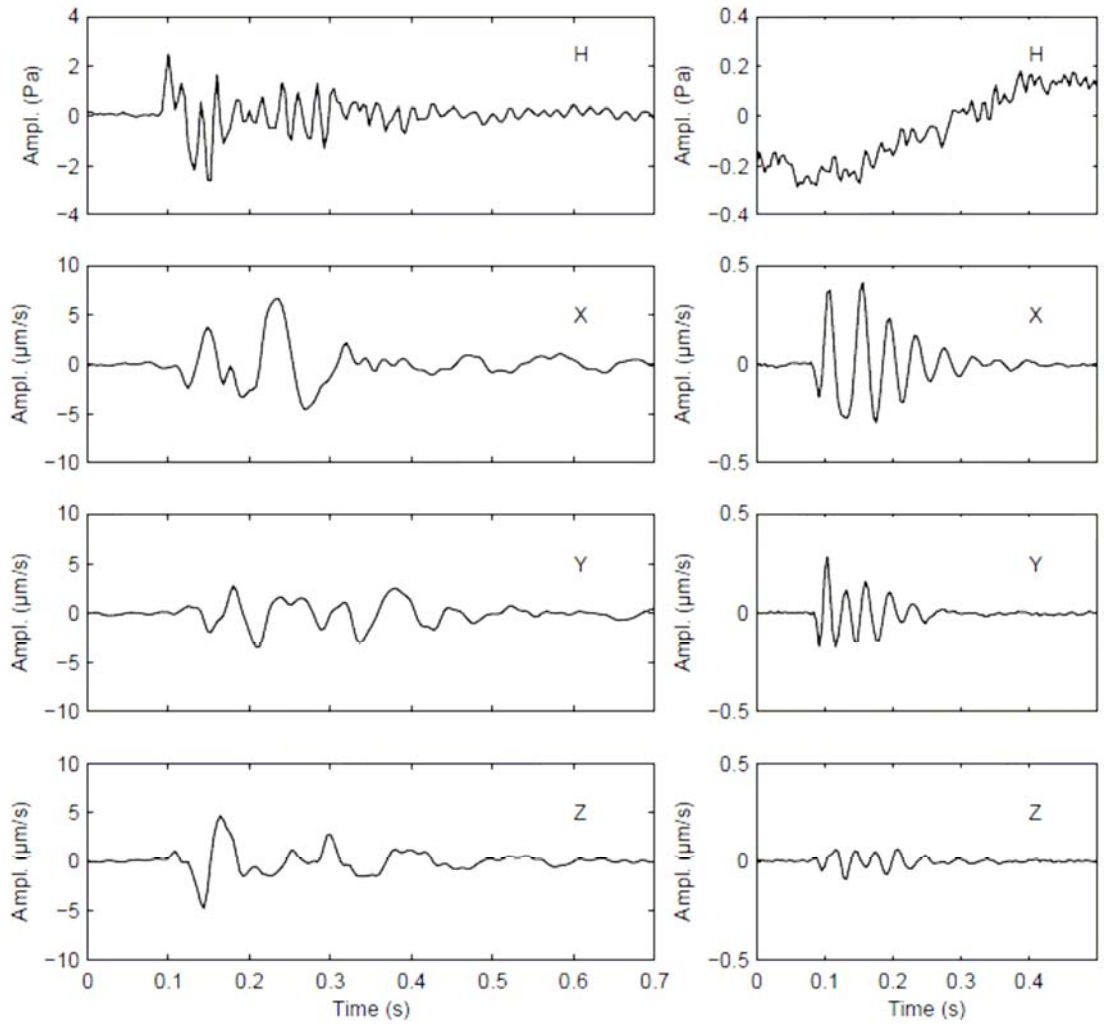

Fig. 3.3. Two examples of micro-events recorded by the OBS 04 on 20/06/2008 at (left) 08:57:42 and (right) 05:31:39 (H: hydrophone, X and Y: horizontal components, Z: vertical component). Note that the signal on the left is clearly visible on the hydrophone.

The most active sites are those of OBSs 03, 02 and 08. These sites are not associated to the E-W main normal fault. Despite its very short recording period (1.5 days), the high activity observed on OBS 08 is likely due to the presence of a nearby pockmark (Fig. 3.2). On the other hand OBSs 1A and 7, situated near the main fault, show relatively low activities.

Interestingly, OBS 04 recorded a crisis of about 300 micro-events over a duration of 1 day on June 21, 2008. In order to perform the principal components analysis of the micro-events of this crisis, the OBS 04 data between June 20 and 22 have been reprocessed. An algorithm was created with parameters adapted to micro-events detection. This algorithm uses a given threshold of the STA/LTA (Short Term Average / Long Term Average) to identify the micro-events. The windows on which the short term and long term averages are calculated have to

be adapted to micro-events detection. Finally, all the detected signals were visually controlled.

Using this algorithm, the number of micro-events detected has been multiplied by ~4 compared to the analysis of *Maury et al.* [2009], even though the temporal evolution of the number of micro-events remains quite similar (Fig. 3.7).

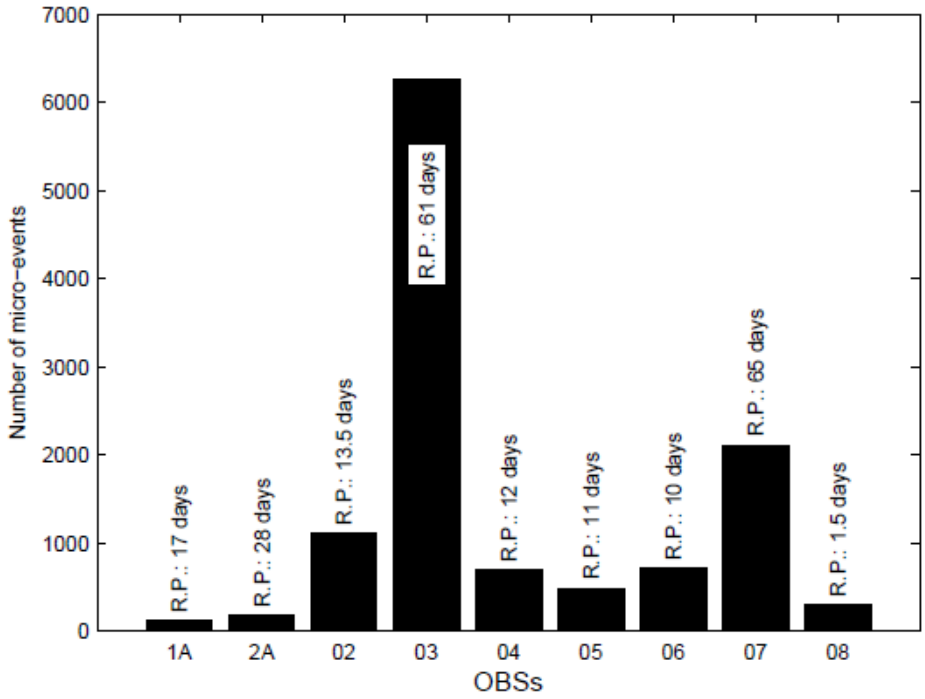

Fig. 3.4. Number of micro-events and recording period (R.P) for all OBSs.

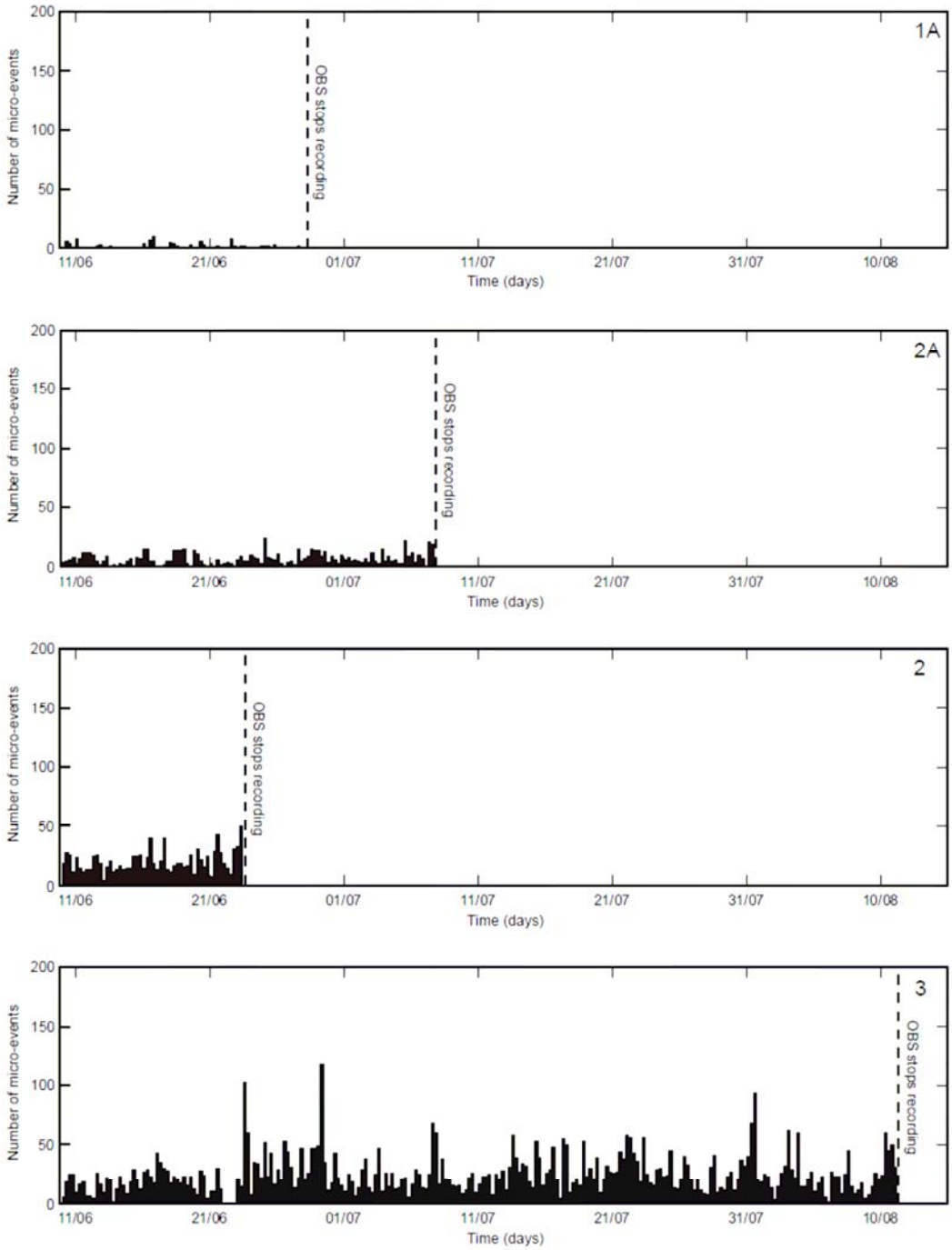

Fig. 3.5. Temporal evolution of the number of micro-events identified on OBSs 1A, 2A, 2, 3.

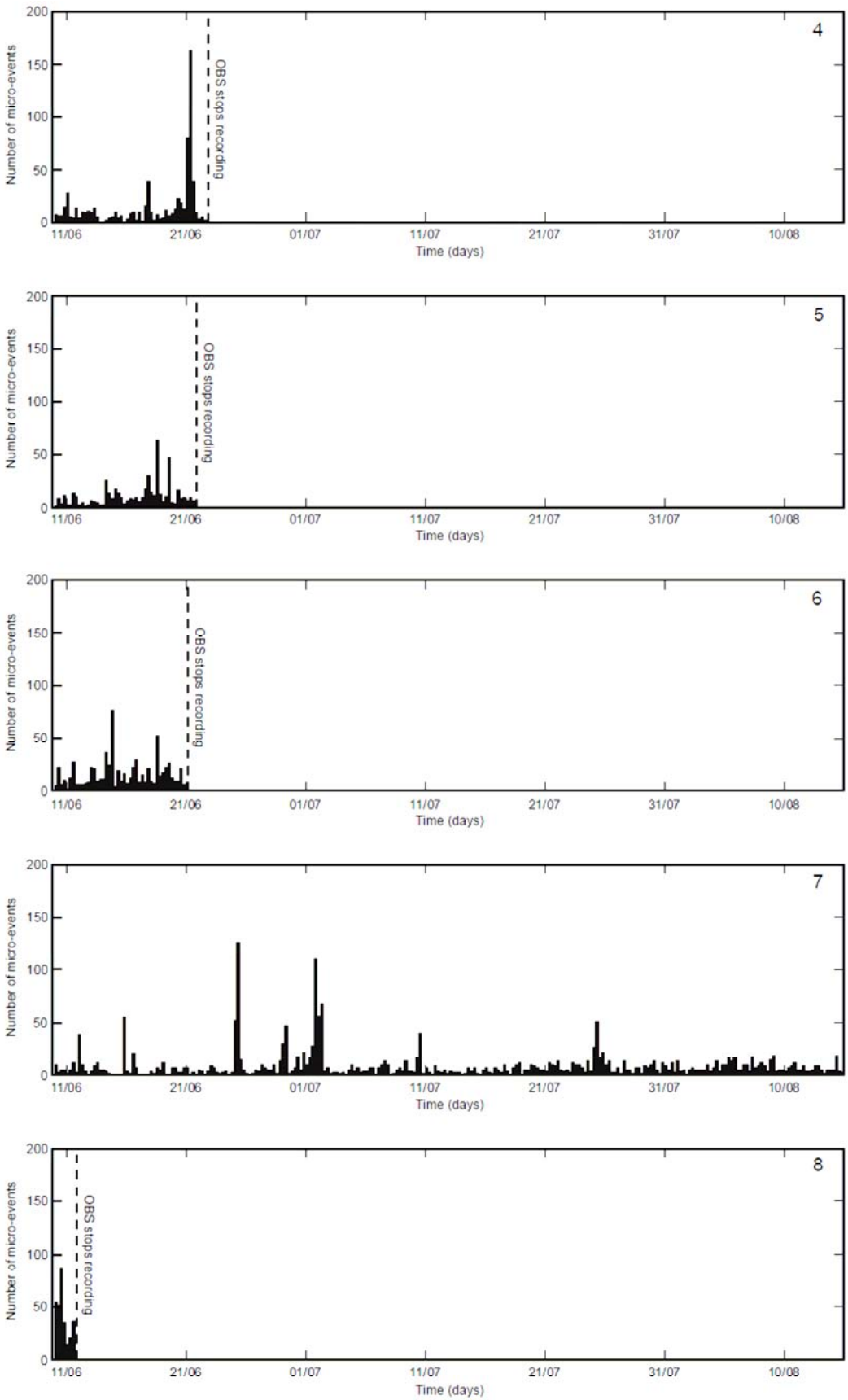

Fig. 3.6. Temporal evolution of the number of micro-events identified on OBSs 4, 5, 6, 7 and 8.

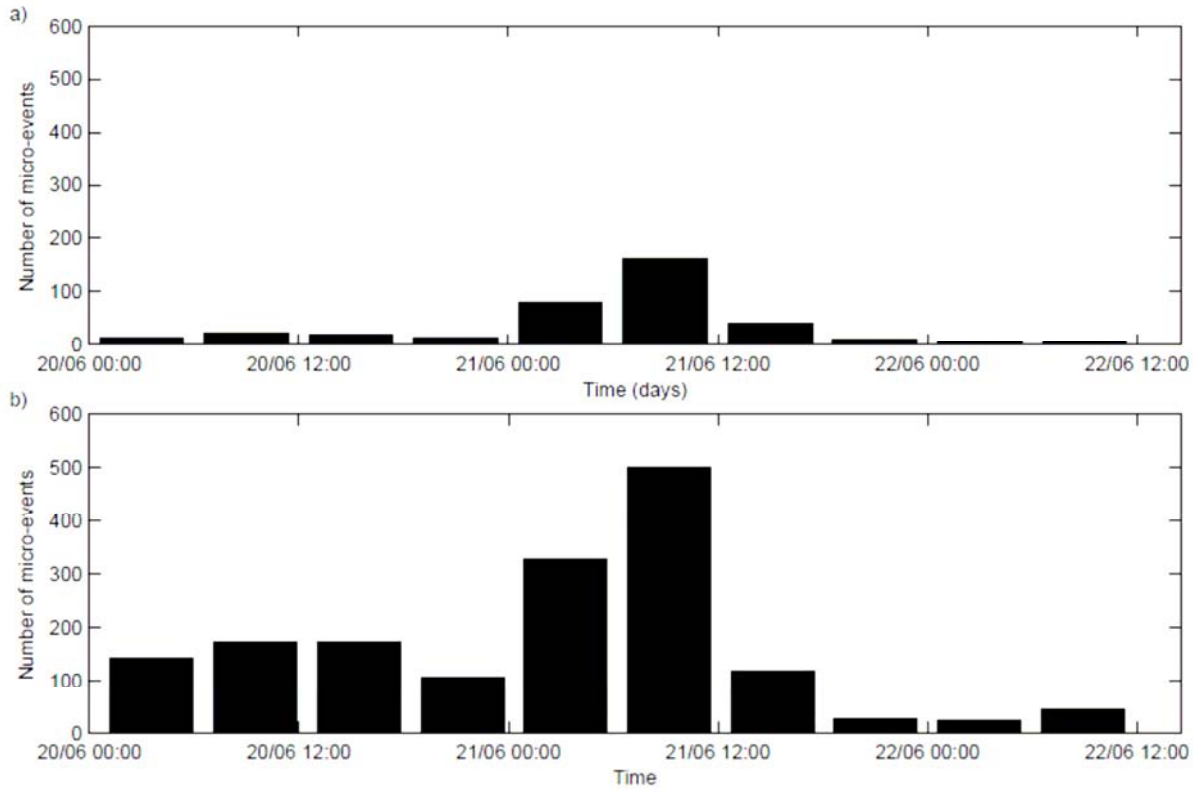

Fig. 3.7. Temporal distribution of the micro-events constituting the swarm recorded by OBS 4 on June 21, 2008. a) Inventory by Maury et al. [2009] with SYTMIS software. B) Inventory made with an adapted algorithm.

- Principal component analysis

The procedure to perform the principal component analysis of the crisis identified on OBS 04 is the same as the one described in section 2.8.2, and applied to the swarm recorded by OBS M in the Sea of Marmara on June 11, 2007. As a reminder:

Step 1: micro-events detection and extraction

Step 2: Signals rotation in the waves frame of reference

Step 3: Signals origin and average control

Step 4: Covariance matrix calculation as

$$\left[C_{tp,tq}\right] = \sum_{1 \le i,\, j \le M} f_i(t_p)\, f_j(t_q) \text{ where } t_1 \le t_p, t_q \le t_N, \qquad (3.1)$$

with f_i and f_j the temporal series, M the number of micro-events, and N the number of samples.

Step 5: Calculation of the characteristic signals (eigenvectors, $\boldsymbol{V_i}$, i = 1, M) together with their data representativeness (eigenvalues, λ_i, i = 1, M). The data representativeness is given as a percentage of the data total energy ($\lambda_i^2/\Sigma\lambda_i^2$).

The first and second eigenvectors are very similar, with a cumulated data representativeness of 73 % on the radial component (Table 3.2). This characteristic signal has frequency contents with one peak between ~16 and ~17 Hz on the radial component, and between 14 and 17 Hz on the vertical component (Fig. 3.8). Its duration is about 0.3 sec.

OBS 04	Eigenvector 1			Eigenvector 2		
947 ME	%	Freq. (Hz)	Dur. (s)	%	Freq. (Hz)	Dur. (s)
Comp. Radial	39	15.7-17.2	0.24	34	15.7	0.29
Comp. Transverse	18	13.7	0.39	14	13.2, 21.6	0.36
Comp. Vertical	29	14.2-16.7	0.26	22	14.7	0.25

Table 3.2. Characteristics of the first and second eigenvectors of the PCA performed for the micro-events of the crisis recorded by OBS 04. The number of micro-events used in the principal component analysis is also indicated (ME: micro-events). Comp.: component; %: data representativeness (energy); Freq.: dominant frequency; Dur.: duration.

The micro-events have similar characteristics in the deep-water Niger delta and in the Tekirdag Basin. However, compared with the sites monitored in the Tekirdag Basin, the sites in the deep-water Niger delta are more active. Indeed, about 7300 micro-events in 395 cumulated recording days were identified during the MarNaut cruise, whereas 11960 micro-events in 220 cumulated recording days were identified during the ERIG3D cruise. This could result from a combination of several factors, (i) the shallower depth of the eastern part of the deep-water Niger Delta, (ii) different sediments properties, (iii) more important gas supplies in the area of the deep-water Niger Delta.

This analysis of the OBS data has proven to be very useful to improve the interpretation of the piezometric data. The combination of the two datasets provides an unique insight on how gas migrates into the upper sediment layers.

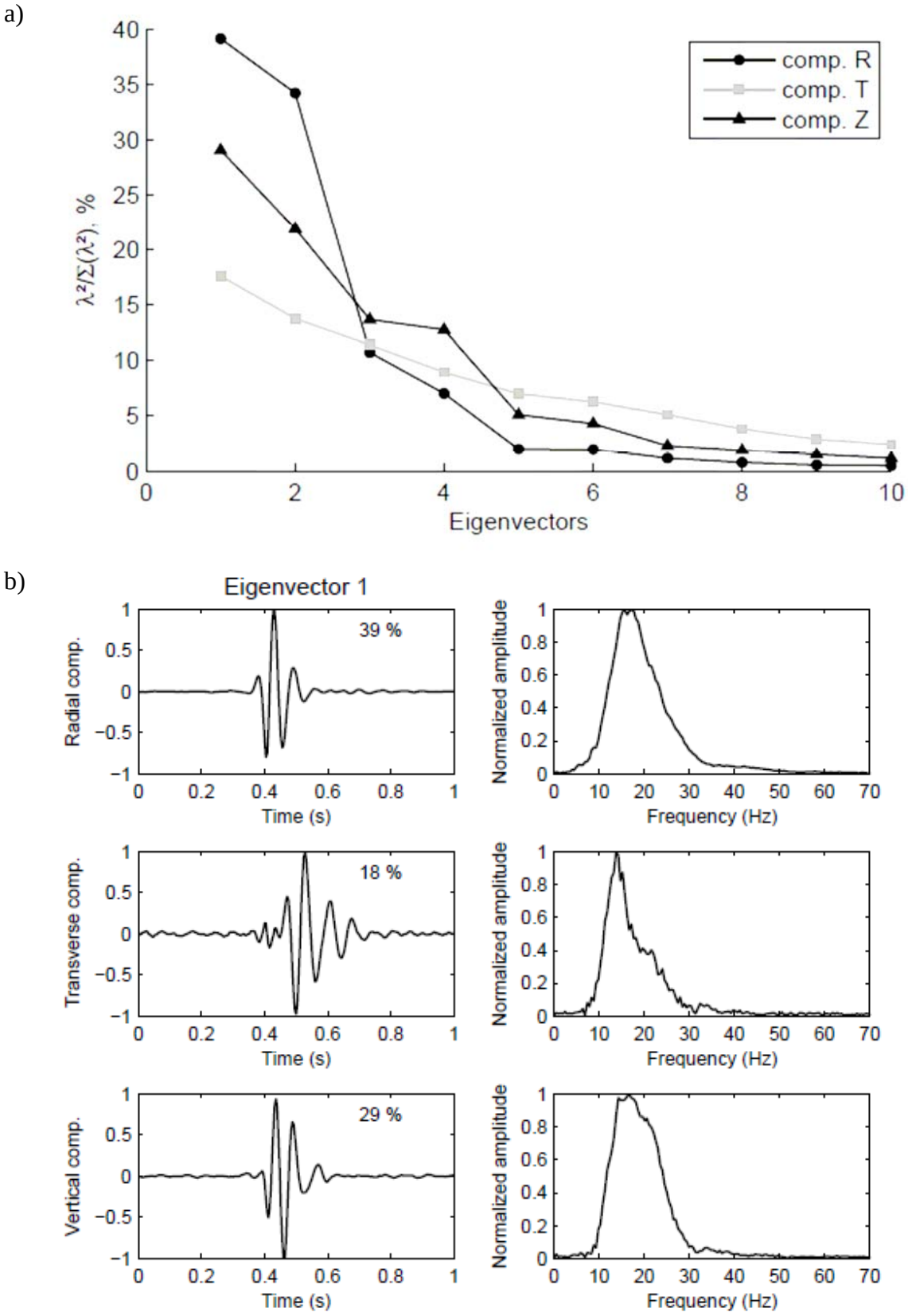

Fig. 3.8. PCA of the micro-events constituting the crisis identified on OBS 04. a) Representativeness of the first 10 eigenvectors (R: Radial, T: Transverse, Z: Vertical). b) First eigenvector for the 3 components in the wave frame of reference. The representativeness of each eigenvector is indicated by its eigenvalue given in percentage of the total energy. On the right is given the eigenvector spectrum.

3.2. Dynamics of fault-fluid-hydrate system around a shale-cored anticline in deepwater Nigeria (Article)

Sultan et al. [2011], accepted by the Journal of Geophysical Research.

This article is presented in Appendix A, because it mainly results from the work of Nabil Sultan and collaborators. My personnal contribution to this paper concerns the interpretation of OBS data. This contribution, however, significantly helped improve our understanding of the degassing processes.

Chapter 4. Conclusion and perspectives

The major conclusions of this PhD work are the following:

1. Recommendations for the future, permanent, mutli-disciplinary seafloor observatories for earthquake monitoring in the Sea of Marmara:

1.1 Because the basins of the Sea of Marmara are filled with more than 5 km of Plio-Quaternary soft ("slow") sediments, the velocity structure of the offshore domain is drastically different from the one onshore. Therefore, merging land and sea-bottom datasets has proven to be very challenging, if not hopeless.

1.2 To improve the real-time, absolute locations of hypocenters near the submerged fault zone and enhance the search for seismic tremors [*Bouchon et al.,* 2011], specific networks of permanent, cabled sea-bottom seismometers are required. Each network should be consistent *per se*, and allow the high-resolution characterization of earthquakes below the Sea of Marmara.

1.3 In addition, it is of critical importance to create a high-resolution, 3D velocity model. This could be achieved by performing velocity analysis using the numerous multi-channel seismic profiles that cover the Sea of Marmara.

1.4 Multi-parameters approaches must be developed. Our work clearly shows that for each measured parameter, the background variability must be assessed. In addition, data processing and research on the physics of the phenomena should be intimately related. The better our understanding on the physics, the better our ability to determine the appropriate criteria for data processing, analysis and interpretation.

2. On Case Study 1:

2.1 Our OBS-based micro-seismic study indicates that the tectonic strain below the western slope of the Tekirdag Basin may contributes to maintain a high permeability in faults zones, suggesting that the fault network might provide conduits for deep-seated fluids to rise up to the seafloor.

2.2 Numerous sites of gas emission have been documented near the Western Slope of the Tekirdag Basin. Our results could explain how and why deep-seated fluids, likely leaking from Thrace Basin hydrocarbon reservoirs, are escaping into the Sea of Marmara.

3. On Case Study 2:

3.1 High-resolution, seismic chirp profiles, reveal that gas occurrence is common within the uppermost sediments that cover the Marmara seafloor.

3.2 Non-seismic micro-events were recorded with different types of OBSs at different sites, over soft sediments covering the seafloor of the Tekirdag Basin. These micro-events are characterized by short durations of less than 0.6 s, frequencies ranging between 10 and 30 Hz and highly variable peak-to-peak amplitudes. In addition, there is no correlation between OBSs, except for those OBSs located ~10 meters apart.

3.3 The presence of gas in superficial sediments suggests that gas expulsion followed by the collapse of a fluid-filled conduit could be the source of the observed micro-events. Hence, OBSs may provide valuable information to improve our understanding of natural degassing processes from the seafloor.

4. On case study 3:

4.1 Our work on the eastern part of the deep-water Niger Delta supports the hypothesis that OBSs enable the detection of individual, local degassing events. Hence, OBSs provide valuable information complementing the piezometric data.

4.2 Natural, submarine degassing processes require a number of generic tools for their detection and monitoring, a subject of critical importance for mitigating gas-related geohazards. The present work promotes the combination of collocated BOBS, piezometers and OBSs to detect the initiation and evolution of episodes of gas accumulation and release in shallow sediment layers.

Perspectives for future work:

Multi-disciplinary, permanent, cabled seafloor observatories represent the ultimate solution to continuously monitor geohazards in exposed submarine areas, such as, for instance, seismically active areas (e.g. the Sea of Marmara), or oil drilling platforms (e.g. the continental slope of the deep-water Niger delta).

However, because the installation of permanent multidisciplinary seafloor observatories represents long-term projects, it is necessary to keep collecting data continuously using autonomous, mobile seafloor instruments to be serviced on a regular basis.

There is an urgent need to develop a multi-parameter approach to detect anomalous events, based on the analysis of combined datasets, including pore pressure data, seismicity and acoustic gas detection. Data from different sites are required, in order to assess the background variability of each parameter and improve our ability to identify and detect anomalous variations.

Some physical parameters are relatively well understood, like microseismicity. In our work, the main limitation is the small size of the network. For further investigations on microseismicity activity and distribution in the Sea of Marmara, either larger networks are needed, deployed for long periods of time (months to years), either land and sea networks could be merged through the construction of a 3-D velocity model including both on-shore and offshore domains.

Also, some limitations arise from instruments themselves:

- Time shifts involved by OBSs clock drift prevent accurate microseismicity location, and limit the impact of location methods based on time delays with an accuracy in the order of magnitude of milliseconds (double-differences method for example). As the true clock behaviour is poorly known, clock drifts are typically corrected linearly. Yet, significant improvements in clock drift correction could be achieved by simple laboratory experiments.

- When using small networks to locate microseismicity, azimuths and dips computed from waves polarization should contribute significantly to the improvement of locations accuracy. Ifremer OBSs are from now on equipped with compass that will enable the use of waves polarization to improve earthquake locations.

- Recordings from short-period OBSs are typically limited to frequencies upper than ~2-4 Hz. Recent observations of long period signals related to degassing events and recorded by the broad-band seismometer (Guralp CMG-40T) of the SN-4 multidisciplinary module of INGV (Francesco Frugoni, personnal communication, 2011), show that broad-band OBSs should be favored for future deployments.

Non-seismic transients (e. g. sediment pore pressure or gas bubble acoustic response) all require further research. The conceptual model proposed for the source of micro-events, as well as the hypotheses on their propagation presented in this work, should be tested through full waveform seismic modeling and laboratory experiments.

The experimental setup could consist in a tank filled by clayey sediments with gas (air) injected through its bottom, and geophones on the surface to record the signals generated while gas is expulsed. Additional geophones could be buried at different levels to investigate the signal attenuation as well as the possible resonance of the fluid-filled conduits. A better knowledge of sediments mechanical properties is required for the development of empirical relationships between the recorded signals and the sources shape and dimensions.

Along with full waveform seismic modelling, the particular propagation mode of micro-events should be further examined and compared to specific characteristics of surface waves (dispersion, polarization...).

Continuous time series are needed to evaluate the real significance of each parameter anomaly and its relevance to hazard occurrence. Our results are encouraging, but long-term observations and further research are needed to confirm the causality link between the different observations: are the observed gas pulses «significant»? In other words: do gas pulses occur randomly or preferentially prior to, during, or after earthquakes?

A major challenge for the future permanent, seafloor observatories is to propose tools and methods for combining all different datasets and detecting anomalous signals that could be correlated with seismic activity and eventually be identified as indicators that a potentially dangerous situation is under way. The real-time processing of the full dataset represents a critical issue that comprises different phases, e.g. data correction and reduction, event detection and characterization, anomaly identification, data cross-correlation, and eventually alarm. It is necessary to work simultaneously on physical processes and on the development of new algorithms for data processing, analysis and interpretation.

References

Adam, S., 2008. Protocole Essais Oedométriques, Rapport Interne Ifremer, 26 pp.

Alpar, B., 1999. Underwater signatures of the Kocaeli earthquake of 17 August 1999 in Turkey, Turkish J. Mar. Sci. 5, 111–130.

Aksu, A. E., Calon, T. J., Hiscott, R. N., and Yaşar, D., 2000. Anatomy of the North Anatolian fault zone in the Marmara Sea. Western Turkey: Extensional basins above a continental transform, GSA Today 10, 1-2.

Ambraseys, N., 2002. The seismic activity of the Marmara Sea region over the last 2000 years, Bull. Seism. Soc. Am. 91, 1397-1416.

Ambraseys, N. N. and Finkel, C. F., 1988. The Anatolian earthquake of 17 August 1668, in Historical Seismograms and Earthquakes of the World, pp. 173-180, eds. Lee, W.H.K., Meyers, H. & Shimazaki, K., Academic Press, New York, NY.

Ambraseys, N., and Finkel, C., 1995. The Seismicity of Turkey and Adjacent Areas 1500-1800, 240 pp., Eren Yayincilik ve Kitapcilik Ltd., Istanbul.

Ambraseys, N., and Jackson, J., 2000. Seismicity of the Sea of Marmara (Turkey) since 1500, Geophys. J. Int. 141, F1–F6.

Armijo, R., Meyer, B., Hubert, A., and Barka, A., 1999. Westward propagation of the North Anatolian Fault into the northern Aegean: Timing and kinematics, Geology 27, 267-270.

Armijo, R., Meyer, B., Navarro, S., G. King and Barka, A., 2002. Slip partitioning in the Sea of Marmara pull-apart: a clue to propagation processes of the North Anatolian Fault ?, Terra Nova 14, 80–86.

Armijo, R., Pondard, N., B. Meyer and Uçarkus, G., 2005. Submarine fault scarps in the Sea of Marmara pull-apart (North Anatolian Fault): implications for seismic hazard in Istanbul, Geochem. Geophys. Geosyst. 6, Q06009.

Baligh, M. M., 1986. Undrained deep penetration, II: pore pressures, Géotechnique, 36(4), 487-501.

Bardainne, T., 2005. Étude de la sismicité de Lacq et analyse des formes d'ondes par décomposition en chirplets, Ph. D. Thesis from Université de Pau et des Pays de l'Adour.

Bardainne, T. and Gaucher, E., 2010. Constrained tomography of realistic velocity models in microseismic monitoring using calibration shots, Geophysical Prospecting 58(5), 739-753, doi: 10.1111/j.1365-2478.2010.00912.x.

Barka, A.A., 1992. The North Anatolian fault zone, Annales Tectonicae, VI suppl., 164-195.

Barka, A., 1996. Slip distribution along the North Anatolian fault associated with the large earthquakes of the period 1939 to 1967, Bull. Seism. Soc. Am. 86, 1238-1254.

Barka, A. A., and Kadinky-Cade, K., 1988. Strike-slip fault geometry in Turkey and its influence on earthquake activity, Tectonics 7, 663-684.

Bayrakci, G., 2009. Hétérogénéité 3D de la croûte supérieure sous la Mer de Marmara : Tomographie sur une grille de sismomètres fond de mer et de profils de tirs. Ph.D. Thesis at IPGP.

Bécel, A., 2006. Structure Sismique de la Faille Nord Anatolienne en Mer de Marmara. Ph.D. Thesis at IPGP.

Bécel, A., Laigle, M., de Voogd, B., Hirn, A., Taymaz, T., Shimamura, H., Murai, Y., Lépine, J.-C., Sapin, M., and Özalaybey, S., 2009. Moho, crustal architecture and deep deformation under the North Marmara Trough, from the SEISMARMARA Leg 1 offshore–onshore reflection–refraction survey, Tectonophysics 467, 1-21, doi: 10.1016/j.tecto.2008.10.022.

Bécel, A., Laigle, M., de Voogd, B., Hirn, A., Taymaz, T., Yolsal-Cevikbilen, S., and Shimamura, H., 2010. North Marmara Trough architecture of basin infill, basement and faults, from PSDM reflection and OBS refraction seismics, Tectonophysics 490, 1-14, doi: 10.1016/j.tecto.2010.04.004

Beck, C., Mercier de Lepinay, B., Schneider, J.-L., Cremer, M., Cagatay, N., Wendenbaum, E., Boutareaud, S., Menot-Combes, G., Schmidt, S., Weber, O., Eris, K., Armijo, R., Meyer, B., Pondard, N., Gutcher, M.-A., Turon, J. L., Labeyrie, L., Cortijo, E., Gallet, Y., Bouquerel, H., Görür, N., Gervais, A., Castera, M. H., Londeix, L., de Resseguier, A., and Jaouen, A., 2007. Late quaternary co-seismic sedimentation in the Sea of Marmara's deep basins, Sedimentary Geology 199 (1-2), 65–89.

Boetius A., Ravenschlag K., Schubert C. J., Rickert D., Widdel F., Giesecke A., Amann R., Jorgensen B. B., Witte U., and Pfannkuche, O., 2000. A marine microbial consortium apparently mediating anaerobic oxidation of methane, Nature 407, 623–626.

Bohnhoff, M., Grosser, H., and Dresen, G., 2006. Strain partitioning and stress rotation at the North Anatolian fault zone from aftershock focal mechanisms of the 1999 Izmit Mw = 7.4 earthquake, Geophys. J. Int. 166, 373-385, doi: 10.1111/j.1365-246X.2006.03027.x.

Bouchon, M., Toksöz, N., Karabulut, H., Bouin, M. P., Dietrich, M., Aktar, M. and Edie, M., 2000. Seismic Imaging of the 1999 Izmit (Turkey) Rupture Inferred from the Near-Fault Recordings, Geophys. Res. Lett. 27(18), 3013-3016.

Bouchon, M. Karabulut, H., Aktar, M., Özalabey, S., Schmittbuhl, and Bouin, M.-P., 2011. Extended Nucleation of the 1999 M_w 7.6 Izmit Earthquake, Science 331, 877-880, doi: 10.1126/science.1197341.

Bouriak, S., Vanneste, M., and Saoutkine, A., 2000. Inferred gas hydrates and clay diapirs near the Storegga Slide on the southern edge of the Voring Plateau, offshore Norway, Marine Geology 163 (1-4), 125–148.

Bourry, C., Chazallon, B., Charlou, J.-L., Donval, J.-P., Ruffine, L., Henry, P., Geli, L., Çagatay, M. N., İnan, S., and Moreau, M., 2009. Free gas and gas hydrates from the Sea of Marmara, Turkey Chemical and structural characterization, Chemical Geology 264, 197-206.

Brune, J. N., 1970. Tectonic Stress and the Spectra of Seismic Shear Waves from Earthquakes, J. Geophys. Res. 75(26), 4997-5009.

Bulut. F., Bohnhoff, M., Ellsworth, W. S., Aktar, M., and Dresen, G., 2009. Microseismicity at the North Anatolian Fault in the Sea of Marmara offshore Istanbul, NW Turkey, J. Geophys. Res. 114, B09302, doi:10.1029/2008JB006244.

Burnard, P., Bourlange, S., Henry, P., Géli, L., Marty, B., Natalin, B., and Sengor, S., 2008. Fluid Sources on the North Anatolian Fault in the Sea of Marmara From He Isotope Measurements. Eos Trans. AGU, 89(53), Fall Meet. Suppl., Abstract U53A-0069.

Burns, S. E., and Mayne, P. W., 1998. Monotonic and dilatory pore pressure decay during piezocone tests in clay, Can. Geotech. J. 35, 1063-1073.

Buskirk, R.E., Frohlich, C., Latham, G. V., Chen, A. T., and J. Lawton (1981), Evidence that biological activity affects ocean bottom seismograph recordings, Mar. Geophys. Res. 5 (2), 189-205.

Çagatay, M. N., Gorur, N., Algan, O., Eastoe, C. S., Tchapalygya, A., Ongan, D., Kuhn, T., and Kuscu, I., 2000. Late Glacial-Holocene palaeoceanography of the Sea of Marmara: timing of connections with the Mediterranean and the Black Sea, Marine Geology 167, 191-206.

Çagatay, M. N., Gorur, N., Polonia, A., Demirbag, E., Sakinc, M., Cormier, M. H., Capotondi, L., McHugh, C., Emre, O., and Eriş, K., 2003. Sea-level changes and depositional environments in the Izmit Gulf, Eastern Marmara Sea, during the Late Glacial-Holocene period, Marine Geology 202 (3-4), 159-173.

Çagatay, M. N., Belucci, L., Polonia, L., Sancar, U., Dikçe, D., Eriş, K., Damci, E., Gasperini, L., Görür, N., Henry P., Zitter T. A. C., Geli, L., and Tryon, M., 2008. Sedimentary earthquake records in the Sea of Marmara, EGU General Assembly 2008, Vienna, EGU2008-A-05412.

Çagatay, M. N., Eriş, K., Ryan, W. B. F. , Sancar, U., Polonia, A., Akcer, S., Biltekin, D., Gasperini, L., Gorur, N., Lericolais, G., and Bard, E., 2009. Late Pleistocene-Holocene evolution of the northern shelf of the Sea of Marmara, Marine Geology 265, 87-100, doi:10.1016/j.margeo.2009.06.011.

Carton, H., 2005. Etudes tectoniques en Méditerranée orientale par analyse de données de sismique réflexion : Mer de Marmara (Bassin de Çinarcik) et marge du Liban, Ph.D. Thesis at IPGP.

Carton, H., Singh, S. C., Hirn, A., Bazin, S., de Voogd, B., Vigner, A., Ricolleau, A., Cetin, S., Oçakoğlu, N., Karakoç, F., and Sevilgen, V., 2007. Seismic imaging of the three-dimensional architecture of the Çinarcık Basin along the North Anatolian Fault. J. Geophys. Res. 112, B06101, doi: 10.1029/2006JB004548.

Chouet, B. (1988), Resonance of fluid-driven crack : radiation properties and implications for the source of long-period events and harmonic tremor, J. Geophys. Res. 93, 4375-4400.

Chouet, B. (1996), Long-period volcano seismicity : its source and use in eruption forecasting, Nature 380, 309-316, doi: 10.1038/380309a0.

Damuth, J. E., 1994. Neogene gravity tectonics and depositional processes on the deep Niger Delta continental margins, Mar. Petrol. Geol., 11, 321-346.

Diaz, J., Gallart, J., and O. Gaspà (2007), Atypical seismic signals at the Galicia Margin, North Atlantic Ocean, related to the resonance of subsurface fluid-filled cracks, Tectonophysics 433, 1-13, doi: 10.1016/j.tecto.2007.01.004.

Dimitrov, L., and Woodside, J., 2003. Deep Sea pockmark environments in the Eastern Mediterranean, Marine Geology 195 (1-4), 263-276.

Dupré, S., Scalabrin, C., Géli, L., Henry, P., Grall, C., Tary, J. B., Cagatay, N., Imren, C., and the Marmesonet cruise Scientific Party, 2010. Widespread gas emissions in the Sea of Marmara in relation with the tectonic and sedimentary environments: Results from shipborne multibeam echosounder water column imagery (MARMESONET expedition, 2009), EGU General Assembly, Vienna, Abstract EGU2010-9429-2.

Elmas, A., 2003. Late Cenozoic tectonics and stratigraphy of northwestern Anatolia: the effects of the North Anatolian Fault to the region, Int. J. Earth Sci. 92, 380-396, doi: 10.1007/s00531-003-0322-2.

Flerit, F., Armijo, R., King, G.C.P., Meyer, B. and Barka, A., 2003. Slip partitioning in the Sea of Marmara pull-apart determined from GPS velocity vectors, Geophys. J. Int., 154, 1–7.

Geli, L., Henry, P., Zitter, T., Dupré, S., Tryon, M., Cagatay, M. N., Mercier de Lépinay, B., Le Pichon, X., Sengor, A. M. C., Görur, N., Natalin, B., Uçarkus, G., Volker, D., Gasperini, L., Burnard, P., Bourlange, S., and the Marnaut Scientific Party, 2008. Gas emissions and active tectonics within the submerged section of the North Anatolian Fault zone in the Sea of Marmara, Earth and Planetary Science Letters 274, 34-39.

Géli, L., Henry, P., and Çagatay, N., 2010. Marmesonet Leg1 Cruise Report, November 4th – November 25th, 2009, http://www.esonet.marmara-dm.itu.edu.tr/ (12, 2010).

Görür, N., and Çağatay, M. N., 2010. Geohazards rooted from the northern margin of the Sea of Marmara since the late Pleistocene: a review of recent results, Natural Hazards, 54(2), 583-603.

Görür, N., and Okay, A. I., 1996. A fore-arc origin for the Thrace Basin, NW Turkey, Geol. Rundsch. 85, 662-668.

Gürbüz, C., Püskülcü, S., and Uçer, B., 1992. A study of crustal to the ruptures. structure in the Marmara region using earthquake data, Isikara, A.M., Honkura, Y. (Eds.), Multidisciplinary Research on Fault Activity in theWestern Part of the North Anatolian Fault Zone. KOERI, pp. 29-42.

Gürbüz, C., Aktar, M., Eyidogan, H., Cisternas, A., Haessler, H., Barka, A., Ergin, M., Türkelli, N., Polat, O., Üçer, S. B., Kuleli, S., Baris, S., Kaypak, B., Bekler, T., Zor, E., Bicmen, F., and Yoruk, A., 2000. The seismotectonics of the Marmara Region (Turkey): results from a micro-seismic experiment, Tectonophysics 316, 1-17.

Gürgey, K., Philp, R.P., Clayton, C., Emiroğlu, H., and Siyako, M., 2005. Geochemical and isotopic approach to maturity/source/mixing estimations for natural gas and associated condensates in the Thrace Basin, NW Turkey, Applied Geochemistry 20(11), 2017-2037.

Halbach, P., Holzbecher, E., Reichel, T., and Moche, R., 2004. Tectonically induced fluid migration of the sulphate-methane reaction zone in marine sediments of the Sea of Marmara-a case study, Chemical Geology 205(1-2), 73-82.

Henry, P., Lallemant, S., Nakamura, K., Tsunogai, U., Mazzotti, S., and Kobayashi, K., 2002. Surface expression of fluid venting at the toe of the Nankai Wedge and implications for flow paths, Marine Geology 187(1-2), 119-143.

Hensen, C., Zabel, M., Pfeifer, K., Schwenk, T., Kasten, S., Riedinger, N., Schulz, H. D., and Boetius, A., 2003. Control of sulfate pore-water profiles by sedimentary events and the significance of anaerobic oxidation of methane for the burial of sulfur in marine sediments, Geochim Cosmochim Acta 67:2631–2647, doi:10.1016/S0016-7037(03)00199-6.

Hergert, T. and Heidbach, O., 2010. Slip-rate variability and distributed deformation in the Marmara Sea fault system, Nature Geoscience 3, 132-135, doi: 10.1038/ngeo739.

Hirata, N., and Matsu'ura, M., 1987. Maximum-likelihood estimation of hypocenter with origin time eliminated using nonlinear inversion technique. Phys. Earth Planet. Inter. 47, 50– 61.

Hubert-Ferrari, A., Barka, A., Jacques, E., Nalbant, S. S., Meyer, B., Armijo, R., Tapponnier, P., and King, G. C. P., 2000. Seismic hazard in the Marmara Sea region following the 17 August 1999, Nature 404, 269-273, doi: 10.1038/35005054.

Ikeda, Y., Suzuki, Y., Herece, E., Şaroğlu, F., Isikara, A. M., and Honkura, Y., 1991. Geological evidence for the last two faulting events on the North Anatolian fault zone in the Mudurnu Valley, western Turkey, Tectonophysics 193, 335–345.

Imren, C., Le Pichon, X., Rangin, C., Demirbağ, E., B. Ecevitoğlu and Görür, N., 2001. the North Anatolian Fault within the Sea of Marmara: a new interpretation based on multichannel seismic and multi-beam bathymetry data, Earth Planet. Sci. Lett. 186,143-158.

Judd, A.G., and Hovland, M., 2007. Seabed Fluid Flow. Impact on Geology, Biology, and the Marine Environment, Cambridge University Press, Cambridge, 470pp.

Juniper, S. K., and Sibuet, M., 1987. Cold seep Benthic communities in Japan subduction zones-spatial-organization, trophic strategies and evidence for temporal evolution, Marine Ecology-Progress Series 40(1-2), 115-126.

Kalafat, D., C. Gürbüz and Üçer, B., 1987. Bati Türkiye'de kabuki ve Üst manto yapisinin arastilmasi, Deprem Arastirma Bülteni 14 (59), 43-64.

Karabulut, H., Bouin, M. P., Bouchon, M., Dietrich, M., Cornou, C., and Aktar, M., 2002. The Seismicity in the Eastern Marmara Sea after the 17 August 1999 Izmit Earthquake, Bull. Seism. Soc. Am. 92, 387-393.

Kastens, K., and Cita, M. B., 1981. Tsunami-induced sediment transport in the abyssal Mediterrranean Sea, Geological Society of America Bulletin 92, 845–857.

Kennett, B. L. N., Engdahl, E. R. and Buland, R., 1995. Constraints on seismic velocities in the Earth from traveltimes, Geophys. J. Int. 122, 108–124.

Ker, S., Le Gall, Y., Marsset, T., and Leon, P., 2008. SYSIF, a low frequency seismic profiler for near-bottom marine geophysics, 70th EAGE Conference & Exhibition, Rome.

Kopf, A. J., 2002. Significance of mud volcanism, Review of Geophysics 40 (2), 1-52.

Le Pichon, X., Kobayashi, K., Cadet, J. P., Ashi, J., Boulegue, J., Chamot-rooke, N., Fiala Medioni, A., Foucher, J. P., Furuta, T., Gamo, T., Henry, P., Iiyama, J. T., Lallemand, S. E., Lallemant, S. J., Ogawa, Y., Sakai, H., Segawa, J., Sibuet, M., Taira, A., Takeuchi, A., Tarits, P., and Toh, H., 1992. Fluid venting activity within the Eastern Nankai Trough Accretionary Wedge-a summary of the 1989 Kaiko-Nankai results, Earth Planet. Sci. Lett. 109 (3-4), 303-318.

Le Pichon, X., Sengor, A.M.C., Demirbag, E., Rangin, C., Imren, C., Armijo, R., Görür, N., Çagatay, N., Mercier de Lépinay, B., Meyer, B., Saatcilar, R., and Tok, B., 2001. The active main Marmara Fault, Earth Planet. Sci. Lett. 192, 595-616.

Le Pichon, X., Chamot-Rooke, N., Rangin, C., and Sengor, A. M. C., 2003. The North Anatolian Fault in the Sea of Marmara, J. Geophys. Res. 108(B4), 2179.

Lee, W. H. K. and J. C. Lahr, 1972. HYP071: A computer program for determining hypocenter, magnitude, and first motion pattern of local earthquakes, Open File Report, U. S. Geological Survey, 100 pp.

Lee , W. H., and S. W. Stewart, 1981. Principles and Applications of Micro-earthquake Network. Advances in Geophysics, Supplement 2, Academic Press, 293 p.

Lienert, B. R., Berg, E., and Frazer, L. N., 1986. Hypocenter: an earthquake location method using centered, scaled and adaptively damped least squares, Bull. Seism. Soc. Am. 76, 771-783.

Marsset, T., Marsset, B., Ker, S., Thomas, Y., and Le Gall, Y., 2010. High and very high resolution deep-towed seismic system: Performance and examples from deep water Geohazard studies, Deep-Sea Research I, doi:10.1016/j.dsr.2010.01.001.

Maury, T., Klingelhoefer, F., Pelleau, P., Géli, L., Sultan, N., and Voisset, M., 2009. Deployment of the LotOBS instrument / passive recording of micro-earthquakes, IFREMER, France.

Mazzini, A., Nermoen, A., Krotkiewski, M., Podladchikov, Y., Planke, S., and Svensen, H., 2009. Strike-slip faulting as a trigger mechanism for overpressure release through piercement structures. Implications for the Lusi mud volcano, Indonesia, Marine Petrol. Geol., 26, 1751-1765.

McHugh, C. M.G., Seeber, L., Cormier, M. H., Dutton, J., Cagatay, N., Polonia, A., Ryan, W. B. F., and Gorur, N., 2006. Submarine earthquake geology along the North Anatolia Fault in the Marmara Sea, Turkey: A model for transform basin sedimentation, Earth Planet. Sci. Lett. 248, 661-684, doi: 10.1016/j.epsl.2006.05.038.

McClusky, S., Balassanian, S., Barka, A., Demir, C., Ergintav, S., Georgiev, I., Gurkan, O., Hamburger, M., Hurst, K., Kahle, H., Kastens, K., Kekelidze, G., King, R., Kotzev, V., Lenk, O., Mahmoud, S., Mishin, A., Nadariya, M., Ouzounis, A., Paradissis, D., Peter, Y., Prilepin, M., Reilinger, R., Sanli, I., Seeger, H., Tealeb, A., Toksoz, M.N., and Veis, G., 2000. Global positioning system constraints on plate kinematics and dynamics in the Eastern Mediterranean and Caucasus, J. Geophys. Res. 105, 5695–5719.

Meade, B. J., Hager, B. H., McClusky, S. C., Reilinger, R., Ergintav, S., Lenk, O., Barka, A., and Ozener, H., 2002. Estimates of seismic potential in the Marmara Sea region from block models of secular deformation constrained by Global Positioning System measurements, Bull. Seismol. Soc. Am. 92, 208-215.

Moore, J. C., Orange, D., and Kulm, L. D., 1990. Interrelationship of fluid venting and structural evolution-alvin observations from the Frontal Accretionary Prism, Oregon, J. Geophys. Res. 95(B6), 8795-8808.

Okay, A. I., Satir, M., Maluski, H., Siyako, M., Monie, P., Metzger, R., and Akyuz, S., 1996. Paleo- and Neo-Tethyan events in northwest Turkey Geological and geochronological constraints, in Tectonic Evolution of Asia, edited by A. Yin and M. Harrison, pp 420-441, Cambridge Univ. Press, New York.

Okay A. I., and Tüysüz, O., 1999. Tethyan sutures of northern Turkey, Geological Society, London, Special Publications, v. 156, p. 475-515, doi:10.1144/GSL.SP.1999.156.01.22.

Okay, A.I., Kaşhlar-Ozcan, A., Imren, C., Boztepe-Güney, A., Demirbağ , E., and Kuşçu, I., 2000. Active faults and evolving strike-slip basins in the Sea of Marmara, northwest Turkey: a multichannel seismic reflection study, Tectonophysics 321, 189-218.

Örgülü, G., and Aktar, M., 2001. Regional Moment Tensor Inversion for Strong Aftershocks of the August 17, 1999 Izmit Earthquake (Mw =7.4), Geophys. Res. Lett. 28, 371-374.

Oth, A., Böse, M., Wenzel, F., Köhler, N., and Erdik, M., 2010. Evaluation and optimization of seismic networks and algorithms for earthquake early warning – the case of Istanbul (Turkey), J. Geophys. Res., 115, B10311, doi:10.1029/2010JB007447.

Özalaybey, S., Ergin, M., Aktar, M., Tapırdamaz, C., Biçmen, F., and Yörük, A., 2002. The 1999 I˙zmit Earthquake Sequence in Turkey: Seismological and Tectonic Aspects, Bull. Seismol. Soc. Am. 92, 376-386.

Papatheodorou, G., Hasiotis, T., and Ferentinos, G., 1993. Gas charged sediments in the Aegean and Ionian Seas, Greece, Marine Geology 112 (1-4), 171-184.

Parsons, T., 2004. Recalculated probability of M 7 earthquakes beneath the Sea of Marmara, Turkey, J. Geophys. Res. 109, B05304, doi:10.1029/2003JB002667.

Parsons, T., Toda, S., Stein, R. S., Barka, A., and Dieterich, J. H., 2000. Heightened odds of large earthquakes near Istanbul: An interaction-based probability calculation, Science 288, 661-665.

Paull, C. K., Hecker, B., Commeau, R., Freemanlynde, R. P., Neumann, C., Corso, W. P., Golubic, S., Hook, J.E., Sikes, E., and Curray, J., 1984. Biological communities at the Florida Escarpment Resemble Hydrothermal Vent, Taxa, Science 226 (4677), 965–967.

Perincek, D., 1991. Possible strand of the North Anatolian Fault in the Thrace Basin, Turkey – An interpretation, AAPG Bulletin 75, 241-257.

Phelion, O., and Tonck, O., 2009. SUBOP V2, Logiciel d'acquisition des données de sondeur de sédiments – Manuel Utilisateur, IPSIS report, ref : SV2-MU-1.03.

Pickering, K.T., and Hiscott, R.N., 1985. Contained (reflected) turbidity currents in the Middle Ordovician Cloridorme Formation, Québec, Canada: an alternative to the antidune hypothesis, Sedimentology 32, 373–394.

Podvin, P., and Lecomte, I., 1991. Finite difference computation of traveltimes in very contrasted velocity model : a massively parallel approach and its associated tools, Geophys. J. Int. 105, 271-284.

Pondard, N., 2006. The Sea of Marmara pull-apart (North Anatolian Fault): morphologic and tectonic evolution, fault interactions, and seismic hazard in the region of Istanbul, PhD thesis at IPGP.

Pondard, N., Armijo, R., King, G. C. P., Meyer, B., and Flerit, F., 2007. Fault interactions in the Sea of Marmara pull-apart (North Anatolian Fault): earthquake clustering and propagating earthquakes sequences, Geophys. J. Int. 171, 1185-1197.

Rangin, C., Demirbağ, E., Imren, C., Crusson, A., Normand, A., E. Le Drezen and Le Bot, A., 2001. Marine Atlas of the Sea of Marmara (Turkey), IFREMER, France.

Rangin, C., Le Pichon, X., Demirbag, E., and Imren, C., 2004. Strain localization in the Sea of Marmara: propagation of the North Anatolian Fault in a now inactive pull-apart, Tectonics 23, TC2014.

Reilinger, R., Ergintav, S., Bürgmann, R., McClusky, S., Lenk, O., Barka, A., Gurkan, O., Hearn, E. H., Feigl, K. L., Cakmak, R., Aktug, B., Özener, H., and Toksöz, M. N., 2000. Coseismic and postseismic fault slip for the 17 August 1999 M = 7.5, Izmit, Turkey earthquake, Science 289, 1519-1524.

Reilinger, R., McClusky, S., Vernant, P., Lawrence, S., Ergintav, S., Cakmak, R., Ozener, H., Kadirov, F., Guliev, I., Stepanyan, R., Nadariya, M., Hahubia, G., Mahmoud, S., Sakr, K., ArRajehi, A., Paradissis, D., Al-Aydrus, A., Prilepin, M., Guseva, T., Evren, E., Dmitrotsa, A., Filikov, S. V., Gomez, F., Al-Ghazzi, R., and Karam, G., 2006. GPS constraints on continental deformation in the Africa-Arabia, Eurasia continental collision zone and implications for the dynamics of plate interactions, J. Geophys. Res., 111, doi:10.1029/2005JB004051.

Sari, E., and Çagatay M. N., 2006. Turbidites and their association with past earthquakes in the deep Cinarcik Basin of the Marmara Sea, Geo-marine Letters 26, 69-76.

Sato, T., Kasahara, J., Taymaz, T., Ito, M., Kamimura, A., Hayakawa, T., and O. Tan, 2004. A study of microearthquake seismicity and focal mechanisms within the Sea of Marmara (NW Turkey) using ocean bottom seismometers (OBSs), Tectonophysics 391, 303-314.

Schweitzer, J., 2001. HYPOSAT – an enhanced routine to locate seismic events, Pure and Applied Geophysics 158, 277-289.

Sen, S., and Yillar, S., 2009. The Korudag anticlinorium in the south Thrace Basin, northwest Turkey: A super giant petroleum trap complex?, AAPG Bulletin 93, 357-377.

Şengör, A. M. C., 1979. The North Anatolian transform fault, its age, offset, and tectonic significance, J. Geol. Soc. London 136, 269-282.

Şengör, A. M. C., and Yilmaz, Y., 1981. Tethyan evolution of Turkey: a plate tectonic approach, Tectonophysics 75, 181-241.

Şengör, A. M. C., Tüysüz, O., Imren C, Sakinç, M., Eyidoğan, H., Görür, N., Le Pichon, X., and Rangin, C., 2004. The North Anatolian Fault: a new look, Annu. Rev. Earth Planet. Sci. 33, 1–75.

Stein, R. S., Barka, A., and Dietrich, J., 1997. Progressive earthquake failure on the North Anatolian fault since 1939 by stress triggering, Geophys. J. Int., 128, 594– 604.

Straub, C., Kahle, H. G., and Schindler, C., 1997. GPS and geologic estimates of the tectonic activity in the Marmara Sea region, NW Anatolia, J. Geophys. Res. 102, B12, 27587-27601.

Sultan, N., Riboulot, V., Lanfumey, V., Ker, S., Marsset, B., Géli, L., Tary, J.-B., Klingelhoefer, F., Voisset, M., Colliat, J.L., Adamy, J., and Grimaud, S., 2011. Dynamics of fault-fluid-hydrate system around a shale-cored anticline in deepwater Nigeria, J. Geophys. Res., submitted (January 2011).

Tarantola, A., and Valette, B., 1982. Inverse problems = quest for information, J. Geophys. Res. 50, 159-170.

Tary, J. B., "Tests oedomètriques sur les carottes MET09GR010 et MET09K02 de Marmesonet", Rapport Interne Ifremer, February, 2010

Toksöz, M. N., A. F. Shakal and Michael, A. J., 1979. Space-time migration of earthquakes along the North Anatolian fault zone and seismic gaps, Pageoph. 117, 1258-1270.

Tryon, M. D., Brown, K. M., Torres, M. E., Trehu, A. M., McManus, J., and Collier, R. W., 1999. Measurements of transience and downward fluid flow near episodic methane gas vents, Hydrate Ridge, Cascadia, Geology 27(12), 1075-1078.

Wong, H. K., Ludmann, T., Uluğ, A., Görür, N., 1995. The Sea of Marmara, a plate boundary sea in escape tectonic regime, Tectonophysics 244, 231-250.

Yaltirak, C., 2002. Tectonic evolution of the Marmara Sea and its surroundings, Marine Geology 190, 493-529.

Zattin, M., Okay, A. I., Cavazza, W., 2005. Fission-track evidence for late Oligocene and mid-Miocene activity along the North Anatolian Fault in south-western Thrace, Terra Nova 17, 95-101.

Zitter, T. A. C., Henry, P., Aloisi, G., Delaygue, G., Çagatay, M. N., Mercier de Lepinay, B., Al-Samir, M., Fornacciari, F., Tesmer, M., Pekdeger, A.,Wallmann, K., and Lericolais, G., 2008. Cold seeps along the main Marmara Fault in the Sea of Marmara (Turkey). Deep Sea Research Part I: Oceanographic Research Papers 55, 552–570.

Appendices

Appendix A. Dynamics of fault-fluid-hydrate system around a shale-cored anticline in deepwater Nigeria

Sultan, N., Riboulot, V., Lanfumey, V., Ker, S., Marsset, B., Géli, L., Tary, J.-B., Klingelhoefer, F., Voisset, M., Colliat, J.L., Adamy, J., and Grimaud, S.

Accepted by the Journal of Geophysical Research.

Dynamics of fault-fluid-hydrate system around a shale-cored anticline in deepwater Nigeria

Nabil Sultan,[1] Vincent Riboulot,[1] Valentine Lanfumey,[1] Stephan Ker,[1] Bruno Marsset,[1] Louis Géli,[1] Jean-Baptiste Tary,[1] Frauke Klingelhoefer,[1] Michel Voisset,[1] Jean-Louis Colliat,[2] Jérome Adamy,[3] and Sylvie Grimaud[2]

Abstract

Gas hydrates were recovered by coring at the eastern border of a shale-cored anticline in the eastern Niger delta. To characterize the link between faults and fluid release and to identify the role of fluid flow in the gas hydrate dynamics, three piezometers were deployed between 387 and 435 days: two of them were deployed within a major fault linked to a shallow hydrocarbon reservoir while the third monitored the fluid pressure from a pockmark aligned above the same major fault. In addition, 10 long recording ocean-bottom seismometers (OBS) were deployed for duration of 2 months. While ocean-bottom seismometers indicate episodic events of fluid release, the two piezometers deployed within the fault, detected simultaneously, an important fluid flow event with duration of around 90 days. By combining and analyzing existing and newly acquired data, it was shown that the studied fluid-fault system operates according to the following three stages: i) slow upward pore fluid migration through existing conduits (mainly the major fault) and free gas accumulation and circulation within several shallow sandy layers intersecting the major fault, ii) pore pressure increases within the sandy-silty layer as evidenced by the data recorded by one piezometer. The free-gas accumulation at these sandy layers was indirectly detected by the amplification of the effect of the tidal cycles on the recorded pore pressure fluctuations and iii) hydro-fracturing and fluid pressure dissipation through sporadic degassing events, eventually causing an interstitial water circulation through the shallow sandy layers and drawing overlying seawater into the sediment.

[1] Ifremer, Département Géosciences Marines, BP 70, 29280 Plouzané, France

[2] Total, 64018 PAU Cedex, France

[3] Total, 92078 Paris La Défense Cedex, France

1. Introduction

Fault-fluid-hydrate systems are presently relatively poorly understood and may present hazards for deep water developments. To date deep water operators have avoided gas hydrate prone areas for development, particularly where they are believed to be underlain by free gas. However, it is clear, that this cautionary approach cannot be applied for all considered sites. It is today essential to evaluate the impact of the fluid circulation and gas hydrates occurrence on the seabed structures using "integrated approaches", during the whole lifetime of an oil field. The Niger delta, is an area in which oil industry activities are highly developed and many seep-related seabed features have been found in the last years in particular during exploration mapping at water depths between 500 and 1500 m [*Hovland and Gallagher*, 1997; *Brooks et al.*, 2000; *Georges and Cauquil*, 2007; *Sultan et al.*, 2010]. Various studies from the Nigerian continental slope have shown different seafloor sedimentary features such as pockmarks, slides and carbonate build-ups associated with fluid flow and gas hydrates [*Damuth*, 1994; *Cohen and McClay*, 1996; *Brooks et al*, 2000; *Haskell et al.*, 1999; *Hovland and Gallagher*, 1997; *Deptuck et al.*, 2003; *Bayon et al.*, 2007; *Georges and Cauquil*, 2007; *Sultan et al.*, 2007 amongst others]. These observations make the Niger delta a prime interest target to study the active interplay of fluid flow processes, gas hydrate dynamics and seafloor deformation.

In this work, the study area is located in the eastern Niger delta. Due to the temperature and pressure conditions of the study site and the geophysical evidence of free gas infiltration through fault networks to the shallow subsurface, gas hydrates were considered as a major hazard source. The understanding of the fault-fluid-hydrate system required the use of an integrated approach going from the detection and quantification of the gas hydrate to the monitoring of the fluid system that controls the gas hydrates stability. Within the context of hazard assessment associated to the occurrence of free-gas and gas hydrates in the study area and in order to evaluate the impact of the fault-fluid-hydrate systems on the seabed engineering structures, the main questions investigated in the present work are: (a) the evaluation of the dynamics (active or not) of the fault-fluid-hydrate system and (b) the determination of the link between fault activities, free gas release and hydrate accumulation.

2. Geological setting

The Niger Delta margin is undergoing deformation by gravity driven tectonism due to the presence of a mobile substratum at the base of the sediment fill [*Bilotti and Shaw*, 2005; *Corredor et al.*, 2005; *Damuth*, 1994]. This substratum is formed by Early Tertiary overpressured shale. The mobile shale has been deformed since the Oligocene, forming the major structures of the Niger Delta [*Wiener et al*., 2006]. The offshore part of the Niger Delta can be divided into several structural zones (Figure 1). The continental shelf is characterized by an extensional zone [*Damuth*, 1994], dominated by listric normal faults (synthetic and antithetic) with extensive growth [*Morley and Guerin*, 1996]. The upper and middle parts of the slope are characterized by a translational zone [*Damuth*, 1994] dominated by folding and faulting in response to rapid sedimentation rates and shale remobilization [*Doust and Omatsola*, 1990; *Morley and Guerin*, 1996]. As the thick stratigraphic column moved down-slope [*Morley and Guerin*, 1996], the lower slope is characterized by a compressional zone [*Damuth*, 1994] dominated by a series of linear toe-thrusts forming a fold-and-thrust belt. The study site (called USAN) is located in the North-Eastern Gulf of Guinea on the continental slope of the modern Niger delta. The site is about 100 km offshore on the eastern Niger Delta

margin coastline at water depths ranging from 700 to 800 meters (Figure 1-A). The investigated area is located to the North-East of a shale-cored anticline with relief of 48 m (Figure 1-B) and is characterized by the presence of (see Figure 2) (1) seafloor undulations around the central anticline, (2) a series of fault scarps to the north and the south of the anticline, (3) a bottom simulating reflector (BSR), and (4) numerous pockmarks and irregular depressions on the north and south sides of the anticline (Figure 1-C).

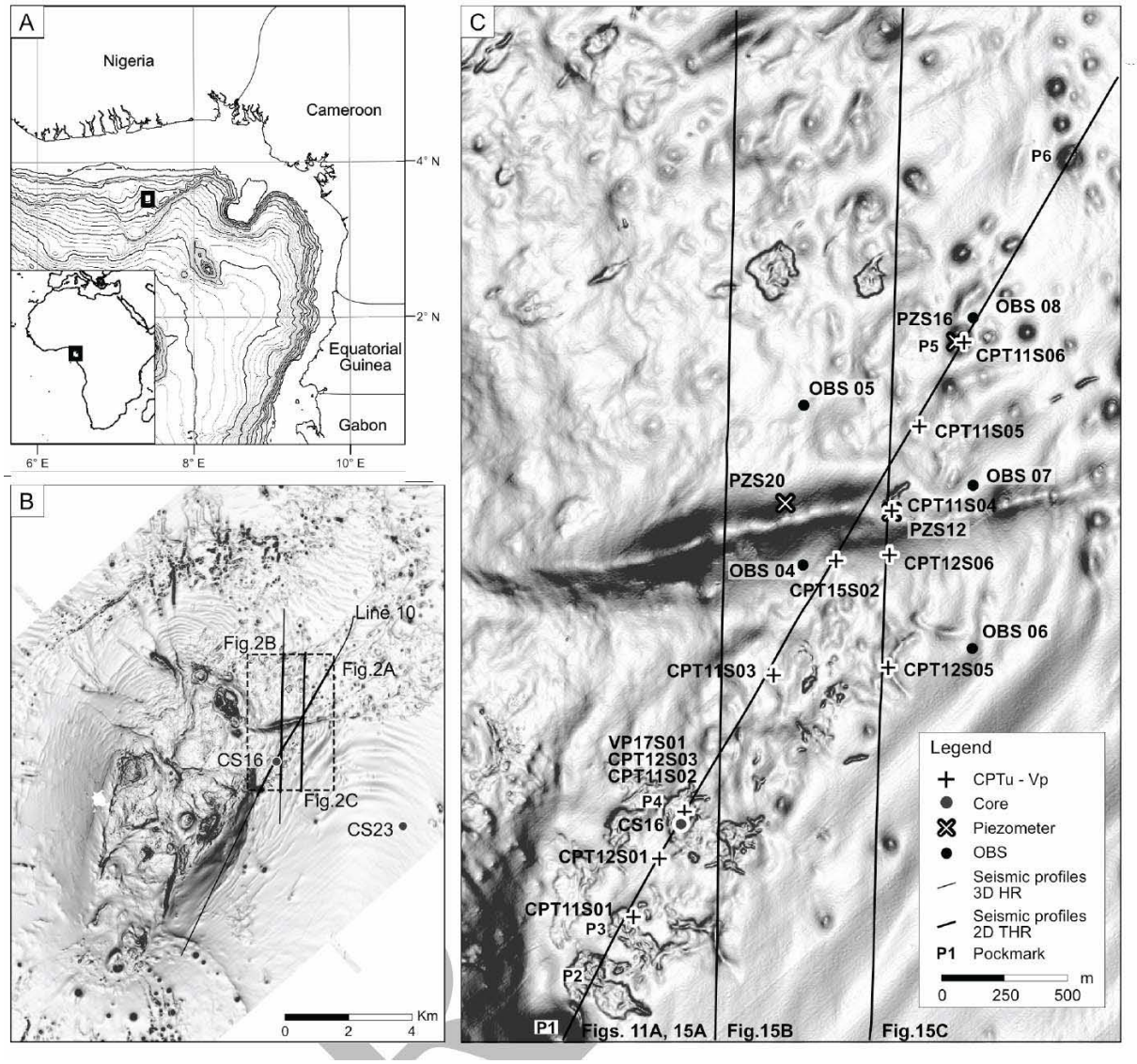

Figure 1. Location maps, A- Gulf of Guinea general bathymetry map and location of the study area 'USAN' on the Niger Delta deep province (bathymetric contours spacing is 100 m). B- Dip map of the study area (Horizontal resolution of this AUV map is 3 m). C- Zoom on the main irregular pockmarks and on the major normal structural fault (see location in figure 1B).

3. Tools and methods

Geotechnical, geophysical and geological data used in this work were acquired within the framework of a joint R&D project [ERIG3D] between Ifremer and TOTAL in 2008.

3.1 Coring and geotechnical tools

Sediment samples (Table 1) were collected in the study area using piston corers. In order to identify the key mechanical and physical parameters of the sediments, an onboard experimental program on undisturbed marine sediment samples has been undertaken. Log sediment cores using the GEOTEK core logging devices (MSCL) was first carried out. Detailed onboard laboratory geotechnical investigations also included classification tests, strength tests and P wave velocity measurements using laboratory celerimeter.

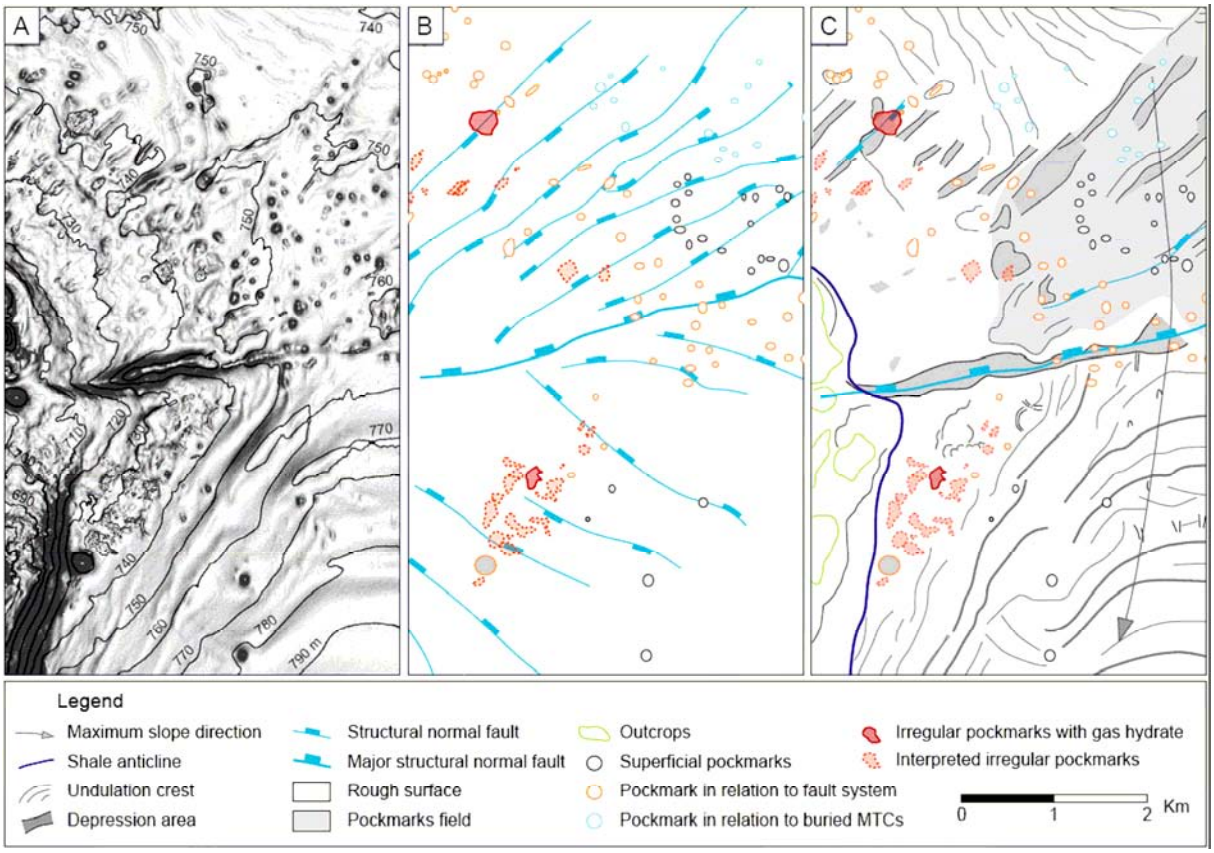

Figure 2. Seafloor and subseafloor characterization. A. Dip map (10 m spaced bathymetric lines), B. Structural map showing normal fault system due to growth fold and the actual seafloor fluid seepage, C. Seismic geomorphologic map.

#	TOOL	CORE LENGTH [m]	BATHY [m]	[DD/MM/YY]	OBSERVATION
CS16	Calypso	14	731	16/05/2008	Hydrates at the base
CS23	Calypso	23.28	786	27/05/2008	Silty layer at around 16 m

Table 1. Calypso cores characteristics.

In situ geotechnical measurements (Table 2) were carried out using the Ifremer CPTu piezocone (PENFELD). It is equipped with a rod which penetrates the sediment to a maximum depth of 30 meters [for more details see *Sultan et al.*, 2010]. The Ifremer piezometer was also used to measure the *in situ* pore pressure (Table 3) during the ERIG3D cruise. It is a free-fall device with a sediment-piercing lance attached to a recoverable instrument part [*Sultan et al.*, 2010]. A total of 3 long-term piezometers measurements were carried out (PZS12, PZS16 and PZS20 - Figure 1) at three different locations surrounding the major eastern fault.

#	TOOL	DEPTH [mbsf]	Water depth [m]	DEPLOYED [DD/MM/YY]	OBSERVATION
CPT11S01	CPTu	12.06	732	16/05/2008	Early refusal
CPT11S02	CPTu	20.36	730	16/05/2008	Early refusal
CPT11S03	CPTu	15.06	734	16/05/2008	Early refusal
CPT11S04	CPTu	26.68	749	16/05/2008	Early refusal
CPT11S05	CPTu	26.4	749	16/05/2008	Early refusal
CPT11S06	CPTu	30	751	16/05/2008	Ok – 30 m
CPT12S01	CPTu	9.74	731	18/05/2008	Early refusal
CPT12S03	CPTu	19.9	733	18/05/2008	Early refusal
CPT12S05	CPTu	30	736	18/05/2008	Ok – 30 m
CPT12S06	CPTu	19.46	738	18/05/2008	Early refusal
CPT15S02	CPTu	18.04	733	23/05/2008	Early refusal

Table 2. CPTUs characteristics.

3.2 Seismic data

The high resolution 3D seismic data used in this study was provided by TOTAL. The 3D seismic volume was short-offset processed and pre-stack time migrated. This processing technique is used to reprocess volumes of 3D seismic data normally acquired for conventional seismic exploration purposes and is designed for maximum preservation of the integrity of the shallow seismic data for precise three-dimensional imaging. The inline spacing of the traces is 6.25 m, and the crossline spacing is 12.5 m. The dominant frequency is 70 Hz in the upper 100 ms, giving a vertical resolution of ~10.5 m (using a velocity of 1500 m/s). The shallow part of the 3D seismic data was re-processed using DeltaStack 3D, an automatic 3D high-resolution velocity picking tool developed by TOTAL [*Arnaud et al.*, 2004; *Cauquil et al.*, 2005] to obtain a high resolution interval velocity field from 3D seismic data. During the NERIS [*Sultan et al.*, 2007] project, it was demonstrated that the interval velocity field obtained using DeltaStack 3D is a valuable tool to identify high amplitude P wave velocity regions associated with the presence of gas hydrates and/or carbonate concretions and low P wave regions associated with the presence of free gas. Thanks to the high quality 3D seismic data available in the studied area, it was possible to process these data in order to provide interval velocity using DeltaStack 3D.

Complementary, high resolution deep-tow seismic data were acquired during the ERIG3D cruise using the recently developed SYSIF deep towed acquisition system [*Marsset et al.*, 2010]. SYSIF is a deep-towed instrument hosting low frequency acoustic transducers (250-1000 Hz, 650-2000 Hz) and a single channel streamer in order to provide High Resolution (HR) images of the sub-bottom. The altitude of SYSIF over the sea floor is about 100 meters

thus reducing the Fresnel zone, i.e. enhancing the lateral resolution compared to conventional surface towed systems.

#	DURATION	Water depth [m]	DEPLOYED [DD/MM/YY]	SENSORS @ [mbsf]
PZS12	435 days	746	19/05/2008	P1-0.83
				P2-3.88
				P3-6.93
				P4-9.98
				P5-11.48
PZS16	387 days	750	22/05/2008	P1-0.83
				P2-2.38
				P3-3.93
				P4-4.73
				P5-5.53
PZS20	393 days	744	26/05/2008	P1-0.83
				P2-3.88
				P3-5.43
				P4-6.98
				P5-7.78

Table 3. Piezometers characteristics.

4. Results

4.1. *In situ* piezocone measurements

The CPTu (cone penetration test with pore pressure measurements) sites were chosen based on the analysis of the bathymetry and the 2D and 3D seismic profiles. Five CPTu measurements (Figure 1 - from south to north: CPT11S01, CPT12S01, CPT11S02, CPT12S03, CPT11S03) were carried out above a shallow horizontal reflector identified in the seismic profile SY08THR-Pr05 and interpreted as an indicator of the presence of gas hydrates. Figure 3-a, b, d, e and f show the corrected cone resistance (qt) versus depth curves obtained from sites CPT11S01, CPT12S01, CPT11S02, CPT12S03 and CPT11S03. The five CPTu profiles have shown the presence of several stronger layers with early refusal. In addition to the high tip resistance, the 5 CPTus have shown locally changes of the excess pore pressure Δu_2 with depth (Figure 4-a, b, d, e and f). Low Δu_2 values with high corrected cone resistance are usually interpreted as an indicator of the presence of silty-sandy layers [e.g. *Lunne et al.*, 1997]. Figure 3-c shows the mass density versus depth curve obtained from core CS16. Gas hydrates were recovered from this core underneath 4 m below the seafloor (mbsf). The large decrease of the mass density at around 4 m from the top corresponds to the presence of the gas hydrates and to the free gas exsolution which occurred during core retrieval.

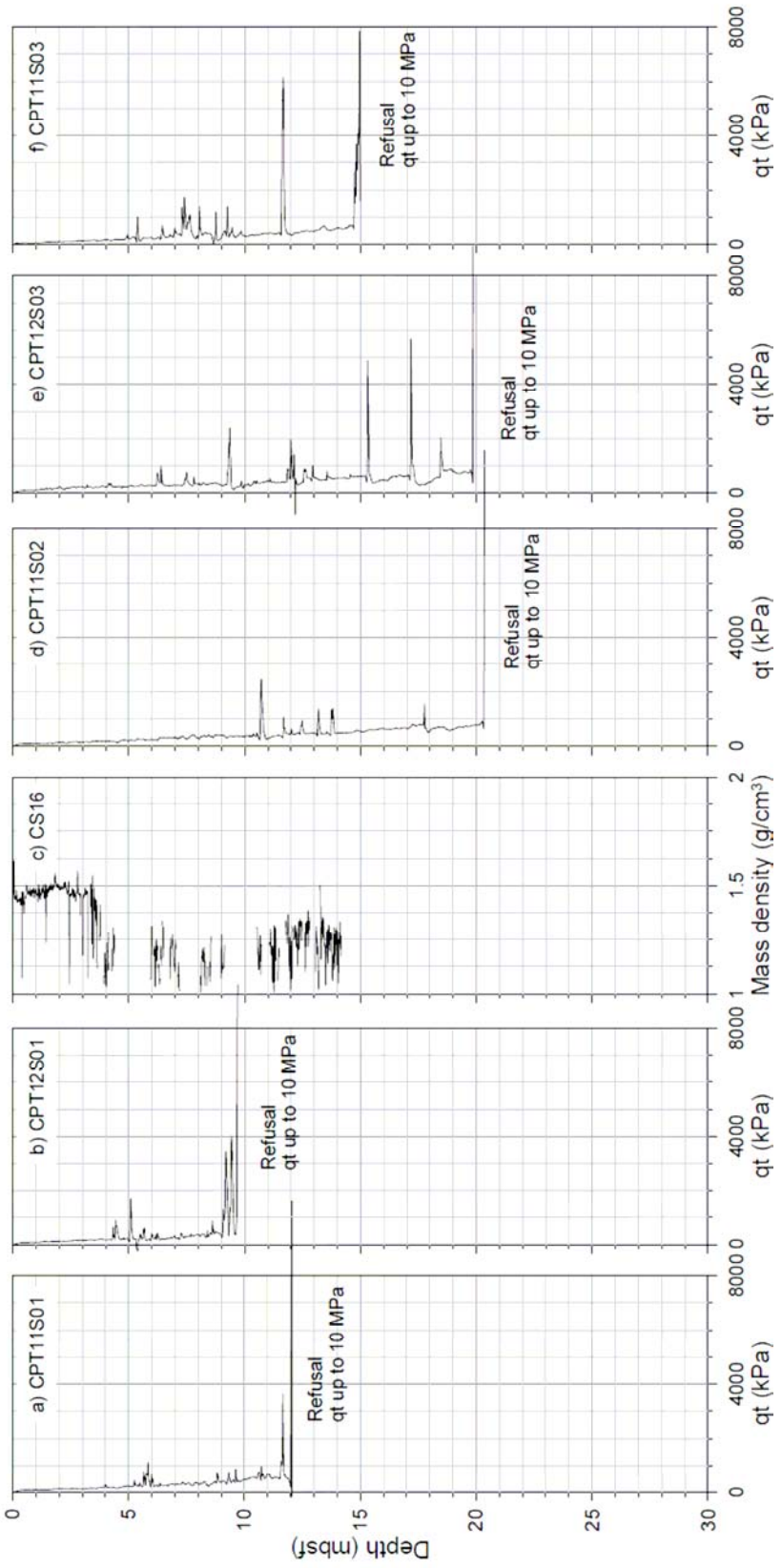

Figure 3. Corrected cone resistance qt versus depth from sites a) CPT11S01, b) CPT12S01, d) CPT11S02, e) CPT12S03 and f) CPT11S03. Mass density values versus depth from core CS16 are presented in (c).

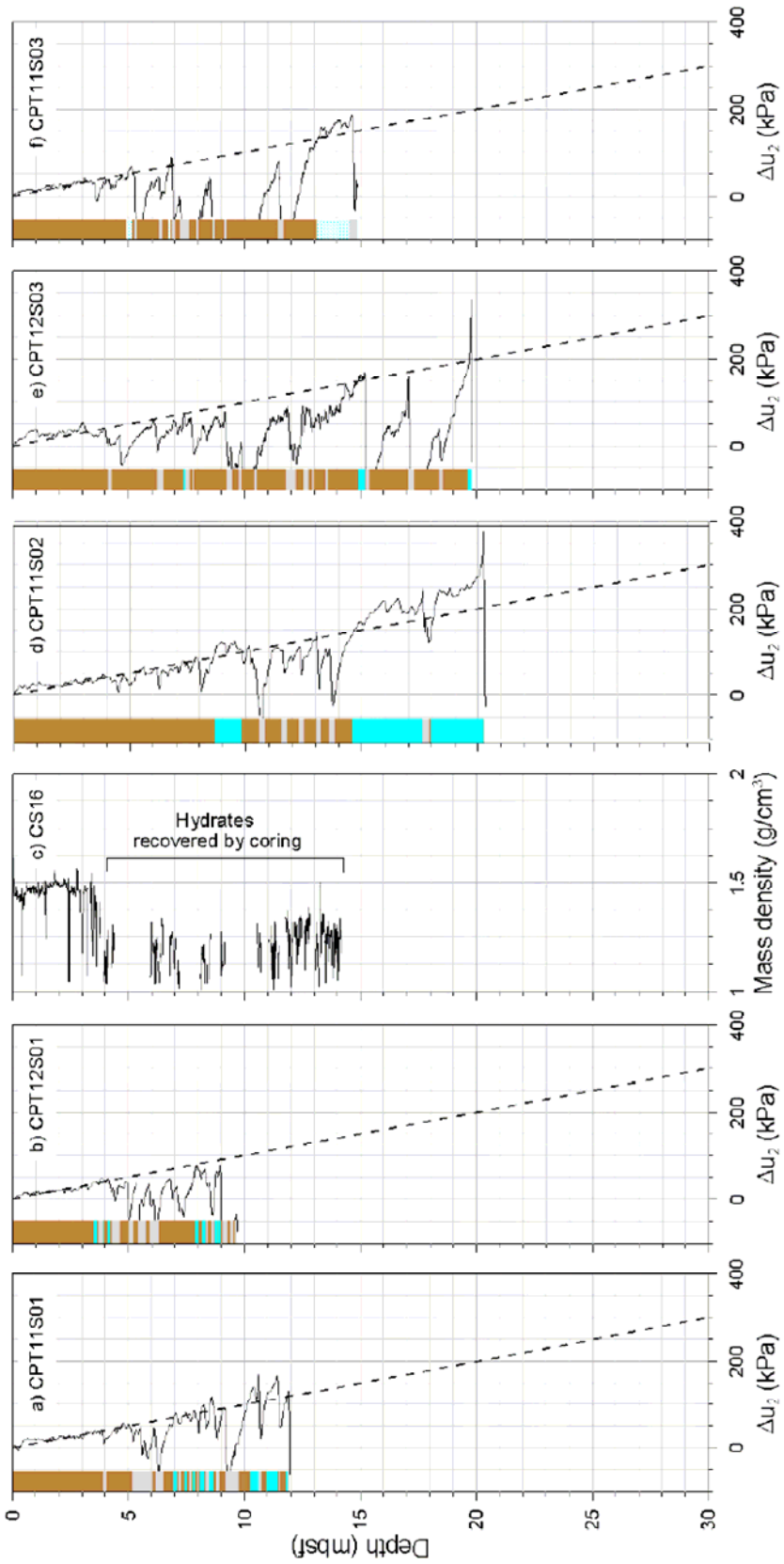

Figure 4. Excess pore pressure Δu_2 versus depth from sites a) CPT11S01, b) CPT12S01, d) CPT11S02, e) CPT12S03 and f) CPT11S03. Grey dashed areas correspond to suspected silty-sandy layers, blue dashed ones to gas hydrates and light blue ones to free gas. Mass density values versus depth from core CS16 are presented in (c).

Four CPTu measurements were carried out within and surrounding the major eastern fault in order to characterize the lateral variability of the sediments (lithology, presence of free gas and gas hydrates) and its mechanical behavior (for location see Figure 1 - from south to north: CPT12S05, CPT15S02, CPT12S06 and CPT11S04). CPT12-S05 shows the presence of relatively stronger layer at around 2 mbsf with a normal linear increase of the qt with depth (Figure 5-a). CPT15S02, CPT1206 and CPT11S04 all indicate the presence of several stronger layers and an early refusal (Figure 5-b, c and d). Several stronger layers detected in the last four CPTu measurements were accompanied by low Δu_2 values indicating the presence of sandy-silty layers (Figure 6).

Two CPTu measurements (CPT11S05 and CPT11S06) were carried out within two pockmarks above the major eastern fault (for location see Figure 1). From the 3D seismic data those two pockmarks seem linked directly to the deep reservoir. The main aim of those two last CPTu measurements was to characterize a chaotic facies observed to north-east of the seismic profile SY08THR-Pr05 (for location, see Figure 1).

Figure 5-e and Figure 5-f show the corrected cone resistance versus depth curves of CPT11S05 and CPT11S06. Both CPTUs (CPT11S05 and CPT11S06) indicate the presence of several stronger layers characterized by high tip resistance, high friction and low excess pore pressure indicating the presence of sandy silty layers (Figure 6-e and Figure 6-f). The detection of the gas hydrates and free gas based on the CPTu data and coring will be discussed later in the paper.

Figure 7 compares the corrected cone resistance versus depth from two different sites in the south (CPT12S06) and in the central part (CPT11S04) of the major eastern fault. The qt values between the seabed and 9.5 mbsf fit well between the two sites. The sandy silty layers seem distributed at different depths between the CPT12S06 and CPT11S04 which are probably the result of the fault movements (Figure 7). Another interesting observation from Figure 7 is the reduced qt values (around 50%) between 10 and 16 mbsf for CPT12S06 with respect to CPT11S04. This rapid decrease of qt values could be an indication of the presence of weak or fractured zones at CPT12S06. This weak zone can be the result of shearing or high fluid activity and hydro-fracturing processes near the fault zone.

4.2. *In situ* pore pressure monitoring

Three piezometers were deployed during approximately one year in the Eastern Usan site (Table 3 and Figure 1). Two of the piezometers (PZS12 and PZS20) were deployed within a major fault linked to a shallow hydrocarbon reservoir while the third (PZS16) monitored the fluid pressure from a pockmark aligned above the same major fault.
In Figure 6-d, the five pressure sensor locations of PZS12 are projected on the CPTu data from site CPT11S04. The upper four sensors of PZS12 are positioned in clayey sediments while the fifth one is just above a sandy-silty layer which is characterized by high tip resistance and almost zero Δu_2. The five pressure sensor locations of PZS16 are (according to the CPT11S06 data) positioned in clayey sediments but above an area which is suspected to contain free gas and/or gas hydrates (Figure 6-f). The presence of free gas/ and or gas hydrates induces an increase of Δu_2 during the CPTu rod penetration. Figure 8 to Figure 10 show for the three piezometers PZS12, PZS16 and PZS20 the excess pore water pressure (a) and the temperature (b) versus time.

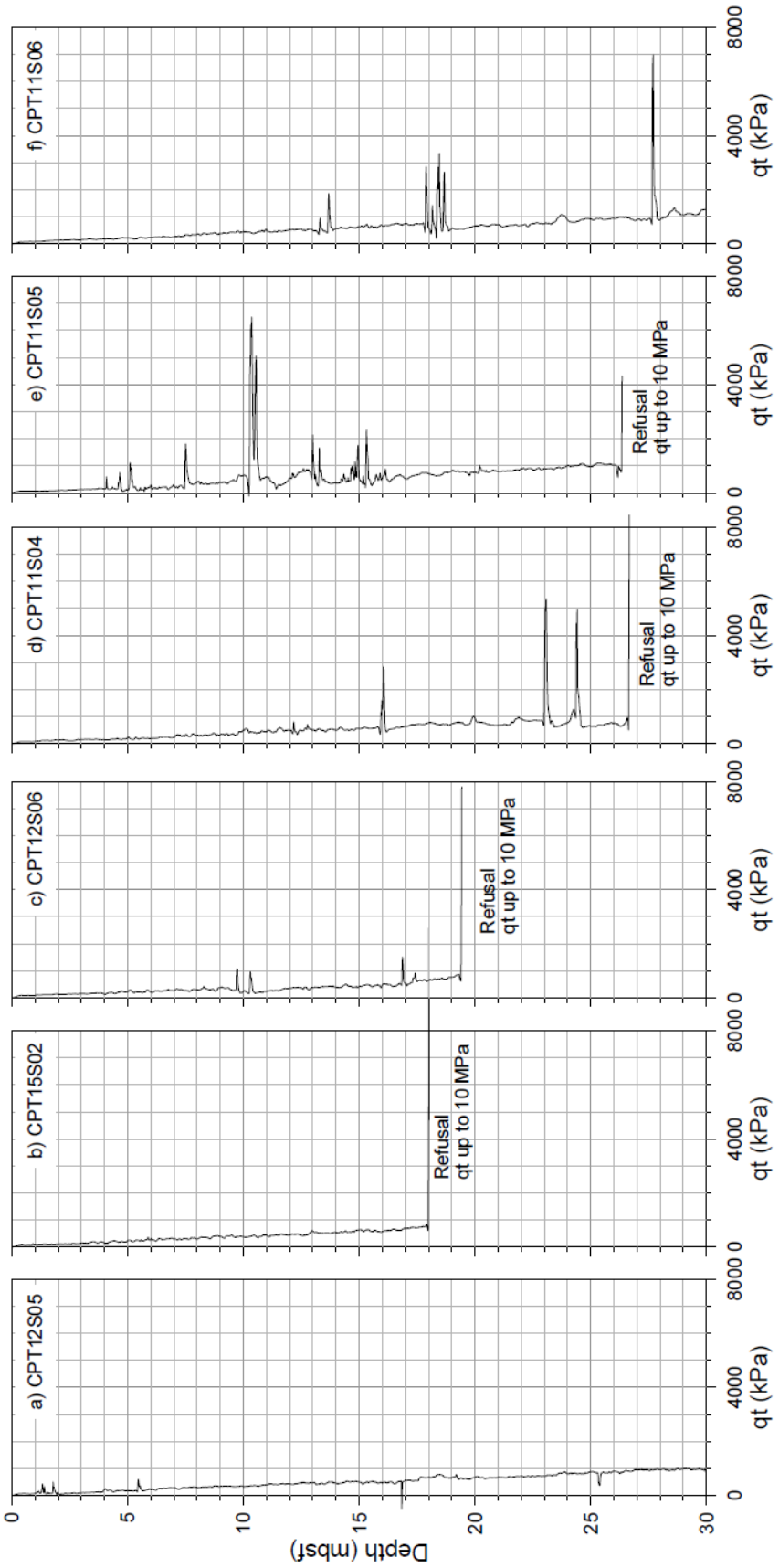

Figure 5. Corrected cone resistance qt versus depth from sites a) CPT12S05, b) CPT15S02, c) CPT12S06, d) CPT11S04, e) CPT11S05 and f) CPT11S06.

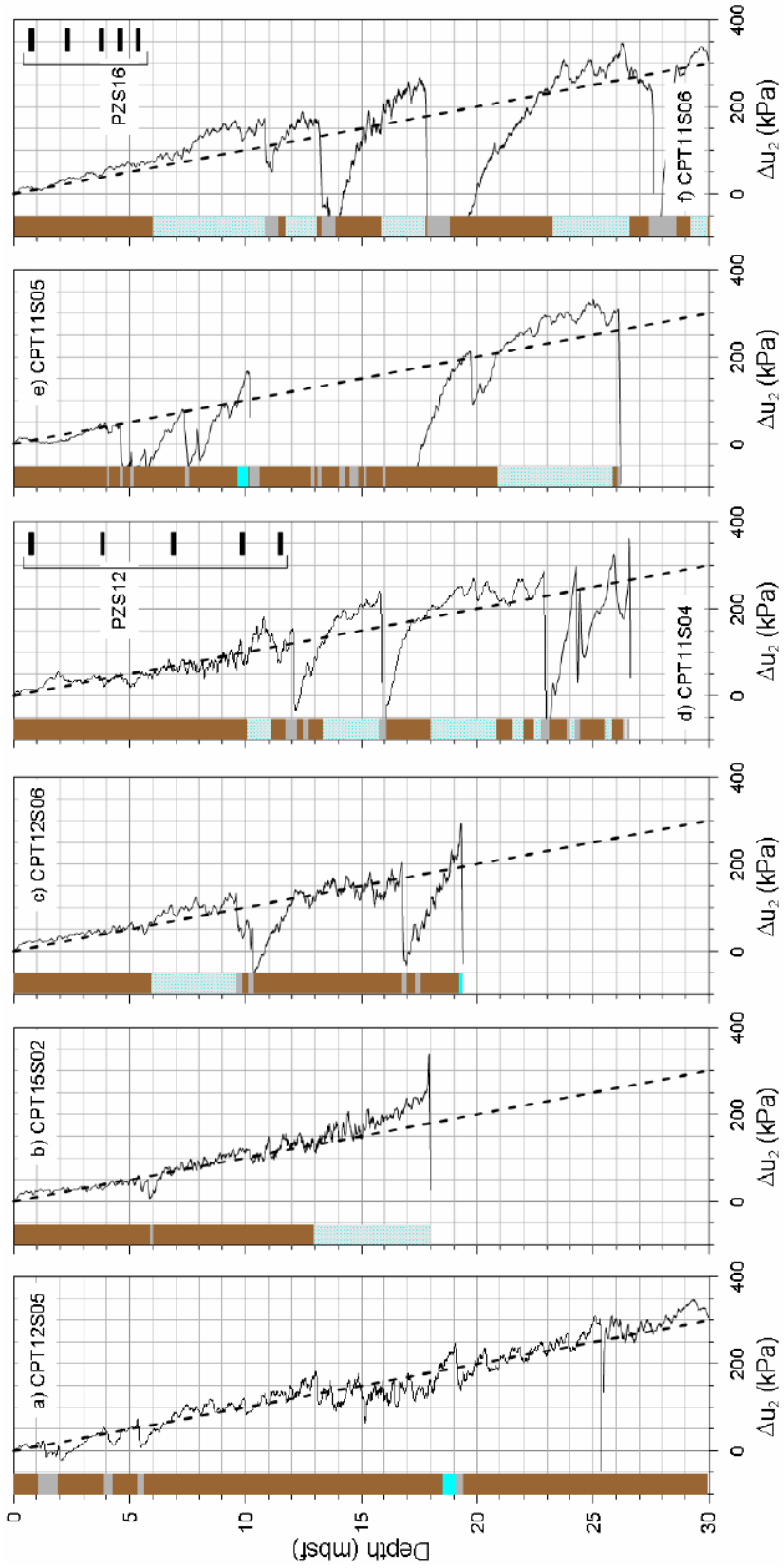

Figure 6. Δu_2 versus depth from sites a) CPT12S05, b) CPT15S02, c) CPT12S06, d) CPT11S04, e) CPT11S05 and f) CPT11S06. Grey dashed areas correspond to suspected silty-sandy layers, blue dashed ones to gas hydrates and light blue ones to free gas. Depth position of the PZS12 and PZS16 sensors are respectively shown in (d) and (f).

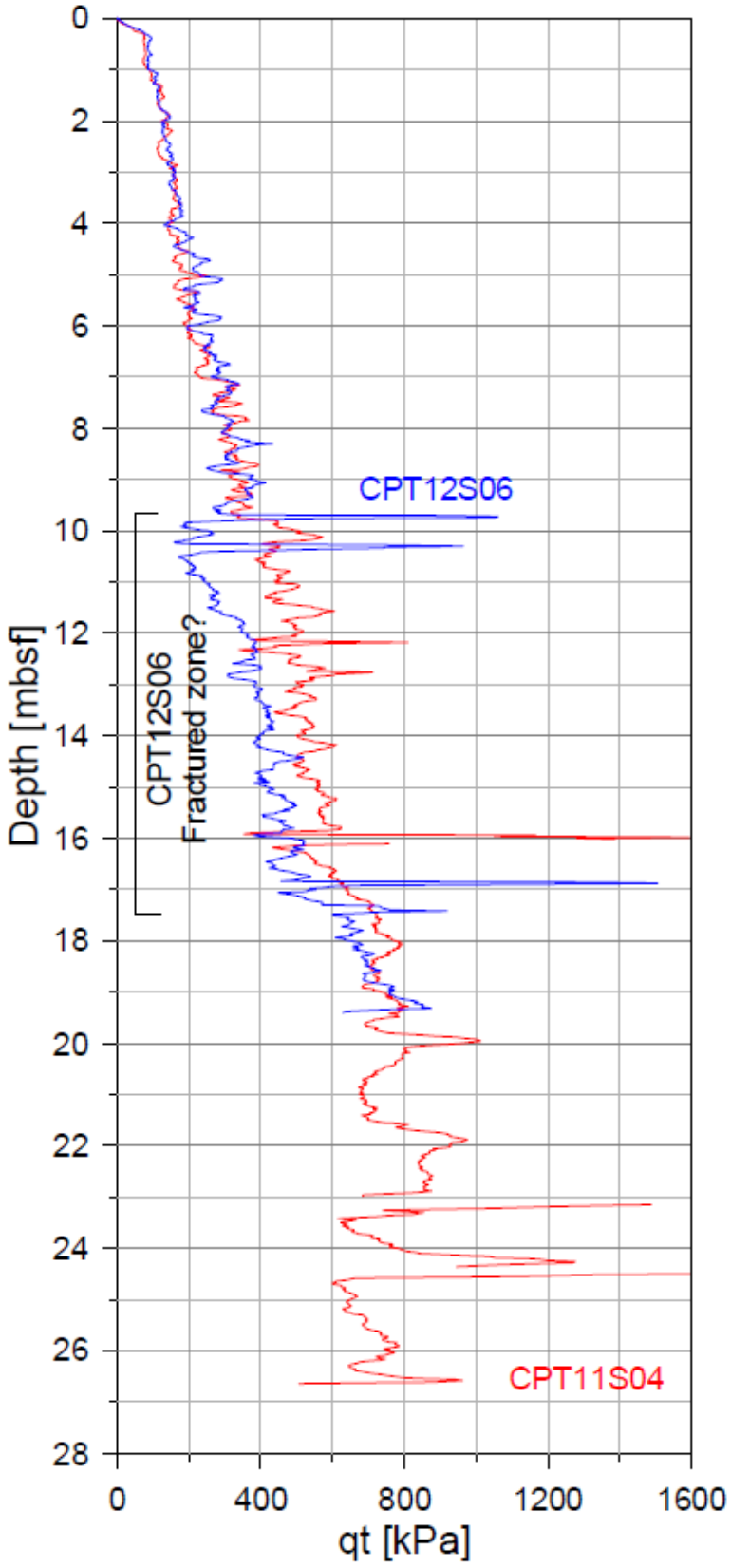

Figure 7. Corrected cone resistance qt *versus depth from sites CP12S06 and CPT11S04.*

4.2.1. Site PZS12

Figure 8-a presents, for PZS12, the initial impulsion and dissipation of the pore water pressure at the 5 sensor levels. Between 36 and 48 hours were needed to reach the pore pressure equilibrium of all 5 sensors. For the upper 4 sensors (P1 to P4), pore pressures remained almost constant until the end of the deployment (Figure 8-a). The P5 sensor was located at 11.48 mbsf, directly above a coarse sediment layer as can be observed from the CPT11-04 data (see Figure 5). From PZS12/P5, the differential pore pressure increases slightly (by ~ 1 kPa) after June 5th, 2008, then a sudden jump of 3 kPa is observed on June 19th, followed by a gradual increase until July 5th (except between June 22nd and June 24th, when a peak reaching a maximum of 13 kPa is observed). After July 5th, 2010, the differential pore pressure decreases during 34 days, until August 9th, 2010. At this date, a sudden increase in pore pressure is observed, followed by a regular decrease, following a diffusion-type curve. It is important to mention that the tidal effect on the differential pore pressure measured by PZS12/P5 was amplified significantly after June 18th, 2008. This is an indication of the increase of the compressibility of the pore fluid at the PZS12/P5 location after the 18th of June.

The temperature measurements carried out at the PZS12 location show, for the shallowest sensor, relatively significant seafloor temperature changes (a maximum variation of 0.3°C at 0.83 mbsf) during the one year piezometer deployment (Figure 8-b). The temperature changes measured at the 4 deeper sensors of PZS12 were less than 0.1°C (Figure 8-b) and almost in the same order of magnitude of the temperature sensor's accuracy (0.05 °C).

4.2.2. Site PZS16

Figure 9-a presents, for PZS16, the initial impulsion and dissipation of the pore water pressure at the 5 sensor levels. On all 5 sensors, pore pressures fluctuated between –1 kPa and 2 kPa during the complete duration of PZS16 deployment (Figure 9-a). The lowest pore pressure (-1 kPa) was measured by the P4 sensor located around 4.73 mbsf. On this sensor (P4), a slight decrease is observed after July 9th. The trend is negative until August 19th, 2010 and positive after this date. As for PZS12, the temperature measurements carried out at PZS16 location show a relatively significant seafloor temperature changes (a maximum variation of 0.3°C at 0.83 mbsf) (Figure 9-b).

4.2.3. Site PZS20

Figure 10-a presents, for PZS20, the initial impulsion and dissipation of the pore water pressure at the 5 sensor levels. Between 36 and 48 hours were needed to reach the pore pressure equilibrium on all 5 sensors. For the upper 4 sensors (P1 to P4), pore pressures were almost constant until the end of recording (Figure 10-a). For the fifth sensor of PZS20 (P5 at around 7.78 mbsf), the pore pressure drops slightly (by ~ 0.5 kPa below hydrostatic) on July 9th, 2010. On July 13th, 2010 a sudden drop is observed, by about 2 kPa. After this date, the pore pressure slightly varies (between 1 and 2 kPa below hydrostatic), until August 9th, 2010, after which it recovers abruptly to hydrostatic pressure. The tidal effect on the differential pore pressure measured by PZS20/P5 was much more pronounced between the 13th of July and the 9th of August, 2008 showing once again the increase of the compressibility of the pore fluid during this transient period.

The temperature measurements carried out at PZS20 location indicate a relatively significant seafloor temperature changes (a maximum variation of 0.3°C at 0.83 mbsf) (Figure 10-b).

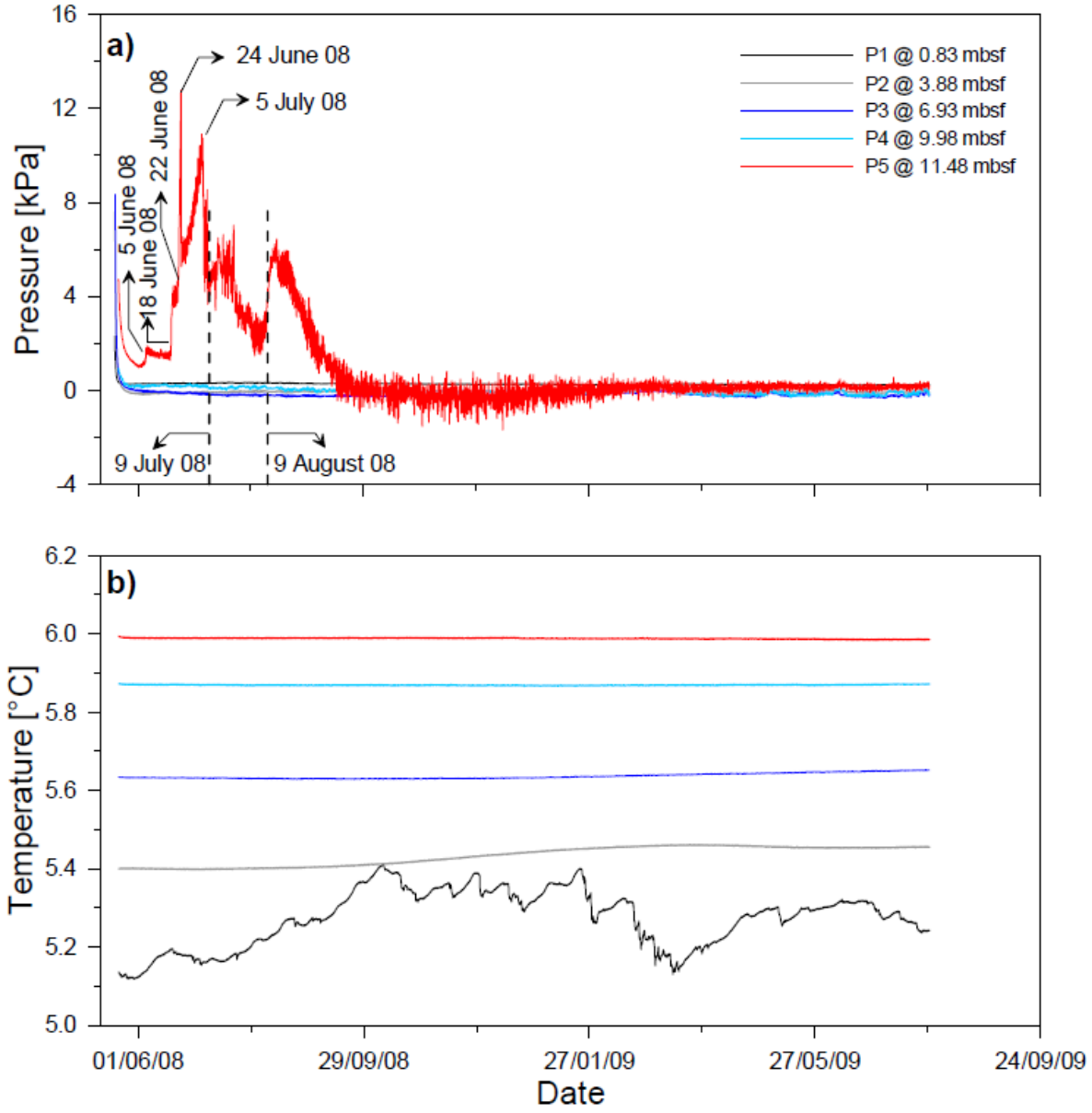

Figure 8. PZS12: a) excess pore water pressure and b) temperature versus time.

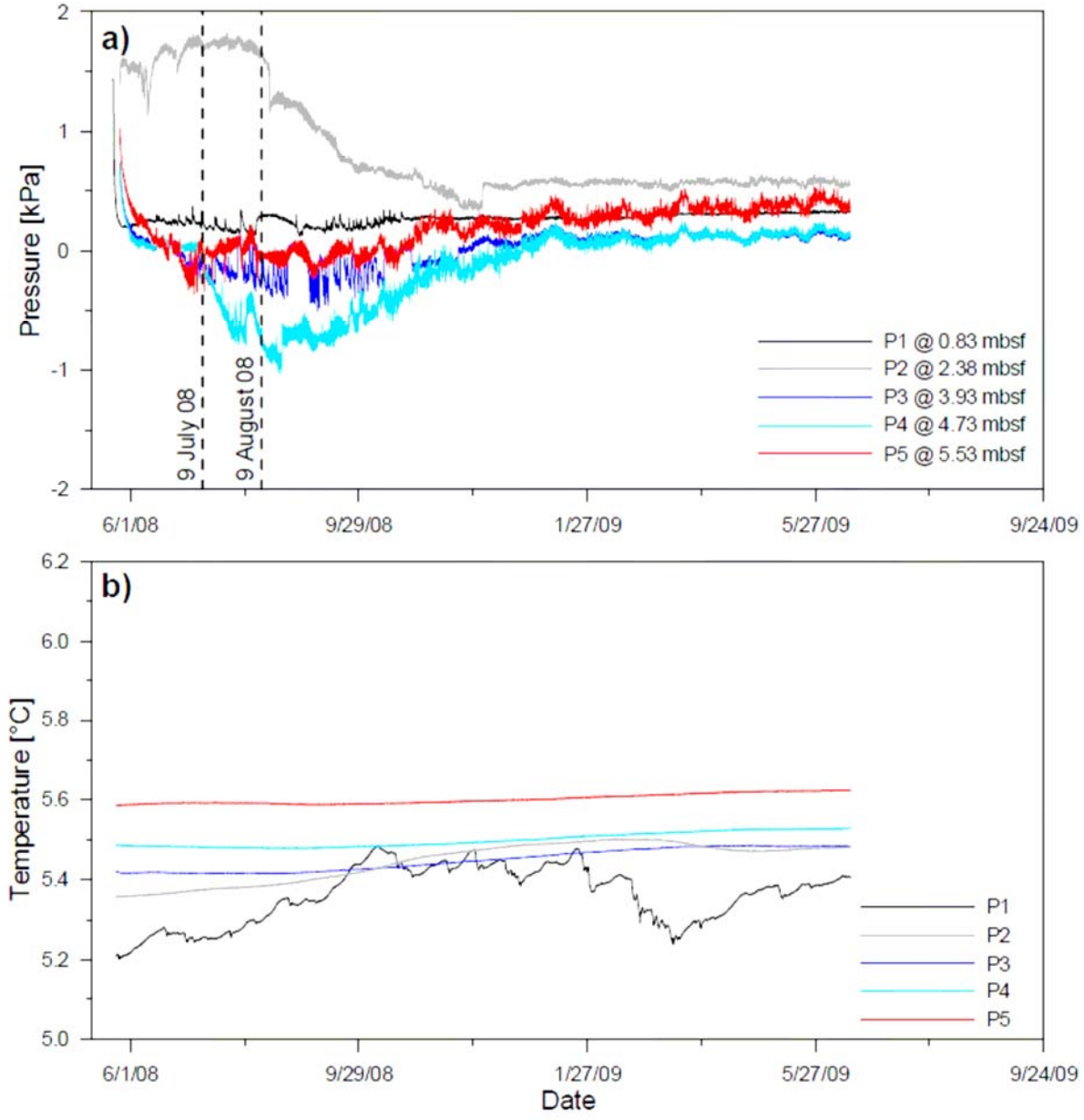

Figure 9. PZS16: a) excess pore water pressure and b) temperature versus time.

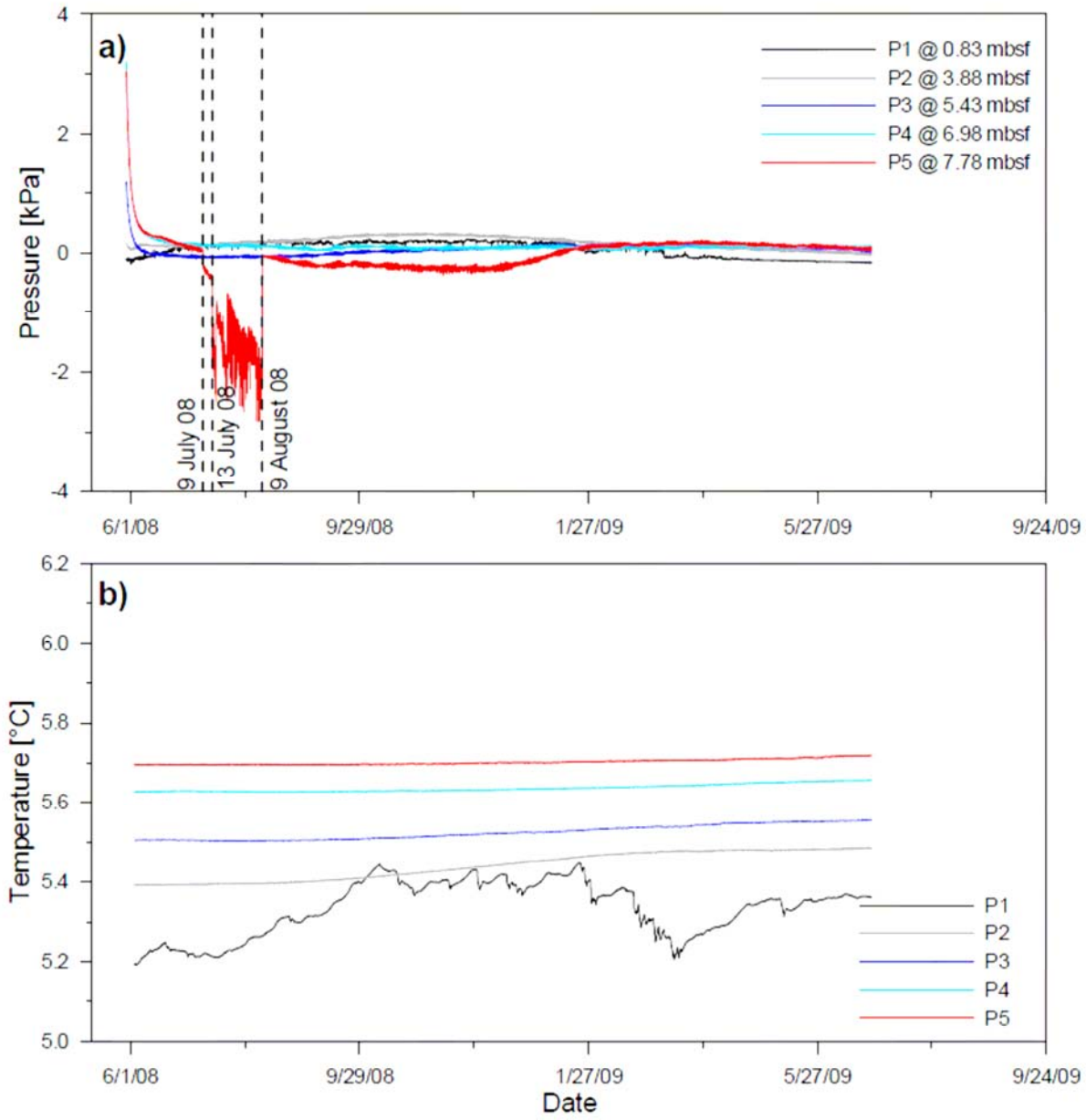

Figure 10. PZS20: a) excess pore water pressure and b) temperature versus time.

4.3. Seafloor and subseafloor characterization

4.3.1. Faults

The geological interpretation of the study area is based on a set of very high-resolution bathymetry (VHR) data and the 3D exploration seismic data (short offset processed). The study site displays various recent and active processes such as slope failures, deformation and fluid escape, as demonstrated by a broad variety of pockmarks (Figure 1 and Figure 2). The very detailed bathymetric data presented in Figure 2-A reveal the presence of two pockmark fields separated by a major E-W structural fault (in the following called the major eastern fault). The stratigraphic interpretation of the 3D seismic data permits to compile a map of

buried structural faults (Figure 2-B) and a very high resolution geomorphologic map presented in Figure 2-C.

The geological structure of the study area reveals a fault system composed of numerous (15) extrados faults related to the uplift of the shale anticline (Figure 2-B). From these 15 long-term growth faults, only 3 faults seem active (Figure 2-C) and they are marked on the seafloor by large depression and in depth by a shift (> 20 m for the D20 reflector: from around 25 mbsf to around 45 mbsf) of the most recent sedimentary layers. The others faults, which are normal faults, are buried under a minimum of 100 meters of sediments.

4.3.2. Pockmarks and undulations

The seafloor morphology of the study site is characterized by several sub-circular depression features. These circular features (pockmarks) with diameters ranging from a few meters to 250 meters are probably the result of fluid seepages. Various studies from the Nigerian continental slope have already shown the importance of fluid activities and related processes in pockmark developments, gas hydrate occurrences, mud volcanoes and carbonate build-ups [*Damuth*, 1994; *Cohen and McClay*, 1996; *Hovland and Gallagher*, 1997; *Brooks et al.*, 2000; *Graue*, 2000; *Deptuck et al.*, 2003; *Sultan et al.* 2007; *Sultan et al* 2010].

Newly acquired and existing seismic data permit to distinguish different types of pockmarks in the study area. Various shapes identified from the seafloor bathymetry and deep structures underneath, permit to characterize different geological processes at the origin of the observed pockmarks: (i) dewatering, (ii) buried mass transport deposits and (iii) presence of fault system as well as fluid escape from petroleum reservoirs. A fourth type of pockmark can be directly linked to the presence of gas hydrates and is probably associated to the dynamics of the hydrate system (Figure 2-C). These hydrate-associated pockmarks have a distorted shape with boundaries less well defined than pockmarks commonly described in literature examples. Gas hydrates were recovered by coring of some of those pockmarks while for other pockmarks, gas hydrates were suspected based on the analyses of seismic and bathymetric data.

The flanks of the anticline which are characterized by step slope angles (locally > 17 degrees) are characterized by many undulations features at the northern and at the south eastern part. Some of those undulations seem related to sedimentary construction (on the eastern flank) while others are the result of either sediment waves or creeping processes [*Sultan et al.*, 2011].

4.3.3. Sandy layers distribution

The interpretation of the VHR seismic profiles (Figure 11) shows several continuous reflectors characterized by high amplitude (called Dxx). 3D seismic data show the continuity of those reflectors in the complete study area (regional reflectors). A calypso core CS23 (23 m long - Table 1) was collected during the ERIG3D cruise in an area far from the free gas perturbation areas, at the eastern periphery of the study site (location in Figure 1-B). This reference core crosses the regional reflector D60 and shows that the high amplitude characterizing this reflector can be correlated to a silty layer between 16 to 17 mbsf (Figure 11-B). *In situ* piezocone measurements data have shown that the high amplitude reflectors named D50 and D30 (Figure 11-A) also corresponds to a sandy/silty layer which is characterized by high tip resistance, high friction and low pore pressure (see CPT11S02, CPT11S05 and CPT11S06 data in Figure 5 and Figure 6). In the following, the Dxx reflectors

presented in Figure 11 are interpreted as sandy-silty layers by extension of observations concerning D60, D50 and D30 ones. The distribution of the sandy layers within and surrounding the eastern fault is important for the understanding of the activity of the whole system going from the reservoir to the subsurface sedimentary layers. Indeed, the high permeability of those sandy layers makes them act as conduits for fluid flow.

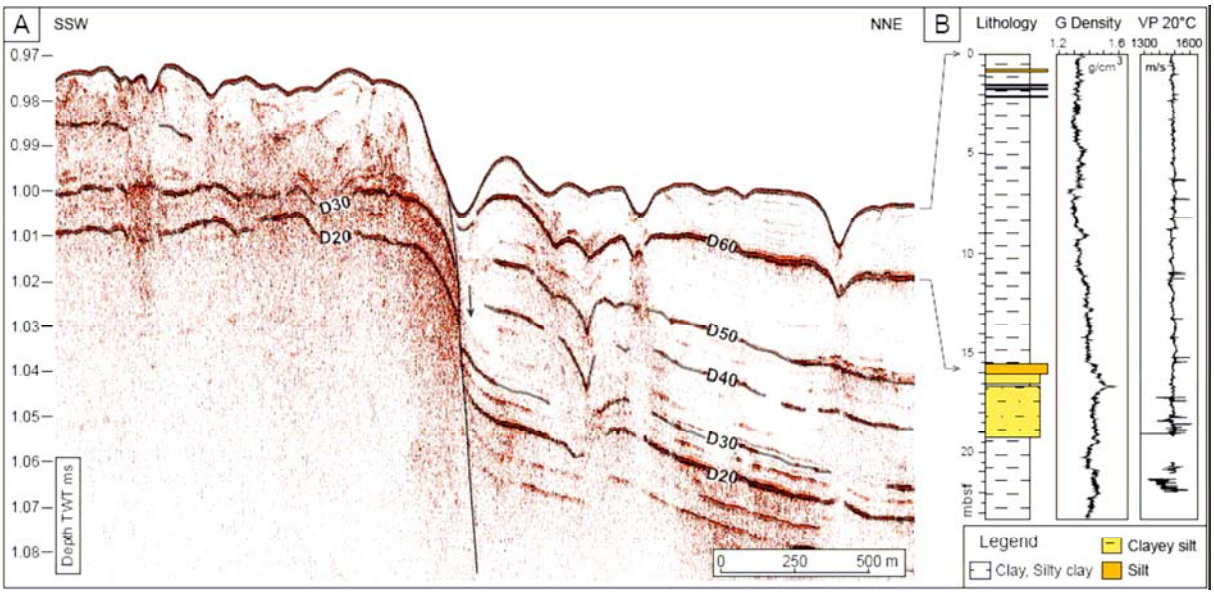

Figure 11. A- Very high resolution (VHR) seismic profile (SY08THR-Pr05). The high amplitude reflectors named Dxx are interpreted like coarse grain layers, B- Core log (ERCS23), densiy curve and Vp laboratory measured curve. The core description shows that the reflector D60 corresponds to a silt layer.

5. Gas-hydrates occurrence and distribution

5.1. From interval velocities

During the NERIS project (Ifremer-Total joint research project: 2003-2006) a new method based on the combination of 3D seismic data to geotechnical site characterizations using piezocone CPTu tests was developed to characterize the presence of free gas, gas hydrates and carbonate concretions which are considered as high-risk factors for sub-sea developments in the Niger delta [*Sultan et al.*, 2007]. A special processing of the 3D seismic data carried out by Total has enabled the calculation of the interval compressional velocity in the study area. Calibration of the P wave velocity anomalies was possible using geotechnical data from two oceanographic surveys [*Sultan et al.*, 2007]. Comparison between in-situ measurement using the piezocone, recovered cores and the prediction of gas and gas hydrate distribution based on the compressional wave velocity derived from the 3D seismic data have shown that 3D seismic data can be a valuable tool to identify heterogeneous areas.

However, the use of in-situ CPTu testing was essential to discriminate between gas hydrate occurrences and carbonate concretions presence. During the ERIG3D cruise we applied the same approach for the Northern-Eastern area of the shale anticline by calibrating the DeltaStack 3D cube made available by Total by coring and *in situ* measurements.

The high resolution interval velocity field was derived from the 3D seismic data available on the shale anticline North-Eastern area, using the DeltaStack 3D analysis. Figure 12-A shows the maximal interval velocities extracted for the first 40 ms TWT of the DeltaStack 3D interval velocity field. The time interval considered of 40 ms TWT (~30 m using a velocity of 1500 m/s) corresponds to the maximal sediment thickness that can be ground-thruthed by CPTu measurements and piston coring.

A part of the high interval velocities are related to the presence of rock outcrops or rocks buried beneath a superficial soft sediment layer sampled during the ERIG3D cruise on the East flank of the shale anticline (Figure 12-A). However, these high interval velocities could be also related to the presence of gas hydrates. Indeed, the temperature and pressure field in the Usan area satisfy the conditions for the occurrence of gas hydrates and a BSR was observed on the 3D seismic data below the shale anticline.

Figure 12-B shows P wave velocities extracted along SY08THR-Pr05 where high P wave velocities are mainly localized to the South of the Eastern fault. For the “Usan” site, it is clear that the distinction between hard rocks and gas hydrates can be only done by “ground-truthing” through coring and *in situ* CPTu measurements.

5.2. From high resolution deep-tow seismic data

Figure 13 shows a zoom on the upper part of the seismic profile SY08THR-Pr05. This seismic profile crosses the eastern fault to the south where the presence of gas hydrates was suspected from the P wave velocity anomalies (Figure 12-B). One of the main features observed in this seismic profile corresponds to the presence of a discontinuous reflector crossing sediment layers between SP 1520 and SP 2000 (Figure 13). This nearly horizontal discontinuous reflector corresponds to several discontinuous high P wave velocities (Figure 12-B) obtained from the DeltaStack 3D cube, and thus possibly related to the top of the gas hydrate occurrence zone (GHOZ). In order to verify this assumption and to determine the significance of this reflector, several *in situ* CPTu measurements (Figure 1-B and Table 2) were carried out along and close to the SY08THR-Pr05 profile (Figure 1).

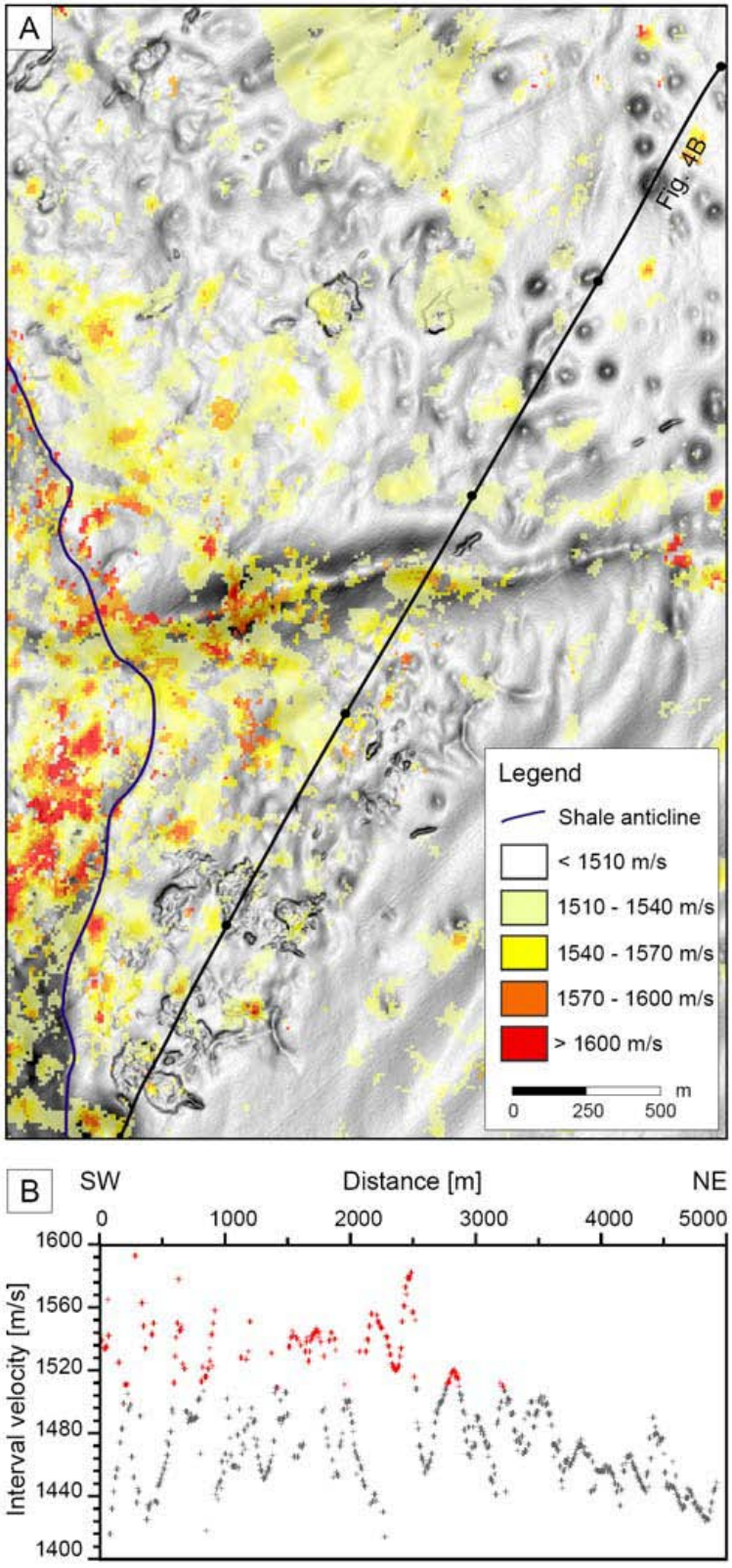

Figure 12. A) Maximal interval velocities extracted over the first 40 ms TWT of the DeltaStack 3D interval velocity field of the Usan North-Eastern area. The location of the SY08THR-Pr05 profile is indicated by the black line. The distance between two consecutive points along the SY08THR-Pr05 profile is 1000 m. B) P wave velocities extracted from the DeltaStack 3D interval velocity cube along the SY08THR-Pr05 profile. P wave velocities could be related in part to the presence of gas hydrates (i.e > 1510 m/s) are represented in red and are mainly located to the South of the major eastern fault.

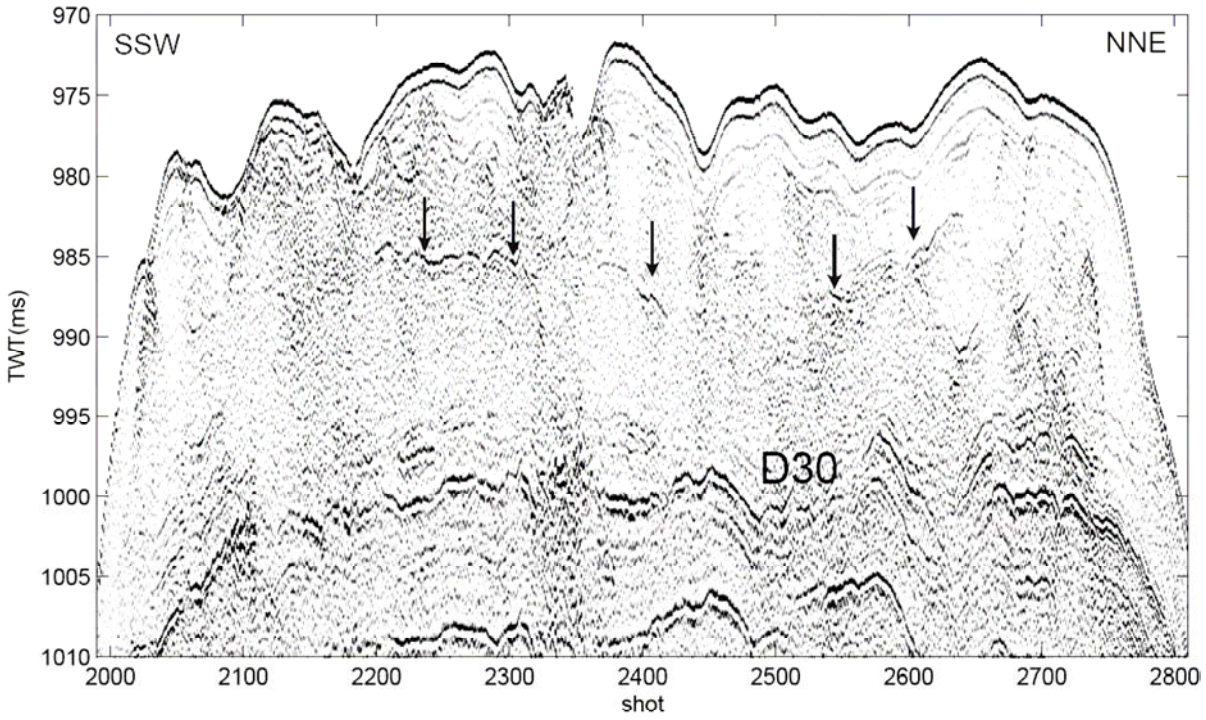

Figure 13. Zoom of seismic profile SY08THR-Pr05 showing a non consistent high amplitude reflector that may correspond to the top of the gas hydrate occurrence zone (shown by arrows).

5.3. Results from coring

Sediment samples collected using the Calypso corer during ERIG3D survey were aimed to identify the key mechanical and physical parameters of the sediments and also to obtain "ground truthing" at sites where hydrates occurrence were proposed based on the seismic data.

A calypso core (CS16; 12.00 m long) was collected at the central part of the irregular morphology of the seafloor on the eastern anticline flank (Figure 14 and location in Figure 1-B). The CS16 core was recovered from above the horizontal reflector indicated in Figure 13 as an indicator of the top of the GHOZ. Gas hydrates were recovered at different depths, from 4 to 12 mbsf. Hydrates were distributed heterogeneously with depth. Gas hydrates recovered at 5 mbsf were less massive than those sampled between 10 mbsf and 11 mbsf. Figure 14 shows lithology and mass-density versus depth curves measured using the MSCL logging device. This last curve shows the limit between water-saturated sediments and gas-hydrate bearing sediments. Indeed a large decrease of the mass-density can be observed at this limit. This discontinuity in the density curve is due to the presence of gas hydrates and to the free gas exsolution occurring after core retrieval. Figure 14-B presents photo images from 2 parts of the core showing the presence of massive gas hydrates in completely reworked sediment.

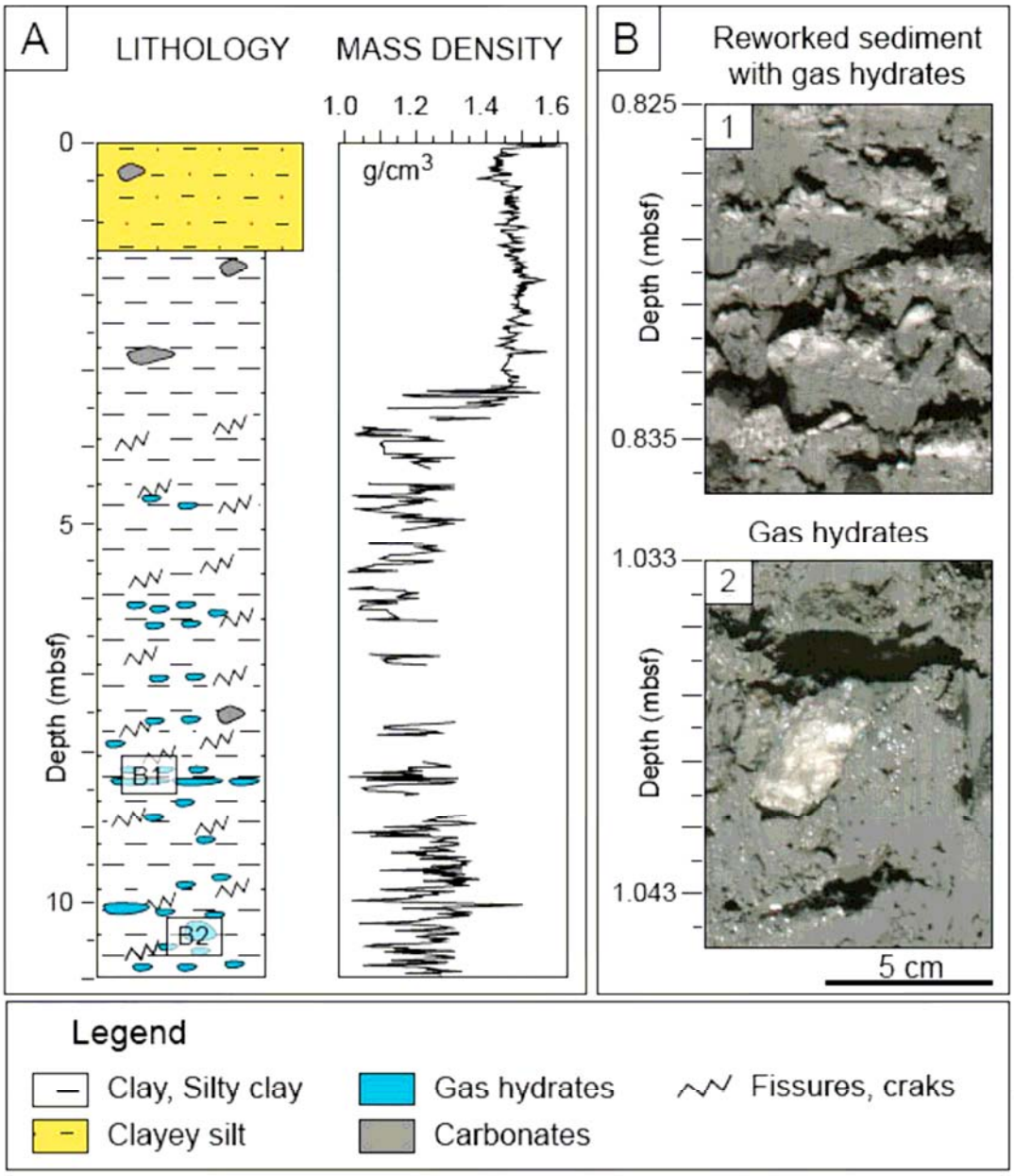

Figure 14. A- Core ERCS16: log and mass density curve, B- Pictures of gas hydrates recovered in this core.

5.4. Results from *in situ* piezocone measurements and correlation with seismic data

CPTu measurements carried out within the NERIS project show, that the distinction between gas hydrates and carbonate concretions or sandy-silty layers is possible using the measured excess pores pressure during piezocone rod penetration. While high excess pore pressure was generated during CPTu testing in gas hydrate bearing areas, a low excess pore pressure (in some cases lower than the hydrostatic pressure) was generated by CPTu testing in carbonate concretions bearing areas. Moreover, high Δu_2 with normal corrected cone resistance values can be an indicator of the presence of free gas [*Sultan et al.*, 2007]. Based on

these previous observations, CPTu data presented in Figure 3 to Figure 6 were interpreted in terms of sandy-silty layers, gas hydrates and free gas. The highest gas hydrates distribution was observed to the south of the Eastern fault and mainly at site CPT11S02 (Figure 4-d). CPT11S02 is close to the position of core CS16 in which gas hydrates were recovered. The CPT11S02 profile indicates that the top of the gas hydrates is at around 9 mbsf while the CS16 core indicates that hydrates were recovered at around 4 mbsf. However, the top of the gas hydrates detected with CPT11S02 fits well with the reflector interpreted as the top of the gas hydrates presented in Figure 13. CPT11S01, CPT12S01 and CPT12S03 also indicate the presence of thin hydrate layers between 7 and 12 mbsf for the first, 3.8 and 9 m for the second and between 15 and 19.7 mbsf for the third layer (Figure 4). Both CPT11S01 and CPT12S01 were positioned in a completely chaotic facies (Figure 15-A). CPT12S03 was positioned near core CS16 and CPT11S02 indicating the important heterogeneity of the gas hydrate distribution in the study area.

Most of the CPTu data presented in Figure 6 show the presence of free gas. CPT15S02, CPT12S06 and CPT11S04 (Figure 6-b, c & d) were positioned in three areas in which high fluid flow activities were proposed based on the seismic profiles (Figure 15). CPT11S05 and CPT11S06 also show the presence of free gas between two pockmarks on the main Eastern fault (Figure 1 and Figure 15). Almost all the gas hydrates and free gas layers were detected above silty sandy layers as can be observed from Figure 4 and Figure 6, thus confirming the role of sandy layers serving as conduits for fluid flow. Additionally, weak/fractured zones detected using the data from CPT12S06 (Figure 7) are also located above a sandy silty layers showing that fluid circulation may occur at the border of the fault by fracturing the superficial clayey layers.

6. Fluid circulation

To understand fluid seeps processes and associated features observed on the seafloor and in the superficial sediments (Figure 2), it is important to have a good understanding of the system from the deep structure to the upper sedimentary layers. This information can be extracted from 3D seismic blocks and VHR seismic profiles which allow interpreting the superficial fluid migration just beneath the seafloor in the gas hydrate stability zone (GHSZ). *In situ* geotechnical properties, pore pressure monitoring and ocean-bottom seismometers (OBS) recording may complement the seismic interpretation by providing a quantitative approach.

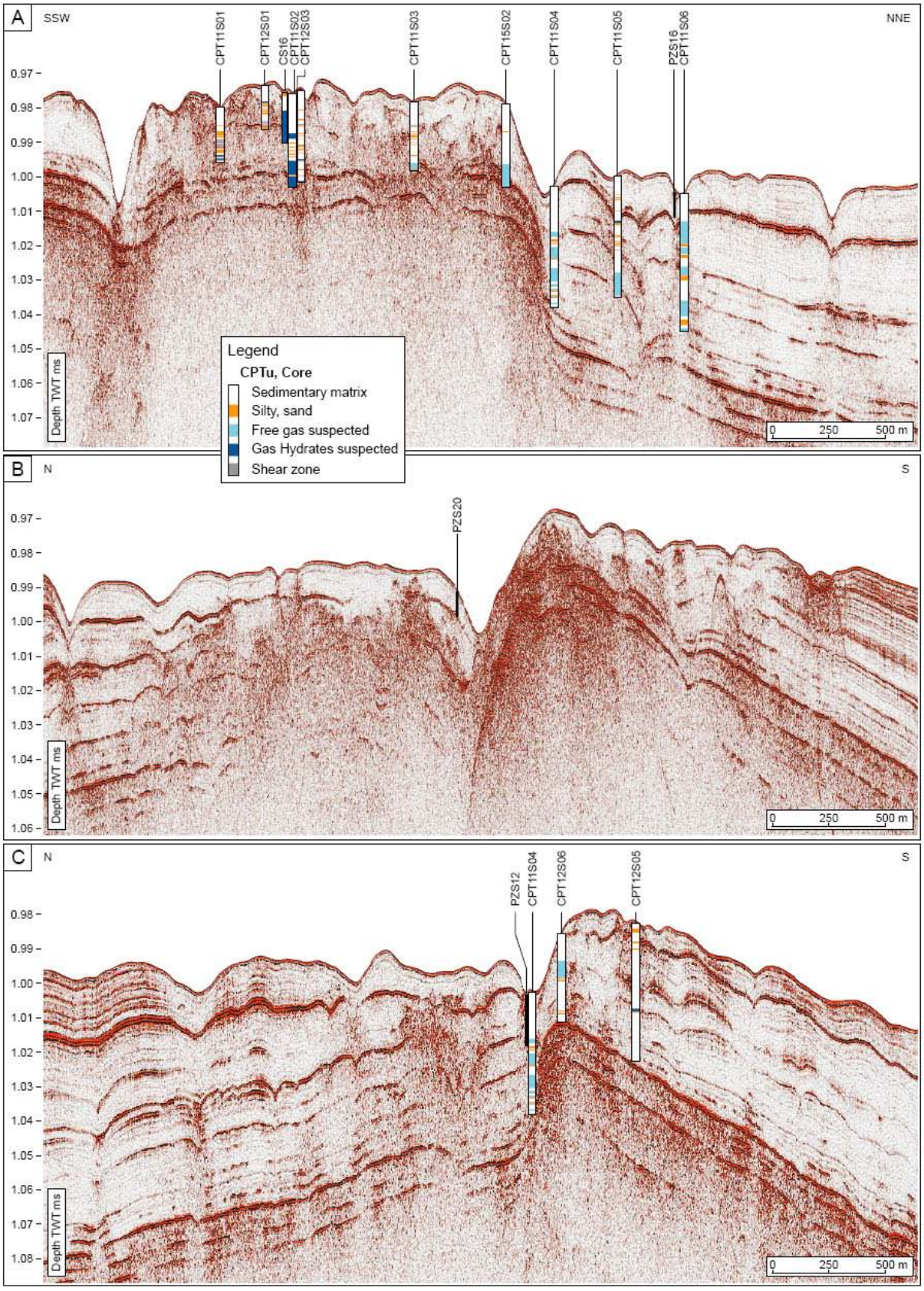

Figure 15. Uninterpreted 2D very high resolution seismic profiles with interpreted CPTU data. A- Profile SY08THR-Pr05, B- Profile SY08THR-Pr02, C- Profile SY08THR-Pr03.

6.1. Evidence from 3D seismic data

The shale anticline (purple colors in Figure 16 and Figure 17) which has been identified beneath the major structural fault is presented in Figure 2. The anticline core plays the role of fluid traps. Some sedimentary layers, marked by grey color in the 2 seismic profiles in Figure 16-B and Figure 17-B, are characterized by high amplitude reflectors indicating the possible location of fluid activities. Many of the normal structural faults presented previously on the dip map in Figure 2 are also indicated on the 3D seismic data in Figure 16-B and Figure 17-B. The connection between the reservoirs (main deep reservoir and intermediate reservoirs) and these extrados faults shows the path that the fluids may follow. Indeed the long-term growth fault acts as the main hydrocarbon migration pathway [*Zhang et al.,* 2006]. The fault system serves as a preferential conduit for fluid flow toward the seafloor analogous to observations by *Papatheodorou et al,* [1993] and *Boe et al.,* [1998]. Intermediate fluid reservoirs in the plio-quaternary canyon can be also observed from the 3D seismic data (Figure 16-B). This plio-quaternary canyon is filled by reworked heterogenous sediments with many fissures and cracks (chaotic facies in Figure 16-B). These intermediate reservoirs are directly connected to the major eastern fault.

The 3D seismic profile presented in Figure 17-B gives important information regarding the presence of fluid near the seafloor. A high-amplitude reflection parallel to the seafloor with a reverse polarity compared to the seafloor reflection, located at around 100 ms twt below the seafloor is interpreted as a BSR. This BSR is the expression of the low P-wave velocities characterizing the gas-charged sediments [*MacKay et al.*,1994].

3D seismic data presented in Figure 16-A and Figure 17-A give important information about the intermediate reservoirs and fluid conduits however these data are not accurate enough to provide a framework for understanding the fluid migration processes and trajectories in the shallower sedimentary layers.

6.2. Evidence from VHR seismic data

Subsurface amplitude anomalies observed from the VHR seismic profiles presented in Figure 15 suggest the occurrence of high fluid activities. The gas front (chaotic facies) identified from VHR seismic profiles suggests that fluid which migrates along the structural faults must diffuse laterally through natural conduits (Figure 16-C and Figure 17-C). Reflectors Dxx which were identified from VHR profiles (Figure 11-A) correspond to high permeable silty-sandy layers and may play the role of lateral fluid conduits. Therefore, fluid migration pathways are largely controlled by the distribution of the silty-sandy permeable layers. This lateral transmission of fluid seems to control the repartition of fluid flow below the seafloor and not only directly above faults.

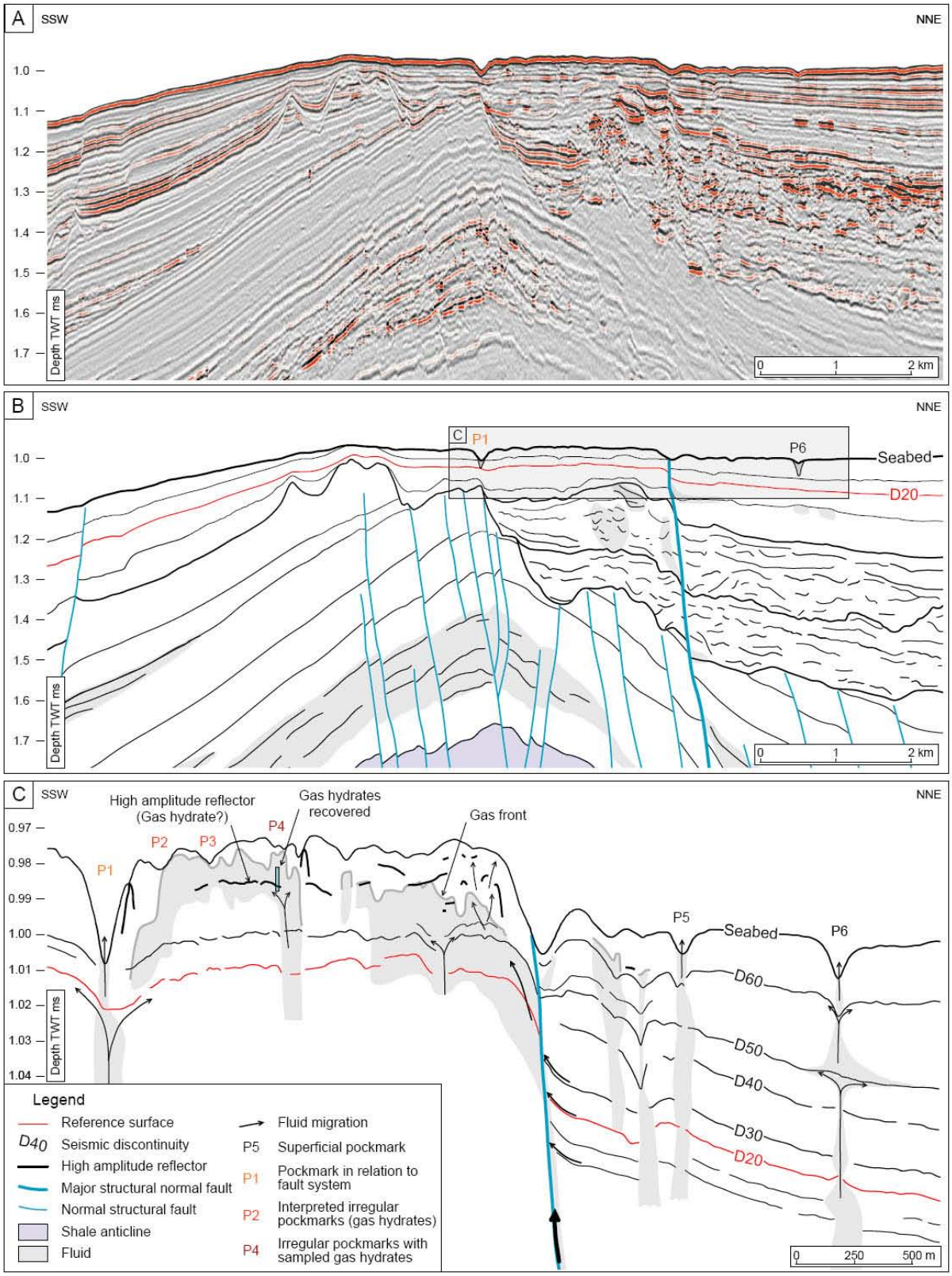

Figure 16. A- Uninterpreted random line extract from 3D high resolution (HR) seismic data showing the seismic morphology and stratigraphy under irregular pockmarks area, the fluid reservoir and fluid migration areas. B- Line showing seismic interpretation of the seismic line 10.A, C- Interpretation of the seismic profile presented in Figure 15-A. It is a seismic profile zoom of the surperficial part of the profile A (located by the dark rectangle in B).

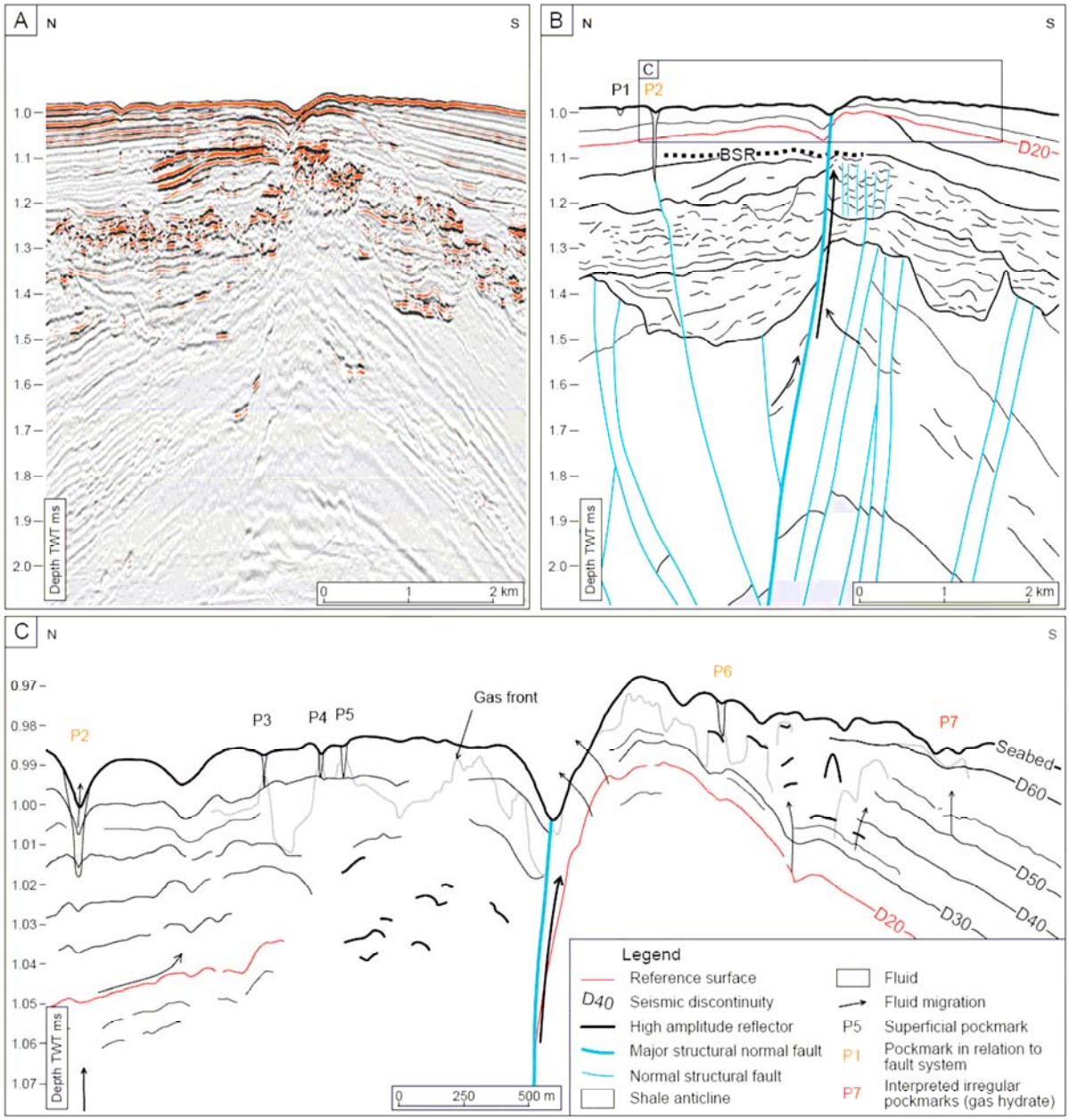

Figure 17. A- Uninterpreted random line extract from 3D HR seismic data (courtesy of Total Oil Compagny) showing the seismic morphology under irregular pockmarks area, the fluid reservoir and fluid migration areas. B- Line showing seismic interpretation of the seismic line 11.A, (BSR= Bottom simulating reflector), C- Interpretation of the VHR seismic profile presented in Figure 15-B. It is a seismic profile zoom of the upper part of the profile A (located by the dark rectangle in B).

Figure 17-C shows that fluid flows can also cross the upper clayey layers by hydro-fracturing and drain directly fluid at the seabed level. This observation was already drawn from to the CPTu data CPT12S06 where hydro-fractured sediments were detected by the important decreases of qt values between 10 and 16 mbsf (Figure 7). Fluid flows seem at the origin of several pockmarks noted “Px” in Figure 16-C and Figure 17-C and also at the origin of gas hydrates. A non-consistent high amplitude reflector indicated in Figure 16-C just underneath P4, could highlight the top of the gas hydrate zone as presented in Figure 13. Indeed, the simultaneous presence of free gas and gas hydrate results in a large velocity contrast marked

by the high amplitude reflector in geophysical data. Furthermore, gas hydrates were recovered in this area (Figure 14) and were suspected using *in situ* CPTu data. VHR seismic data confirmed the link between fluid migration in sub-surface through faults and sandy-silty layers, gas hydrate accumulations and several pockmark locations.

6.3. Evidence from micro-seismic signatures

During the ERIG3D cruise 10 long recording ocean-bottom seismometers (OBS) were deployed in the study area for duration of 2 months. The main objective of the experiment was to establish a baseline of the micro-seismicity in the Eastern fault area of the Usan field. The instruments were designed to record very small events using externally deployed geophones, to ensure good sea-floor coupling. The deployments were carried out using a cable and ultra-short baseline positioning relative to the ship to exactly determine the position of the instrument on the sea-floor. The experimental layout was chosen to ensure recording of micro-seismicity around the major eastern fault and with an instrument density sufficient to eventually relocate the source position of events recorded eventually by four or more OBS. However, due to technical problems, the instruments stopped recording prematurely and most instruments recorded only for 14 and 28 days after the deployment. Although between 68 and 652 events were recorded by individual seismometers, no events were recorded by more than one instrument simultaneously preventing the localization of micro-seismic events (Table 4). During the recording period, no earthquake (with arrivals recorded at different distant OBSs) was detected. Instead, the instruments recorded a great number of micro-events having the following characteristics:

1) micro-events are frequent but not isolated; instead, they appear to occur as part of crisis, each crisis being made of a few tens of individual of events;

2) there is no correlation between distant (1 km) OBSs;

3) the duration of each event is less than 300 to 400 msec, with frequencies ranging between 10 and 30 Hz (Figure 18); peak amplitudes are highly variable, comprised between 0.5 and 20 μm/s. As an example, local earthquakes with moment magnitudes 2 to 3, distant by a few tens of km and recorded on the OBSs have amplitudes of a few tens of μm/s.

4) the micro-event signals are detected by all geophone components (x, y, z); only those micro-events that have the largest amplitude are detected on the hydrophone.

During the recording period, the most significant micro-events were detected on OBSs 04, 05, 07 and 08. OBS08 stopped recording on June 11th, while OBSs 05 and 04 stopped on June 21st and June 22nd, respectively. So, among these four instruments, OBS07 was the only one functioning after June 22nd (OBS 07 did record until August 15th, 2008). The first series of micro-events was recorded on June 10th and 11th on OBSs 04, 05, 07 and 08 (Figure 20). A second series, with events of relatively small amplitude was recorded on OBSs 04 and 05 on June 19th and 20th. Then, the most prominent crisis was recorded by OBS04 between June 21st and June 22nd, 2008 just couple of hours before the important peak measured by PZS12. After June 22nd, OBS07 recorded two crises, on June 25th and July 2nd, respectively.

From the above, we conclude that the micro-events recorded by the OBSs are not due to instrumental artefacts, neither related to biological (fish) activity. Instead, the results of a

study conducted to identify similar signals from the Sea of Marmara [*Tary et al., 2011*] strongly suggest the hypothesis that the micro-events are likely related to natural degassing processes from the seafloor or from the near sub-surface.

#	Water depth (m)	Recording period
OBS04	734	10/06/2008 02:00 - 22/06/2008 14:22
OBS05	739	10/06/2008 02:00 - 21/06/2008 16:31
OBS06	743	10/06/2008 02:00 - 20/06/2008 18:40
OBS07	748	10/06/2008 02:00 - 15/08/2008 01:58
OBS08	716	10/06/2008 02:00 - 11/06/2008 16:14

Table 4. OBSs characteristics and recording period. Natural frequency of geophones: 4.5 Hz; Sampling frequency: 250 Hz.

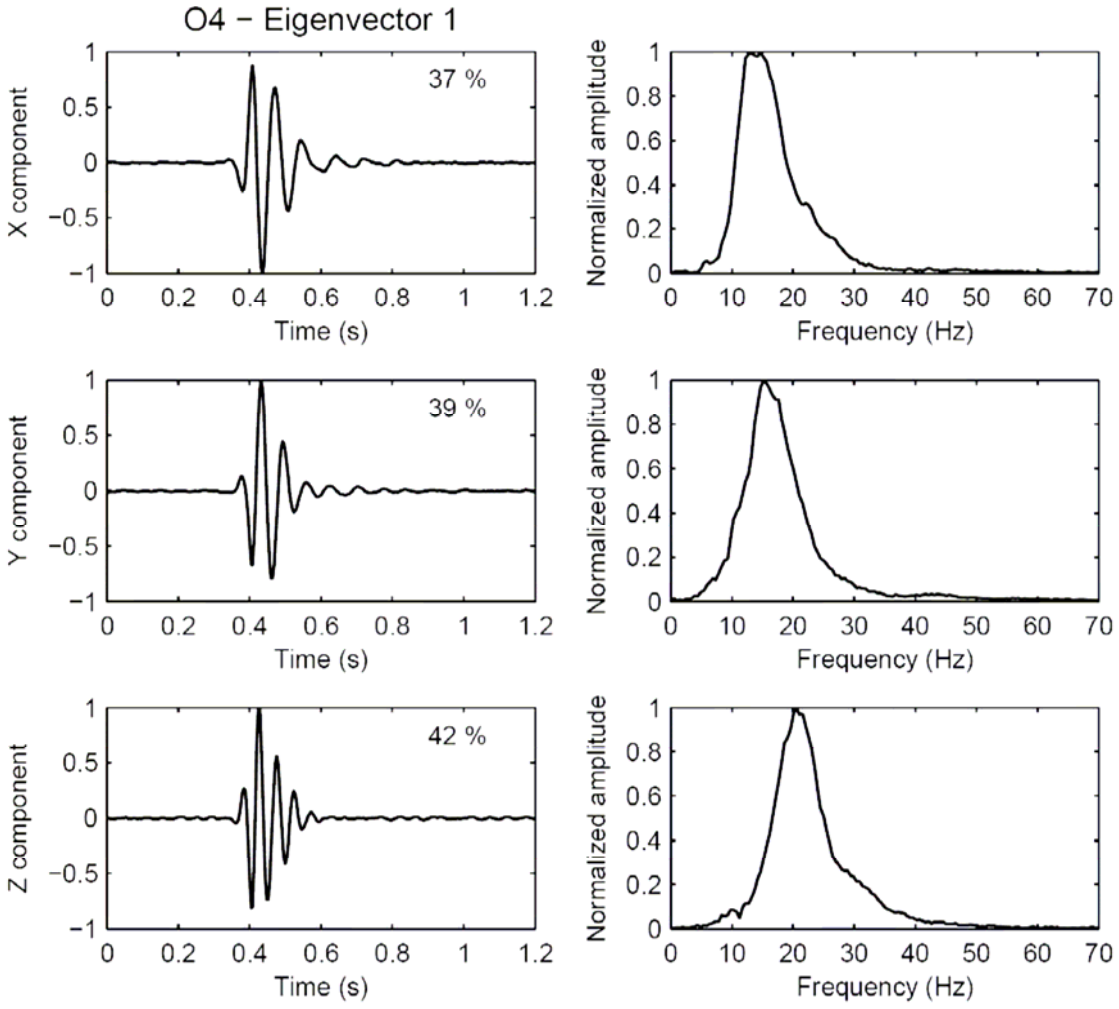

Figure 18. First eigenvector coming from the Principal Component Analysis of the micro-events constituting the crisis (from June 20, to June 22, 2008) observed on OBS 4 (components X, Y and Z). The representativeness of each eigenvector is indicated by its eigenvalue given in percentage of the total energy. On the right is given the eigenvector spectrum.

6.4. Evidence from piezometer measurements: Thermal and pore pressure regimes

Figure 19-a shows the temperature evolution (around 1 year) measured by the upper first sensor (between 0.83 and 0.92 mbsf) of 6 piezometers deployed surrounding the Usan anticline. The six piezometers were deployed at water depths between 736 m and 761 m. PZS13 and PZS14 were positioned west of the Usan anticline while the PZS17 was positioned to the East. Temperature fluctuations from the 6 piezometers presented in Figure 19-a show similar seasonal variations with a similar range of variations during the one year monitoring. In addition, inter-seasonal fluctuations can be observed on the six piezometers recordings.
The temperature measured by the upper sensor of the six piezometers varies during the monitoring period between 5.05°C and 5.5°C. The concordance between the temperature curves presented in Figure 19-a is sufficiently marked to show that no large influence is exerted by a local process that could perturb the seabed temperature field during the monitoring period.

Figure 19-b shows geothermal profiles recorded by PZS12, PZS16 and PZS20 between the 18th of June 2008 and 17th of May 2009. For all three piezometers, it is obvious that the thermal transient regime is only linked to the seawater temperature changes without any input from an external mechanism that could perturb the geothermal profiles (appendix A). Moreover, the pore pressure changes observed by PZS12 and PZS20 around the 9th of July 2008 did not produce any thermal perturbation.

The important pore pressure perturbations measured by PZS12 and PZS20 (Figure 8 and Figure 10) at the base of the piezometer lances seem to diffuse very slowly vertically through the sedimentary column (see appendix B). It is clear from the calculation presented in appendix B that during the 1-year period monitoring, only a limited area surrounding the sensors P5 of PZS12 and PZS20 is affected by the pore pressure variations. Data from PZS12 and PZS20 confirm the influence of the fluid activities surrounding the eastern fault. The main conduits of those fluid flows are the sandy-silty layers as it can be observed from Figure 6-d for PZS12.

Fluid circulations within the clayey sediments are only possible by hydro-fracturing or by opening existing fractures as it was assumed from the reduced qt values on CPT12S06 location (Figure 7). Fluid flow seems to occur more laterally in the upper sedimentary layers (above PZS12/P5 and PZS20/P5) as the pore pressure accumulations were not accompanied by any temperature changes. Moreover, the amplification of the tidal effect on the differential pore pressure after the18th of July, 2008, for PZS12/P5 (Figure 8) and between the 9th of July and the 9th of August, 2008, for PZS20/P5 (Figure 10) is a direct indication of the increase of the compressibility of the pore fluid and therefore an indirect indication of the presence of free gas and fluid circulation at those two levels.

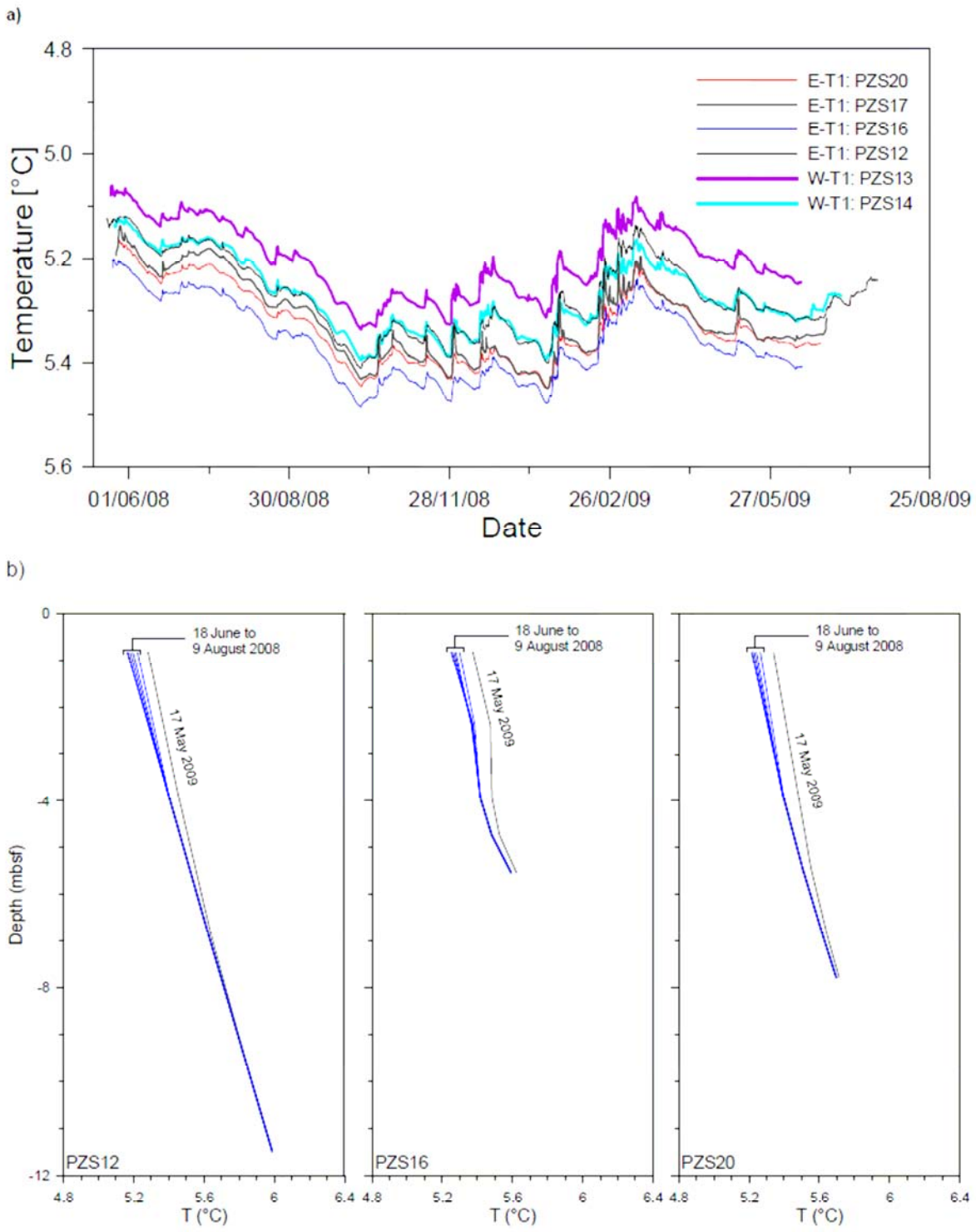

Figure 19. a) Temperature histories (around 1 year) measured by the upper first sensor (between 0.83 and 0.92 mbsf) of 6 piezometers deployed surrounding the Usan anticline. PZS13, PZS14 and PZS17 were deployed at water depths of 761 m, 753 m and 736 m, respectively. PZS13 and PZS14 are positioned to the West of the Usan anticline while the PZS17 is positioned to the East and b) Geothermal profiles recorded between the 18th of June 2008 and 17th of May 2009 from a) PZS12, b) PZS16 and d) PZS20.

7. Discussion: faults, microseismicity, fluid release and hydrate distribution

Figure 20 summarizes seven measurements from, respectively, PZS12, PZS16, PZS20, OBS04, 05, 07, and OBS08. A small increase in differential pore pressure of 1 kPa is first recorded at PZS12 (sensor P5) on June 5th, 2008. On June 10th and June 11th, two small crises with micro-events are detected on all four OBSs (Figure 20 d, e, f & g). Then, on June 19th, an abrupt increase in pore pressure is observed at PZS12 (sensor P5), followed by a regular, positive trend until July 5th (reaching 11 kPa). Superposed on this regular trend, a strong peak – reaching a maximum value of 13 kPa – occurs between July 22nd and July 24th, shortly after the most significant crisis in micro-events detected by OBS4 between June 21st and June 22nd. After July 5th, the pore pressure decreases abruptly. On august 9th, a sudden increase in pore pressure is detected at PZS12, followed by a progressive recovery to hydrostatic (Figure 20-a).

The geometry of the sandy silty layer below PZS12 pulls-up to around 5 mbsf at the northern flank of the fault (Figure 17-c) and can explain the sudden decrease of the pore pressure measured by PZS12/P5 the 24th of June and the 5th of July 2008. Indeed, pore pressures of 13 kPa and 11 kPa corresponds, respectively, to around 82% and 70% of the vertical effective stress at 5 mbsf (for a submerged mass density of 0.33 g/cm^3). This high pore pressure is enough to create hydro-fracturing or to open existing fractures in the above 5 m of clayey sediments. In addition, hydro-fracturing on the northern flank of the Eastern fault was already detected thanks to CPT12S06 (Figure 7).

The hydraulic diffusivity D_H value was calculated from the dissipation curve, which took place after July 5th (see Figure 21). The hydraulic diffusivity D_H was found equal to 1.3 10^{-4} m^2/s for a drainage path of 5 m corresponding to the depth of the sandy layer at the northern flank of the eastern fault. This unusual high D_H value (4 orders of magnitude higher than the values presented in Appendix B) confirms that dissipation occurs through fractured sediments. On the other hand, the pore fluid accumulation which occurs on August 9th is followed by pore pressure dissipation with a hydraulic diffusivity comparable to the one presented in Appendix B. Indeed, the pressure of 6 kPa accumulated, at the base of PZS12, on August 9th was not enough to open preexisting fractures and the dissipation might have occurred with diffusion through the clayey matrix. The presence of the free gas at PZS12/P5 position (after the 18th of July 2008) can be indirectly observed from the amplification of the tidal effect on pore pressure fluctuations and therefore on fluid compressibility as it can be clearly seen from Figure 20-a. Based on PZS12 data, we propose that migration of gas (in the sandy-silty layer that has been identified as a fluid conduit) results in the increase of pore pressure detected at 11.48 m below seafloor at PZS12 after June 5th, 2010.

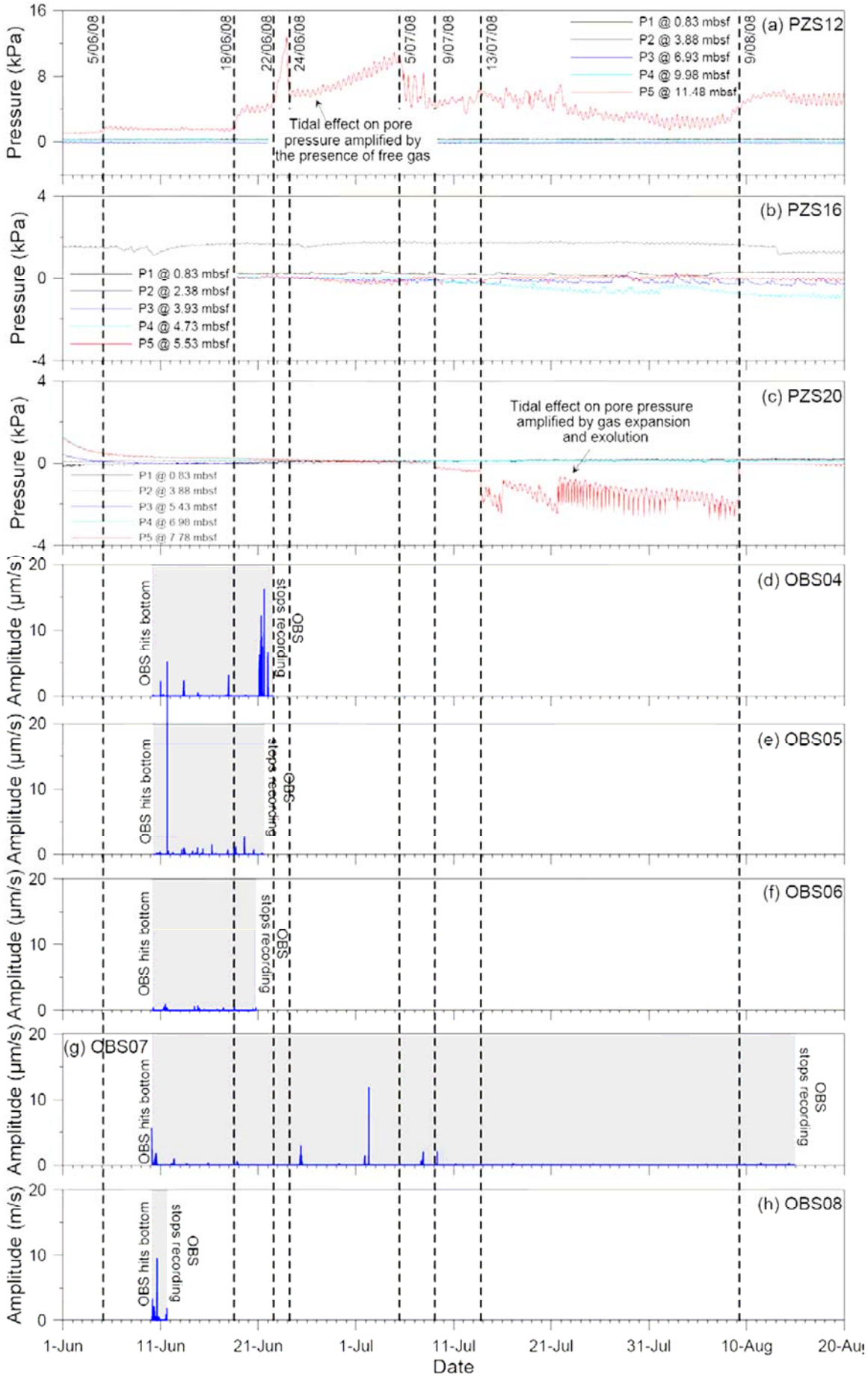
(a) PZS12
P1 @ 0.83 mbsf
P2 @ 3.88 mbsf
P3 @ 6.93 mbsf
P4 @ 9.98 mbsf
P5 @ 11.48 mbsf
5/06/08
18/06/08
22/06/08
24/06/08
5/07/08
9/07/08
13/07/08
9/08/08
Tidal effect on pore pressure amplified by the presence of free gas
Pressure (kPa)
(b) PZS16
P1 @ 0.83 mbsf
P2 @ 2.38 mbsf
P3 @ 3.93 mbsf
P4 @ 4.73 mbsf
P5 @ 5.53 mbsf
(c) PZS20
Tidal effect on pore pressure amplified by gas expansion and exolution
P1 @ 0.83 mbsf
P2 @ 3.88 mbsf
P3 @ 5.43 mbsf
P4 @ 6.98 mbsf
P5 @ 7.78 mbsf
Amplitude (µm/s)
(d) OBS04
(e) OBS05
(f) OBS06
(g) OBS07
(h) OBS08
OBS hits bottom
stops recording
OBS
Amplitude (m/s)
1-Jun
11-Jun
21-Jun
1-Jul
11-Jul
21-Jul
31-Jul
10-Aug
20-Aug
Date

Figure 20. Correspondence between Piezometers records [a) PZS12, b) PZS16 and c) PS20] and OBS records [d) OBS04, e) 05, f) 06, g) 07 and h) 08]. The locations of the different instruments are indicated in Figure 1. This figure suggests that PZS12 records two-phase episodes: during Phase 1, from June 5th to July 5th, 2008, gas accumulation results in pore pressure increase; during phase 2, pore pressure slowly returns to equilibrium, from July 2008 to February 2009. Note that: 1) micro-events occur as the OBSs hit bottom after deployment at sea; 2) micro-events recorded at different OBSs are not correlated; 3) the most prominent crisis of micro-events occur near OBS04 on June 21st/22nd, 2008; our analysis suggest that this crisis likely results from the release of gas which accumulated in excess in the sub-surface sandy, silty layers; 4) a peak in pore pressure occurred during phase 1 between June 22nd and June 24th, suggesting a sudden injection of gas by hydro-fracturing and/or opening of existing fractures. The free gas circulation expansion and exsolution (after the 18th of July, 2008 for PZS12/P5 and between the 13th of July and the 9th of August, 2008 for PZS20/P5) are evidenced by the amplification of the tidal effect on the fluctuation of the differential pore pressure due to the increase of the pore fluid compressibility.

Gas accumulation in this layer near PZS12 site appears to be a non-steady process with, different phases:

1) continuous free gas flow and gas accumulation from June 5th to July 5th, with marked increases on June18th and June 22nd;

2) hydro-fracturing and/or open existing fractures and degassing phase starting on July 5th;

3) gas accumulation resuming abruptly on August 9th eventually followed by a phase of fluid release with slow pressure recovery (diffusion) to hydrostatic.

Pore pressure depression recorded at PZS20 site (Figure 20 -c) occurs almost simultaneously with the decrease of the pore pressure measured at PZS12 location (5th to 9th of July 2009).

The end of the pore pressure depressions measured at PZS20 site coincides with the second phase of pore pressure accumulation measured by PZS12 (9th of August 2009). This pore pressure depression indicates that seawater penetrates into the bottom sediments at the level of PZS20. The origin of this depression could be a fast circulation of free gas in the sandy silty layers.
The expulsion of free gas generates two processes that may induce depressions in the surrounding medium: 1) a negative volume balance due to the fast gas bubbles expulsion and 2) depending on the gas velocities, a pressure depression field can be created behind the gas bubbles. The decrease of the pore pressure recorded by PZS20/P5 is accompanied by gas exsolution and expansion which increases the compressibility of the pore fluid and amplify the pore pressure fluctuations under tidal cycles (Figure 20-c).

The pore pressure regime observed at PZS16 is local, as it is very different from what is observed at PZS12 and PZS 20 sites (Figure 20-b).

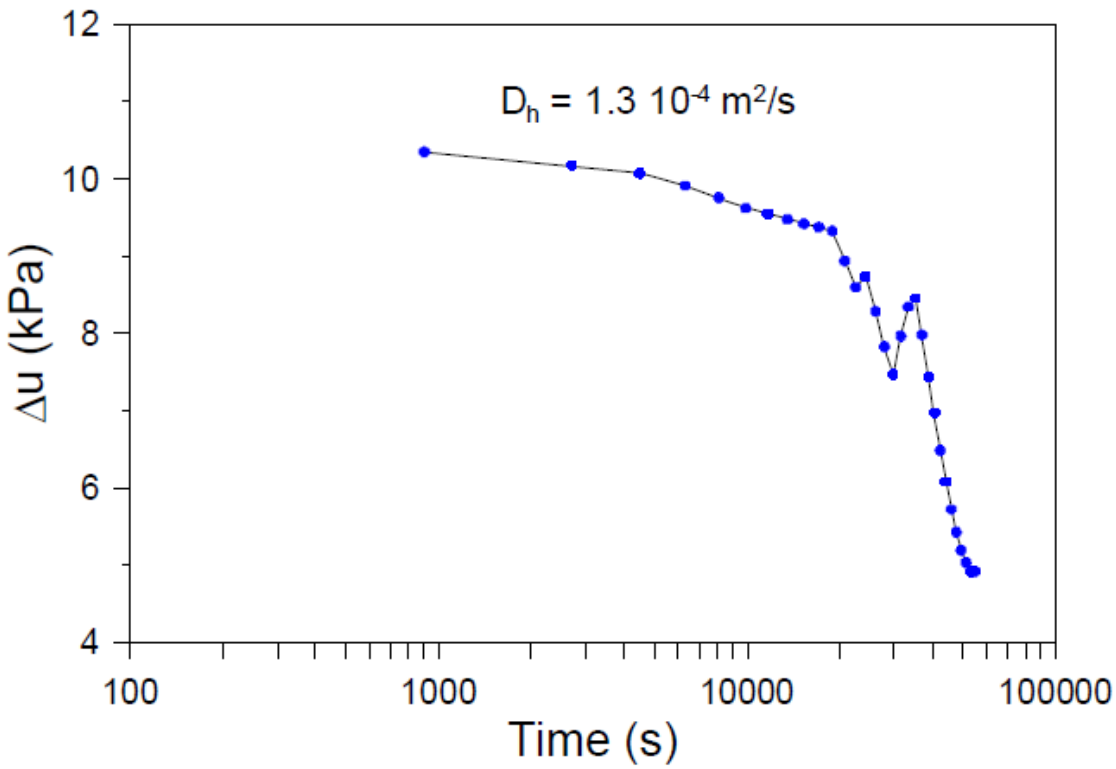

Figure 21. Dissipation pore pressure curve measured by PZS12/P5 between July 5th and July 6th. The hydraulic diffusivity D_H was calculated from a drainage path of 5 m corresponding to the depth of the sandy layer at the northern flank of the eastern fault.

For the discussion hereafter, we recall our working hypothesis, according which the micro-events measured by OBSs are related to degassing processes from the seafloor or from the near sub-surface. The micro-events recorded at one given OBS are not detected by the other OBSs, although located less than 750 m apart. This can be explained assuming that the micro-events are produced at very shallow depth (a few tens of meters) below seafloor, in very attenuating sediments. This suggests that the non-seismic micro-events originate in the immediate vicinity of the OBSs.

The source of the micro-events recorded at the OBSs are too distant from PZS12 to be directly related to the degassing processes that could occur at the piezometer site, even though one can suspect that a causal, indirect relationship could exist between the micro-events crisis detected on OBS04 between June 21st and June-22nd and the peak in pore pressure recorded at PZS12 on June 23rd and 24th. To obtain the full picture on the relationships between the pore pressure and the micro-seismic events, the exact collocation of OBSs and piezometers is required.

However, altogether the OBSs provide valuable information at the scale of the formation. The data indicate that gas migration processes occur within the sandy-silty layer over a whole area centered on PZS12. These processes result in gas accumulation and increase in pore pressure at PZS12 site, within the permeable, sandy-silty layer, 11.48 meters below seafloor.

The local process described in the present paper has some bearing to the one presented by *Tryon et al.* [1999] and is summarized in Figure 22 with the following three stages:

Stage 1: slow upward pore fluid (mainly free gas) migration through existing conduits (mainly the major eastern fault) and free gas accumulation and circulation within several shallow sandy layers intersecting the major eastern fault;

Stage 2: pore pressure increases within the sandy-silty layers as evidenced by the data recorded by PZS12. The free-gas accumulation at these sandy layers was indirectly detected by the amplification of the effect of the tidal cycles on the recorded pore pressure fluctuations;

Stage 3: hydro-fracturing and/or opening existing fractures and fluid pressure dissipation through sporadic degassing events (with some of them being detected at the OBSs). This process can eventually causes an interstitial water circulation through the shallow sandy layers and drawing overlying seawater into the sediment (as it was observed from PZS20/P5).

Due to the geological complexity of the study area with the presence of several intermediate gas caps (Figure 16) and sandy-silty conduits, it is obvious that processes of free gas circulation, free gas accumulation, pore pressure increases and degassing, may occur simultaneously or separately at several locations surrounding the major eastern fault. This is supported by the several shallow chaotic facies that can be observed from the VHR seismic profiles presented in Figure 15 and the non-synchronous micro seismic events detected by the deployed OBSs (Figure 20).
However, the good synchronization between the pore pressure dissipation at PZS12/P5 and the pore fluid depression at PZS20/P5 raises the question about the important spatial extension and the time scale of such degassing phenomena and the potential link between gas hydrates distribution and fluid circulation processes. Indeed, gas hydrates were recovered by coring and indirectly detected by geophysical data and *in situ* geotechnical measurements to the south of the major eastern fault. Therefore, at shallow depth below the seafloor, gas accumulation and fluid release seem to favor gas hydrate formation above sandy-silty conduits to the south of the fault while downward flow of seawater prevent the accumulation of gas hydrates to the north of it.
This observation can be only drawn for the upper explored sedimentary layers. The complexity of the piping system going from the main reservoir to intermediate gas caps through the major eastern fault and the sandy-silty conduits prevents any conclusion about the functioning of the deep system.

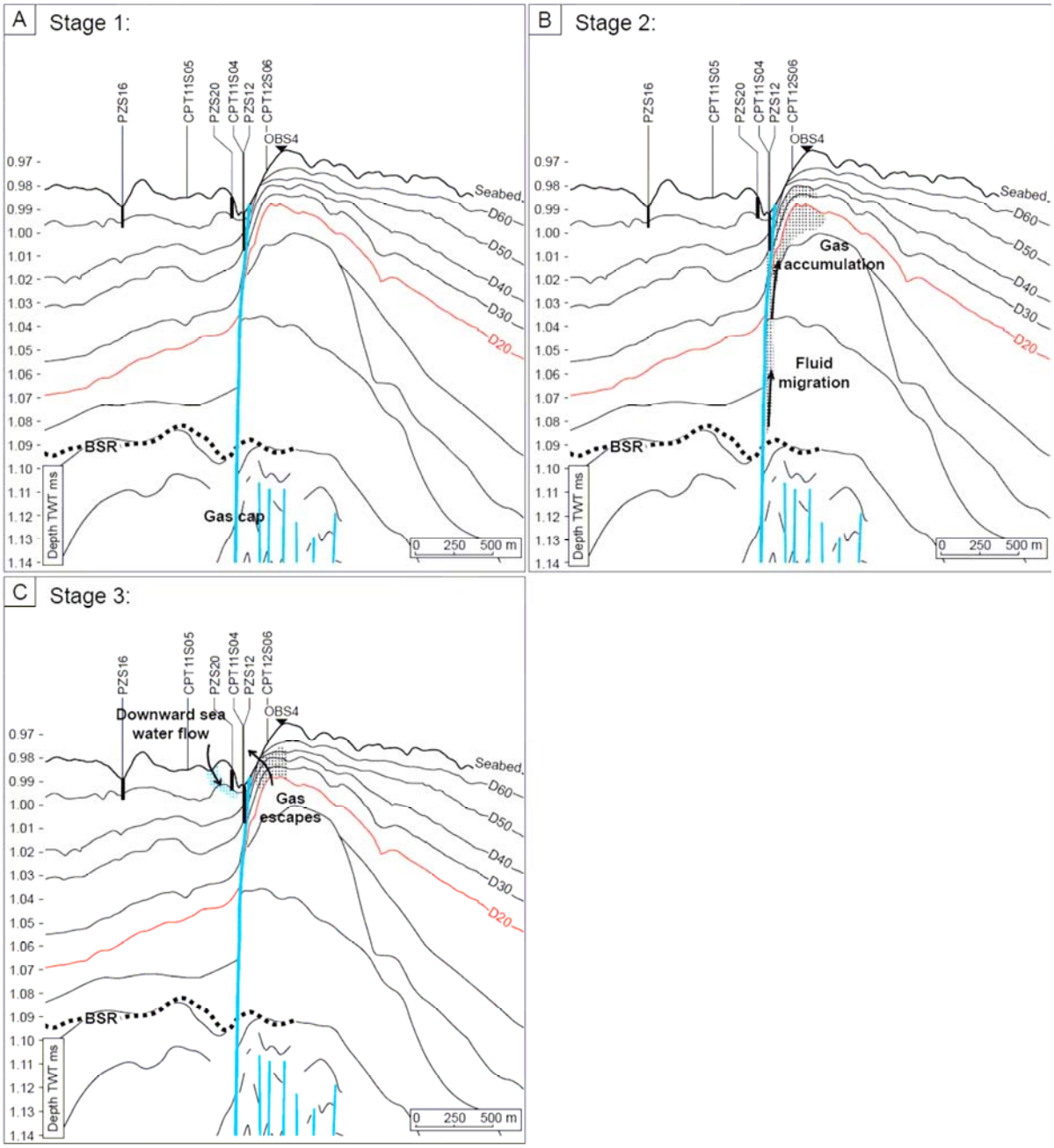

Figure 22. The studied hydrate-fault system operates according to the following three stages: A- Stage 1: slow upward pore fluid (mainly free gas) migration through existing conduits (mainly the major eastern fault) and free gas accumulation within several shallow sandy layers intersecting the major eastern fault; B- Stage 2: pore pressure increases within the sandy-silty layer as evidenced by the data recorded at PZS12; C- Stage 3: hydro-fracturing and fluid pressure dissipation through sporadic degassing events (with some of them being detected at the OBSs), eventually causing an interstitial water circulation through the shallow sandy layers and drawing overlying seawater into the sediment.

8. Conclusions

In summary, seismic, *in situ* geotechnical measurements, pore pressure and temperature data acquired within the present work show that important mechanisms controlling the fluid activities in the studied fault-fluid-hydrate system were: pore fluid (mainly free gas) migration, free gas accumulation and pore pressure increases and hydro-fracturing and fluid pressure dissipation. This last phase can causes an interstitial water circulation through the shallow sandy layers and drawing overlying seawater into the sediment. Free gas circulation, expansion and exsolution were evidenced by the amplification of the tidal effect on the fluctuation of the differential pore pressure due to the increase of the pore fluid compressibility. At shallow depth below the seafloor, gas accumulation and fluid release seem to favor gas hydrate formation above sandy-silty conduits to the south of the major eastern fault while downward flow of seawater prevent the accumulation of gas hydrates to the north of it. Although, micro seismologic data using OBSs allow the detection of individual degassing events, it is not clear whether or not pore pressure accumulations, hydro-fracturing and recorded micro events are directly linked. That is why further experiments, with collocated OBSs and piezometers could provide important insight on the timing of natural degassing processes from the seafloor.

9. Appendix A – Thermal regimes at piezometer locations

Temperature changes occurring in the upper sedimentary layers could be the result of the seafloor temperature fluctuations (diffusion) and/or water flow through high permeable levels (advection through faults and sandy layers). In order to identify the main thermal processes affecting the temperature field for the different studied sites, we consider as a working hypothesis the seafloor temperature changes as the main source of temperature fluctuations. In order to calculate the effect of these seafloor temperature changes on the different deeper temperature sensors, we use the heat equation which is given by:

$$\frac{\partial T}{\partial t} = D_T \frac{\partial^2 T}{\partial x^2} \qquad \text{(A1)}$$

where $T = T(x, t)$ is the temperature variable, D_T is the thermal diffusivity, t is the time ($t \geq 0$) and x ($0 \leq x \leq L$) is the space variable.

Solution to equation (A-1) requires specification of boundary conditions at $x = 0$ and $x = L$, and initial conditions at $t = 0$. For the case of the piezometer measurements, $T(0,t)$ was taken equal to the temperature measured at P1 (upper first sensor), $\frac{\partial T(L,t)}{\partial x}$ was taken equal to the mean temperature gradient (0.078°C/km) measured in the area (Figure 19-b). Equation A-1 is numerically solved by approximating all the derivatives by finite differences and by using an explicit numerical method.

Comparison of the measured and calculated temperatures at the level of the 4 deepest sensors from PZS12, PZS16 and PZS20 shows that for PZS12, the imposed temperature fluctuations diffuse very slowly through the sedimentary column for the three different D_T values ($2\ 10^{-7}$ m²/s, $3\ 10^{-7}$ m²/s and $5\ 10^{-7}$ m²/s) (Figure A - 1). D_T values were derived from the temperature-time decay curves obtained after the PZS12 installation.

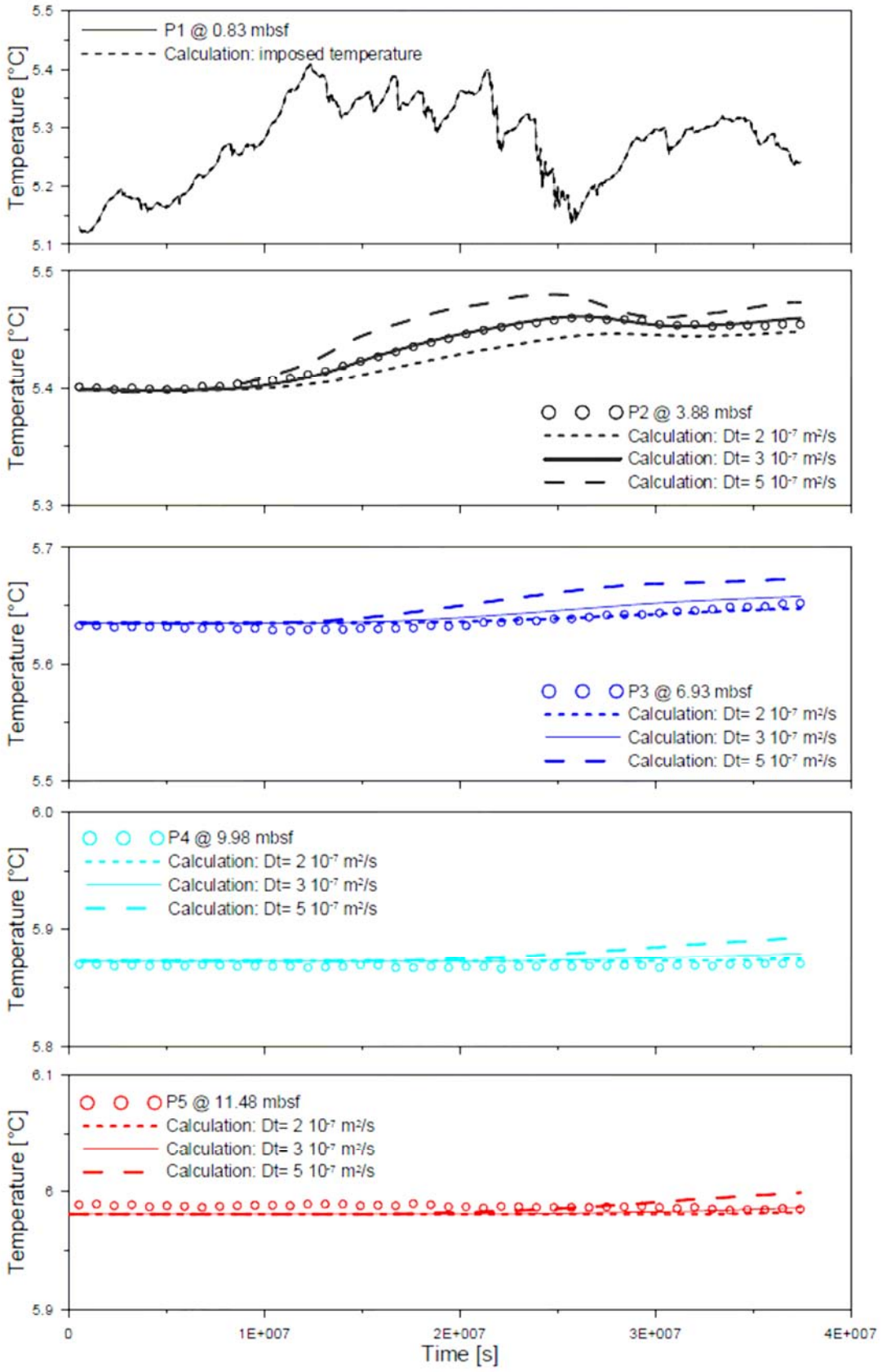

Figure A - 1. PZS12: Temperature changes imposed at the level of the first sensor (at 0.83 mbsf) and calculated temperature for the four other sensor levels and for three thermal diffusivity values. The calculated temperature changes are obtained by solving the heat equation in one dimension.

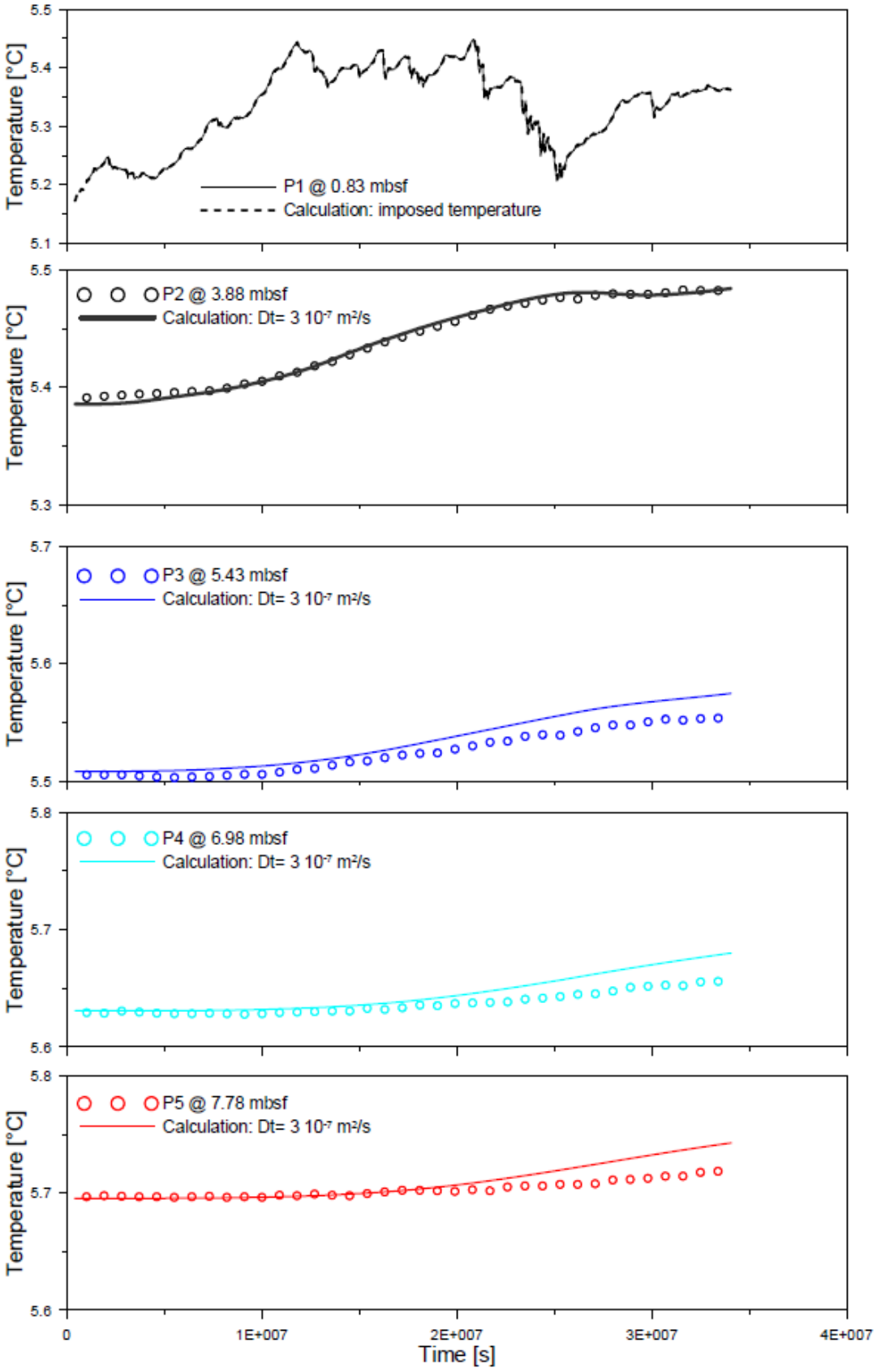

Figure A - 2. PZS20: Temperature changes imposed at the level of the first sensor (at 0.83 mbsf) and calculated temperature for the four other sensor levels and for one thermal diffusivity value. The calculated temperature changes are obtained by solving the heat equation in one dimension.

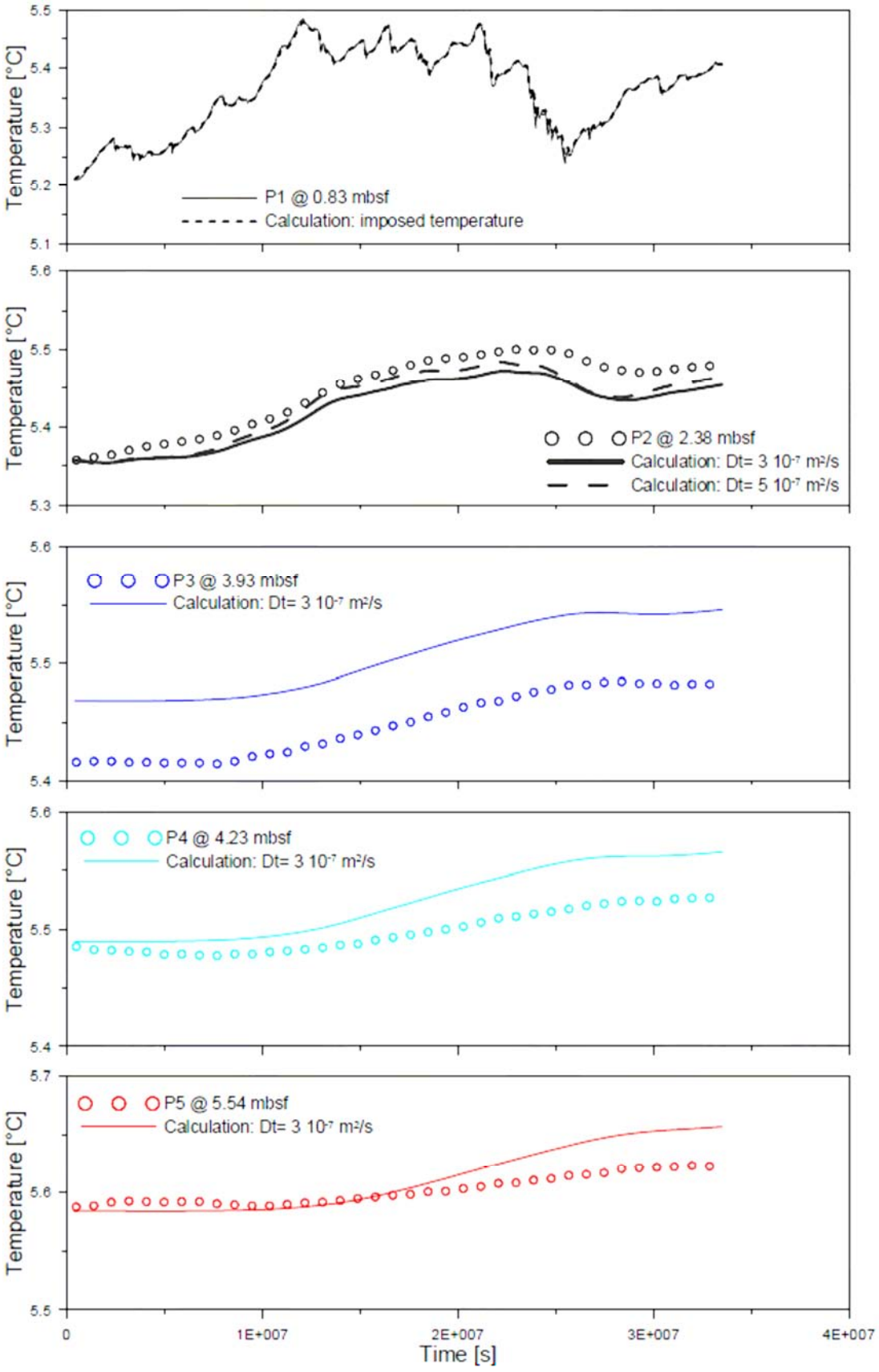

Figure A - 3. PZS16: Temperature changes imposed at the level of the first sensor (at 0.83 mbsf) and calculated temperature for the four other sensor levels and for two thermal diffusivity values. The calculated temperature changes are obtained by solving the heat equation in one dimension.

From PZS12 (Figure A - 1) and PZS20 (Figure A - 2), it is clear that the temperature diffusion is the major process controlling the temperature in the upper sedimentary layers. Indeed, for a thermal diffusivity of 3.10^{-7} m2/s the discrepancies between measured and calculated temperatures are significantly lower than the accuracy of the used temperature sensors (0.05 °C).

For PZS16 (Figure A - 3), the difference between measured and calculated temperatures is comparable to the accuracy of the used temperature sensors (0.05 °C). The highest difference between measured and calculated temperature is localized at P3 and P4 levels showing that if advection is influencing the temperature at the location of PZS16, this may occur laterally through sandy-silty layers and not vertically through faults. Additionally, the PZS16 piezometer was deployed within a pockmark where the suspected presence of free gas and disturbed sediment (Figure 15) could decrease locally but significantly the thermal diffusivity of the medium inducing an important perturbation of the temperature field.

10. Appendix B – Hydraulic regimes at piezometer locations

Important pore pressure perturbations were measured by PZS12 and PZS20 at the base of the piezometer lances. Durations of the pore pressure perturbation for PZS12 and PZS20 were, respectively, around 90 days and 30 days. For the two piezometers, these pore pressure variations were localized at the level of the two lowest sensors and none of the other 8 sensors have measured a significant pore pressure change during these perturbation periods. In order to check the validity of the pore pressure measurements and to evaluate theoretically the expected extension of these localized pore pressure perturbations, a one-dimensional transient fluid flow is used (equation B-1):

$$\frac{\partial U(x,t)}{\partial t} = D_H \frac{\partial^2 U(x,t)}{\partial x^2} \qquad \text{(B1)}$$

where U(x, t) is the pore pressure variable, D_H is the hydraulic diffusivity, t is the time ($t \geq 0$) and x ($0 \leq x \leq L$) is the space variable. D_H values were derived from the pore pressure dissipation curves obtained after piezometers installation (Figure B - 1).

Solution to equation (B-1) requires specification of boundary conditions at x = 0 and x = L, and initial conditions at t = 0. For the case of the piezometer measurements, U(L,t) was taken equal to the pressure measured at P5 and at the seafloor level, U(0,t) was taken equal to zero. Equation B-1 is numerically solved by approximating all the derivatives by finite differences and by using an explicit numerical method.

Figure B - 2 shows the iso-contours of the calculated pore pressure U at site PZS12 using the flow diffusion equation (equation B-1) for a hydraulic diffusivity value of 5.10-8 m^2/s. At 11.48 mbsf, the imposed pore pressure U was taken from the P5 sensor of PZS12 (Figure 8-a). The imposed pore pressure fluctuations diffuse very slowly through the sedimentary column for the considered D_H value. From Figure B - 2, it is clear, that during the 1-year period calculation, only an area of 1 m above the sensor 5 is affected by the pore pressure variations. A similar calculation was carried out to simulate the extension of the pore pressure depression measured by PZS20 at P5. Again, the duration of the pore pressure perturbations measured at the base of PZS20 was not sufficiently important to diffuse and reach the sensor P4.

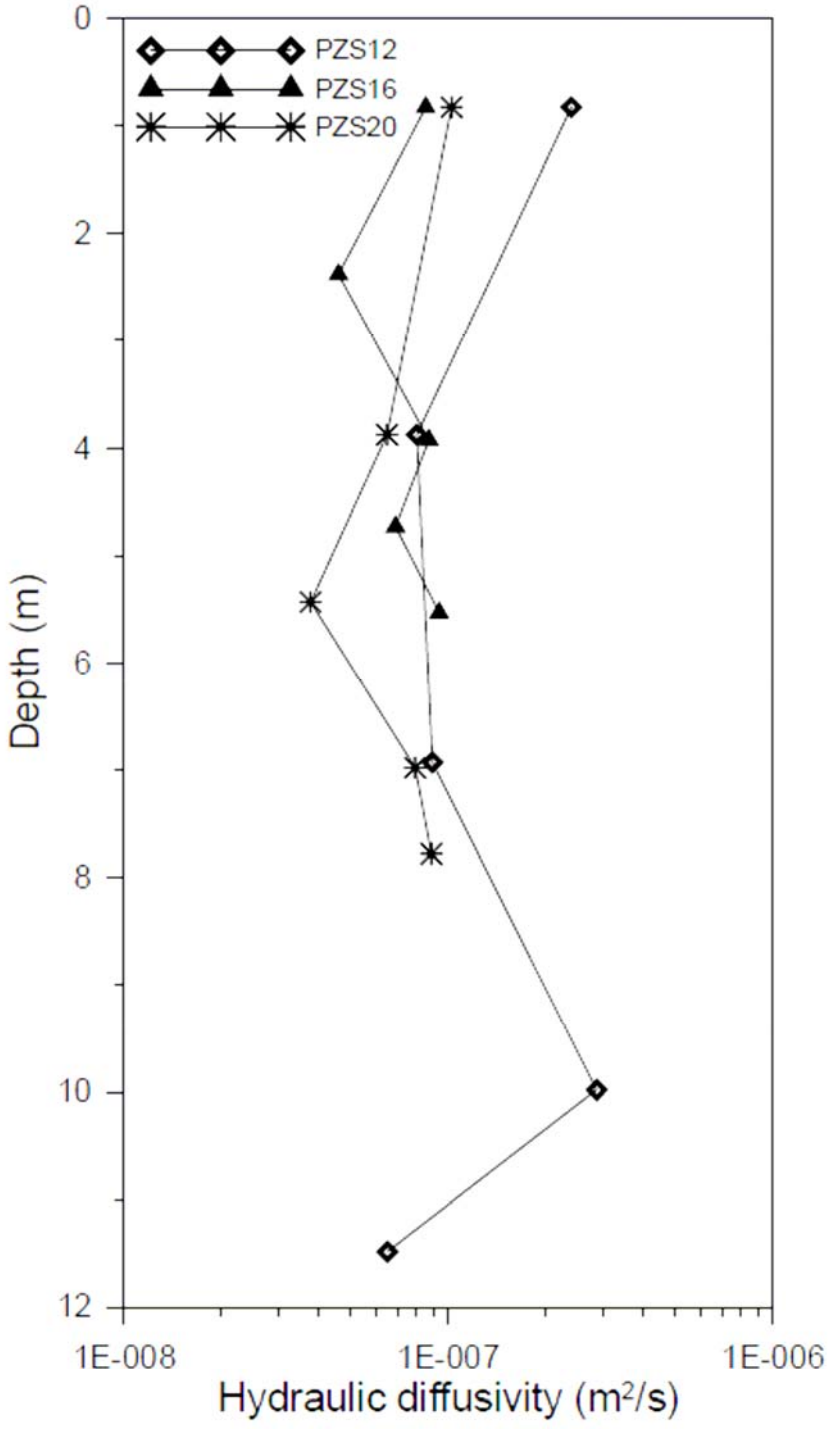

Figure B - 1. Hydraulic diffusivity values from PZS12, PZS16 and PZS20 obtained from pore pressure dissipation curves.

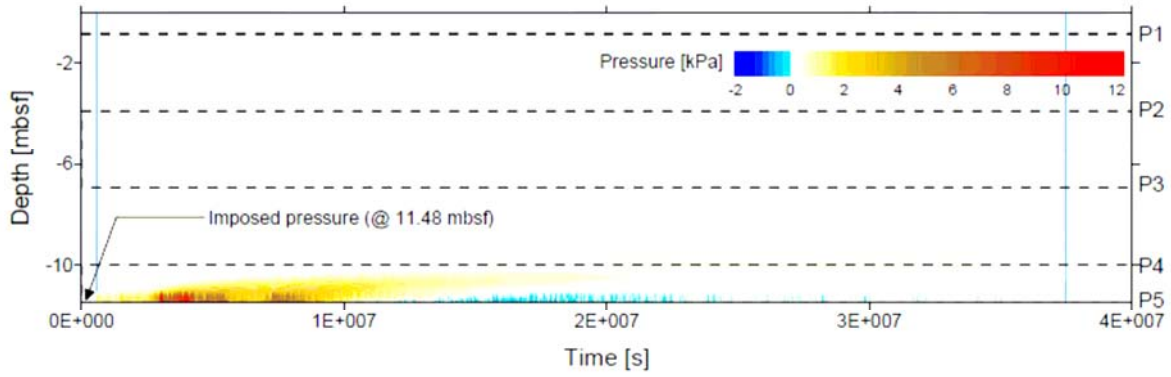

Figure B - 2. PZS12: Pressure perturbation imposed at the level of the last sensor (at 11.48 mbsf) and iso-contours of calculated pore pressure using the diffusion equation for hydraulic diffusivity D_h equal to 5.10^{-8} m^2/s.

11. References

Arnaud, J., D. Rappin, J-P. Dunand, and V. Curinier (2004), High-Density picking for accurate velocity and anisotropy determination, in Proceedings, *74th Ann. Internat. Mtg, Soc. Of Expl. Geophysics, Session RC P2.3*, 1627-1629.

Bayon, G., C. Pierre, J. Etoubleau, M. Voisset, E. Cauquil, T. Marsset, N. Sultan, E. Le Drezen, and Y. Fouquet (2007), Sr/Ca and Mg/Ca ratios in Niger Delta sediments: Implications for authigenic carbonate genesis in cold seep environments, *Marine Geology, 241*(1-4), 93-109.

Bilotti, F., and J. H. Shaw (2005), Deep-water Niger Delta fold and thrust belt modeled as a critical-taper wedge: The influence of elevated basal fluid pressure on structural styles, *Aapg Bulletin, 89(11)*, 1475-1491.

Boe, R., L. Rise, and D. Ottesen (1998), Elongate depressions on the southern slope of the Nowegian trench (Skagerrak) : morphology and evolution, *Marine Geology, 146*, 191-203.

Brooks, J. M., W. R. Bryant, B. B. Bernard, and N. R. Cameron (2000), The nature of gas hydrates on the Nigerian continental slope, *Gas Hydrates: Challenges for the Future, 912*, 76-93.

Cohen, H. A., and K. McClay (1996), Sedimentation and shale tectonics of the northwestern Niger Delta front, *Marine and Petroleum Geology, 13*(3), 313-328.

Corredor, F., J. H. Shaw, and F. Bilotti (2005), Structural styles in the deep-water fold and thrust belts of the Niger Delta, *Aapg Bulletin, 89*(6), 753-780.

Damuth, J. E. (1994), Neogene gravity tectonics and depositional processes on the deep Niger Delta continental margins, *Marine and Petroleum Geology, 11*(3), 320-346.

Deptuck, M. E., G. S. Steffens, M. Barton, and C. Pirmez (2003), Architecture and evolution of upper fan channel-belts on the Niger Delta slope and in the Arabian Sea, *Marine and Petroleum Geology, 20*(6-8), 649-676.

Doust, H., and E. Omatsola E., (1990), Niger Delta in divergent/passive margin basins, in J. D. Edwards and P. A. Santogrossi, eds., *Aapg Memoir, 48*, 201-238.

Georges, R.A, and E. Cauquil (2007), AUV Ultrahigh-Resolution 3D Seismic Technique for Detailed Subsurface Investigations, *Offshore Technology Conference*, Houston, OTC18784.

Graue, K. (2000), Mud volcanoes in deepwater Nigeria, *Marine and Petroleum Geology*, *17*, 959-974.

Haskell, N., S. Nissen, M. Hughes, J. Grindhaug, S. Dhanani, R. Heath, J. Kantorowicz, L. Antrim, M. Cubanski, R. Nataraj, M. Schilly, and S. Wigger (1999), Delineation of geologic drilling hazards using 3-D seismic attributes, *The Leading Edge*, Tulsa, 373–382.

Hovland, M., J. W. Gallagher, M. B. Clennell, and K. Lekvam (1997), Gas hydrate and free gas volumes in marine sediments: Example from the Niger Delta front, *Marine and Petroleum Geology*, *14*(3), 245-255.

Lunne, T., P.K. Robertson, and J.J.M Powell (1997), *Cone Penetration Testing in Geotechnical Practice*, Spon Press, London, 312.

Mackay, M. E., R. D. Jarrard, G. K. Westbrook, and R. D. Hyndman (1994), Origin of bottom- simulating reflectors: Geophysical evidence from the Cascadia accretionary prism, *Geology*, *22*(5), 459-462.

Marsset, T., B. Marsset, S. Ker, Y. Thomas, and Y. Le Gall (2010), High and very high resolution deep-towed seismic system: Performance and examples from deep water Geohazard studies, *Deep-Sea Research Part I-Oceanographic Research Papers*, *57*(4), 628-637.

Morley, C. K., and G. Guerin (1996), Comparison of gravity-driven deformation styles and behavior associated with mobile shales and salt, *Tectonics*, *15*(6), 1154-1170.

Papatheodorou, G., T. Hasiotis, and G. Ferentinos (1993), Gas-charged sediments in the Aegean and Ionian Seas, Greece, *Marine Geology*, *112*(1-4), 171-184.

Sultan, N., M. Voisset, T. Marsset, A. M. Vernant, E. Cauquil, J. L. Colliat, and V. Curinier (2007), Detection of free gas and gas hydrate based on 3D seismic data and cone penetration testing: An example from the Nigerian Continental Slope, *Marine Geology*, *240*(1-4), 235-255.

Sultan, N., B. Marsset, S. Ker, T. Marsset, M. Voisset, A. M. Vernant, G. Bayon, E. Cauquil, J. Adamy, J. L. Colliat, and D. Drapeau (2010), Hydrate dissolution as a potential mechanism for pockmark formation in the Niger delta, Journal of Geophysical Research-Solid Earth, 115., B08101, doi:10.1029/2010JB007453.

Sultan, N., S. Garziglia, and J.-L. Colliat (2011), Gas hydrate occurrences and seafloor deformation: investigation of strain-softening of gas-hydrate bearing sediments and its consequence in terms of submarine slope instabilities, *Offshore Technology Conference*, Houston, OTC21294.

Tary, J. B., L. Géli, C. Guennou, P. Henry, N. Sultan, N. Çagatay, and V. Vidal (2011), Micro-events produced by gas migration and expulsion at the seabed: a study based on sea bottom recordings from the Sea of Marmara, submitted (April 2011).

Tryon, M. D., K. M. Brown, M. E. Torres, A. M. Trehu, J. McManus, and R. W. Collier (1999), Measurements of transience and downward fluid flow near episodic methane gas vents, Hydrate Ridge, Cascadia, *Geology*, *27*(12), 1075-1078.

Wiener, R.W., M.G. Mann, D.M. Advocate, M.T. Angelich, and S.A. Barboza (2006), Mobile Shale Characteristics and Impact on Structural and Stratigraphic Evolution of the Niger Delta, *AAPG/GSTT* Hedberg conference, Port of Spain, Trinidad & Tobago.

Zhang, C., X. N. Xie, T. Jiang, and X. F. Liu (2006), Hydrocarbon migration and accumulation along a long-term growth fault: Example from the BZ25-1 oilfield of Bohai basin, eastern China, *Journal of Geochemical Exploration*, *89*(1-3), 460-464.

Appendix B. Shipboard CHIRP data

Shipboard chirp profiles have been acquired during Marmarascarps (September-November 2002), MarNaut (May-June 2007), and Marmesonet (November-December 2009) cruises in the Sea of Marmara. These high-resolution reflection profiles are used to image the upper sedimentary layers, up to about 100 m bsf (below sea floor) depending on the physical properties of the sediments. Seismic reflections depend on layer's impedance, which, in turn, depend on lithology, porosity, pore fluid and pressure. With these data, the main objectives are to study the sediment's structure, highlight fault escarpments and determine the gas distribution in the subseafloor sediments of the Sea of Marmara.
Data acquisition and treatments are described in SUBOP v2 software manual (Phelion and Tonck, 2009).

B.1. Marmesonet chirp profiles

A total of 304 chirp profiles (~2300 km) were collected during the Marmesonet cruise (~1815 km during Leg 1 and ~485 km during Leg 2), along with EM302 recordings.
The quality of the chirp data is good, especially in the basins, where the penetration is about 60-90 ms twtt. Almost all the Marmara Shear zone was systematically covered with chirp profiling to improve fault geometry and gas distribution knowledge.

Marmesonet cruise chirp profiles distribution:
Leg 1 (Nov. 4 – Nov. 25, 2009): 243 profiles (Fig. B1)

Cinarcik Basin: 58 profiles
Southern shelf: 26 profiles
Kumburgaz Basin: 30 profiles
Central High: 18 profiles
Central Basin: 36 profiles
Western High: 41 profiles
Tekirdag Basin: 34 profiles

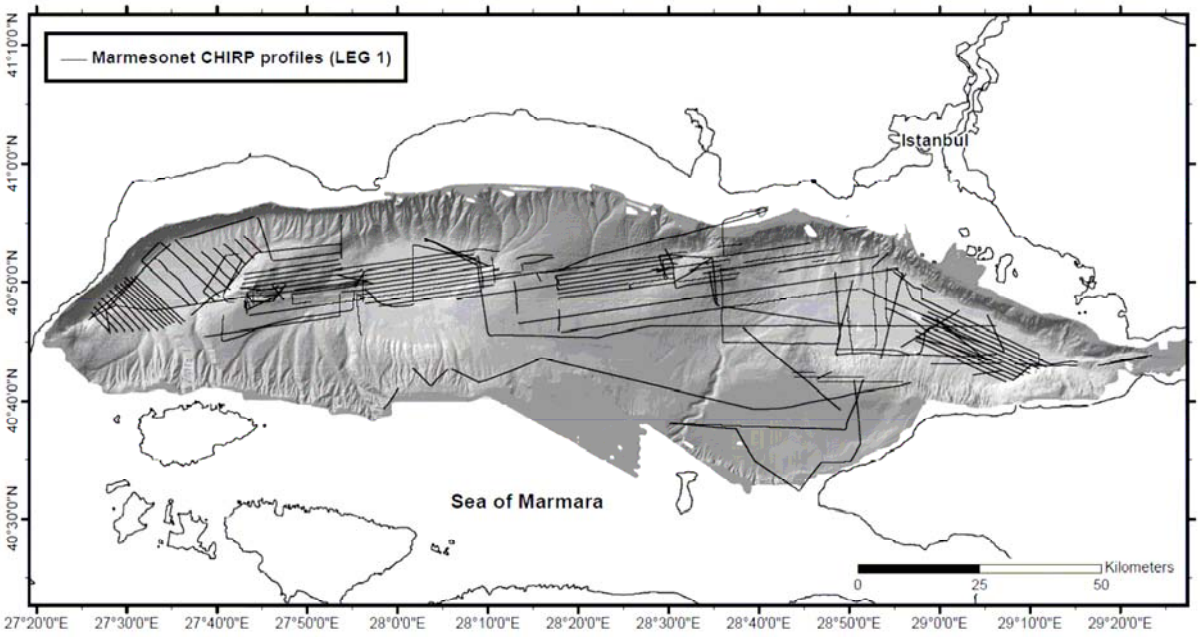

Fig. B1. Marmesonet cruise, Leg 1: chirp profiles distribution.

Leg 2 (Nov. 29 – Dec. 10, 2009): 61 profiles (Fig. B2)

Cinarcik Basin: 21 profiles
Southern shelf: 4 profiles
Kumburgaz Basin: 3 profiles
Central High: 10 profiles
Central Basin: 7 profiles
Western High: 9 profiles
Tekirdag Basin: 7 profiles

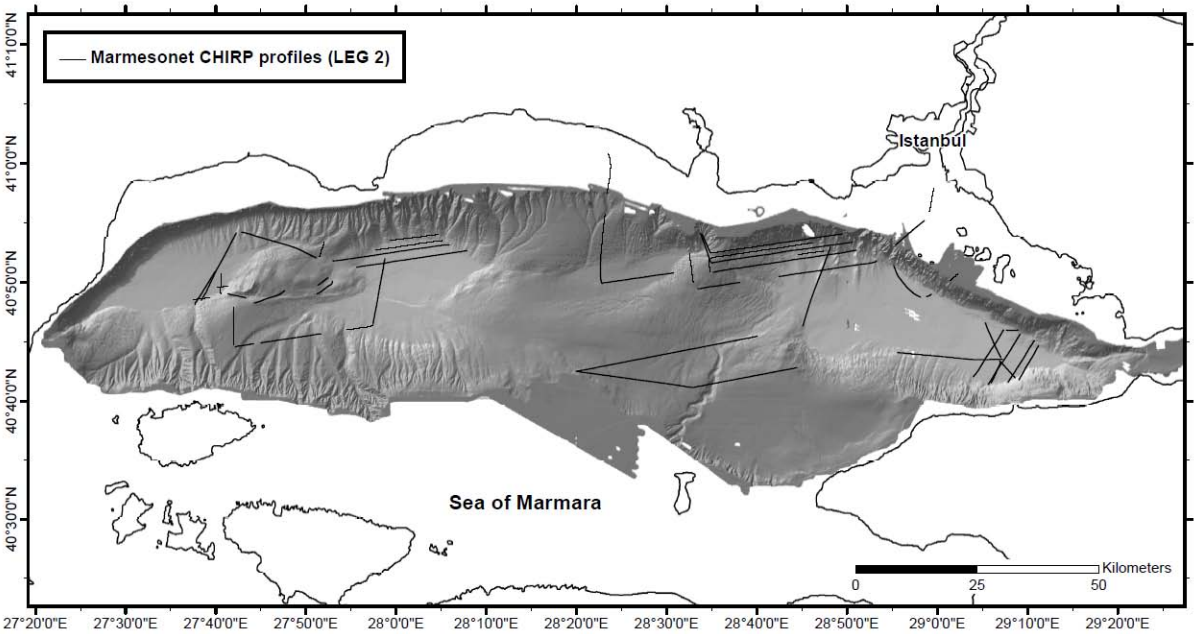

Fig. B2. Marmesonet cruise, Leg 2: chirp profiles distribution.

B.2. Characteristic patterns on CHIRP profiles

B.2.1. "Heterogeneous masses" and landslides

Some profiles exhibit transparent patches, either on the sub-surface or at depth. When located on the slope foot, these transparent patches can be interpreted as landslides.

An example is shown at the foot of the eastern slope of the Tekirdag Basin, which exhibit a transparent patch that is probably a landslide (Fig. B3 and B4). This "heterogeneous mass" has a lenticular shape typical of landslides, and a volume around 5.8 millions of m^3 (half of: 1150 m x 1350 m x 0.01 s twt at 1.5 km/s).

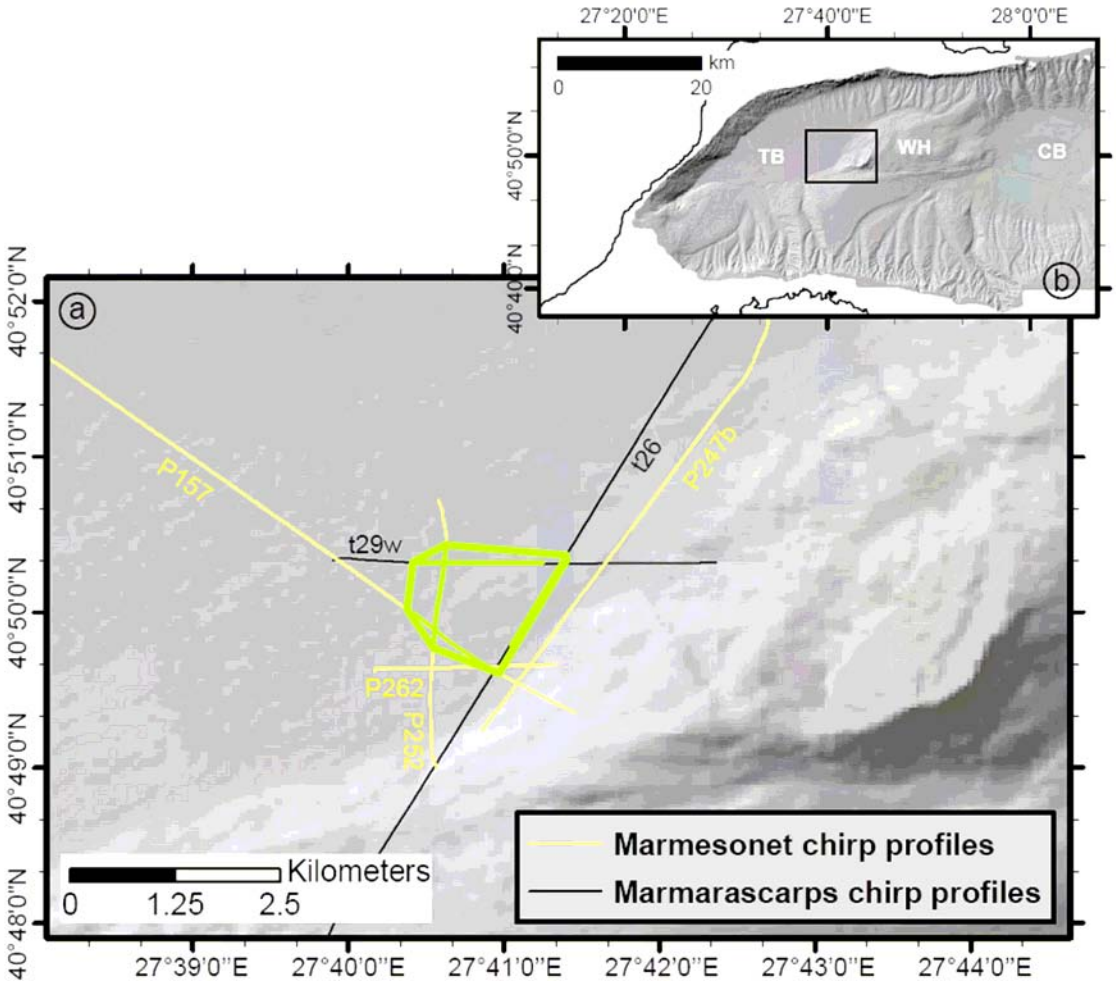

Fig. B3. a) Location and size of the landslide (bordered by the green line) in the Tekirdag Basin inferred from CHIRP profiles (Fig. B4). The Marmesonet CHIRP profiles are indicated by the yellow lines and the Marmarascarps CHIRP profiles by the black lines. Where present, the landslide extension on CHIRP profiles is shown by the green lines. b) Map of the Sea of Marmara showing the location of the area given in a). TB, Tekirdag Basin; WH, Western High; CB, Central Basin.

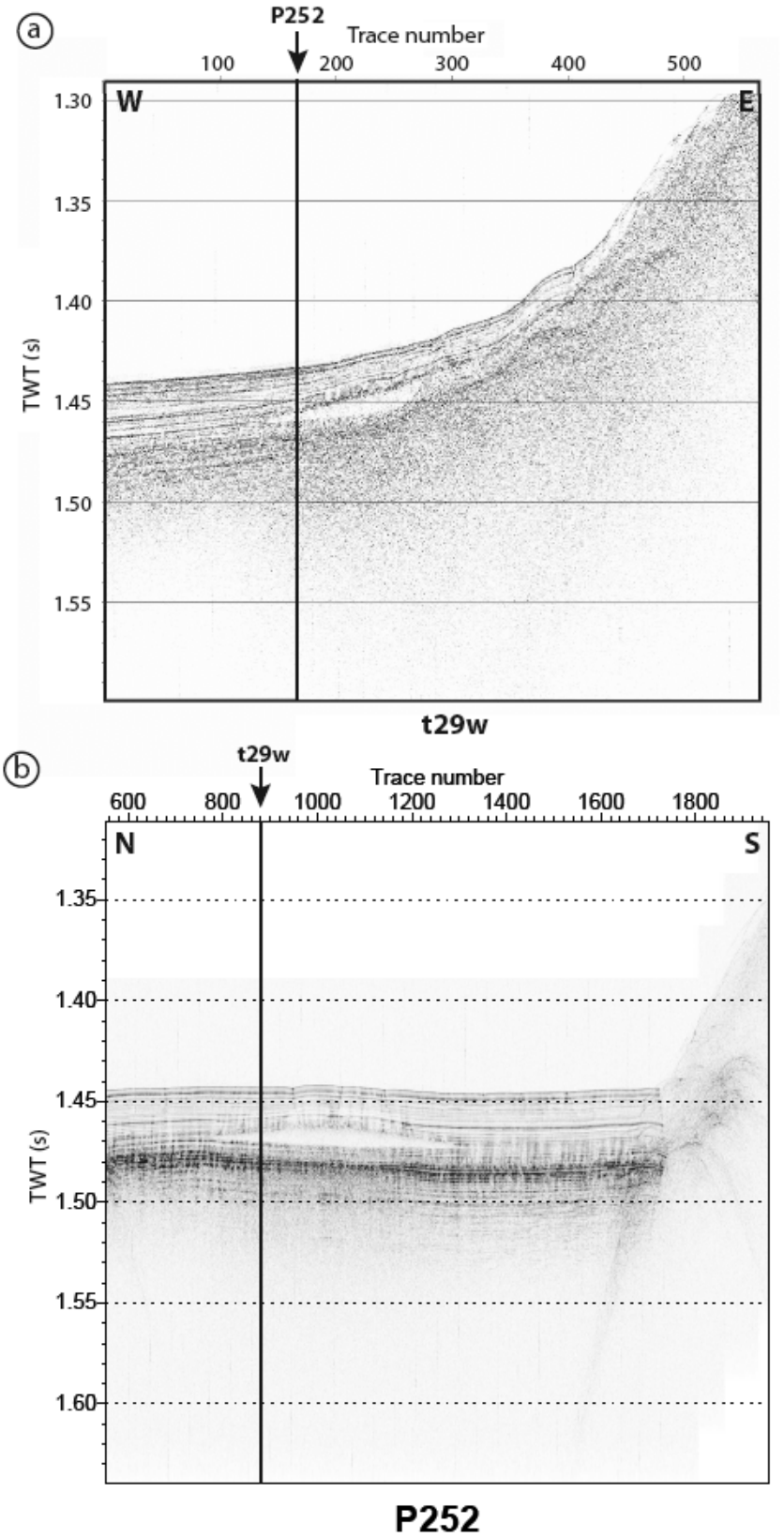

Fig. B4. a) Chirp profile t29w acquired during the Marmarascarps cruise (TWT: Two Way Travel time, in seconds). b) Chirp profile P252 acquired during the Marmesonet cruise. The profile's location is given in Fig. B3. The black vertical lines correspond to the intersection between the two profiles.

The landslide is buried under 0.025 s twtt of sediments (~19 m with a velocity of 1.5 km/s), but is above a strong black reflector interpreted as the lacustrine-marine transition dated around 12 kyr BP [*Çagatay et al.,* 2000, 2003]. With an average sedimentation rate of 2 mm/yr, compatible with the date of the lacustrine to marine transition, the age of the landslide is about 9.4 kyr BP. Two mains reasons could have promoted the triggering of this landslide. First, the recent eustatic change brought an important amount of sediments, providing the material to slide. This slow increase of the sea level come-along with more "high-frequency" eustatic variations, which could have weaken the superficial sedimentary cover. Secondly this area is frequently prone to strong earthquakes that might have triggered the landslide, which, in turn, may have triggered large tsunamis in the Sea of Marmara [*Görür and Çagatay,* 2010].

B.2.2. A transparent layer: the "homogenite"

The chirp profiles crossing the Central Basin and the western part of the Çinarcik Basin show an acoustically transparent layer (Fig. B5). This layer is buried under ~35 ms twt of sediments (26 m at 1.5 km/s) and its thickness is up to 10-15 ms twt (8-11 m at 1.5 km/s) in the centre of the Central Basin. This homogeneous layer has been interpreted as a homogenite by *Beck et al.* [2007], following the concept of *Kastens and Cita* [1981]. The homogenite differs from landslides by its larger extension relatively to the basin and hence the way it was deposited. The homogenite is present mainly in the Central Basin and its thickness increase with increasing depth.

The cores retrieved during the MARMARACORE cruise (2001) with R/V Marion-Dufresne allowed *Beck et al.* [2007] to describe the sediment characteristics of the homogenite. The homogenite is composed by very fine-grained allochtonous sediments transported and deposited as suspended load. The depositional mechanism could be either a high velocity turbidity current reflected on the slope of the basin ("contained turbidites", *Pickering and Hiscott,* 1985), or an oscillatory movement of the whole mass of water (like tsunami or seiche effects) activated by a sudden change in the sea-bottom topography.

As mentioned above for the landslide in the Tekirdag Basin, the same combination of factors, i. e. an important amount of terrigenous sediment available and a major earthquake, could led to the formation of the homogenite.

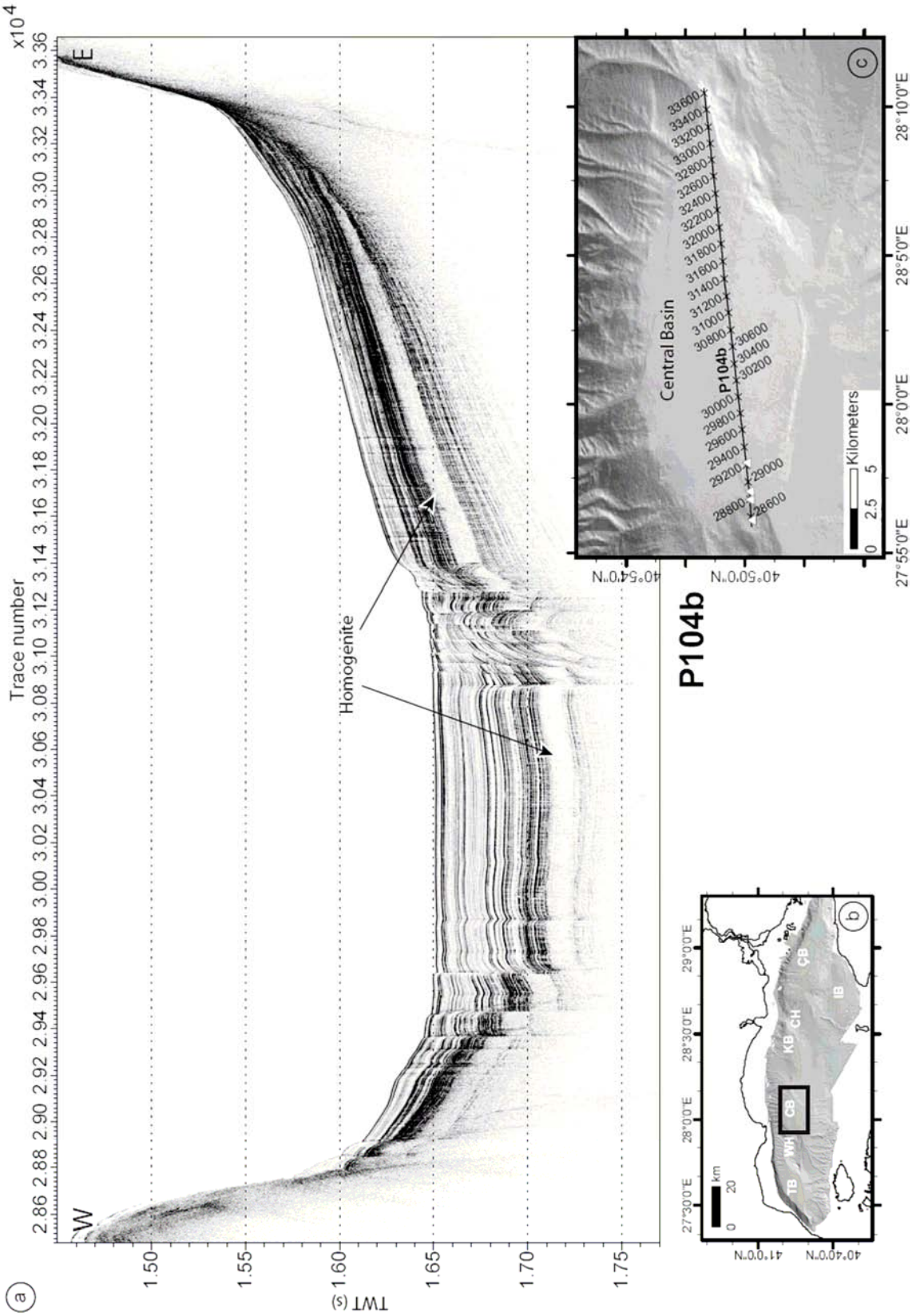

Fig. B5. a) Marmesonet cruise, chirp profile P104b in the Central Basin (TWT, Two Way Travel time in seconds). The homogenite is indicated by black arrows. b) Map of the Sea of Marmara showing the location of the area given in c). TB, Tekirdag Basin; WH, Western High; CB, Central Basin; KB, Kumburgaz Basin; CH, Central High; ÇB, Çinarcik Basin; IB, Imrali Basin. c) Ship's track of the P104b profile in a). Shotpoint numbers are indicated. Acoustic anomalies detected by the EM302 echosounder in the water column are indicated by white triangles.

B.2.3. Gas signature

Gas in sediments will typically induce two types of signatures on CHIRP profiles. First, an important amount of gas will decrease the density as well as the wave's velocity in sediments, involving a high, negative amplitude reflector in the CHIRP data (Fig. B6). Secondly, free gas bubbles strongly attenuate and scatter acoustic signals, masking the sedimentary horizons, this effect is called "acoustic blanking".

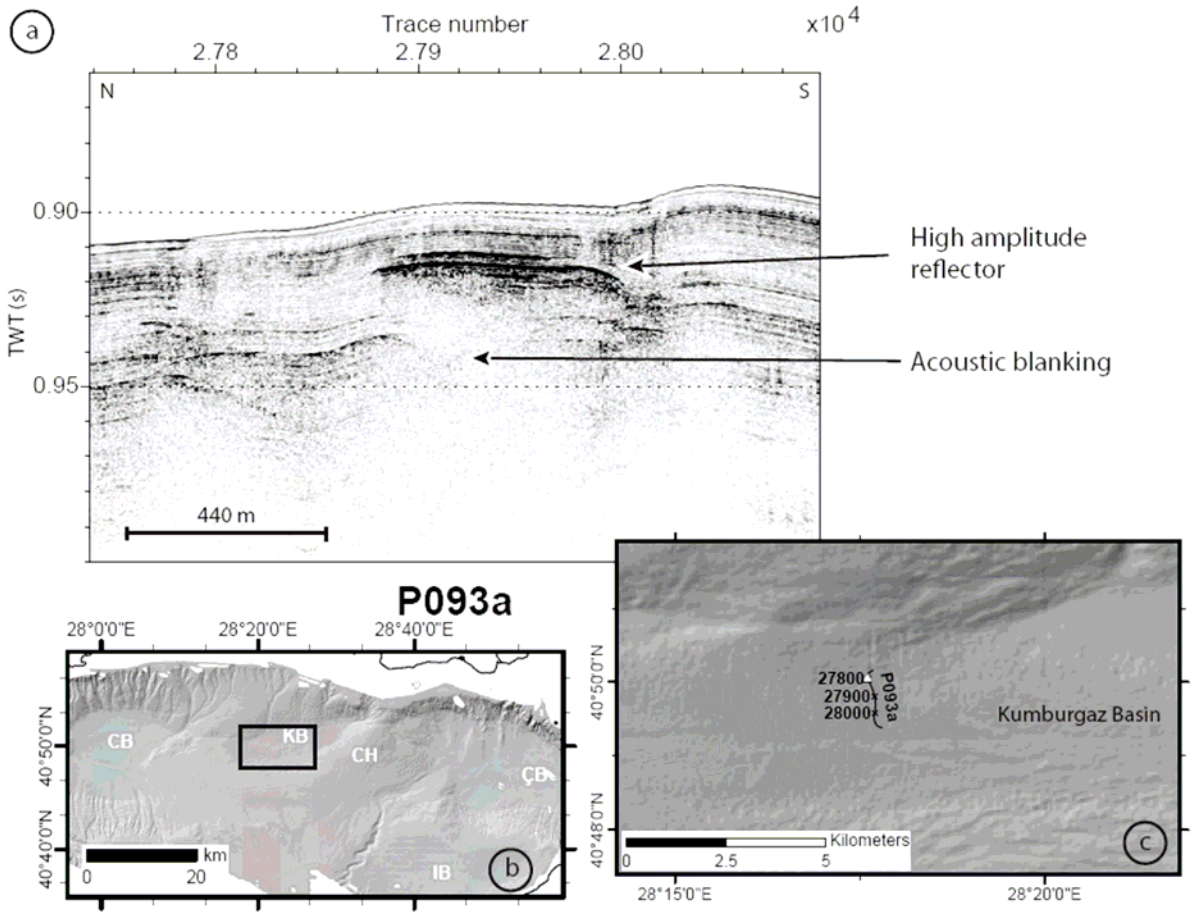

Fig. B6. a) Marmesonet cruise, chirp profile P093a in the Kumburgaz Basin (TWT, Two Way Travel time in seconds). Gas evidence is highlighted by a high amplitude reflector followed by an acoustic blanking of the sedimentary layers. b) Map of the Sea of Marmara showing the location of the area given in c). TB, Tekirdag Basin; WH, Western High; CB, Central Basin; KB, Kumburgaz Basin; CH, Central High; ÇB, Çinarcik Basin; IB, Imrali Basin. c) Ship's track of the P093a profile in a). Shotpoint numbers are indicated. Acoustic anomalies detected by the EM302 echosounder in the water column are indicated by white triangles.

However, this effect has to be interpreted with caution. If vertical acoustic blanking is generally interpreted as an indicator of gas within the sediments, debris flow and under-compacted clay rich sediments [*Papatheodorou et al.*, 1993; *Bouriak et al.*, 2000] also appear as transparent acoustic layer (Fig. B4 and B5). In addition, localized high amplitude reflectors can be generated by interferences with side echoes or high density materials like carbonate crusts and turbidites.

As the distribution of the gas plumes detected in the water column (Fig. 2.20) indicates the widespread presence of gas in the Sea of Marmara seafloor, besides any consideration on the origin of fluids, typical signatures like the one shown in Fig. B6 are preferentially interpreted here as an evidence of gas trapped in the sediments.

B.3. Gas distribution in the Sea of Marmara from Marmesonet CHIRP profiles

During the Marmesonet cruise, the deeper part of the Sea of Marmara has been fully covered with CHIRP profiles (Fig. B1 and B2), from the Dardanelle strait to the Izmit Gulf and from the Bosphorous strait to the Imrali Basin.

In the following, a distinction has been made between gas evidences that we considered as "sure" (Fig. B6) and the ones we considered as "probable (Fig. B7 and B8).

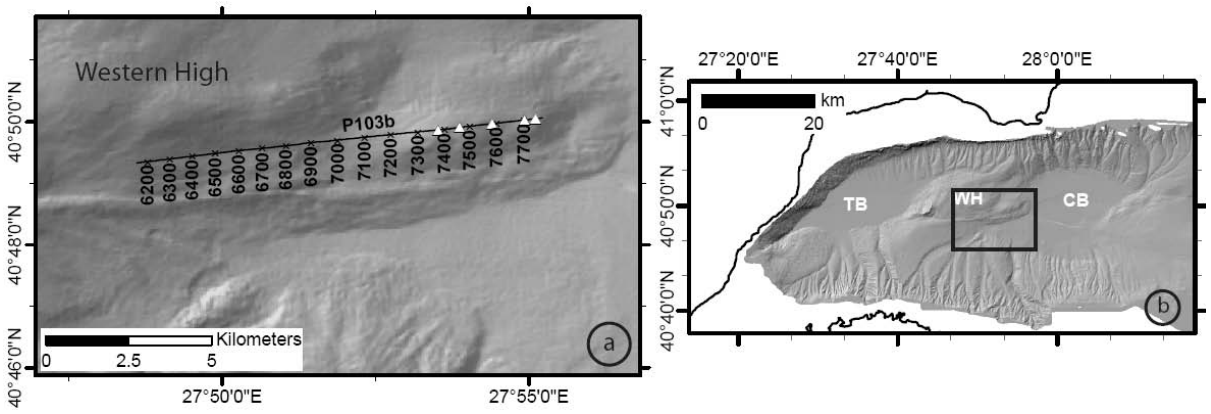

Fig. B7. a) Marmesonet cruise, ship's track of the chirp profile P103b in the Kumburgaz Basin (Fig. B8). Shotpoint numbers are indicated. Acoustic anomalies detected by the EM302 echosounder in the water column are indicated by white triangles. b) Map of the Sea of Marmara showing the location of the area given in a). TB, Tekirdag Basin; WH, Western High; CB, Central Basin; KB, Kumburgaz Basin; CH, Central High; ÇB, Çinarcik Basin; IB, Imrali Basin.

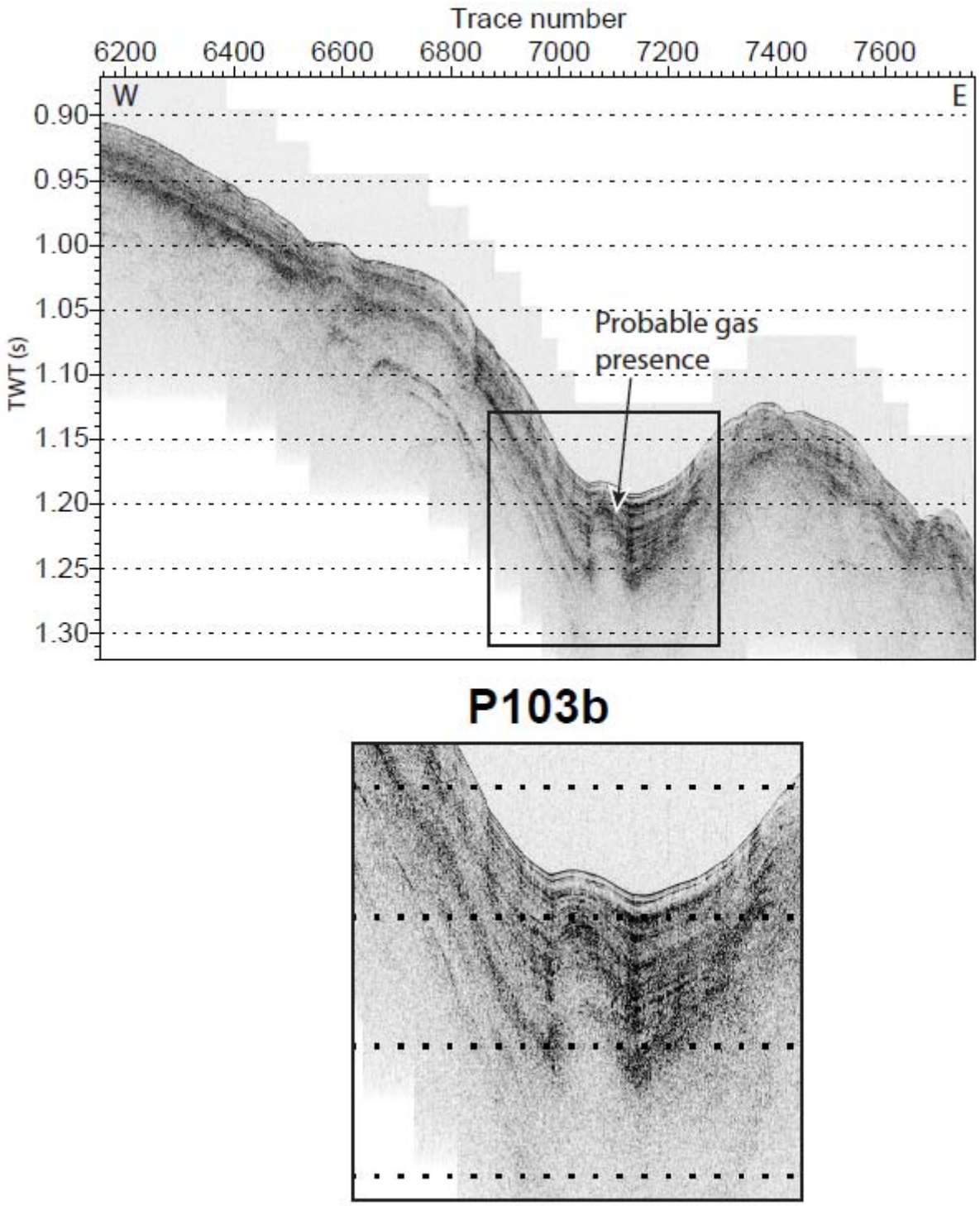

Fig. B8. a) Marmesonet cruise, chirp profile P103b in the Kumburgaz Basin (TWT, Two Way Travel time in seconds, see Fig. B7 for location). A probable gas evidence is indicated by the black arrow. The black rectangle indicates the location of the zoom presented below the profile.

A total of 304 profiles from the Marmesonet cruise have been examined, and 324 evidences were picked (Fig. 2.21).

Gas occurrence is more common in basins than on highs, because sediment deposits are thicker but also because gas is easier to detect within basins, where sedimentary horizons are well-defined, than on highs or in slopes, where wave's scattering is important and penetration limited.

- The Tekirdag Basin

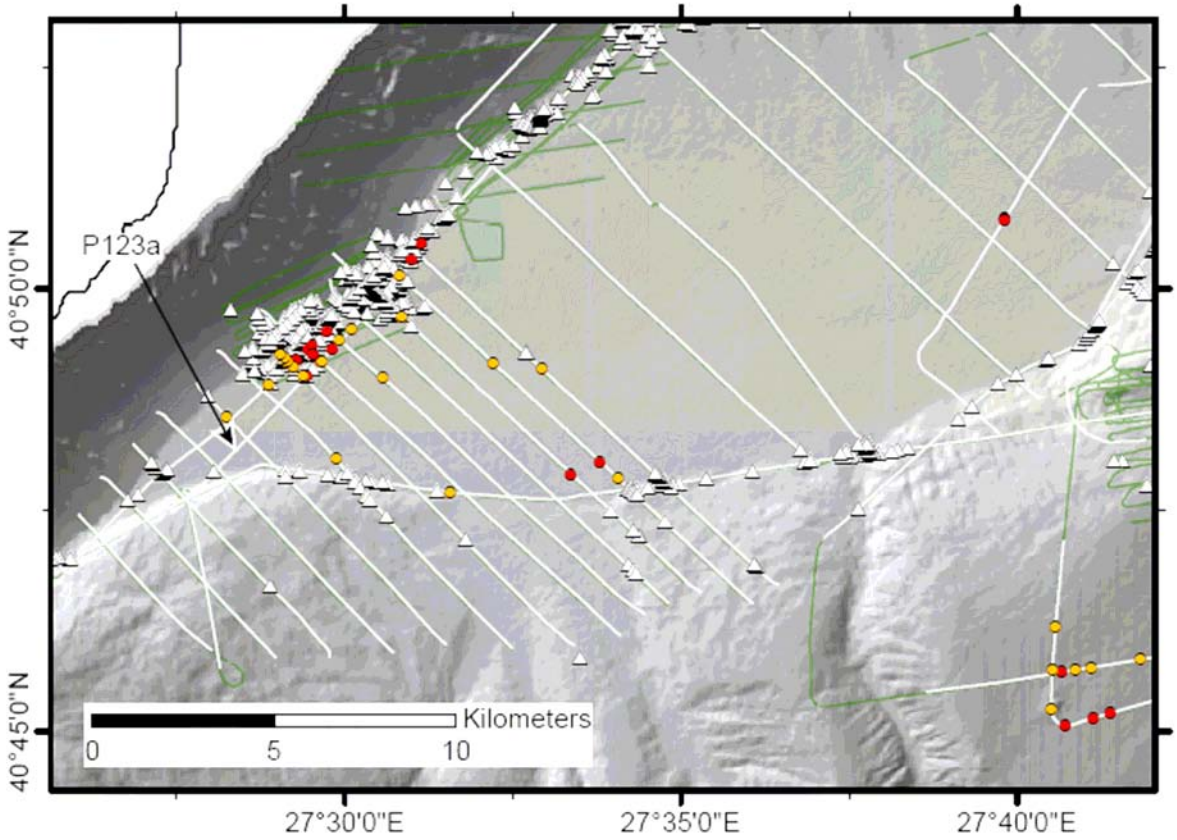

Fig. B9. Tekirdag Basin. Distribution of gas evidences in sediments from CHIRP profiles and acoustic anomalies in the water column (white triangles) detected by the Simrad EM302 multibeam system during the Marmesonet cruise, leg 1, in the Sea of Marmara. Gas evidences that we considered as "sure" are indicated by red dots while the ones we considered as "probable" are indicated by orange dots. Green and gray lines correspond to EM302 lines and CHIRP profiles acquired during the Marmesonet cruise leg 1, respectively.

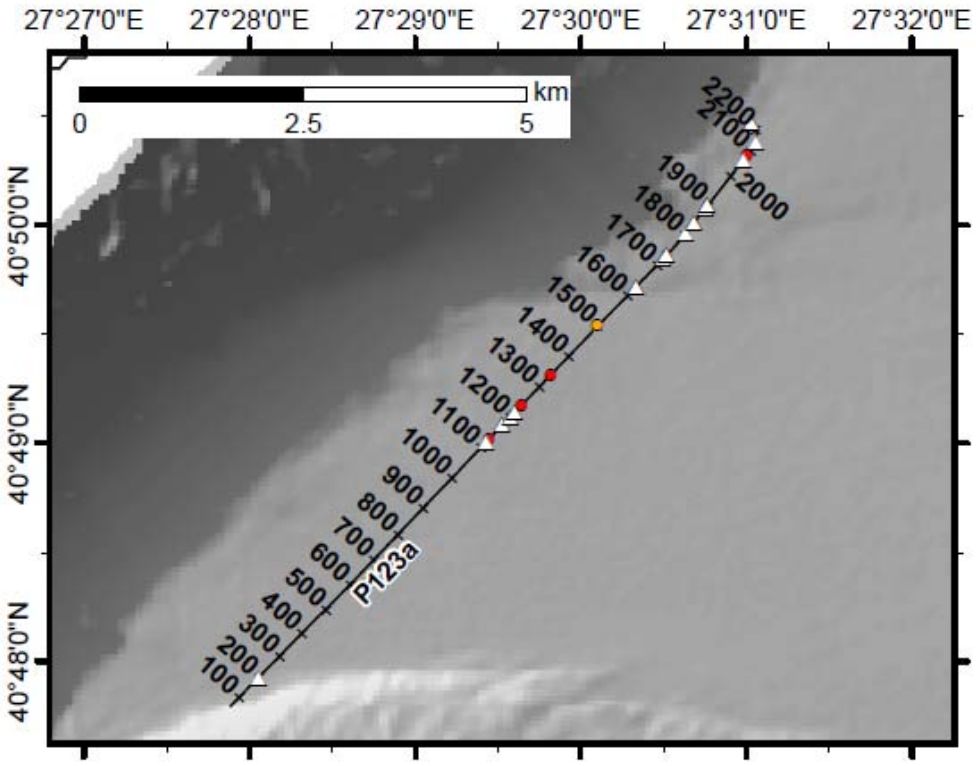

Fig. B10. Tekirdag Basin, chirp profile P123a. Distribution of gas evidences in sediments and acoustic anomalies in the water column (white triangles) detected by the Simrad EM302 multibeam system during the Marmesonet cruise, leg 1, in the Sea of Marmara. The symbology is the same as Fig. B9.

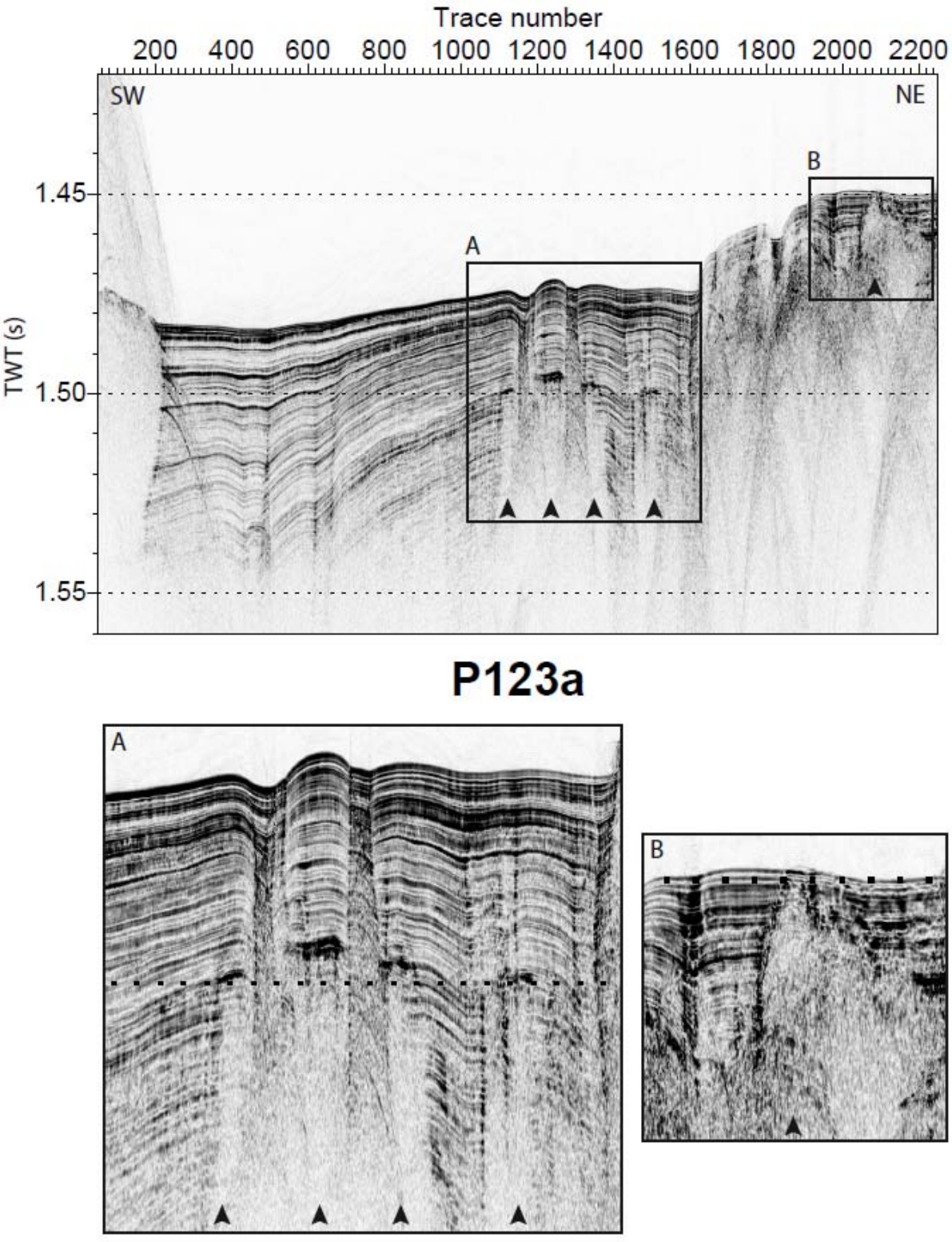

Fig. B11. a) Marmesonet cruise, chirp profile P123a in the Tekirdag Basin (TWT, Two Way Travel time in seconds). Gas evidences, corresponding to red and orange dots in Fig. B10, are indicated by black arrows. Black rectangles indicate the location of the zooms presented below the profile.

- The Central Basin

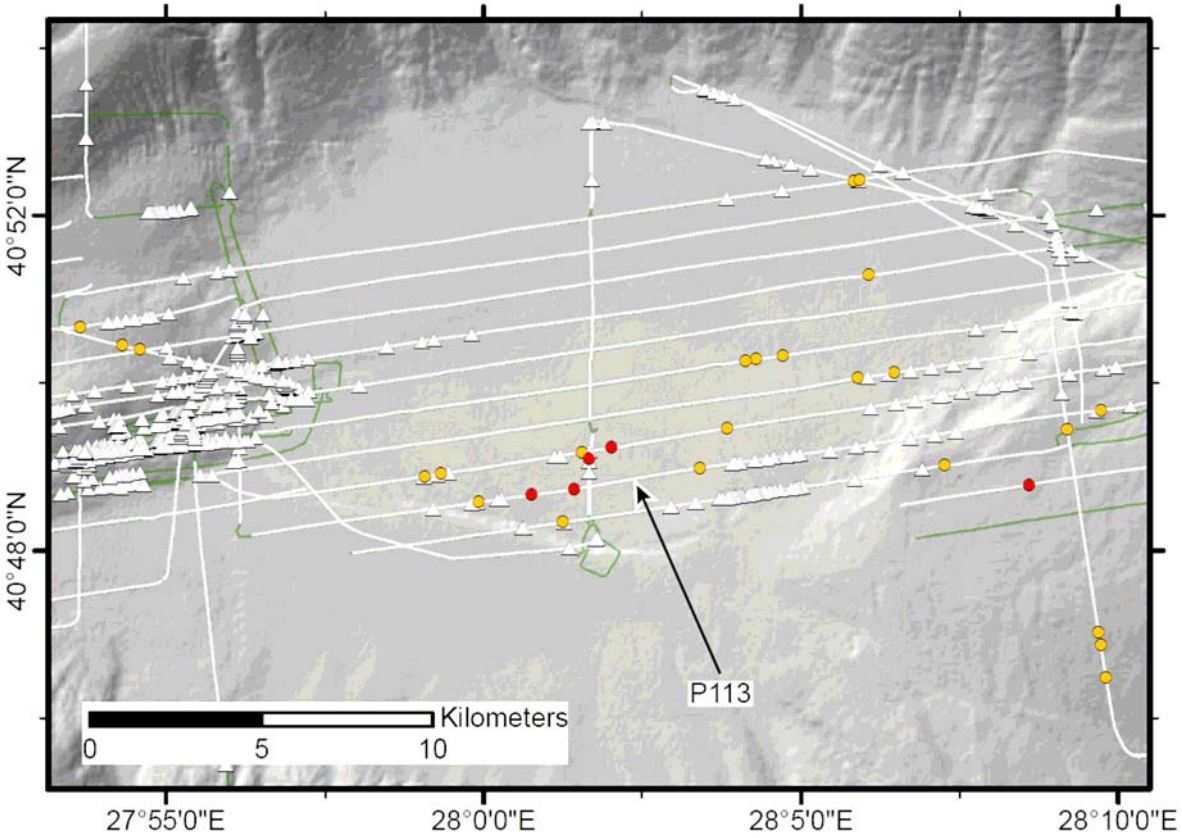

Fig. B12. Central Basin. Distribution of gas evidences in sediments from CHIRP profiles and acoustic anomalies in the water column (white triangles) detected by the Simrad EM302 multibeam system during the Marmesonet cruise, leg 1, in the Sea of Marmara. The symbology is the same as Fig. B9.

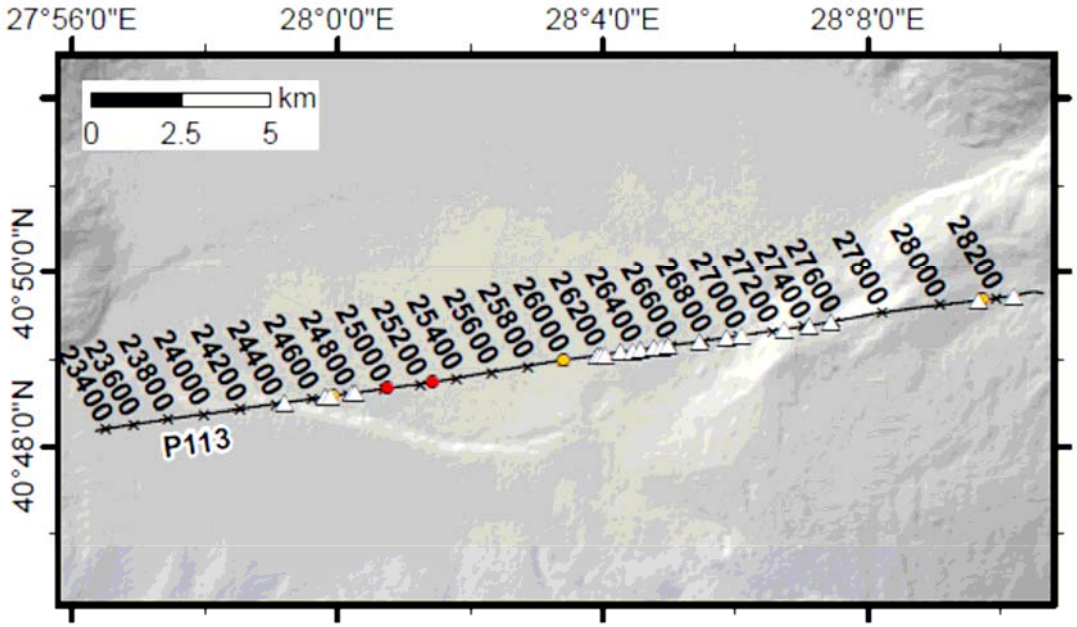

Fig. B13. Central Basin, chirp profile P113. Distribution of gas evidences in sediments and acoustic anomalies in the water column (white triangles) detected by the Simrad EM302 multibeam system during the Marmesonet cruise, leg 1, in the Sea of Marmara. The symbology is the same as Fig. B9.

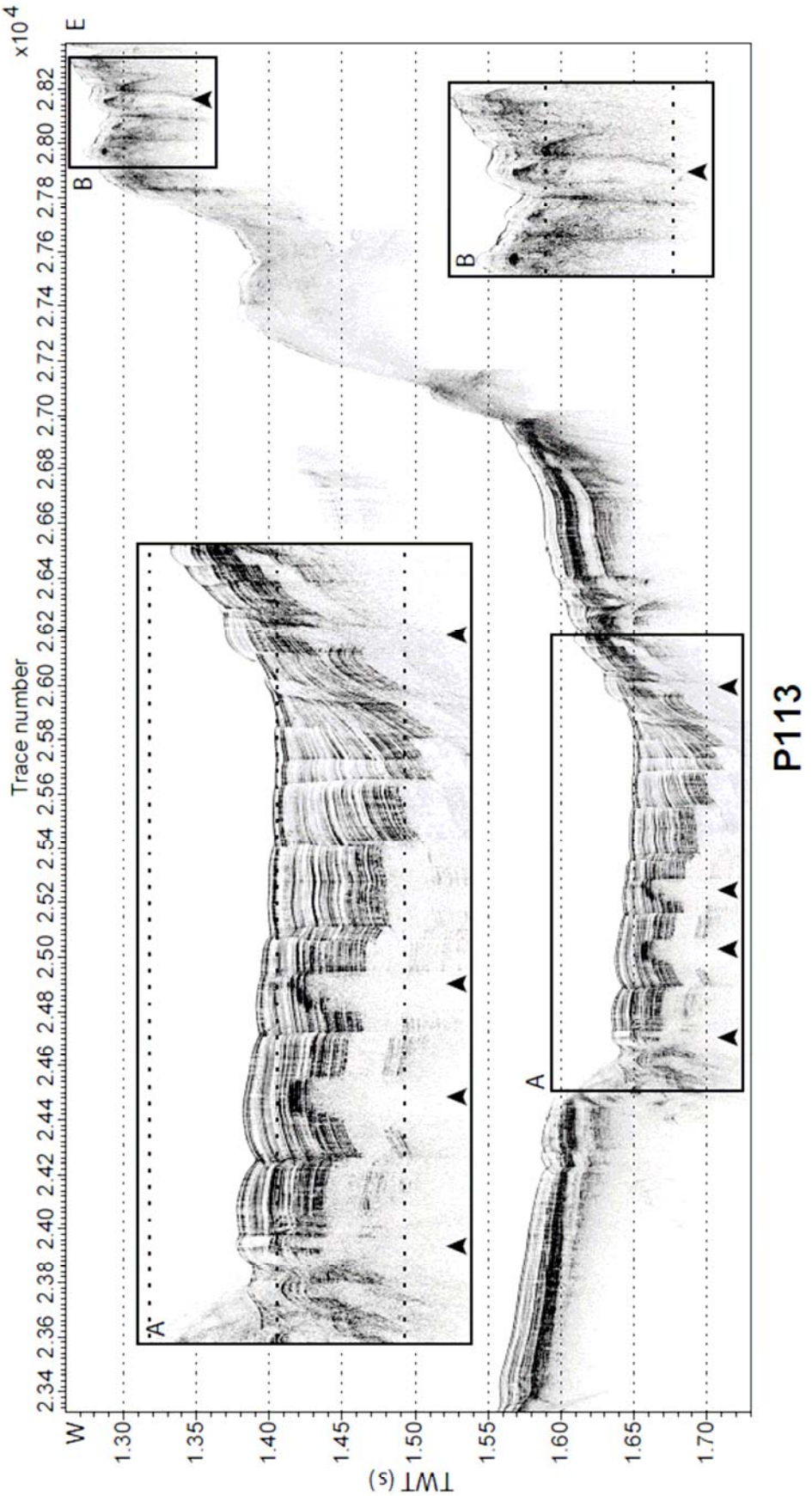

Fig. B14. a) Marmesonet cruise, chirp profile P113 in the Tekirdag Basin (TWT, Two Way Travel time in seconds). Gas evidences, corresponding to red and orange dots in Fig. B13, are indicated by black arrows. Black rectangles indicate the location of the zooms.

- The Kumburgaz Basin

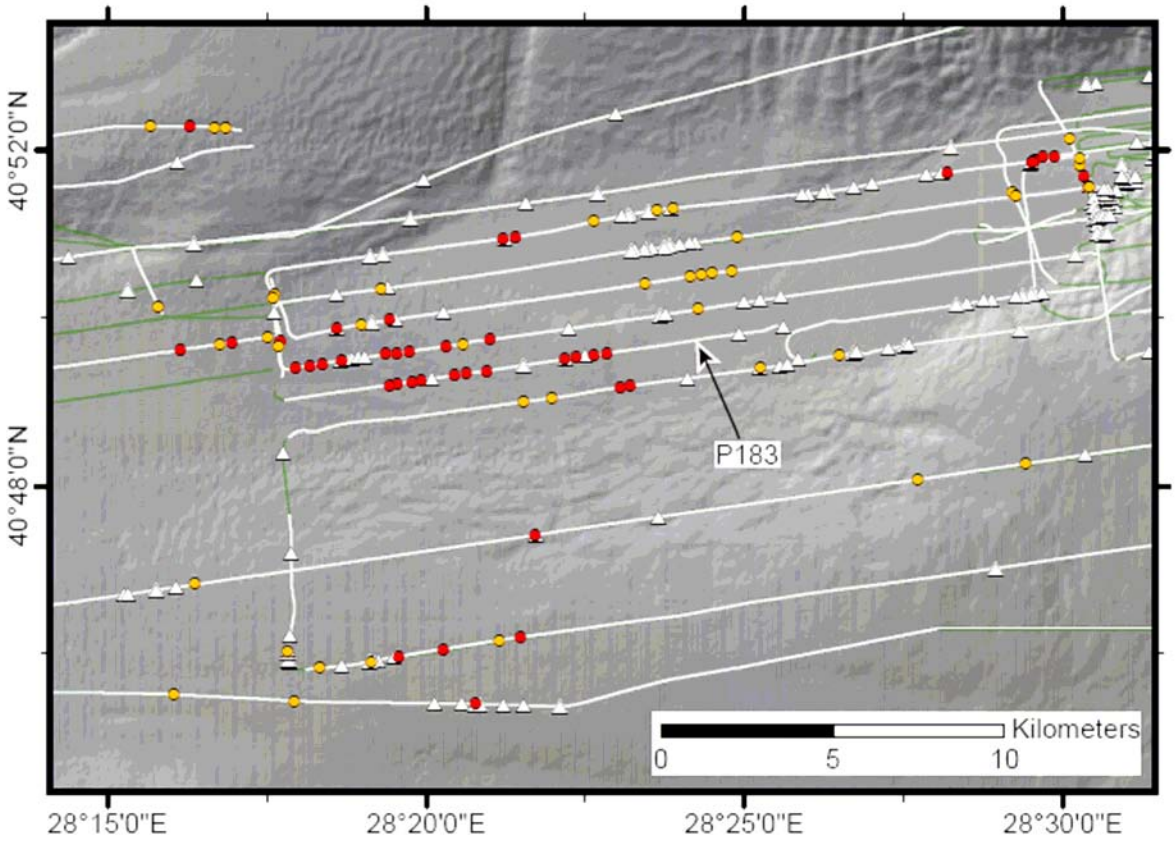

Fig. B15. Kumburgaz Basin. Distribution of gas evidences in sediments from CHIRP profiles and acoustic anomalies in the water column (white triangles) detected by the EM302 multibeam system during the Marmesonet cruise, leg 1, in the Sea of Marmara. The symbology is the same as Fig. B9.

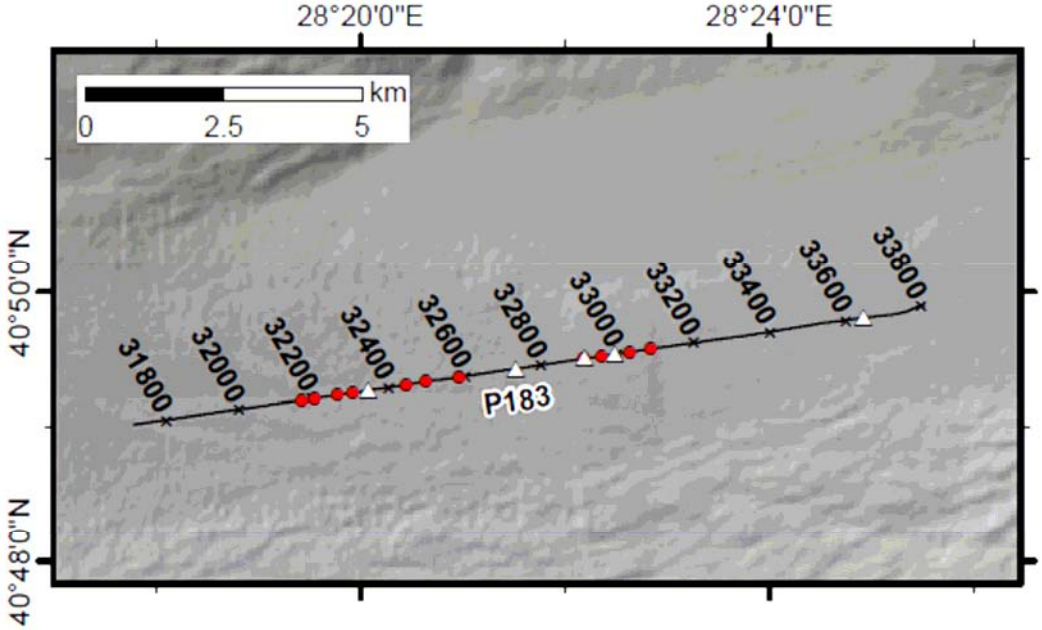

Fig. B16. Kumburgaz Basin, chirp profile P183. Distribution of gas evidences in sediments and acoustic anomalies in the water column (white triangles) detected by the Simrad EM302 multibeam system during the Marmesonet cruise, leg 1, in the Sea of Marmara. The symbology is the same as Fig. B9.

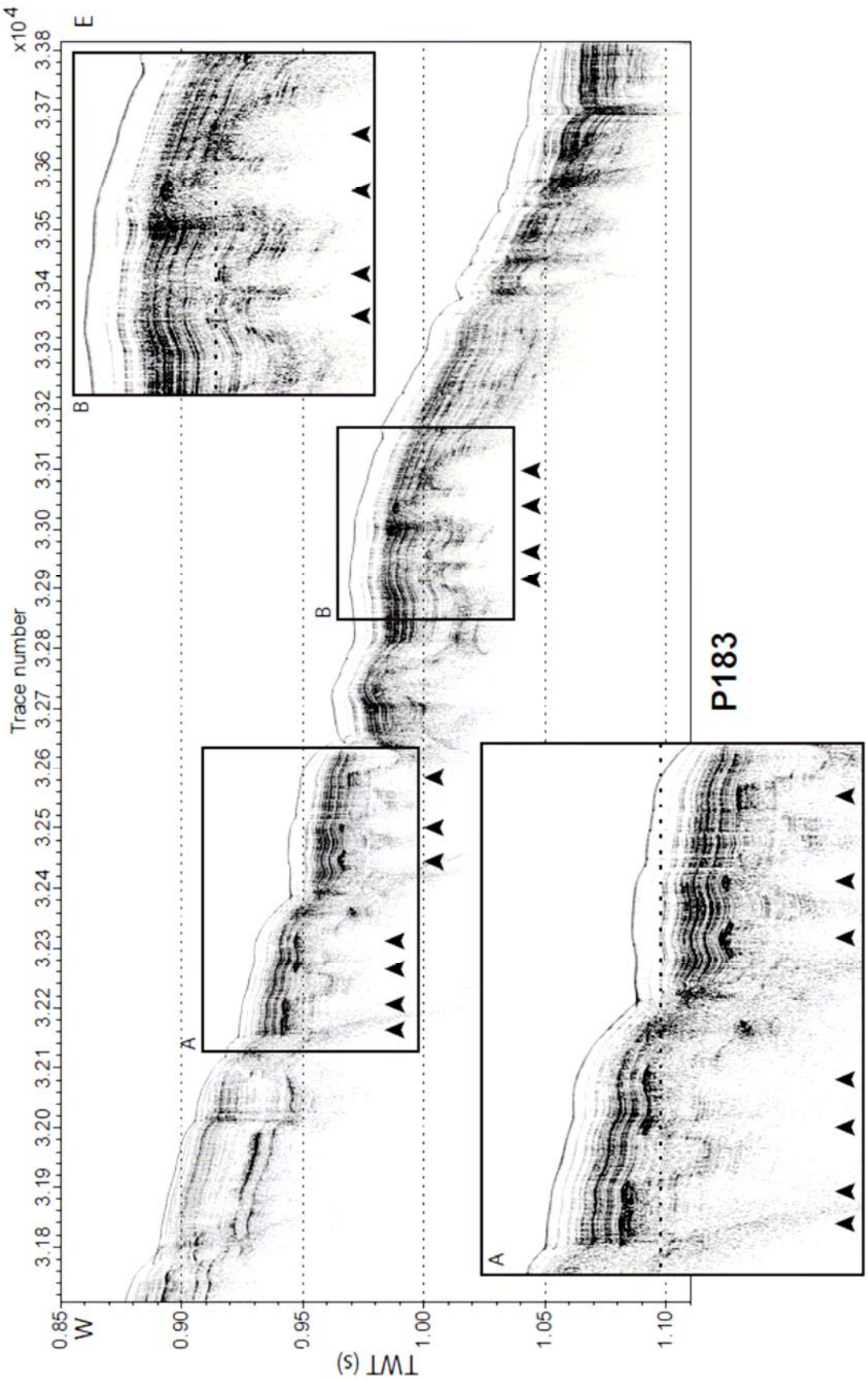

Fig. B17. a) Marmesonet cruise, chirp profile P183 in the Kumburgaz Basin (TWT, Two Way Travel time in seconds). Gas evidences, corresponding to red and orange dots in Fig. B16, are indicated by black arrows. Black rectangles indicate the location of the zooms.

- Central High

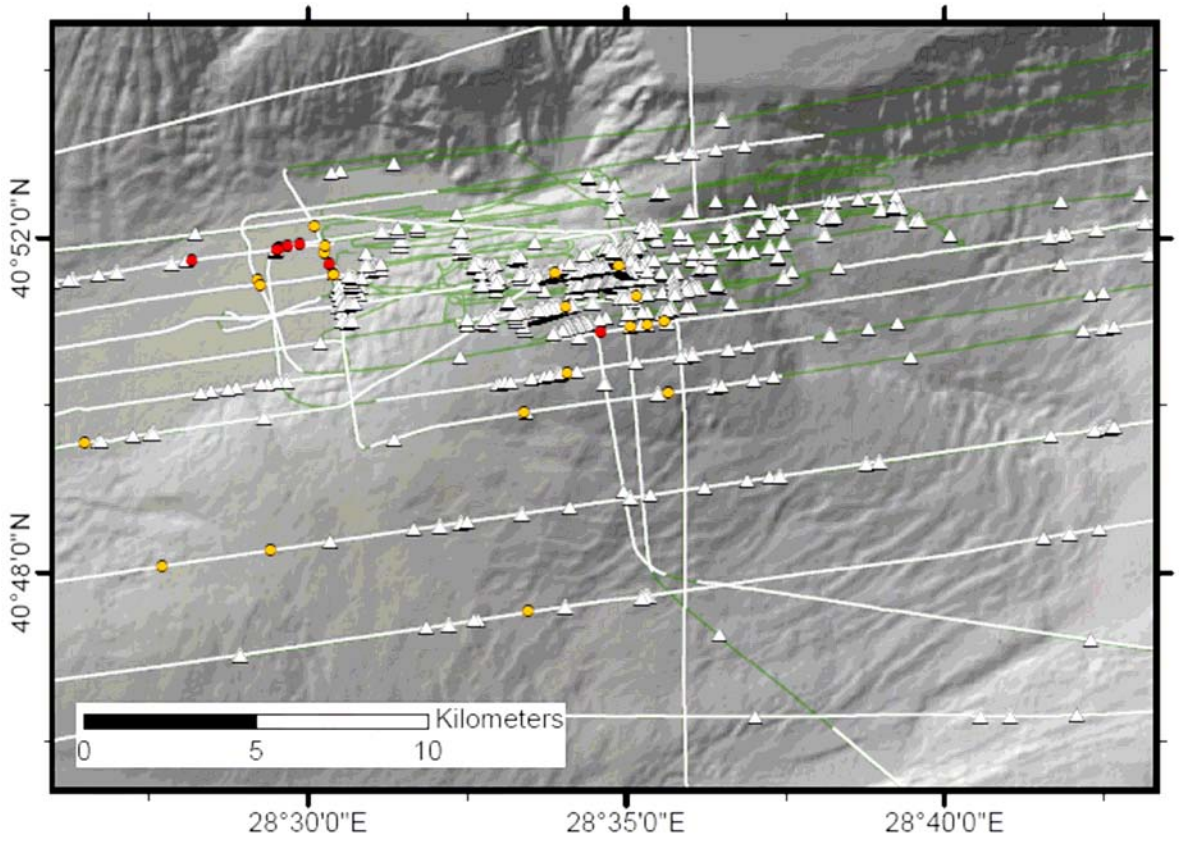

Fig. B18. Central High. Distribution of gas evidences in sediments from CHIRP profiles and acoustic anomalies in the water column (white triangles) detected by the Simrad EM302 multibeam system during the Marmesonet cruise, leg 1, in the Sea of Marmara. The symbology is the same as Fig. B9.

- Çinarcik Basin

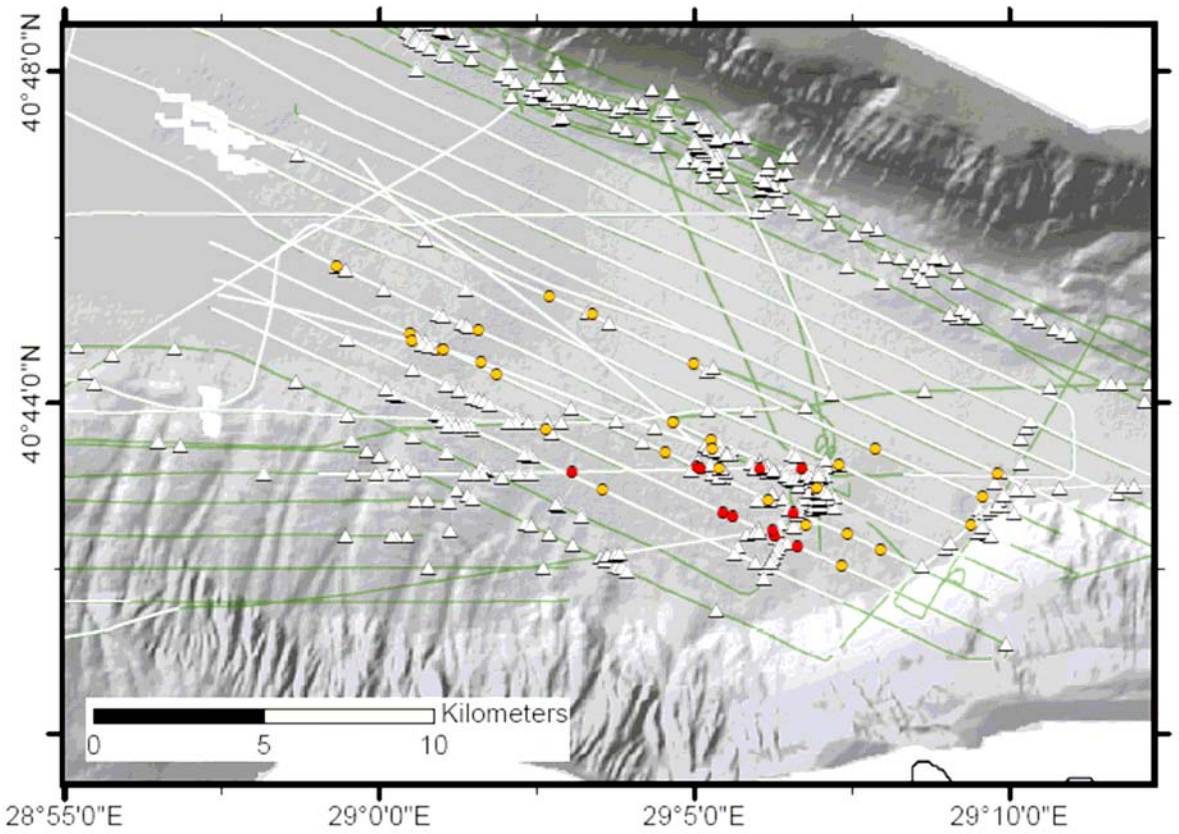

Fig. B19. Çinarcik Basin. Distribution of gas evidences in sediments from CHIRP profiles and acoustic anomalies in the water column (white triangles) detected by the Simrad EM302 multibeam system during the Marmesonet cruise, leg 1, in the Sea of Marmara. The symbology is the same as Fig. B9.

- Imrali Basin

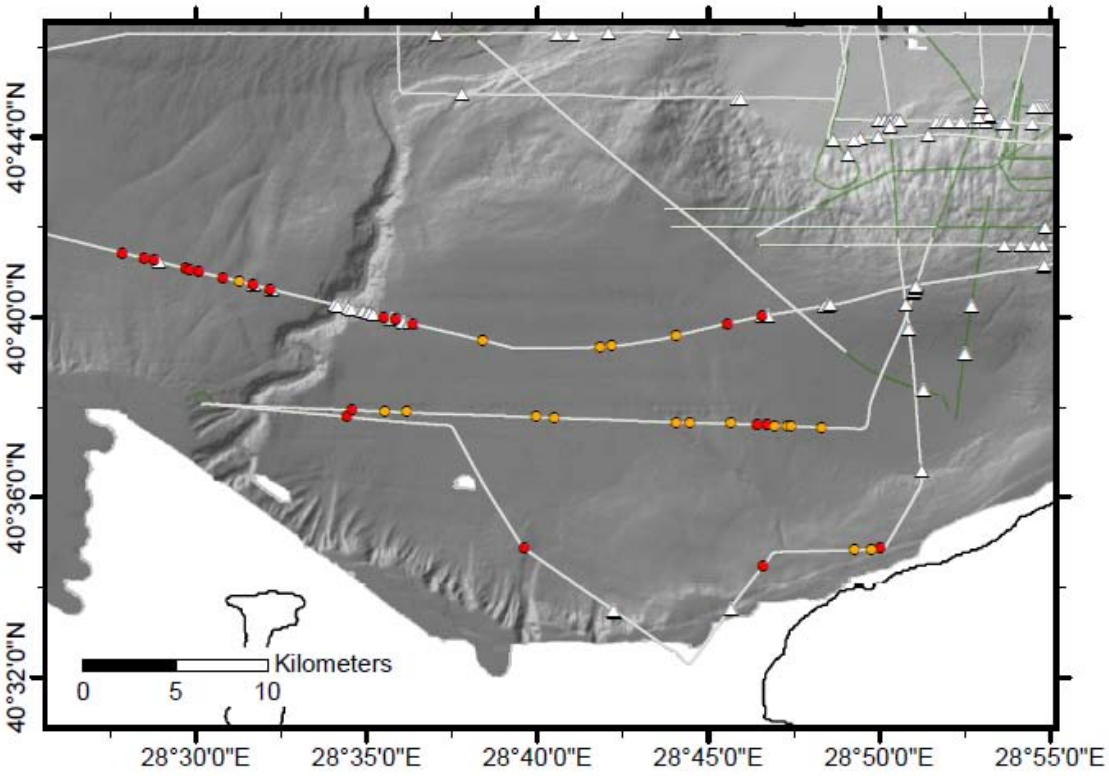

Fig. B20. Imrali Basin. Distribution of gas evidences in sediments from CHIRP profiles and acoustic anomalies in the water column (white triangles) detected by the Simrad EM302 multibeam system during the Marmesonet cruise, leg 1, in the Sea of Marmara. The symbology is the same as Fig. B9.

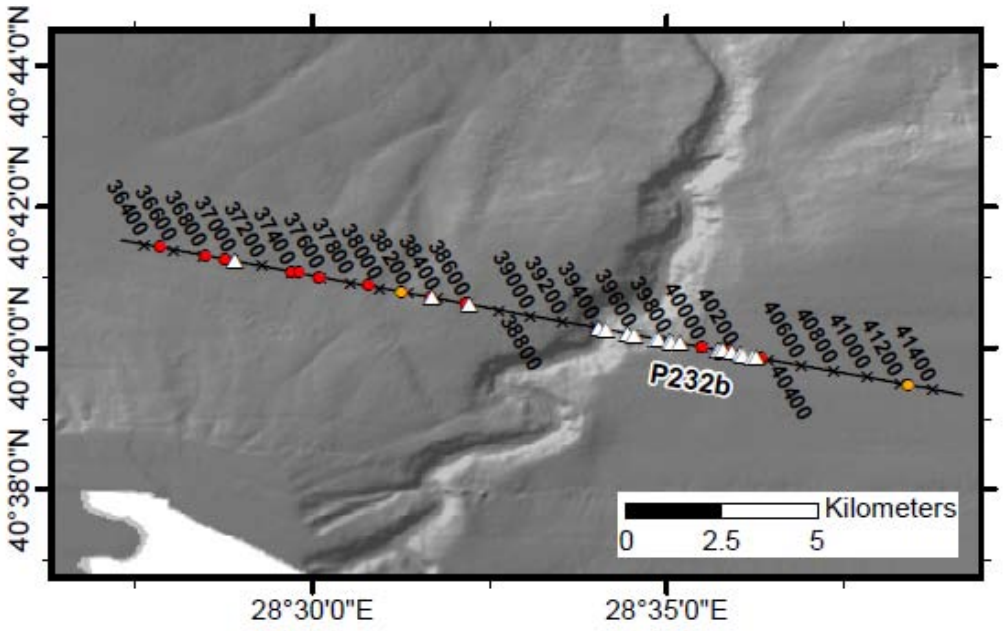

Fig. B21. Imrali Basin, chirp profile P232b. Distribution of gas evidences in sediments and acoustic anomalies in the water column (white triangles) detected by the Simrad EM302 multibeam system during the Marmesonet cruise, leg 1, in the Sea of Marmara. The symbology is the same as Fig. B9.

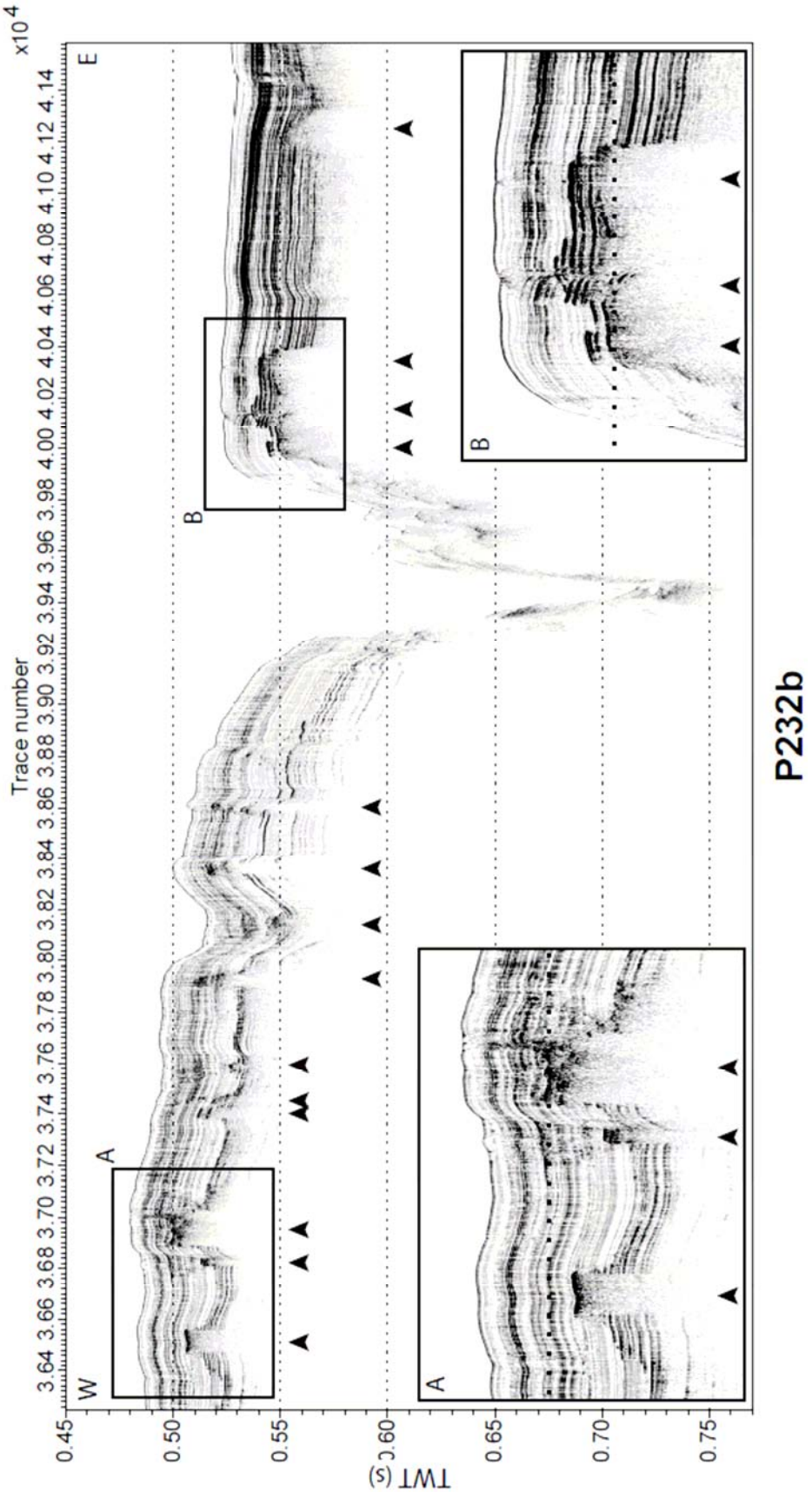

Fig. B22. a) Marmesonet cruise, chirp profile P232b in the Imrali Basin (TWT, Two Way Travel time in seconds). Gas evidences, corresponding to red and orange dots in Fig. B21, are indicated by black arrows. Black rectangles indicate the location of the zooms.

Appendix C. Detailed OBS characteristics

During MarNaut (May-August, 2007) and ERIG3D (June-August, 2008) cruises, 6 types of OBSs were deployed. Among those 6, 3 were provided by IFREMER (OldOBS, MicrOBS and LotOBS) and 3 by CGG-Veritas (ARMSS, NEEDLE, SPAN). The structure and information available vary from one OBS to the others. In this appendix has been gathered all useful information on each OBS.

C.1. IFREMER OBSs

C.1.1. OldOBS (MarNaut cruise, OBSs J, K, L and M)

These OBS are 1.5 meters tall (Fig. C1). Although their heavy weighs of 240 kg in air, they have negative buoyancies of -16 kg in water, allowing them to automatically rise to the surface when they are freed from their ground weight (65 kg).

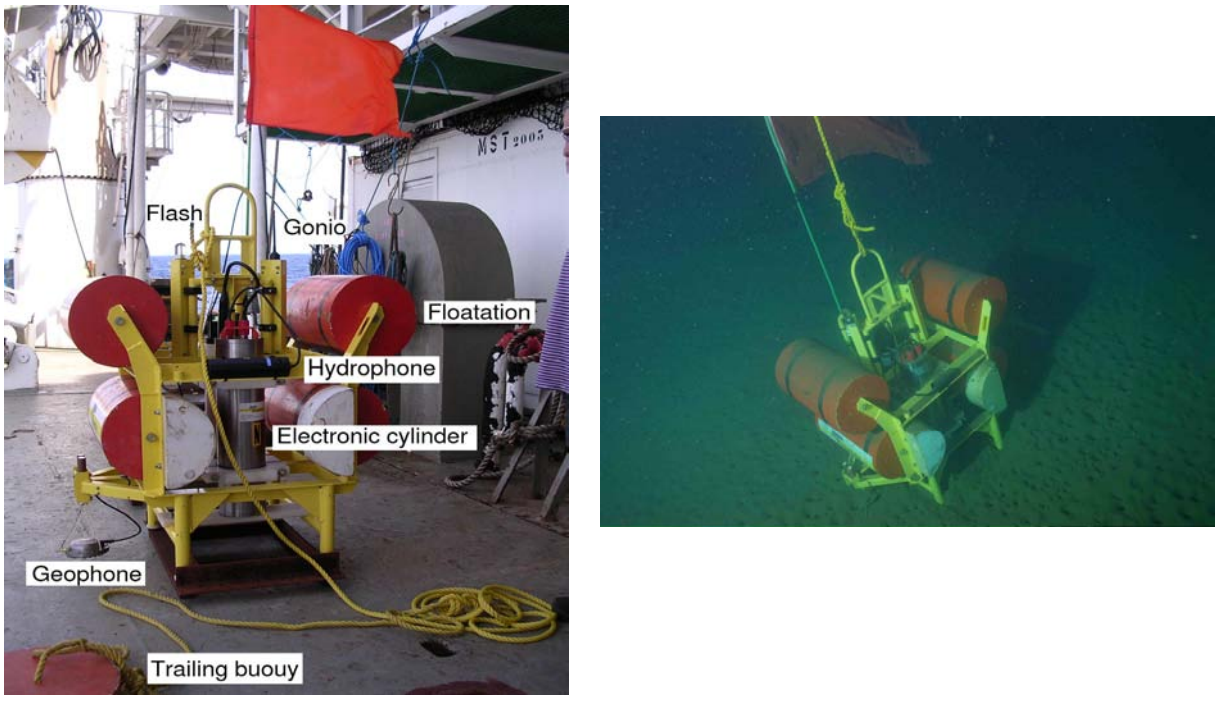

Fig. C1. Overview of an OldOBS with its ground weight, onboard (Left) and on the seabed (Right).

The geophones (Geospace 4.5 Hz GS11-D, 2 horizontals and 1 vertical) are located in a pressure-resistant case and liying directly on the seafloor. The hydrophone (OAS E-2PD) is fixed on the instrument's frame, ~0.9 m above the seafloor.

General characteristics of the geophone Geospace 4.5 Hz GS11-D (Fig. C2) and its acquisition chain:

Natural frequency: 4.5 Hz
Sampling frequency: 250 Hz
Frequency bandwidth: 4.5 to 1000 Hz
Sensibility: 0.81 V/inch/s (32 V/m/s)
ADC conversion factor (card Cirrus Logic 24 bits): 3.974E-7 V/count
Gain: 34.7 dB (May 14 to June 9, 2007) and 40.2 dB (June 9 to August 30, 2007)
Descaling factor: 2.286E-10 and 1.213E-10 m/s/count

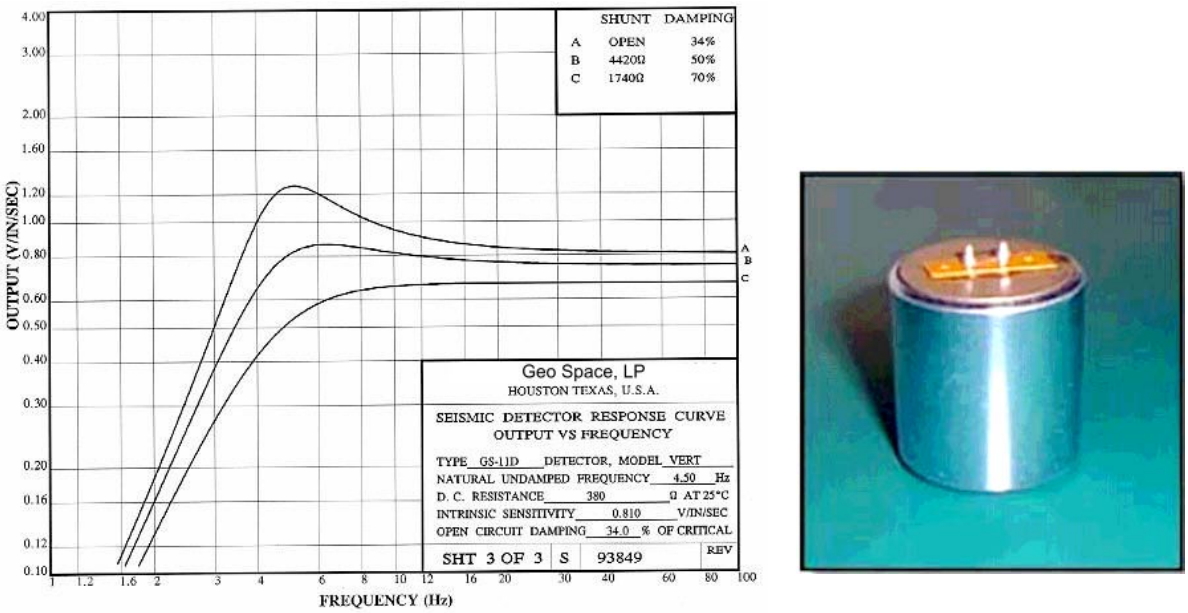

Fig. C2. (Left) Geophone Geospace 4.5 Hz GS11-D characteristics and frequency response curve. (Right) Picture of geophone Geospace 4.5 Hz GS11-D (height: 3.35 cm).

General characteristics of the hydrophone OAS E-2PD (Fig. C3) and its acquisition chain:

Sampling frequency: 250 Hz
Frequency bandwidth: 0-5000 Hz
Sensibility: -92 dB ref 1V/µPa (~2.512E-4 V/Pa)
ADC conversion factor: unknown
Gain: 14.7 dB (May 14 to June 9, 2007) and 20.24 dB (June 9 to August 30, 2007)
Descaling factor: unknown

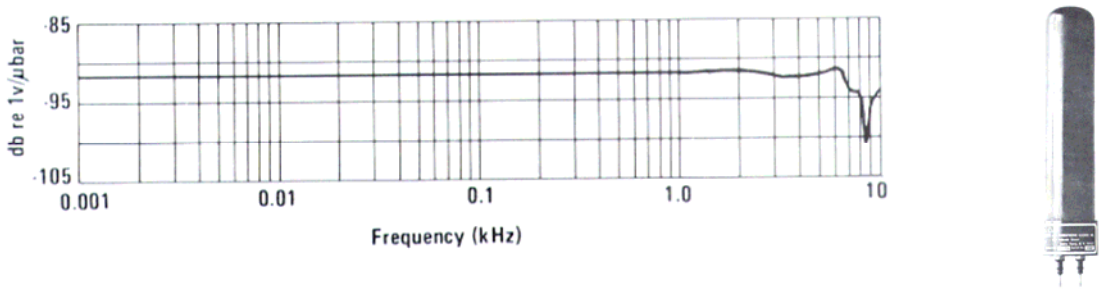

Fig. C3. (Left) Hydrophone OAS E-2PD frequency response curve. (Right) Picture of hydrophone OAS E-2PD (height: 22.9 cm).

C.1.2. MicrOBS (MarNaut cruise, OBS J2)

These OBS, much smaller than the OldOBS, have a height of 60 cm (Fig. C4). They weigh ~20 kg in air in addition to a ground weight of 17 kg. The three geophones (Geospace 4.5 Hz GS11-D), electronics and batteries are included in a 13" glass sphere. The hydrophone (High Tech. Inc. HTI 90U) is fixed on the instrument's frame, ~0.3 m above the seafloor. The geophones acquisition chain is the same as the one of the OldOBS.

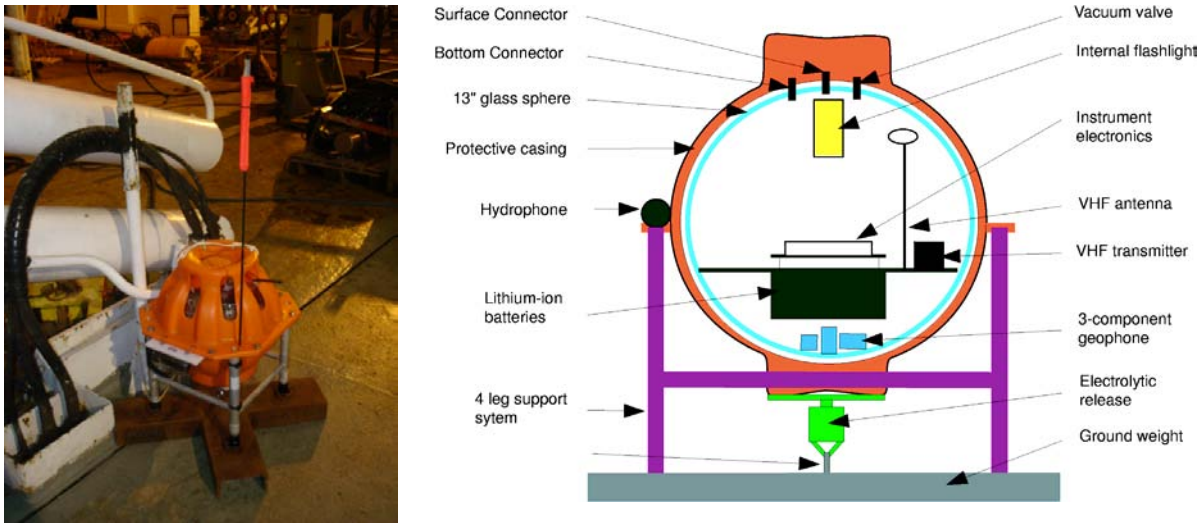

Fig. C4. (Left) Overview of a MicrOBS. (Right) Internal structure of a MicrOBS.

General characteristics of the hydrophone HTI 90U (Fig. C5) and its acquisition chain:

Sampling frequency: 250 Hz
Frequency bandwidth: 2-20000 Hz
Sensibility: -158 dB ref 1V/µPa (~1.26E-2 V/Pa)
ADC conversion factor (card Cirrus Logic 24 bits): 3.974E-7 V/count
Gain: 14.7 dB (May 14 to June 9, 2007) and 20.24 dB (June 9 to August 30, 2007)
Descaling factor: 5.81E-6 and 3.07E-6 Pa/count

Fig. C5. Picture of hydrophone HTI 90U (length: 10.2 cm)

C.1.3. LotOBS (ERIG3D cruise)

The LotOBS is a combination of OldOBS and MicrOBS. This OBS have a height of ~70 cm cm and a weight of 65 kg in air including a ground weight of 23 kg. Electronics and batteries are housed in a 17" glass sphere, while the geophones (Geospace 4.5 Hz GS11-D) lie directly on the seafloor (Fig. C6). The hydrophone (HTI 90U) is fixed on the instrument's frame, ~0.4 m above the seafloor.

Fig. C6. Overview of a LotOBS with the arm that deploys the pressure-resistant case containing the geophones. The hydrophone, visible in the photograph on the right, is fixed on the instrument's frame, ~0.4 m above the seafloor.

General characteristics of the geophone Geospace 4.5 Hz GS11-D (Fig. C2) and its acquisition chain:

Natural frequency: 4.5 Hz
Sampling frequency: 250 Hz
Frequency bandwidth: 4.5 to 1000 Hz
Sensibility: 0.81 V/inch/s (32 V/m/s)
ADC conversion factor (card Cirrus Logic 24 bits): 3.974E-7 V/count
Gain: 46 dB
Descaling factor: 6.2234 m/s/count

General characteristics of the hydrophone HTI 90U (Fig. C5) and its acquisition chain:

Sampling frequency: 250 Hz
Frequency bandwidth: 2-20000 Hz
Sensibility: -158 dB ref 1V/µPa (~1.26E-2 V/Pa)
ADC conversion factor (card Cirrus Logic 24 bits): 3.974E-7 V/count
Gain: 20.24 dB
Descaling factor: 3.07E-6 Pa/count

C.2. CGG OBSs (MarNaut cruise)

C.2.1. ARMSS

ARMSS is constituted by a 0.9 m long body that lies horizontally on the seafloor (Fig. C7), connected to a head containing all the sensors (3 geophones and one hydrophone). The instrument's head is equipped with a vibrating system to enhance the coupling with the seafloor. Inside the head are located three geophones (Geospace LT101) arranged in a Galperin configuration (Fig. C8) and a hydrophone Benthos AQ4.

General characteristics of the geophone Geospace LT101 (Fig. C9) and its acquisition chain:

Natural frequency: 14 Hz
Sampling frequency: 500 Hz
Frequency bandwidth: 6 to 800 Hz
Sensibility: 1.07 V/inch/s (42.1 V/m/s)
ADC conversion factor: 4.54E-07 V/count
Gain: unknown
Descaling factor: unknown

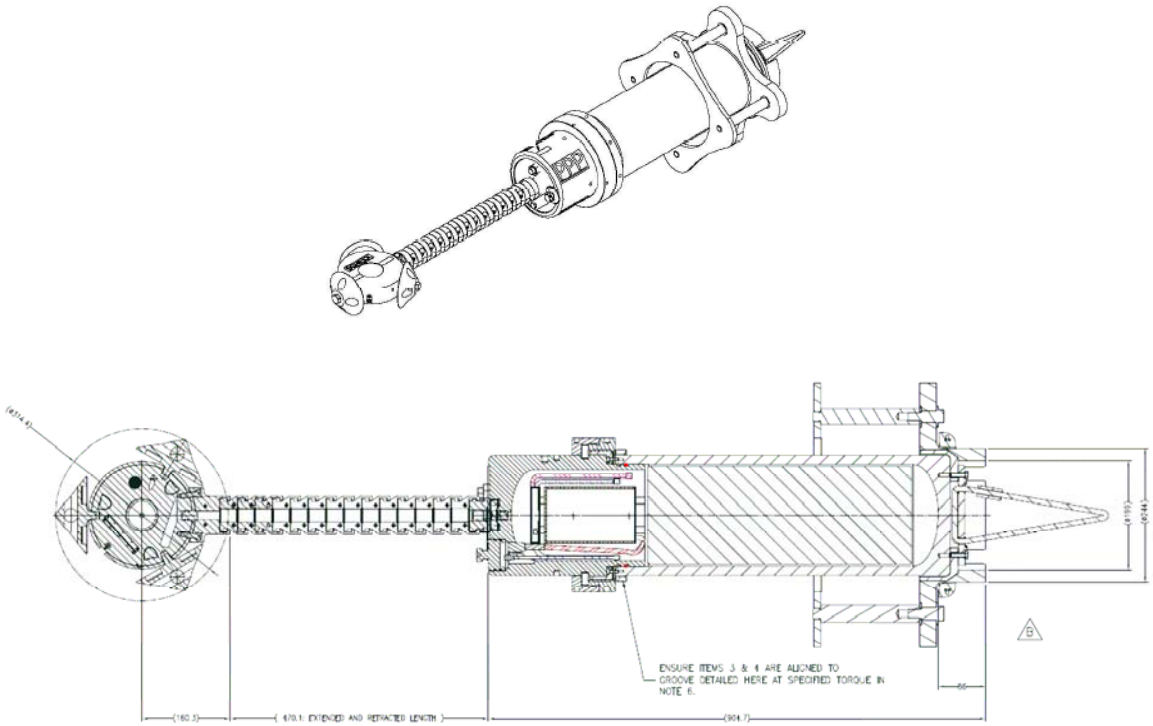

Fig. C7. (Top) Overview of OBS ARMSS. (Bottom) ARMSS general structure with dimensions (in mm).

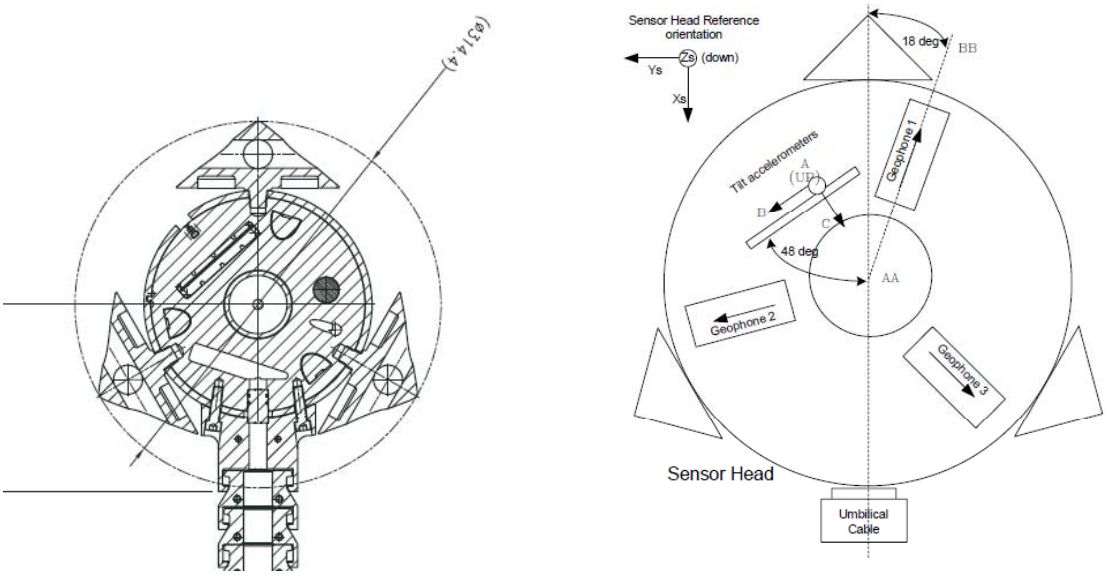

Fig. C8. (Left) Zoom in and dimension (in mm) of the ARMSS head. (Right) Geophones configuration within ARMSS head. The hydrophone is located in the center (AA).

In Galperin arrangement, the three geophones are in identical positions (tilted by 35.3 deg. relatively to the horizontal and separated by 120 deg.), there are no vertical or horizontal geophones.

Amplitudes in Galperin configuration (G1, G2, G3) are converted into amplitudes in orthogonal configuration (X, Y, Z), using the follows

$$Ampl.X = \sin(60).\sin\left(\arctan\sqrt{2}\right).(Ampl.G_2 - Ampl.G_3), \quad \text{(C1)}$$

$$Ampl.Y = \frac{1}{2}\sin\left(\arctan\sqrt{2}\right).(Ampl.G_2 + Ampl.G_3 - 2.Ampl.G_1), \quad \text{(C2)}$$

$$Ampl.Z = \cos\left(\arctan\sqrt{2}\right).(Ampl.G_1 + Ampl.G_2 + Ampl.G_3). \quad \text{(C3)}$$

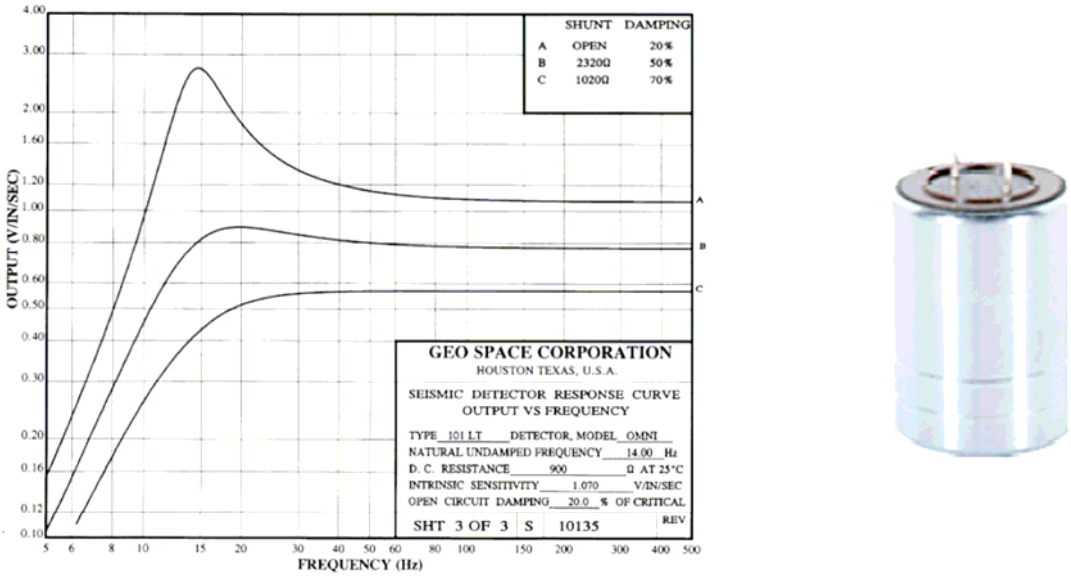

Fig. C9. (Left) Geophone Geospace LT101 characteristics and frequency response curve. (Right) Picture of geophone Geospace LT101 (height: 3.73 cm).

General characteristics of the Benthos AQ4 (Fig. C10) hydrophone and its acquisition chain:

Sampling frequency: 500 Hz
Frequency bandwidth: 1-15000 Hz
Sensibility: -201 dB ref 1V/µPa (~8.9E-05 V/Pa)
ADC conversion factor: 4.54E-07 V/count
Gain: unknown
Descaling factor: unknown

Fig. C10. Picture of the hydrophone Benthos AQ4 (length: 3.3 cm).

C.2.2. NEEDLE

OBS NEEDLE consists in a ~1.5 m long upper part (Fig. C11), and a ~3 m long needle containing the sensors (three geophones and a hydrophone). This instrument is installed following geothechnical coring method (Kullenberg coring apparatus), ensuring deep burying of the sensors. The upper part, mechanically decoupled from the needle by a self corroding system, lie on the seafloor. Three geophones SEND "Full Tilt" and one hydrophone are located at the lower extremity of the needle.

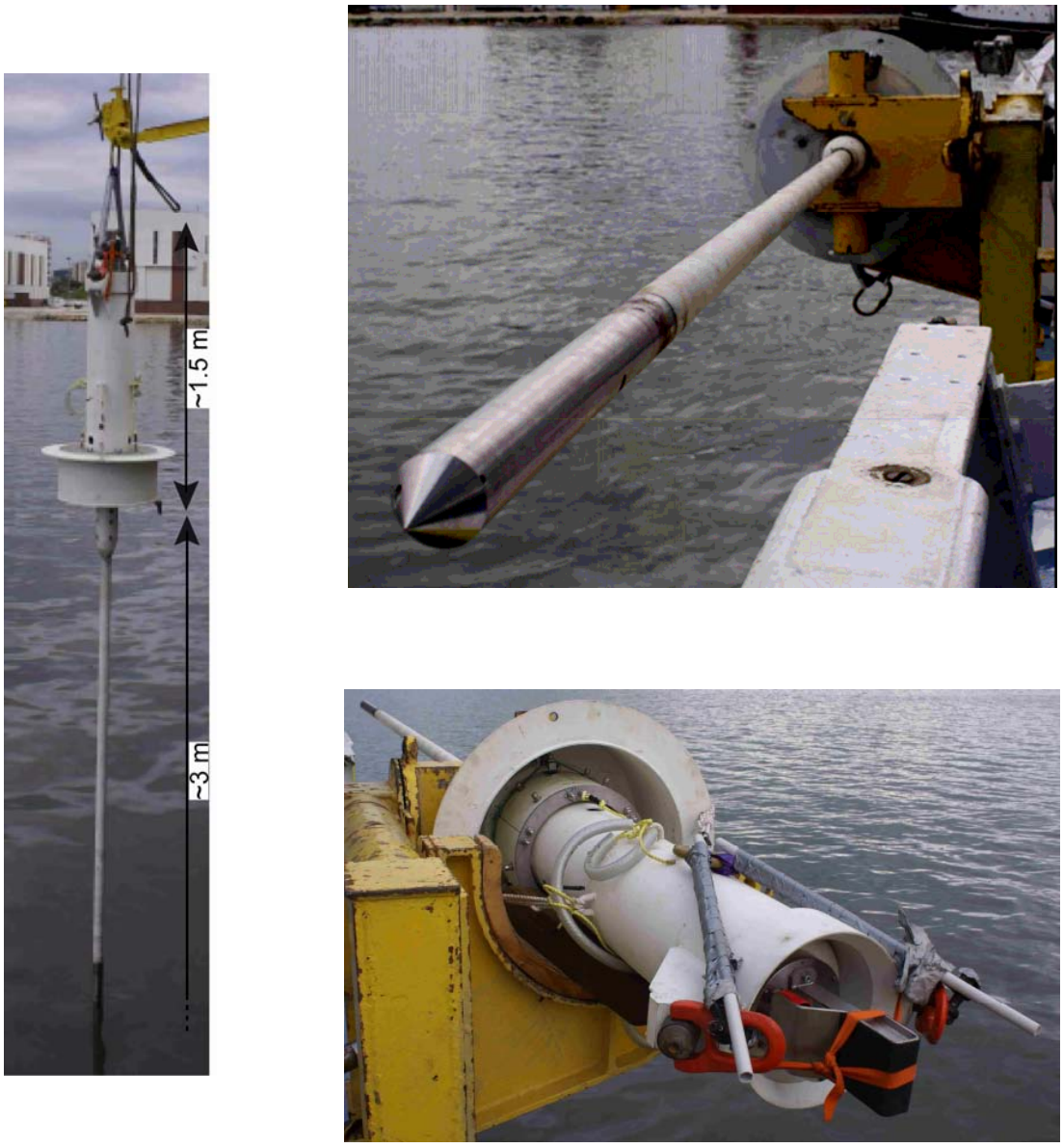

Fig. C11. Pictures of OBS NEEDLE, (Left) overview, (Top right) view from below, (Bottom right) view from above.

General characteristics of the geophone SEND “Full Tilt” (Fig. C12) and its acquisition chain:

Natural frequency: 4.5 Hz
Sampling frequency: 500 Hz
Sensibility: 35 V/m/s
ADC conversion factor: 4.54E-07 V/count
Gain: unknown
Descaling factor: unknown

Fig. C12. Picture of geophone SEND “Full Tilt” (height: ~5 cm).

General characteristics of the hydrophone and its acquisition chain:

Sampling frequency: 500 Hz
Sensibility: 8.1E-05 V/Pa
ADC conversion factor: 4.54E-07 V/count
Gain: unknown
Descaling factor: unknown

C.2.3. SPAN

The SPAN is a ~1 m long shrapnel-like OBS that lied horizontally on the seafloor during the MarNaut cruise (Fig. C13). Three geophones SEND “Full Tilt” are located inside the titanium container. The hydrophone is fixed on the container inside the instrument’s tail. The geophones and the hydrophone are identical to those of the NEEDLE.

Fig. C13. Overview of OBS SPAN.

The main technical specifications of all instruments are summarized in Table C1.

Cruises	ERIG 3D	MarNaut						
Providers		IFREMER			CGG-Veritas			
OBS Types	LotOBS	MicrOBS		OldOBS	ARMSS	NEEDLE	SPAN	
Geophones								
Sensors		Geospace GS11-D			Geospace LT101	SEND "Full Tilt"		
Natural frequency (Hz)	4.5	4.5		4.5	14	4.5	4.5	
Sampling frequency (Hz)	250	250		250	500	500	500	
Sensibility (V/m/s)	32	32		32	42.1	35	35	
ADC factor (V/count)	3.97E-07	3.97E-07		3.97E-07	4.54E-07	4.54E-07	4.54E-07	
Gain (dB)	46	34.7/40.2		34.7/40.2		Unknown		
Descaling factor (m/s/count)	6.22E-11	2.286E-10/1.213E-10		2.286E-10/1.213E-10		Unknown		
Hydrophones								
Sensors		HTI 90U		OAS E-2PD	Benthos AQ4	Unknown	Unknown	
Sampling frequency (Hz)	250	250		250	500	500	500	
Frequency bandwidth (Hz)	2-20000	2-20000		0-5000	1-15000	Unknown	Unknown	
Sensibility (V/Pa)	1.26E-02	1.26E-02		2.51E-04	8.90E-05	8.10E-05	8.10E-05	
ADC factor (V/count)	3.97E-07	3.97E-07		Unknown	4.54E-07	4.54E-07	4.54E-07	
Gain (dB)	20.24	14.7/20.24		14.7/20.24		Unknown		
Descaling factor (Pa/count)	3.07E-06	5.81E-06/3.07E-06		Unknown		Unknown		

Table C1. Main technical specifications of all OBSs.

C.3. OBSs noise analysis (MarNaut cruise)

Temporal evolutions of the average of the noise amplitude for all OBSs deployed during the MarNaut cruise (2007) are presented in Fig. C14, C15, C16 and C17 and summarized in Table C2. Amplitudes have been calibrated according to section 2.6.2 methodology.

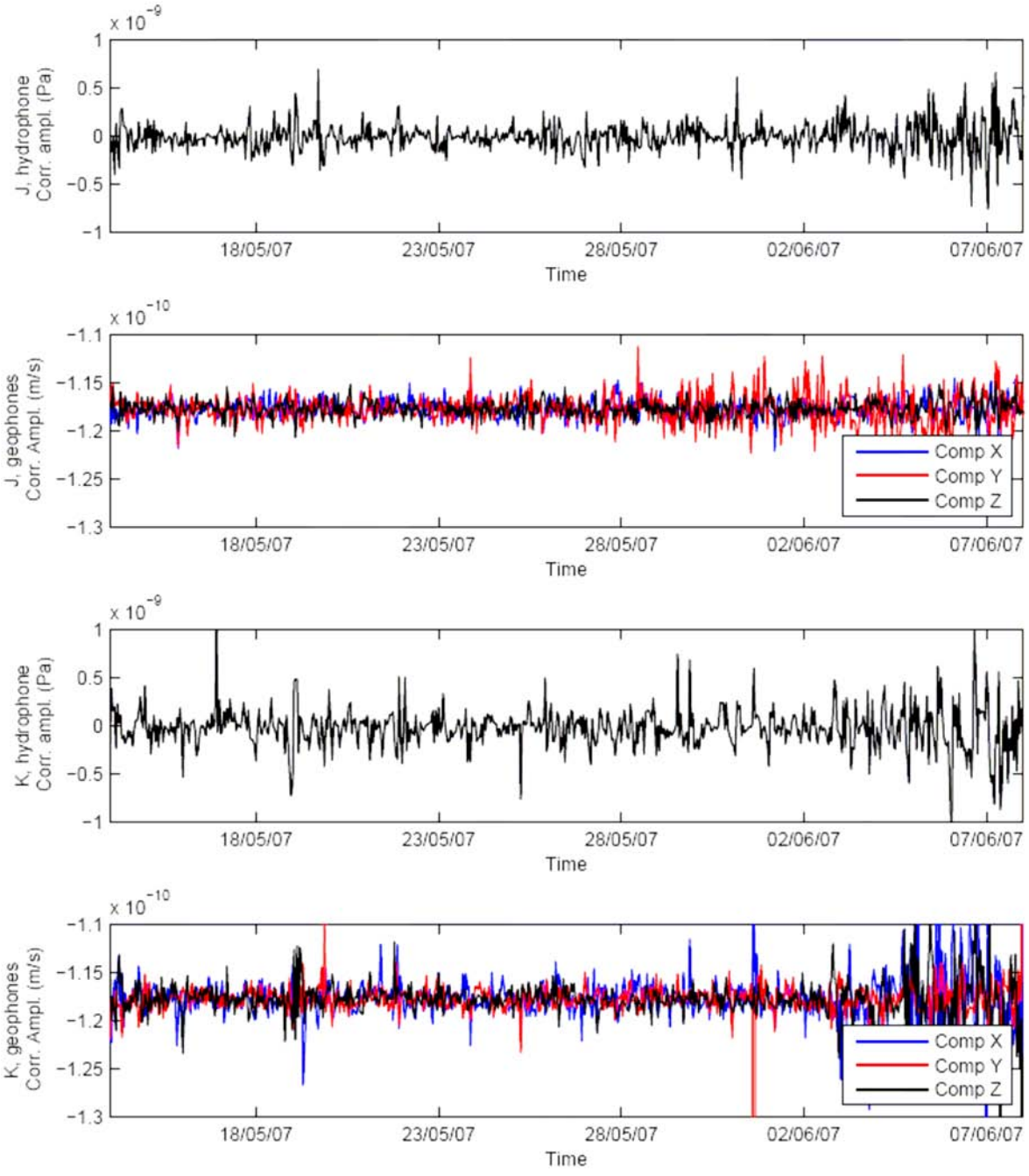

Fig. C14. Temporal evolution of the average of the noise amplitude (in Pa and m/s) of OBSs J and K (hydrophone and geophones) for the period 14 May – 08 June, 2007. The noise amplitude average was computed over the first 10 minutes of each hour.

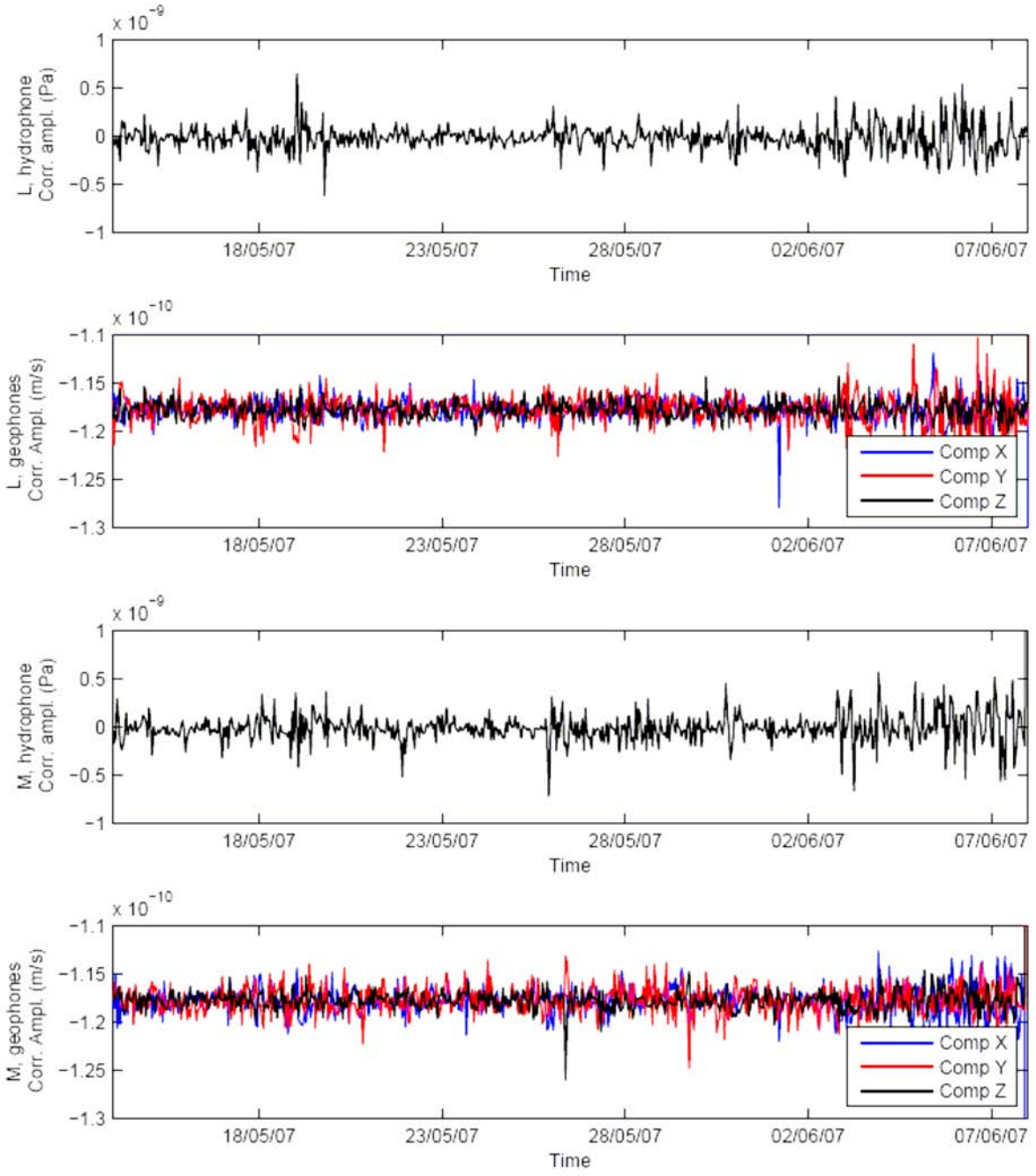

Fig. C15. Temporal evolution of the average of the noise amplitude (in Pa and m/s) of OBSs L and M (hydrophone and geophones) for the period 14 May – 08 June, 2007. The noise amplitude average was computed over the first 10 minutes of each hour.

The average of the noise amplitude is ± 1E-9 Pa on OldOBS and MicrOBS hydrophones, and ranges from about -1E-10 to about -6E-11 m/s on OldOBS and MicrOBS geophones. The average of the noise amplitude is very stable on IFREMER OBSs. On the other hand the average of the noise amplitude on CGG-Veritas OBSs drifts, either linearly (ARMSS) or not

(NEEDLE, SPAN). The noise amplitude on these OBSs is several order of magnitude superior to the noise amplitude of OldOBS and MicrOBS instruments.

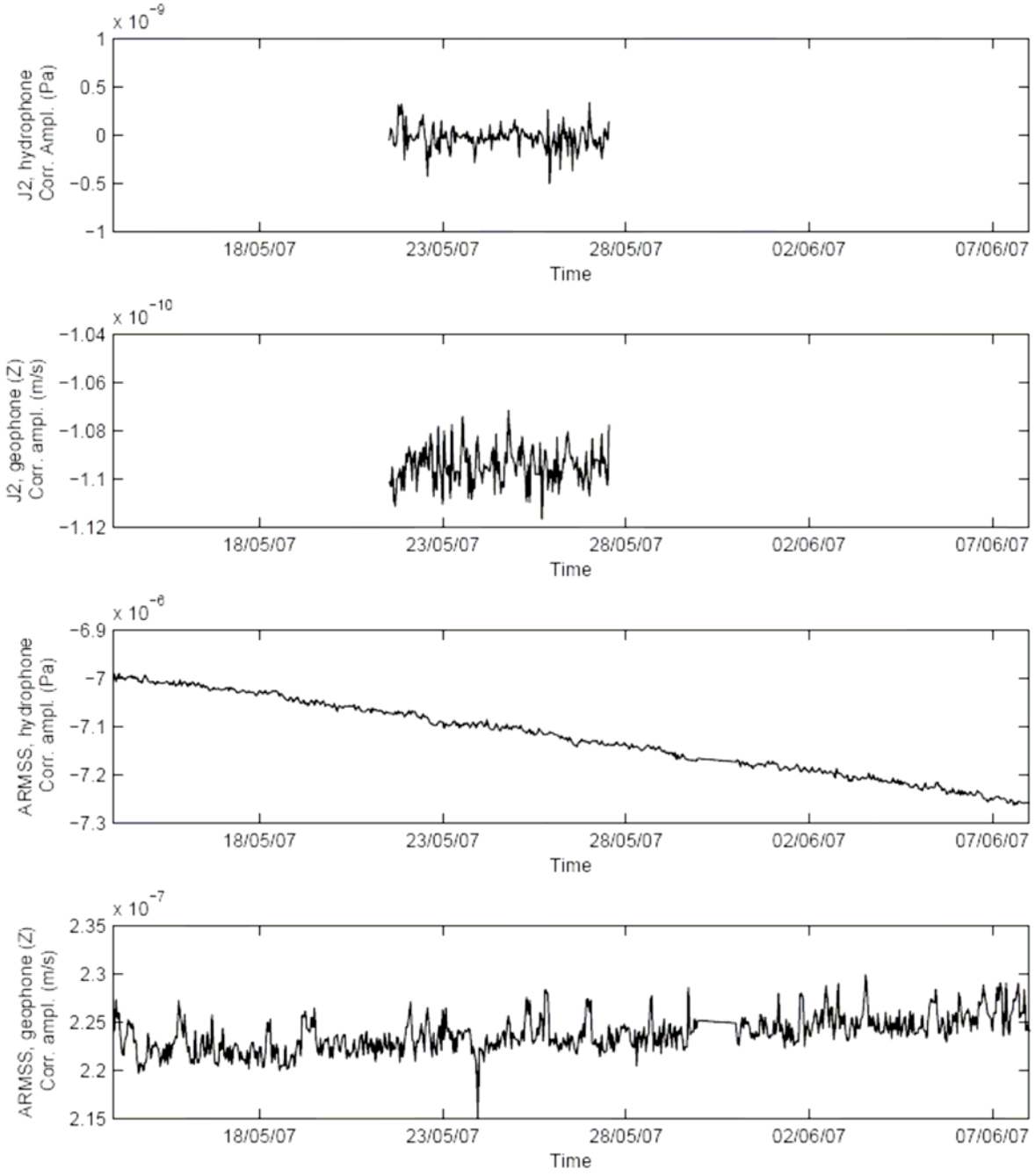

Fig. C16. Temporal evolution of the average of the noise amplitude (in Pa and m/s) of OBSs J2 and ARMSS (hydrophone and vertical geophone) for the period 14 May – 08 June, 2007. The noise average was computed over the first 10 minutes of each hour.

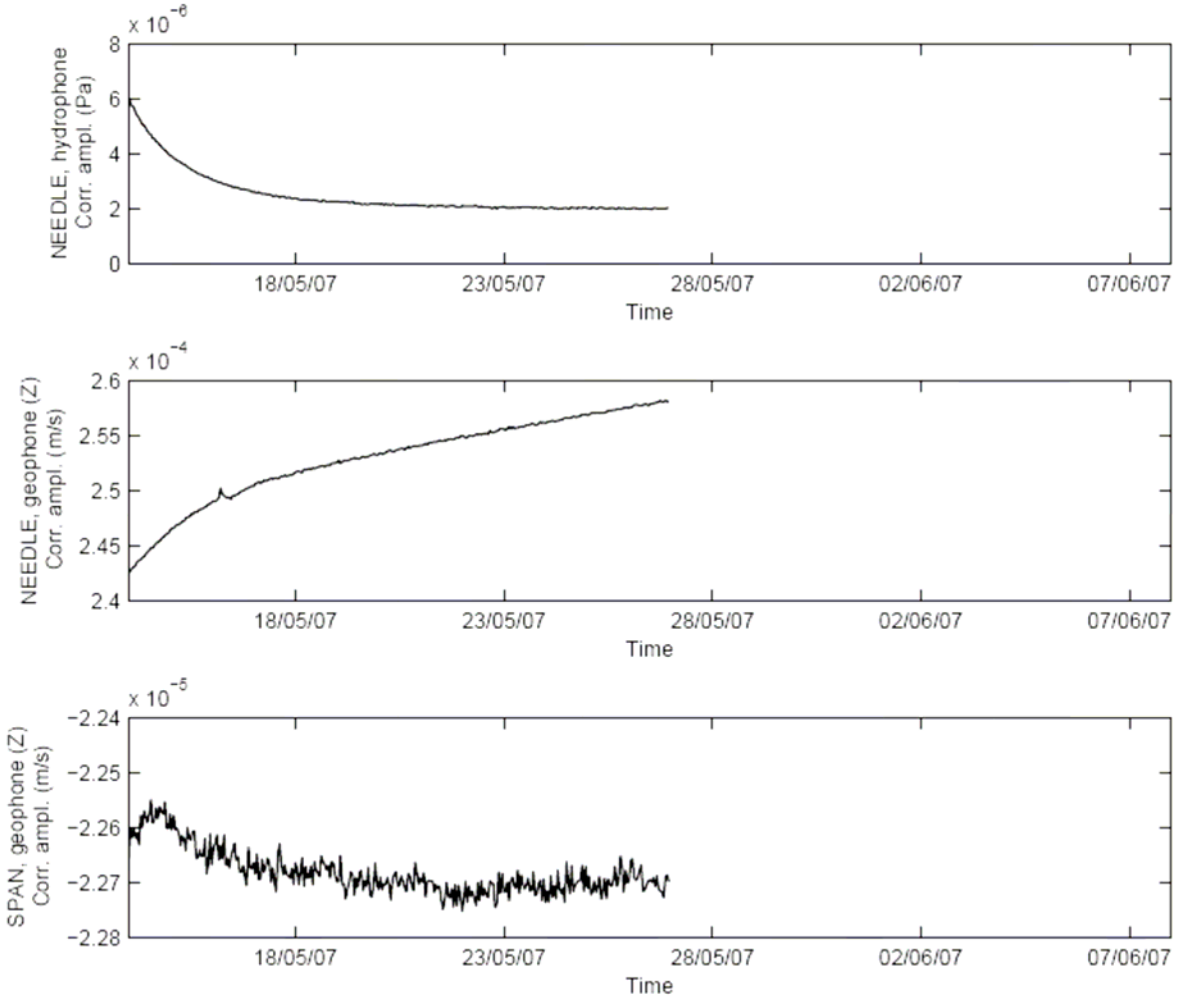

Fig. C17. Temporal evolution of the average of the noise amplitude (in Pa and m/s) of OBSs NEEDLE (hydrophone and vertical geophone) and SPAN (vertical geophone) for the period 14 May – 08 June, 2007. The noise average was computed over the first 10 minutes of each hour.

	Hydrophone	Geophones (May 14 to June 9)
J	± 1E-9	-1.17E-10 ± 0.5E-10
K	± 1E-9	-1.18E-10 ± 0.07E-10
L	± 0.5E-9	-1.17E-10 ± 0.04E-10
M	± 1E-9	-1.17E-10 ± 0.04E-10
J2	± 0.5E-9	-1.1E-10 ± 0.02E-10
ARMSS	7.15E-6 ± 0.15E-6	2.25E-7 ± 0.05E-7
NEEDLE	4.5E-6 ± 2.5E-6	2.5E-4 ± 0.1E-4
SPAN	No signal	-2.265E-5 ± 0.01E-5

Table C2. Noise amplitudes (in m/s) of OBSs deployed during the MarNaut cruise (2007).

Noise frequency contents of all OBSs, computed over a period of 10 seconds on May 22, 2007 at 19:15:33, are presented in Fig. C18 and C19. Generally, noises affect the complete frequency spectrum. In the case of OBSs L and M, noises are concentrated in a frequency range higher than 20 Hz. The noise frequency content is significantly different for OBSs J2 (geophone X), ARMSS (hydrophone), NEEDLE (geophone Z) and SPAN (hydrophone and geophone Y).

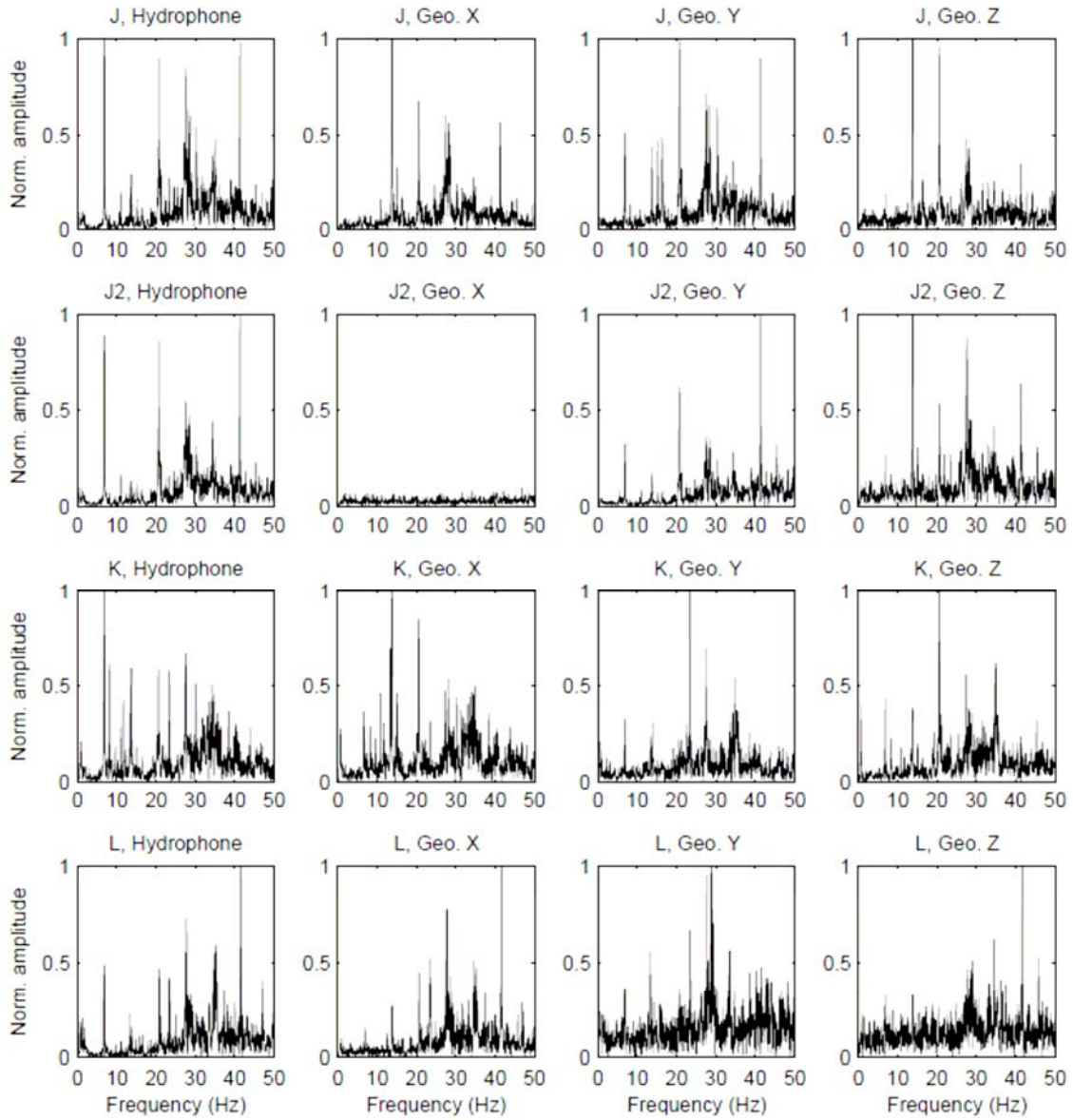

Fig. C18. Noise frequency content computed over a period of 10 seconds on May 22, 2007 at 19:15:33, for OBSs J, J2, K and L (normalized amplitudes). Geo.: geophones.

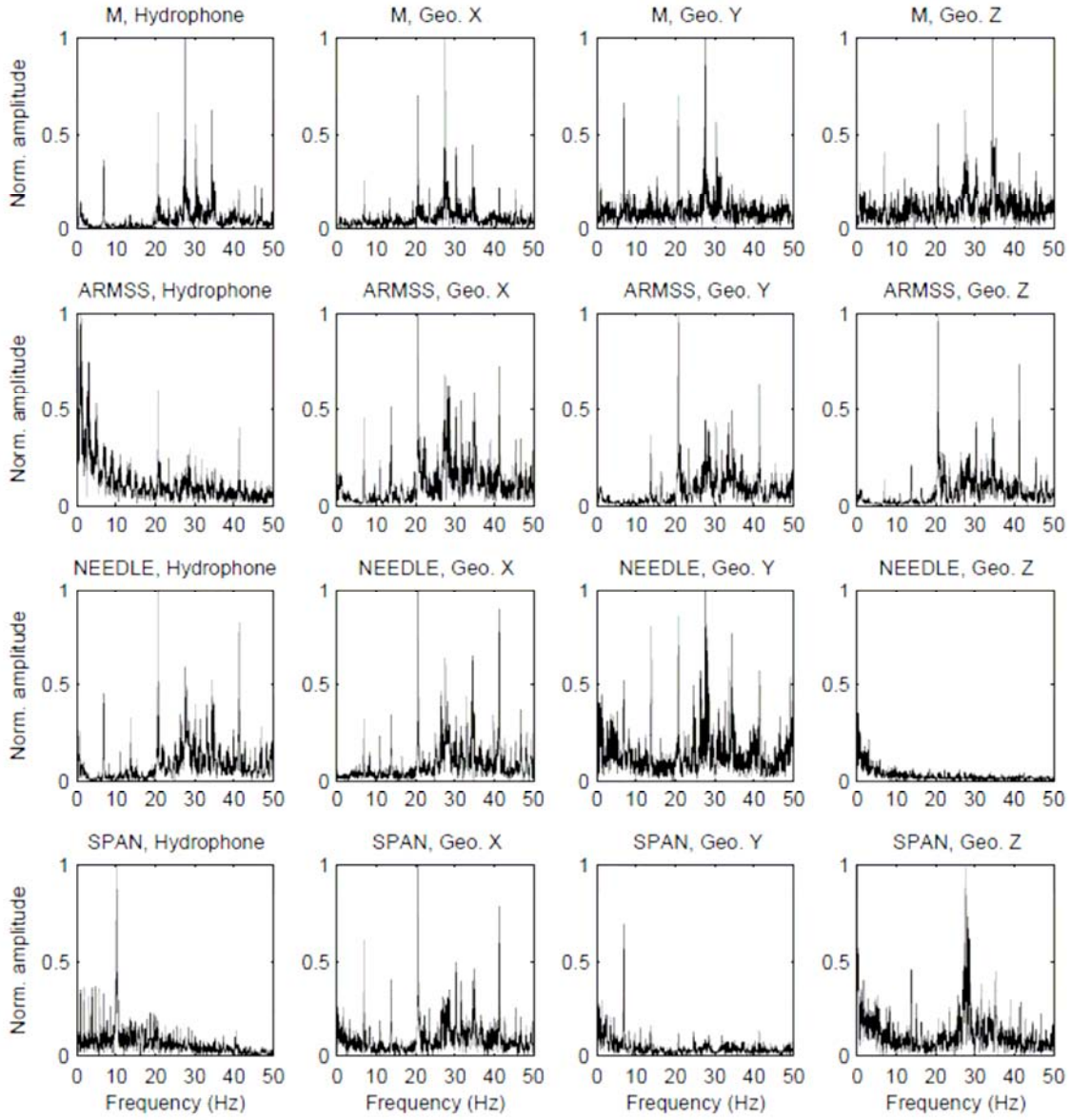

Fig. C19. Noise frequency content computed over a period of 10 seconds on May 22, 2007 at 19:15:33, for OBSs M, ARMSS, NEEDLE and SPAN (normalized amplitudes). Geo.: geophones.

In addition, CGG-Veritas instruments present specific noises. The SPAN hydrophone recorded only 0.1 s-long crenel-shaped signals and higher amplitude pulses every 1 and 11 s (Fig. C20). Sometimes, the crenel-shaped signals have higher amplitudes and hide the other noises.

A comb-like signal is regularly recorded by ARMSS hydrophones and geophones and by NEEDLE geophones (Fig. C21 and C22). At the same moment, horizontal geophones of OBS NEEDLE also described opposite curves. This noise appears regularly, every ~17 minutes and ~21 minutes for OBSs ARMSS and NEEDLE, respectively, suggesting that it likely corresponds to the start-up of the internal hard disk.

Another noise is visible about 2 s before the comb-like signal on the hydrophone recording of ARMSS (Fig. C21). This signal is composed by 4 pulses followed by a gradual return to the background level. It appears every 10 s and corresponds to a LED flash. The number and period of pulses contain information on the current status of the data logger and battery voltage level.

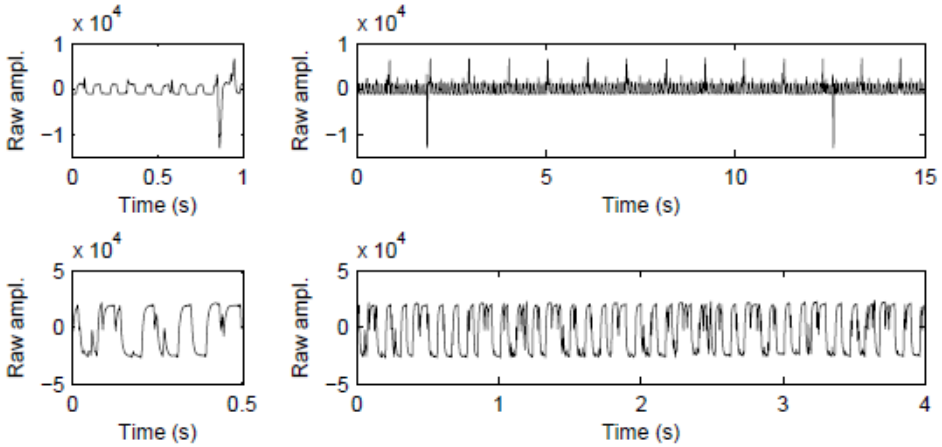

Fig. C20. Typical recordings of SPAN hydrophone. (Top) Crenel signals lasting 0.1 s with higher amplitude pulses every 1 and 11 s. (Bottom) High amplitude crenel signals.

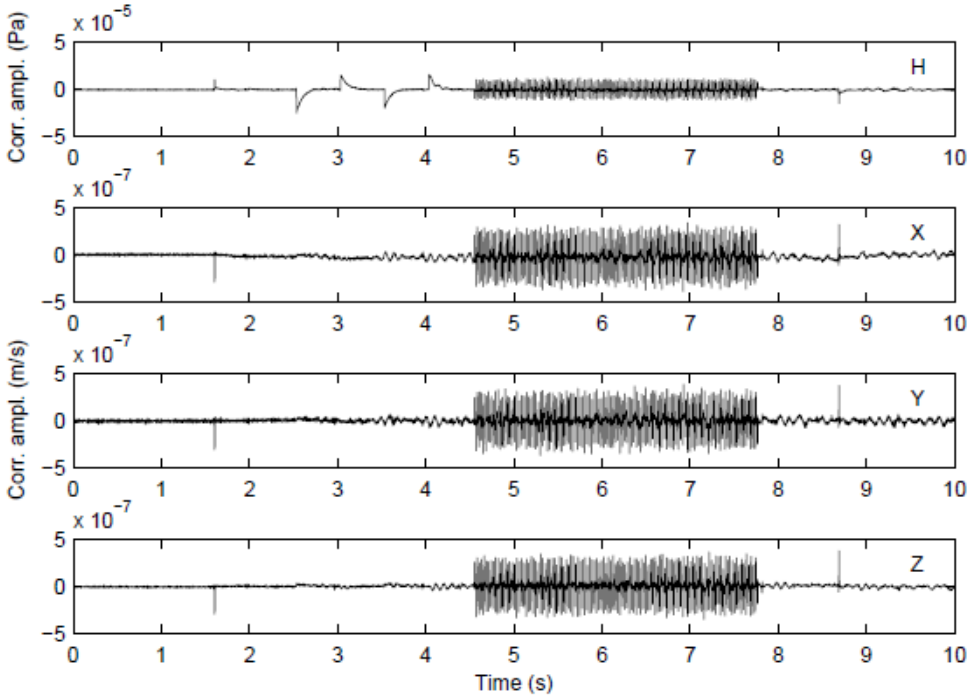

Fig. C21. ARMSS recording (H: hydrophone, X and Y: horizontal geophones, Z: vertical geophone), showing a comb-like signal between 4 and 8 s preceded by 4 pulses on the hydrophone.

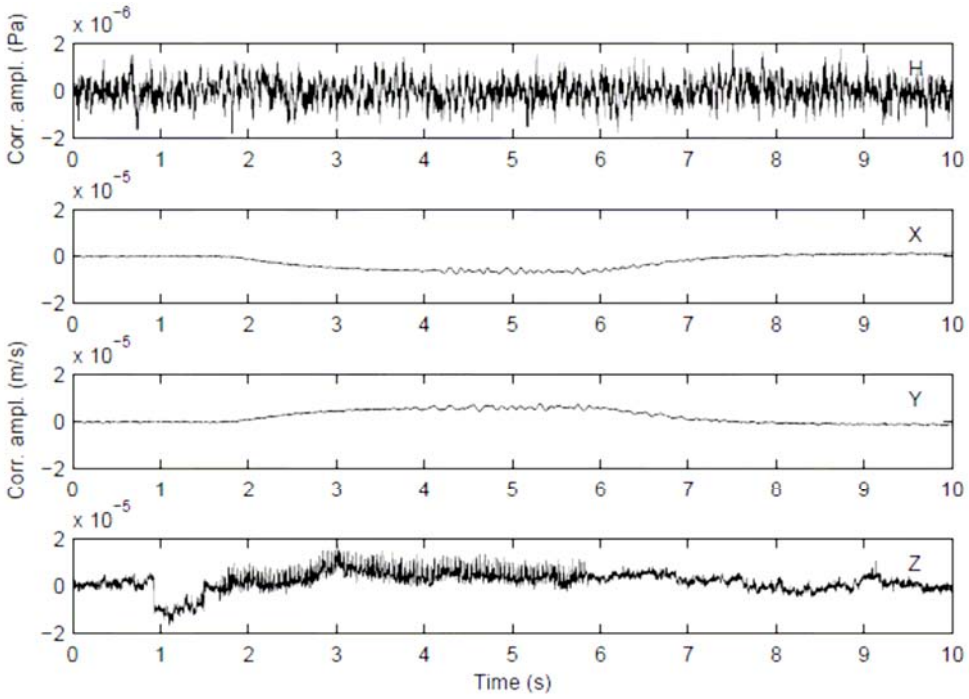

Fig. C22. NEEDLE recording (H: hydrophone, X and Y: horizontal geophones, Z: vertical geophone), showing a comb-like signal and geophones drift.

Appendix D. Piezometers: instrument and preliminary works

D.1. Piezometers: instrument's characteristics

Ifremer piezometers are used to measure the *in situ* pore pressure during short-term and long-term experiments. These instruments are constituted by a several meters long needle (5-15 m) buried in the sediments and lost after the cruise, and a recoverable part that contains data storage and batteries (Fig. D1). Generally, piezometers needle is equipped by 5 or 6 differential pore pressure and temperature sensors. Differential pore pressure sensors measure the difference between hydrostatic pressure and *in situ* pore pressure at various levels *via* porous stone filters. These sensors measure a current which depends on the deformation of a quartz fixed on a membrane. A positive excess pore pressure corresponds to a higher pressure compared to hydrostatic pressure.

Fig. D1. An Ifremer piezometer with a 3 m long needle presented in its cradle.

In the original version of Ifremer piezometers (v1, Fig. D2), the differential pore pressure sensors are located within the retrievable part on the seafloor. The sensors are connected to *in situ* porous stone and an oil-filled equipressure bladder at hydrostatic pressure in the seawater by oil-filled cables.

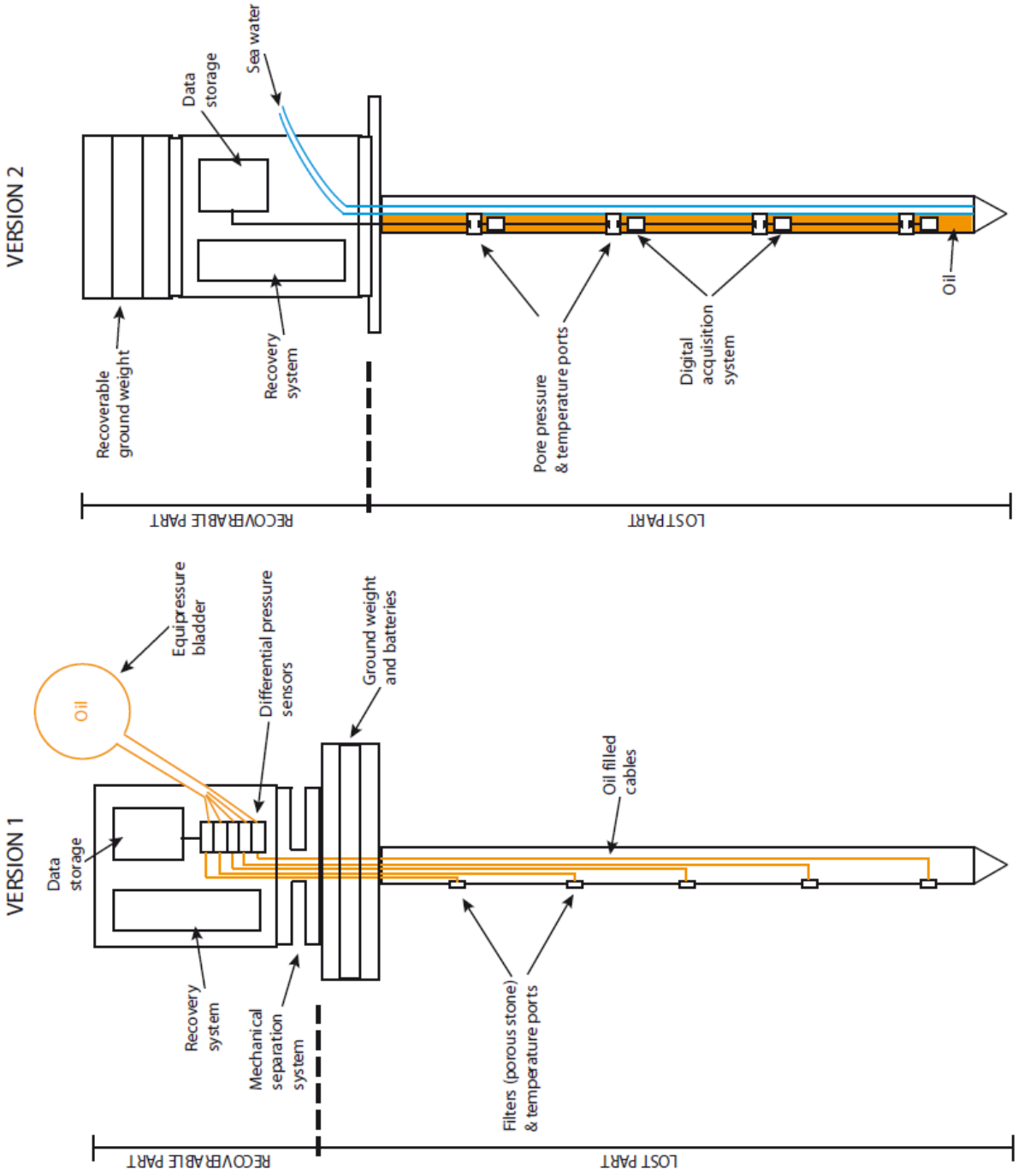

Fig. D2. Ifremer piezometers used for long-term pore pressure and temperature measurements in superficial sediments.

In the new version of Ifremer piezometers (v2, Fig. D2), the sensors are inside the soil, in contact with sediments. A cable filled with seawater connects the sensor with the reference pressure up to the seafloor.

Both versions have one sensor per monitored depth, with separated clocks and electronics.

The sampling interval is 30 s during MarNaut (2007) and ERIG 3D (2008) cruises and 1 s during the Marmesonet cruise (2009). The clock drift depends on the temperature and range from 1.1 s/day at 0°C to –0.3 s/day at 20°C. Assuming a linear variation of the clock drift with temperature, the clock drift should be about 0.1 s/day on the Sea of Marmara seafloor (14.5 °C). The pore pressure and temperature sensors are calibrated for pressure and temperature conditions ranging from 0 to 350 kPa and 0 to 50 °C. Pore pressure sensors precision alone is ± 0.2 kPa, however, because of electronics, various oil behavior depending on *in situ* conditions, homogeneity of the system (possible presence of gas inside oil-filled cables), and calibration difficulties, the real measure precision is about ± 0.5 kPa.

D.2. Data processing

D.2.1. MarNaut cruise (2007)

During this cruise, one piezometer v1 was deployed in the Tekirdag Basin close to OBS J (Fig. D3). This piezometer monitored pore pressure and temperature at 5 depths (P1: 0.5 m bsf - below sea floor -, P2: 3.5 m bsf, P3: 5.5 m bsf, P4: 7.0 m bsf, P5: 8.0 m bsf) during 3 months (08/06/2007-12/09/2007) with a sampling frequency of 1 sample/30 s.

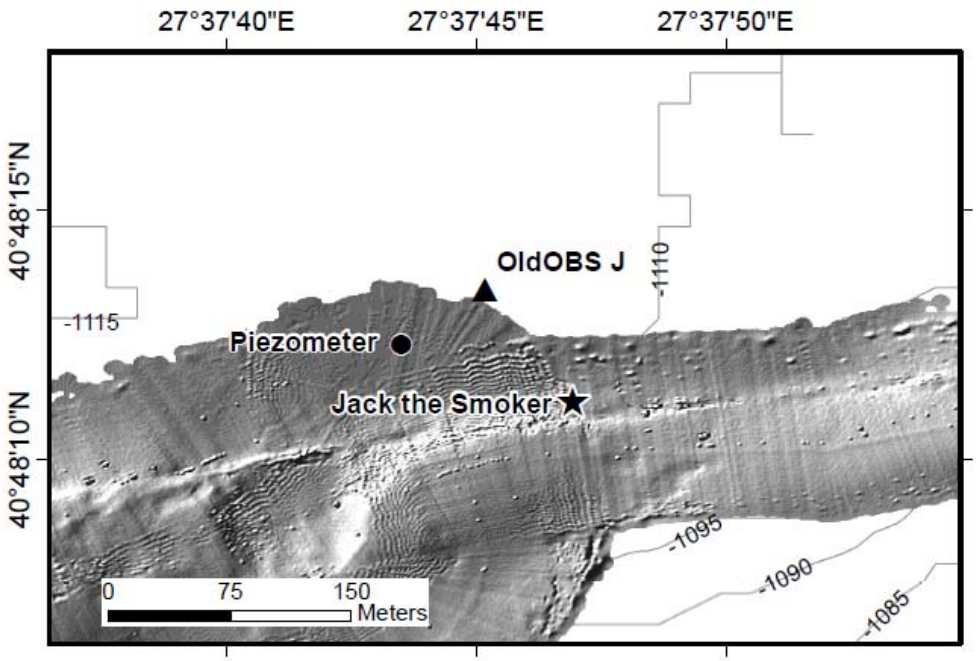

Fig. D3. Zoom in the area near OBS J (black triangle). The piezometer is indicated by the black dot (N 40.803417, E 27.62875, 1110 m). The black star shows the location of "Jack the Smoker" site where fresh water has been found escaping from the seafloor through carbonate chimneys.

Before the piezometer penetrates into the seafloor, the differential pore pressure should be ~0. Usually, there is a small offset attributable to *in situ* conditions that has to be corrected. During the instrument fall in the water column, up to three 10 minutes stops are made to control the offset in "real" conditions. In the case of the MarNaut cruise, only one stop has been made at the sea bottom, just before the penetration (Fig. D4). The offsets, ranging from –8 kPa (P3) to 30.2 kPa (P2), have all been corrected.

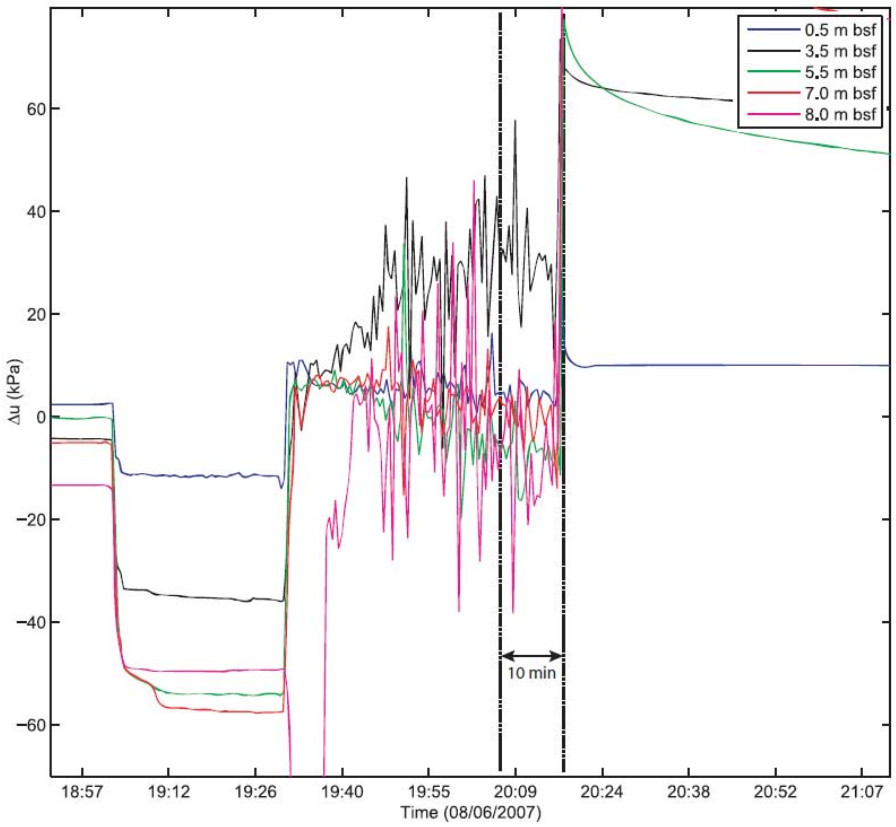

Fig. D4. Pre-penetration period of the piezometer measurements. The two dashed lines indicate the period used for offsets calculation.

Piezometers measurements corrected from offsets are presented in Fig. D5. The pore pressure equilibrium was reached in two stages by all sensors. On June 15, 2007, a second differential pore pressure drop occurred on all sensors. A slow pore pressure increase is visible on P3 (5.5 m) on June 23. Possible origins of these slow variations are discussed in section D.5.

After 20 days, the pore pressure equilibrium was finally reached by all sensors (Fig. D6). The observed differences in equilibrium pore pressure suggest overpressure in the sediment layer at 5.5 m depth.

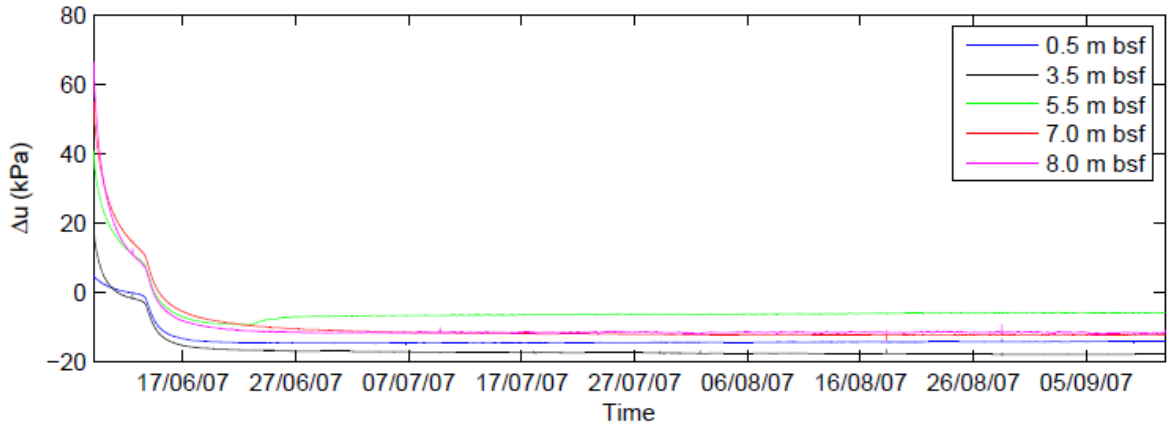

Fig. D5. Post-penetration differential pore pressure measurements. Two slow variations occur on June 15 (all sensors) and June 23 (sensor located at 5.5 bsf, green line).

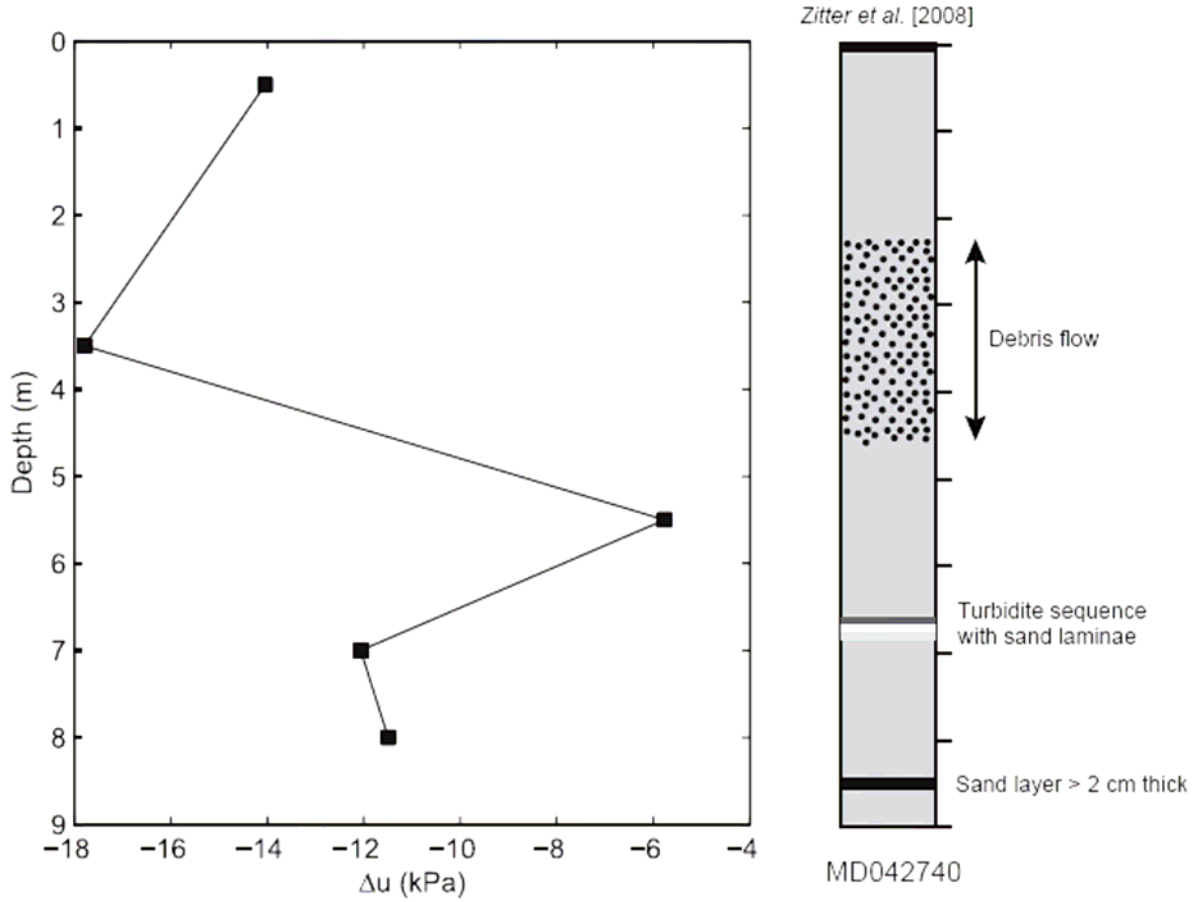

Fig. D6. Equilibrium pore pressure of the 5 sensors of the piezometer deployed in the Tekirdag Basin (Left). Interpretation log of core MD042740 (total core length: 24.47 m, see location in Fig. D7) from the MARMARA-VT cruise in 2004 [Zitter et al., 2008] located close to the piezometer (Right).

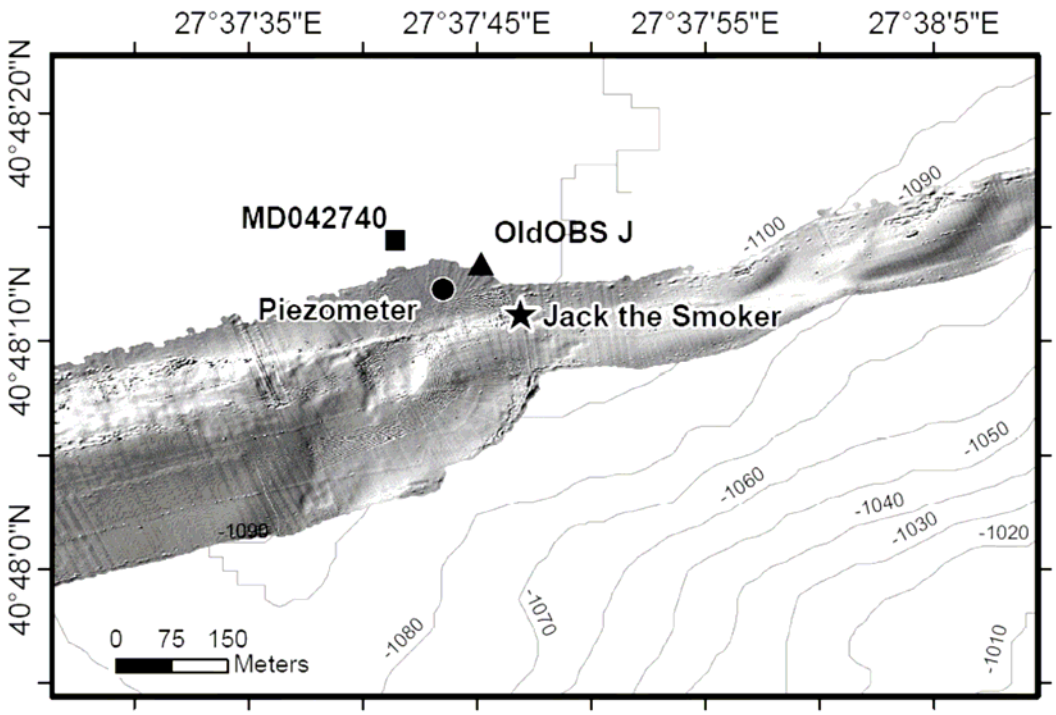

Fig. D7. Map of the piezometer (black dot) area with the location of the core MD042740 (black square). Locations of OBS J and "Jack the Smoker" site are indicated by a black triangle and a black star, respectively.

D.2.3. Marmesonet cruise (Sept. 2009-Febr. 2010)

During the Marmesonet cruise, five piezometers v2 were deployed in the Çinarcik Basin (eastern Sea of Marmara) for 5 months (Fig. D8). Their coordinates, recording period and characteristics are summarized in Table D1. All piezometers were equipped with 6 sensors, recording the differential pore pressure at a sampling frequency of 1 sample/s.

	Lat. (deg.)	Long. (deg.)	Depth (m)	Duration	Recording period
PZ-A	N 40.758417	E 28.797767	1199	153 days	27/09/2009 - 27/02/2010
PZ-B	N 40.719317	E 29.117067	1248	3 days	28/09/2009 - 01/10/2009
PZ-C	N 40.734083	E 29.120033	1265	106 days	28/09/2009 - 12/01/2010
PZ-D	N 40.728217	E 29.385950	168	147 days	29/09/2009 - 23/02/2010
PZ-E	N 40.833383	E 28.937050	1219	11 days	29/09/2009 - 10/10/2009

Sensors depth (m)
P1: 0.79 m
P2: 3.84 m
P3: 5.39 m
P4: 6.94 m
P5: 7.74 m
P6: 8.54 m

Table D1. Coordinates, recording period and sensors depth of piezometers that were deployed during the Marmesonet cruise (sampling frequency: 1 Hz).

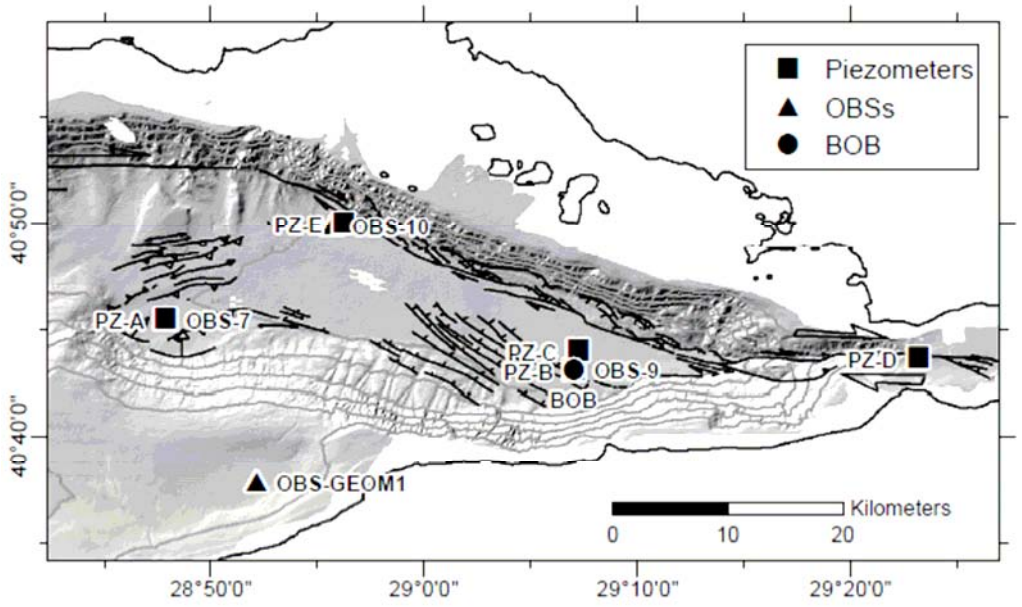

Fig. D8. Location of piezometers (black squares), OBSs (black triangles) and BOB (acoustic detector of bubbles in the water column, black dot) deployed in the Çinarcik Basin during the Marmesonet cruise.

One stop has been made during the instruments fall in the water column. The Marmesonet data were then corrected from offsets in the same way as the ones of MarNaut piezometer. The corrected data are shown in Fig. D9-D13.

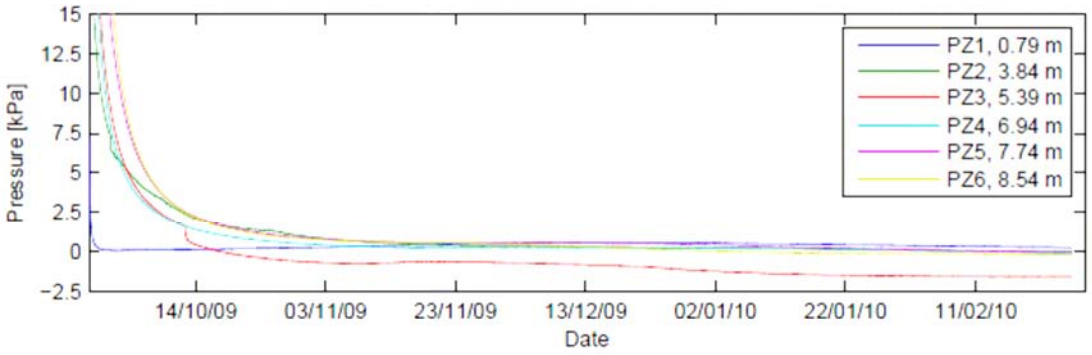

Fig. D9. Post-penetration differential pore pressure measurements of PZ-A.

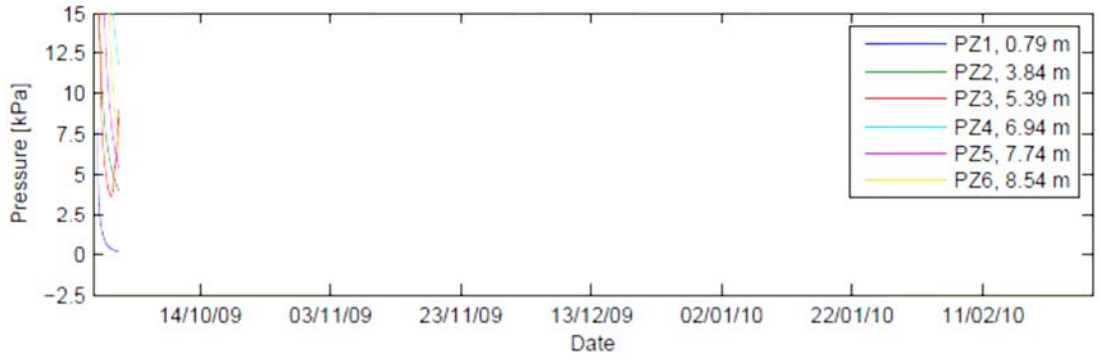

Fig. D10. Post-penetration differential pore pressure measurements of PZ-B.

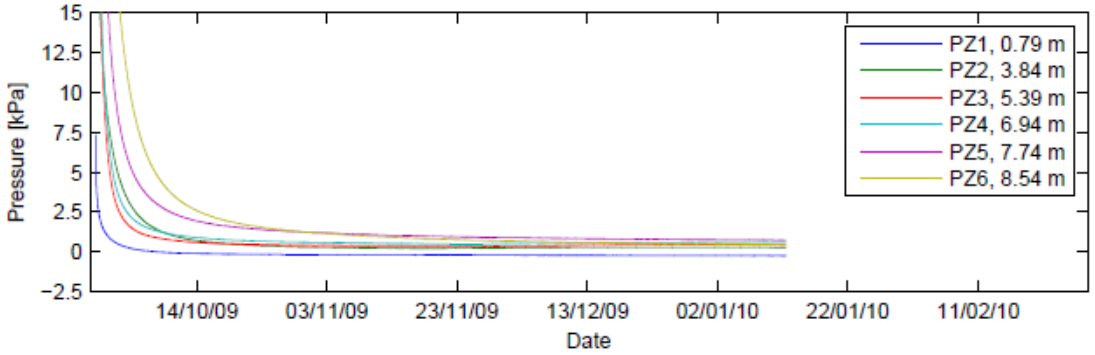

Fig. D11. Post-penetration differential pore pressure measurements of PZ-C.

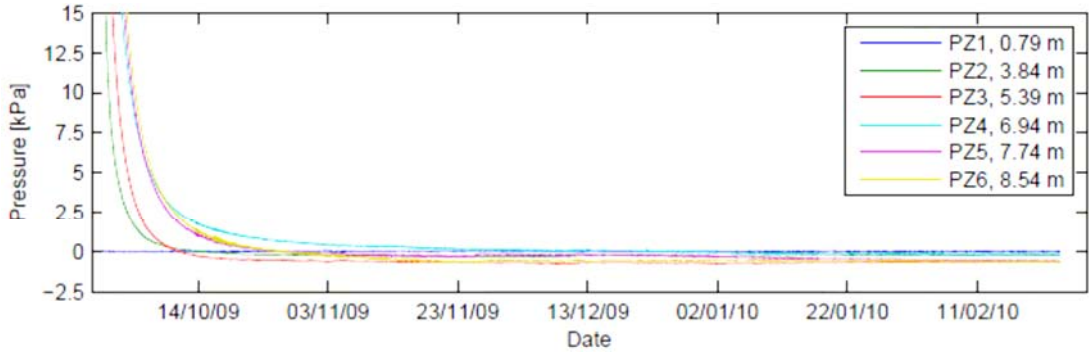

Fig. D12. Post-penetration differential pore pressure measurements of PZ-D.

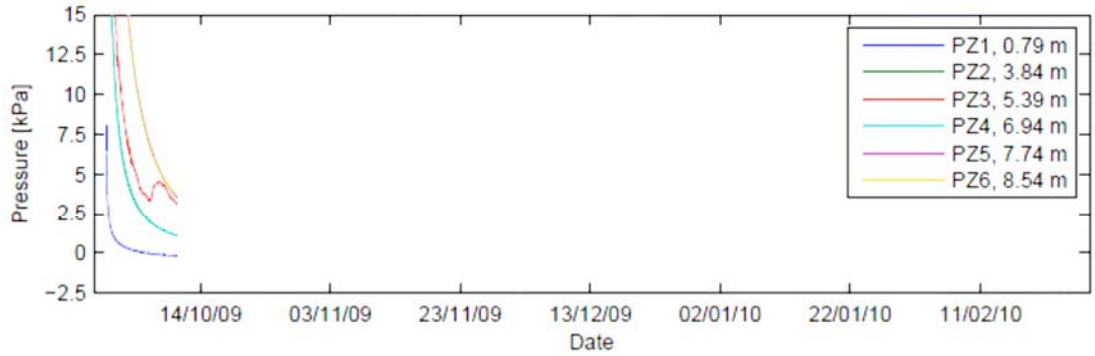

Fig. D13. Post-penetration differential pore pressure measurements of PZ-E.

D.3. Piezometer penetration

Piezometer penetration changes the soil pore-fluid conditions around the probe. The piezometer insertion involves an increase in pore pressure which dissipates over time. The pore pressure increase results from the change in normal stress (soil and fluid displacements) and shear stress (soil shearing). The excess pore pressure dissipation, *i. e.* the soil consolidation, depends on the soil permeability.

The sensor position on the piezometer (under the cone tip or along the shaft) determines the parts of normal and shear stresses. Under the cone tip, shear stresses are small compared to normal stresses and can be neglected (<20 %, [*Baligh*, 1986]). Along the piezometer shaft, shear stresses are significant due to the large amount of normal stresses already undergone by the cone tip. The excess pore pressure Δu, generated by the piezometer penetration can be written as follows

$$\Delta u = u_T - u_0 = \Delta\sigma_{oct} + \Delta\tau_{oct}, \qquad \text{(D1)}$$

where u_T the total pore pressure, u_0 the hydrostatic pressure, $\Delta\sigma_{oct}$ and $\Delta\tau_{oct}$ the excess pore pressure due to changes in the mean octahedral normal and shear stresses.

The coefficient of consolidation of a soil can be determined from the excess pore pressure dissipation measured by the piezometer after its penetration. Either empirical or analytical solutions can be used, however, in both cases, the solution depends on two interrelated parameters: the rigidity index (zone of influence of the octahedral normal stress) and the coefficient of consolidation [*Burns and Mayne*, 1998].

The empirical solution, given by Eq. D2, can be used only where the pore pressure have reached the equilibrium.

$$\Delta u_f = \frac{(\Delta\sigma_{oct})_i}{1+50T^*} + \frac{(\Delta\tau_{oct})_i}{1+5000T^*} \text{ with } T^* = \frac{c_h\, t}{a^2\, Ir^{0.75}}, \qquad \text{(D2)}$$

where Δu_f is the excess pore pressure at equilibrium, c_h the consolidation coefficient, t the time, a the piezometer's tip radius, and Ir the rigidity index. Subscripts i indicate variables at initial state.

The second term can be neglected when the excess pore pressure decrease immediately after the penetration, meaning that shear stresses are small.
In long-term experiments, equilibrium is generally reached. However, when it is not the case, like during the MarNaut cruise, the dissipation curve has to be modeled [*Burns and Mayne*, 1998].
In order to better constrain the solution, oedometer tests have been carried out to determine one of the two interrelated parameters, the vertical coefficient of consolidation.

D.4. Oedometer tests: one-dimensional compression, consolidation and permeability tests

To apply an isotropic load to a spherical sample is pretty complicated. In oedometer tests, the sample is usually confined in a steel ring and squeezed vertically [*Adam*, 2008]. During the process, only small shape changes occur and the main mode of deformation is compression.
A soil sample is inserted in a steel ring (5 x 2 cm) and placed in a larger steel cell, between 2 porous stone covered by paper-made filters (Fig. D14 and D15). Then the cell is filled by water in order to maintain the sample fully saturated during the test. Another small soil sample is weighed and placed in a drying oven to obtain its initial void index (e_0) given by,

$$e_0 = \frac{2.65 * \left(Initial\,Wet\,Weight_{sediment}\,(g) - Final\,Dry\,Weight_{sediment}\,(g) \right)}{Final\,Dry\,Weight_{sediment}\,(g)}, \quad \text{(D3)}$$

where 2.65 is the density of the solid grains of the sediment.

Finally, a set of weight is applied on the sample, twice the previous load every 24 hours (usually from 100 g = 5.52 kPa to 32 kg = 1765.1 kPa). The sediment's compressibility is given by the final deformation (i. e. height decrease) of the sample, and the sediment's coefficient of consolidation is obtained from the deformation history of the sample (Fig. D16). Between each load increase, the soil sample's permeability has been measured.

Fig. D14. Picture of a permeametric cell with its accessories (assembled on the left).

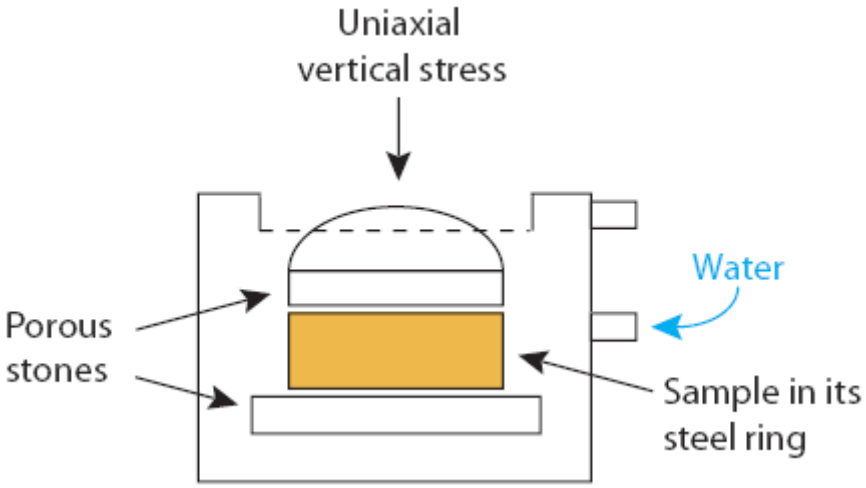

Fig. D15. Schema of the internal structure of the permeametric cell

To summarize, an oedometer test provides:

- The initial void index (e_0)
- The compressibility coefficient (λ)
- The effective pre-consolidation stress (pc')
- The swelling coefficient
- The overconsolidation ratio (OCR)
- The vertical consolidation coefficient (c_v)
- The permeability

During an oedometer test, the soil sample shows different mechanical behaviors in function of the uniaxial vertical stress (Fig. D16). The first deformation stage is non-linear elastic (linear in semi-log plots) until a threshold, the pre-consolidation stress (pc'), from then on the deformation becomes plastic. The pre-consolidation stress corresponds to the highest stress experienced by the soil sample in its history. The overconsolidation ratio is defined as the pre-consolidation stress divided by in situ stress condition. An overconsolidation ratio superiors to one means that the soil undergone in its history a higher stress than the current in situ stress, and inversely for an overconsolidation ratio inferiors to one.

As shown by the soil sample discharge in Fig. D16, only the elastic part of the deformation can be recovered. The coefficient of compressibility is defined during the plastic deformation of the sample. It indicates which amount of deformation you will get from a given stress.

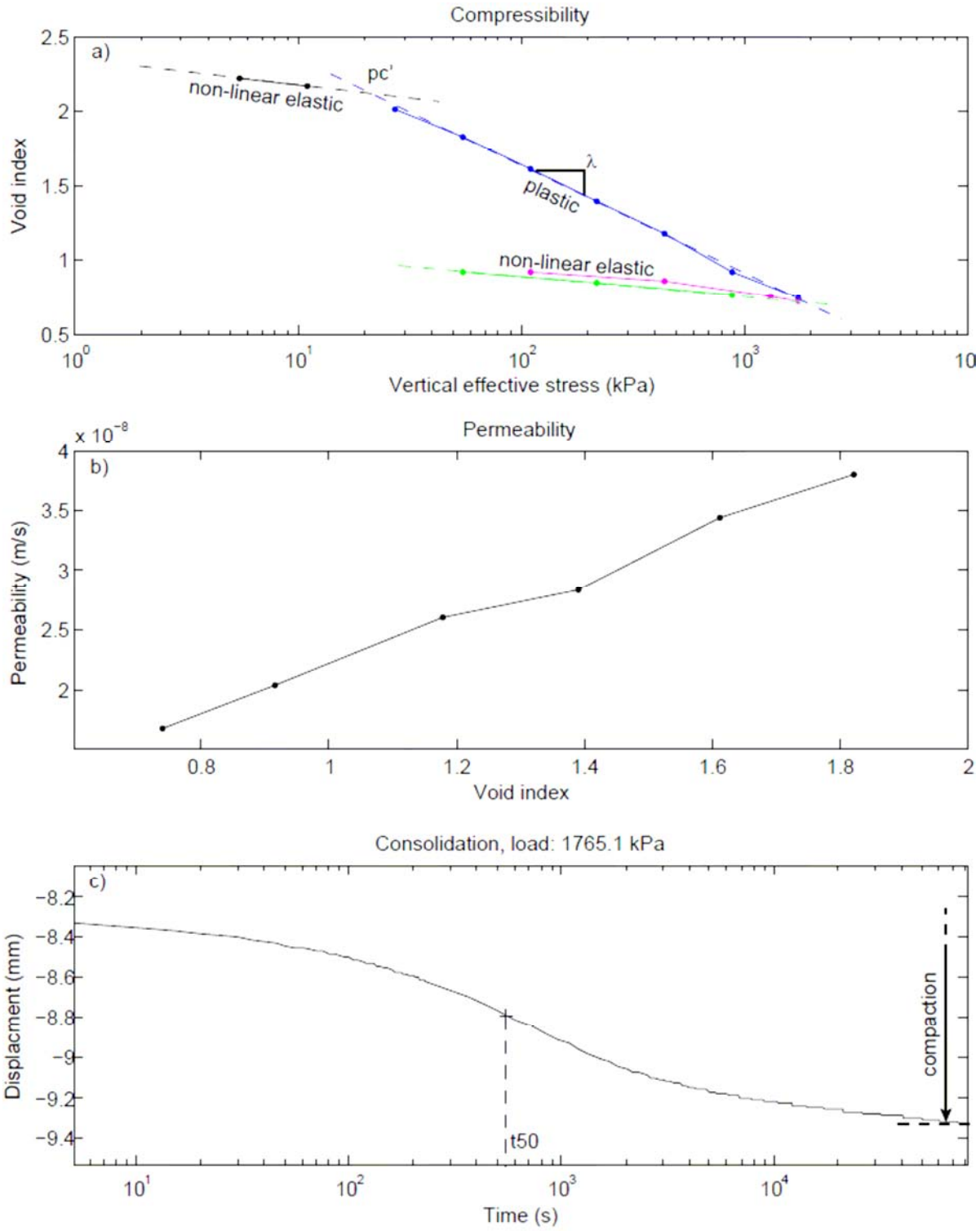

Fig. D16. Oedometer test: compressibility, permeability and consolidation of a sample taken from MET09K02 core at a depth of 380-385 cm. a) Volumetric strain (given as void index e*) in function of the log of vertical effective stress (kPa). Sample loading is indicated by the black (non-linear elastic) and blue (plastic) lines. Sample discharge and re-loading are shown by the pink and green lines, respectively. The pre-consolidation stress (pc') and coefficient of compressibility (λ) are also indicated. b) Permeability measurements (in m/s) in function of the void index (*e*). c) Consolidation curve for a load of 1765.1 kPa, showing the vertical strain (given as vertical displacement in mm) in function of the log of the time. The half-compaction time t50 is indicated.*

Soil consolidation is a time-dependent behavior resulting from the expulsion of fluids in response to a load increase. The coefficient of consolidation (in m²/s) for a soil compacted during ~24 hours is given by

$$c_v = \frac{Tv * h^2}{t_{50}} \text{ with } h = \frac{h_0 - \Delta h}{2}, \quad \text{(D4)}$$

where *Tv* is a time factor equal to 0.197, t_{50} the half-compaction time in seconds (Fig. D16), h the compacted height of the sample in mm, h_0 its original height (20 mm here) and Δh its compaction in mm.

Five oedometer tests were carried out on two cores collected in the Sea of Marmara during the Marmesonet cruise: MET09GR010 and MET09K02 (Table D2).

Core name	Corer type	Cruise	Lat. (deg.)	Long. (deg.)	Depth (m)	Length (m)	Site-comments
MNTKS06	Kullenberg	MarNaut	40.7338	29.1249	1274	9.25	PZ-C site
MNTKS30	Kullenberg	MarNaut	40.8036	27.6298	1118	9.8	Jack the Smoker site
MET09GR010	Gravity	Marmesonet	40.8037	27.6291	1122	3.1	Jack the Smoker site
MET09K02	Kullenberg	Marmesonet	40.7348	29.1198	1271	6.6	PZ-C site

Table D2. Cores coordinates and main characteristics.

MET09GR010 and MNTKS30 (MarNaut core) cores are located in the Tekirdag Basin, close to the position of MarNaut piezometer. MET09K02 and MNTKS06 (MarNaut core) cores are located in the Çinarcik Basin, close to the position of the Marmesonet piezometer PZ-C. The main results of oedometer tests are given hereafter (Fig. D17-21). The full report of these tests are summarized in a specific report available on request to the authors (Tary, J. B., “Tests oedomètriques sur les carottes MET09GR010 et MET09K02 de Marmesonet”, Rapport Interne Ifremer, February, 2010).

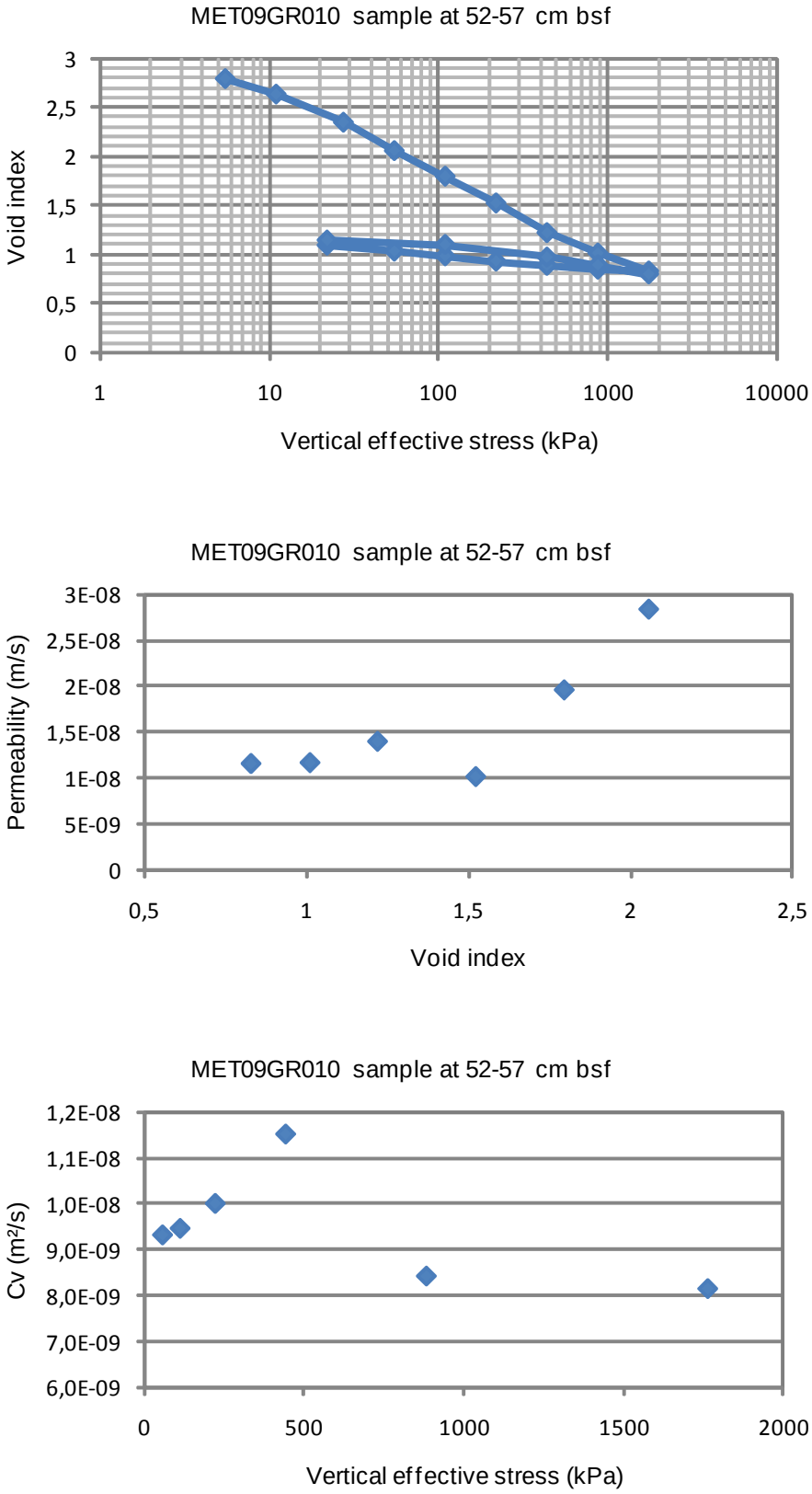

Fig. D17. (Top) Volumetric strain (given as void index), (Center) permeability (in m/s) and (Bottom) vertical coefficient of consolidation (in m²/s) of a sample taken from MET09GR010 core at a depth of 52-57 cm.

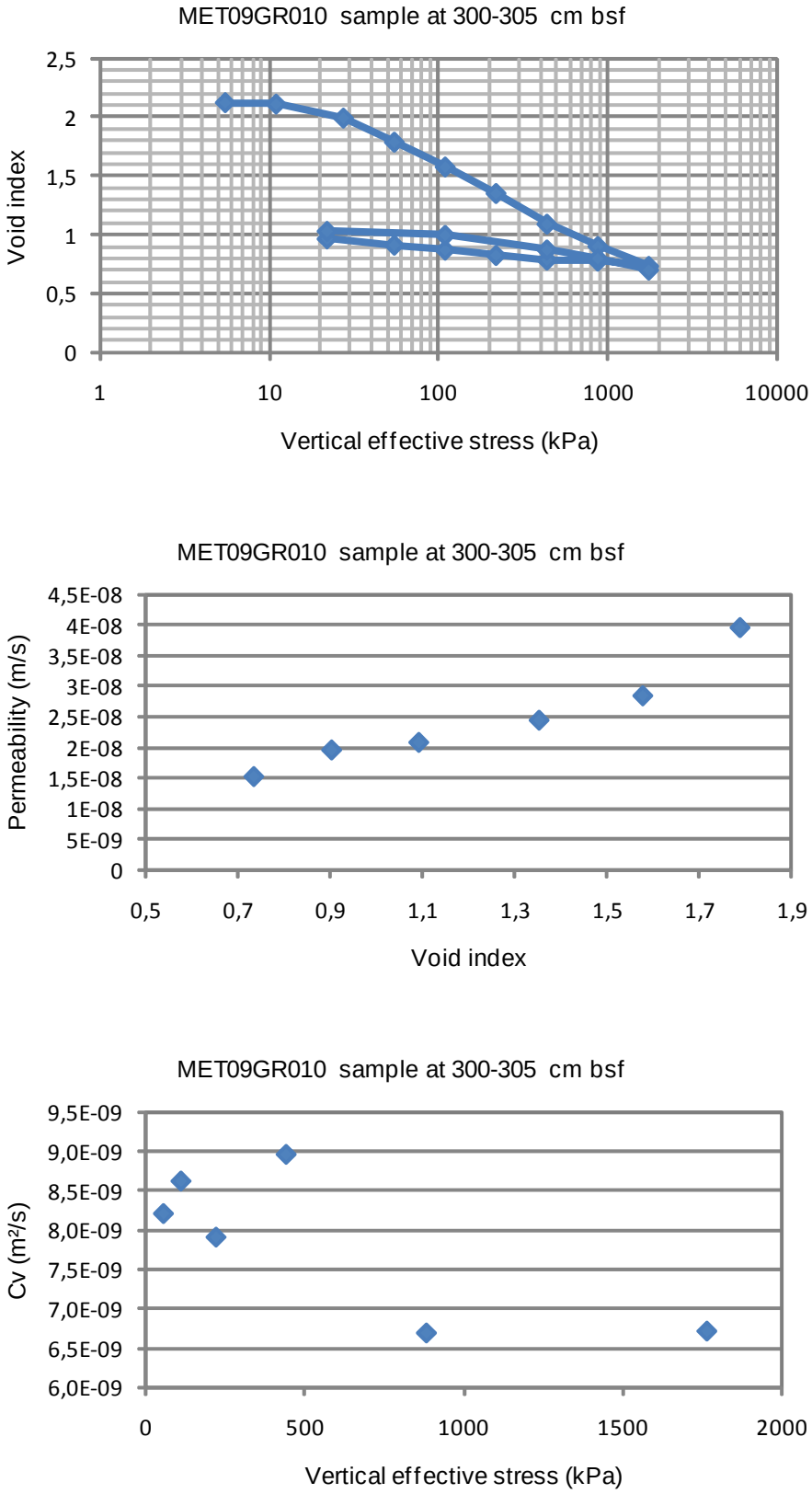

Fig. D18. (Top) Volumetric strain (given as void index), (Center) permeability (in m/s) and (Bottom) vertical coefficient of consolidation (in m²/s) of a sample taken from MET09GR010 core at a depth of 300-305 cm.

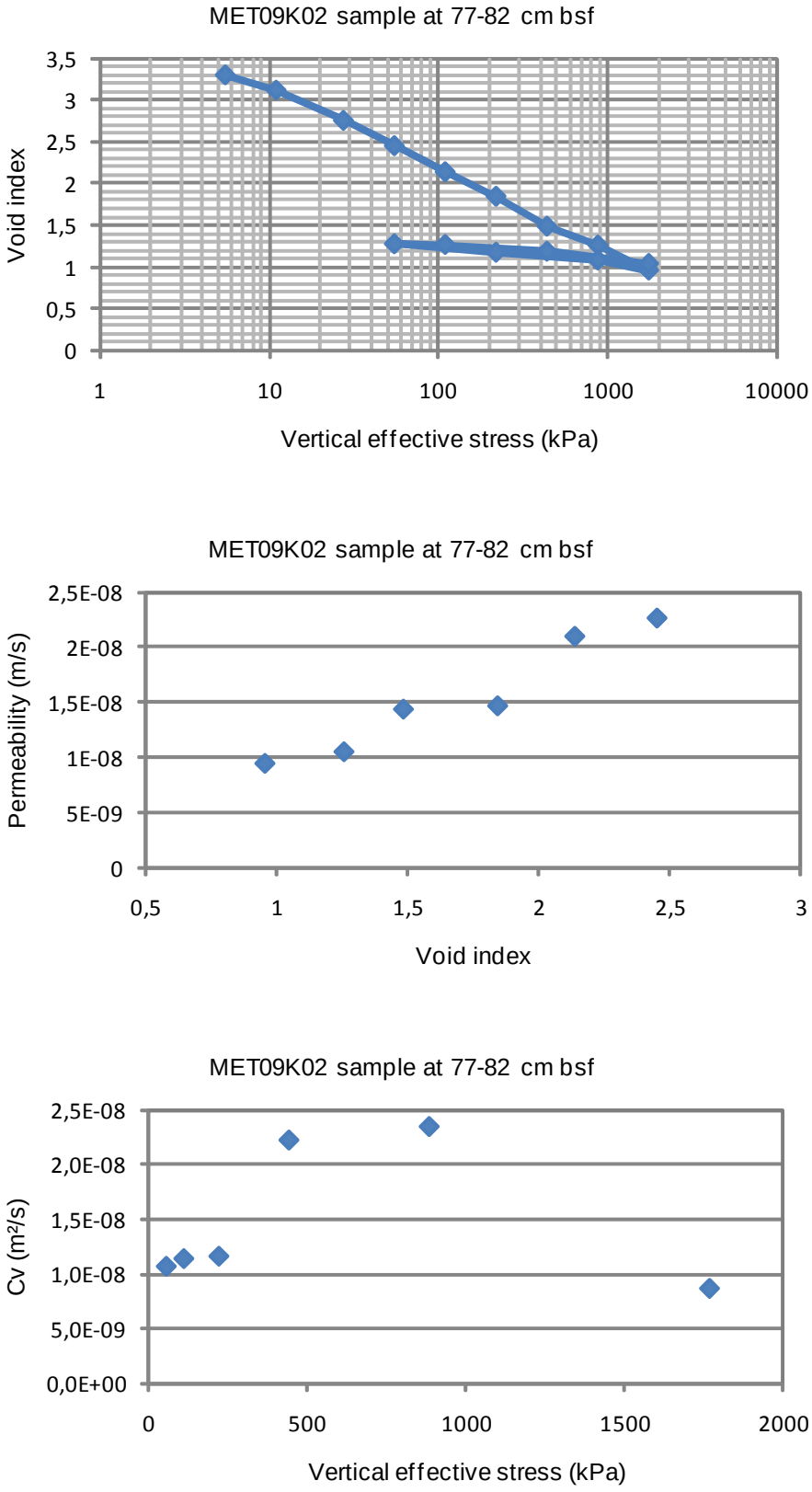

Fig. D19. (Top) Volumetric strain (given as void index), (Center) permeability (in m/s) and (Bottom) vertical coefficient of consolidation (in m²/s) of a sample taken from MET09K02 core at a depth of 77-82 cm.

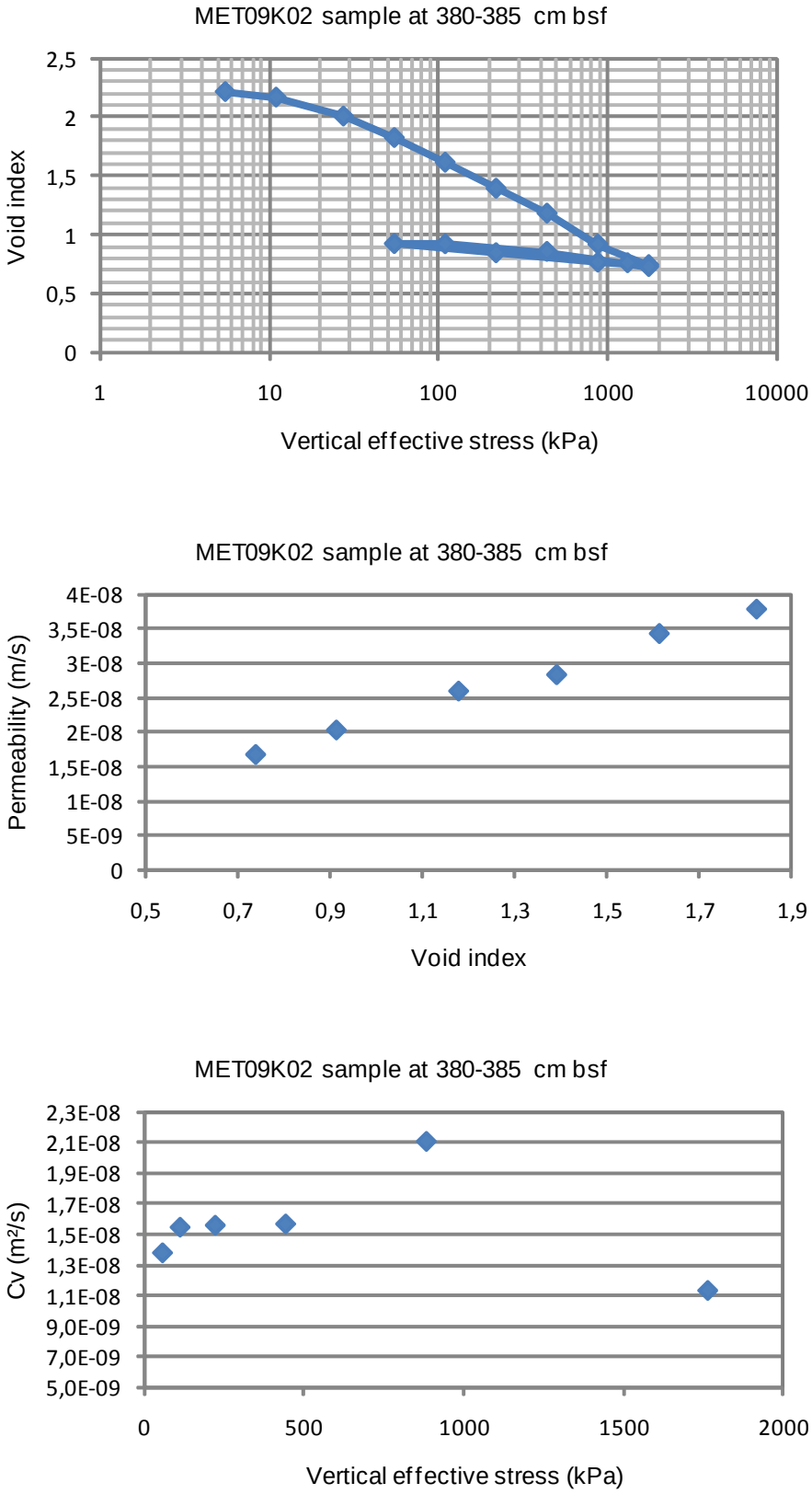

Fig. D20. (Top) Volumetric strain (given as void index), (Center) permeability (in m/s) and (Bottom) vertical coefficient of consolidation (in m²/s) of a sample taken from MET09K02 core at a depth of 380-385 cm.

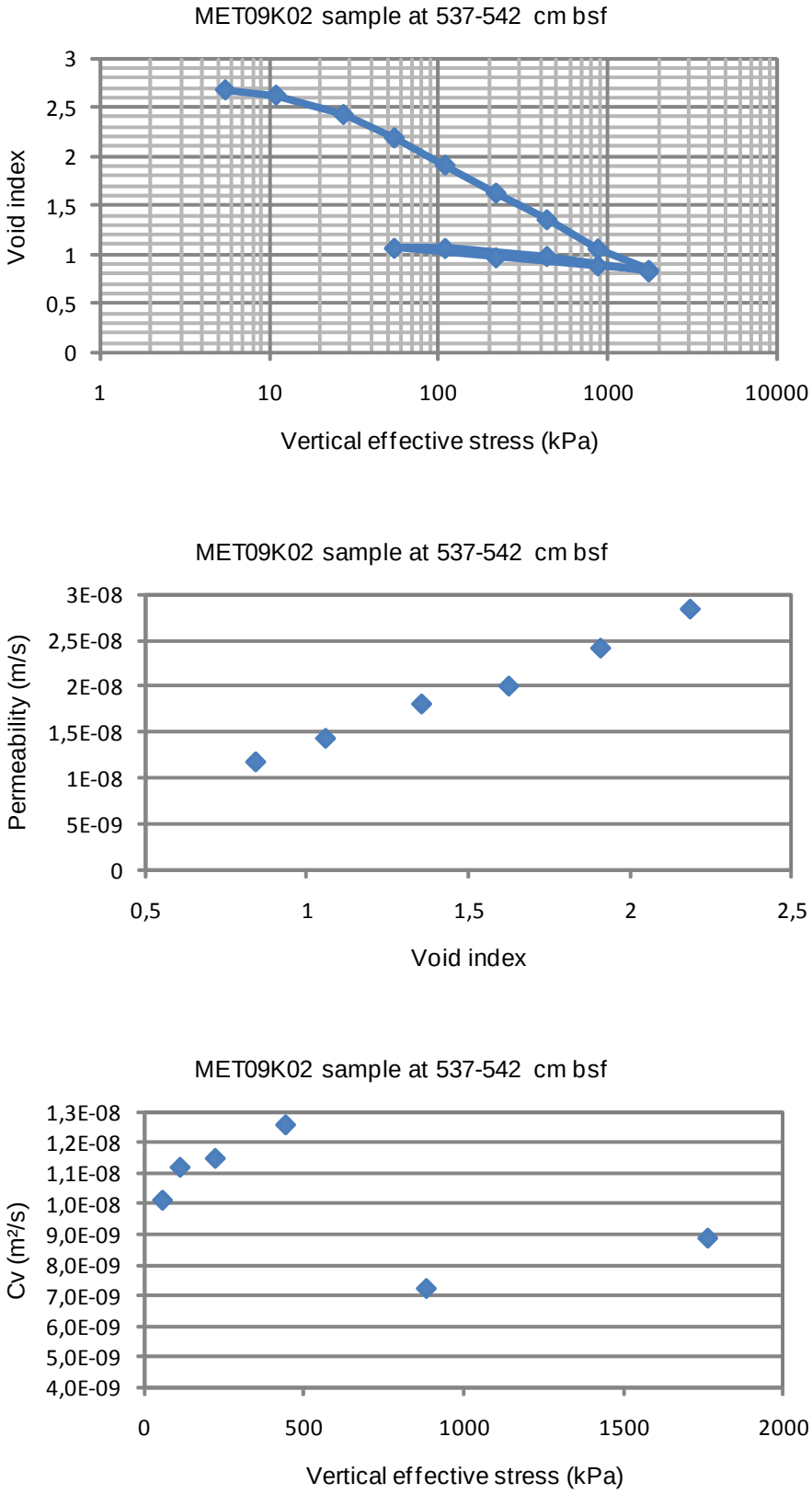

Fig. D21. (Top) Volumetric strain (given as void index), (Center) permeability (in m/s) and (Bottom) vertical coefficient of consolidation (in m²/s) of a sample taken from MET09K02 core at a depth of 537-542 cm.

D.5. Preliminary works

Anomalous pressure transients recorded by piezometers can be divided in two categories. Pore pressure variations can be slow in drained conditions (e. g. Fig. D5 or D9) or sudden (undrained conditions). While slow variations typically last days, sudden variations last between seconds to hours.

D.5.1. Slow pore pressure variations

Slow variations are observed on recordings whatever the version of the piezometer. Remarkably, their amplitudes can be quite large (up to 20 kPa during the MarNaut cruise) but their origins and the influence of the ground weight (piezometer v1) are still unclear.

-The MarNaut cruise (2007)

In the case of the MarNaut cruise, two slow variations are visible on the piezometer recording, one on 15 June (pore pressure drop) and the other on 23 June (pore pressure increase). No correlations between the seismic activity and the slow pore pressures variations were found. Instead, the first slow pore pressure drop could be due to a small probe readjustment in the sediments, slowly enough to prevent any positive pore pressure transient to be recorded, or an episode of sediments degassing. Conversely, the following pore pressure increase could correspond to gas incoming into the sedimentary layer. A sediment settling can be discarded as no sensors apart from the fifth show any pore pressure variations at the same time.

-The Marmesonet cruise (2009-2010)

Slow pore pressure increases or decreases were recorded by 3 piezometers, PZA, PZB and PZE (Fig. D22). Possible relations with the intense seismic activity of the area have not been investigated yet.

D.5.2. Sudden pore pressure variations

-Spikes

Some “spikes” (Fig. D23) were recorded during the MarNaut and Maradja2 cruises. They are characterized by a sharp pore pressure increase followed by a progressive, diffusion-like, decrease in pore pressure. Their characteristics (amplitudes, durations, number of sensors), summarized in Table D3, are highly variable.

SPIKES MARNAUT			
Date	Dur. (min)	Ampl. max (kPa)	Visible on sensor(s)
10/06/07 08:14:43	11,5	1,1	P2, P4, **P5**
12/06/07 13:10:13	9,5	1,9	P1, P2, P3, P4, **P5**
21/06/07 08:32:13	9	0,5	P4, **P5**
09/07/07 18:28:43	55	1,3	P2, P3, P4, **P5**
01/08/07 18:59:03	0,5	0,8	**P2**
18/08/07 07:40:32	5	1,7	P2, P3, **P4**, P5
28/08/07 12:50:43	245	2,4	P1, P2, P3, P4, **P5**

SPIKES MARADJA2			
Date	Dur. (min)	Ampl. max (kPa)	Visible on sensor(s)
23/11/2005 15:48:29	2	0,5	**PZD-2**

Table D3. Inventory of the spikes identified during the MarNaut and Maradja2 cruises. For each spike is given its duration, amplitude maximum, and on which sensor(s) the signal is visible. Values of duration and amplitude correspond to the signal of the sensor whose name is in bold.

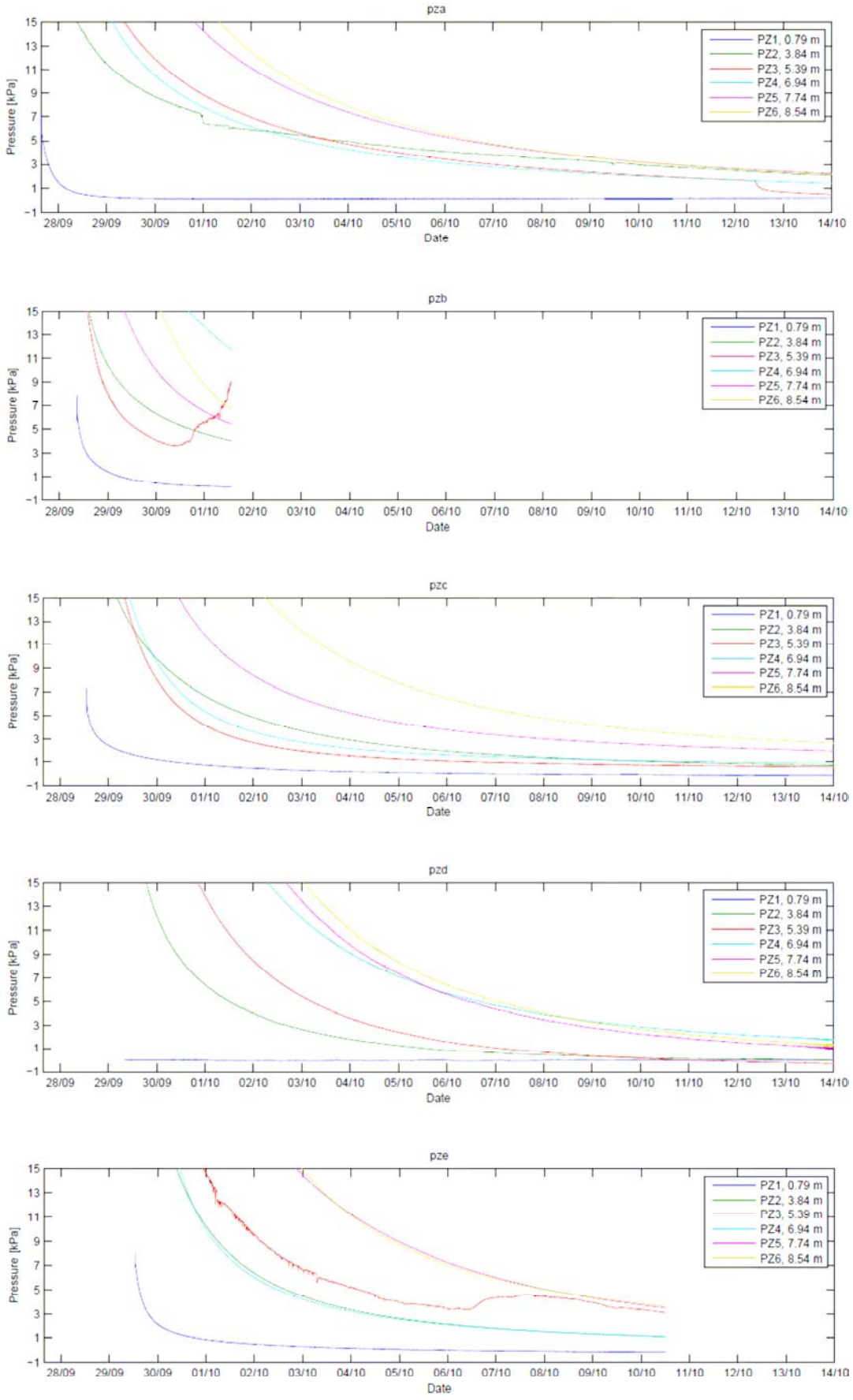

Fig. D22. Post-penetration differential pore pressure measurements of the five piezometers deployed during the Marmesonet cruise during the period 28/10/2009 – 14/10/2009.

EARTHQUAKES								
Date	Tp (OBS J)	Ts (OBS J)	Lon. (deg)	Lat. (deg)	Ampl. (µm/s)	Dur. (s)	M	Provider
10/06/07	08:15:48	08:16:22	26,38	38,87	3,6	66	3,8	EMSC
12/06/07	13:10:11	13:10:43	26,33	38,87	2,5	72	3,6	EMSC
No earthquakes								
09/07/07	18:27:03	18:27:11	27,765	40,4	36,4	13	3,3	KOERI
01/08/07	18:57:25	18:57:32	27,629	40,4126	13,3	19	3,1	Our study
18/08/07	07:37:44	07:37:41	27,6076	40,3858	60,7	12	3,4	Our study
28/08/07	12:45:17	12:45:38	25,94	40,38	36,4	45	4,6	EMSC

EARTHQUAKES								
Date	Tp (OBS 5)	Ts (OBS 5)	Lon. (deg)	Lat. (deg)	Ampl. (µm/s)	Dur. (s)	M	Provider
23/11/05	15:46:44	15:46:45	3,8445	36,9904	Saturated	22	3,4	Our study

Table D4. Characteristics of earthquakes that could be related to the spikes. For each earthquake is given, the amplitude, the duration and the arrival times of P and S waves on the OBS located nearby the piezometer, as well as its magnitude and location. Providers of the earthquakes location are indicated.

Apart from one of them (21/06/2007 08:32:13), the spikes are generally correlated with an earthquake recorded by a nearby OBS (Table D4). However, some earthquakes with similar characteristics (amplitudes, distance, frequency content and duration) did not generate spikes on piezometer measurements. Hence, spikes origin remains unclear. Is it a signal due to the response of pore fluid to earthquakes, a small readjustment of the probe (due to earthquakes or not), or produced at the interface between the probe and the sediments?

-Earthquakes

Earthquakes involve variations in static stress near the fault (near-field), and in dynamic stress due to seismic waves propagation (intermediate- and far-field). Depending on the level of stress increase, the porous media will deform either elastically or plastically. In the latter case, permanent deformation will occur leading to pore pressure diffusion and fluids flow. Interestingly, two piezometers (PZA and PZD) deployed during the Marmesonet cruise recorded a mb 5.2 earthquake 300 km away (Fig. D24). At the same location of PZA, the ground velocity was also recorded by an OBS. No permanent deformation or pore pressure build-up occurred at any depth, showing a purely elastic response of the system piezometers-sediments. Due to higher permeability of the first meter of sediments, the first sensor at 0.79 m below sea floor did not record the earthquake.

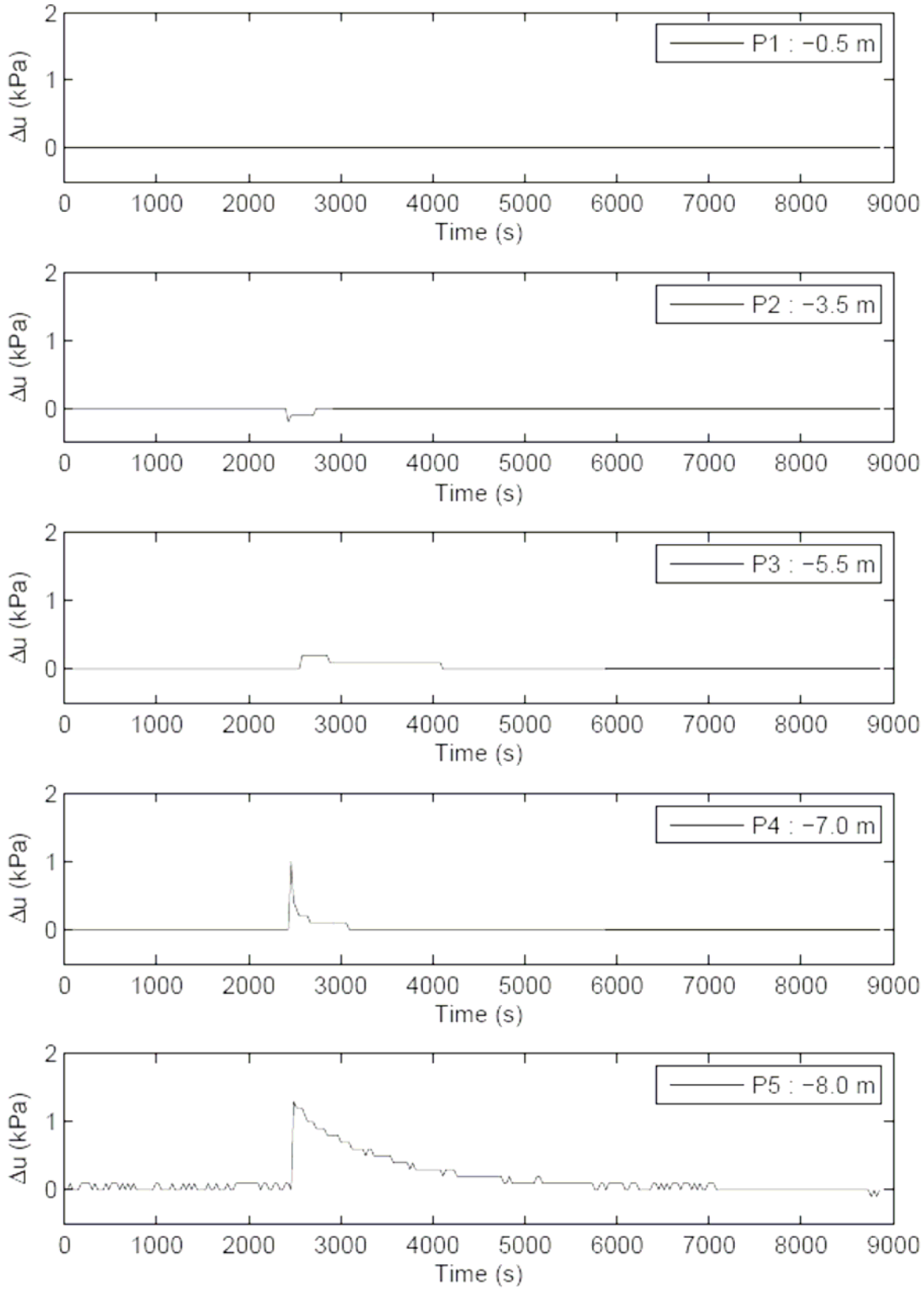

Fig. D23. Differential pore pressure measurements of the piezometer deployed during the MarNaut cruise showing a spike recorded on July 09, 2007, 18:28:43.

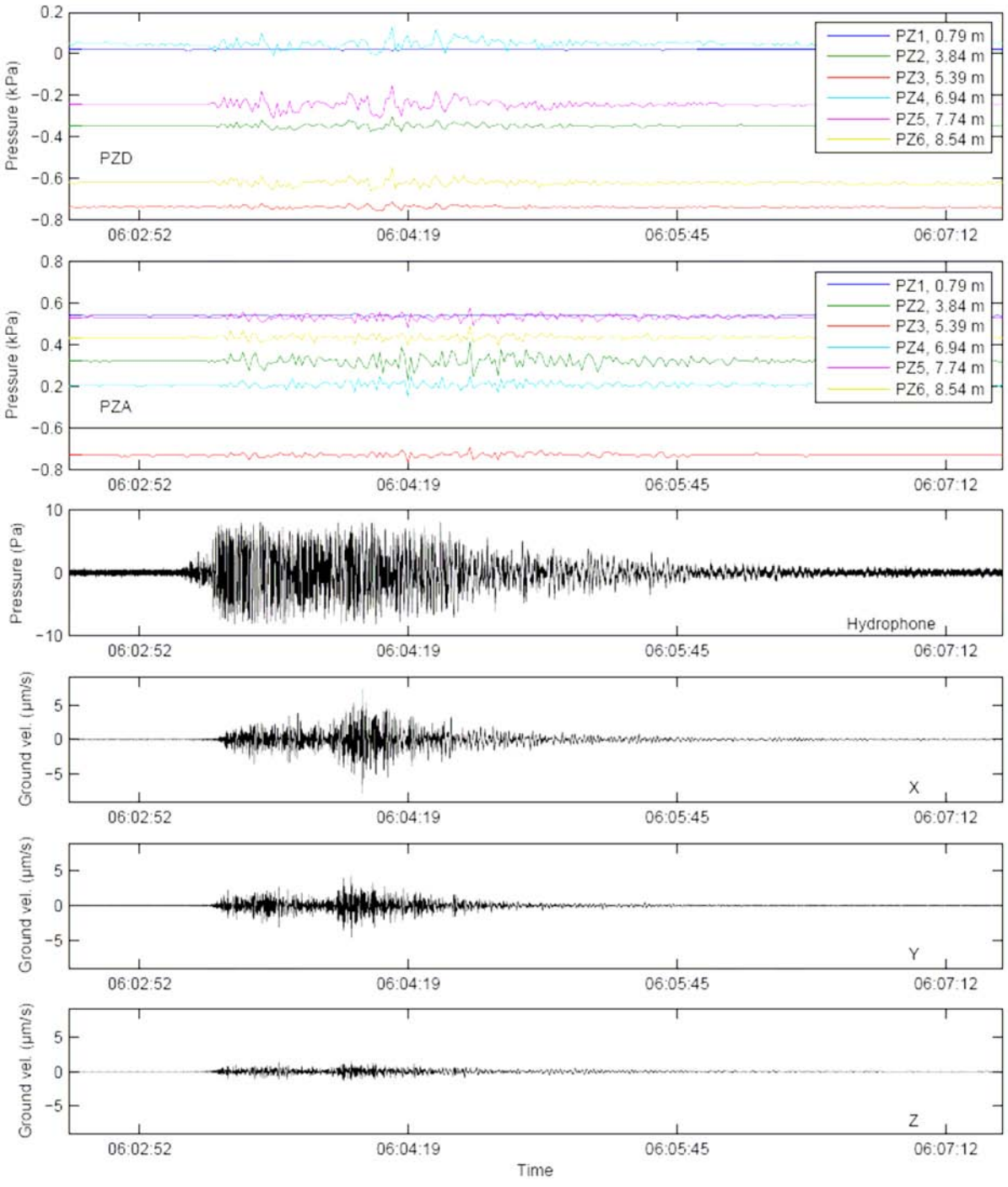

Fig. D24. Differential pore pressure recorded by PZA and PZD piezometers (1 sample/sec.) together with hydrophone and three-component seismogram (X, Y, Z) recorded by OBS 7 (see Fig. D11 for location) at the same location as PZA of a mb 5.2 earthquake (04/12/2009 06:02:21.6, N 37.91, E 28.83). Sensors depth of the two piezometers are indicated in the boxes on the right.

Résumé

Le présent travail de thèse aborde la question du couplage entre fluides et déformation en milieu sous-marin, un sujet d'importance dans le domaine des risques, naturels (séismes, glissements de terrain) ou industriels (stabilité des plateformes de forage en mer, par exemple). Trois études de cas sont présentées : les deux premières concernent la Mer de Marmara, en Turquie, une zone fortement exposée au risque sismique, du fait de la proximité de la Faille Nord-Anatolienne ; la troisième concerne une zone pétrolifère offshore, sur la pente continentale du delta profond du Niger.

La **première étude de cas** en Mer de Marmara porte sur l'activité micro-sismique qui caractérise l'escarpement ouest du Bassin de Tekirdag. Notre étude montre que la déformation contribue à maintenir des perméabilités élevées associées au réseau de failles sous l'escarpement, ce qui permet aux fluides de remonter, des réservoirs gaziers du Bassin de Thrace jusqu'à la surface.

La **deuxième étude de cas** porte sur des micro-évènements enregistrés par les sismographes de fond de mer (OBS : Ocean Bottom Seismometers), non sismiques, de courtes durées (200 à 600 msec), et caractérisés par des fréquences comprises entre 10 et 30 Hz. Notre étude montre que ces micro-évènements sont liés à des expulsions de gaz. Les OBS fournissent donc des informations inattendues pour l'étude des processus de dégazage naturel en fond de mer.

La **troisième étude de cas,** sur la pente continentale du Niger, démontre que la combinaison de piézomètres et d'OBS voisins en fond de mer permet de suivre l'évolution des phases d'accumulation et de vidange de gaz dans les sédiments superficiels. La détection et la surveillance des phénomènes de dégazage naturel en fond de mer est d'une importance qui pourrait s'avérer critique dans les zones d'exploitation pétrolière en domaine offshore.

D'une manière générale, ce travail plaide pour la nécessité : i) de disposer de plusieurs réseaux d'observatoires sous-marins câblés en Mer de Marmara et d'un modèle de vitesse-3D rendant compte du fort gradient de vitesses sismiques dans les couches superficielles (la structure de vitesses du domaine sous-marin étant radicalement différente de celle du domaine émergé, la combinaison des données sismologiques à terre et en mer s'avère très difficile); ii) de développer des approches de surveillance multi-paramètres. Pour chaque paramètre, il est nécessaire de connaître la variabilité naturelle "normale", de manière à détecter les variations anormales. La recherche sur les processus physiques et le développement algorithmique doivent être conduits de front.

Mots clés : sismicité, fluides, risques naturels, sismographes de fond de mer, piézomètre, Mer de Marmara, Delta du Niger, failles.